

DYNAMICS OF THE SHELL MODEL

C. MAHAUX

Institute of Physics B5, University of Liège, Sart Tilman, B-4000 Liège 1, Belgium

P.F. BORTIGNON

Istituto di Fisica Galileo Galilei, I-35100 Padova, Italy

R.A. BROGLIA

Niels Bohr Institutet, University of Copenhagen, DK-2100 Copenhagen Ø, Denmark

and

C.H. DASSO

NORDITA, Blegdamsvej 17, DK-2100 Copenhagen Ø, Denmark

Received March 1984

Contents

1. Introduction	3	3. Single-particle motion in uniform systems	35
2. Empirical information on the shell model	4	3.1. Introduction	35
2.0. Preview	4	3.2. Definitions	36
2.1. Selected evidence for the validity of single-particle motion in nuclei	6	3.3. The independent particle model	43
2.2. The independent particle model	8	3.4. Quasiparticle approximation	45
2.3. Weakly bound single-particle states	9	3.5. Single-particle wave equation	50
2.4. Scattering single-particle states	11	3.6. Effective mass	56
2.5. Deeply bound single-particle states	13	3.7. Hartree-Fock approximation	58
2.6. Effective mass	15	3.8. Attractive part of the second-order contribution	64
2.7. Density of single-particle energies	17	3.9. Repulsive part of the second-order contribution	82
2.8. Group velocity	22	3.10. Full second-order contribution	91
2.9. Spectroscopic factors	22	3.11. Momentum distribution	106
2.10. Single-particle spreading width	24	3.12. Quasiparticle strength	109
2.11. A simple model for the spreading of a single-particle configuration	28	3.13. Screening corrections	112
2.12. Hindsight	34	3.14. Hard-sphere dilute Fermi gas	115
		3.15. Hole line expansion	120
		3.16. Role of the high-energy virtual excitations	128

Single orders for this issue

PHYSICS REPORTS (Review Section of Physics Letters) 120, Nos. 1-4 (1985) 1-274.

Copies of this issue may be obtained at the price given below. All orders should be sent directly to the Publisher. Orders must be accompanied by check.

Single issue price Dfl. 178.00, postage included.

DYNAMICS OF THE SHELL MODEL

C. MAHAUX

*Institute of Physics B5, University of Liège, Sart Tilman,
B-4000 Liège 1, Belgium*

P.F. BORTIGNON

Istituto di Fisica Galileo Galilei, 1-35100 Padova, Italy

R.A. BROGLIA

*Niels Bohr Institutet, University of Copenhagen, DK-2100,
Copenhagen, Ø, Denmark*

and

C.H. DASSO

NORDITA, Blegdamsvej 17, DK-2100 Copenhagen Ø, Denmark



NORTH-HOLLAND - AMSTERDAM

3.17. Statistical and dynamical quasiparticle energies	130	4.6. Microscopic calculations of the quasiparticle energies of the valence shells in ^{208}Pb	215
3.18. The method of correlated basis functions	137	4.7. Distribution of the single-particle strength and sub-shell occupation probabilities	229
3.19. Normal liquid ^3He	142	4.8. Level dependence of the dispersion corrections	249
3.20. The electron gas	158	4.9. Level-averages of the dispersion corrections	252
3.21. Hindsight	178	4.10. Dispersion corrections in spatial coordinate representation	260
4. Single-particle motion in nuclei	179	4.11. Implications, applications and questions	263
4.1. Introduction	179	5. Postface	266
4.2. The mass operator in finite systems	180	References	267
4.3. The average nucleon–nucleus potential	189	Note added in proof	274
4.4. Dispersion relation approach	196		
4.5. Core excitations in ^{208}Pb	212		

Abstract:

Many Fermi liquids are amenable to a shell-model description, where the particles move in an average potential. The coupling of the single-particle degrees of freedom to other modes of excitation strongly affects the properties of the shell-model potential. It is empirically found, however, that these couplings preserve the approximate validity of the shell model. Significant theoretical progress has recently been accomplished in the understanding of the resulting “dynamical shell model” in nuclear matter, normal liquid ^3He , the electron gas and nuclei. The dominant modes which couple to the single-particle motion are particle-hole excitations in the case of nuclear matter, paramagnons in the case of ^3He , phonons for electrons in metals and surface vibrations in the case of nuclei. For the latter, the dynamical shell model can be viewed as an extension of the optical model to encompass both positive and negative energies. It thus provides a unified description of scattering and of bound single-particle states. The associated potential is energy dependent. This feature is characterized by the nucleon effective mass. The theoretical and experimental evidence which testifies to the existence of a strong energy dependence of this effective mass around the Fermi energy and near the nuclear surface is the central subject of the present review.

1. Introduction

One of the most striking features exhibited by nuclei is the validity of the shell model where each nucleon moves independently in a smooth potential. This potential is static but nonlocal in the space variables, which implies that the mean field is velocity (or momentum) dependent.

The fluctuations of the average potential lead to collective modes. When one takes into account the couplings of these modes to the single-particle motion, the shell model acquires *dynamical content*. As a consequence the average potential becomes also nonlocal in time, a property which can be characterized by an energy (or frequency) dependence. The present review is mainly devoted to these dynamical aspects of the shell model.

In chapter 2, we recall some of the empirical information which is at the basis of the shell model as well as the experimental evidence which points to the need of going beyond the static mean field approximation.

The velocity dependence of the single-particle potential can be characterized by the *k-mass*, and its frequency dependence by the *ω -mass*. Most experiments only probe the product of these two quantities, which is the *effective mass*. Particular attention is devoted in the present review to the ω -mass, since this quantity is the one which characterizes the *dynamical shell model*.

We feel that the present review is timely. Indeed, it is only recently that a significant breakthrough has been achieved in the quantitative understanding of the properties of the ω -mass in nuclei, although the interest of this problem had been emphasized long ago [1]. The main difficulties which had to be overcome were connected partly with the strong character of the nucleon–nucleon interaction, which hinders a straightforward use of perturbation theory, and partly with the definition of average quantities. The latter problem is twofold. Because of the *state dependence* expected in the coupling

between the low-lying collective modes and the single-particle states, the question indeed arises of whether it is possible to define an average potential which describes the coupled situation and still retains the original simplicity of the shell model. In addition, the existence of discrete levels and of isolated resonances makes it necessary to perform *energy averages* in order to define the quantities of interest. These two problems do not exist in an infinite system. Hence, it is not surprising that it is in the latter case that significant theoretical progress was first made.

The dynamics of nuclear matter is rather different from that of finite nuclei, where surface vibrations play an important role. It would thus not be justified to compare in detail the results of nuclear matter calculations with experiments. Nevertheless, the investigation of nuclear matter is instructive for the following three main reasons. (i) All relevant quantities are smooth, so the problem of averaging does not blur the main issues. (ii) It is in the case of nuclear matter that methods have been developed to replace the strong nucleon–nucleon interaction by a weak effective force. (iii) Many properties of the ω -mass are shared by most normal Fermi liquids of which nuclear matter provides an instructive illustration. This is why a significant fraction (chapter 3) of this review is devoted to uniform systems, in particular to nuclear matter.

Already in this simplified case, the dynamics of the shell model has a bearing on different nuclear properties such as the single-particle spreading widths, the imaginary component of the single-particle field, the density of single-particle states near the Fermi energy, the single-particle spectroscopic factors, the nucleon group velocity, the possible occurrence of a pion condensate, some of the properties of neutron stars, etc.

The importance of the dynamical couplings was first demonstrated in the case of electrons in metals and of normal liquid ^3He . In the latter case it was found that the specific heat at low temperature displays a marked temperature dependence. This was interpreted in terms of an energy dependence of the effective mass. These results inspired the work of Bertsch and Kuo [2] on the enhancement of the effective mass near the Fermi energy in finite nuclei. The recent progress accomplished in the understanding of the effective mass in nuclear matter and in nuclei has in turn stimulated a reexamination of the temperature dependence of the specific heat of liquid ^3He at low temperature [3–5].

After having been introduced in chapter 3 to the relevant concepts and techniques in the case of nuclear matter, the reader will be prepared to be confronted to finite nuclei in chapter 4.

The dynamical shell model is an attempt to extend the optical model [6] to negative energies. Hence, techniques first developed in the framework of the theory of nuclear reactions are useful. In the process of calculating microscopically the energy dependence of the optical potential one employs, on the other hand, methods which are more familiar in the field of nuclear spectroscopy, in particular the particle-vibration coupling model. The conjunction of these two formalisms proves to be very fruitful.

A unified description of single-particle motion at *positive* and at *negative* energy eventually emerges. Its implications are probably not yet fully apprehended. Some consequences and open problems are discussed in chapter 5.

2. Empirical information on the shell model

2.0. Preview

In the independent particle model, the wave function of each nucleon is a solution of the

single-particle Schrödinger equation whose most general form reads

$$i\hbar \frac{\partial \Psi(\mathbf{r}, t)}{\partial t} = -\frac{\hbar^2}{2m} \nabla^2 \Psi(\mathbf{r}, t) + \int d\mathbf{r} \int dt' \mathcal{M}(\mathbf{r}, \mathbf{r}'; t - t') \Psi(\mathbf{r}', t') \quad (2.0.1)$$

where for simplicity we drop explicit reference to the spin degree of freedom.

The single-particle potential \mathcal{M} which appears in eq. (0.1) can be very complicated since it is nonlocal in the spatial and in the time coordinates. The nonlocality in time is reflected by a dependence upon the difference $t - t'$ because we assumed that the nucleon-nucleon interaction is independent of time.

The dependence of \mathcal{M} upon $t - t'$ can be transformed into a frequency dependence. Let us indeed consider a stationary state with a well-defined frequency:

$$\Psi(\mathbf{r}, t) = \varphi_\omega(\mathbf{r}) e^{-i\omega t}. \quad (2.0.2)$$

Equation (0.1) then becomes

$$\hbar\omega \varphi_\omega(\mathbf{r}) = -\frac{\hbar^2}{2m} \nabla^2 \varphi_\omega(\mathbf{r}) + \int d\mathbf{r}' \mathcal{M}(\mathbf{r}, \mathbf{r}'; \omega) \varphi_\omega(\mathbf{r}') \quad (2.0.3)$$

where $\mathcal{M}(\mathbf{r}, \mathbf{r}'; \omega)$ is the Fourier transform of $\mathcal{M}(\mathbf{r}, \mathbf{r}'; t - t')$ over $t - t'$. *The nonlocality in time of the mean field therefore amounts to a frequency dependence.*

Let us now assume that the potential has the form $\mathcal{M}(\mathbf{r}, \mathbf{r}')$, i.e. is only nonlocal in space. In simple cases it can be shown that this nonlocality is equivalent to a velocity (momentum) dependence. This essentially implies that there exists a local potential $M(\mathbf{r}; E)$ which yields the same bound state energies and elastic scattering phase shifts as the nonlocal field [7].

There are thus two sources for an energy dependence of the empirical shell-model potential; one arises from the nonlocality in time and one from an approximate treatment of the nonlocality in space.

There is empirical evidence that the shell-model potential is indeed energy dependent. In fact, the following simple single-particle wave equation

$$E \varphi_E(\mathbf{r}) = -\frac{\hbar^2}{2m} \nabla^2 \varphi_E(\mathbf{r}) + M(\mathbf{r}; E) \varphi_E(\mathbf{r}) \quad (2.0.4)$$

provides a satisfactory description of many experimental data. It is difficult to determine separately the two types of contributions to the energy dependence displayed by the potential, since most data only involve their combined effects.

The main purpose of the present chapter is to gather some *empirical information* on the potential $M(\mathbf{r}; E)$ introduced in eq. (0.4). There is no way to “measure” directly a potential. We learn about this quantity through the theoretical analysis of experimental data on single-particle energies and scattering cross sections. To account for the elastic scattering and for the total cross sections one must introduce an imaginary part in $M(\mathbf{r}; E)$

$$M(\mathbf{r}; E) = V(\mathbf{r}; E) + i W(\mathbf{r}; E). \quad (2.0.5)$$

It is customary to assume that the real part $V(r; E)$ of $M(r; E)$ has a Woods–Saxon shape, namely

$$V(r; E) = \frac{V_0(E)}{1 + \exp\{(r - R_v)/a_v\}}. \quad (2.0.6)$$

The geometry is usually kept fixed, with the typical parameter values [8]

$$R_v = r_0 A^{1/3}; \quad r_0 = 1.25 \text{ fm}; \quad a_v = 0.65 \text{ fm}. \quad (2.0.7)$$

This leaves one with V_0 as the only adjustable parameter. The fit to the experimental data requires V_0 to depend upon energy, with typically

$$V_0(E) = V^0 + 0.3E \quad (2.0.8)$$

for $E > 10 \text{ MeV}$ as well as for $E < -20 \text{ MeV}$. In contradiction, it turns out that for E close to the separation energy, V_0 is approximately independent of energy in medium-weight and in heavy nuclei.

These properties imply that the *effective mass* m^* , which is defined by

$$m^*(E)/m = 1 - dV_0(E)/dE, \quad (2.0.9)$$

is a function of the energy E . More precisely, $m^*(E)/m$ is approximately equal to unity near the separation energy, while it is equal to about 0.7 for large values of $|E|$ [1].

At positive energies, the imaginary part of the potential, W , accounts for the depopulation of the entrance (elastic) channel. At negative energies, W is related to the spreading width Γ^\downarrow of a single-particle state.

By studying in section 2.11 this spreading in the framework of a simple model, we shall introduce some of the concepts and quantities which play a basic role in the present review and are useful for the understanding of the empirical data presented below.

2.1. Selected evidence for the validity of single-particle motion in nuclei

2.1.1. Positive energies

Information on the mean free path of a nucleon in the nucleus can be obtained from measurements of total reaction cross sections. Let us consider the scattering of neutrons by a target nucleus. The wave function which describes this process is asymptotically of the form

$$\Psi \sim \left\{ \exp(i k_n z) + \sum_{\beta} \frac{\exp(ik_{\beta} r)}{r} f_{n\beta}(k_n, \theta) \right\} \exp(i E_n t/\hbar). \quad (2.1.1)$$

It is the sum of a plane wave with momentum

$$\hbar k_n = \{2mE_n\}^{1/2} \quad (2.1.2)$$

where m is the reduced mass and E_n the bombarding energy, and of outgoing spherical waves with momentum k_{β} . The label β denotes the final channel while θ is the scattering angle.

The neutron total cross section is defined by

$$\sigma_{n,\text{tot}} = \sum_{\beta} \int |f_{n\beta}|^2 d\Omega \quad (2.1.3)$$

and is given by the optical theorem:

$$\sigma_{n,\text{tot}} = \frac{4\pi}{k_n} \text{Im} f_{nn}(k_n, \theta = 0). \quad (2.1.4)$$

These two expressions correspond to the existence of two possible ways of determining the total reaction cross section, namely: (i) Integrating the differential cross section for all reaction channels over all scattering angles. (ii) In terms of the attenuation of the incoming beam.

If the target nucleus would act as a perfect absorber for the incident nucleon, the reaction cross section would be a smooth, monotonically decreasing function of the incident energy E_n [9]. This can be understood in terms of the change of the wavelength as a function of E_n . The experimental data are in contradiction with this “black nucleus” model. Indeed, the measured total cross sections exhibit marked oscillations when the neutron energy varies [10]. An example is shown in fig. 2.1. These oscillations are due to the interference of the transmitted neutron wave (i.e. the part of the incident wave which passes through the target nucleus) and the incident wave [12]. Oscillations in the cross section appear when the phase difference between the two waves changes over multiples of π . From the magnitude of the oscillations one may estimate the mean free path λ of a nucleon in the nucleus. It turns out to be of the order of the nuclear radius. We shall return in section 2.4 to the theoretical analysis of the data shown in fig. 2.1.

2.1.2. Negative energies

The first empirical evidence of the approximate validity of the independent particle model in nuclei came from the systematics of ground state properties. The striking irregularities displayed by several observed quantities were interpreted in terms of shell closures. These, in turn, could be accounted for by assuming that the nucleons move independently of one another in an average potential well [13]. In order to be able to ascribe orbit quantum numbers to the motion of a nucleon it is necessary that this nucleon travels a significant fraction of its orbit before making a collision. Thus, the approximate validity of the shell model implies that the nucleons have a mean free path λ which is at least of the order of the nuclear size. This result came as a surprise since early estimates of λ based on measured nucleon–nucleon cross section lead to values of the order of 0.4 fm [9, p. 340]. In these estimates the essential role of the Pauli principle had been overlooked.

The value of the “magic numbers” at which shell closures occur can only be reproduced if one assumes that the mean field contains a strong spin-orbit interaction term of the form

$$V_{ls}(r) = V_{ls}(l \cdot s) \frac{r_0^2}{r} \frac{d}{dr} \left[\frac{1}{1 + \exp((r - R_v)/a_v)} \right]. \quad (2.1.5)$$

In the present review we focus on the central part of the nuclear mean field; some of the conclusions might be affected by a possible dependence of the spin-orbit term on the energy of the nucleon.

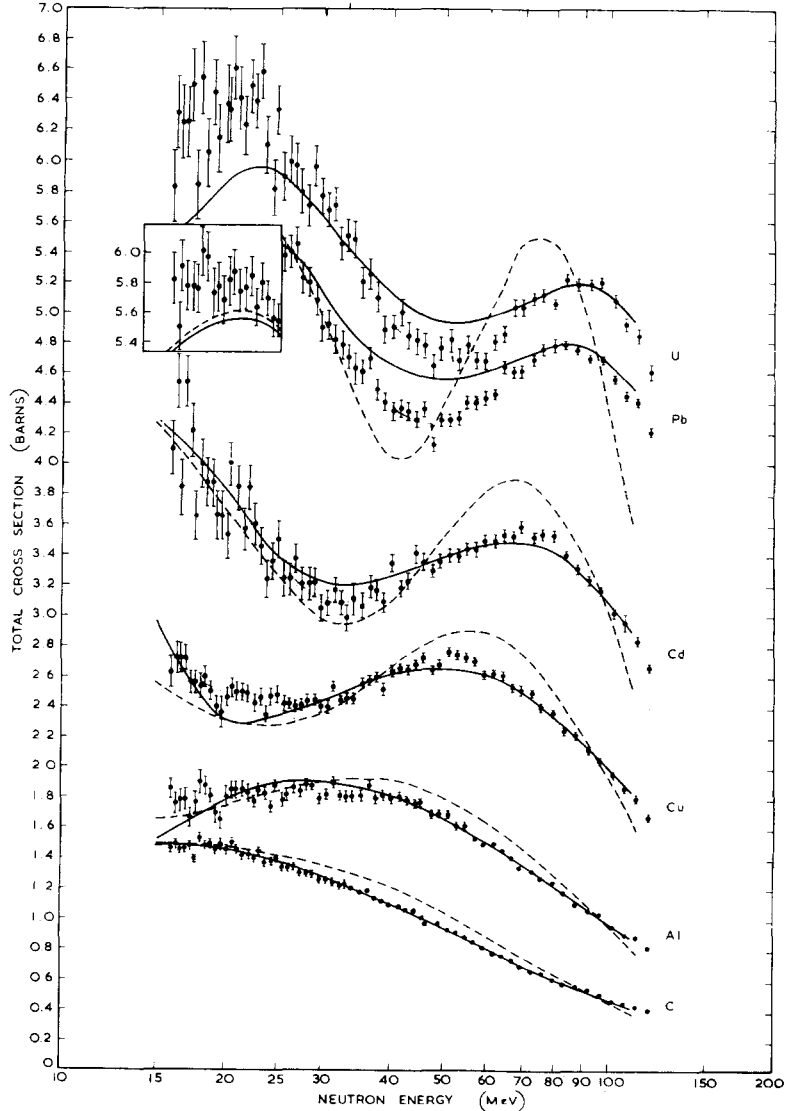


Fig. 2.1. Taken from ref. [11]. The dots show the dependence upon incident energy of the neutron total cross sections of (from bottom to top) carbon, aluminium, copper, cadmium, lead and uranium. The solid and broken lines are calculated from the optical model. As discussed in section 2.4, the broken lines are obtained when the depth of the real part of the potential is not allowed to depend upon energy, while the solid curves correspond to the energy dependence shown in fig. 2.9.

2.2. The independent particle model

In its simplest form, the nuclear shell model assumes that each nucleon moves independently of the others in a smooth potential well. In most empirical analyses the central part of this average potential is assumed to have the “Woods-Saxon” radial dependence (0.6) illustrated in fig. 2.2

$$V(r) = \frac{V_0}{1 + \exp\{(r - R_v)/a_v\}}. \quad (2.2.1)$$

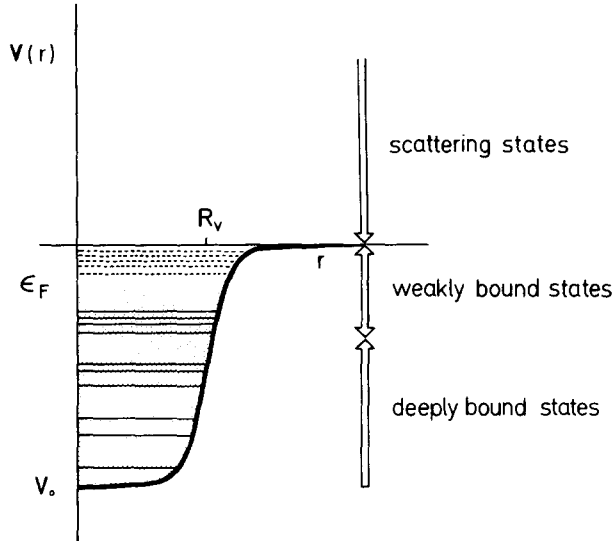


Fig. 2.2. Sketch of the three energy domains discussed in sections 2.3, 2.4 and 2.5. The Fermi energy is denoted by ϵ_F . The shaded region corresponds to the occupied states in the independent-particle model description of the ground state.

The potential radius R_v and the potential diffuseness a_v are expected to be slightly larger than the corresponding parameters of the ground state density distributions. One typically uses the values (0.7). This leaves V_0 as the only adjustable parameter.

In the next three sections we discuss the main empirical information on V_0 as obtained from the analyses of the experimental data concerning weakly bound states, scattering states and deeply bound states, respectively. These three domains are sketched in fig. 2.2. Our discussion will be illustrated by examples taken from ^{208}Pb and ^{40}Ca .

2.3. Weakly bound single-particle states

In the independent particle model, the ground state wave function of ^{208}Pb is viewed as a Slater determinant in which all neutron levels up to the $3p_{1/2}$ subshell and all proton levels up to the $3s_{1/2}$ subshell are filled. The ground state of ^{209}Pb is obtained by adding a neutron in the $2g_{9/2}$ orbit. This picture is consistent with the ease with which the ground state of ^{209}Pb is populated in the $^{208}\text{Pb}(\text{d}, \text{p})$ ^{209}Pb stripping reaction (cf. fig. 2.3), and with the $l = 4$ signature of the associated angular distribution. A quantitative measure of the single-particle character of a level is provided by the associated spectroscopic factor (cf. section 2.9). In particular, the large spectroscopic factor of the $l = 6$ level which lies at 0.77 MeV excitation energy in ^{209}Pb leads one to interpret it as a $1i_{11/2}$ neutron added to the ^{208}Pb core. Similarly for the other levels of ^{209}Pb which are displayed in fig. 2.4.

The pick-up reaction $^{208}\text{Pb}(\text{d}, \text{t})$ ^{207}Pb shown in fig. 2.5 preferentially feeds those excited states in ^{207}Pb which can be interpreted as a one neutron hole punched in the ^{208}Pb core, in the appropriate subshell. For instance, the $5/2^-$ level at 0.57 MeV excitation energy in ^{207}Pb is interpreted as a $2f_{5/2}$ hole in the ^{208}Pb core. Similarly for the other levels of ^{207}Pb which are displayed in fig. 2.4.

The “observed” single-particle neutron and proton spectra are collected in fig. 2.6. Also shown are single-particle energies as calculated from the Woods-Saxon potential (2.1), with the following

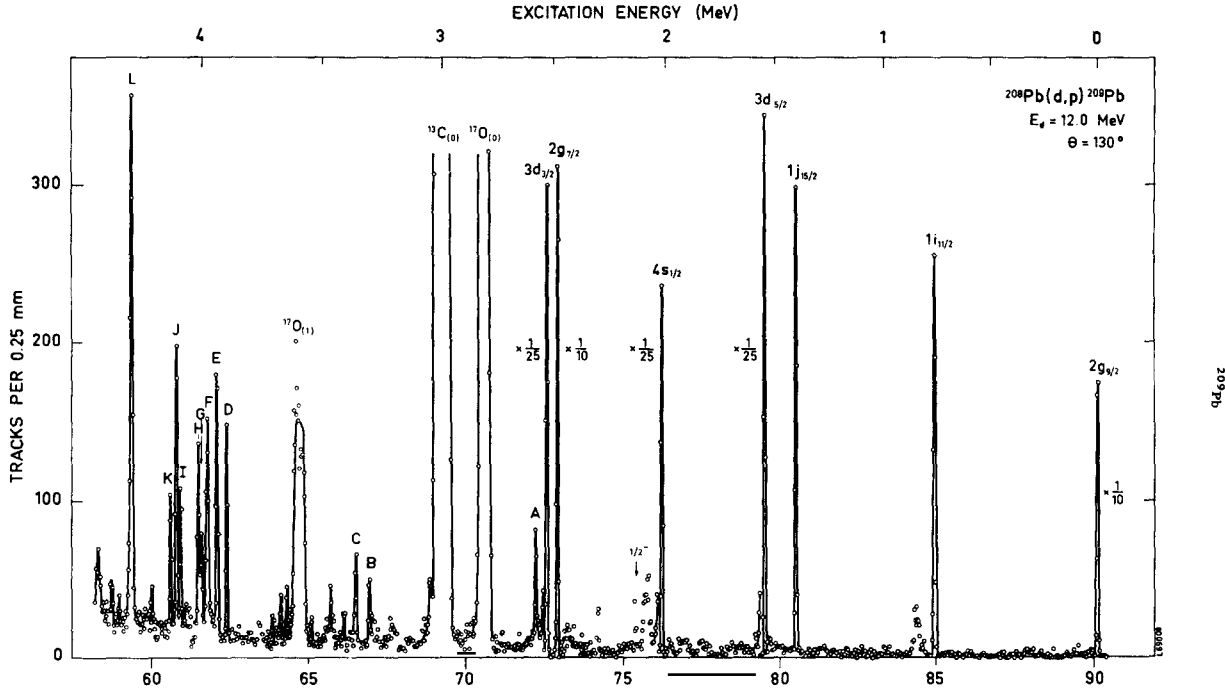


Fig. 2.3. Taken from ref. [14]. Proton spectrum from the $^{208}\text{Pb}(\text{d}, \text{p})^{209}\text{Pb}$ reaction, at $E_{\text{d}} = 12$ MeV and $\theta = 130^\circ$. The intense peaks are labelled by their shell-model assignment.

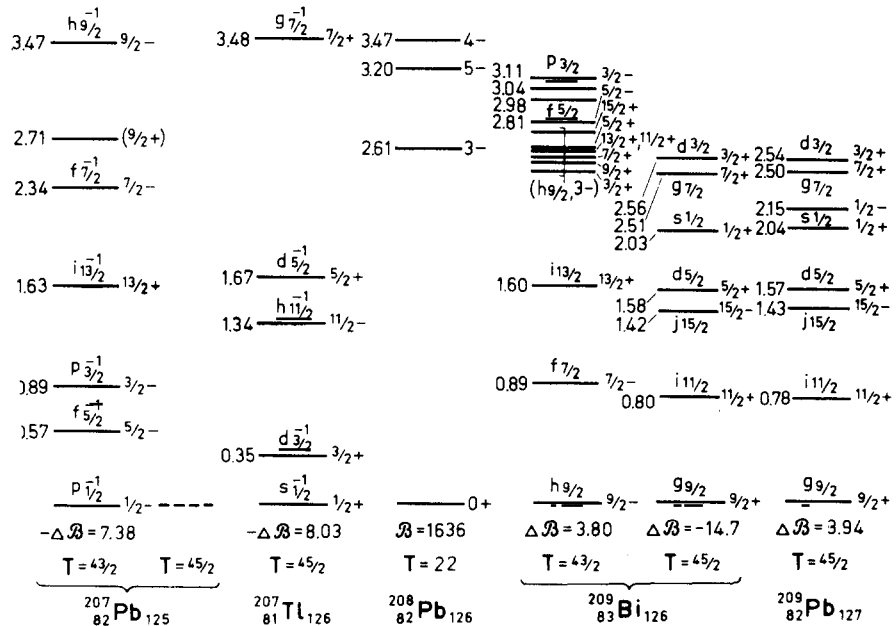


Fig. 2.4. Taken from ref. [15]. Level spectra of ^{207}Pb , ^{207}Tl , ^{208}Pb , ^{209}Bi and ^{209}Pb , from which one deduces the single-particle spectrum shown in fig. 2.6.

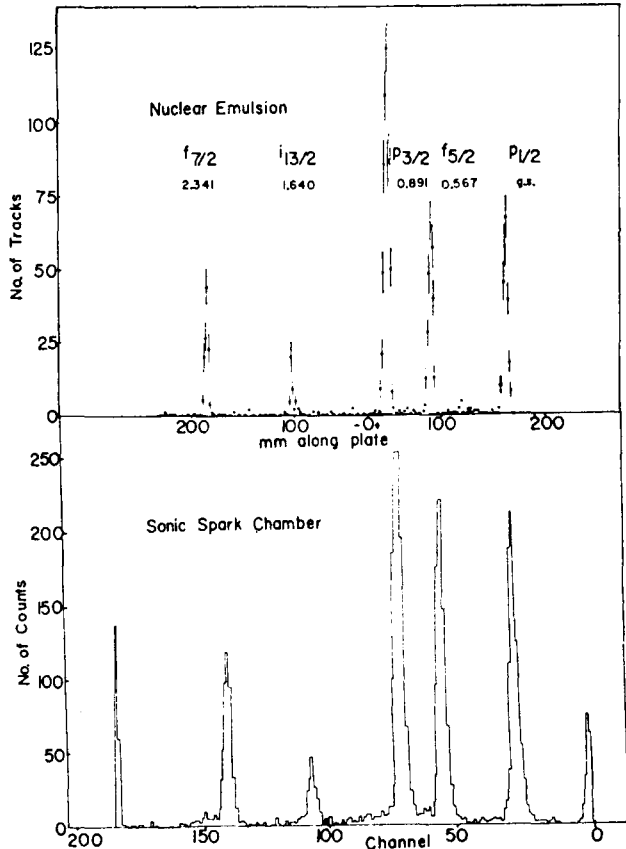


Fig. 2.5. Taken from ref. [16]. Triton spectrum for the reaction $^{208}\text{Pb}(\text{d}, \text{t})^{207}\text{Pb}$ at $E_{\text{d}} = 24.8$ MeV and $\theta = 30^\circ$. The peaks in the upper part are labelled by their shell-model assignment.

parameters: $V_0 = -44$ MeV for neutrons, -58 MeV for protons, and

$$R_v = 1.27 A^{1/3} \text{ fm}, \quad a_v = 0.67 \text{ fm}, \quad V_{ls} r_0^2 = 34 \text{ MeV fm}^2. \quad (2.3.1)$$

This example shows that *the energies of weakly bound single-particle states in medium-weight and in heavy nuclei are reasonably well reproduced by the independent particle model based on the static potential (2.1)* [1]. Here, the word static is meant to emphasize that V_0 and V_{ls} are constant, i.e. are independent of the energy of the single-particle state.

The validity of this statement is questionable in the case of lighter nuclei like ^{40}Ca (see figs. 2.7 and 2.8). Indeed, in this case the calculated value of the energy gap between the s-d shell and the f-p shell is somewhat too small.

2.4. Scattering single-particle states

The differential elastic scattering and the total nucleon-nucleus cross sections can be accurately reproduced by assuming that the bombarding nucleon is scattered by a potential well of the Woods-Saxon form (2.1), provided that one adds to it an imaginary component $W(r; E)$ to which we shall

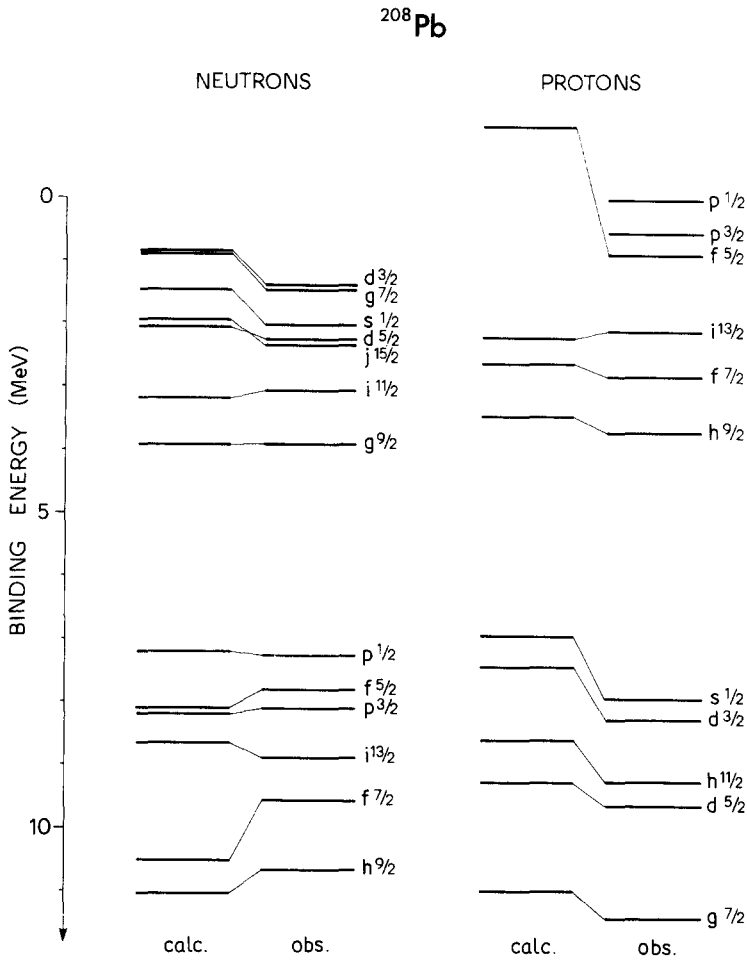


Fig. 2.6. Adapted from ref. [15]. Observed (“obs.”) single-particle states in ^{208}Pb , and single-particle energies calculated (“calc.”) from the central Woods-Saxon potential (2.1) with $V_0 = -51 \text{ MeV}$, $R_v = 1.27A^{1/3} \text{ fm}$, $a_v = 0.67 \text{ fm}$ [8], supplemented by spin-orbit, symmetry and Coulomb components.

return in section 2.10. However, the fits are not satisfactory unless one allows V_0 to depend upon the incident nucleon energy E , according to the law

$$V_0(E) = V^0 + 0.3E. \quad (2.4.1)$$

For instance, the broken curve in fig. 2.1 corresponds to a constant V_0 , while the solid lines correspond to the linear dependence (4.1) which is illustrated in fig. 2.9.

Figures 2.10 and 2.11 present a compilation of potential depths for ^{208}Pb and ^{40}Ca respectively. For $E > 0$, they were obtained from fits to proton elastic scattering data. For $E < 0$, they were determined from the single-particle energies. The solid straight line shows that the linear energy dependence (4.1) is supported by this compilation, in the domain $100 \text{ MeV} > E > 0 \text{ MeV}$.

We conclude from these examples that *for positive energies the depth of the empirical average potential depends upon the energy according to the law (4.1)*. This energy dependence is rather insensitive to the

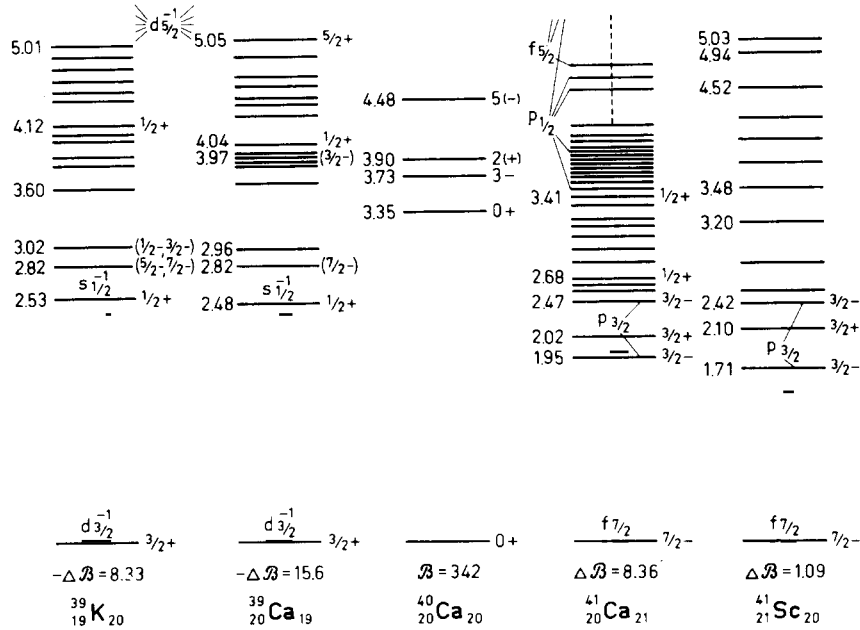


Fig. 2.7. Taken from ref. [15]. Level spectra of ^{39}K , ^{39}Ca , ^{40}Ca , ^{41}Ca and ^{41}Sc from which one deduces the single-particle spectrum shown in fig. 2.8.

precise choice of the geometrical parameters R_v and a_v . This choice mainly affects the value of the constant V^0 .

2.5. Deeply bound single-particle states

The successes of the independent particle model and of the closely related Hartree–Fock calculations [19] suggest that it may be reasonable to ascribe a physical meaning to the deeply bound single-particle states. This has been confirmed during the last decade, although most experimental data are restricted to light and medium-light nuclei. These data are obtained from pick-up reactions (e.g. ($^3\text{He}, \alpha$)) [20] or from knock-out reactions (e.g. ($e, e'p$)) [21].

In fig. 2.12 we give an example of this type of data, obtained from the analysis of the $^{40}\text{Ca}(e, e'p)$ ^{39}K knock-out reaction. It shows that the probability of knocking-out one nucleon from the 1p shell in ^{40}Ca has a maximum for $E \sim 35$ MeV, which is identified with the binding energy of the 1p shell. Only part of the width of the bump can be ascribed to the experimental energy resolution, which is not good enough to separate the spin partners. Part of the width arises from the fact that the probability of finding a nucleon with the quantum numbers 1p is spread over a finite energy interval. This reflects the fact that the independent particle model is an oversimplification. We shall come back to this point in sections 2.10, 2.11.

The example of ^{40}Ca given in fig. 2.11 shows that in order to reproduce the observed binding energies of deeply bound single-particle states it is necessary, as in the case of the scattering states, to let the depth V_0 of the potential well (2.1) depend upon energy. The broken line in fig. 2.11 corresponds to the linear law

$$V_0(E) = V^0 + 0.40E, \quad (2.5.1)$$

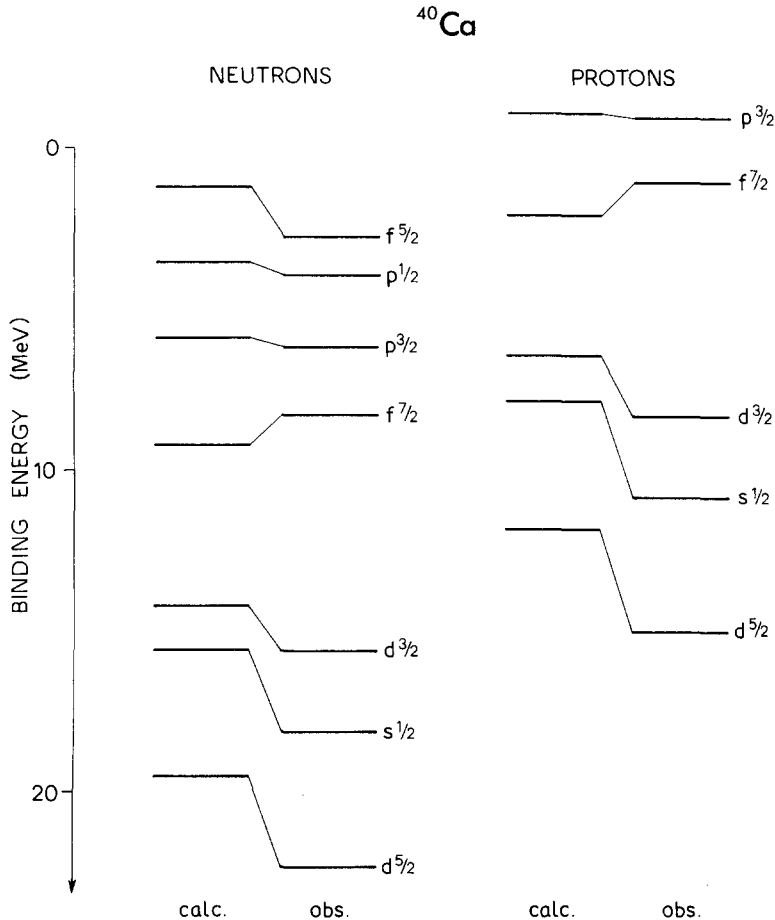


Fig. 2.8. Adapted from ref. [15]. Observed ("obs.") single-neutron states in ^{40}Ca , and single-neutron energies calculated ("calc.") from the Woods-Saxon potential (1.1), with $V_0 = -51 \text{ MeV}$, $R_v = 1.27A^{1/3} \text{ fm}$, $a_v = 0.67 \text{ fm}$, supplemented by spin-orbit, symmetry and Coulomb components.

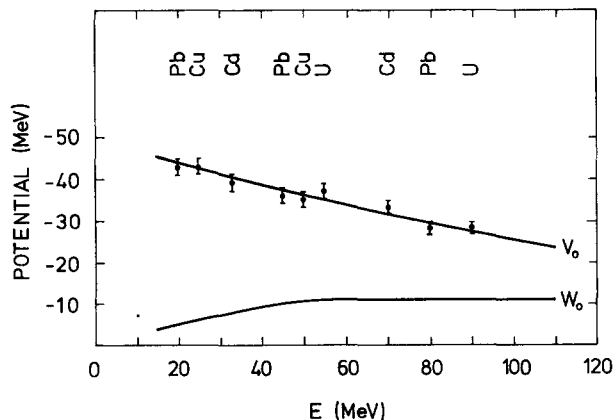


Fig. 2.9. Taken from ref. [11]. Dependence upon incident neutron energy of the depth of the real part and of the imaginary part of the optical-model potential used to generate the solid lines in fig. 2.1. Each empirical point is labelled by the data which led to its determination, i.e. (from left to right) the location of the second maximum of the total cross section in Pb, the location of the first minimum of the total cross section in Cu, etc. The real part and the imaginary parts have been assumed to have the same Woods-Saxon radial shape. The fits below 50 MeV are improved if one allows the shape of the imaginary part to change from a Woods-Saxon to a surface peaked function as the energy decreases.

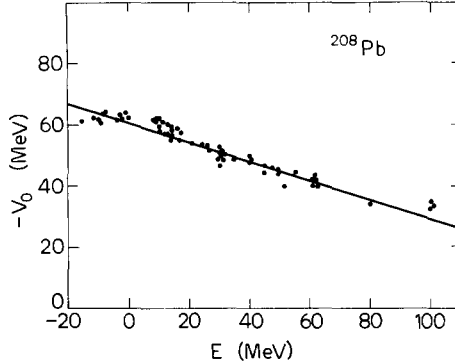


Fig. 2.10. Adapted from ref. [17]. Dependence upon proton bombarding energy of the depth V_0 of the potential well (2.1) which reproduces the $^{208}\text{Pb}(p, p)$ differential cross section [18] and the weakly bound single-proton states. The geometry parameters are $R_v = 1.24A^{1/3} \text{ fm}$ and $a_v = 0.65 \text{ fm}$. The full straight line represents the linear law (4.1), with $V^0 = -62 \text{ MeV}$.

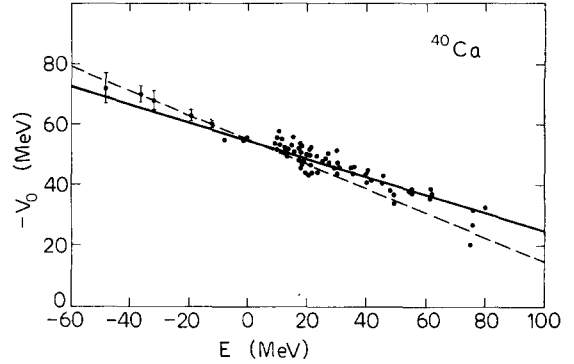


Fig. 2.11. Adapted from ref. [17]. Dependence upon proton bombarding energy of the depth V_0 of the potential well (2.1) which reproduces the $^{40}\text{Ca}(p, p)$ differential cross section for $E > 10 \text{ MeV}$, and the experimental single-proton energies for $E < 0 \text{ MeV}$. The potential parameters are $R_v = 1.24A^{1/3} \text{ fm}$, $a_v = 0.65 \text{ fm}$. The full straight line corresponds (in MeV) to $V_0(E) = -55 + 0.3E$, and the dashed straight line represents $V_0(E) = -55 + 0.4E$.

with $V^0 = -55 \text{ MeV}$. Note that the energy dependence appears to be slightly more pronounced in the case of deeply bound single-particle states (eq. (5.1)) than in the case of scattering states (eq. (4.1)).

2.6. Effective mass

2.6.1. Definition

The effective mass m^* of a nucleon in the bulk of the nucleus is defined by the relation

$$m^*(E)/m = 1 - dV_0(E)/dE. \quad (2.6.1)$$

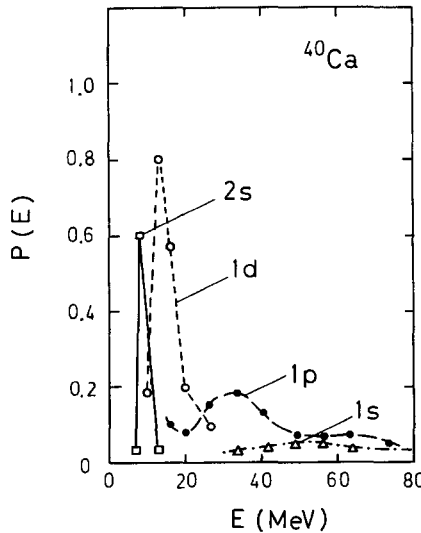


Fig. 2.12. Adapted from ref. [22]. Energy distribution of the bound single-proton states in ^{40}Ca . The squares correspond to the 2s state, the open circles to the 1d states, the full dots to the 1p state and the triangles to the 1s state. The curves are only a help to the eye.

The origin of the expression “effective mass” will be explained in sections 2.6.3 and 2.8. When the energy dependence of the potential depth is linear, the effective mass is constant. In general, however, m^* is a function of the energy E .

2.6.2. Empirical energy dependence of the effective mass

The empirical data surveyed in sections 2.3–2.5 indicate that the effective mass depends upon the single-particle energy. Indeed, they yield $m^*/m \approx 0.65$ for either positive energies or for large negative energies and $m^*/m \approx 1$ for small negative energies.

Let us be somewhat more quantitative. We define the *Fermi energy* ε_F as the average between the energy ε_F^- of the last occupied orbit and the energy ε_F^+ of the first unoccupied orbit

$$\varepsilon_F = (\varepsilon_F^+ + \varepsilon_F^-)/2. \quad (2.6.2)$$

In the case of neutrons in ^{208}Pb for example, one has $\varepsilon_F = -5.6$ MeV (see fig. 2.6). With this definition we can summarize as follows the empirical evidence:

$$m^*/m \approx 0.7 \quad \text{for } |E - \varepsilon_F| > 20 \text{ MeV}, \quad (2.6.3)$$

$$m^*/m \approx 1 \quad \text{for } |E - \varepsilon_F| < 10 \text{ MeV}. \quad (2.6.4)$$

The property that *the effective mass presents a narrow enhancement near the Fermi energy* was first pointed out by Brown, Gunn and Gould [1]. We shall devote much attention to its theoretical investigation, because this enhancement is one of the features which directly reveals the dynamical content of the shell model.

2.6.3. Nuclear matter

We now explain the origin of the expression “effective mass”. Let us consider the case of infinite nuclear matter, which is a hypothetical *uniform* medium with equal number of neutrons and protons and with the Coulomb interaction turned off.

In nuclear matter the independent particle model amounts to assuming that each nucleon with momentum k has a well-defined potential energy V . Then, it also has a well-defined total energy E , which is given by the energy-momentum relation

$$E = \hbar^2 k^2 / 2m + V(E). \quad (2.6.5)$$

Let us suppose that the simple linear law

$$V(E) = V^0 + (1 - m^*/m)E \quad (2.6.6)$$

is a good approximation. Substituting eq. (6.6) into eq. (6.5), we find

$$E = \frac{\hbar^2 k^2}{2m^*} + \frac{m}{m^*} V^0. \quad (2.6.7)$$

Thus, instead of letting $V(E)$ depend linearly on energy, one can equivalently consider that the

potential energy is constant (and equal to mV^0/m^*), provided that the nucleon mass is replaced by m^* . This justifies the expression “effective mass” for m^* .

2.7. Density of single-particle energies

2.7.1. Density of states in nuclear matter

From the energy-momentum relation

$$E = \hbar^2 k^2 / 2m + V(E) \quad (2.7.1)$$

and from the definition

$$m^*/m = 1 - dV(E)/dE \quad (2.7.2)$$

of the effective mass, one derives

$$dE/dk = \hbar^2 k / m^*. \quad (2.7.3)$$

One can interpret the left-hand side of this equation as the rate of change in energy when the momentum changes or, equivalently, when the number of nodes per unit length changes. Since the latter can be used to label the single-particle states, the energy spacing between levels decreases for increasing values of m^* . Thus, *the effective mass is proportional to the density of single-particle energies*.

2.7.2. Harmonic oscillator potential

To bridge the gap between infinite nuclear matter and the case of potential wells of finite range let us consider a particle of mass m in a one-dimensional harmonic potential. The Hamiltonian describing its motion

$$H = p^2/2m + kx^2/2 \quad (2.7.4)$$

leads to discrete energy levels with a constant spacing (cf. fig. 2.13a)

$$\hbar\omega_0 = \hbar\sqrt{k/m}. \quad (2.7.5)$$

It follows from this expression that the density of states is proportional to the square root of m .

We notice, however, that this result is derived assuming that the potential remains unchanged. If this is the case, the ground state wave function for a particle of mass $m^* > m$ will shrink in space as compared to the one of mass m and consequently the mean square radius of the system will decrease (fig. 2.13b). If we would like to establish a comparison between the energy level spacings for a constant extension in space we are forced to change the potential well. For this purpose it is more convenient to express the relevant quantities in terms of the oscillator length b which is defined by assuming that the ground state wave function is of the form

$$\Psi_0(x) \propto \exp(-x^2/2b^2). \quad (2.7.6)$$

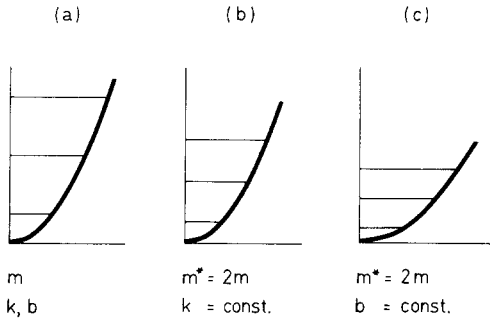


Fig. 2.13. Schematic representation of the first three energy levels of a one-dimensional harmonic oscillator. In (a) the position of the eigenstates is shown for a particle of mass m moving in a potential $V = kx^2/2$ and corresponding to an oscillator length b . The levels in (b) belong to a particle of mass $m^* = 2m$ moving in the same potential, leading to a higher density of states but also to a smaller oscillator length. Finally, in (c) the energy levels are shown for the particle of mass $m^* = 2m$ requiring the radial extent of the wave functions to be the same as those in (a), i.e. for $b = \text{const.}$ In this case the density of states is precisely double of the one displayed in (a).

Substitution in the Schrödinger equation leads to the following results

$$b^4 = 2\hbar^2/mk \quad (2.7.7)$$

$$\hbar\omega_0 = \hbar^2(mb^2)^{-1}. \quad (2.7.8)$$

Thus, if we replace the mass of the particle by $m^* > m$ while requiring the ground state wave function to have the same radial spread ($b = \text{const.}$, fig. 2.13c), the density of levels turns out to be proportional to the effective mass, as in nuclear matter.

For the sake of simplicity we have worked out this example in one dimension. What we have presented, however, can be generalized straightforwardly to the $l=0$ states of a three-dimensional harmonic oscillator. In this case, the change in energy corresponds to the separation in energy between states with different number of nodes. This involves the energy gap between major shells in the harmonic oscillator picture.

2.7.3. Potential wells of finite range

Let us proceed to the more realistic case of a Woods-Saxon potential well of radius R_v and diffuseness a_v , and with an energy-dependent depth given by the linear law

$$V_0(E) = V^0 + (1 - m^*/m)E. \quad (2.7.9)$$

The energy levels are characterized by the principal quantum number n and by the orbital angular momentum l . The equation for the radial wave function $\Psi_{nl}(r)$ reads

$$\frac{\hbar^2}{2m} \left[\frac{d^2}{dr^2} - \frac{l(l+1)}{r^2} \right] \Psi_{nl}(r) + \left[\epsilon_{nl} - \frac{V^0 + (1 - m^*/m) E_{nl}}{1 + \exp\{(r - R_v)/a_v\}} \right] \Psi_{nl}(r) = 0 \quad (2.7.10)$$

where ϵ_{nl} are the energy eigenvalues. Due to the radial dependence of the potential, it is no longer

possible to reduce this equation to an equivalent one for a particle of mass m^* moving in a Woods-Saxon potential of constant depth.

We illustrate with a numerical example that this equivalence is nevertheless satisfied in practice to a very good approximation. With the same geometrical parameters used in the calculation of the neutron levels of ^{208}Pb displayed in fig. 2.6, i.e.

$$R_v = 7.5 \text{ fm}, \quad a_v = 0.65 \text{ fm}, \quad (2.7.11)$$

we have calculated the energies of the single-particle levels in a family of Woods-Saxon potential wells of different depth V_0 . The results are presented in fig. 2.14. In (a) we show schematically the profiles of the different potentials and indicate in each case only one of the single-particle levels. The value of V_0 has been adjusted in each instance to follow the law

$$V_0 = -44 + 0.3(\varepsilon - \varepsilon_F), \quad (2.7.12)$$

where ε stands for the energy of the selected level. The Fermi energy ε_F has been taken half-way between the 1h and 2f levels, i.e.

$$\varepsilon_F = \frac{1}{2}(\varepsilon_{1\text{h}} + \varepsilon_{2\text{f}}) = -11.5 \text{ MeV}. \quad (2.7.13)$$

The sequence of single-particle levels has been collected in (b). Notice that, at this point, they do not

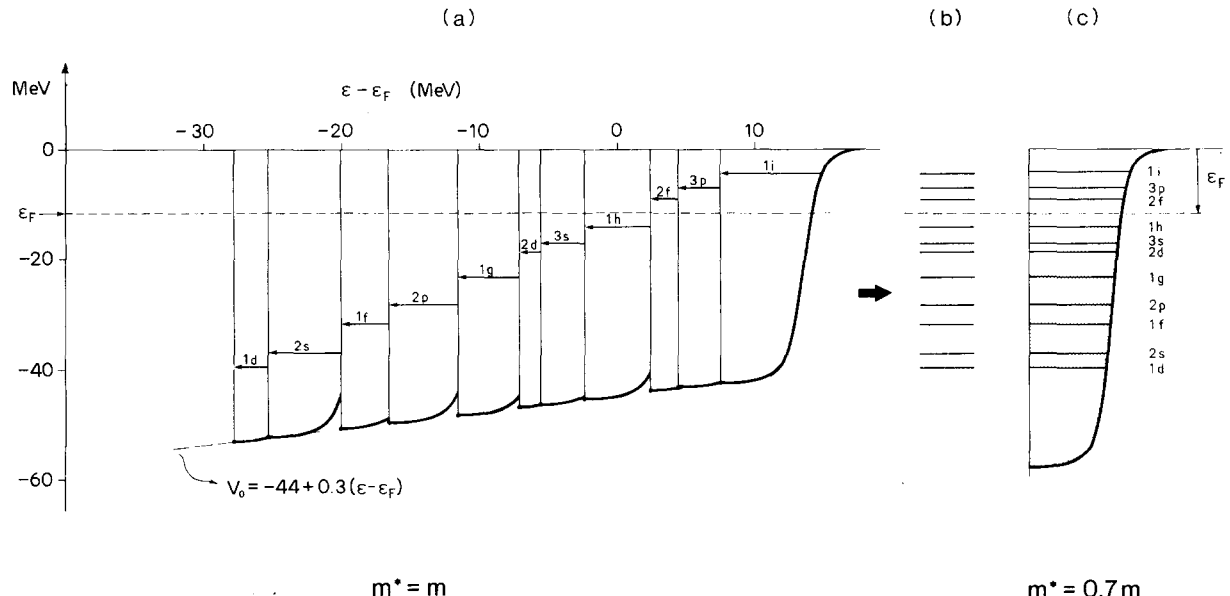


Fig. 2.14. In (a) a family of Woods-Saxon potentials with radius $R = 7.5 \text{ fm}$ ($A = 208$) and diffuseness 0.65 fm is shown. The energy levels for a particle of mass $m^* = m$ have been calculated for all these potentials. In each of these cases one energy level is singled out. The depth V_0 of the corresponding potential has been adjusted as a function of the energy ε_{nl} of this level and follows the linear law $V_0 = -44 + 0.3(\varepsilon_{nl} - \varepsilon_F)$, where $\varepsilon_F = -11.5 \text{ MeV}$. These energy levels have been collected in (b). In (c) it is shown that essentially the same single-particle energies are obtained when using an energy-independent Woods-Saxon potential with depth $V^0 = -57 \text{ MeV}$ provided that the eigenstates are calculated for a particle of mass $m^* = 0.7m$.

come out as eigenvalues of a “common” static potential. This is emphasized in the figure, as they are displayed without any potential profile.

In (c) we show, however, that an almost identical set of energy eigenvalues results from the energy-independent Woods-Saxon potential

$$\bar{V}(r) = \frac{\bar{V}_0}{1 + \exp\{(r - R_v)/a_v\}} \quad (2.7.14)$$

provided that the corresponding radial wave equation

$$\frac{\hbar^2}{2m^*} \left[\frac{d^2}{dr^2} - \frac{l(l+1)}{r^2} \right] \bar{\Psi}_{nl}(r) + [\bar{\varepsilon}_{nl} - \bar{V}(r)] \bar{\Psi}_{nl}(r) = 0 \quad (2.7.15)$$

is solved for a particle of mass $m^* = 0.7m$. The value of \bar{V}_0 ($= -57$ MeV in this example) was chosen to reproduce the value of ε_F , that is

$$\varepsilon_F = \frac{1}{2}(\bar{\varepsilon}_{1h} + \bar{\varepsilon}_{2f}). \quad (2.7.16)$$

In fig. 2.15, the same numerical example illustrates that the distance between single-particle levels is

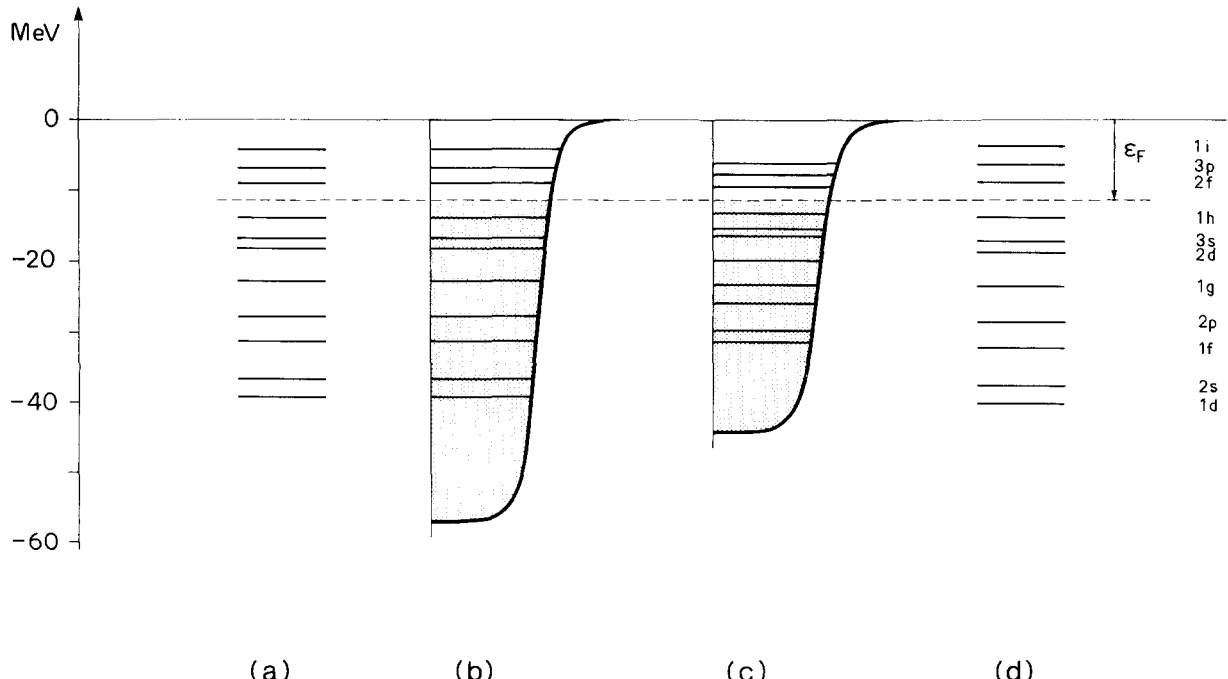


Fig. 2.15. The energy levels shown in column (a) are identical to those contained in column (a) of fig. 2.14; column (b) is identical to column (c) in fig. 2.14. Column (c) displays the energy levels of a particle of mass m in a Woods-Saxon potential with the same geometry and with a depth taken equal to -44 MeV, in order to yield the same value $\varepsilon_F = -11.5$ MeV for the Fermi energy. Column (d) shows the energies obtained by multiplying by $(0.7)^{-1}$ all energy differences $\varepsilon_{nl} - \varepsilon_F$ shown in column (c).

almost proportional to the ratio m^*/m . We remark that it is the full single-particle spectrum which is compressed when m^* is replaced by m , not only the difference between levels with the same value of l and different values of n . Notice that the depth -57 MeV differs from $mV_0/m^* = -63$ MeV. This is discussed in the next section.

2.7.4. Radial dependence of the effective mass

We have shown in section 2.7.3 that the eigenvalue problem posed in eq. (7.10) is not equivalent to solving (7.15) for $\bar{V}_0 = mV_0/m^*$. The reason lies in the radial dependence of the potential well or, equivalently, in the fact that we have assumed that m^* is independent of the distance r from the nuclear centre.

We could have defined a radial-dependent effective mass from the relation

$$m^*(r; E)/m = 1 - \partial V(r; E)/\partial E. \quad (2.7.17)$$

Let us assume a linear energy dependence for the potential depth, i.e.

$$V(r; E) = \frac{V^0 + (1 - m_0^*/m)E}{1 + \exp\{(r - R_v)/a_v\}} \quad (2.7.18)$$

where the index on m_0^* indicates the effective mass for $r = 0$. One has then

$$1 - \frac{m^*(r)}{m} = \frac{1 - m_0^*/m}{1 + \exp\{(r - R_v)/a_v\}}. \quad (2.7.19)$$

Note that the effective mass m^* does not depend on E because of the linear energy dependence which has been assumed for the potential. The single-particle equation

$$\frac{\hbar^2}{2m} \left[\frac{d^2}{dr^2} - \frac{l(l+1)}{r^2} \right] \Psi_{nl}(r) + [\varepsilon_{nl} - V(r; \varepsilon_{nl})] \Psi_{nl}(r) = 0 \quad (2.7.20)$$

then has exactly the same bound and scattering eigenstates as the equation

$$\frac{\hbar^2}{2m^*(r)} \left[\frac{d^2}{dr^2} - \frac{l(l+1)}{r^2} \right] \Psi_{nl}(r) + [\varepsilon_{nl} - \bar{V}(r)] \Psi_{nl}(r) = 0 \quad (2.7.21)$$

with the *energy-independent potential*

$$\bar{V}(r) = \frac{mV^0/m^*(r)}{1 + \exp\{(r - R_v)/a_v\}}. \quad (2.7.22)$$

This can be extended to other radial dependences.

The situation just described is similar to the one encountered in self-consistent calculations based on Skyrme-type effective nucleon–nucleon interactions.

2.8. Group velocity

In free space the velocity of a nucleon with momentum $\hbar k$ is given by

$$v = \hbar k/m. \quad (2.8.1)$$

Inside a uniform medium, the physical velocity of the wave packet associated with the nucleon is the group velocity

$$v_g = \frac{1}{\hbar} \frac{dE}{dk}. \quad (2.8.2)$$

The definition (7.2) of m^* yields

$$v_g = \hbar k/m^* \quad (2.8.3)$$

which gives further support to the expression “effective mass” used for m^* .

We have seen in section 2.5 that $m^* < m$. This leads to the conclusion that in general one has

$$v_g > v, \quad (2.8.4)$$

i.e. that *the velocity of a nucleon with momentum $\hbar k$ in the nuclear medium is larger than the velocity that it would have in free space*. This is somewhat surprising. One could have expected the group velocity to be *smaller*, since the nucleon has to cut its way through the medium.

2.9. Spectroscopic factors

Figures 2.3 and 2.5 illustrate the fact that one calls single-particle states those which are strongly populated in stripping or pick-up reactions. The “ease” with which a final state is populated in a one-particle transfer reaction is measured by its spectroscopic factor.

2.9.1. Addition and removal probabilities

The cross section for adding to a target A a nucleon in an orbit characterized by the quantum numbers $\alpha = \{n, l, j, m\}$ is proportional to the square of the matrix element

$$M_{if}(A \rightarrow A + 1) = \langle \Psi_f(A + 1) | a_{jm}^+ | \Psi_i(A) \rangle \quad (2.9.1)$$

where $|\Psi_i(A)\rangle$ is the normalized wave function of the target ground state, while $|\Psi_f(A + 1)\rangle$ denotes the normalized wave function of the final state in the $(A + 1)$ nucleon system. Similarly, the cross section for removing a nucleon from an orbit j, m is proportional to the square of the matrix element

$$M_{if}(A \rightarrow A - 1) = \langle \Psi_f(A - 1) | a_{jm}^- | \Psi_i(A) \rangle. \quad (2.9.2)$$

2.9.2. Sum rules

If the target state A is a closed shell configuration and the final state f is a pure single-particle configuration added to that core, the matrix element M_{if} has modulus unity. This is approximately the case for the levels shown in figs. 2.3 and 2.5. In general, Ψ_i and Ψ_f describe more complicated configurations, and the matrix element M_{if} has modulus smaller than unity. The sum of the cross sections leading to all final states can, however, be expressed in closed form. One has indeed

$$\sum_f |\langle \Psi_f(A-1) | a_{jm} | \Psi_i(A) \rangle|^2 = \langle \Psi_i(A) | n_{jm} | \Psi_i(A) \rangle \quad (2.9.3)$$

where

$$n_{jm} = a_{jm}^+ a_{jm} \quad (2.9.4)$$

is the *occupation number* operator. Equation (9.3) expresses the fact that the sum of the cross sections involving the removal of a particle from the orbit (jm) is proportional to the probability that this orbit is occupied in the target. Similarly the sum of the particle-addition probabilities is given by

$$\sum_f |\langle \Psi_f(A+1) | a_{jm}^+ | \Psi_i(A) \rangle|^2 = \langle \Psi_i(A) | (1 - n_{jm}) | \Psi_i(A) \rangle. \quad (2.9.5)$$

Equations (9.3) and (9.4) yield

$$\sum_f M_{if}(A \rightarrow A+1) + \sum_f M_{if}(A \rightarrow A-1) = 1. \quad (2.9.6)$$

2.9.3. Average single-particle strength

Pure single-particle states are encountered only exceptionally. In general, the operator a_{jm}^+ or a_{jm} may lead to several or even many different states with comparable intensity. Thus the wave function constructed by coupling the target to a single particle with quantum numbers (jm) is not associated with a single eigenstate of the Hamiltonian. Rather, it is distributed over many eigenstates as a result of interactions which couple the single-particle motion to other, more complicated, degrees of freedom.

When many quantum states are populated by the particle-addition or removal process, it is convenient to define the average single-particle strength per energy interval at energy E as follows

$$P_{jm}^{(+)}(E) = \frac{1}{\Delta} \sum_{|E_f - E| < \Delta/2} |\langle \Psi_f(A+1) | a_{jm}^+ | \Psi_i(A) \rangle|^2 \quad (2.9.7)$$

$$P_{jm}^{(-)}(E) = \frac{1}{\Delta} \sum_{|E_f - E| < \Delta/2} |\langle \Psi_f(A-1) | a_{jm} | \Psi_i(A) \rangle|^2 \quad (2.9.8)$$

where Δ is an appropriately chosen averaging interval.

The sum rules (9.3), (9.5) and (9.6) respectively yield

$$\int_0^{\infty} P_{jm}^{(+)}(E) dE = \langle \Psi_i(A) | n_{jm} | \Psi_i(A) \rangle \quad (2.9.9)$$

$$\int_0^{\infty} P_{jm}^{(-)}(E) dE = \langle \Psi_i(A) | (1 - n_{jm}) | \Psi_i(A) \rangle \quad (2.9.10)$$

$$\int_0^{\infty} \{P_{jm}^{(+)}(E) + P_{jm}^{(-)}(E)\} dE = 1. \quad (2.9.11)$$

Note that in these sum rules the integration over energy extends to infinity; this points to the caution which must be exercised when using sum rules in connection with experimental data, since these only cover a limited energy domain.

Above, we have considered as fully specified the projection of the angular momentum of the transferred particle on the quantization axis. The dependence of the matrix elements on this quantity is determined by tensor algebra. "Spectroscopic factors" $S_j^{(+)}$ or $S_j^{(-)}$ are thereby related to $P_{jm}^{(+)}$ and $P_{jm}^{(-)}$. It is customary to attach part of the isospin dependence to S_j and to consider quantities conventionally denoted by $C_{\pm}^2 S_j^{(\pm)}$ where C_{\pm}^2 is a Clebsch-Gordan coefficient which corresponds to the isospin transfer.

The value of $C^2 S_j$ is extracted from experiment through the relation

$$C^2 S_j (A+1) = (\frac{d\sigma}{d\Omega})_{\text{exp}} / (\frac{d\sigma}{d\Omega})_{\text{th}}. \quad (2.9.12)$$

Here, $(d\sigma/d\Omega)_{\text{exp}}$ is the experimental differential cross section and $(d\sigma/d\Omega)_{\text{th}}$ the theoretical differential cross section usually calculated in the distorted wave Born approximation. It depends on the wave functions assumed for the projectile and the outgoing particle, on the interaction responsible for the transfer and on the optical-model potentials. As a consequence, the absolute value of a spectroscopic factor associated with an almost pure single-particle state cannot be determined with an accuracy better than 50 per cent and that of a less pure state within a factor larger than two. Relative values of the spectroscopic factors are, however, much more accurately determined.

2.10. Single-particle spreading width

Any model is an approximation of the physical reality. In the case of the independent particle model the approximation is rather extreme. It ignores the collisions of a nucleon with the others, i.e. those dynamical aspects of the nucleon motion on which we focus our attention in the present review.

Pure single-particle levels are encountered only exceptionally. They are in practice limited to a few levels near the Fermi energy in doubly closed shell nuclei plus or minus one nucleon. Most generally, it is found that the total strength corresponding to a single-particle orbital is distributed over several

states; those of them which display the larger spectroscopic factors are contained in an energy interval whose size is called the *single-particle spreading width* Γ^\downarrow .

2.10.1. Examples

Figure 2.7 indicates that the strength of the $d_{5/2}$ neutron- or proton-hole configuration is distributed over a number of states in ^{39}Ca or in ^{39}K . This distribution of the spectroscopic factors can be investigated by means of pick-up reactions on ^{40}Ca . Let us first consider the case of ^{39}K . Figure 2.16 shows the distribution of the $l = 2$ spectroscopic factors in ^{39}K , as obtained from the analysis of the $^{40}\text{Ca}(\text{d}, ^3\text{He})^{39}\text{K}$ pick-up reaction [23]. All the spectroscopic factors above 5 MeV of excitation energy are assumed to correspond to levels with $j = \frac{5}{2}^+$. The solid line represents the quantity $P_{5/2}^{(-)}(E)$ as calculated from a Gaussian average rather than from a square average as in eq. (9.8). We see that most of the large $d_{5/2}$ spectroscopic factors are contained in an energy interval of width $\Gamma^\downarrow \sim 2$ MeV. The occupation probability of the $d_{5/2}$ single-particle level as obtained from these data with the help of eq. (9.8) is $\langle n_d \rangle \sim 0.7$ [24].

Similar results are shown in fig. 2.17 for the case of the $^{40}\text{Ca}(\text{d}, \text{t})^{39}\text{Ca}$ neutron pick-up reaction [24]. The $l = 2$ spectroscopic factors of the states above 4 MeV excitation energy are believed to be associated with $5/2^+$ states in ^{39}Ca . Here, again, most of the large $d_{5/2}$ spectroscopic factors are distributed in an energy interval of width $\Gamma^\downarrow \sim 2$ MeV, centered at about 7 MeV excitation energy.

When the excitation energy in the $(A - 1)$ nucleus increases, the level density becomes so large that experimentally one can at best observe a bump in the measured distribution of the single-particle spectroscopic factors (cf. fig. 2.12). The same holds true for fixed excitation energy when A increases [25, 26]. The example of the $f_{7/2}$ proton-hole configuration in ^{89}Y is shown in fig. 2.18.

2.10.2. Physical interpretation

In the independent particle model, all the strength of a $\{n, l, j\}$ configuration should be contained in a single state of the residual nucleus. The examples shown above indicate that in practice this is an

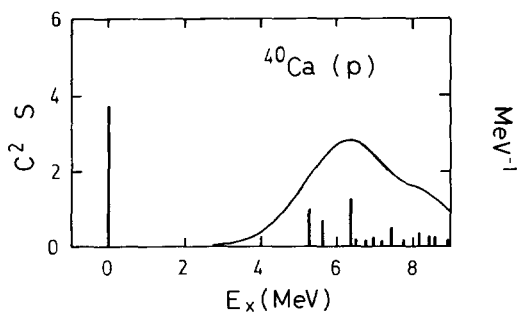


Fig. 2.16. Adapted from ref. [23]. Plot versus excitation energy (E_x) of the spectroscopic factors as measured from the $^{40}\text{Ca}(\text{d}, ^3\text{He})$ pick-up reaction. The vertical bar at $E_x = 0$ corresponds to the $(d_{3/2})^{-1}$ ground state of ^{39}K . The other bars are believed to be associated with $\frac{5}{2}^+$ levels and measure the amount of $(d_{5/2})^{-1}$ admixture. The full curve is obtained by folding the spectroscopic factors with a Gaussian of 0.7 MeV standard deviation. The scale for this curve is given at the right-hand side of the frame.

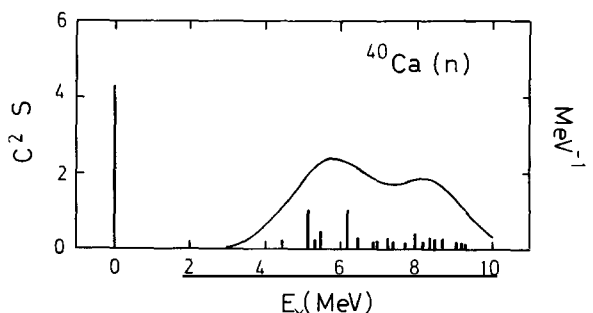


Fig. 2.17. Adapted from ref. [24]. Neutron spectroscopic factor as measured from the $^{40}\text{Ca}(\text{d}, \text{t})$ pick-up reaction. The notation is the same as in fig. 2.16.

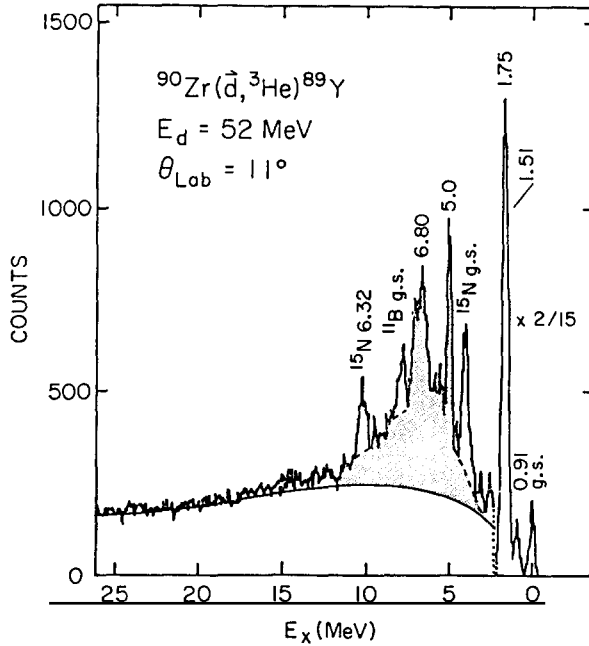


Fig. 2.18. Taken from ref. [27]. Energy spectrum of ^3He in the proton pick-up reaction $^{90}\text{Zr}(\vec{d}, ^3\text{He})^{89}\text{Y}$. The shaded area has been identified with the $f_{7/2}$ orbit from angular distribution and analysing power measurements.

idealization. This is natural, since in reality nucleons do not move totally independently of one another. They can make collisions with other nucleons, or couple to collective vibrations of the nucleus. The collective modes at low-lying excitation energy are, in spherical nuclei, surface vibrations. For example, the hole created in ^{40}Ca in a pick-up reaction can make a collision with the nuclear surface and excite the low-lying quadrupole vibration. Estimates of the strength distribution based on this coupling mechanism yield fair agreement with the observed distribution of the $d_{5/2}$ strength shown in figs. 2.16 and 2.17 [23, 24].

The existence of damping in the single-particle motion implies that on the average nucleons only stay a finite time τ in a given orbit. These states are therefore not stationary and do not have a well-defined energy. The uncertainty in the energy is called the single-particle spreading width Γ^\downarrow . It is related to the lifetime τ by the uncertainty relation

$$\Gamma^\downarrow \tau = \hbar. \quad (2.10.1)$$

2.10.3. Complex average potential

We now indicate how, in a simplified case, the effect of collisions can be included in an *average way* by adding an imaginary component to the shell-model potential.

We consider a particle moving with positive momentum k towards positive x in a one-dimensional infinite medium. Let us assume that the particle has been added at $x = 0$. For $x > 0$, the particle undergoes collisions with other particles in the medium. In analogy with optics we can describe the

wave motion in the region $x > 0$ by the function e^{ikx} where now the momentum takes a complex value

$$k = k_R + ik_1, \quad (2.10.2)$$

with $k_1 > 0$. This assumption leads to

$$\exp(ikx) = \exp(ik_R x) \cdot \exp(-k_1 x); \quad (2.10.3)$$

the amplitude decreases exponentially as x increases. One can ascribe a *mean free path* λ to the particle, defined as

$$\lambda = 1/2k_1. \quad (2.10.4)$$

The corresponding *mean lifetime* τ is given by

$$\lambda = v_g \tau, \quad (2.10.5)$$

where v_g is the group nucleon velocity.

The introduction of a complex wave number for a nucleon with energy E entails that of a *complex potential* energy. In fact, substituting (10.2) into the energy-momentum relation (6.7), it becomes necessary to replace the potential V by a complex potential $V - iW$ where

$$W = \hbar^2 k_R k_1 / m^*. \quad (2.10.6)$$

To derive this formula we have assumed $k_R \gg k_1$. Using equations (10.4), (10.5), (10.6) and the expression

$$v_g = \hbar k_R / m^* \quad (2.10.7)$$

we obtain

$$2W\tau = \hbar. \quad (2.10.8)$$

The analogy with Heisenberg's principle allows one to interpret $2W$ as an uncertainty in the particle energy and to identify it with the spreading width Γ^\downarrow of the single-particle states

$$\Gamma^\downarrow = 2W. \quad (2.10.9)$$

This relationship between the spreading width and the imaginary part of the potential will be discussed further in section 3.5.3. It can be extended to finite nuclei where W is a function of r ; then,

$$\Gamma^\downarrow = 2\langle W \rangle \quad (2.10.10)$$

where the brackets stand for an average over the nuclear volume. We note that this reasoning applies to the propagation of a hole as well as to that of a particle.

In the preceding very simple example, the introduction of an imaginary component in the average potential can account for the *global* effect of collisions, whose presence only shows up through the existence of a finite mean free path and of a finite mean lifetime. In the case of positive energies, i.e. of scattering states, the introduction of the imaginary component W corresponds to the familiar *optical model*. In fact, we have just argued that this extension of the shell model is useful at *negative* energies as well.

2.11. A simple model for the spreading of a single-particle configuration

In section 2.10, the spreading of a single-particle state was described in terms of a single quantity, namely the single-particle spreading width Γ^\downarrow . We now discuss a simple but instructive theoretical model [15, 28, 29] which enables one to investigate this spreading width in more detail. We exploit this example to make some of our earlier statements more precise, and to introduce important concepts which will be used in the following chapters. The main features of the model are illustrated in fig. 2.19.

2.11.1. The model

Let us denote by H_0 the Hamiltonian of the independent particle model for $A + 1$ nucleons, by ϕ_β its eigenstates and by E_β the corresponding eigenvalues. For simplicity, we restrict the discussion to a *finite*

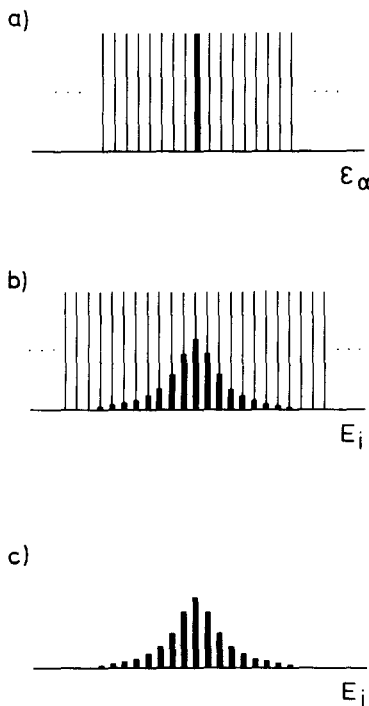


Fig. 2.19. Schematic representation of the model considered in section 2.11. The top part (a) of the figure corresponds to the unperturbed Hamiltonian, the thick bar corresponds to the single-particle state ϕ_0 , and the thin bars the complicated states ϕ_α . The thick bars in the middle part (b) of the figure show the spectroscopic factor $(C_\beta^0)^2$, i.e. the admixture probability of the single-particle state ϕ_0 into each eigenstate Ψ_i of the full Hamiltonian. Stripping experiments only probe that component $C_\beta^0 \phi_0$ of the wave function; the spectroscopic factors $(C_\beta^0)^2$ are shown in the bottom part (c) of the figure. For the purpose of illustration, the quantities $(C_\beta^0)^2$ shown in (b) and (c) have been multiplied by a factor 3.

number of bound eigenstates ($\beta = 0, 1, \dots, M$). We call ϕ_0 the single-particle configuration whose spreading we want to investigate:

$$|\phi_0\rangle = a_{jm}|A\rangle. \quad (2.11.1)$$

The other eigenstates ϕ_α ($\alpha = 1, 2, \dots, M$) are two hole-one particle, three hole-two particle, or more complicated configurations.

We call H the exact Hamiltonian. It is the sum of H_0 and of a “residual” interaction v

$$H = H_0 + v. \quad (2.11.2)$$

Let us first diagonalize H among the *complicated* configurations ($\alpha = 1, \dots, M$). For simplicity, we still denote by ϕ_α ($\alpha = 1, \dots, M$) the new complicated states and by ε_α their eigenvalues

$$\langle\phi_\alpha|H|\phi_\alpha\rangle = \varepsilon_\alpha \delta_{\alpha\alpha'}. \quad (2.11.3)$$

Note that the complicated states ϕ_α ($\alpha = 1, \dots, M$) now may contain collective components.

Let us call ε_0 the expectation value of H in the single-particle configuration ϕ_0

$$\langle\phi_0|H|\phi_0\rangle = \varepsilon_0 \quad (2.11.4)$$

and $v_{\alpha 0}$ the matrix elements of H which couple ϕ_0 to ϕ_α

$$\langle\phi_0|H|\phi_\alpha\rangle = v_{\alpha 0}. \quad (2.11.5)$$

The eigenvalues E_i and the eigenfunctions Ψ_i ($i = 0, 1, \dots, M$) of H are obtained by diagonalizing the matrix $\langle\phi_\beta|H|\phi_\beta'\rangle$,

$$|\Psi_i\rangle = \sum_{\alpha=0}^M C_\alpha^i |\phi_\alpha\rangle, \quad (2.11.6)$$

$$\langle\Psi_i|H|\Psi_j\rangle = E_i \delta_{ij}. \quad (2.11.7)$$

The eigenvalues E_i are the roots of the equation

$$E_i - \varepsilon_0 - \sum_{\alpha=1}^M \frac{v_{\alpha 0}^2}{E_i - \varepsilon_\alpha} = 0 \quad (2.11.8)$$

while the probability of finding the single-particle component ϕ_0 in the state Ψ_i is given by

$$(C_0^i)^2 = \left[1 + \sum_{\alpha=1}^M \frac{v_{\alpha 0}^2}{(E_i - \varepsilon_\alpha)^2} \right]^{-1}. \quad (2.11.9)$$

2.11.2. Average over levels

The following identity holds for *all* values of the complex variable z

$$\left\{ z - \varepsilon_0 - \sum_{\alpha=1}^M \frac{v_{\alpha 0}^2}{z - \varepsilon_\alpha} \right\}^{-1} = \sum_{i=0}^M \frac{(C_0^i)^2}{(z - E_i)}. \quad (2.11.10)$$

This can be checked by noticing that the two sides of eq. (11.10) have the same poles and residues, and vanish for large z .

Let us take the identity (11.10) at the complex value $z = E + i\Delta/2$, where Δ will be identified with an energy-averaging interval. If Δ is larger than the average distance d between two consecutive energies ε_α , $\varepsilon_{\alpha+1}$, and if one can define a smooth function $C_0^2(E')$ which represents the local average of the quantities $(C_0^i)^2$ in the energy interval $(E' - \frac{1}{2}\Delta, E' + \frac{1}{2}\Delta)$, the discrete sums can be converted into integrals:

$$\sum_{\alpha=1}^M \frac{v_{\alpha 0}^2}{E + i\Delta/2 - \varepsilon_\alpha} \approx \int_{-\infty}^{\infty} \frac{\rho(E') v^2(E') dE'}{E + i\Delta/2 - E'} \quad (2.11.11)$$

$$\sum_{i=0}^M \frac{(C_0^i)^2}{E + i\Delta/2 - E_i} \approx \int_{-\infty}^{\infty} \frac{\rho(E') C_0^2(E') dE'}{E + i\Delta/2 - E'}. \quad (2.11.12)$$

We have introduced the same density function $\rho(E')$ in both expressions since the density of the α states is close to that of the i states.

If the functions $v^2(E')$ and $C_0^2(E')$ are almost constant over an energy interval of size Δ , the integrals can be divided into their real and imaginary parts by using the property

$$\int_{-\infty}^{\infty} \frac{f(x) dx}{x - x_0 \mp i\eta} = \mathcal{P} \int_{-\infty}^{\infty} \frac{f(x)}{x - x_0} dx \pm i\pi f(x_0) \quad (2.11.13)$$

where

$$\mathcal{P} \int_a^b \frac{f(x)}{x - x_0} dx = \lim_{\delta \rightarrow +0} \left[\int_a^{x_0-\delta} \frac{f(x)}{x - x_0} dx + \int_{x_0+\delta}^b \frac{f(x)}{x - x_0} dx \right] \quad (2.11.14)$$

is the principal value integral. The content of the curly brackets on the left-hand side of (11.10) can thus be written as follows

$$E + i\frac{\Delta}{2} - \varepsilon_0 - \left[\mathcal{P} \int_{-\infty}^{\infty} \frac{v^2(E') \rho(E') dE'}{(E - E')} - i\pi v^2(E) \rho(E) \right] = (E - \tilde{E}_0) + \frac{i}{2} (\Gamma^\downarrow(E) + \Delta) \quad (2.11.15)$$

where we have introduced the definitions

$$\tilde{E}_0 = \varepsilon_0 + \mathcal{P} \int_{-\infty}^{\infty} \frac{v^2(E') \rho(E')}{(E - E')} dE', \quad (2.11.16)$$

$$\Gamma^\downarrow(E) = 2\pi v^2(E) \rho(E). \quad (2.11.17)$$

Equating the real and imaginary parts of the left- and right-hand sides of (11.10) one obtains

$$\mathcal{P} \int_{-\infty}^{\infty} \frac{C_0^2(E') \rho(E') dE'}{E - E'} = \frac{(E - \tilde{E}_0)}{(E - \tilde{E}_0)^2 + \frac{1}{4}(\Gamma(E) + \Delta)^2} \quad (2.11.18)$$

$$C_0^2(E) \rho(E) = \frac{1}{2\pi} \frac{(\Gamma^\downarrow(E) + \Delta)}{2\pi(E - \tilde{E}_0)^2 + \frac{1}{4}(\Gamma^\downarrow(E) + \Delta)^2}. \quad (2.11.19)$$

The product

$$P_0(E) = C_0^2(E) \rho(E) \quad (2.11.20)$$

is called the *strength function* and represents the probability of finding the configuration ϕ_0 (cf. eq. (11.1)) per unit energy interval. It is identical to the quantity $P^{(+)}(E)$ defined in eq. (9.7). It is expressed in terms of two functions of the energy, namely $\Gamma(E)$ and

$$\delta_0(E) = \tilde{E}_0 - \varepsilon_0 = \mathcal{P} \int_{-\infty}^{\infty} \frac{v^2(E') \rho(E')}{(E - E')} dE'. \quad (2.11.21)$$

This quantity $\delta_0(E)$ is the energy shift of the ϕ_0 state resulting from the coupling to the states α ; it is thus related to its self-energy.

The particular case where the matrix elements $v_{\alpha 0}$ are all equal to \bar{v} and where the complicated states are equally spaced with a distance D is illustrated in fig. 2.19. Then, the quantity (11.21) vanishes and the strength function reads [30]

$$P_0(E) = \frac{1}{2\pi} \frac{\Gamma^\downarrow + \Delta}{(E - \varepsilon_0)^2 + \frac{1}{4}(\Gamma^\downarrow + \Delta)^2}, \quad (2.11.22)$$

where

$$\Gamma^\downarrow = 2\pi\bar{v}^2/D \quad (2.11.23)$$

is now independent of the energy. The strength function has a Breit–Wigner shape centered around ε_0

with a full width at half-maximum equal to $\Gamma^\downarrow + \Delta$. The quantity Γ^\downarrow is identified with the spreading width of the single-particle state.

The shape of the strength function will, in general, have a more complicated energy dependence than (11.22). The centroid of the distribution in an energy interval $E_1 < E < E_2$ is defined as

$$\langle E \rangle = \int_{E_1}^{E_2} E P_0(E) dE / \int_{E_1}^{E_2} P_0(E) dE. \quad (2.11.24)$$

A number representative of the spread is provided by the second central moment σ^2 defined as

$$\sigma^2 = \int_{E_1}^{E_2} (E - \langle E \rangle)^2 P_0(E) dE / \int_{E_1}^{E_2} P_0(E) dE. \quad (2.11.25)$$

For nonsingular interactions the integrals can be extended over all energies [31]. One can then make use of the fact that

$$\int_{-\infty}^{\infty} P_0(E) dE = 1. \quad (2.11.26)$$

If the centroid of the distribution is close to the unperturbed energy of the state, i.e. $\langle E \rangle \approx \varepsilon_0$, one can show that the second moment can be expressed in terms of the square of the matrix elements according to the relation

$$\begin{aligned} \sigma^2 &= \int (E - \varepsilon_0)^2 P_0(E) dE \cong \sum_i \langle 0 | i \rangle \langle i | (H - \varepsilon_0)^2 | i \rangle \langle i | 0 \rangle \\ &= \sum_{\alpha} v_{\alpha 0}^2 \approx \int v^2(E) \rho(E) dE. \end{aligned} \quad (2.11.27)$$

This quantity can be infinite, for instance when the matrix element $v(E)$ is independent of the energy, as in the model (11.22). In practical applications one limits oneself to the central region of the structure associated with the single-particle state and considers it as a Gaussian distribution. In such an approximation one has

$$\Gamma^\downarrow \sim \sqrt{8 \ln 2} \sigma \sim 2.4 \sigma. \quad (2.11.28)$$

2.11.3. Time evolution

Let us assume that at time $t = 0$ the system is in the state ϕ_0 . The probability amplitude for finding

the system in the same state ϕ_0 at a later time $t > 0$ is given by

$$G_0(t) = i \langle \phi_0 | \exp\{-iHt/\hbar\} | \phi_0 \rangle \quad (2.11.29)$$

$$= i \sum_j (C_0^j)^2 \exp\{-iE_j t/\hbar\}. \quad (2.11.30)$$

If one replaces the sum over j by an integral over the energy and uses the expression (11.19) for $C_0^2(E)\rho(E)$, one obtains [15]

$$\begin{aligned} G_0(t) &= \frac{i}{2\pi} \int_{-\infty}^{\infty} \frac{\exp\{-iE t/\hbar\} (\Gamma^\downarrow(E) + \Delta)}{(E - \tilde{E}_0)^2 + \frac{1}{4}(\Gamma(E) + \Delta)^2} dE \\ &= -i \exp\{-i\tilde{E}_0 t/\hbar\} \exp\{-(\Gamma^\downarrow(E) + \Delta)t/2\hbar\}. \end{aligned} \quad (2.11.31)$$

For the case where the matrix elements and the density are independent of the energy, and consequently $\Gamma(E) = \Gamma^\downarrow$, the probability of finding the system in the state ϕ_0 after time t decreases exponentially with a mean lifetime $\tau = \hbar/\Gamma^\downarrow$.

2.11.4. Single-particle Green function

In the present context, the initial state $\phi_0 \equiv \phi_{nlj}$ of interest is the one which corresponds to punching a hole with quantum numbers $\{n, l, j\}$ in the ground state of the nucleus with wave function $|A\rangle$. Then, the quantity $G_{nlj}(t)$ is given by

$$G_{nlj}(t) = i \langle A | a_{nlj}^+(t) a_{nlj}(t=0) | A \rangle. \quad (2.11.32)$$

When going from eq. (11.29) to the approximation (11.31), we had to replace $(C_0^j)^2$ by its *average*. In the case of our model, the Fourier transform $G_0(E)$ of the single-particle Green function $G_0(t)$ can be obtained in closed form [32]: one has

$$G_0(E) = \langle A | a_0^+ \frac{1}{E - H} a_0 | A \rangle \quad (2.11.33)$$

$$= \left[E - \varepsilon_0 - \sum_{\alpha=1}^M \frac{v_{\alpha 0}^2}{E - \varepsilon_\alpha} \right]^{-1}. \quad (2.11.34)$$

By comparing this result with eq. (11.8), we see that *the single-particle Green function has poles at the eigenvalues of H* . This is a very general property.

2.11.5. The mass operator

The single-particle Green function can be written in the form

$$G(E) = 1/(E - \varepsilon_0 - M(E)) \quad (2.11.35)$$

where $M(E)$ is by definition the *mass operator*, also called the *self-energy*. In the case of our model, one has

$$M(E) = \sum_{\alpha} \frac{v_{\alpha 0}^2}{E - \varepsilon_{\alpha}}. \quad (2.11.36)$$

(It would be more consistent with the notation of chapter 4 to call $M(E)$ the dispersion contribution to the mass operator and to denote it by $N(E)$, since the shell-model contribution is contained in ε_0 .)

Note that the energy dependence of the mass operator arises from the coupling between the configuration ϕ_0 and the other modes ϕ_{α} .

The value $M(E + i\Delta/2)$ can be evaluated as described in eqs. (11.12)–(11.14). One gets

$$M\left(E + i\frac{\Delta}{2}\right) = \delta_0(E) - \frac{i}{2}(\Gamma(E) + \Delta). \quad (2.11.37)$$

The quantity $G(E + i\Delta/2)$ is given by

$$\langle G(E) \rangle = G(E + i\Delta/2) = 1 / \left\{ (E - \tilde{E}_0) + \frac{i}{2}(\Gamma(E) + \Delta) \right\}. \quad (2.11.38)$$

Its Fourier transform reads

$$\langle G(t) \rangle = \theta(t) \exp\left[-\frac{(\Gamma(E) + \Delta)}{2\hbar} t - i \frac{\tilde{E}_0 t}{\hbar} \right]. \quad (2.11.39)$$

We thus recover the result (11.22). We retain from this example that the quantities $M(E + i\Delta/2)$ and $G(E + i\Delta/2)$ are of interest when considering the energy average of the distribution of spectroscopic factors. This was emphasized and discussed by Engelbrecht and Weidenmüller [32] in a more general framework.

2.12. Hindsight

In the independent particle model, the nucleons are assumed to move independently of one another in some average potential. It turns out that it is not possible to reproduce the essential features of the experimental data on bound and scattering single-particle states if one assumes that this potential is local and independent of energy. If one takes a local potential with a fixed geometry and only lets its depth V_0 be a function of energy, one finds that the effective mass m^* , defined by the relation

$$m^*/m = 1 - dV_0/dE \quad (2.12.1)$$

is a function of energy. In medium-weight and heavy nuclei, one has $m^*/m \approx 0.7$ in the case of scattering states ($E > 10$ MeV) and of deeply bound states ($E < -20$ MeV), while $m^*/m \approx 1$ near the separation energy.

Another characteristic shown by the experimental data is that the excited states of nuclei with one

nucleon outside closed shells are usually not pure single-particle states. One observes that the main part of the single-particle strength, as measured by the spectroscopic factors, is spread over an energy interval called the single-particle spreading width. The magnitude of this quantity is about 2 MeV for weakly bound states ($|\epsilon - \epsilon_F| \lesssim 10$ MeV), and increases to several MeV further away from the Fermi surface.

The spreading of single-particle states is a consequence of the fact that actually the nucleons do not move independently of one another. They can make collisions among themselves, or inelastically against the nuclear surface. This is responsible for the existence of a spreading width and leads to the necessity of introducing an imaginary component W in the average potential. The two quantities are related since $\Gamma^\downarrow = 2\langle W \rangle$.

As a nucleon moves through the nucleus it feels the presence of the other nucleons whose configurations change as time proceeds. It takes some time for this information to be fed back on the nucleon. This renders the average potential nonlocal in time. A time-dependent operator can always be transformed into an energy-dependent operator by taking its Fourier transform. Hence, the empirical energy dependence of $V_0(E)$ as measured by the effective mass might be taken as a direct reflection of the nonlocality in time of the average field. This is not the full story. Indeed, the average field is nonlocal in space; this also gives rise to an energy dependence in the empirical local shell-model potential.

3. Single-particle motion in uniform systems

3.1. Introduction

The present chapter is devoted to the study of particle motion through a Fermi gas, especially to the motion of nucleons through nuclear matter. The latter is a hypothetical uniform medium with equal number of neutrons and protons, and with the Coulomb interaction turned off. Some reasons for considering this idealized system are:

(i) All relevant physical quantities are smooth functions of energy, and averages need not be taken. In particular, this holds true for the mass operator $M(E)$. We have seen in the simple model discussed in section 2.11 that, for finite nuclei, $M(E)$ has poles at discrete, real values of E ; a smooth behaviour of M as a function of the energy was obtained by analytic continuation into the complex E -plane. It was shown that the replacement of E by $E + i\Delta/2$ corresponds to an energy averaging over an interval Δ . In nuclear matter, the particle and hole states are represented by plane waves; they are identified by a continuous variable $\hbar k$ which is the linear momentum of the single-particle states. The single-particle energy spectrum is also continuous, and it is thus not necessary to perform local averages over the energy to reveal the smooth energy dependence of the quantities of interest.

(ii) Translational invariance entails that the spatial non-locality of the average nuclear field is simple in nuclear matter.

(iii) Reliable methods for handling the strong short-range part of the nucleon-nucleon interaction have been developed for normal infinite systems in the framework of either perturbation theory or of variational approaches.

(iv) Several infinite Fermi systems exist in nature (liquid ^3He , electron gas, neutron stars).

(v) Many concepts and techniques can more easily be introduced and investigated in the case of uniform systems and then be extended to “finite” nuclei.

(vi) The usefulness of the shell model lies in the fact that the average nucleon–nucleus potential is a smooth function of the mass number A . It thus makes sense to take the limit $A \rightarrow \infty$. Although nuclear matter lacks important degrees of freedom directly connected with the finite size of nuclei, in particular surface vibrations, we shall see that the dynamical content of the shell model is *qualitatively* similar in the two cases.

Many recent reviews of nuclear matter theory exist, see e.g. [33] and references quoted therein. Moreover, most of the concepts used below are described in textbooks, e.g. [34, 35]. Hence, we mainly emphasize the physical meaning of the various quantities and of the approximations, omitting in many cases references to the original papers.

3.2. Definitions

The quantities defined in the present section correspond to an exact description of the ground state of nuclear matter and of the excited states obtained by adding one nucleon to this ground state or by taking out one nucleon from it. The quantities introduced here thus describe the “motion” of an actual nucleon (particle or hole) through the medium. This motion is quite complicated. Hence the quantities and the exact properties listed in the present section have little direct relationship with most available numbers extracted from the analyses of the experimental data, which only exhibit global aspects of the nucleon motion. The experimental data are usually interpreted in the framework of either the independent particle model, or of the dynamical shell model. These models emerge when approximations to the exact quantities are introduced. In order to learn the nature of the approximations involved and to be aware of the limitations that result from those, we shall compare the model quantities with the exact ones. This is the main motivation for the present section. More details and proofs can be found in [36] and references quoted therein.

3.2.1. Momentum distribution in the ground state

Let us first consider the *free Fermi gas*, i.e. an ideal system in which the particles are not interacting with one another but are moving in some average external potential field. Then, the ground state wave function ψ_0 is a Slater determinant built with plane waves $\exp(i\mathbf{k} \cdot \mathbf{r})$ in which all momentum states are occupied from $k = 0$ up to the *Fermi momentum* k_F . Henceforth, we set $\hbar = 1$. The momentum distribution in the free Fermi gas is thus given by

$$n_0(k) = \langle \psi_0 | a^\dagger(\mathbf{k}) a(\mathbf{k}) | \psi_0 \rangle \quad (3.2.1)$$

$$= \theta(k_F - k). \quad (3.2.2)$$

The step function $n_0(k)$ is represented by the dashed line in fig. 3.1. The Fermi momentum is related to the density ρ of the medium by

$$\rho = \frac{2}{3\pi^2} k_F^3, \quad (3.2.3)$$

where the spin degeneracy has been considered. The factor 2 should be included only when two types of particles (e.g. protons and neutrons) exist.

We denote by $|\psi\rangle$ the *exact* normalized ground state. It includes the effect of correlations between

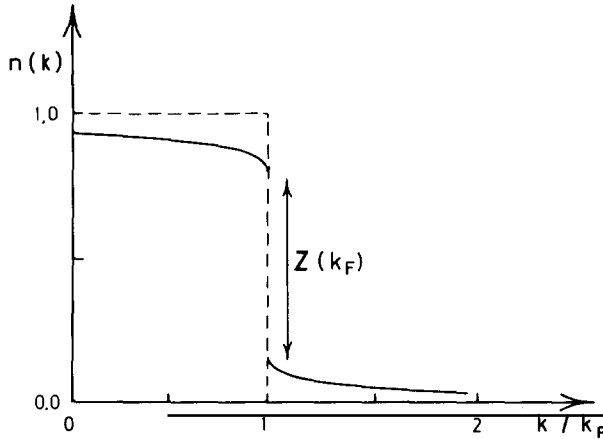


Fig. 3.1. Sketch of the momentum distribution of the nucleons in a free (dashes) and in a correlated (full curve) normal Fermi system.

the particles. The average momentum distribution in this correlated ground state is given by

$$n(k) = \langle \psi | a^\dagger(k) a(k) | \psi \rangle ; \quad (3.2.4)$$

it only depends upon $k = |\mathbf{k}|$. A typical shape for $n(k)$ is given by the full drawn curve in fig. 3.1. It can be shown that $n(k)$ is discontinuous at k_F for all *normal* Fermi liquids [37, 38]

$$n(k_F - 0) - n(k_F + 0) = Z(k_F) . \quad (3.2.5)$$

3.2.2. Hole part of the Green function

Let us create at time t , a hole with momentum \mathbf{k} inside the correlated ground state. The resulting state

$$|\phi(\mathbf{k}; t)\rangle = a(\mathbf{k}; t)|\psi\rangle , \quad (3.2.6)$$

is not normalized to unity since

$$\langle \phi(\mathbf{k}; t) | \phi(\mathbf{k}; t) \rangle = n(k) . \quad (3.2.7)$$

The probability amplitude of finding a hole with the same momentum \mathbf{k} in the correlated ground state at a time $t' > t$ is given by

$$\mathcal{G}_h(k; t' - t) = +i \langle \psi | a^\dagger(k; t') a(k; t) | \psi \rangle \theta(t' - t) . \quad (3.2.8)$$

Here we have introduced the step function $\theta(t' - t)$ so that $\mathcal{G}_h(k; t' - t)$ is also defined (and equal to zero) for $t' < t$. We shall call $\mathcal{G}_h(k; t' - t)$ the *hole part of the one-body Green function* (see eq. (2.11.32)).

The Fourier transform of $\mathcal{G}_h(k; t' - t)$ with respect to $t' - t$ reads

$$\mathcal{G}_h(k; \omega) = \langle \psi | a^\dagger(k) (\omega - H - i\eta)^{-1} a(k) | \psi \rangle, \quad (3.2.9)$$

where H is the full Hamiltonian of the system.

3.2.3. Hole spectral function

In general the state $a(k)|\psi\rangle$ is not an eigenstate of the system with $(A - 1)$ particles. Rather, it is distributed over the eigenstates $|\psi_{E'}^{(A-1)}\rangle$ of H according to

$$a(k)|k\rangle = \int_{-\infty}^{\varepsilon_F} |\psi_{E'}^{(A-1)}\rangle \langle \psi_{E'}^{(A-1)}| a(k) | \psi \rangle dE' \quad (3.2.10)$$

where the *Fermi energy* ε_F is the maximum value of the energy of the $(A - 1)$ system and where $\psi_{E'}^{(A-1)}$ is normalized to a delta function,

$$\langle \psi_{E'}^{(A-1)} | \psi_{E''}^{(A-1)} \rangle = \delta(E' - E'').$$

Substituting eq. (2.10) in eq. (2.9), we obtain the following *Lehmann representation* of the hole Green function

$$G_h(k; \omega) = \int_{-\infty}^{\varepsilon_F} \frac{S_h(k; \omega')}{\omega - \omega' - i\eta} d\omega', \quad (3.2.11a)$$

where the *hole spectral function* is given by

$$S_h(k; \omega') = |\langle \psi_{\omega'}^{(A-1)} | a(k) | \psi \rangle|^2. \quad (3.2.11b)$$

The quantity $S_h(k; \omega) d\omega$ is equal to the joint probability of removing of a nucleon with momentum k from the correlated ground state, and of finding the resulting system (with $(A - 1)$ nucleons) with an energy contained in the interval $(\omega, \omega + d\omega)$. The excitation energy of the $(A - 1)$ system is $|\omega - \varepsilon_F|$. The quantity $S_h(k; \omega)$ differs from zero even for $k > k_F$, although S_h is the hole spectral function. This is because momentum states with $k > k_F$ are partially occupied in the correlated ground state, see fig. 3.1. The hole spectral function $S_h(k; \omega)$ vanishes for $\omega > \varepsilon_F$.

3.2.4. Centroid energy

We just saw that the energy of a hole state is distributed over a wide energy range, which can extend from $-\infty$ to ε_F . The centroid energy for the hole state of momentum k is defined by

$$\langle \epsilon_h(k) \rangle = \int_{-\infty}^{\varepsilon_F} \omega S_h(k; \omega) d\omega / \int_{-\infty}^{\varepsilon_F} S_h(k; \omega) d\omega. \quad (3.2.12)$$

This is also referred to as the *mean removal energy* [39, 40]. The denominator on the right-hand side of eq. (2.12) can be shown to be equal to the average number of nucleons with momentum k (see eq. (2.4))

$$n(k) = \int_{-\infty}^{\epsilon_F} S_h(k; \omega) d\omega. \quad (3.2.13)$$

In nuclear matter (and in nuclei), the centroid energy is usually larger in absolute magnitude than what is empirically called the single-particle energy (section 3.4.2). The reason is that nuclear forces are very strong at short distances. This gives rise to short-range correlations which produce a long tail in $S_h(k; \omega)$ for $\omega \rightarrow -\infty$. This tail is very difficult to measure, and so is consequently the mean removal energy. From eq. (2.13) and by making use of the conservation of the number of particles, one can obtain the following sum rule

$$\int_0^{\infty} k^2 dk n(k) = \int_0^{\infty} k^2 dk \int_{-\infty}^{\epsilon_F} S_h(k; \omega) d\omega = \frac{1}{3} k_F^3. \quad (3.2.14)$$

In a finite nucleus, the measurement of the hole spectral function $S_h(k; \omega)$ for all values $-\infty < \omega < \epsilon_F$ and for all $0 < k < \infty$ should enable one to fulfill a sum rule analogous to (2.14) [41]. If it is not fulfilled, this implies that the analysis of the data is incorrect and/or that the experiment only yields too little information on $S_h(k; \omega)$ for $k > k_F$ or for large $|\omega|$.

When only two-body forces exist, the centroid energy (2.12) presents the interest of being connected with the total energy B of the system by [39, 42]

$$B = \frac{1}{2} \sum_k n(k) \left\{ \frac{k^2}{2m} + \langle \varepsilon_h(k) \rangle \right\}. \quad (3.2.15)$$

Attempts to detect a violation of the sum rule (2.15), i.e. the existence of three-body forces, have failed [43, 44], mainly because of the lack of knowledge of $n(k)$ for $k > k_F$ and of $S_h(k; \omega)$ for large $|\omega|$. For a semi-empirical application of eq. (2.15), see ref. [45].

3.2.5. Particle part of the Green function

The particle part of the one-body Green function is defined by

$$G_p(k; t' - t) = -i \langle \psi | a(k, t') a^\dagger(k, t) | \psi \rangle \theta(t' - t). \quad (3.2.16)$$

It describes the probability amplitude of finding at time t' a nucleon with momentum k on top of the correlated ground state, knowing that it had been created at an earlier time t .

Most of the relations and concepts introduced in the case of the hole Green function can be transferred to the particle Green function.

The Lehmann representation is

$$\mathcal{G}_p(k; \omega) = \int_{\epsilon_F}^{\infty} d\omega' \frac{S_p(k; \omega')}{\omega - \omega' + i\eta}, \quad (3.2.17)$$

where the *particle spectral function* reads

$$S_p(k; \omega') = |\langle \psi_{\omega'}^{(A+1)} | a^\dagger(k) | \psi \rangle|^2. \quad (3.2.18)$$

The quantity $S_p(k; \omega) d\omega$ measures the joint probability of adding a nucleon with momentum k to the correlated ground state and of finding the energy of the resulting system (with $(A+1)$ nucleons) contained in the interval $(\omega, \omega + d\omega)$. The excitation energy of the state $\psi_{\omega}^{(A+1)}$ is equal to $\omega - \epsilon_F$.

The following sum rule holds

$$\oint_{-\infty}^{\epsilon_F} S_h(k; \omega) d\omega + \int_{\epsilon_F}^{\infty} S_p(k; \omega) d\omega = 1; \quad (3.2.19)$$

it is equivalent to eq. (2.11.26). Equations (2.13) and (2.19) yield

$$\int_{\epsilon_F}^{\infty} d\omega S_p(k; \omega) = 1 - n(k). \quad (3.2.20)$$

In the case of a hard-core interaction, the quantity

$$\int_{\epsilon_F}^{\infty} \omega S_p(k; \omega) d\omega \quad (3.2.21)$$

diverges [46]. This quantity is thus quite sensitive to the short-range behaviour of the interaction and one should avoid to relate it to observables as was proposed in ref. [47] for instance.

3.2.6. Time-ordered Green function

The time-ordered one-body Green function, or for short the *Green function*, is defined by

$$\mathcal{G}(k; t' - t) = \begin{cases} \mathcal{G}_p(k; t' - t) & \text{for } t' > t, \\ \mathcal{G}_h(k; t - t') & \text{for } t' < t. \end{cases} \quad (3.2.22a)$$

If $\mathcal{G}(k; \omega)$ denotes its Fourier transform, one has

$$\mathcal{G}(k; \omega) = \mathcal{G}_h(k; \omega) + \mathcal{G}_p(k; \omega). \quad (3.2.22b)$$

This quantity thus combines the information for the propagation of a hole as well as of a particle. The full *spectral function* given by

$$S(k; \omega) = S_p(k; \omega) + S_h(k; \omega) \quad (3.2.23)$$

fulfills the sum rule (2.19).

3.2.7. Coordinate space representation

In coordinate space representation, the one-body Green function $G(\mathbf{r}, \mathbf{r}'; t, t')$ is given by

$$\mathcal{G}(k; \omega) = \int d^3(\mathbf{r} - \mathbf{r}') \int d(t - t') \exp[-ik \cdot (\mathbf{r} - \mathbf{r}')] \exp[i\omega(t - t')] G(\mathbf{r}, \mathbf{r}'; t, t'). \quad (3.2.24a)$$

In a uniform medium, G only depends upon the two quantities $|\mathbf{r} - \mathbf{r}'|$ and $t' - t$. One has

$$G(\mathbf{r}, \mathbf{r}'; t, t') = \begin{cases} -i \langle \psi | a(\mathbf{r}, t) a^\dagger(\mathbf{r}', t') | \psi \rangle & \text{for } t > t', \\ i \langle \psi | a^\dagger(\mathbf{r}', t') a(\mathbf{r}, t) | \psi \rangle & \text{for } t < t'. \end{cases} \quad (3.2.24b)$$

This exhibits that \mathcal{G} describes the propagation of a hole from a location \mathbf{r} at time t to a location \mathbf{r}' at time $t' > t$, and of a particle from (\mathbf{r}', t') to (\mathbf{r}, t) with $t > t'$. For the following, it is important to keep in mind that the variables k and $|\mathbf{r} - \mathbf{r}'|$ correspond to one another in a Fourier transformation. Similarly for the variables ω and $t - t'$.

3.2.8. Mass operator

In the example discussed in section 2.11, the mass operator $M(E)$ plays the role of a potential energy which is added to the energy ε_0 of the uncoupled single-particle state ϕ_0 . Similarly, one can introduce the mass operator $\mathcal{M}(k; \omega)$ through the relation

$$\mathcal{G}(k; \omega) = \frac{1}{\omega - k^2/2m - \mathcal{M}(k; \omega)}. \quad (3.2.25)$$

The quantity $\mathcal{M}(k; \omega)$ can be identified with the potential energy felt by a nucleon with momentum k and frequency ω .

This interpretation of $\mathcal{M}(k; \omega)$ will be discussed in detail in chapter 4. Here, we anticipate the main results. In a finite system and in coordinate space, the mass operator is a function of \mathbf{r} , \mathbf{r}' and ω . When it is inserted in a one-body Schrödinger equation, the mass operator $\mathcal{M}(\mathbf{r}, \mathbf{r}'; \omega)$ yields the exact value of the elastic scattering phase shift at the energy $\omega > 0$ [48, 49]. This confirms that $\mathcal{M}(k; \omega)$ can be identified with the nucleon-nucleus potential in the case of nuclear physics, or with the electron-atom potential in the case of atomic physics (see e.g. [50]). In what follows, we list some properties of $\mathcal{M}(k; \omega)$. Note that $\mathcal{M}(k; \omega)$ coincides also with the self-energy of the nucleon $(k; \omega)$. The equation which determines the poles of (2.25) is known as the Dyson equation.

The mass operator is a complex quantity. We shall write it in the form

$$\mathcal{M}(k; \omega) = \mathcal{V}(k; \omega) - i \mathcal{W}(k; \omega), \quad \text{for } \omega > \varepsilon_F, \quad (3.2.26)$$

$$\mathcal{M}(k; \omega) = \mathcal{V}(k; \omega) + i \mathcal{W}(k; \omega), \quad \text{for } \omega < \varepsilon_F. \quad (3.2.27)$$

The function

$$\Sigma(k; \omega) = \mathcal{V}(k; \omega) + i \mathcal{W}(k; \omega) \quad (3.2.28)$$

is analytic in the whole ω -plane except on the real axis, where it has a cut [51, 76]. One has $\mathcal{W}(k; \omega) \geq 0$ for all values of ω .

The imaginary part vanishes when ω approaches ε_F , according to [51, 52]

$$\mathcal{W}(k; \omega) \sim (\omega - \varepsilon_F)^2, \quad (3.2.29)$$

where the Fermi energy ε_F is the root of the equation

$$\varepsilon_F = k_F^2/2m + \mathcal{M}(k_F; \varepsilon_F) = k_F^2/2m + \mathcal{V}(k_F; \varepsilon_F). \quad (3.2.30)$$

At equilibrium in a self-bound system, the Fermi energy is equal to the average binding energy per nucleon

$$B/A = \varepsilon_F. \quad (3.2.31)$$

Making use of eqs. (2.11a), (2.17) and (2.23), one obtains the following expression for the full spectral function

$$S(k; \omega) = \pi^{-1} \frac{\mathcal{W}(k; \omega)}{[\omega - k^2/2m - \mathcal{V}(k; \omega)]^2 + [\mathcal{W}(k; \omega)]^2}. \quad (3.2.32)$$

In view of the behaviour (2.29), one has

$$S(k; \omega) \sim (\omega - \varepsilon_F)^2 \quad (3.2.33)$$

when ω is close to the Fermi energy ε_F . The spectral function in the cases $k > k_F$ and $k < k_F$ is sketched in fig. 3.2.

Finally, it can be proved that in the case of nonsingular interactions, the following dispersion relation holds

$$\mathcal{V}(k; \omega) = V_{HF}(k) + \frac{\mathcal{P}}{\pi} \int_{-\infty}^{\infty} d\omega' \frac{\mathcal{W}(k; \omega')}{\omega - \omega'}. \quad (3.2.34)$$

Here, $V_{HF}(k)$ is independent of frequency and is equal to the Hartree–Fock single-particle field. This quantity is infinite in the case of a singular (e.g. a hard core) particle–particle interaction; one should then use “subtracted” dispersion relations. This will be discussed in sections 3.14 and 3.17. The dispersion relation (2.34) derives from the property that $\Sigma(k; \omega)$ is analytic [51, 76].

3.2.9. Summary

The Green function $\mathcal{G}(k; t' - t)$ describes the propagation from time t to time t' of a nucleon (particle

or hole) with momentum k on top of the exact (correlated) ground state of the system. It is customary to work with the Fourier transform $\mathcal{G}(k; \omega)$ which depends on the nucleon momentum k and on its frequency ω .

The mass operator $\mathcal{M}(k; \omega)$, which is a complex quantity, can be identified with the potential felt by a nucleon with momentum k and frequency ω . A Fourier transform over k yields the operator $\mathcal{M}(|\mathbf{r} - \mathbf{r}'|; \omega)$ which is nonlocal in coordinate space. A Fourier transform over ω yields the operator $\mathcal{M}(k; t' - t)$ which is nonlocal in time, see eq. (2.0.1). For the following, it is essential to keep in mind that the momentum dependence is associated with nonlocality in space, while the frequency dependence is associated with nonlocality in time.

For a particle-particle interaction which is not singular, the following dispersion relation holds

$$\mathcal{V}(k; \omega) = V_{HF}(k) + \frac{\mathcal{P}}{\pi} \int_{-\infty}^{\infty} d\omega' \frac{\mathcal{W}(k; \omega')}{\omega - \omega'} \quad (3.2.35)$$

where \mathcal{P} refers to a principal value integral and $V_{HF}(k)$ is the Hartree-Fock field. For $\omega > \varepsilon_F$, the spectral function $S(k; \omega)$ has the property that $S(k; \omega) d\omega$ is equal to the joint probability of being able to add to the correlated ground state a nucleon with momentum k and of finding that the energy of the resulting system with $(A + 1)$ nucleons is contained in the interval $(\omega, \omega + d\omega)$. For $\omega < \varepsilon_F$, the quantity $S(k; \omega) d\omega$ is equal to the joint probability of being able to extract from the correlated ground state a nucleon with momentum k and of finding that the energy of the resulting system with $(A - 1)$ nucleons is contained in the interval $(\omega, \omega + d\omega)$.

3.3. The independent particle model

In the independent particle model one assumes that each nucleon moves in a potential $U(k)$ which may be momentum- (or velocity-) dependent. Although this potential results from the presence of the other nucleons, we can consider it as an external potential insofar as the nucleon moves in this field without colliding with the other nucleons.

In this approximation, each nucleon has a well-defined energy, namely

$$e_0(k) = k^2/2m + U(k). \quad (3.3.1)$$

As a consequence, the spectral function is given by

$$S_0(k; \omega) = \delta(\omega - e_0(k)), \quad (3.3.2)$$

which expresses the fact that k and ω are no longer independent variables, since they are connected through the energy-momentum relationship (3.1).

In the ground state the system is a free Fermi gas whose momentum distribution is given by the step function

$$n_0(k) = \theta(k_F - k), \quad (3.3.3)$$

while the Fermi energy is related to the Fermi momentum through

$$\varepsilon_F^{(0)} = e_0(k_F). \quad (3.3.4)$$

The Green function (2.22b) becomes

$$\mathcal{G}_0(k; \omega) = \frac{n_<(k)}{\omega - e_0(k) - i\eta} + \frac{n_>(k)}{\omega - e_0(k) + i\eta} \quad (3.3.5)$$

where

$$n_<(k) \begin{cases} = 1 & \text{if } k < k_F, \\ = 0 & \text{if } k > k_F; \end{cases} \quad (3.3.6)$$

$$n_>(k) \begin{cases} = 0 & \text{if } k < k_F, \\ = 1 & \text{if } k > k_F. \end{cases} \quad (3.3.7)$$

Its Fourier transform for $k > k_F$ reads

$$\mathcal{G}_0(k; t) = -i \exp[-i e_0(k) t] \theta(t). \quad (3.3.8)$$

Equation (2.15) shows that the binding energy of the system is equal to

$$B_0 = \frac{1}{2} \sum_k n_<(k) \left[\frac{k^2}{2m} + e_0(k) \right]. \quad (3.3.9)$$

By definition the mass operator is given by

$$\mathcal{M}_0(k; \omega) = U(k). \quad (3.3.10)$$

It is real and does not display any dependence on ω ; the dispersion relation (2.34) shows that one of these two properties entails the other. We shall see in section 3.7 that the Hartree–Fock potential is like $U(k)$, i.e. it is independent of ω and real. Hence, the Hartree–Fock approximation corresponds to an independent particle model in which collisions are neglected. In this sense, it is a *static* model.

Collisions lead to an ω -dependence in the mass operator. Then, the mass operator becomes complex and the spectral function no longer reduces to a delta function. Since, however, we know that the independent particle approximation is a fairly good starting point, the quantities predicted by the independent particle model must retain some of the features displayed by the true quantities. For instance, the spectral function displays a peak instead of being a delta function, compare figs. 3.2 and 3.3.

The dynamical shell model or quasiparticle model discussed in the next section aims at the description of only the peak of the spectral function. The investigation of the full shape of the spectral function or, equivalently of the mass operator $\mathcal{M}(k; \omega)$ as a function of k and ω , lies outside the scope of a dynamical description of single-particle motion in terms of average potentials. It is nevertheless within reach of some experiments in which a nucleon can be added or knocked out with an energy independent of its momentum, as in $(e, e'p)$ reactions or in stripping reactions which lead to unbound residual states.

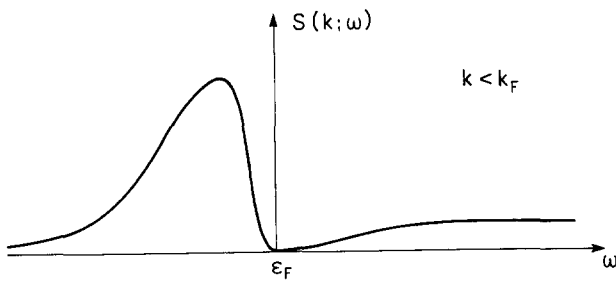
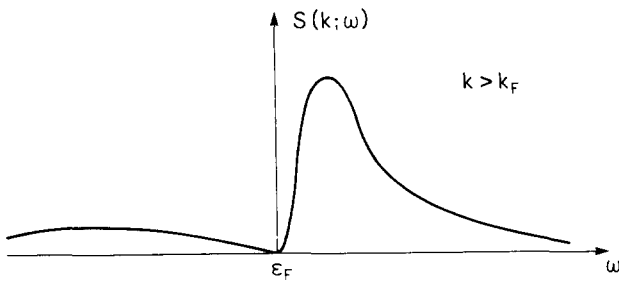


Fig. 3.2. Sketch of the spectral function $S(k; \omega)$ in the cases $k > k_F$ (upper part) and $k < k_F$ (lower part).

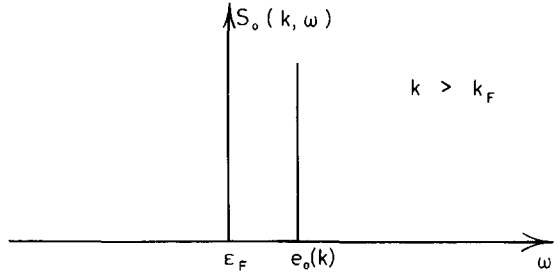


Fig. 3.3. Spectral distribution in the independent particle model for $k > k_F$ (upper part) and for $k < k_F$ (lower part). The vertical line represents the delta function $\delta(\omega - \epsilon_0(k))$.

3.4. Quasiparticle approximation

In the independent particle model, the nucleon has a well-defined energy. A particle which is created (or annihilated) with momentum k at time $t = 0$ has unit probability of keeping the same momentum k at all subsequent times. This is expressed by the fact that the modulus of the corresponding time-dependent one-body Green function is equal to unity, see eq. (3.8). When collisions are taken into account, the modulus of the Green function is expected to decrease with increasing time. The quasi-particle approximation consists in assuming that this decrease is exponential. This assumption leads to the *optical model* in nuclear reaction theory.

3.4.1. The optical model

In the optical model (OM), the particle part of the Green function is approximated by the expression (see eq. (3.8))

$$\mathcal{G}_p^{(OM)}(k; t) = -i e^{-i e(k)t} e^{-t/2\tau(k)} n_>(k) \theta(t), \quad (3.4.1)$$

where $e(k)$ is defined by the relation (4.5) below and where we have included the possibility that the lifetime τ (see section 2.10.3) may depend upon the momentum k . By taking a Fourier transform over t , we obtain

$$\mathcal{G}_p^{(OM)}(k; \omega) = \frac{n_>(k)}{\omega - e(k) + iW(k)}, \quad (3.4.2)$$

where $W(k)$ is related to $\tau(k)$ by (see eq. (2.10.8))

$$W(k) = [2 \tau(k)]^{-1}. \quad (3.4.3)$$

The optical model Green function (4.2) is very similar to the independent particle model Green function

$$\mathcal{G}_p^{(0)}(k; \omega) = \frac{n_>(k)}{\omega - e_0(k) + i\eta}. \quad (3.4.4)$$

In order to exhibit the main difference between the two models, let us define a real potential $V(k)$ by

$$V(k) = e(k) - k^2/2m. \quad (3.4.5)$$

Then eqs. (4.2) and (4.4) become

$$\mathcal{G}_p^{(\text{OM})}(k; \omega) = \frac{n_>(k)}{\omega - k^2/2m - V(k) + iW(k)}, \quad (3.4.6)$$

$$\mathcal{G}_p^{(0)}(k; \omega) = \frac{n_>(k)}{\omega - k^2/2m - U(k) + i\eta}. \quad (3.4.7)$$

The quantity

$$M(k) = V(k) - iW(k) \quad (3.4.8)$$

is the *optical-model potential*. In the optical model, the effect of collisions is thus taken into account by the introduction of an imaginary component in the potential energy. We note that $M(k)$ cannot be directly identified with the mass operator $\mathcal{M}(k; \omega)$ of eq. (2.26), since the latter quantity depends upon two variables. However, we shall see that $M(k)$ can be constructed from $\mathcal{M}(k; \omega)$ by taking into account the energy-momentum relation (4.12) below.

The spectral function of the optical model can be obtained from eqs. (2.17) and (4.6). It reads

$$S^{(\text{OM})}(k; \omega) = \frac{1}{\pi} \frac{W(k)}{[\omega - e(k)]^2 + [W(k)]^2} n_>(k). \quad (3.4.9)$$

Notice the close analogy with eq. (2.11.22). In the optical model, the energy of a nucleon with momentum k is thus distributed according to a Breit-Wigner law, centred on the quasiparticle energy $e(k)$ and with a full width at half-maximum given by $2 W(k)$.

3.4.2. Quasiparticle pole

The empirical success of the optical model demonstrates that it is a good approximation. Hence, we should be able to derive it by making suitable approximations on the quantities defined in section 3.2. Let us first write eq. (4.6) in the form

$$\mathcal{G}_p^{(\text{OM})}(k; \omega) = \frac{1}{\omega - k^2/2m - M(k)}, \quad (3.4.10)$$

where we have dropped the index p since the propagation of a hole can be treated on exactly the same footing as that of a particle. Equation (4.10) shows that the optical-model Green function has a pole (with residue unity) in the complex ω -plane located at $\omega = k^2/2m + M(k)$.

Since the optical model yields an accurate description of the experimental data, one can assume that the exact Green function (2.25) has a pole close to the real ω -axis. This pole is a root of the equation

$$\omega = k^2/2m + \mathcal{M}(k; \omega). \quad (3.4.11)$$

It is convenient to expand all quantities in the denominator on the right-hand side of eq. (2.25) in the vicinity of the root $\omega = E(k)$ of the following energy-momentum relation, which only involves real quantities

$$E = k^2/2m + \mathcal{V}(k; E); \quad (3.4.12)$$

$E(k)$ is real and is called the *quasiparticle energy* of the nucleon with momentum k . We thus write

$$\mathcal{V}(k; \omega) \approx V^{\text{NL}}(k) + [\omega - E(k)] [\partial \mathcal{V}(k; \omega)/\partial \omega]_{\omega=E(k)} \quad (3.4.13)$$

where we introduced the function

$$V^{\text{NL}}(k) = \mathcal{V}(k; E(k)). \quad (3.4.14)$$

It is appropriate to discuss our notation. The mass operator $\mathcal{M}(k; \omega)$ is a function of the two variables k and ω . We have seen that these are associated with different physical entities. Indeed, the dependence on k carries (through Fourier transformation) the information about the nonlocality in space of the single-particle field, while the dependence upon ω arises from its nonlocality in time. However, the optical-model potential only aims at the description of that part of the nucleon wave packet whose amplitude decays approximately exponentially in time. We shall see that this limited aim only requires the knowledge of $\mathcal{M}(k; \omega)$ and of its first derivatives at ω equal to the root $E(k)$ of the energy-momentum relation (4.12). In the quasiparticle approximation, the relation (4.12) can be used to eliminate the explicit dependence of $\mathcal{V}(k; E)$ upon E , as we did in eq. (4.14). We could as well have used (4.12) to eliminate the explicit dependence of $V(k; E)$ upon k ; this will be made in eq. (5.8) below. Henceforth, we shall always reserve the latter E to denote the quasiparticle energy, i.e. the quantity which is related to k by the energy-momentum relation (4.12). Hence, k and E are *not* independent of one another, as opposed to k and ω .

If the ω -dependence of $\mathcal{V}(k; \omega)$ is smooth, one can write the following approximate expression for the Green function (2.25):

$$\mathcal{G}(k; \omega) \approx \frac{Z(k)}{\omega - k^2/2m - V^{\text{NL}}(k) + i Z(k) W^{\text{NL}}(k)} + \mathcal{G}^{\text{B}}(k; \omega), \quad (3.4.15)$$

where the superscript B in \mathcal{G}^{B} refers to a “background” contribution, while

$$[Z(k)]^{-1} = [1 - \partial \mathcal{V}(k; \omega)/\partial \omega]_{\omega=E(k)}, \quad (3.4.16)$$

and

$$W^{\text{NL}}(k) = \mathcal{W}(k; E(k)). \quad (3.4.17)$$

Comparing eq. (4.6) with eq. (4.15), we see that the quasiparticle approximation essentially corresponds to replacing the Green function by the pole term on the right-hand side of eq. (4.15). A residue $Z(k)$ now appears which, in general, differs from unity in contrast to eq. (4.6).

Neglecting the background term \mathcal{G}^B on the right-hand side of eq. (4.15), we get the following quasiparticle approximation for the spectral function

$$S^{\text{QP}}(k; \omega) = \pi^{-1} \frac{Z^2(k) W^{\text{NL}}(k)}{[\omega - k^2/2m - V^{\text{NL}}(k)]^2 + [Z(k) W^{\text{NL}}(k)]^2}. \quad (3.4.18)$$

This function is represented by the dashed curves in fig. 3.4. It corresponds to the assumption that if a nucleon with momentum k is taken out (or is added to) the ground state, the energy of the resulting system with $(A-1)$ (or $(A+1)$) nucleons is distributed according to a Breit–Wigner law, centred on the *single-particle energy* $E(k)$, with a full width at half-maximum equal to

$$\Gamma^\downarrow = 2 Z(k) W^{\text{NL}}(k). \quad (3.4.19)$$

3.4.3. Quasiparticle strength

The appearance of the residue $Z(k)$ in eqs. (4.15), (4.18) and (4.19) is the main difference with the corresponding expressions introduced in the optical model. In what follows, we discuss the physical interpretation of this “quasiparticle strength” $Z(k)$.

We first point out that our present notation is compatible with the one used in eq. (2.5) to denote the discontinuity of the momentum distribution at the Fermi momentum. This follows from the fact that

$$\int_{-\infty}^{\infty} d\omega S_h^{\text{QP}}(k; \omega) = Z(k), \quad (3.4.20)$$

and that the pole part $S_h^{\text{QP}}(k; \omega)$ of $S_h(k; \omega)$ no longer contributes to the right-hand side of eq. (2.13) when k becomes larger than k_F [37, 38].

The Fourier transform of the pole (quasiparticle) contribution to the right-hand side of eq. (4.15) reads

$$\mathcal{G}^{\text{QP}}(k; t) = -i Z(k) \exp\{-i E(k) t\} \exp\{-t Z(k) W^{\text{NL}}(k)\} \theta(t). \quad (3.4.21)$$

Therefore, the quasiparticle strength $Z(k)$ measures the probability amplitude that a one-particle (or a one-hole) excitation with momentum k propagates like a damped plane wave, with well-defined frequency ($E(k)$) and lifetime ($\tau = \{2 Z(k) W^{\text{NL}}(k)\}^{-1}$).

The strength $Z(k)$ is equal to the area below the dashed curve (“quasiparticle peak”) in fig. 3.4. The area under the full curve is equal to unity. Note that $Z(k)$ may be larger than unity. For k close to k_F , however, one always has $Z(k) < 1$. This property is implied by eq. (2.5); it can be proved on the basis of

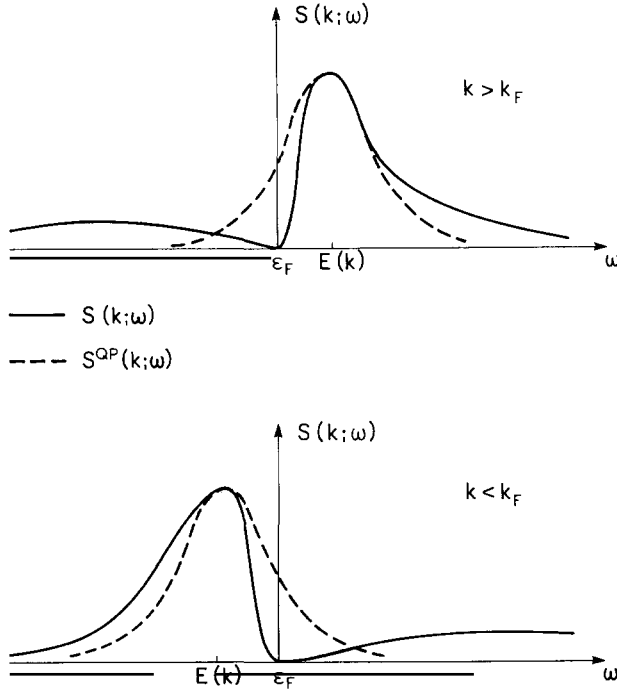


Fig. 3.4. The full curves represent a sketch of realistic spectral functions, see fig. 3.2. The dashed curves correspond to the quasiparticle approximation. Note that the difference $S(k; \omega) - S^{QP}(k; \omega)$ can be positive or negative, depending on the value of ω . The areas have the following values $\int_{-\infty}^{\infty} S(k; \omega) d\omega = 1$; $\int_{E(k)}^{\infty} S(k; \omega) d\omega = n(k)$; $\int_{\epsilon_F}^{\infty} S(k; \omega) d\omega = 1 - n(k)$, where $n(k)$ is the average number of nucleons with momentum k . The area below the dashed curve is equal to the quasiparticle strength $Z(k)$. The quasiparticle energy $E(k)$ is given by the location of the maximum of $S(k; \omega)$.

the dispersion relation (2.34) as will become clear in sections 3.8–3.16. For k close to k_F , the width of the quasiparticle peak is moreover approaching zero (see eq. (2.29)). Then one can safely interpret $Z(k)$ as measuring the fraction of the bare particle which is contained in the quasiparticle peak. Equivalently, one can say that for k close to k_F , the strength $Z(k)$ measures that fraction of the wave packet associated with the nucleon k which has a well-defined frequency and a well-defined lifetime.

3.4.4. Background contribution

The reason why $Z(k)$ may become larger than unity when k is not close to k_F can be traced to the fact that when making the quasiparticle approximation we have neglected the background term \mathcal{G}^B on the right-hand side of eq. (4.15). The physical meaning of this background can be obtained by going back to the time-dependent description of the propagation of the initial particle state $|\phi(k; t=0)\rangle$ (see eq. (2.6)). This initial state is viewed as composed of two parts [53]. (i) A coherent part of norm $Z(k)$ which oscillates with the frequency $E(k)$ over times t less than $\{2 Z(k) W^{NL}(k)\}^{-1}$ and which is called the quasiparticle part. (ii) An incoherent background; this part dominates for large ω , i.e. for small times. For $t \ll [E(k) - \epsilon_F]^{-1}$, the time dependence of $\mathcal{G}_n(k; t)$ is thus very complicated because all frequency components of $a(k; t)|\psi\rangle$ are large. These short times appear in the following definition of the “instantaneous” single-particle energy [53]

$$\mathcal{E}(k) = [\mathcal{d}\mathcal{G}(k; t)/dt]_{t=-0} - [\mathcal{d}\mathcal{G}(k; t)/dt]_{t=+0}, \quad (3.4.22)$$

whose use in nuclear physics has been suggested by Baranger [54]. In view of our preceding comments, $\mathcal{E}(k)$ appears to be remote from directly observable quantities. A somewhat more transparent form of $\mathcal{E}(k)$ is

$$\mathcal{E}(k) = \frac{1}{n(k)} \left\{ \int_{-\infty}^{\varepsilon_F} \omega S_h(k; \omega) d\omega + \int_{\varepsilon_F}^{\infty} \omega S_p(k; \omega) d\omega \right\} = \langle \varepsilon_h(k) \rangle + \langle \varepsilon_p(k) \rangle, \quad (3.4.23)$$

see eq. (2.12). The second term inside the curly brackets is infinite in the case of a singular (e.g. hard core) particle-particle interaction. This confirms that $\mathcal{E}(k)$ could be useful only in the framework of some approximation schemes. In the case of hole states and if one uses the quasiparticle approximation one finds that [32]

$$\mathcal{E}(k) \approx Z(k) E(k). \quad (3.4.24)$$

In the independent particle model, one has $Z(k) = 1$, and $\mathcal{E}(k) = e_0(k)$.

3.4.5. Summary

In the independent particle model, a particle with momentum k has a well-defined energy $e_0(k)$. The associated spectral function is a δ -function. When collisions are taken into account, the δ -function becomes a peak superimposed upon a background. This peak is centred on the quasiparticle energy or single-particle energy $E(k)$ and has a full width at half-maximum equal to $Z(k) W^{NL}(k)$. The dynamical shell model, which is equivalent to the optical model in the case of positive energies, aims at the description of only this quasiparticle peak, i.e. at the description of a fraction $Z(k)$ of the full wave packet associated with the nucleon moving with momentum k . We emphasize that this does *not* necessarily imply that the dynamical shell model is useful only if $Z(k)$ is close to unity. Although the background is not explicitly described, its existence is nevertheless globally taken into account via the appearance of the quasiparticle strength $Z(k)$. Note that the latter quantity involves the partial derivative of the single-particle potential $\mathcal{V}(k; \omega)$ with respect to the variable ω . We noted in section 3.2 that this variable ω is associated with the time variable, i.e. with the dynamics of the shell model.

3.5. Single-particle wave equation

3.5.1. Energy-momentum relation

In a uniform system, single-particle excitations are described by plane waves. The single-particle wave equation then takes a particularly simple form since the wave function can be divided out. This leaves the wave equation in the form of the energy-momentum relation (4.11), namely

$$\omega = k^2/2m + \mathcal{V}(k; \omega) \mp i \mathcal{W}(k; \omega), \quad (3.5.1)$$

where the upper sign corresponds to $\omega > 0$ and the lower sign to $\omega < 0$.

We now show explicitly that eq. (5.1) indeed corresponds to a wave equation. To make contact with finite systems and to establish the physical meaning of the variables k and ω , it is instructive to turn to the space-time representation. The most general form of the single-particle wave equation reads, see eq.

(2.0.1)

$$-\frac{1}{2m} \nabla^2 \psi(\mathbf{r}, t) + \int d\mathbf{r}' \int dt' \mathcal{M}(\mathbf{r}, \mathbf{r}'; t - t') \psi(\mathbf{r}', t') = i \frac{\partial}{\partial t} \psi(\mathbf{r}, t). \quad (3.5.2)$$

In the case of a stationary state, one has

$$\psi(\mathbf{r}, t) = \psi_\omega(\mathbf{r}) e^{-i\omega t} \quad (3.5.3)$$

and eq. (5.2) becomes

$$-\frac{1}{2m} \nabla^2 \psi_\omega(\mathbf{r}) + \int d\mathbf{r}' \mathcal{M}(\mathbf{r}, \mathbf{r}'; \omega) \psi_\omega(\mathbf{r}') = \omega \psi_\omega(\mathbf{r}). \quad (3.5.4)$$

In a uniform system, \mathcal{M} only depends upon $|\mathbf{r} - \mathbf{r}'|$ and ω , while $\psi_\omega(\mathbf{r})$ is a plane wave

$$\psi_\omega(\mathbf{r}) = \exp(i\mathbf{k} \cdot \mathbf{r}). \quad (3.5.5)$$

When eq. (5.5) is inserted into eq. (5.4), the latter reduces to

$$k^2/2m + \mathcal{M}(k; \omega) = \omega \quad (3.5.6)$$

which defines k as a function of ω and is identical to eq. (5.1).

This confirms that the dependence of $\mathcal{M}(k; \omega)$ upon k reflects the nonlocality of the single-particle field in space, while its dependence upon ω corresponds to its nonlocality in time. Here, nonlocality refers to the fact that in order to calculate $\psi(\mathbf{r}, t)$ at location \mathbf{r} and at time t , one needs $\psi(\mathbf{r}', t')$ at other locations and times.

Nonlocality in space is familiar because it is already encountered in the Hartree–Fock approximation (section 3.7). In the Hartree approximation, the particle–target potential is local unless the particle–particle interaction contains exchange forces. Antisymmetrization leads to the Fock term, which is nonlocal. Nonlocality in time is less familiar because most theoretical analyses are based on stationary states rather than on the time evolution of wave packets. In these works, the nonlocality in time therefore appears in the form of an energy or frequency dependence. Since nonlocality in time is usually treated as a frequency dependence, the word “nonlocality” will henceforth refer to nonlocality in space, unless otherwise specified.

Time- (or frequency-) dependent operators also appear in the theory of effective interactions. In that case, the frequency dependence of the effective interaction can be avoided by using “folded diagrams” [54]. This also holds true for the energy dependence of $\mathcal{M}(\mathbf{r}, \mathbf{r}'; \omega)$ [55, 56]. In other words, one can construct an energy-independent nonlocal operator $\bar{\mathcal{M}}(\mathbf{r}, \mathbf{r}')$ which yields *exactly* the same (off- as well as on-the-energy-shell) value for the transition amplitude. The operator $\bar{\mathcal{M}}$ can have an awkward type of nonlocality; it is, for instance, not symmetric in the variables \mathbf{r} and \mathbf{r}' [56]. The usefulness of $\bar{\mathcal{M}}$ remains to be demonstrated.

3.5.2. Equivalent potentials

The energy-momentum relation (4.12) can be solved to express k as a function $k(E)$ of E , or E as a

function $E(k)$ of k . The functions

$$M^{\text{NL}}(k) = \mathcal{M}(k; E(k)) = V^{\text{NL}}(k) \mp i W^{\text{NL}}(k) \quad (3.5.7)$$

and

$$M(E) = \mathcal{M}(k(E); E) = V(E) \mp i W(E) \quad (3.5.8)$$

are “equivalent” in the sense that they are both equal to the difference between the total energy $E(k)$ of the quasiparticle and its kinetic energy $k^2/2m$. Since $M^{\text{NL}}(k)$ is independent of frequency but depends on momentum, it is nonlocal in space (whence the subscript NL). Since $M(E)$ does not depend upon k , it is local. The potential $M(E)$ is thus called the *local equivalent* of the nonlocal potential $M^{\text{NL}}(k)$. One is obtained from the other by using the energy–momentum relation (4.12). This procedure was introduced by Perey and Buck [7]. As discussed in section 3.5.3 below, it would be more appropriate to use the complex energy–momentum relation (4.11) rather than (4.12).

Inasmuch as the single-particle wave equation is concerned, the quantities $\mathcal{M}(k; \omega)$, $M^{\text{NL}}(k)$ and $M(E)$ are thus “equivalent”. Since, however, $\mathcal{M}(k; \omega)$ depends on two variables, some information is lost when one of these variables is eliminated with the help of the energy–momentum relation. For instance, the knowledge of $M^{\text{NL}}(k)$ does not enable one to calculate the quasiparticle strength $Z(k)$, which involves the partial derivative of $\mathcal{M}(k; \omega)$ with respect to ω , for fixed k , see eq. (4.16). In a finite system, this loss of information corresponds to the fact that the “on-the-energy-shell” value of the transition operator yields the elastic scattering phase shift, but does not enable one to obtain the elastic scattering wave function at finite distances.

3.5.3. Nonlocality correction to the mean-free path

In order to avoid the complication that the solution $k(\omega)$ of eq. (4.11) is complex for ω real, we had used in sections 3.4 and 3.5.2 the real part (4.12) of eq. (4.11). We now discuss this approximation [57–60].

Let us assume that $|W| \ll |E - V|$ and write the solution of eq. (4.11) in the form

$$k(\omega) = k_R(\omega) + i k_I(\omega). \quad (3.5.9)$$

Let us expand all quantities about the real root $k_0(E)$ of eq. (4.12):

$$E = k_0^2/2m + \mathcal{V}(k_0; E). \quad (3.5.10)$$

This yields

$$k_R = k_0, \quad (3.5.11)$$

$$k_I = \frac{m}{k_0} \mathcal{W}(E; k_0) \frac{m_k}{m}, \quad (3.5.12)$$

where the k -mass m_k is defined by

$$\frac{m_k(E)}{m} = \left[1 + \frac{m}{k_0} \frac{\partial \mathcal{V}(k; \omega)}{\partial k} \right]_{\omega=E(k)}^{-1}, \quad (3.5.13)$$

and may, as indicated, depend upon $E(k)$.

We note the appearance of the factor m_k/m on the right-hand side of eq. (5.12) (see also ref. [61]). This factor did not appear in section 2.10. The reason is that the factor m_k/m reflects the nonlocality (momentum dependence) of \mathcal{V} , which had been neglected in section 2.10. This factor enters in the expression of the mean free path, which reads

$$\lambda = (2k_1)^{-1} = \frac{k_0}{m_k} \{2 \mathcal{W}(k_0(E); E)\}^{-1}. \quad (3.5.14)$$

Equation (4.21) shows that the mean lifetime is equal to

$$\tau = \{2 Z(k) \mathcal{W}(k_0(E); E)\}^{-1}. \quad (3.5.15)$$

The mean free path is related to the mean lifetime by

$$\lambda = v_g \tau, \quad (3.5.16)$$

where (see eq. (2.8.2)) $v_g = \hbar k_0/m^*$ is the group velocity. Indeed, the following relation is fulfilled (see section 3.6 below)

$$\frac{m^*(E)}{m} = \frac{m_k(E)}{m} \frac{m_\omega(E)}{m}, \quad (3.5.17)$$

where the ω -mass m_ω is defined by

$$m_\omega(E)/m = [1 - \partial \mathcal{V}(k; \omega)/\partial \omega]_{\omega=E(k)} \quad (3.5.18)$$

$$= \{Z(k)\}^{-1}. \quad (3.5.19)$$

Early estimates on the mean free path were based on the approximation

$$\lambda \approx \lambda_0 = \frac{k_0}{m} \{2 \mathcal{W}(k_0(E); E)\}^{-1}. \quad (3.5.20)$$

The values of λ_0 are considerably smaller than the empirical ones [62]. The appearance of the k -mass $m_k < m$ on the right-hand side of eq. (5.14) removes most of this discrepancy [57, 58, 60].

The reasoning carried out in the preceding paragraph can be applied to obtain the modification of the local equivalent potential when a (real or complex) perturbation Δ is added to a nonlocal potential

$\mathcal{V}(k; \omega)$. Let us consider the solution $k_0(E)$ of the relation

$$E = k_0^2/2m + \mathcal{V}(k_0; E). \quad (3.5.21)$$

The local equivalent potential of $\mathcal{V}(k; E)$ is $V(E) = \mathcal{V}(k_0(E); E)$. Let us add a perturbation Δ to the nonlocal potential $\mathcal{V}(k; \omega)$. The energy momentum relation becomes

$$E = k^2/2m + \mathcal{V}(k; E) + \Delta, \quad (3.5.22)$$

with the solution $k_\Delta(E)$. When $|\Delta| \ll |E - V|$, one finds that

$$\mathcal{V}(k_\Delta(E); E) \sim \mathcal{V}(k_0(E); E) + (m_k/m - 1)\Delta. \quad (3.5.23)$$

This result corresponds to the following rule. *When a perturbation Δ is added to a nonlocal field $\mathcal{V}(k; \omega)$, the local equivalent field is only increased by the amount $(m_k/m)\Delta$.* This was pointed out by Dabrowski [63] in the case when Δ is the symmetry potential due to neutron excess. It had also been applied to the case when Δ is a Coulomb field V_c . Then, however, care must be exercised. Indeed, it may be shown that if $\mathcal{V}_n(k; \omega)$ is the potential for a neutron, the potential for a proton is given by

$$\mathcal{V}_p(k; \omega) = \mathcal{V}_n(k; \omega - V_c) + V_c, \quad (3.5.24)$$

where we disregarded the symmetry potential. The latter has been included in [64]. The local equivalent of $\mathcal{V}_p(k; \omega)$ is [65]

$$V_p(E) = V_n(E) + (m^*/m)V_c. \quad (3.5.25)$$

The appearance of the factor m^*/m instead of m_k/m in front of the Coulomb field V_c is due to the appearance of V_c in the first term on the right-hand side of eq. (5.24). The quantity

$$(m^*/m - 1)V_c \quad (3.5.26)$$

is called the *Coulomb correction*. It is usually approximated by $-0.4 ZA^{-1/3}$, but recent theoretical [65] and empirical [66] arguments indicate that this may be an underestimate. For recent discussions of these problems, see refs. [64, 67].

3.5.4. Local density approximation

Finite systems will be considered in chapter 4. It may, however, be useful to make contact between uniform and finite systems by using the following very rough *local density approximation*.

Let us first exhibit by an index ρ the fact that all the quantities calculated in an infinite system depend upon the density ρ of the medium. For instance, $k_\rho(\omega)$ is defined by the energy-momentum relation

$$\frac{1}{2m} [k_\rho^2(E)] + \mathcal{V}_\rho(k_\rho(E); E) = E, \quad (3.5.27)$$

$$V_\rho^{\text{NL}}(k) = \mathcal{V}_\rho(k; E_\rho(k)), \quad (3.5.28)$$

$$V_\rho(E) = \mathcal{V}_\rho(k_\rho(E); E). \quad (3.5.29)$$

The simplest local density approximation consists in assuming that the value of the nucleon–core (particle–target, hole–core) potential at the distance r from the centre is the same as in an infinite system whose density would be equal to that ($\rho(r)$) of the finite system at location r . For instance, the real part of the local energy-dependent real potential is then approximated by

$$V(r; E) = V_{\rho(r)}(E). \quad (3.5.30)$$

This approximation is crude but has enjoyed semi-quantitative success [68]. It suffers from the following two main drawbacks. (i) It neglects surface corrections related to the range of the particle-particle interaction. This can be cured either by adopting a folding prescription [68], or by making a local density approximation on the effective nucleon–nucleon interaction [69–71] rather than on the nucleon–nucleus potential itself. (ii) It ignores the fact that in a finite nucleus a nucleon can excite surface vibrations. This should mainly affect those quantities which are particularly sensitive to dynamical effects, namely the imaginary part $\mathcal{W}(k; \omega)$ of the potential and the dependence of the potential $\mathcal{V}(k; \omega)$ upon the variable ω . The importance of these finiteness effects will appear when comparing the results obtained in the case of infinite nuclear matter on the one hand and in the case of finite nuclei on the other hand.

3.5.5. Perey correction

We mentioned that in a finite system the potential $M(E)$ and the nonlocal potential $M^{\text{NL}}(|r - r'|)$ are “equivalent” in the sense that they give almost the same elastic scattering phase shift. However, it can be shown that they do *not* give the same scattering wave function in the target *interior*. There, the amplitude of the wave function $\phi^{\text{NL}}(r)$ calculated from the nonlocal potential M^{NL} is, in general, smaller than the amplitude of the wave function $\phi_L(r)$ calculated from the local potential. One has [72]

$$\phi^{\text{NL}}(r) \approx (m_k/m)^{1/2} \phi_L(r). \quad (3.5.31)$$

This is often called the *Perey correction* and plays a significant role in the extraction of spectroscopic factors from stripping or pick-up experiments. For recent discussions, see refs. [59, 73, 74].

3.5.6. Summary

We have seen that the quantity

$$\mathcal{M}(k; \omega) = \mathcal{V}(k; \omega) \mp i \mathcal{W}(k; \omega) \quad (3.5.32)$$

may be identified with the momentum- and frequency-dependent mean field. The momentum dependence is equivalent to a nonlocality in spatial coordinates, in which the average field is given by the Fourier transform $\mathcal{M}(|r - r'|; \omega)$ of $\mathcal{M}(k; \omega)$. The frequency dependence is equivalent to a nonlocality in time, as expressed by taking the Fourier transform $\mathcal{M}(k; t - t')$ of $\mathcal{M}(k; \omega)$.

The complex potential felt by a *quasiparticle* is the value of $\mathcal{M}(k; \omega)$ when the two variables k and ω

are related by the energy-momentum relation

$$k^2/2m + \mathcal{M}(k; \omega) = \omega. \quad (3.5.33)$$

Its real part can be approximated by $\mathcal{V}(k; E(k))$ where $E(k)$ is defined by the real energy-momentum relation

$$k^2/2m + \mathcal{V}(k; E) = E. \quad (3.5.34)$$

The latter equation can also be used to express k as a function of E , namely $k(E)$. The quasiparticle complex potential can thus be approximated by the equivalent forms

$$\mathcal{M}^{NL}(k) = \mathcal{M}(k; E(k)), \quad (3.5.35)$$

$$\mathcal{M}(E) = \mathcal{M}(k(E); E). \quad (3.5.36)$$

In $\mathcal{M}^{NL}(k)$, the ω -dependence has disappeared; $\mathcal{M}^{NL}(k)$ is thus a nonlocal energy-independent potential. In $\mathcal{M}(E)$, the momentum dependence has disappeared; $\mathcal{M}(E)$ is thus a local energy-dependent potential; it is called the *local equivalent* potential of the nonlocal potential $\mathcal{M}^{NL}(k)$.

While the potentials $\mathcal{M}(E)$ and $\mathcal{M}^{NL}(k)$ are essentially equivalent to $\mathcal{M}(k; \omega)$ inasmuch as the potential felt by a quasiparticle is concerned, a more detailed description of the quasiparticle properties involves values of $\mathcal{V}(k; \omega)$ which are “off-shell” in the sense that eq. (5.33) is not fulfilled. One does not, however, need to go far off-shell, since only partial derivatives of $\mathcal{V}(k; \omega)$ at $\omega = E(k)$ are required. For instance, the quasiparticle strength is measured by

$$Z(k) = m/m_\omega = \{1 - [\partial\mathcal{V}(k; \omega)/\partial\omega]_{\omega=E(k)}\}^{-1}, \quad (3.5.37)$$

where m_ω is the “ ω -mass”. The quantity $Z(k)$ enters into the value of mean lifetime τ (eq. (5.15)) of the quasiparticle. The mean free path of the quasiparticle involves the “ k -mass” m_k , which is defined by

$$m_k/m = \left\{ 1 + \frac{m}{k} \frac{\partial\mathcal{V}(k; \omega)}{\partial k} \right\}_{\omega=E(k)}^{-1}. \quad (3.5.38)$$

3.6. Effective mass

The effective mass is defined by eq. (2.7.3), namely

$$dE/dk = k/m^*, \quad (3.6.1)$$

where E is the energy of the quasiparticle and k its momentum. These two quantities are connected by the energy-momentum relation

$$E = k^2/2m + \mathcal{V}(k; E). \quad (3.6.2)$$

In view of our definitions (5.7) and (5.8) of the quantities $V^{NL}(k)$ and $V(E)$, eq. (6.2) can be put into

the equivalent forms

$$E = k^2/2m + V(E), \quad (3.6.3)$$

$$E = k^2/2m + V^{\text{NL}}(k). \quad (3.6.4)$$

Equations (6.1) and (6.3) yield the following expression for the effective mass

$$m^*/m = 1 - dV(E)/dE, \quad (3.6.5)$$

in which we recognize eq. (2.7.2). Equations (6.1) and (6.4) lead to

$$\frac{m^*}{m} = \left\{ 1 + \frac{m}{k} \frac{dV^{\text{NL}}(k)}{dk} \right\}^{-1}. \quad (3.6.6)$$

This derivation shows that the right-hand side of eqs. (6.5) and (6.6) are equal. Let us write these expressions in terms of the original nonlocal and frequency-dependent potential $\mathcal{V}(k; \omega)$. Equation (6.5) amounts to

$$\frac{m^*(E)}{m} = 1 - \frac{d}{dE} \{ [\mathcal{V}(k; \omega)]_{\omega=E(k)} \}, \quad (3.6.7)$$

while eq. (6.6) amounts to

$$\frac{m^*(E)}{m} = \left\{ 1 + \frac{m}{k} \frac{d}{dk} [\mathcal{V}(k; \omega)]_{\omega=E(k)} \right\}^{-1}. \quad (3.6.8)$$

These expressions for the effective mass m^* can be compared with those of the k -mass m_k and of the ω -mass m_ω . These are given by eqs. (5.13) and (5.18), namely

$$\frac{m_k(E)}{m} = \left\{ 1 + \frac{m}{k} \left[\frac{\partial \mathcal{V}(k; \omega)}{\partial k} \right] \right\}_{\omega=E(k)}^{-1}, \quad (3.6.9)$$

$$\frac{m_\omega(E)}{m} = 1 - \left[\frac{\partial}{\partial \omega} \mathcal{V}(k; \omega) \right]_{\omega=E(k)}. \quad (3.6.10)$$

The difference between the quantities (6.7) and (6.10) is that in eq. (6.10) the limit $\omega \rightarrow E(k)$ is taken *after* having computed the *partial* derivative $\partial/\partial\omega$, while in eq. (6.7) the limit $\omega \rightarrow E(k)$ is taken *before* computing the derivative. As a consequence, the effective mass m^* and the ω -mass m_ω would be equal if the potential $\mathcal{V}(k; \omega)$ would be independent of k , i.e. local in space. The difference between the ω -mass m_ω and the effective mass m^* thus reflects the nonlocality of the potential $\mathcal{V}(k; \omega)$. Similarly, the k -mass m_k and the effective mass m^* would be equal if the potential $\mathcal{V}(k; \omega)$ would be independent of ω , i.e. would be static (local in time). The difference between the k -mass m_k and the effective mass m^* thus reflects the frequency dependence of the potential $\mathcal{V}(k; \omega)$, i.e. its dynamical content.

In summary, the k -mass m_k characterizes the spatial nonlocality in space of the field, while the ω -mass m_ω characterizes its nonlocality in time, i.e. the dynamics of the shell-model potential $\mathcal{V}(k; \omega)$. The relationship between m_k and the range of nonlocality will be illustrated in section 3.7.5.

The quantities m^* , m_k and m_ω are not independent. Indeed, the following identity holds

$$\frac{m^*(E)}{m} = \frac{m_k(E)}{m} \cdot \frac{m_\omega(E)}{m} \quad (3.6.11)$$

provided that k and E are related by eq. (5.34), namely

$$[k(E)]^2/2m + \mathcal{V}(k(E); E) = E. \quad (3.6.12)$$

The k -mass m_k and the ω -mass m_ω were introduced in ref. [75] where it was first pointed out that in nuclear matter the function $m_\omega(E)$ has a peak when E is close to the Fermi energy ε_F . However, the identity (6.11) had previously appeared in the literature, see e.g. eq. (6) of ref. [76] or eq. (2.3.12) of ref. [35].

3.7. Hartree–Fock approximation

3.7.1. Definition

We recall that we restrict the discussion to *normal systems*, i.e. to systems which can be described either by straightforward perturbation theory, or by performing partial summations in the perturbation series. The perturbation series we are referring to is the expansion in powers of the strength s of the effective interaction sv , and in which one ultimately sets $s = 1$. In the present section, we discuss the first-order term of the perturbation expansion of the mass operator $\mathcal{M}(k; \omega)$. This first-order term is called the *Hartree–Fock potential*. Its algebraic expression reads

$$\mathcal{M}_1(k) = V_{\text{HF}}(k) = \sum_j n_<(j) \{ \langle \mathbf{k}, \mathbf{j} | v | \mathbf{k}, \mathbf{j} \rangle - \langle \mathbf{k}, \mathbf{j} | v | \mathbf{j}, \mathbf{k} \}. \quad (3.7.1)$$

We recall that $n_<(j)$ means that $j = |\mathbf{j}|$ is restricted to values $j < k_F$, where k_F is the Fermi momentum. We used the notation

$$|\mathbf{k}, \mathbf{j} \rangle = \exp\{i(\mathbf{k} \cdot \mathbf{r}_1 + \mathbf{j} \cdot \mathbf{r}_2)\}, \quad (3.7.2)$$

and we omitted explicit reference to the spin and isospin quantum numbers.

The Hartree–Fock field is the sum of the Hartree (direct) potential

$$V_{\text{H}}(k) = \sum_j n_<(j) \langle \mathbf{k}, \mathbf{j} | v | \mathbf{k}, \mathbf{j} \rangle, \quad (3.7.3)$$

and of the Fock (exchange) contribution

$$V_{\text{F}}(k) = - \sum_j n_<(j) \langle \mathbf{k}, \mathbf{j} | v | \mathbf{j}, \mathbf{k} \rangle. \quad (3.7.4)$$

The latter arises from the Pauli principle.

3.7.2. Graphical representation

Graphs or diagrams are very useful to gain a physical interpretation of the approximation and also to perform partial summations of the perturbation series. The convention for representing the various contributions to the perturbation expansion of the mass operator are somewhat author-dependent. Here, we adopt those which are most commonly used in nuclear physics. We do not attempt to give general rules, since we shall use only a few graphs.

The Hartree–Fock approximation is represented by the graph at the left in fig. 3.5. Often, one draws the middle or right diagrams when one discusses quasiparticle ($k > k_F$) or quasihole ($k < k_F$) potentials, respectively. However, the three diagrams in fig. 3.5 correspond to the *same* algebraic expression, namely (7.1).

3.7.3. Nonlocality in space

The Hartree–Fock potential is static, i.e. is independent of ω and thus local in time. Relatedly, it is real since the dispersion relation (2.35), which holds in any order of perturbation theory, implies that a frequency-dependent approximation to the mass operator is necessarily complex, and conversely.

The Hartree–Fock potential is momentum-dependent, i.e. nonlocal in space. Let us first consider the case when the particle–particle interaction v is local and contains no exchange operator. Then, the Hartree potential is independent of k and is simply given by the product of the density by the volume integral of the interaction

$$V_H = \rho \int v^3(r') d^3r'. \quad (3.7.5)$$

We recall that for simplicity we omit spin-statistical factors. In that case, the momentum dependence of the Hartree–Fock potential originates from the Fock contribution. When v contains exchange forces and has finite range, as is the case for most effective nucleon–nucleon interactions, even the Hartree potential is nonlocal. In nuclear physics there is therefore only little interest in distinguishing between the direct and the exchange contributions to the first-order approximation $V_{HF}(k)$. We shall thus usually treat them together and write eq. (7.1) in the form

$$V_{HF}(k) = \sum_j n_{<}(j) \langle \mathbf{k}, j | v | \mathbf{k}, j \rangle_i, \quad (3.7.6)$$

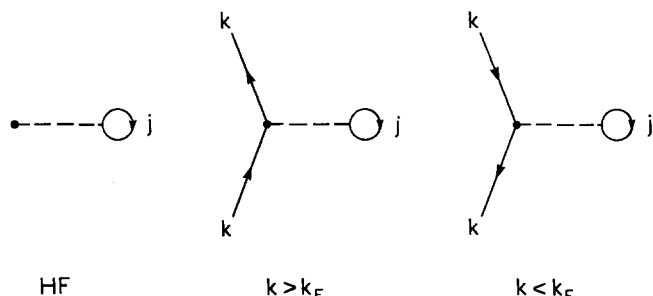


Fig. 3.5. Graphs which represent the Hartree–Fock approximation (7.6) to the mass operator. Downward pointing arrows are associated with hole states and upward pointing arrows correspond to particle states. An integration is carried out over all “internal” lines, which in the present case mean over the momentum j , with $j < k_F$. Only the direct (Hartree) term is shown.

where

$$|\mathbf{k}, \mathbf{j}\rangle_t = |\mathbf{k}, \mathbf{j}\rangle - |\mathbf{j}, \mathbf{k}\rangle. \quad (3.7.7)$$

3.7.4. Effective mass of the Hartree–Fock potential

Since the Hartree–Fock potential is independent of the frequency ω , the corresponding ω -mass is equal to the bare mass m . In the Hartree–Fock approximation, the effective mass therefore reduces to the k -mass m_k^* :

$$m_{\text{HF}}^* = m_k^{\text{HF}}. \quad (3.7.8)$$

As early as 1957, Weisskopf [77] had argued that in nuclear matter the effective mass m^* for hole states, i.e. for $k < k_F$, is on the average smaller than the bare mass m . His reasoning went as follows:

(i) The Fermi energy ε_F of a self-bound system at equilibrium is exactly equal to the average binding energy per nucleon, B/A , see eq. (2.31). In nuclear matter, the empirical numbers are

$$k_F \approx 1.35 \text{ fm}^{-1}, \quad \varepsilon_F = B/A \approx -16 \text{ MeV}. \quad (3.7.9)$$

(ii) One can approximate the binding energy by the independent-particle model formula (3.9), which yields

$$\frac{B}{A} = \sum_k n_<(k) \left[\frac{k^2}{2m} + \frac{1}{2} U(k) \right] \approx \frac{\bar{k}^2}{2m} + \frac{1}{2} U(\bar{k}), \quad (3.7.10)$$

where

$$\bar{k} = \int_0^{k_F} k d^3k / \int_0^{k_F} d^3k = 0.75k_F \quad (3.7.11)$$

is the average value of k for $k < k_F$. One then has

$$-16 \text{ MeV} = k_F^2/2m + U(k_F) = \bar{k}^2/2m + \frac{1}{2} U(\bar{k}), \quad (3.7.12)$$

$$-16 \text{ MeV} = 0.56k_F^2/2m + \frac{1}{2} U(\bar{k}). \quad (3.7.13)$$

This yields

$$U(k_F) = -54 \text{ MeV}, \quad (3.7.14)$$

and

$$U(\bar{k}) = -76 \text{ MeV}. \quad (3.7.15)$$

Hence the shell-model potential $U(k)$ is deeper at $k = 0.75k_F$ than at $k = k_F$. This implies that the

effective mass is smaller than m . We emphasize that these estimates rely upon the assumption (7.10), which is only valid in the Hartree–Fock approximation.

3.7.5. Range of nonlocality

In their analysis of nucleon–nucleus scattering in terms of a nonlocal potential well, Perey and Buck [7] considered a phenomenological Gaussian nonlocality, i.e. a potential well of the form

$$V_{\text{PB}}(r; |\mathbf{r} - \mathbf{r}'|) = f_{\text{WS}}(r) V_{\text{NL}}(|\mathbf{r} - \mathbf{r}'|), \quad (3.7.16)$$

where $f_{\text{WS}}(r)$ is a Woods–Saxon form factor normalized to unity at $r = 0$, while

$$V_{\text{NL}}(|\mathbf{r} - \mathbf{r}'|) = \pi^{-3/2} a^{-3} V_0 \exp(-|\mathbf{r} - \mathbf{r}'|^2/a^2). \quad (3.7.17)$$

The length a is the *range of nonlocality*. The Fourier transform of $V_{\text{NL}}(|\mathbf{r} - \mathbf{r}'|)$ is equal to

$$V^{\text{NL}}(k) = V_0 \exp(-\frac{1}{4} a^2 k^2). \quad (3.7.18)$$

The local equivalent potential is given by the relation

$$V_{\text{PB}}(r; E) = V_0 f_{\text{WS}}(r) \exp\left\{-\frac{ma^2}{2}[E - V_{\text{PB}}(r; E)]\right\}. \quad (3.7.19)$$

The momentum dependence of the Perey–Buck potential is measured by k -mass (eq. (6.9)) which in the present case is given by

$$m_k^{\text{PB}}(r; E)/m = \{1 - \frac{1}{2}ma^2 V_{\text{PB}}(r; E)\}^{-1}. \quad (3.7.20)$$

In order to estimate this quantity, let us take the typical values $V_0 = -70$ MeV, $a = 0.8$ fm. Then, we find that $m_k(r = 0)/m$ increases in a monotonic way from 0.64 at $k = 0$ to unity at $k = \infty$. We emphasize that this increase is very slow. Indeed, $k = 0$ corresponds to the energy $E = -70$ MeV. At $k = k_F = 1.35$ fm $^{-1}$, one has $E = -14.5$ MeV and $m_k/m = 0.71$.

3.7.6. Numerical example

The Hartree–Fock field (7.6) can be calculated analytically for simple choices of the potential $v(r_{12})$ between the particles 1 and 2. This is, in particular, the case for the Yukawa interaction

$$v_Y(r_{12}) = v_0 \frac{b}{r_{12}} \left\{ \exp\left(-\frac{r_{12}}{b}\right) \right\} (1 - \alpha + \alpha P_x), \quad (3.7.21)$$

where P_x is the Majorana operator which exchanges the spatial coordinates of particles 1 and 2. The corresponding expression of the Hartree–Fock field can be found in refs. [78–83]. The interest of taking $\alpha \neq 0$ in the nuclear case is that in momentum representation the dependence upon relative momentum of the diagonal elements of the effective nucleon–nucleon interaction can be fairly well reproduced by a potential which has a finite range and only acts in low-even relative partial waves [84, 85]. Setting $\alpha = 0.5$ restricts the interaction (7.21) to even partial waves.

In order to illustrate our discussion in the present and in the next sections, we shall use an exponential interaction

$$v(r) = v_0 \exp(-\mu r) \delta_{l=0}, \quad (3.7.22)$$

where $\delta_{l=0}$ indicates that it acts only in the relative $l=0$ partial wave. More precisely, we adopt the following model for the matrix elements of v :

$$\langle \mathbf{k}, \mathbf{j} | v | \mathbf{a}, \mathbf{b} \rangle = \frac{8r\mu v_0}{[\mu^2 + \frac{1}{4}|\mathbf{k} - \mathbf{j}|^2 + \frac{1}{4}|\mathbf{a} - \mathbf{b}|^2]^2}. \quad (3.7.23)$$

This expression can be shown to be very close to the matrix element of the interaction (7.22) [86]. The corresponding Hartree–Fock potential in symmetric nuclear matter can be calculated analytically and reads

$$V_{HF}(k) = \frac{6\sqrt{2}}{\pi} v_0 \left\{ \tan^{-1}\left(\frac{k+k_F}{\mu\sqrt{2}}\right) \tan^{-1}\left(\frac{k-k_F}{\mu\sqrt{2}}\right) - \frac{1}{\sqrt{2}} \ln \frac{(k+k_F)^2 + 2\mu^2}{(k-k_F)^2 + 2\mu^2} \right\}. \quad (3.7.24)$$

The quantity (7.24) is plotted in fig. 3.6 for the parameter values

$$\mu = 2 \text{ fm}^{-1}, \quad v_0 = 240 \text{ MeV}, \quad (3.7.25)$$

and for the Fermi momentum $k_F = 1.35 \text{ fm}^{-1}$. The latter corresponds (eq. (2.3)) to the density at the centre of a medium-weight or heavy nucleus, since one has

$$k_F = 1.35 \text{ fm}^{-1} \quad \text{for } \rho = 0.166 \text{ fm}^{-3}. \quad (3.7.26)$$

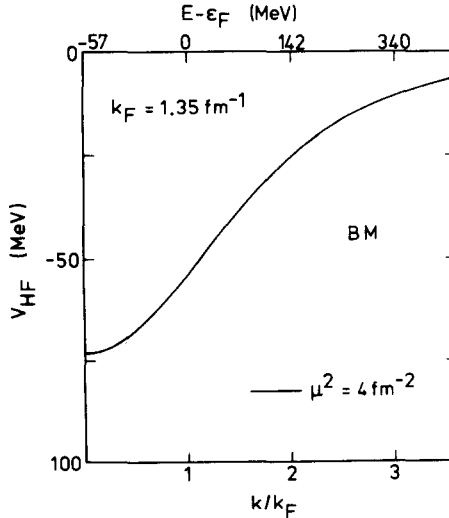


Fig. 3.6. Adapted from ref. [86]. Dependence upon k/k_F of the Hartree–Fock potential for $k_F = 1.35 \text{ fm}^{-1}$, in the case of the model interaction (7.23) with the parameter values (7.25).

The k -dependence shown in fig. 3.6 is typical of the one which would be obtained with other semi-realistic models, see e.g. ref. [80]. It furthermore resembles the Gaussian shape considered by Perey and Buck [7].

The k -mass $m_k^{\text{HF}} = m_{\text{HF}}^*$ associated with the Hartree–Fock field (7.24) is represented in fig. 3.7. The momentum dependence of this k -mass is typical of that obtained in other Hartree–Fock calculations, e.g. that based on the Yukawa interaction (7.21). It is also similar to the one calculated from the phenomenological nonlocal potential of Perey and Buck [7].

We conclude that most effective interactions lead to a Hartree–Fock potential which is a smoothly increasing function of the momentum, or equivalently of the energy. The corresponding effective mass is thus smaller than unity; it usually increases monotonically with increasing energy.

3.7.7. Skyrme interaction

Velocity-dependent interactions are of current use in nuclear physics. In particular, the “*Skyrme interaction*” is adopted in many modern Hartree–Fock calculations, see e.g. references contained in [19]. The matrix elements of the two-body part of the Skyrme interaction are of the form [87]

$$\langle \mathbf{k}, \mathbf{j} | v | \mathbf{a}, \mathbf{b} \rangle = t_0(1 + x_0 P_\sigma) + \frac{1}{2} t_1 [| \mathbf{k} - \mathbf{j} |^2 + | \mathbf{a} - \mathbf{b} |^2] + t_2 (\mathbf{k} - \mathbf{j}) \cdot (\mathbf{a} - \mathbf{b}); \quad (3.7.27a)$$

the Skyrme interaction also contains a three-body force

$$v^{(3)} = t_3 \delta(\mathbf{r}_1 - \mathbf{r}_2) \delta(\mathbf{r}_1 - \mathbf{r}_3). \quad (3.7.27b)$$

The matrix element (7.27a) increases with increasing relative momenta, in contrast with the model (7.23) for instance. In this sense, the Skyrme interaction appears unsuited for calculating the coupling between single-particle configurations and highly excited core configurations.

The Skyrme–Hartree–Fock value m_{Sk}^* of the effective mass is given by [87]

$$\frac{m_{\text{Sk}}^*}{m} = \frac{8}{8 + m\rho(3t_1 + 5t_2)}. \quad (3.7.28)$$

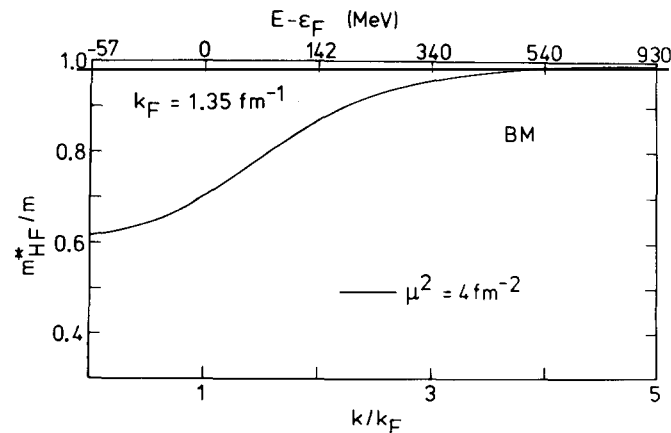


Fig. 3.7. Adapted from ref. [86]. Dependence upon k/k_F of the k -mass $m_k/m = m_{\text{HF}}^*/m$ as calculated from the Hartree–Fock potential shown in fig. 3.6.

It is independent of the nucleon momentum. Therefore, it also has the property that it does not have an enhancement near the Fermi energy. This remains true in finite nuclei.

3.7.8. Conclusions

The Hartree–Fock potential in nuclear matter is momentum-dependent, i.e. is nonlocal in spatial coordinates. It is independent of frequency, i.e. is local in time. The Hartree–Fock potential is thus a *static* approximation.

The effective mass m_{HF}^* is then equal to the k -mass. In general, it smoothly increases with increasing nucleon momentum. In the case of the Skyrme interaction, the effective mass is constant. Therefore, the Hartree–Fock approximation does not explain the enhancement of the empirical effective mass near the Fermi energy (see section 2.6). In principle, the possibility exists that the existence of an enhancement of the effective mass might be typical of “finite” nuclei. We shall see below that this is not the case, although the size of the enhancement is considerably increased when going from infinite nuclear matter to a finite nucleus. We also note that at least two other uniform systems, namely liquid ${}^3\text{He}$ and the electron gas, exist for which the experimental effective mass has a pronounced enhancement near the Fermi energy (sections 3.19 and 3.20). In order to reproduce this enhancement, we must therefore carry the perturbation series beyond the Hartree–Fock approximation. Since the higher-order contributions are frequency-dependent (or nonlocal in time), they contain the *dynamics of the shell model*. They form the subject of the next sections.

3.8. Attractive part of the second-order contribution

3.8.1. Introduction

Sections 3.8, 3.9 and 3.10 are devoted to the second-order contribution $\mathcal{M}_2(k; \omega)$ to the expansion of the mass operator in powers of the strength of the interaction. This contribution is represented by the graph at the left in fig. 3.8. In an infinite medium, total momentum is conserved in the matrix elements of the interaction v . This implies that at least one of the lines has to correspond to a hole ($j < k_F$) and at least one of the lines to a particle ($d > k_F$). This still leaves the freedom that the third line can be either a particle or a hole. Accordingly, the second-order contribution $\mathcal{M}_2(k; \omega)$ can be written as a sum of two terms

$$\mathcal{M}_2(k; \omega) = \mathcal{M}_{2a}(k; \omega) + \mathcal{M}_{2b}(k; \omega). \quad (3.8.1)$$

The contributions \mathcal{M}_{2a} and \mathcal{M}_{2b} are represented on the right-hand side of fig. 3.8. The present section is devoted to the study of the term \mathcal{M}_{2a} .

In many references, see e.g. [26, 86, 88–91] the term $\mathcal{M}_{2a}(k; \omega)$ was called the *polarization*

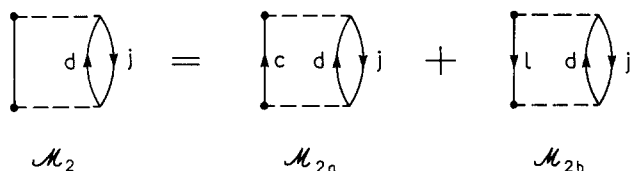


Fig. 3.8. Graphical representation of the second-order contribution $\mathcal{M}_2(k; \omega)$ to the mass operator. It is the sum of two contributions, denoted by $\mathcal{M}_{2a}(k; \omega)$ and $\mathcal{M}_{2b}(k; \omega)$, respectively. Only the direct terms are shown.

contribution. This followed a terminology introduced by Bertsch and Kuo [2], in the case of quasiparticles with momentum $k > k_F$. We shall see in section 3.8.5 that in the case of *quasihole* states ($k < k_F$), graph (2a) is associated with the blocking of ground state *correlations* rather than with core polarization. Hence, we avoid referring here to \mathcal{M}_{2a} as a polarization contribution and simply label it by an index (2a) as in ref. [88]. We call it *the attractive part of the second-order contribution* because we shall see that its real part is attractive for quasiparticles close to the Fermi surface ($k \approx k_F$).

One of the reasons for distinguishing between the contributions $\mathcal{M}_{2a}(k; \omega)$ and $\mathcal{M}_{2b}(k; \omega)$ is that these two terms have very different analytical properties. In particular, this leads to the fact that the second-order approximation to the momentum distribution $n(k)$ (e.g. (2.4)) must be computed from \mathcal{M}_{2a} for $k < k_F$, and from \mathcal{M}_{2b} for $k > k_F$. Moreover, the imaginary part of \mathcal{M}_{2a} describes the spreading of particle states (with momentum $k > k_F$), while that of \mathcal{M}_{2b} describes the spreading of hole states ($k < k_F$). The distinction between categories (a) and (b) can be made in any order of perturbation theory.

The present section is organized as follows. We first give in section 8.2 the algebraic expression of $\mathcal{M}_{2a}(k; \omega)$ and further discuss the motivation for distinguishing between two types ((a) and (b)) of contributions. We discuss a numerical example for \mathcal{M}_{2a} in section 8.3 and describe qualitative and physical interpretations of \mathcal{M}_{2a} and of its properties in sections 8.4 and 8.5, respectively. Conclusions are drawn in section 8.6.

3.8.2. Definition and properties

3.8.2.1. Definition of \mathcal{M}_{2a}

The algebraic expression of $\mathcal{M}_{2a}(k; \omega)$ is the following [36]

$$\mathcal{M}_{2a}(k; \omega) = \frac{1}{2} \sum_{j, c, d} n_<(j) n_>(c) n_>(d) \frac{|\langle k, j | V | c, d \rangle|^2}{\omega - e(c) - [e(d) - e(j)] + i\eta}. \quad (3.8.2)$$

We emphasize that this equation holds for *all* values of ω and k , namely $0 < k < \infty$; $-\infty < \omega < \infty$. Momentum conservation requires that

$$k + j = c + d. \quad (3.8.3)$$

3.8.2.2. Auxiliary potential

The energies $e(q)$ which appear in eq. (8.2) are given by

$$e(q) = q^2/2m + U(q), \quad (3.8.4)$$

where $U(q)$ is an “auxiliary” potential energy which is, in principle, arbitrary. In practice, it is chosen in such a way as to optimize the rate of convergence of the perturbation expansion.

The simplest choice consists in setting $U(q)$ to zero, i.e. in taking

$$e(q) = q^2/2m. \quad (3.8.5)$$

While this choice is convenient in numerical work, it presents the drawback that the imaginary part $\mathcal{W}_{2a}(k; \omega)$ of $\mathcal{M}_{2a}(k; \omega)$ then vanishes at $\omega = T_F = k_F^2/2m$. This is very different from the empirical Fermi energy ε_F (≈ -16 MeV) at which the imaginary part of the *exact* $\mathcal{M}(k; E)$ vanishes, see eq. (2.29).

Indeed, in nuclear matter, one has at saturation

$$k_F \approx 1.35 \text{ fm}^{-1}, \quad T_F \approx 37.8 \text{ MeV}, \quad \varepsilon_F \approx -16 \text{ MeV}. \quad (3.8.6)$$

Mainly for this reason [36, 42, 92], it appears preferable to adopt the following self-consistent choice for *all* values of q :

$$e(q) = E(q), \quad (3.8.7)$$

where $E(q)$ is defined by eq. (4.12). We thus write eq. (8.2) in the form

$$\mathcal{M}_{2a}(k; \omega) = \frac{1}{2} \sum_{j, c, d} n_<(j) n_>(c) n_>(d) \frac{|\langle \mathbf{k}, \mathbf{j} | \mathbf{v} | \mathbf{c}, \mathbf{d} \rangle_t|^2}{\omega - E(c) - [E(d) - E(j)] + i\eta}. \quad (3.8.8)$$

In practice, $\mathcal{V}(q; \omega)$ is not known, and in eq. (8.7) one must replace $E(q)$ by an approximation. For instance, one can use the Hartree–Fock approximation and take

$$e(q) = q^2/2m + V_{HF}(q). \quad (3.8.9)$$

Many numerical works are based on an approximate form of (8.9), namely on the following *effective mass approximation* (see eq. (2.6.7))

$$e(q) = \frac{q^2}{2m_{HF}^*} + \frac{m}{m_{HF}^*} V_{HF}(k_F) \quad (3.8.10)$$

where m_{HF}^* is the value of the Hartree–Fock effective mass at $k = k_F$.

It can be argued [26, 93] that most of the relevant physical quantities, in the present case $\mathcal{V}_{2a}(k; \omega)$ and $\mathcal{W}_{2a}(k; \omega)$, are not very sensitive upon the choice of $U(q)$, provided that these quantities are plotted versus the difference

$$\omega - e(k_F), \quad (3.8.11)$$

where $e(k_F)$ is the model Fermi energy, namely

$$e(k_F) = k_F^2/2m + U(k_F). \quad (3.8.12)$$

3.8.2.3. Real and imaginary parts of \mathcal{M}_{2a}

We follow the convention (2.26) and write

$$\mathcal{M}_{2a}(k; \omega) = \mathcal{V}_{2a}(k; \omega) - i \mathcal{W}_{2a}(k; \omega), \quad (3.8.13)$$

with

$$\mathcal{V}_{2a}(k; \omega) = \frac{\mathcal{P}}{2} \sum_{j, c, d} n_<(j) n_>(c) n_>(d) \frac{|\langle \mathbf{k}, \mathbf{j} | \mathbf{v} | \mathbf{c}, \mathbf{d} \rangle_t|^2}{\omega - E(c) - [E(d) - E(j)]}, \quad (3.8.14)$$

$$\mathcal{W}_{2a}(k; \omega) = \frac{\pi}{2} \sum_{j, c, d} n_<(j) n_>(c) n_>(d) |\langle k, j | v | c, d \rangle|^2 \cdot \delta(\omega - E(c) - [E(d) - E(j)]). \quad (3.8.15)$$

The symbol \mathcal{P} in eq. (8.14) means that one must calculate a principal value integral when the energy denominator vanishes.

In practice, $E(q)$ is an increasing function of q . Accordingly, one has ($E(k_F) = \varepsilon_F$, see eq. (2.30))

$$\mathcal{W}_{2a}(k; \omega) = 0 \quad \text{for } \omega < \varepsilon_F. \quad (3.8.16)$$

One can check that the summation on the right-hand side of eq. (8.13) restricts the phase space in such a way that [42, 94]

$$\mathcal{W}_{2a}(k; \omega) \sim C(\omega - \varepsilon_F)^2 \quad \text{for } \omega \rightarrow \varepsilon_F + 0, \quad (3.8.17)$$

where C is a positive constant. Note that

$$\mathcal{W}_{2a}(k; \omega) \geq 0, \quad (3.8.18)$$

which was our motivation for introducing a minus sign on the right-hand side of eq. (8.13).

3.8.2.4. Categories (a) and (b)

The property (8.16) is the basic characteristic of all the graphs that we shall label with an index a. More explicitly, any n th order approximation to the mass operator can be written as a sum of two terms, namely

$$\mathcal{M}_n(k; \omega) = \mathcal{M}_{na}(k; \omega) + \mathcal{M}_{nb}(k; \omega), \quad (3.8.19)$$

where $\mathcal{M}_{na}(k; \omega)$ has the following properties

$$\mathcal{M}_{na}(k; \omega) = \mathcal{V}_{na}(k; \omega) - i \mathcal{W}_{na}(k; \omega), \quad (3.8.20)$$

with

$$\mathcal{W}_{na}(k; \omega) = 0 \quad \text{for } \omega < \varepsilon_F, \quad (3.8.21)$$

$$\mathcal{W}_{na}(k; \omega) > 0 \quad \text{for } \omega > \varepsilon_F. \quad (3.8.22)$$

Conversely, the b-component \mathcal{M}_{nb} is *defined* by the following properties

$$\mathcal{M}_{nb}(k; \omega) = \mathcal{V}_{nb}(k; \omega) + i \mathcal{W}_{nb}(k; \omega), \quad (3.8.23)$$

with

$$\mathcal{W}_{nb}(k; \omega) = 0 \quad \text{for } \omega > \varepsilon_F, \quad (3.8.24)$$

$$\mathcal{W}_{nb}(k; \omega) > 0 \quad \text{for } \omega < \varepsilon_F. \quad (3.8.25)$$

Our convention is thus that *all graphs* (a) *have a negative imaginary part which vanishes for ω smaller than the Fermi energy*, while *all graphs* (b) *have a positive imaginary part which vanishes for ω larger than the Fermi energy*.

3.8.2.5. Dispersion relations

The following dispersion-type relation holds

$$\mathcal{V}_{2a}(k; \omega) = \frac{\mathcal{P}}{\pi} \int_{\varepsilon_F}^{\infty} \frac{\mathcal{W}_{2a}(k; \omega')}{\omega - \omega'} d\omega', \quad (3.8.26)$$

as can be checked by inserting in the integral the value of $\mathcal{W}_{2a}(k; \omega')$ given by eq. (8.15). We shall henceforth refer to eq. (8.26) as a dispersion relation without further qualification. The subtracted dispersion relation reads

$$\mathcal{V}_{2a}(k; \omega) = \mathcal{V}_{2a}(k; \omega_0) + (\omega - \omega_0) \frac{\mathcal{P}}{\pi} \int_{\varepsilon_F}^{\infty} \frac{\mathcal{W}_{2a}(k; \omega')}{(\omega' - \omega_0)(\omega - \omega')} d\omega', \quad (3.8.27)$$

where ω_0 is arbitrary.

Dispersion relations like (8.27) are quite useful from many points of view.

(i) From a *numerical* point of view, its interest resides in the fact that in some simple models the quantity $\mathcal{W}_{2a}(k; \omega)$ can be obtained in *algebraic form*. Then, $\mathcal{V}_{2a}(k; \omega)$ can be computed with great accuracy from eq. (8.27).

(ii) From a *formal* point of view, we shall see that the dispersion relation (8.27) enables one to establish the sign of $\mathcal{V}_{2a}(k; \omega)$ and of $\partial\mathcal{V}_{2a}(k; \omega)/\partial\omega$ for ω close to ε_F .

(iii) From a *physical* point of view, the dispersion relation (8.27) can be used to find the influence on $\mathcal{V}_{2a}(k; \omega)$ of those intermediate two particle-one hole states whose energy $E(c) + E(d) - E(j)$ is either larger or smaller than ω . It suffices indeed to write eq. (8.27) in the form

$$\mathcal{V}_{2a}(k; \omega) = \mathcal{V}_{2a}^{(+)}(k; \omega) + \mathcal{V}_{2a}^{(-)}(k; \omega), \quad (3.8.28)$$

where by definition

$$\mathcal{V}_{2a}^{(+)}(k; \omega) = \frac{1}{\pi} \int_{\varepsilon_F}^{\omega-0} \frac{\mathcal{W}_{2a}(k; \omega')}{\omega - \omega'} d\omega', \quad (3.8.29)$$

$$\mathcal{V}_{2a}^{(-)}(k; \omega) = \frac{1}{\pi} \int_{\omega+0}^{\infty} \frac{\mathcal{W}_{2a}(k; \omega')}{\omega - \omega'} d\omega'. \quad (3.8.30)$$

The superscripts (+) and (−) refer to the following properties

$$\mathcal{V}_{2a}^{(+)}(k; \omega) \geq 0, \quad (3.8.31)$$

$$\mathcal{V}_{2a}^{(-)}(k; \omega) \leq 0. \quad (3.8.32)$$

The dispersion relation (8.26) can be extended to any term of the perturbation series. Our definition (8.20)–(8.25) of the graphs of categories (a) and (b) implies the following dispersion relations

$$\mathcal{V}_{na}(k; \omega) = \frac{\mathcal{P}}{\pi} \int_{\epsilon_F}^{\infty} \frac{\mathcal{W}_{na}(k; \omega')}{\omega - \omega'} d\omega', \quad (3.8.33)$$

$$\mathcal{V}_{nb}(k; \omega) = \frac{\mathcal{P}}{\pi} \int_{-\infty}^{\epsilon_F} \frac{\mathcal{W}_{nb}(k; \omega')}{\omega - \omega'} d\omega', \quad (3.8.34)$$

where n refers to the order of the graph in the perturbation series. By summing over all orders, one gets the dispersion relations

$$\mathcal{V}_a(k; \omega) = \frac{\mathcal{P}}{\pi} \int_{\epsilon_F}^{\infty} \frac{\mathcal{W}_a(k; \omega')}{\omega - \omega'} d\omega', \quad (3.8.35)$$

$$\mathcal{V}_b(k; \omega) = \frac{\mathcal{P}}{\pi} \int_{-\infty}^{\epsilon_F} \frac{\mathcal{W}_b(k; \omega')}{\omega - \omega'} d\omega'. \quad (3.8.36)$$

The real part $\mathcal{V}(k; \omega)$ of the exact mass operator $\mathcal{M}(k; \omega)$ is given by

$$\mathcal{V}(k; \omega) = V_{HF}(k) + \mathcal{V}_a(k; \omega) + \mathcal{V}_b(k; \omega). \quad (3.8.37)$$

Equations (8.35) and (8.36) yield the general dispersion relation (2.35).

3.8.3. Numerical example

The quantity $\mathcal{W}_{2a}(k; \omega)$ has been calculated in algebraic form for *all* values of k and ω in the case of the dilute hard sphere Fermi gas model [88] which will be discussed in section 3.14. It corresponds to replacing in eq. (8.8) all the matrix elements $\langle k, j | v | a, b \rangle$ by a constant. Once $\mathcal{V}_{2a}(k; \omega)$ is known, one can calculate $\mathcal{V}_{2a}(k; \omega)$ and related quantities by making use of the dispersion relation (8.27). One important conclusion of the dilute hard sphere Fermi gas model is that the dependence upon ω' of $\mathcal{W}_{2a}(k; \omega')$ is approximately the same for all values of k in the domain $k/k_F < 2$ and for $\omega' - \epsilon_F$ smaller than about 50 MeV. This had been foreseen by Orland and Schaeffer [93] on the basis of phase space arguments and has been confirmed in refs. [83, 95]. This property has been applied by many authors [26,

89–91, 93] who only computed $\mathcal{W}_{2a}(k; \omega)$ as a function of ω for a *fixed* value of k , usually for $k = k_F$. We thus introduce the *definitions*

$$W_{2a}(\omega) = \mathcal{W}_{2a}(k_F; \omega), \quad (3.8.38)$$

$$V_{2a}(\omega) = \mathcal{V}_{2a}(k_F; \omega). \quad (3.8.39)$$

The dispersion relation (8.26) then yields

$$V_{2a}(\omega) = \frac{\mathcal{P}}{\pi} \int_{\epsilon_F}^{\infty} \frac{W_{2a}(\omega')}{\omega - \omega'} d\omega'. \quad (3.8.40)$$

The quantity $W_{2a}(\omega)$ has been calculated in algebraic form for all values of ω in the case of the model interaction (7.23) and in the framework of the effective mass approximation (8.10) [86]. The result for $k_F = 1.35 \text{ fm}^{-1}$ is shown in fig. 3.9, where

$$\omega_F = k_F^2/2m + V_{HF}(k_F) \approx \epsilon_F \quad (3.8.41)$$

is the Hartree–Fock approximation to the Fermi energy.

For ω close to ω_F , one has (see eq. (8.17))

$$W_{2a}(\omega) \sim C(\omega - \omega_F)^2 \quad (3.8.42)$$

with $C \approx 3 \times 10^{-3} \text{ MeV}^{-1}$ for $k_F = 1.35 \text{ fm}^{-1}$.

The decrease of $\mathcal{W}_{2a}(\omega)$ for large $|\omega|$ is due to the decrease of the matrix element (7.23) with increasing relative momentum. This is a common feature of all nonsingular potentials.

The real part $V_{2a}(\omega)$ as calculated from the dispersion relation (8.40) is plotted in the lower part of fig. 3.9. In the present context, we are mainly interested in the vicinity of the Fermi energy. There, one has

$$V_{2a}(\omega) < 0 \quad \text{for } \omega \approx \omega_F, \quad (3.8.43)$$

$$\frac{d}{d\omega} V_{2a}(\omega) < 0 \quad \text{for } \omega \approx \omega_F. \quad (3.8.44)$$

Property (8.43) is the origin of the expression “attractive part of the second-order contribution” that we coined for graph (2a). We shall see in the next section that the features (8.43) and (8.44) are largely independent of the specific nature of the interaction which is being used.

Property (8.44) implies that for $\omega \approx \omega_F$ graph (2a) yields a positive contribution to the ω -mass m_ω defined in eq. (6.10). Let us call $m_\omega^{(2a)}$ the value that the ω -mass would take if graph (2a) alone would be responsible for the full ω -dependence of the mass operator, namely

$$m_\omega^{(2a)}(E)/m = 1 - dV_{2a}(E)/dE. \quad (3.8.45)$$

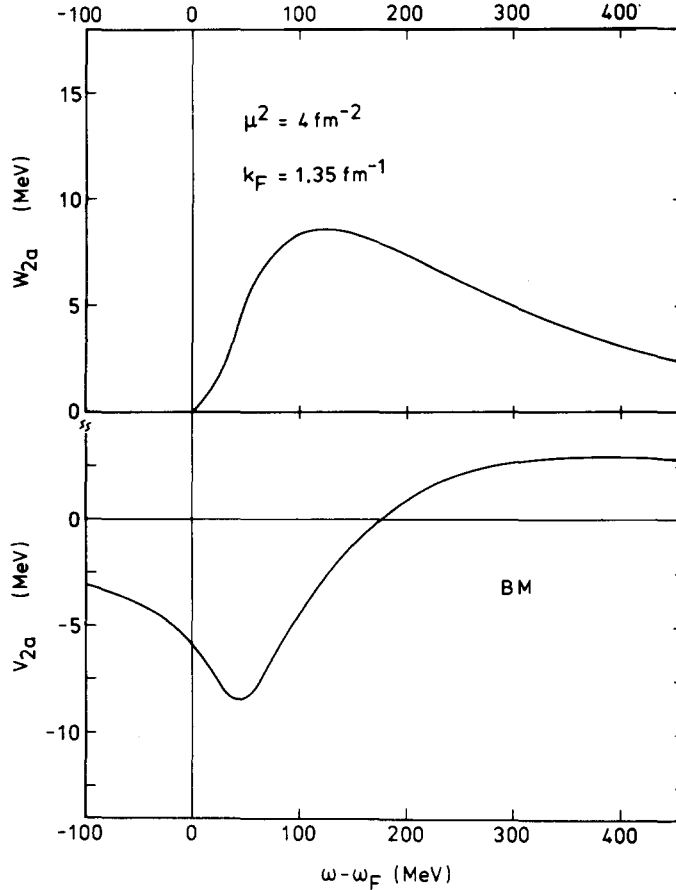


Fig. 3.9. Adapted from ref. [86]. Dependence upon $\omega - \omega_F$ of the imaginary part (upper graph) and of the real part (lower graph) of the contribution (2a), in the case of the model interaction (7.23) with the parameter values (7.25), and for the Fermi momentum $k_F = 1.35 \text{ fm}^{-1}$. The Fermi energy ω_F is defined by eq. (8.41).

The quantity $m_\omega^{(2a)}(E)/m$ is plotted versus $E - \omega_F$ in fig. 3.10. We note that it has a maximum located slightly above the (approximate) Fermi energy ω_F .

The investigation of the E -dependence of $m_\omega^{(2a)}(E)$ requires an accurate calculation of the derivatives of $V_{2a}(\omega)$, and therefore a very accurate knowledge of $V_{2a}(\omega)$. This is the reason why it was important to use an algebraic expression of $W_{2a}(\omega)$ as input in the dispersion relation (8.40).

3.8.4. Qualitative discussion

In the present section, we argue that the main features of the results displayed in figs. 3.9 and 3.10 are expected to hold for other choices of the effective interaction v .

We already stated that the threshold properties (8.16) and (8.42) hold for any uniform normal Fermi system and that for finite range nonsingular and velocity-independent interactions, $W_{2a}(\omega)$ approaches zero for $|\omega| \rightarrow \infty$. (The case of singular and of velocity-dependent interactions will be discussed in sections 3.14–3.17). Hence, the bell shape of $W_{2a}(\omega)$ shown on the top of fig. 3.9 is quite general, see other examples in e.g. refs. [83, 93]. Once the shape of $W_{2a}(\omega)$ is known, the ω -dependence of $V_{2a}(\omega)$ can be discussed on the basis of the dispersion relation (8.40).

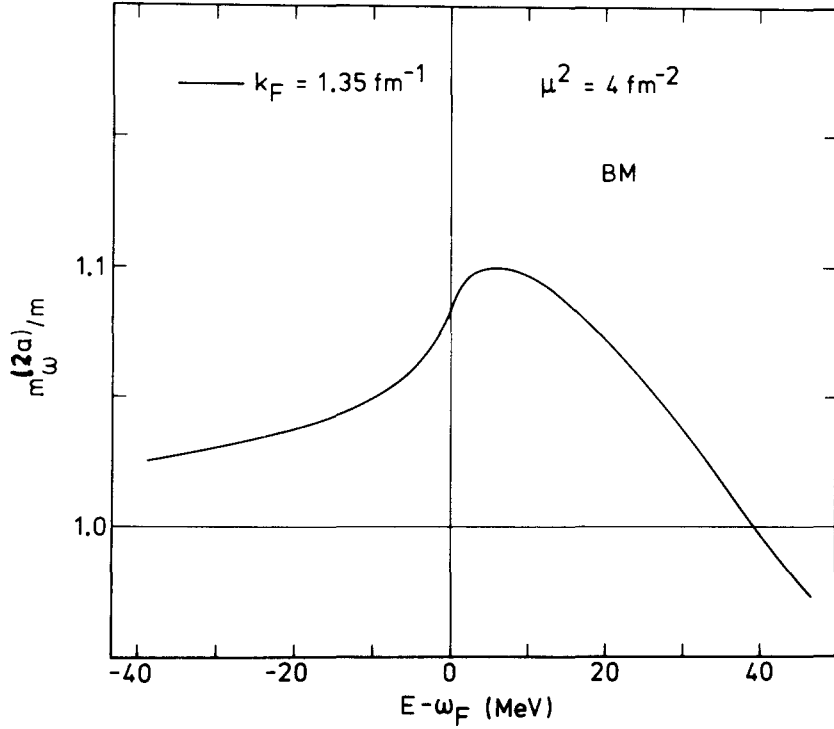


Fig. 3.10. Adapted from ref. [86]. Dependence upon $E - \omega_F$ of the quantity $m_\omega^{(2a)}(E)/m$, as calculated from eq. (8.45) and from the values of $V_{2a}(E)$ shown in fig. 3.9.

Let us first consider the domain $\omega < \omega_F$. Then, the integrand on the right-hand side of eq. (8.40) is negative definite and one has

$$V_{2a}(\omega) < 0 \quad \text{for } \omega < \omega_F. \quad (3.8.46)$$

Since $V_{2a}(\omega)$ is a continuous function of ω , it remains negative at least for ω slightly larger than ω_F . This leads to the property (8.43).

We now turn to the contribution $m_\omega^{(2a)}(E)$ of the graph (2a) to the ω -mass. In the domain $\omega < \omega_F$, the energy denominator in the integrand on the right-hand side of eq. (8.40) never vanishes. One has thus

$$\frac{d}{dE} V_{2a}(E) = -\pi^{-1} \int_{\omega_F}^{\infty} \frac{W_{2a}(\omega')}{(E - \omega')^2} d\omega' \quad (3.8.47)$$

for $E < \varepsilon_F$. This quantity is negative definite and, by continuity, remains negative at least for E somewhat larger than ω_F . Consequently, one has

$$m_\omega^{(2a)}(E) > m \quad \text{for } E \approx \omega_F. \quad (3.8.48)$$

Furthermore, one has for $E < \omega_F$

$$\frac{d}{dE} [m_\omega^{(2a)}(E)] = -2\pi^{-1} \int_{\omega_F}^{\infty} \frac{W_{2a}(\omega')}{(E - \omega')^3} d\omega'. \quad (3.8.49)$$

This implies that $m_\omega^{(2a)}(E)$ is an increasing function of E for $E < \omega_F$ and, by continuity, at least for E slightly larger than ω_F . From the threshold behaviour (8.42), one finds that

$$\lim_{E \rightarrow \omega_F^-} \left\{ \frac{d}{dE} m_\omega^{(2a)}(E)/m \right\} = -2C \lim \ln \frac{|E - \omega_F|}{-|\omega_F|} = +\infty. \quad (3.8.50)$$

We conclude that $m_\omega^{(2a)}(E)/m$ is larger than unity and is increasing with increasing E for $E < \omega_F$ and also for E slightly larger than ω_F . It has an inflection point with a positive infinite slope at $E = \omega_F$.

If $W_{2a}(\omega)$ decreases for large ω , $V_{2a}(\omega)$ will vanish at some energy $E_M^{(2a)} > \omega_F$. Hence, it must have a minimum at an energy $E_q^{(2a)}$, with

$$\omega_F < E_q^{(2a)} < E_M^{(2a)}. \quad (3.8.51)$$

This implies that $m_\omega^{(2a)}(E_q^{(2a)}) = m$. Together with inequality (8.48), this result shows that $m_\omega^{(2a)}(E)$ reaches a maximum at an energy $E_{\max}^{(2a)}$, with

$$\omega_F < E_{\max}^{(2a)} < E_q^{(2a)}. \quad (3.8.52)$$

Since the slope of $m_\omega^{(2a)}(E)$ is positive definite at $E = \omega_F$, the energy $E_{\max}^{(2a)}$ is likely to be only slightly larger than ω_F , or else the maximum value $m_\omega^{(2a)}(E_{\max})/m$ would be quite large.

We conclude that $m_\omega^{(2a)}(E)$ presents an enhancement in the vicinity of the Fermi energy. The maximum is located somewhat above the Fermi surface.

In the example of figs. 3.9 and 3.10, one has $E_M^{(2a)} - \omega_F \approx 180$ MeV, $E_q^{(2a)} - \omega_F \approx 40$ MeV, $E_{\max}^{(2a)} - \omega_F \approx 7$ MeV, $m_\omega^{(2a)}(E_{\max})/m \approx 1.1$, $m_\omega^{(2a)}(E = 0)/m \approx 1.02$.

Since the enhancement peak of $m_\omega^{(2a)}(E)$ is asymmetric, one can only give a rough measure of its width Δ_{2a} . In the case of fig. 3.10, one has $\Delta_{2a} \approx 30$ MeV, which is of the order of the kinetic energy of a nucleon at the Fermi surface ($k_F^2/2m = 37.8$ MeV for $k_F = 1.35$ fm $^{-1}$). The peak is narrower for smaller k_F . For $k_F = 1$ fm $^{-1}$, for instance, its width reduces to $\Delta_{2a} \approx 20$ MeV [86], which is again of the order of $k_F^2/2m$. Finally, the width Δ_{2a} decreases when the range of the interaction v increases, i.e. when μ decreases in eq. (7.23) [86].

3.8.5. Physical interpretation

3.8.5.1. Potential energy and spreading width

The most direct physical interpretation of the mass operator $M(k; \omega)$ is made in terms of the quasiparticle properties. The potential energy felt by a quasiparticle of momentum k is $V^{\text{NL}}(k)$ (eq. (4.14)), and its spreading width is (eq. (4.19))

$$\Gamma^\downarrow = 2 Z(k) W^{\text{NL}}(k). \quad (3.8.53)$$

Equivalently, the potential energy of a quasiparticle with energy E is given by $V(E)$ (eq. (5.8)) and its spreading width is (eq. (5.15))

$$\Gamma^\downarrow = 2 Z(E) W(E). \quad (3.8.54)$$

Here, we expressed the residue Z as a function of E rather than of k but kept the same symbol for simplicity. Note that

$$Z(E) = m/m_\omega(E). \quad (3.8.55)$$

We now give a simple physical interpretation of the results presented in section 8.3. We restrict the discussion to the on-shell values ($\omega = E(k)$). In the present case, this is quite automatic since we have assumed that the nonlocality of $\mathcal{M}_{2a}(k; \omega)$ can be neglected for k close to k_F and for $\omega - \omega_F < 50$ MeV (see section 8.5.6). We thus consider the functions $V_{2a}(E)$ and $W_{2a}(E)$ (eqs. (8.38) and (8.39)) where E is the Hartree–Fock approximation to the quasiparticle energy

$$E(k) \approx k^2/2m + V_{HF}(k). \quad (3.8.56)$$

The physical interpretation of $V_{2a}(E)$ is that it yields a second-order contribution to the potential energy of a quasiparticle with energy E . A more accurate estimate to this shift to the Hartree–Fock value is given by

$$\bar{V}_{2a} = \frac{m_{HF}^*}{m} V_{2a}(E),$$

where the origin of the factor m_{HF}^*/m has been discussed in section 3.5 (see eq. (5.23)).

The physical interpretation of $2W_{2a}(E)$ is that it yields the second-order approximation to the spreading width of a quasiparticle with energy E . More precisely, this spreading width is given by (see eqs. (8.54) and (8.56))

$$\Gamma^\downarrow(E) = 2Z_{2a}(E)W_{2a}(E), \quad (3.8.57)$$

where

$$Z_{2a}(E) = m/m_\omega^{(2a)}(E) \quad (3.8.58)$$

is the value of $Z(E)$ as evaluated from graph (2a) (see also eq. (9.10) below).

For $E > 0$, one can also interpret

$$\bar{W}_{2a}(E) = W_{2a}(E) m_{HF}^*/m \quad (3.8.59)$$

as being the *second-order approximation to the imaginary part of the optical-model potential*.

3.8.5.2. Graphical representation

The graphical representation of $\mathcal{M}_{2a}(k; \omega)$ was given in fig. 3.8, and is recalled at the top of fig. 3.11. Whenever quasiparticle properties are concerned, the contribution of graph (2a) is often drawn in two different ways depending on whether one considers particle states ($k > k_F$) or hole states ($k < k_F$). This is shown at the bottom of fig. 3.11.

We emphasize that the two graphs shown at the bottom of fig. 3.11 correspond to the same algebraic expression, namely (8.8). The reason for sometimes using two different graphical representations is that graph 2a is often interpreted as associated with a polarization (PO) effect for quasiparticle states above the Fermi surface, and with a correlation (CO) effect for quasiparticle states below the Fermi surface (quasiholes). This is explained in the next section.

3.8.5.3. Polarization and correlation effects

Let us first consider the case $k > k_F$ (or equivalently $E > \varepsilon_F$), i.e. quasiparticle states above the Fermi surface (“unoccupied” bound or scattering single-particle states). Graph (2a) is then often drawn as the polarization (PO) graph in fig. 3.11, which has the following physical interpretation. An incoming nucleon with momentum k and energy ω interacts with one core nucleon (j). As a result, a two particle (c, d) –one hole (j) configuration of the ($A + 1$) system is excited. In other words, the extra nucleon with energy $E > \varepsilon_F$ “polarizes” the core (with A nucleons), in which it excites a one particle (d) –one hole (j) configuration. This can be an energy-conserving collision if ω is larger than the Fermi energy. These energy-conserving collisions give a contribution to the imaginary part of the mass operator or equivalently of the optical-model potential.

We now turn to the case $k < k_F$ (or equivalently $E < \varepsilon_F$), i.e. quasiparticle states below the Fermi surface (“quasiholes” or “occupied” single-particle states). The physical meaning of the graph CO of fig. 3.11 is then illustrated in fig. 3.12 and is the following. The single-particle energy of a hole state with momentum k is defined by

$$E(k) = B(A) - B_k(A - 1), \quad (3.8.60)$$

where $B(A)$ is the energy of the nucleus with A nucleons, while $B_k(A - 1)$ is the energy of the nucleus with $(A - 1)$ nucleons which is formed by punching a hole with quantum number k ($k \rightarrow \{n, l, j\}$ for a finite system) in the core A .

Let us call $B^{\text{HF}}(A)$ the value of $B(A)$ in the Hartree–Fock approximation. The latter amounts to an independent particle model (see section 3.7). In reality, the ground state of the system is correlated; its wave function ψ_0 (see eq. (2.1)) contains two particle (c, d) –two hole (k, j) (and more complicated) admixtures. These correlations decrease $B(A)$ as compared to the Hartree–Fock approximation. The creation of a hole eliminates some of the ground state correlations. Thus, the gain in binding energy with respect to the Hartree–Fock value is larger for the A -particle system than what it is for the $(A - 1)$ -particle system, i.e.

$$B^{\text{HF}}(A) - B^{\text{CO}}(A) > B_k^{\text{HF}}(A - 1) - B_k^{\text{CO}}(A - 1),$$

or

$$B^{\text{HF}}(A) - B_k^{\text{HF}}(A - 1) > B^{\text{CO}}(A) - B_k^{\text{CO}}(A - 1).$$

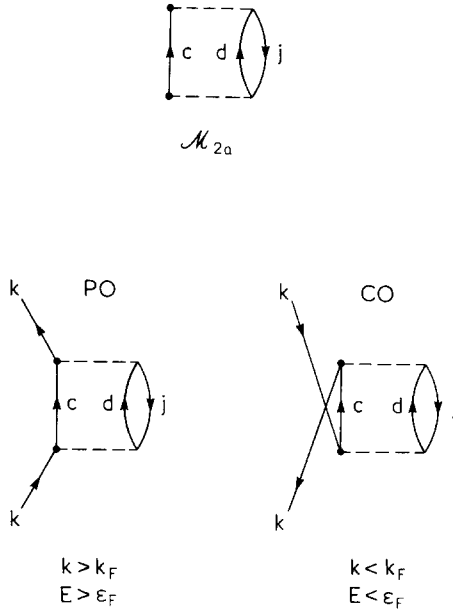


Fig. 3.11. The graph at the top represents the contribution $\mathcal{M}_{2a}(k; \omega)$ to the mass operator (see fig. 3.8). Quite often, the corresponding contributions to the quasiparticle properties are drawn as shown at the bottom, where the left-hand diagram is used for particle states ($k > k_F, E > \epsilon_F$), and the right-hand diagram is used for hole states ($k < k_F, E < \epsilon_F$). The labels CO and PO stand for *correlation* and *polarization*, respectively.

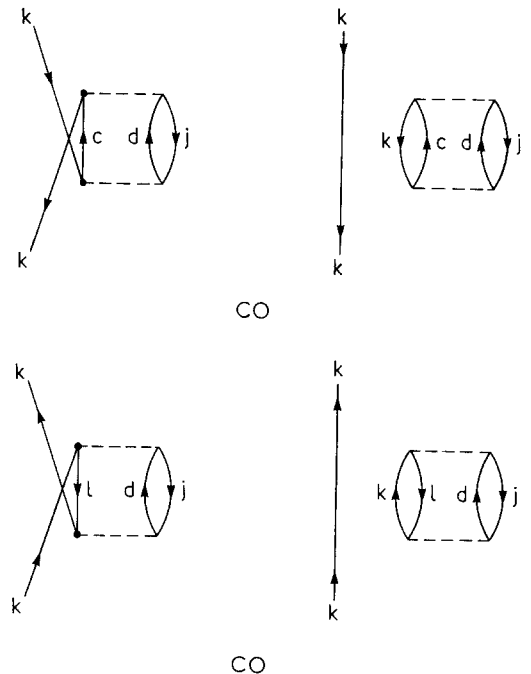


Fig. 3.12. Interpretation of graphs CO in fig. 3.11 and in fig. 3.16 below as “correlation” diagrams. They depict the influence of the core correlations on the quasiparticle energies.

Following the definition of the single-particle energy for a hole state given above we obtain

$$E^{\text{HF}}(k) > E^{\text{CO}}(k)$$

which establishes the attractive character of this effect.

Figure 3.12 may thus be interpreted as follows. The additional hole (k) in nucleus ($A - 1$) “blocks” (because of the Pauli principle) those two particle–two hole admixtures in the ground state of nucleus A in which one hole was in state k . This is why the correlation graph (i.e. $V_{2a}(E)$ for $E < \epsilon_F$) is sometimes called a *Pauli blocking diagram*, or a *rearrangement diagram*, or is said to depict an “interference with a ground state correlation” [2].

In many recent papers, contribution (2a) is called the polarization contribution. While this terminology is appropriate for $k > k_F$, it is somewhat misleading in the case of quasiholes ($k < k_F$), for which the polarization effect arises from contribution (2b) [93].

Other terminologies have also been used in the literature. For instance, Brandow [97] and Engelbrecht and Weidenmüller [32] called graphs CO of fig. 3.12 the *on-shell part* of the second-order contribution for hole (top) and for particle (bottom) states, and graph PO of fig. 3.11 the *off-shell part* of the second-order contribution *for particle states*. The reason for this denomination is that when a self-energy (or mass operator) insertion is made on a Goldstone graph for the *total* energy of the system, this insertion can be put “on-the-energy-shell” by using the time-ordering theorem of Bethe,

Brandow and Petscheck [98] if the two external lines are crossed. In the present context, this terminology would be confusing since we call “on-shell” the value of the mass operator $\mathcal{M}(k; \omega)$ at the frequency $\omega = E(k)$ of the quasiparticle.

3.8.5.4. Depletion of the Fermi sea

From the preceding interpretation, one expects that for $k < k_F$ a close relationship exists between graph (2a) and the *depletion*

$$\kappa = 1 - n(k) \quad (3.8.61)$$

of the Fermi sea (see eq. (2.4) and fig. 3.1). This is the case. For $k \leq k_F - 0$ and in the framework of second-order perturbation theory [36], one has indeed

$$\kappa_2(k) = \frac{1}{2} \sum_{j, c, d} n_<(j) n_>(c) n_>(d) \frac{|\langle \mathbf{k}, j | v | \mathbf{c}, d \rangle|^2}{[E(k) + E(j) - E(c) - E(d)]^2}. \quad (3.8.62a)$$

Comparing eqs. (8.8), (8.45) and (8.61), we obtain for $k < k_F - 0$

$$\kappa_2(k) = m_\omega^{(2a)} / m - 1. \quad (3.8.62b)$$

This quantity is closely related to the smallness parameter which characterizes the rate of convergence of Brueckner’s theory of nuclear matter (section 3.15). There one introduces a *correlated two-body wave function* which is written in the form

$$\psi_{\mathbf{k}, j} = |\mathbf{k}, j\rangle + D_{\mathbf{k}, j}. \quad (3.8.63)$$

The quantity $D_{\mathbf{k}, j}$ is called the *defect function*. It reads, in first-order perturbation theory,

$$D_{\mathbf{k}, j} = \sum_{c, d} \frac{n_>(c) n_>(d)}{e(k) + e(j) - e(c) - e(d)} \langle \mathbf{c}, \mathbf{d} | v | \mathbf{k}, j \rangle | \mathbf{c}, \mathbf{d} \rangle. \quad (3.8.64)$$

For $k < k_F$, one has [42]

$$\kappa_2(k) = \sum_j n_<(j) \langle D_{\mathbf{k}, j} | D_{\mathbf{k}, j} \rangle. \quad (3.8.65)$$

This shows the relationship between the “smallness parameter” κ_2 and the “volume of the defect function” or “volume of the wound”. Here, the word “wound” refers to the fact that for a hard-core interaction, $D_{\mathbf{k}, j}$ gives rise to a wound in the plane wave $|\mathbf{k}, j\rangle$, since the correlated two-body wave function $\psi_{\mathbf{k}, j}$ must vanish for $r_{12} < c$, where c is the hard-core radius.

The volume of the wound is of the order of $(4\pi/3)c^3$, while ρ is equal to $((4\pi/3)r_0^3)^{-1}$ where r_0 is the constant which appears in the expression $R = r_0 A^{1/3}$ for the nuclear radius. Hence, one expects the smallness parameter to be of the order of $(c/r_0)^3$. This indicates why the Bethe–Brueckner expansion is believed to be applicable only to dilute normal systems, i.e. to normal systems in which the distance

between neighbouring particles is larger than the range of the strong part of the particle-particle interaction.

3.8.5.5. Open and closed channels

In eq. (8.28), we wrote $\mathcal{V}_{2a}(k; \omega) \approx V_{2a}(\omega)$ as a sum of two terms. The first one, $V_{2a}^{(+)}(E)$, is positive for $E > \varepsilon_F$ and vanishes for $E < \varepsilon_F$. We recall that $V_{2a}^{(+)}(E)$ is that part of $V_{2a}(E)$ which is due to the excitation of two particle-one hole configurations with energy smaller than E . In the terminology used in the field of nuclear reactions, one could think of $V_{2a}^{(+)}(E)$ as being that contribution to the single-particle potential at the energy $E > 0$ which originates from the coupling between the entrance channel and those inelastic channels which are open at the energy E . Correspondingly, it appears tempting to associate $V_{2a}^{(-)}$ with the coupling between the entrance channel and the closed channels. These interpretations would, however, not be quite correct, as we now discuss.

In eqs. (8.29) and (8.30), the energy ω' of the intermediate two particle-one hole state is (see fig. 3.11)

$$\omega' = E(c) + E^*, \quad (3.8.66)$$

where

$$E^* = E(d) - E(j) \quad (3.8.67)$$

is the excitation energy of the core. Writing $V_{2a}(E)$ as the sum $V_{2a}^{(+)}(E) + V_{2a}^{(-)}(E)$ corresponds to a subdivision between the domains $\omega' < E$ and $\omega' > E$, respectively. Equation (8.67) shows that the inequalities $\omega' < E$ and $E^* > E$ can be simultaneously fulfilled, because $E(c)$ can be negative (in a finite nucleus, this corresponds to c being a bound unoccupied orbit). Hence, $V_{2a}^{(+)}(E)$ contains some contributions from closed channels ($E^* > E$).

When the energy E is only slightly larger than E^* (i.e. when the incoming nucleon is close to the inelastic threshold or is close to the top of the Coulomb barrier in that inelastic channel), the corresponding $W_{2a}(\omega')$ is very small for $\omega' < E$. Hence, $V_{2a}(E)$ is then dominated by $V_{2a}^{(-)}(E)$. In other words, channels which are barely open yield an attractive contribution to the single-particle potential in the entrance channel, i.e. to the real part of the optical model potential. This explains the results recently published in ref. [99].

We note that if a channel is closed with a far away threshold ($E^* \gg E$), then $\omega' \gg E$, and $V_{2a}(E)$ reduces to $V_{2a}^{(-)}(E)$ which is attractive. Thus, barely open channels and closed channels both yield an attractive contribution to the real part of the optical-model potential at positive energy.

3.8.5.6. Coupled-channel approach

In the preceding section, we established some contact between $V_{2a}(E)$ for $E > 0$ (i.e. the polarization contribution, see fig. 3.11) on the one hand, and the terminology and concepts used in the field of nuclear reactions on the other hand. In the latter field, one often uses the coupled-channel formalism. In the present section, we briefly outline the relationship between this formalism and our expressions.

Let us denote the entrance (elastic) channel by the index e and the inelastic channel by an index i (see fig. 3.13). The coupled-channel equations read

$$(E - H_{ee}) \chi_e(E) = V_{ei} \chi_i(E), \quad (3.8.68a)$$

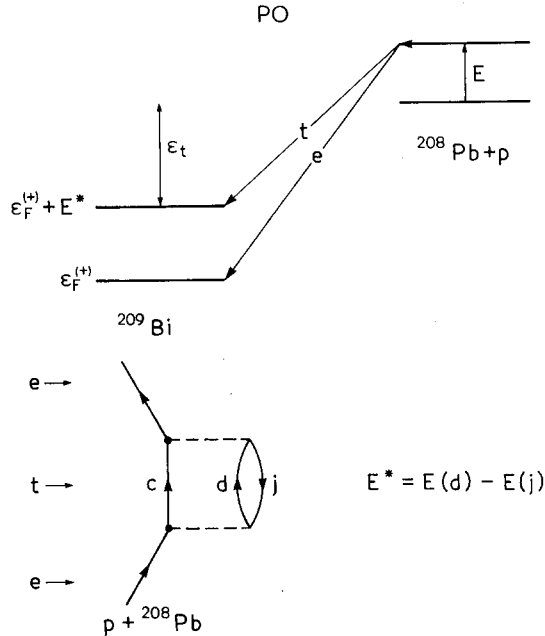


Fig. 3.13. Illustration of the polarization of a core (^{208}Pb in this example) by an incoming proton. The core (target) is excited to the energy $E^* = E(d) - E(j)$ (cf. fig. 3.11). The “entrance” channel ($^{208}\text{Pb} + \text{incoming proton with energy } E$) is denoted by e , the inelastic channel by t .

$$(E - H_{tt}) \chi_t(E) = V_{te} \chi_e(E). \quad (3.8.68b)$$

From eq. (8.68b), one finds

$$\chi_t(E) = \frac{1}{E - H_{tt} + i\eta} V_{te} \chi_e(E), \quad (3.8.69)$$

where the $+i\eta$ in the denominator corresponds to the boundary condition that χ_t is an outgoing wave. Equations (8.68a) and (8.69) then yield

$$(E - \tilde{H}_{ee}) \chi_e(E) = 0, \quad (3.8.70)$$

where \tilde{H}_{ee} is the effective Hamiltonian in the entrance channel [100] and reads

$$\tilde{H}_{ee} = H_{ee} + V_{et} \frac{1}{E - H_{tt} + i\eta} V_{te}. \quad (3.8.71)$$

Hence, the expectation value of the correction to H_{ee} due to the “polarization” (i.e. to the excitation) of the target is given by

$$\mathcal{P} \int_{\varepsilon_t}^{\infty} d\omega' \frac{|\langle \chi_e(E) | V | \chi_t(\omega') \rangle|^2}{E - \omega'} - i\pi |\langle \chi_e(E) | V | \chi_t(E) \rangle|^2 \theta(e - \varepsilon_t) \quad (3.8.72)$$

where ε_t is the threshold energy of channel t . Equations (8.26) and (8.66) show that the expression (8.72) is equivalent to the contribution of channel t to $\mathcal{M}_{2a}(E)$, see eqs. (8.13)–(8.15). The dispersion relation (8.40) is fulfilled by (8.72).

When the channel is closed ($E < \varepsilon_t$), the real part of (8.72) is negative. A closed channel thus yields an attractive contribution to the real part of the effective nucleon–nucleus potential in the entrance channel, and does not contribute to its imaginary part. A barely open channel also leads to an attractive correction. If the channel t is wide open, its contribution to the real part of the nucleon–nucleus potential can have either sign.

We showed that the coupled-channel formalism quite naturally leads to the contribution (2a). In our derivation, however, we did not encounter the equivalent of correction (2b) (see fig. 3.8). This is because contribution (2b) at positive energy (i.e. in the case of nucleon–nucleus scattering) is associated with a Pauli blocking effect. Hence, it is a consequence of the existence of core correlations. The latter are omitted in the coupled-channel formalism sketched here, and more generally in most applications of nuclear reaction theory.

3.8.5.7. Nonlocality

In sections 3.8.3–3.8.5, we have assumed that the nonlocality of \mathcal{M}_{2a} (the k -dependence of $\mathcal{V}_{2a}(k; \omega)$ and of $\mathcal{W}_{2a}(k; \omega)$) can be neglected; i.e. that \mathcal{W}_{2a} is local in coordinate space. This is an approximation, whose accuracy we now briefly discuss.

In order to evaluate the effect of the k -dependence of \mathcal{V}_{2a} upon the full k -mass m_k (eq. (6.9)), let us consider the following model (see eq. (7.18))

$$\mathcal{V}_{2a}(k; \omega) \approx V_0^{(2a)}(\omega) \exp(-\frac{1}{4}a^2 k^2), \quad (3.8.73)$$

in the domain $\omega - \omega_F \approx$ several tens MeV, with (see fig. 3.9)

$$V_0^{(2a)}(\omega) \approx -7 \text{ MeV}. \quad (3.8.74)$$

From eqs. (7.18), (7.20) and (8.73), we obtain the following expression for the k -mass associated with the sum $V_{PB}(k) + \mathcal{V}_{2a}(k; \omega)$:

$$m_k(\omega_F)/m \approx \left\{ 1 - \frac{1}{2} m a^2 [V_{HF} + V_0^{(2a)}]_{\omega=\omega_F} \right\}^{-1}. \quad (3.8.75)$$

Using $V_0 \approx -70$ MeV in eq. (7.18), we find

$$m_k(\varepsilon_F)/m \approx 0.68, \quad (3.8.76)$$

as compared to the value $m_k(\varepsilon_F)/m \approx 0.71$ obtained from eq. (7.20). Hence, the nonlocality of $\mathcal{V}_{2a}(k; \omega)$ decreases the value of the k -mass from its Hartree–Fock value.

This conclusion is verified in fig. 3.14. There, the quantity

$$\frac{m_k^{(2a)}}{m} = \left[1 + \frac{m}{k} \frac{\partial \mathcal{V}^{(2a)}(k; \omega)}{\partial k} \right]_{\omega=k^2/2m}^{-1} \quad (3.8.77)$$

is plotted versus k/k_F , in the case of a Yukawa interaction whose range (0.3 fm) corresponds to

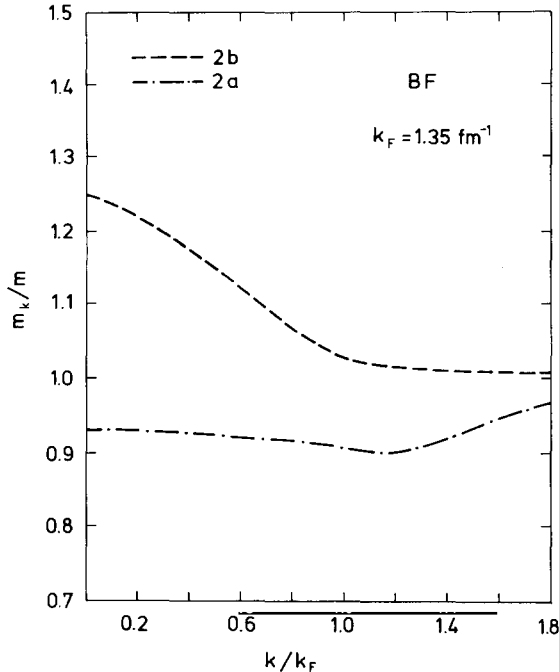


Fig. 3.14. Obtained from Blaizot and Friman [101]. Dependence upon k/k_F of the quantities $m_k^{(2a)}/m$ (eq. (8.77), dash-and-dot) and $m_k^{(2b)}/m$ (eq. (9.39), dashes) in the case of a Yukawa interaction of range 0.3 fm which acts in the $S = 1, L = 1$ state only. The energies $e(q)$ have been taken equal to $q^2/2m$ (eq. (8.5)). The Fermi momentum k_F is equal to 1.35 fm^{-1} .

ρ -exchange and which only acts in the $S = 1, L = 1$ state. The choice (8.5) is made for $e(q)$ (all q). The inequality $m^{(2a)} < m$ reflects the property that $\partial V^{(2a)}/\partial k > 0$, in keeping with our assumptions (8.73) and (8.74).

The nonlocality range a_W of $\mathcal{W}_{2a}(k; \omega)$ has been evaluated in refs. [36, 102] (see also [83]) in the case of uniform nuclear matter and in refs. [61, 103–105] in the case of finite nuclei at positive energy. It is equal to about 1.5 fm. If we make the simple assumption

$$\mathcal{W}_{2a}(k; \omega) \approx W_0^{(2a)}(\omega) \exp(-\frac{1}{4}a_W^2 k^2), \quad (3.8.78)$$

we see that the dependence upon E of the imaginary part of the local equivalent potential, i.e. of

$$W_{2a}(E) = \mathcal{W}_{2a}(k(E); E), \quad (3.8.79)$$

is *smaller* than the ω -dependence of $\mathcal{W}_{2a}(k; \omega)$. However, this difference is fairly small for $\omega \approx \varepsilon_F$. In other words, the E -dependence of $W_{2a}(E)$ mainly reflects the ω -dependence of $\mathcal{W}_{2a}(k; \omega)$. This is illustrated by the fact that one has typically [36]

$$\frac{m^*}{k} \left[\frac{\partial}{\partial k} \mathcal{W}_{2a}(k; \omega) \right]_{\omega=E(k)} \approx 0.1 \left[\frac{\partial}{\partial \omega} \mathcal{W}_{2a}(k; \omega) \right]_{\omega=E(k)} \quad (3.8.80)$$

for $E(k) \approx$ several tens MeV.

3.8.6. Summary

The second-order contribution $\mathcal{M}_2(k; \omega)$ to the mass operator can be written as the sum of two terms (see fig. 3.8), namely

$$\mathcal{M}_2(k; \omega) = \mathcal{M}_{2a}(k; \omega) + \mathcal{M}_{2b}(k; \omega). \quad (3.8.81)$$

The present section 3.8 was devoted to $\mathcal{M}_{2a}(k; \omega)$. It is a fairly good approximation to assume that $\mathcal{M}_{2a}(k; \omega)$ is independent of k for $k/k_F < 2$ and for $|\omega - \omega_F| < 50$ MeV. Thus, one can write

$$\mathcal{M}_{2a}(k; \omega) \approx M_{2a}(\omega), \quad (3.8.82)$$

$$M_{2a}(E) = V_{2a}(E) - i W_{2a}(E). \quad (3.8.83)$$

The real part V_{2a} typically gives a ten per cent correction to the Hartree–Fock approximation to the potential energy of a quasiparticle with energy E . It is *negative (attractive)* for E smaller or slightly larger than the Fermi energy. Its contribution to the ω -mass is enhanced for E close to the Fermi energy ε_F . The maximum of this contribution lies slightly above ε_F . The width of this enhancement peak is about 30 MeV in a uniform medium with a density close to that encountered in the nuclear interior ($\rho \approx 0.17 \text{ fm}^{-3}$). It decreases with decreasing density.

The imaginary part $W_{2a}(E)$ of the contribution (2a) vanishes for $E < \varepsilon_F$. For $E > 0$, it can be identified with the leading term of the perturbation expansion of the imaginary part of the optical model potential. For $\varepsilon_F < E < 0$, it is connected to the spreading width of a bound (“unoccupied”) single-particle state with energy E by the relation $\Gamma^\downarrow \approx 2 W_{2a}(E)$.

For quasiparticle states below the Fermi energy (occupied bound single-particle states), the contribution (2a) arises from the fact that some correlations are suppressed in the core (“Pauli blocking” or correlation correction). For quasiparticles above the Fermi energy (unoccupied bound single-particle states or scattering states with positive energy), the physical meaning of the contribution (2a) is that the additional nucleon excites the core (polarization correction).

3.9. Repulsive part of the second-order contribution

3.9.1. Definition and properties

In eq. (8.1), we wrote the second-order contribution $\mathcal{M}_2(k; \omega)$ to the power series expansion of the mass operator as the sum of two terms, $\mathcal{M}_{2a}(k; \omega) + \mathcal{M}_{2b}(k; \omega)$. The preceding section contains a detailed investigation of $\mathcal{M}_{2a}(k; \omega)$. The present one is devoted to $\mathcal{M}_{2b}(k; \omega)$. Many of the arguments developed in the case of \mathcal{M}_{2a} can easily be adapted to the discussion of \mathcal{M}_{2b} . Accordingly, we can often paraphrase part of section 3.8 and give fewer explanations.

The quantity $\mathcal{M}_{2b}(k; \omega)$ is graphically represented in fig. 3.8. Its algebraic expression reads

$$\mathcal{M}_{2b}(k; \omega) = \frac{1}{2} \sum_{j, l, d} n_<(l) n_<(j) n_>(d) \frac{|\langle l, j | v | k, d \rangle|^2}{\omega - e(l) + [e(d) - e(j)] - i\eta} \quad (3.9.1)$$

where $e(q)$ is given by eq. (8.4). Henceforth, we write all expressions as though the self-consistent value (8.7) would be adopted for $e(q)$, although in practice calculations are usually based on the ap-

proximations (8.5), (8.9) or (8.10). Momentum conservation implies that

$$\mathbf{l} + \mathbf{j} = \mathbf{k} + \mathbf{d}. \quad (3.9.2)$$

The quantity $\mathcal{M}_{2b}(k; \omega)$ is complex. In keeping with our convention (2.27), we write

$$\mathcal{M}_{2b}(k; \omega) = \mathcal{V}_{2b}(k; \omega) + i \mathcal{W}_{2b}(k; \omega), \quad (3.9.3)$$

with

$$\mathcal{V}_{2b}(k; \omega) = \frac{\mathcal{P}}{2} \sum_{\mathbf{j}, \mathbf{l}, \mathbf{d}} n_<(l) n_<(j) n_>(d) \frac{|i\langle \mathbf{l}, \mathbf{j} | v | \mathbf{k}, \mathbf{d} \rangle|^2}{\omega - E(l) + [E(d) - E(j)]} \quad (3.9.4)$$

$$\begin{aligned} \mathcal{W}_{2b}(k; \omega) &= \frac{\pi}{2} \sum_{\mathbf{j}, \mathbf{l}, \mathbf{d}} n_<(l) n_<(j) n_>(d) |i\langle \mathbf{l}, \mathbf{j} | v | \mathbf{k}, \mathbf{d} \rangle|^2 \\ &\times \delta\{\omega - E(l) + [E(d) - E(j)]\}. \end{aligned} \quad (3.9.5)$$

One has

$$\mathcal{W}_{2b}(k; \omega) > 0 \quad \text{for } \omega < \varepsilon_F, \quad (3.9.6)$$

$$\mathcal{V}_{2b}(k; \omega) = 0 \quad \text{for } \omega > \varepsilon_F, \quad (3.9.7)$$

$$\mathcal{W}_{2b}(k; \omega) \sim C(\omega - \varepsilon_F)^2 \quad \text{for } \omega \rightarrow \varepsilon_F - 0. \quad (3.9.8)$$

The constant C is the same as the one which appears in eq. (8.17).

The following dispersion relation holds

$$\mathcal{V}_{2b}(k; \omega) = \frac{\mathcal{P}}{\pi} \int_{-\infty}^{\omega_F} \frac{\mathcal{W}_{2b}(k; \omega')}{\omega - \omega'} d\omega', \quad (3.9.9)$$

provided that $\mathcal{W}_{2b}(k; \omega') \rightarrow 0$ for $|\omega'| \rightarrow \infty$. In contrast to the case of $\mathcal{W}_{2a}(k; \omega')$, this requirement is always fulfilled because $\mathcal{W}_{2b}(k; \omega')$ vanishes identically for large $|\omega'|$. Indeed, the argument of the delta function on the right-hand side of eq. (9.5) cannot vanish for large $|\omega'|$ since $E(l) - [E(d) - E(j)]$ is bounded from below because of eq. (9.2). Here, $\omega_F = E(k_F)$ is an approximation to the Fermi energy ε_F .

3.9.2. Numerical example

The quantity $\mathcal{W}_{2b}(k; \omega)$ has been obtained in algebraic form for all values of k and ω in the dilute hard sphere Fermi gas model, which will be discussed in section 3.14. This model has shown that the dependence of $\mathcal{W}_{2b}(k; \omega)$ upon k is weaker than its dependence upon ω , at least in the domain $k/k_F < 2$, $|\omega_F - \omega| < 50$ MeV. Hence, it is sufficient for semi-quantitative purposes to calculate $\mathcal{W}_{2b}(k; \omega)$ as a function of ω for a fixed value of k . Since here we are mainly interested in the vicinity of the Fermi

surface, let us take $k = k_F$ and introduce the definitions

$$W_{2b}(\omega) = \mathcal{W}_{2b}(k_F; \omega), \quad (3.9.10)$$

$$V_{2b}(\omega) = \mathcal{V}_{2b}(k_F; \omega). \quad (3.9.11)$$

The dispersion relation (9.9) then yields

$$V_{2b}(\omega) = \frac{\mathcal{P}}{\pi} \int_{-\infty}^{\varepsilon_F} \frac{W_{2b}(\omega')}{\omega - \omega'} d\omega'. \quad (3.9.12)$$

The quantity $W_{2b}(\omega')$ has been calculated in algebraic form for all values of ω' in the case of the model interaction (7.23) and in the framework of the effective mass approximation (8.10) [86]. The result is shown in the upper part of fig. 3.15. Its “bell” shape is in keeping with the asymptotic behaviour (9.8) on the one hand, and with the fact that $W_{2b}(\omega)$ vanishes identically for $|\omega_F - \omega| > 8\omega_F$ as a consequence of energy and momentum conservation on the other hand.

The real part $V_{2b}(\omega)$ as calculated from the dispersion relation (9.12) (where ε_F is replaced by ω_F) is plotted in the lower part of fig. 3.15. In the present context, we are mainly interested in the vicinity of

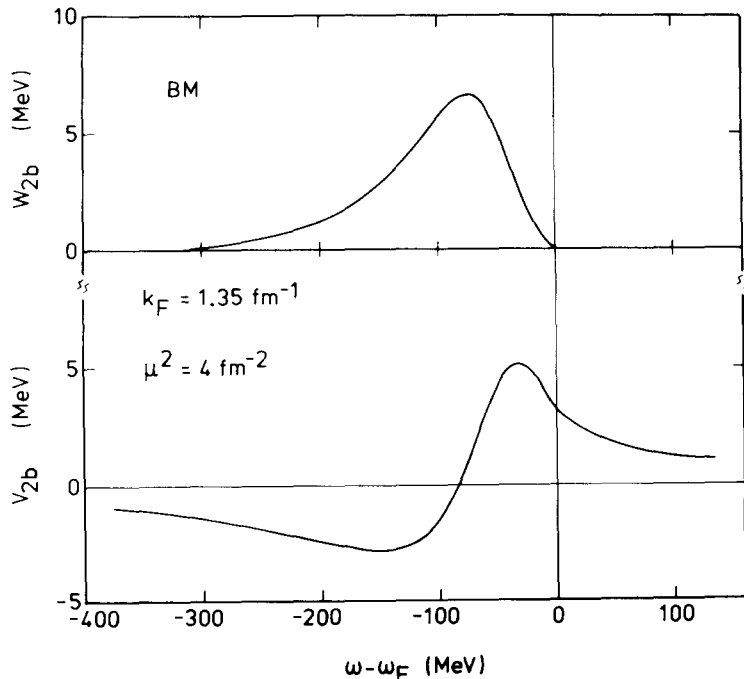


Fig. 3.15. Adapted from ref. [86]. Dependence upon $\omega - \omega_F$ of the imaginary part (upper graph) and of the real part (lower graph) of the contribution (2b), in the case of the model interaction (7.23) with the parameter values (7.25), and for the Fermi momentum $k_F = 1.35 \text{ fm}^{-1}$. The Fermi energy ω_F is defined by eq. (8.41).

the Fermi energy. There, one has

$$V_{2b}(\omega) > 0 \quad \text{for } \omega \approx \omega_F, \quad (3.9.13)$$

$$\frac{d}{d\omega} V_{2b}(\omega) < 0 \quad \text{for } \omega \approx \omega_F. \quad (3.9.14)$$

The inequality (9.13) is the origin of the expression “repulsive part of the second-order contribution” that we coined for graph (2b). The property (9.14) shows that for $\omega \approx \omega_F$ the graph (2b) yields a positive contribution to the ω -mass m_ω defined in eq. (6.10). Let us call $m_\omega^{(2b)}$ the value that the ω -mass would take if graph (2b) alone would be responsible for the full ω -dependence of the mass operator, namely

$$m_\omega^{(2b)}(E)/m = 1 - dV_{2b}(E)/dE. \quad (3.9.15)$$

The quantity $m_\omega^{(2b)}(E)/m$ is plotted versus $E - \omega_F$ in fig. 3.16.

3.9.3. Qualitative discussion

In the present section, we show that the main features of the results displayed in figs. 3.15 and 3.16 hold for most other choices of the effective interaction v .

We already discussed that the “bell” shape of $W_{2b}(\omega)$ shown on the top of fig. 3.15 is quite independent of the choice of v . Once the shape of $W_{2b}(\omega)$ is known, the ω -dependence of $V_{2b}(\omega)$ can be discussed on the basis of the dispersion relation (9.12). For $\omega > \omega_F$, the integrand on the right-hand side

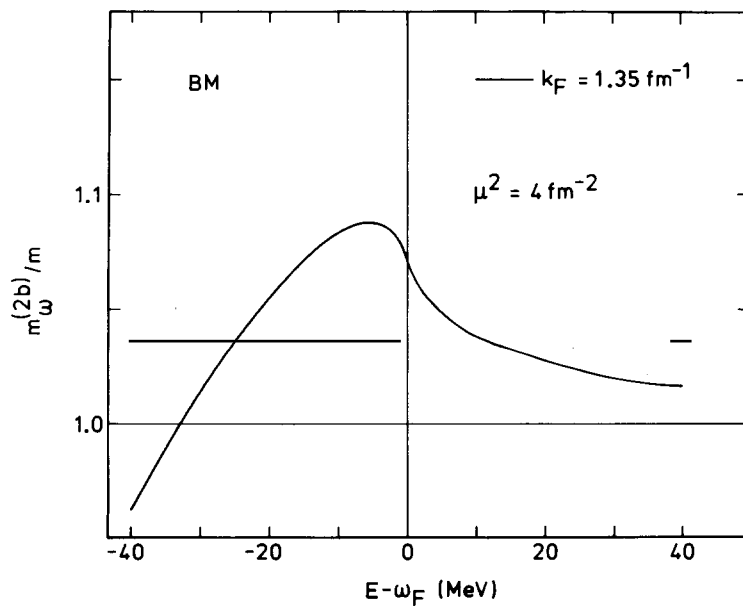


Fig. 3.16. Adapted from ref. [86]. Dependence upon $E - \omega_F$ of the quantity $m_\omega^{(2b)}(E)/m$, as calculated from eq. (9.15) and the values of $V_{2b}(E)$ shown in fig. 3.14.

of eq. (9.12) is positive definite, and one has

$$V_{2b}(\omega) > 0 \quad \text{for } \omega > \omega_F. \quad (3.9.16a)$$

By continuity, $V_{2b}(\omega)$ remains positive at least for ω slightly smaller than ω_F . For $E > \varepsilon_F$, one can write

$$\frac{d}{dE} V_{2b}(E) = -\pi^{-1} \int_{-\infty}^{\omega_F} \frac{W_{2b}(\omega')}{(E - \omega')^2} d\omega' < 0. \quad (3.9.16b)$$

By continuity, this derivative remains negative at least for E somewhat smaller than ω_F . Consequently, one has

$$m_\omega^{(2b)}(E) > m \quad \text{for } E \approx \omega_F. \quad (3.9.17)$$

Furthermore, one has for $E > \omega_F$

$$\frac{d}{dE} [m_\omega^{(2b)}(E)] = -2\pi^{-1} \int_{-\infty}^{\omega_F} \frac{W_{2b}(\omega')}{(E - \omega')^3} d\omega' < 0. \quad (3.9.18)$$

Hence, $m_\omega^{(2b)}(E)$ is a decreasing function of E for $E > \omega_F$ and, by continuity, at least for E slightly smaller and ω_F . From the threshold behaviour (9.8), one finds that

$$\lim_{E \rightarrow \omega_F+0} \left\{ \frac{d}{dE} m_\omega^{(2b)}(E)/m \right\} = 2C \lim \left\{ \ln \frac{|E - \omega_F|}{|\omega_F|} \right\} \quad (3.9.19)$$

$$= -\infty. \quad (3.9.20)$$

We conclude that $m_\omega^{(2b)}(E)/m$ is larger than unity and decreasing with increasing E for $E > \omega_F$ and also for E slightly smaller than ω_F . It has an inflection point with a negative infinite slope at $E = \omega_F$.

Since $W_{2b}(\omega)$ vanishes for large $|\omega|$, $V_{2b}(\omega)$ vanishes at some energy $E_M^{(2b)} < \omega_F$. Hence, it must have a maximum at an energy $E_q^{(2b)}$, with

$$E_M^{(2b)} < E_q^{(2b)} < \omega_F. \quad (3.9.21)$$

This implies that $m_\omega^{(2b)}(E_q^{(2b)}) = m$. Together with inequality (9.17), this result shows that $m_\omega^{(2b)}(E)$ reaches a maximum at $E_{\max}^{(2b)}$, with

$$E_q^{(2b)} < E_{\max}^{(2b)} < \omega_F. \quad (3.9.22)$$

Since the slope of $m_\omega^{(2b)}(E)$ is negative infinite at $E = \omega_F$, the energy $E_{\max}^{(2b)}$ is likely to be only slightly smaller than ω_F , or else the maximum value $m_\omega^{(2b)}(E_{\max}^{(2b)})/m$ would probably be very large. In the example of figs. 3.15 and 3.16, one has $|\omega_F - E_M^{(2b)}| \approx 90$ MeV; $|\omega_F - E_q^{(2b)}| \approx 35$ MeV; $|\omega_F - E_{\max}^{(2b)}| \approx 7$ MeV; $m^{(2b)}(E_{\max}^{(2b)})/m \approx 1.08$; $m^{(2b)}(\omega_F)/m \approx 1.07$.

We conclude that $m_\omega^{(2b)}(E)$ presents an enhancement in the vicinity of the Fermi energy. The maximum is located slightly below the Fermi energy.

Since the enhancement peak is asymmetric, one can only give a rough measure of its width Δ_{2b} . In the case of fig. 3.16, one has $\Delta_{2b} \approx 30$ MeV. This is close to the width of the enhancement peak of $m_\omega^{(2a)}(e)$, see fig. 3.10. The peak is narrower for smaller k_F . For $k_F = 1.00 \text{ fm}^{-1}$, one has $\Delta_{2b} \approx 20 \text{ MeV} \approx \Delta_{2a}$ [86].

3.9.4. Physical interpretation

The discussion below closely follows the one carried out in section 3.8.5 in the case of M_{2a} .

3.9.4.1. Potential energy and spreading width

The quantity $V_{2b}(E)$ is the contribution of graph (2b) to the potential energy of a quasi-hole with energy E . A more accurate estimate of this energy shift is given by

$$\bar{V}_{2b}(E) = \frac{m_{\text{HF}}^*}{m} V_{2b}(E) \quad (3.9.23)$$

see eq. (5.23). The quantity

$$\Gamma^\downarrow(E) \approx 2 W_{2b}(E) \quad (3.9.24)$$

gives an approximation to the spreading width of a quasi-hole with energy E . A more precise value of the second-order spreading width is given by (see eq. (8.57))

$$\Gamma^\downarrow(E) = 2Z_2(E) W_{2b}(E) \quad (3.9.25)$$

in the case of quasiholes ($E < \varepsilon_F$), and

$$\Gamma^\downarrow(E) = 2Z_2(E) W_{2a}(E) \quad (3.9.26)$$

in the case of quasiparticles ($E > \varepsilon_F$). Here,

$$[Z_2(E)]^{-1} = 1 - \frac{d}{dE} [V_{2a}(E) + V_{2b}(E)] \quad (3.9.27)$$

$$= m_\omega^{(2a)}(E)/m + m_\omega^{(2b)}(E)/m - 1 \quad (3.9.28)$$

is the second-order approximation to the strength of the quasiparticle, see eq. (4.16).

3.9.4.2. Graphical representation

The graphical representation of $M_{2b}(k; \omega)$ was given in fig. 3.8 and is recalled at the top of fig. 3.17. Whenever quasiparticle properties are concerned, the contribution of graph (2b) is often drawn in two different ways, depending on whether one considers particle or hole states. This is shown at the bottom of fig. 3.17, where (PO) and (CO) stand for *polarization* and for *correlation*, respectively, in keeping with

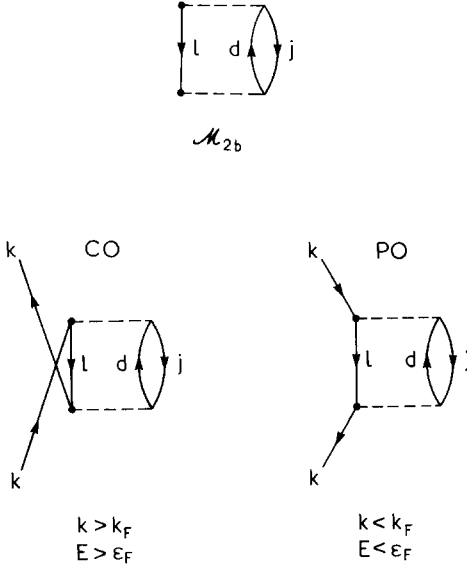


Fig. 3.17. The graph at the top represents the contribution $\mathcal{M}_{2b}(k; \omega)$ to the mass operator (see fig. 3.8). Quite often, the corresponding contributions to the quasiparticle properties are drawn as shown at the bottom, where the left-hand diagram is used for particle states ($k > k_F$, $\omega > \epsilon_F$), and the right-hand diagram is used for hole states ($k < k_F$, $\omega < \epsilon_F$). The labels CO and PO stand for correlation and polarization, respectively.

the physical interpretation given below. We emphasize that $\mathcal{M}_{2b}(k; \omega)$ is given by the same algebraic expression (9.1) for E larger as well as smaller than ϵ_F .

3.9.4.3. Polarization and correlation effects

We now explain that the contribution \mathcal{M}_{2b} describes correlation effects for quasiparticle states ($k > k_F$) and polarization effects for quasi-hole states ($k < k_F$), in keeping with the notation adopted in fig. 3.17.

Let us first consider the case $k < k_F$. The configuration obtained by punching a hole with momentum k in the core (with A nucleons) is coupled to two hole (l, j)–one particle (d) configurations. In other words, the hole with momentum k *polarizes* the core by giving rise to one particle (d)–one hole (j) core excited states.

In the case $k > k_F$, graph CO in fig. 3.17 is a consequence of the existence of correlations in the core; this is depicted in the lower part of fig. 3.12. Figure 3.15 shows that the core correlations yield a positive correction to the Hartree–Fock energy for particle states ($k > k_F$), while we recall (see section 3.8.5) that it leads to a negative contribution in the case of hole states ($k < k_F$). This can be understood as follows.

Let us for instance consider a “bound unoccupied” single-particle state with quantum number k ($k \rightarrow \{n, l, j\}$ in a finite nucleus). This corresponds to $k > k_F$ in nuclear matter. The presence of the extra particle introduces, on the one hand, new interaction bounds in the $(A + 1)$ particle spectrum. It also blocks those existing correlations of the ground state of the A -particle system which are responsible for the partial occupation of the single-particle state k . In this sense, and following our discussion in section 3.8.5, we could write

$$E^{\text{HF}}(k) = B_k^{\text{HF}}(A + 1) - B^{\text{HF}}(A) \quad (3.9.29a)$$

in the Hartree–Fock approximation, and

$$E^{\text{CO}}(k) = B_k^{\text{CO}}(A+1) - B_k^{\text{CO}}(A) \quad (3.9.29\text{b})$$

when we take into account the effect of the diagram displayed in fig. 3.12. Since some correlation energy is lost in the $(A+1)$ particle system we have

$$B_k^{\text{HF}}(A+1) - B_k^{\text{CO}}(A+1) < B^{\text{HF}}(A) - B^{\text{CO}}(A), \quad (3.9.29\text{c})$$

or

$$E^{\text{HF}}(k) < E^{\text{CO}}(k), \quad (3.9.29\text{d})$$

which establishes the repulsive character of the correlation correction.

3.9.4.4. Momentum distribution outside the Fermi sea

Correlations inside the core are responsible for the fact that in the actual ground state of the medium the average number of nucleons with momentum k does not vanish for $k > k_F$, see fig. 3.1. This is also the origin of the correlation graph shown at the bottom left of fig. 3.12. We thus expect a relationship between $\mathcal{V}_{2b}(k; \omega)$ in the domain $k > k_F$ and $\omega > \varepsilon_F$ on the one hand and the momentum distribution $n(k)$ for $k > k_F$ on the other hand. This is the case. In the second-order approximation, the value of $n_2(k)$ for $k > k_F$ is indeed given by [42]

$$n_2(k) = [\partial \mathcal{V}_{2b}(k; \omega) / \partial \omega]_{\omega=E(k)} \quad (3.9.30)$$

$$= m_\omega^{(2b)} / m - 1. \quad (3.9.31)$$

This may be compared with the expression (see eqs. (8.61) and (8.62))

$$n_2(k) = 2 - m_\omega^{(2a)} / m \quad (3.9.32)$$

which holds for $k < k_F$. The exact sum rule

$$\int_0^\infty n(k) d^3k = \frac{4\pi}{3} k_F^3 \quad (3.9.33)$$

remains fulfilled when $n(k)$ is replaced by its second-order approximation (9.31), (9.32):

$$\int_0^\infty n_2(k) d^3k = \frac{4\pi}{3} k_F^3. \quad (3.9.34)$$

3.9.4.5. Nuclear reaction theory

In section 3.8.5.5, we showed that the contribution (2a) (which at positive energy yields the

polarization graph PO in fig. 3.11) is included in the coupled-channel formulation of nuclear reaction theory or in other approaches to nuclear reaction theory, e.g. those used in refs. [106, 170]. This is not the case for the contribution (2b) discussed in the present section. The reason is the following. Nuclear reactions focus on positive energies. Then, contribution (2b) arises from core correlations (i.e. from target correlations in the terminology used in the field of nuclear reactions) and from the Pauli principle. It is very difficult to build a nuclear reaction model in which these core correlations would be correctly taken into account. For instance, the graph PO in fig. 3.11 shows that this model should take into account configurations in which two nucleons (\mathbf{k} and \mathbf{d}) are in scattering states. This gives rise to severe difficulties analogous to those encountered in the three-body scattering problem.

3.9.4.6. Nonlocality of \mathcal{M}_{2b}

In the preceding sections, we have usually assumed that the k -dependence of $\mathcal{W}_{2b}(k; \omega)$ and of $\mathcal{V}_{2b}(k; \omega)$ can be neglected, i.e. that \mathcal{M}_{2b} is local in coordinate space. We now briefly discuss the accuracy of this approximation. It appears natural to expect that the nonlocality range of $\mathcal{V}_{2b}(k; \omega)$ is (roughly) the same as that of $\mathcal{V}_{2a}(k; \omega)$, i.e. $a \approx 0.8$ fm. Indeed, the value of a in both cases is mainly determined by the range and by the exchange mixture of the effective nucleon–nucleon interaction. In order to evaluate the effect of the k -dependence of \mathcal{V}_{2b} upon the full effective mass, let us make the approximation (see eqs. (7.18) and (8.73))

$$\mathcal{V}_{2b}(k; \omega) \approx V_0^{(2b)}(\omega) \exp(-\frac{1}{4}a^2 k^2), \quad (3.9.35)$$

where (see fig. 3.15)

$$V_0^{(2b)} \approx +5 \text{ MeV} \quad (3.9.36)$$

for $|\omega - \omega_F| \leq 50$ MeV. From eqs. (7.20) and (9.35), we obtain the following expression for the k -mass associated with the sum $V_{HF}(k) + \mathcal{V}_{2b}(k; \omega)$

$$m_k(\varepsilon_F)/m \approx \{1 - \frac{1}{2}ma^2[V_{HF} + V_0^{(2b)}]\}^{-1}. \quad (3.9.37)$$

Taking $V_0 \approx -70$ MeV in eq. (7.18) and using eq. (9.36), we find

$$m_k(\varepsilon_F)/m \approx 0.73, \quad (3.9.38)$$

as compared to the value $m_k(\varepsilon_F)/m \approx 0.71$ obtained from eq. (7.20). Hence, the nonlocality of $\mathcal{V}_{2b}(k; \omega)$ gives rise to an increase of the value of the k -mass from its Hartree–Fock value.

This property is verified in fig. 3.14. There, the quantity

$$\frac{m_k^{(2b)}(k)}{m} = \left[1 + \frac{m}{k} \frac{\partial \mathcal{V}^{(2b)}(k; \omega)}{\partial k} \right]_{\omega=k^2/2m}^{-1} \quad (3.9.39)$$

is plotted versus k/k_F , for the model described in connection with eq. (8.77). The increase of $m_k^{(2b)}(k)$ when $k \rightarrow 0$ can probably be ascribed to the increase of the on-shell value $\mathcal{V}_{2b}(k^2/2m)$.

3.9.5. Summary

It is a fairly good approximation to assume that the contribution $\mathcal{M}_{2b}(k; \omega)$ to the second-order approximation to the mass operator is independent of k for $k/k_F < 2$ and $|\omega - \omega_F| < 50$ MeV. Hence, one can write

$$\mathcal{M}_{2b}(k; \omega) \approx M_{2b}(\omega), \quad (3.9.40)$$

$$M_{2b}(E) \approx V_{2b}(E) + i W_{2b}(E). \quad (3.9.41)$$

The real part $V_{2b}(E)$ typically gives a ten per cent correction to the Hartree–Fock approximation to the potential energy of a quasiparticle with energy E . It is positive for all E larger than the Fermi energy ε_F , and also for E somewhat smaller than ε_F . Its contribution to the ω -mass is enhanced for E close to the Fermi energy. This enhancement reaches a maximum slightly below ε_F ; the width of the enhancement peak is about 30 MeV in a uniform medium with a density close to that encountered in the interior of a nucleus ($\rho \approx 0.17 \text{ fm}^{-3}$). This width decreases with decreasing density.

The imaginary part $W_{2b}(E)$ vanishes for $E > \varepsilon_F$. For $E < \varepsilon_F$, it is connected to the spreading width of a bound (“occupied”) single-particle state with energy E by the relation (see eq. (9.25))

$$\Gamma^\downarrow \approx 2 Z_2(E) W_{2b}(E). \quad (3.9.42)$$

For quasiparticle states above the Fermi energy (“unoccupied” bound single-particle states or scattering states with positive energy), the contribution V_{2b} arises from correlations in the core. For quasi-hole states, i.e. quasiparticle states below the Fermi energy, the physical meaning of the contribution (2b) is that the hole can excite the core (polarization correction).

3.10. Full second-order contribution

3.10.1. Introduction

In eq. (8.1), we wrote the second-order contribution as the sum of two terms

$$\mathcal{M}_2(k; \omega) = \mathcal{M}_{2a}(k; \omega) + \mathcal{M}_{2b}(k; \omega). \quad (3.10.1)$$

The diagrams most commonly adopted to represent the first-order (Hartree–Fock) and the second-order approximations to the mass operator are gathered in fig. 3.18. The sum of the first- and second-order contributions to the real part of $\mathcal{M}_2(k; \omega)$ will be written in the form

$$\mathcal{V}_{1+2}(k; \omega) = V_{HF}(k) + \mathcal{V}_{2a}(k; \omega) + \mathcal{V}_{2b}(k; \omega). \quad (3.10.2)$$

We shall particularly focus on its on-shell value, i.e. on

$$\mathcal{V}_{1+2}(E) = \mathcal{V}_{1+2}(k(E); E), \quad (3.10.3)$$

where $k(E)$ is defined either by

$$E = k^2/2m + \mathcal{V}_{1+2}(k; E), \quad (3.10.4)$$

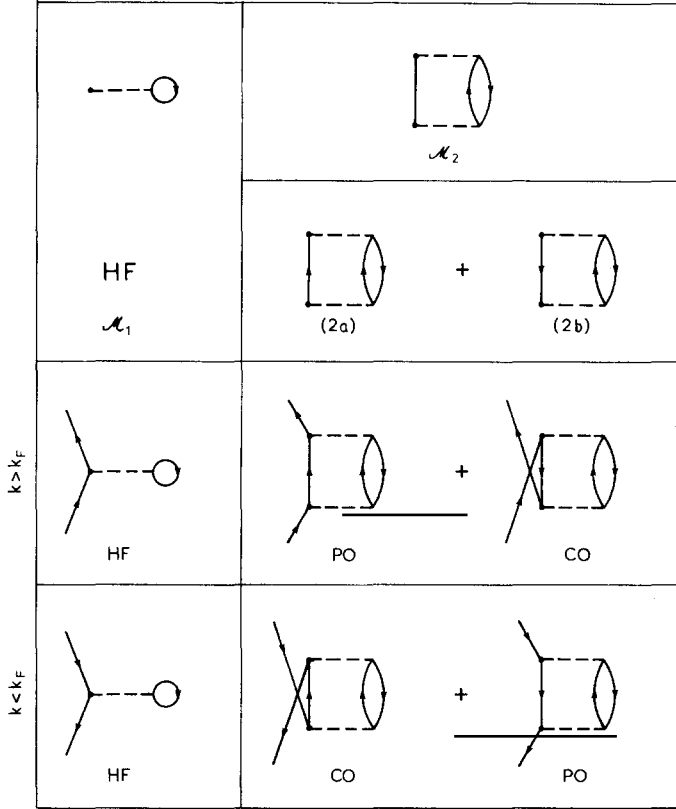


Fig. 3.18. Diagrams most commonly used to represent the first-order (\mathcal{M}_1) and the second-order (\mathcal{M}_2) contributions to the mass operator $\mathcal{M}(k; \omega)$. The second-order term is the sum of two terms, namely \mathcal{M}_{2a} and \mathcal{M}_{2b} . For quasihole states ($k < k_F$), \mathcal{M}_{2a} can be interpreted as arising from the existence of *correlations* (CO) in the ground state of the core, while for quasiparticle states above the Fermi surface ($k > k_F$), \mathcal{M}_{2a} arises from the excitations of the core, i.e. from core *polarization* (PO). For quasihole states ($k < k_F$), on the contrary, it is \mathcal{M}_{2b} that describes the core *polarization* (PO) while for quasiparticle states above the Fermi surface ($k > k_F$), \mathcal{M}_{2b} arises from the existence of *correlations* (CO) in the ground state of the core.

or by the simpler approximation (see eq. (8.9))

$$E = k^2/2m + V_{HF}(k). \quad (3.10.5)$$

In the latter case, we shall often use the notation $e(k)$.

3.10.2. The imaginary part

The second-order approximation to the imaginary part of the mass operator is given by

$$\text{Im } \mathcal{M}_2(k; \omega) = -\mathcal{W}_{2a}(k; \omega) \quad \text{for } \omega > \varepsilon_F, \quad (3.10.6)$$

$$\text{Im } \mathcal{M}_2(k; \omega) = \mathcal{W}_{2b}(k; \omega) \quad \text{for } \omega < \varepsilon_F. \quad (3.10.7)$$

The minus sign on the right-hand side of eq. (10.6) is due to our definition (8.13) which had been introduced in order to render $\mathcal{W}_{2a}(k; \omega)$ positive.

The values of $W_{2a}(\omega) = \mathcal{W}_{2a}(k_F; \omega)$ and of $W_{2b}(\omega) = \mathcal{W}_{2b}(k_F; \omega)$ as calculated from the model interaction (7.23), (7.25) have been plotted in figs. 3.9 and 3.15, respectively. These curves show that $W_{2a}(\omega)$ and $W_{2b}(\omega)$ are almost symmetric with respect to ω_F , i.e. that

$$W_{2a}(\omega - \omega_F) \approx W_{2b}(\omega_F - \omega) \quad \text{for } |\omega - \omega_F| < 80 \text{ MeV}. \quad (3.10.8)$$

This is exhibited in fig. 3.19.

The approximate equality (10.8) is confirmed by the results presented in refs. [83, 89] and [108]. In these works, the k -dependence of $\mathcal{W}_{2a}(k; \omega)$ and of $\mathcal{W}_{2b}(k; \omega)$ was taken into account; the domain of validity of the approximation

$$\omega_{2a}(k; \omega - \omega_F) \approx \mathcal{W}_{2b}(k; \omega_F - \omega)$$

is reduced to $|\omega - \omega_F| < 30$ MeV when $k/k_F < 0.5$ or $k/k_F > 1.3$.

3.10.3. The real part

In keeping with our estimates in sections 3.8.5 and 3.9.4, let us neglect the k -dependence of \mathcal{V}_{2a} and of \mathcal{V}_{2b} . We thus write (see eqs. (8.39), (9.11))

$$V_{2a}(E) = \mathcal{V}_{2a}(k_F; E) \approx \mathcal{V}_{2a}(k; E), \quad (3.10.9)$$

$$\mathcal{V}_{2b}(E) = \mathcal{V}_{2b}(k_F; E) \approx \mathcal{V}_{2b}(k; E). \quad (3.10.10)$$

The quantities $V_{2a}(E)$ and $V_{2b}(E)$ have been plotted in figs. 3.9 and 3.15 in the case of the model interaction (7.23), (7.25). Let us have a closer look at these results in the vicinity of the Fermi energy. Figure 3.20 shows the values of $V_{2a}(E)$, of $V_{2b}(E)$ and of their sum

$$V_2(E) = V_{2a}(E) + V_{2b}(E). \quad (3.10.11)$$

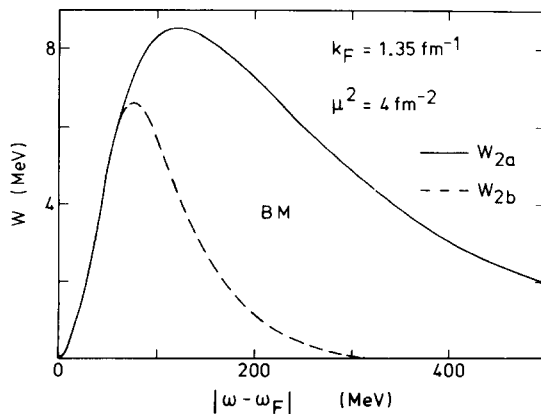


Fig. 3.19. Comparison between the dependence upon $|\omega - \omega_F|$ of the quantities $W_{2a}(\omega)$ and $W_{2b}(\omega)$ as calculated from the model interaction (7.23), (7.25) (see figs. 3.9 and 3.15), for $k_F = 1.35 \text{ fm}^{-1}$. The Fermi energy $\varepsilon_F = \omega_F$ is defined by eq. (8.41).

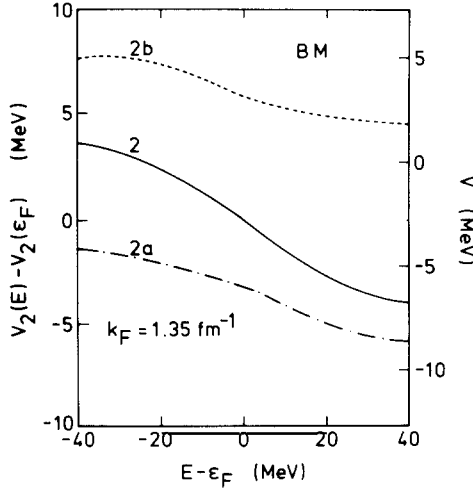


Fig. 3.20. Adapted from ref. [86]. The right-hand ordinate scale gives the dependence upon $E - \epsilon_F$ of the quantities V_{2a} (see fig. 3.9), V_{2b} (see fig. 3.15) and of their sum V_2 in the vicinity of the Fermi energy. The model interaction is defined by eqs. (7.23) and (7.25), and the Fermi energy $\epsilon_F = \omega_F$ by eq. (8.41). The Fermi momentum has the value $k_F = 1.35 \text{ fm}^{-1}$. The left-hand ordinate scale gives the value of the difference $V_2(E) - V_2(\omega_F)$.

As emphasized in sections 3.8 and 3.9, the quantities $V_{2a}(\epsilon_F)$ and $V_{2b}(\epsilon_F)$ have opposite signs. In fig. 3.20, their sum $V_2(\epsilon_F)$ turns out to be negative. We shall argue later that the sign of $V_2(\epsilon_F)$ depends upon the choice of the model (“effective”) interaction v or, equivalently, is sensitive to the truncation of the configuration space in a finite nucleus. However, we shall also see that the value of $V_2(\epsilon_F)$ is largely irrelevant: it is the E -dependence of $V_2(E)$ which matters.

For most purposes, the only meaningful quantity is thus the difference

$$\bar{V}_2(E) = V_2(E) - V_2(\epsilon_F) \quad (3.10.12)$$

in the domain $|E - \epsilon_F| < 50 \text{ MeV}$. This difference can be read on the left ordinate scale in figs. 3.20 and 3.21. The former is based on the model interaction (7.23), (7.25). Figure 3.21 is associated with the

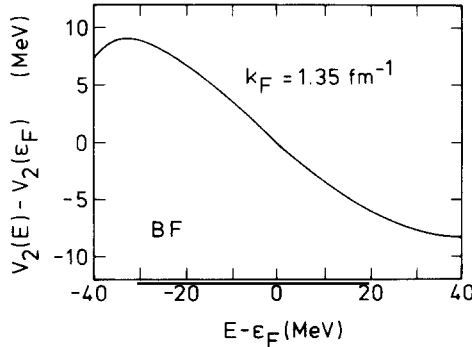


Fig. 3.21. Derived from ref. [83]. Dependence upon $E - \epsilon_F$ of the difference $V_2(E) - V_2(\epsilon_F)$, where $V_2(E)$ is the second-order contribution to the real part of the mass operator, as calculated from the model interaction defined by eqs. (10.13a, b). The Fermi momentum has the value $k_F = 1.35 \text{ fm}^{-1}$.

following effective interaction which acts in the $S = 1$, $T = 1$ channel only:

$$v(q) = \frac{f_\pi^2}{m_\pi^2} \Gamma(q) \left\{ g'(\boldsymbol{\sigma}_1 \cdot \boldsymbol{\sigma}_2) - \gamma_1 \frac{(\boldsymbol{\sigma}_1 \cdot \mathbf{q})(\boldsymbol{\sigma}_2 \cdot \mathbf{q})}{q^2 + m_\pi^2} - \gamma_2 \frac{(\boldsymbol{\sigma}_1 \times \mathbf{k}_1)(\boldsymbol{\sigma}_2 \times \mathbf{k}_2)}{q^2 + m_\rho^2} \right\} (\boldsymbol{\tau}_1 \cdot \boldsymbol{\tau}_2); \quad (3.10.13a)$$

q denotes the momentum transfer. The parameter values

$$g' = 0.5, \quad \gamma_1 = 0.85, \quad \gamma_2 = 1.2 \quad (3.10.13b)$$

have been adjusted to fit the matrix elements of a realistic effective interaction which had been previously computed [109]; $\Gamma(q) = \Lambda^2 / (\Lambda^2 + q^2)$ is a form factor ($\Lambda = 1$ GeV); m_π and m_ρ denote the masses of the π - and of the ρ -meson, respectively. The authors of ref. [83] have made the choice $U(q) = 0$ (see eqs. (8.4), (8.5)) for the energies which appear in the denominator on the right-hand side of eqs. (8.2) and (9.1). However, they used eq. (10.4) to relate k and E . We believe that this leads to an overestimate of the size (ordinate scale) of the second-order correction by a factor $m/m_{HF}^{**} \approx 1.4$ [36].

The values of $V_{2a}(k; e(k))$ and of $V_{2b}(k; e(k))$ in the case of the interaction of Hammann and Ho-Kim [110] have been evaluated in ref. [26].

The results shown in figs. 3.20 and 3.21 share two main features. (i) The first one is that the difference $\bar{V}_2(E) = V_2(E) - V_2(\varepsilon_F)$ decreases by about 10 MeV between $E = \varepsilon_F - 40$ MeV and $E = \varepsilon_F + 40$ MeV. The smaller decrease in the case of fig. 3.20 can be ascribed to the fact that the strength of the effective interaction is too small in that case [86]; we shall argue in section 3.10.4 that this does not affect our main conclusions. (ii) The second common feature is that the slope of $V_2(E)$ varies with energy; its magnitude is largest for E close to ε_F . This property is actually barely visible on figs. 3.20 and 3.21. In order to better exhibit it, we investigate in the next section the dependence upon E of the quantity

$$m_\omega^{(2)}(E) = 1 - dV_2(E)/dE, \quad (3.10.14)$$

i.e. the second-order approximation to the ω -mass.

3.10.4. The ω -mass

3.10.4.1. Introduction

The ω -mass is defined by

$$\frac{m_\omega(E)}{m} = \left[1 - \frac{\partial}{\partial \omega} \mathcal{V}(k; \omega) \right]_{\omega=E(k)}. \quad (3.10.15)$$

The first-order (Hartree–Fock) approximation to $\mathcal{V}(k; \omega)$ is independent of ω and thus yields no contribution to the ω -mass. From eqs. (10.2), (10.11) and (10.15), we obtain the following expression for the second-order approximation to the ω -mass:

$$\frac{M_\omega^{(2)}(E)}{m} = 1 - \frac{d}{dE} V_{2a}(E) - \frac{d}{dE} V_{2b}(E). \quad (3.10.16)$$

From eqs. (8.45) and (9.15), we find that

$$m_\omega^{(2)}(E)/m = m_\omega^{(2)}(E)/m + m_\omega^{(2b)}(E)/m - 1. \quad (3.10.17)$$

The dependence upon E of the quantity $m_\omega^{(2a)}(E)/m$ has been discussed in sections 3.8.3 and 3.8.4, and that of $m_\omega^{(2b)}(E)/m$ in sections 3.9.2 and 3.9.3. We showed that $m_\omega^{(2a)}(E)$ reaches a maximum for E somewhat larger than the Fermi energy ϵ_F , while $m_\omega^{(2b)}(E)$ has a maximum for E somewhat smaller than ϵ_F . We argued in section 3.8.4 and 3.9.3 that these properties hold for practically any choice of the nucleon-nucleon interaction v .

3.10.4.2. Numerical examples

Let us first consider the model interaction defined by eq. (7.23). The corresponding quantities $m_\omega^{(2a)}/m$ and $m_\omega^{(2b)}/m$ have been plotted in figs. 3.10 and 3.16. These results are reproduced in fig. 3.22, together with the second-order approximation $m_\omega^{(2)}(E)/m$ to the ω -mass. We see that while $m_\omega^{(2a)}(E)$ and $m_\omega^{(2b)}(E)$ reach their maximum value on opposite sides of the Fermi energy ϵ_F , the maximum of their sum is located practically at $E = \epsilon_F$.

The strength (7.25) of the effective interaction used in ref. [86] is too weak for a realistic evaluation of the second-order contribution, even though it yields a fairly realistic value for the Hartree-Fock field. This has been related to the fact that the model interaction (7.23) has no tensor component [86]. We note that the shapes of the curves shown in fig. 3.22 are independent of the strength of the effective interaction adopted to calculate the second-order correction, provided that eq. (10.5) is used to compute the on-shell value of the mass operator and the Fermi energy. Indeed, a modification of the strength of v would simply modify the ordinate scale in fig. 3.22.

The full width at half-maximum (Δ) of the enhancement peak of $m_\omega^{(2)}(E)$ in fig. 3.22 is equal to about 50 MeV for $k_F = 1.35 \text{ fm}^{-1}$. It is thus slightly smaller than two times the width of the enhancement peaks of $m_\omega^{(2a)}$ and of $m_\omega^{(2b)}$. The width decreases with decreasing density. This is illustrated in fig. 3.23 which shows that the width Δ reduces to about 30 MeV for $k_F = 1.00 \text{ fm}^{-1}$.

In figs. 3.22 and 3.23, the quantity $m_\omega^{(2)}(E)/m$ has been plotted versus the energy E . One could have plotted $m_\omega^{(2)}/m$ versus the momentum k , by using the relation (10.5) between E and k . Then, one would have found that the width Γ of the enhancement peak that $m_\omega^{(2)}/m$ displays when plotted versus k/k_F

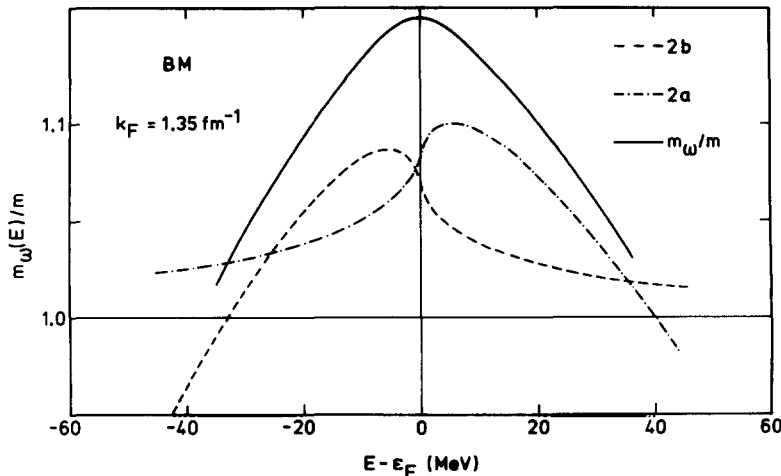


Fig. 3.22. Adapted from ref. [86]. Dependence upon $E - \epsilon_F$ of the quantities $m_\omega^{(2a)}(E)/m$ (dash-and-dot curve), $m_\omega^{(2b)}(E)/m$ (dashes) and $m_\omega^{(2)}(E)/m$ (full curve), in the case of the model interaction (7.23) with the parameter values (7.25), and for the Fermi momentum $k_F = 1.35 \text{ fm}^{-1}$. The Fermi energy $\epsilon_F = \omega_F$ is defined by eq. (8.41).

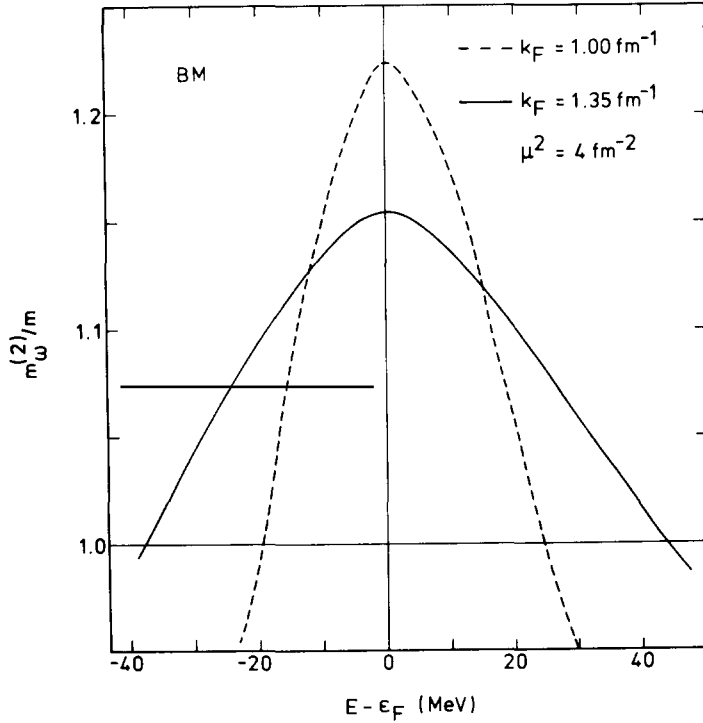


Fig. 3.23. Adapted from ref. [86]. Dependence upon $E - \epsilon_F$ of the second-order approximation to the ω -mass in the case of the model interaction (7.23), (7.25). The full curve corresponds to $k_F = 1.35 \text{ fm}^{-1}$ (see fig. 3.22) and the dashed curve to $k_F = 1.00 \text{ fm}^{-1}$.

increases with decreasing k_F ; this width Γ is a well-defined and decreasing function of the ratio k_F/μ . The width Δ which characterizes the dependence of $m_{\omega}^{(2)}$ upon E is related to the width Γ which characterizes its dependence upon k/k_F by [86]

$$\Delta \approx 2|\omega_F|\Gamma, \quad (3.10.18)$$

where ω_F is the value of the Fermi energy in the Hartree-Fock approximation. Hence, the decrease with decreasing k_F of the width Δ is related to the decrease of $|\omega_F|$.

We now turn to the model that we briefly described in relationship with fig. 3.14. The corresponding values of $m_{\omega}^{(2a)}$, $m_{\omega}^{(2b)}$ and $m_{\omega}^{(2)}$ are shown in fig. 3.24. We recognize the same main features as in fig. 3.22.

Figure 3.25 gives the value of $m_{\omega}^{(2)}/m$ for the model defined by eqs. (10.13a, b) and discussed in connection with fig. 3.21. The shape of the enhancement peak is similar to those shown in figs. 3.22, 3.24. However, its height is much higher than the one displayed in fig. 3.22. This is in keeping with the fact that the model (10.13a,b) involves a tensor term; it is a more realistic model than the one defined by (7.23).

Another fairly realistic example has been studied by Krotscheck, Smith and Jackson [89]. These authors started from Reid's soft core “ v_6 ” nucleon-nucleon interaction (i.e. essentially Reid's interaction stripped off its L^2 and spin-orbit components). They constructed an effective two-body interaction with the help of the correlated basis function approach [111]. Then $V_{2a}(k; e(k))$ and $V_{2b}(k; e(k))$

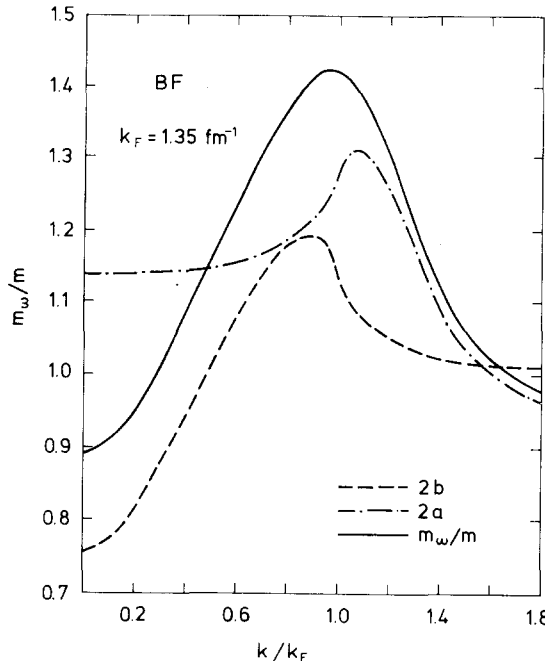


Fig. 3.24. Provided by Blaizot and Friman [101]. Dependence upon k/k_F of the quantities $m_\omega^{(2a)}/m$ (dash-and-dot), $m_\omega^{(2b)}/m$ (dashes) and $m_\omega^{(2)}/m$ in the case of a Yukawa interaction of range 0.3 fm which acts in the $S = 1$, $L = 1$ state only. The energies $e(q)$ have been taken equal to $q^2/2m$ (eq. (8.5)). The Fermi momentum k_F is equal to 1.35 fm^{-1} .

were computed with a choice close to (10.5) for $e(q)$. Monte Carlo techniques were used to evaluate the right-hand side of eqs. (8.14), (9.4) [112]. The corresponding ω -mass is plotted in fig. 3.26. The height of the peak is close to that shown in fig. 3.25 but the width is larger. The origin of this difference perhaps lies in the fact that the density is larger by a factor 1.4 in the case of fig. 3.26 than in fig. 3.25. The authors of ref. [89] also mention the possible explanation that the effective interaction derived from the correlated basis function approach implicitly contains some screening corrections (section 3.13).

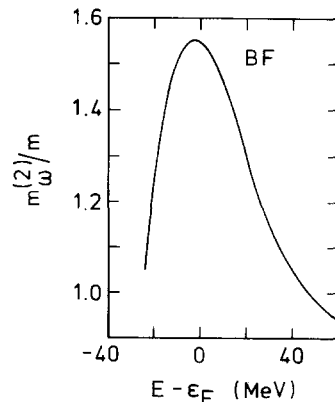


Fig. 3.25. Adapted from ref. [83]. Dependence upon $E - \epsilon_F$ of the second-order approximation to the ω -mass in the case of the model interaction (10.13a, b), as computed from the curve shown in fig. 3.21.

The dashed line in fig. 3.27 shows the dependence upon k/k_F of the quantity

$$\frac{\tilde{m}_\omega^{(2)}(k)}{m} = \left\{ 1 - \frac{\partial}{\partial \omega} \mathcal{V}_{1+2}(k; \omega) \right\}_{\omega=e(k)} \quad (3.10.19)$$

in a model very close in spirit to the one which leads to fig. 3.26 [95]. Here, the twiggle on $\tilde{m}_\omega^{(2)}$ emphasizes that the content of the curly brackets on the right-hand side is calculated at the Hartree-Fock energy $e(k)$ (see eq. (10.5)) rather than at the self-consistent energy defined by eq. (10.4). The difference between the quantities $\tilde{m}_\omega^{(2)}$ and $m_\omega^{(2)}$ will be discussed in section 3.10.7.

We conclude from this survey of numerical calculations that the second-order contribution to the ω -mass displays an enhancement centred very close to the Fermi energy, with a full width at half-maximum equal to about 40 MeV for $k_F = 1.35 \text{ fm}^{-1}$.

3.10.5. Schematic models

In section 3.8.4, we showed that the origin of the positive infinite slope of $m_\omega^{(2a)}(E)$ at $E = \varepsilon_F$ lies in the asymptotic behaviour $\mathcal{W}_{2a}(k; \omega) \sim C(\omega - \varepsilon_F)^2$ for $\omega \rightarrow \varepsilon_F + 0$, with $C > 0$. We saw in section 3.9.3 that, correspondingly, $m_\omega^{(2b)}(E)$ has a negative infinite slope at $E = \varepsilon_F$ because $\mathcal{W}_{2b}(k; \omega) \sim C(\omega - \varepsilon_F)^2$ for $\omega \rightarrow \varepsilon_F - 0$. The constant C is exactly the same in the two cases. Therefore, the slope of the sum $m_\omega^{(2a)}(E) + m_\omega^{(2b)}(E) = m_\omega^{(2)}(E)$ is finite at $E = \varepsilon_F$.

In other words, the terms which behave asymptotically like $|(\omega - \varepsilon_F)|^2$ in $\mathcal{W}_{2a}(k; \omega)$ and in $\mathcal{W}_{2b}(k; \omega)$ cancel when one computes the second derivative with respect to ω of the sum $\mathcal{V}_{2a}(k; \omega) + \mathcal{V}_{2b}(k; \omega) = \mathcal{V}_2(k; \omega)$. In order to investigate the ω -dependence of $\mathcal{V}_2(k; \omega)$, it is thus necessary to take

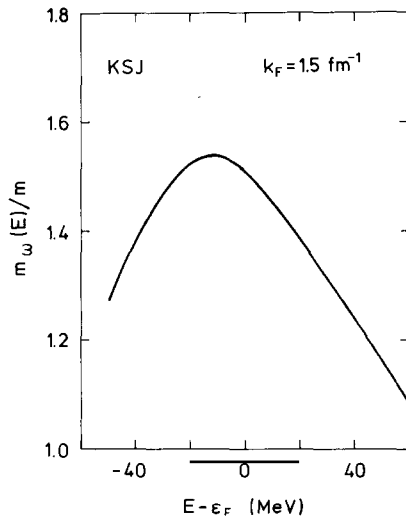


Fig. 3.26. Adapted from ref. [89]. Dependence upon $E - \varepsilon_F$ of the second-order approximation to the ω -mass in the case of an effective interaction constructed from Reid's v_6 soft core nucleon-nucleon potential by means of the correlation functions method. The Fermi momentum is equal to 1.5 fm^{-1} .

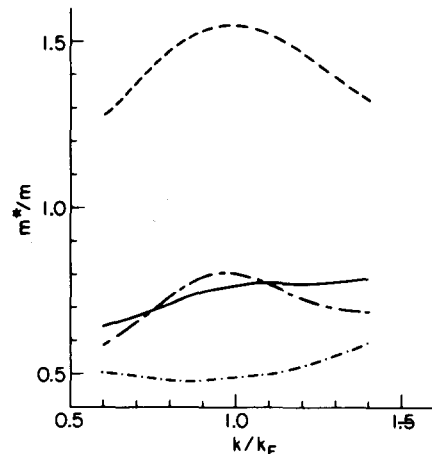


Fig. 3.27. Taken from ref. [95]. Dependence upon k/k_F of the quantities $\tilde{m}_\omega^{(2)}/m$ (eq. (10.30), dashed curve), $\tilde{m}_k^{(2)}/m$ (eq. (10.31), dash-and-dot line), $\tilde{m}_2^{(2)}/m$ (eq. (10.35), full curve) and m_2^*/m (eq. (10.34), long-short dashes) in the case of an effective interaction constructed from the v_6 nucleon-nucleon potential by means of the correlation functions method. The Fermi momentum is equal to 1.5 fm^{-1} .

into account the next order term in the asymptotic expansion of $\mathcal{W}_2(k; \omega)$ for $\omega \rightarrow \varepsilon_F$. One has

$$\mathcal{W}_2(k; \omega) \sim C(\omega - \varepsilon_F)^2 - \alpha|\omega - \varepsilon_F|^3 - \beta(\omega - \varepsilon_F)^3, \quad (3.10.20)$$

where the coefficient β allows for a possible asymmetry of $\mathcal{W}_{2a}(k; \omega)$ and of $\mathcal{W}_{2b}(k; \omega)$ with respect to the Fermi energy. It can be checked [76] that the term proportional to β only yields a constant (i.e. independent of E) contribution to the ω -mass $m_\omega(E)$. We thus drop it and take

$$\mathcal{W}_2(k; \omega) \sim C(\omega - \varepsilon_F)^2 - \alpha|\omega - \varepsilon_F|^3. \quad (3.10.21)$$

This expression can be used as input in the dispersion relations (8.26) and (9.9). Since, however, the right-hand side then diverges, one is led to introduce an energy cut-off Q and to write the dispersion relation in the approximate form

$$\mathcal{V}_2(k; \omega) \approx \frac{\mathcal{P}}{\pi} \int_{-Q}^Q \frac{\mathcal{W}_2(k; \omega')}{\omega - \omega'} d\omega'. \quad (3.10.22)$$

The shape of the enhancement peak of $m_\omega^{(2)}(E)$ in the domain $|E - \varepsilon_F| \ll Q$ should be rather insensitive to the value of the cut-off Q . Substituting (10.21) into eq. (10.22) and retaining the leading terms in the limit $\omega \rightarrow \varepsilon_F$, one finds [83]

$$\mathcal{V}_2(k; \omega) \approx \mathcal{V}_2(k; \varepsilon_F) - 2CQ(\omega - \varepsilon_F) - 2\alpha(\omega - \varepsilon_F)^3 \ln \{|\omega - \varepsilon_F|/Q\}. \quad (3.10.23)$$

This result accounts for the main numerical findings shown in figs. 3.20 and 3.21 and in figs. 3.23–3.26. Indeed, the approximation (10.23) leads to the following expression for the ω -mass:

$$m_\omega^{(2)}(E)/m \approx 1 + 2CQ + 6\alpha(E - \varepsilon_F)^2 \ln \{ |E - \varepsilon_F|/Q \}. \quad (3.10.24)$$

The right-hand side of (10.24) has a maximum at $E = \varepsilon_F$, and decreases on both sides of ε_F ; it is symmetric about $E = \varepsilon_F$; this symmetry would not be maintained if we would use input (10.20) instead of (10.21). The maximum value is equal to $1 + 2CQ$. It depends upon the cut-off parameter Q but it is independent of α . The rate of decrease of $m_\omega^{(2)}(E)$ when $|E - \varepsilon_F|$ increases depends upon the three quantities C , α and Q . It can be verified that the cut-off energy Q only has a minor influence on the shape of $m_\omega^{(2)}(E)$ for E close to ε_F . This shape thus mainly depends upon the value of α . The latter quantity measures the energy at which $\mathcal{V}(k; \omega)$ departs from the quadratic law. Indeed, the right-hand side of (10.21) has inflection points at the energies

$$E_i = \varepsilon_F \pm \frac{1}{3}C/\alpha, \quad (3.10.25)$$

where we neglected the term proportional to $(E - \varepsilon_F)^2$ on the right-hand side of eq. (10.24).

The analytical model (10.21) has the merit of explicitly exhibiting that the enhancement peak of $m_\omega^{(2)}(E)$ for E close to ε_F is due to the fact that the quadratic approximation $\mathcal{W}_2(k; \omega) \sim C(\omega - \varepsilon_F)^2$ is no longer valid away from ε_F . For large values of $|\omega - \varepsilon_F|$, the increase of $\mathcal{W}_2(k; \omega)$ is less rapid than the quadratic law would predict.

We pointed out that the inclusion of a cut-off energy Q in the dispersion relation (10.22) only has a small influence on the shape of $m_\omega^2(E)$ for E close to ε_F , provided that Q is sufficiently large (several tens MeV). One way of avoiding this cut-off would be to use another input for $\mathcal{W}(k; \omega)$, for instance [93]

$$\mathcal{W}^{\text{OS}}(k; \omega) \approx D(\omega - \varepsilon_F)^2 \exp[-|\omega - \varepsilon_F|/G], \quad (3.10.26)$$

where D and G are adjustable constants. One more general way consists in using “subtracted” dispersion relations (see section 3.14).

Another analytic model has been worked out by Brown and Rho [113]. These authors adopt the input

$$W^{\text{BR}}(k; \omega) = \frac{d(\omega - \varepsilon_F)^2}{(\omega - \varepsilon_F)^2 + E_0^2} \quad (3.10.27)$$

in the dispersion relation (10.22). Here, d and E_0 are adjustable constants ($C = d/E$). Wambach, Mishra and Li [114] have recently considered the parametric form

$$W^{\text{WML}}(\omega) = \frac{d(\omega - \varepsilon_F)^2}{(\omega - \varepsilon_F)^2 + E_0^2} + \frac{A}{(\omega - \varepsilon_F - E_1)^2 + a^2} - \frac{A}{E_1^2 + a^2}, \quad (3.10.28a)$$

which amounts to adding to (10.27) a Lorentzian which vanishes at $\omega = \varepsilon_F$ and takes negative values for $|\omega| \rightarrow \infty$. The generalization (10.28a) of (10.27) had been introduced in order to fit the results obtained by Wambach et al. from a microscopic calculation of $W(\omega)$ in ^{208}Pb in the domain $|\omega - \varepsilon_F| < 10$ MeV, see section 4.6. The results derived from (10.27) and (10.28a) are compared in ref. [115].

The following set of parameter values has been considered by Wambach et al. [116]:

$$\begin{aligned} A &= 3.06 \text{ MeV}^3, & E_1 &= 8.5 \text{ MeV}, & a &= 1.08 \text{ MeV}, \\ d &= 14.78 \text{ MeV}, & E_0 &= 69.10 \text{ MeV}. \end{aligned} \quad (3.10.28b)$$

The corresponding energy dependence of $W^{\text{WML}}(E)$ is represented in the upper part of fig. 3.28. A comparison with nuclear matter results shows that the model (10.28a) is quite different. In particular, $W^{\text{WML}}(E)$ has a resonance-like peak at $E \approx 8.5$ MeV. It increases linearly for E close to ε_F :

$$W^{\text{WML}}(E) \sim 2 \frac{AE_1}{(E_1^2 + a^2)^2} (E - \varepsilon_F), \quad (3.10.29)$$

while in the case of nuclear matter the quadratic threshold behaviour (2.29) holds quite generally.

The value $V(\omega)$ which is obtained when (10.28a) is introduced on the right-hand side of the dispersion relation (10.22) can be calculated algebraically and is shown in the middle part of fig. 3.28. The energy dependence of the corresponding ω -mass is represented in the lower part. The energy dependence of $V(E)$ and of $m_\omega(E)$ can easily be understood from the shape of $W(E)$ and the dispersion relation (10.22). We shall discuss this model in section 4.4. At the present stage, we only point out that it illustrates the variety of the schematic models which can be constructed.

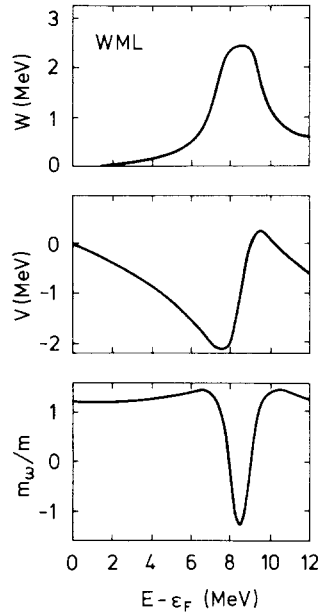


Fig. 3.28. Adapted from ref. [115]. Dependence upon $E - \epsilon_F$ of the imaginary (top) and real (middle) parts of the dispersive part of the mass operator, in the case of the schematic model defined by eqs. (10.28a, b). The corresponding ω -mass is shown at the bottom.

3.10.6. The k -mass

Most calculations described above focus upon the ω -mass. The k -mass $m_k(E)$ defined by eq. (5.13) was believed to be a smooth monotonic function of E , analogous to the result found in the Hartree–Fock approximation (section 3.7) and in the Brueckner–Hartree–Fock approximation (section 3.15). The first indication that this belief may be ill-founded has been provided by the hard sphere dilute Fermi gas model in which $m_k(E)$ presents a shallow dip centred near the Fermi energy (section 3.14). Figure 3.14 suggests that this feature may hold in other models. This is confirmed by fig. 3.29 which

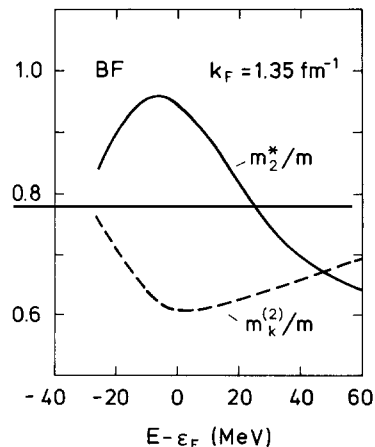


Fig. 3.29. Adapted from ref. [83]. Dependence upon $E - \epsilon_F$ of the k -mass $m_k^{(2)}$ (dashes) and of the effective mass m_2^*/m (full curve) as calculated from second-order perturbation theory in the case of the model defined by eqs. (10.13a, b). The Fermi momentum is equal to 1.35 fm^{-1} .

shows the quantity

$$\frac{m_k^{(2)}(E)}{m} = \left\{ 1 + \frac{m}{k} \frac{\partial \mathcal{V}_{1+2}(k; \omega)}{\partial k} \right\}_{\omega=E(k)}^{-1} \quad (3.10.30)$$

in the case of the model defined by eqs. (10.13a,b). Here, $\mathcal{V}_{1+2}(k; \omega)$ is given by eq. (10.2), and the on-shell energy $E(k)$ by eq. (10.4). In this model, the Hartree–Fock effective mass $m_{\text{HF}}^* = m_k^{\text{HF}}$, eq. (7.8), is a smooth monotonically increasing function of E [101]. Hence, the dip displayed by $m_k^{(2)}$ should be ascribed to the second-order contributions \mathcal{V}_{2a} and \mathcal{V}_{2b} . Figure 3.14 and the discussions carried out in sections 3.8.5.6 and 3.9.4.6 indicate that the increase of $m_k^{(2)}(E)$ at low E reflects the increase of $V_{2b}(E)$.

The dash-and-dot line in fig. 3.27 shows the dependence upon k/k_F of the quantity

$$\frac{\tilde{m}_k^{(2)}}{m} = \left\{ 1 + \frac{m}{k} \frac{\partial \mathcal{V}_{1+2}(k; \omega)}{\partial k} \right\}_{\omega=e(k)}^{-1} \quad (3.10.31)$$

in the model of ref. [95]. As in eq. (10.19), the twiggle on $\tilde{m}_k^{(2)}$ recalls that the content of the curly brackets on the right-hand side of eq. (10.31) is calculated at the Hartree–Fock energy $e(k)$ (see eq. (10.5)) rather than at the self-consistent energy defined by eq. (10.4). The quantities $m_k^{(2)}$ and $\tilde{m}_k^{(2)}$ are not expected to be very different. We return to this point in the next section.

3.10.7. The effective mass

The effective mass $m^*(E)$ is defined by eq. (6.7). It can be computed from the k -mass (eq. (6.9)) and from the ω -mass (eq. (6.10)) by using the relation (6.11), namely

$$\frac{m_2^*(E)}{m} = \frac{m_k^{(2)}(E)}{m} \cdot \frac{m_\omega^{(2)}(E)}{m} \quad (3.10.32)$$

We emphasized that eq. (10.32) holds only if the derivatives which appear in the three effective quantities are calculated at the same self-consistent energy determined by

$$k^2/2m + \mathcal{V}_{1+2}(k; E) = E. \quad (3.10.33)$$

It is not clear whether the condition (10.33) has been fulfilled in the investigation of the model defined by eqs. (10.13a,b). The corresponding value of $m_\omega^{(2)}(E)$ given in ref. [83] has been shown in fig. 3.25. The quantity $m_k^{(2)}(E)$ is represented by the dashed line in fig. 3.29 in which the full curve gives the energy dependence of the effective mass as calculated from (10.32). Despite the dip of $m_k^{(2)}(E)$ for E close to the Fermi energy ϵ_F ($\epsilon_F = -16$ MeV), the effective mass $m_2^*(E)$ displays an enhancement which reflects that of the ω -mass. The asymmetry of the enhancement peak of $m_2^*(E)$ is no longer present in $m_2^*(E)$ because it is compensated by the increase of $m_k^{(2)}(E)$ when E decreases. This should be a rather general feature. Indeed, the discussion in section 3.9.4.6 suggests that the sharp decrease of $m_\omega^{(2)}(E)$ and the sharp increase of $m_k^{(2)}(E)$ below ϵ_F are both due to the increase of $\mathcal{V}_{2b}(k; \omega)$ when ϵ decreases.

It appears likely that in ref. [83] the partial derivatives which appear in eqs. (6.9) and (6.10) have been taken at the free kinetic energy $\omega = k^2/2m$ and that the self-consistent relation (10.33) was used only to convert the dependence upon k of all calculated quantities into a dependence upon $E(k)$. If that

interpretation is correct, the quantities $m_k^{(2)}$ and $m_\omega^{(2)}$ shown in figs. 3.29 and 3.25 should more appropriately be denoted by $\tilde{m}_k^{(2)}$ and $\tilde{m}_\omega^{(2)}$ in keeping with eqs. (10.19) and (10.31).

It appears that most authors calculated the quantities $\tilde{m}_\omega^{(2)}$ (eq. (10.19)) and $\tilde{m}_k^{(2)}$ (eq. (10.31)) and that they used these results to construct the following approximation \tilde{m}_2^* to the effective mass:

$$\frac{\tilde{m}_2^*}{m} = \frac{\tilde{m}_k^{(2)}}{m} \cdot \frac{\tilde{m}_\omega^{(2)}}{m}. \quad (3.10.34)$$

One example is shown by the full curve in fig. 3.27. There, the long-short dashes represent still another approximation to the effective mass, namely

$$\frac{m_2^*(k)}{m} = \left\{ 1 + \frac{m}{k} \frac{d}{dk} \mathcal{V}_{1+2}(k; e(k)) \right\}^{-1}, \quad (3.10.35)$$

where the function $e(k)$ is defined by the Hartree–Fock approximation (10.5). The difference between the two approximations (10.34) and (10.35) illustrates the importance of fulfilling the proper self-consistency condition. It is not easy to decide which one of the two approximations (10.34) or (10.35) is the most accurate; the authors of ref. [95] believe that in their case (10.35) is the most reliable of the two quantities. We note that \mathcal{V}_{2a} and \mathcal{V}_{2b} involve multiple integrals. In refs. [89, 95, 108] these are computed via Monte-Carlo techniques which necessarily involve numerical uncertainties. The dependence of $m_\omega^{(2)}$, $m_k^{(2)}$ and m_2^* upon k requires the calculation of second derivatives of $\mathcal{V}_{2a}(k; \omega)$ and $\mathcal{V}_{2b}(k; \omega)$; it is difficult to evaluate these quantities accurately.

The full curve in fig. 3.30 shows the value obtained for m^*/m when the ω -mass given in fig. 3.26 is multiplied by the Hartree–Fock approximation to the k -mass (dashes), in the model of ref. [89]. The

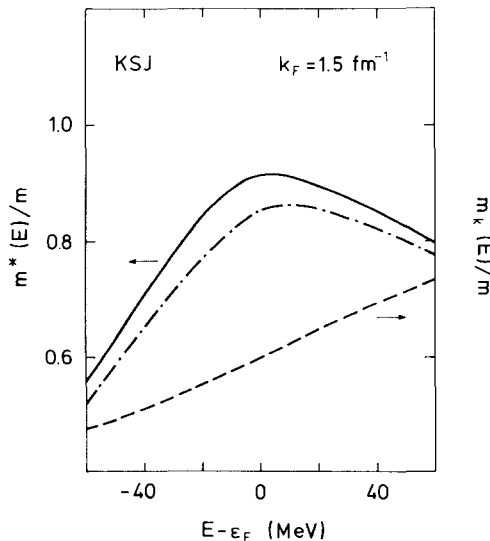


Fig. 3.30. Adapted from ref. [89]. Dependence upon $E - \epsilon_F$ of the effective mass as evaluated from the Hartree–Fock approximation (m_{HF}^*/m , dashes) and from the product $m_{HF}^{(2)}/m^2$ (full curve), where $m^{(2)}/m$ is taken from fig. 3.26. The dash-and-dot curve is evaluated from eq. (10.35). The Fermi momentum k_F is equal to 1.5 fm^{-1} .

difference between the full curve and the dash-and-dot line provides another illustration of the sensitivity of the calculated effective mass to the choice of the self-consistent definition for the energy.

The quantity (10.35) has also been evaluated in ref. [117]. The results are shown in fig. 3.31 for two values of the Fermi momentum, namely 1.33 fm^{-1} and 1.06 fm^{-1} .

3.10.8. The full mass operator

The mass operator $M(k; \omega)$ is a function of two variables. The quasiparticle potential energy is given by the real part $\mathcal{V}(k; E(k))$ of its on-shell value. However, the quasiparticle strength, the k -mass and the ω -mass involve slightly off-the-energy-shell values of $\mathcal{V}(k; \omega)$. It is thus instructive to investigate the dependence of $\mathcal{V}(k; \omega)$ upon k and ω separately. This has been performed in ref. [95]. These authors call $e(k)$ the Hartree–Fock energy, see eq. (10.5), and plot versus Δe and k/k_F the quantity

$$\Sigma(k; e(k) + \Delta e) = \mathcal{V}_{1+2}(k; e(k) + \Delta e). \quad (3.10.36)$$

The results are shown in fig. 3.32. The dependence of $m_\omega^{(2)}$ upon k/k_F is determined by the slope of the lines parallel to the front face at the intersection with the $\Delta e = 0$ plane. The value of the effective mass (10.35) versus k/k_F is determined by the slope of the curve located at $\Delta e = 0$ and parallel to the sides.

3.10.9. Summary

The ω -mass $m_\omega^{(2)}(E)$ displays a maximum which is centred near the Fermi energy ε_F and whose width is about 40 MeV for $k_F = 1.35 \text{ fm}^{-1}$. The height of the maximum is found to be $m_\omega^{(2)}(\varepsilon_F)/m \approx 1.4$ in various semi-realistic models.

The energy dependence of the k -mass $m_k(E)$ is much less known. It appears that $m_k(E)$ probably displays a shallow minimum centred near ε_F .

Many authors compute the effective mass $m^*(E)$ by using the relation $m^*(E) = m_\omega(E) \cdot m_k(E)/m$.

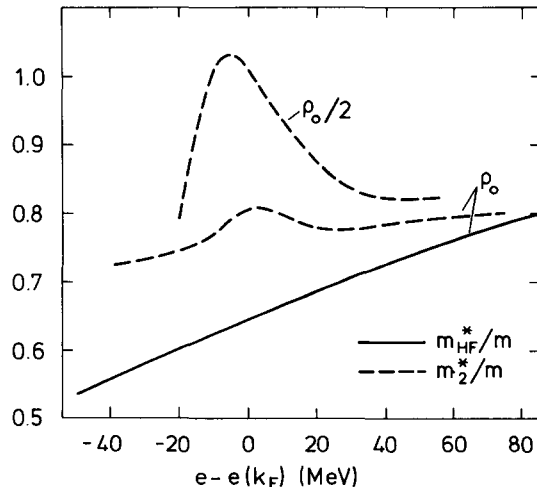


Fig. 3.31. Adapted from ref. [117]. Dependence upon $e(k) - e(k_F)$ of the effective mass as calculated in the Hartree–Fock (full line) and in the second-order (dashed curves, eq. (10.35)) approximations, for the Fermi momenta 1.33 fm^{-1} (density ρ_0) and 1.06 fm^{-1} (density $\rho_0/2$). The effective interaction is derived via correlation operators from the Urbana v_{14} nucleon–nucleon potential supplemented by a three-body interaction approximated by a density-dependent two-body potential.

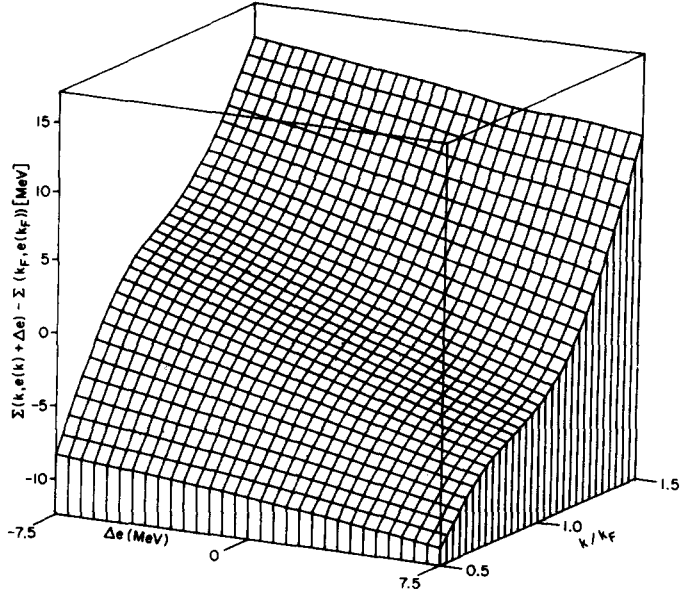


Fig. 3.32. Taken from ref. [95]. Dependence upon Δe and upon k/k_F of the quantity $\Sigma(k; e(k) + \Delta e) - \Sigma(k_F; e(k_F))$ (see eq. (10.36)) in the case of the model illustrated in fig. 3.27. The Fermi momentum is equal to 1.35 fm^{-1} .

This is justified only if the energy derivatives which appear in the definition of these quantities (see eqs. (6.8)–(6.10)) are calculated at the self-consistent energy $E(k)$ determined by the energy-momentum relation (10.4). It seems doubtful that this condition has been fulfilled in any of the available models. It nevertheless appears from various approximations and models that the effective mass $m^*(E)$ also displays an enhancement centred on ε_F . This enhancement is, however, less pronounced and broader than that of $m_\omega(E)$.

3.11. Momentum distribution

3.11.1 Second-order approximation

The average momentum distribution in the correlated ground state is defined by eq. (2.4) and has been sketched in fig. 3.1. In second-order perturbation theory, it is given by [36]

$$n_{2a}(k) = 1 - \frac{1}{2} \sum_{j, c, d} n_<(j) n_>(c) n_>(d) \frac{|\langle \mathbf{k}, \mathbf{j} | v | \mathbf{c}, \mathbf{d} \rangle_t|^2}{\{E(k) - E(c) - [E(d) - E(j)]\}^2} \quad (3.11.1)$$

for $k < k_F$, as indicated by eqs. (8.61), (8.62a). For $k > k_F$, the mean occupation number is equal to

$$n_{2b}(k) = \frac{1}{2} \sum_{j, l, d} n_<(l) n_<(j) n_>(d) \frac{|\langle \mathbf{l}, \mathbf{j} | v | \mathbf{k}, \mathbf{d} \rangle_t|^2}{\{E(k) - E(l) - [E(d) - E(j)]\}^2}. \quad (3.11.2)$$

It can be checked that the exact sum rule (2.14) is fulfilled by the second-order expressions (11.1),

(11.2) regardless of the precise choice of the energies $E(q)$ in the denominators:

$$\int_0^{k_F} k^2 n_{2a}(k) dk + \int_{k_F}^{\infty} k^2 n_{2b}(k) dk = \frac{1}{3} k_F^3. \quad (3.11.3)$$

3.11.2. Physical interpretation

The relations (11.1) and (11.2) can be interpreted with the help of the graphs shown on the right-hand side of fig. 3.12. Let us for instance consider $1 - n_{2a}(k)$, i.e. the probability that a momentum $k < k_F$ is not fully occupied. In lowest order, this depletion probability arises because two nucleons of the Fermi sea, with momenta \mathbf{k} and \mathbf{j} , interact and acquire momenta \mathbf{c} and \mathbf{d} , with $c > k_F$, $d > k_F$. The relation (11.2) can be interpreted similarly with the help of the diagram at the bottom right corner of fig. 3.12.

3.11.3. Relationship to the ω -mass

Figure 3.12 strongly suggests that for $k < k_F$ the depletion probability is closely related with the contribution $\mathcal{V}_{2a}(k; \omega)$ represented in the upper left corner. This is confirmed by eqs. (8.14) and (11.1) which yield

$$n_{2a}(k) = \left\{ 1 + \frac{\partial}{\partial \omega} \mathcal{V}_{2a}(k; \omega) \right\}_{\omega=E(k)}. \quad (3.11.4)$$

The contribution of \mathcal{V}_{2a} to the ω -mass is defined by

$$\frac{m_{\omega}^{(2a)}(E(k))}{m} = \left\{ 1 - \frac{\partial}{\partial \omega} \mathcal{V}_{2a}(k; \omega) \right\}_{\omega=E(k)}. \quad (3.11.5)$$

Equations (11.4) and (11.5) give for $k < k_F$

$$n_{2a}(k) = 2 - m_{\omega}^{(2a)}(k)/m, \quad (3.11.6)$$

where we have for simplicity used the same notation to denote the dependence of $m_{\omega}^{(2a)}$ upon k as upon $E(k)$.

One can show in the same way that for $k > k_F$

$$n_{2b}(k) = m_{\omega}^{(2b)}(k)/m - 1, \quad (3.11.7)$$

where

$$\frac{m_{\omega}^{(2b)}(k)}{m} = \left\{ 1 - \frac{\partial}{\partial \omega} \mathcal{V}_{2b}(k; \omega) \right\}_{\omega=E(k)}. \quad (3.11.8)$$

Relations (11.6) and (11.7) illustrate the interest of computing separately the contributions $m_{\omega}^{(2a)}$ and $m_{\omega}^{(2b)}$ to the ω -mass $m_{\omega}^{(2)}$.

3.11.4. Numerical results

The first reliable calculation of $n_{2a}(k)$ and of $n_{2b}(k)$ has been performed by Sartor [118] who used as input the reaction matrix (section 3.15) derived from the semi-realistic nucleon–nucleon interaction of Hammann and Ho-Kim [110]. The multiple integrals on the right-hand side of eqs. (11.1) and (11.2) have been computed with Monte-Carlo techniques. The results are shown in fig. 3.33. The dashed curve is obtained by identifying $E(q)$ with the Hartree–Fock (more precisely the Brueckner–Hartree–Fock) self-consistent relation (10.5), while the full curve is based on eq. (10.4). The difference between the two curves illustrates the sensitivity of the results to the choice of the energies in the denominators on the right-hand side of eqs. (11.1) and (11.2). The quantities $m_\omega^{(2a)}$, $m_\omega^{(2b)}$ and $m_\omega^{(2)}$ shown in several previous figures are expected to display the same type of sensitivity. The sum rule (11.3) is fulfilled within 0.1 per cent in both cases; this gives a measure of the numerical accuracy of the Monte-Carlo procedure in this example. The infinite slope of $n_{2a}(k)$ and $n_{2b}(k)$ at $k = k_F$ reflects the existence of an infinite slope in $m^{(2a)}(k_F)$ and $m^{(2b)}(k_F)$, see eqs. (8.50) and (9.20).

In the case of a free Fermi gas, the average kinetic energy per nucleon is given by

$$T_0/A = 3k_F^{-3} \int_0^\infty \frac{k^4}{2m} n_0(k) dk = \frac{3}{5} \frac{k_F^2}{2m}, \quad (3.11.9)$$

where $n_0(k)$ is the step function (2.2). In the correlated system, the average kinetic energy per nucleon is given by

$$T/A = 3k_F^{-3} \int_0^\infty \frac{k^4}{2m} n(k) dk. \quad (3.11.10)$$

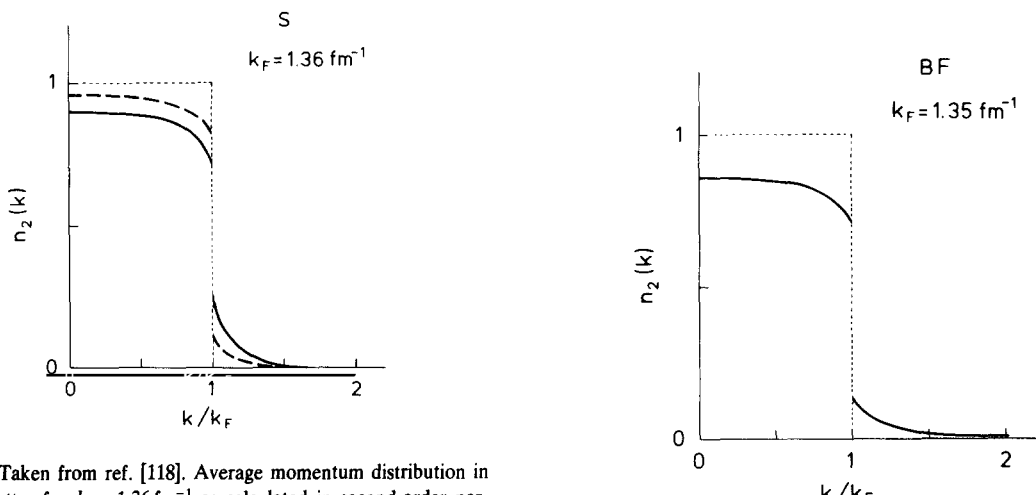


Fig. 3.33. Taken from ref. [118]. Average momentum distribution in nuclear matter for $k_F = 1.36 \text{ fm}^{-1}$ as calculated in second-order perturbation theory with an effective interaction derived from the semi-realistic potential of Hammann and Ho-Kim [110]. The energy $E(q)$ on the right-hand side of eqs. (11.1) and (11.2) have been calculated from the self-consistent relation (10.5) (dashes) or (10.4) (full curve).

Fig. 3.34. Average momentum distribution in nuclear matter as derived from fig. 3.24 and eqs. (10.42), (10.43). It corresponds to a Yukawa potential, and to a Fermi momentum equal to 1.35 fm^{-1} .

One has $T > T_0$ since momentum states $k > k_F$ are partly occupied in the correlated system. The value of T/A computed from fig. 3.33 is 27.3 MeV/nucleon (dashes) and 29.8 MeV/nucleon (full curve), as compared to $T_0/A = 23$ MeV/nucleon for the free Fermi gas.

Figure 3.34 shows the momentum distribution computed by using in eqs. (11.6) and (11.7) the values of $m_\omega^{(2a)}$ and $m_\omega^{(2b)}$ shown in fig. 3.24, and derived from a simple Yukawa interaction.

Fantoni and Pandharipande [108] recently computed $n(k)$ in the case of the effective interaction mentioned in the caption of fig. 3.31. Their result is shown in fig. 3.35. The discontinuity of $n(k)$ at $k = k_F$ is equal to $Z(k_F) = m/m_\omega(k_F)$, see eqs. (2.5), (4.16) and (5.18). Figure 3.35 yields $m_\omega(k_F)/m = 1.43$. This result is close to those shown in figs. 3.24, 3.25, 3.26 and 3.27.

Poggiali and Jackson [119] have computed the quantity $Z(k_F)$ in the framework of Brueckner's theory and found $Z(k_F) = n(k_F - 0) - n(k_F + 0) \approx 0.7$.

3.11.5. Summary

The average momentum distribution $n(k)$ in nuclear matter is characterized by a discontinuity at the Fermi momentum k_F , where $n(k)$ has an infinite slope. The calculated difference $n(k_F - 0) - n(k_F + 0)$ is close to 0.7. This value is sensitive to the nature of the self-consistent choice made for the energies which enter in the denominators of the propagators.

3.12. Quasiparticle strength

3.12.1. Dependence upon the quasiparticle energy

The quasiparticle strength is defined by eq. (4.16). In second-order approximation, it is given by eq. (9.28), namely

$$Z_2(E) = m/m_\omega^{(2)}(E). \quad (3.12.1)$$

Let us consider the semi-realistic model illustrated in fig. 3.24. The corresponding values of Z_2 are

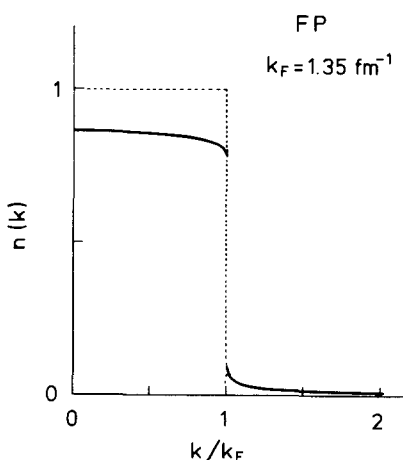


Fig. 3.35. Adapted from ref. [108]. Average momentum distribution in nuclear matter, for the Fermi momentum $k_F = 1.33 \text{ fm}^{-1}$. The input is the same effective interaction as the one used in fig. 3.31. The calculational method is the correlated basis function approach.

plotted versus k/k_F in fig. 3.36. They display a minimum at the Fermi surface. This minimum is a direct reflection of the existence of a maximum of $m_\omega^{(2)}(E)$.

3.12.2. Physical interpretation

The fact that the quasiparticle strength has a minimum at the Fermi surface may at first sight appear surprising. Indeed, the quasiparticle approximation is claimed to be most accurate near the Fermi energy. The reason for this claim is that the quasiparticle lifetime then approaches zero, see eq. (2.29). This implies that for k close to k_F the spectral function $S(k; \omega)$ has a very narrow peak at the quasiparticle energy. This property is schematically represented in fig. 3.37 in the case when k is slightly smaller than k_F . This narrow quasiparticle peak can be fitted with a Lorentzian. The latter delimits an area $Z(k)$, see eq. (4.20). It is apparent from fig. 3.37 that $Z(k) < 1$ for k close to k_F . The reason is that the quasiparticle peak does not include the background part of $S(k; \omega)$.

One can distinguish two different contributions to this background. The first one is located in the domain $\omega > \omega_F$, i.e. in the single-particle strength contained in the $(A + 1)$ particle system. The second one is contained in the domain $\omega \ll E(k) - W_{2b}(k) < \varepsilon_F$.

The background in the domain $\omega > \varepsilon_F$ arises from the fact that the momentum state $k < k_F$ is not fully occupied in the correlated ground state. This is reflected in the appearance of the factor $Z_{2a}(E)$ in the following approximation to $Z_2(E)$:

$$Z_2(E) \approx Z_{2a}(E) \cdot Z_{2b}(E), \quad (3.12.2)$$

with

$$Z_{2a}(E) = m/m_\omega^{(2a)}(E) \approx n_{2a}(E), \quad (3.12.3)$$

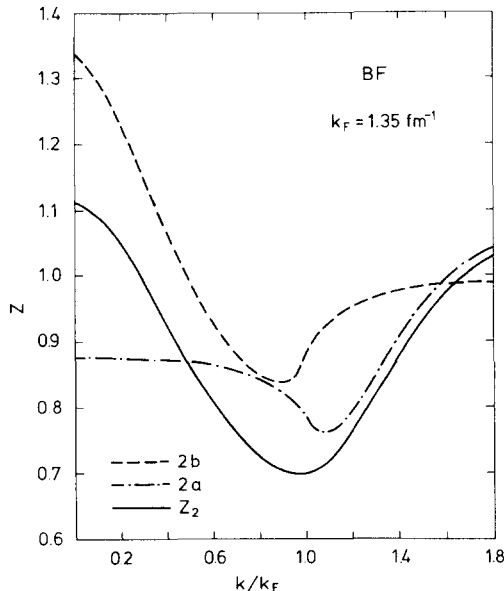


Fig. 3.36. Dependence upon k/k_F of the quasiparticle strength $Z(k)$ associated with the ω -mass shown in fig. 3.24. The full curve represents $Z_2 = m/m_\omega^{(2)}$, the dash-and-dot $Z_{2a} = m/m_\omega^{(2a)}$ (eq. (12.2)) and the dashes $Z_{2b} = m/m_\omega^{(2b)}$ (eq. (12.4)).

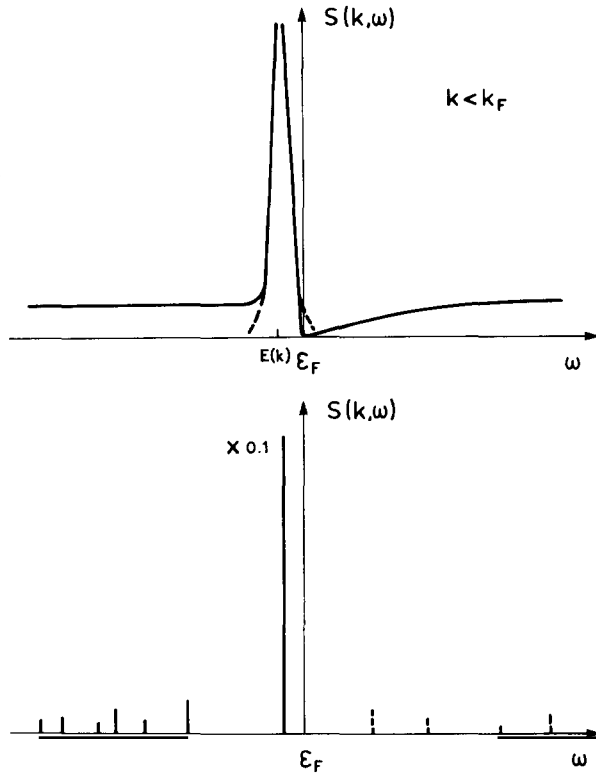


Fig. 3.37. The full curve in the upper part schematically represents the spectral function in nuclear matter when k is smaller than but very close to k_F . The area under the full curve is equal to unity. The quasiparticle peak is then very narrow. Its fit with a quasiparticle Lorentzian (dashes) delimits an area of size $Z(k) < 1$, see eq. (4.20). The bottom part of the figure sketches the analog situation in the case of a finite nucleus. The condition $k \approx k_F - 0$ then refers to a situation in which the orbit quantum numbers $\{n, l, j\}$ correspond to a normally occupied valence shell located just below the Fermi energy. One state of the $(A - 1)$ system is strongly excited in pick-up reactions, i.e. has a very large spectroscopic factor. States with higher excitation energy in the $(A - 1)$ system have very small spectroscopic factors, represented by solid segments. The dotted segments correspond to spectroscopic factors which would be found in the analysis of stripping reactions to the normally occupied single-particle state. Here, the word "normally" recalls that this state is partly empty because of the existence of core correlations. The sum of all the full and dotted vertical segments is equal to unity, see eq. (2.9.11). A physical example will be shown in fig. 4.37c.

$$Z_{2b}(E) = m/m_{\omega}^{(2b)}(E). \quad (3.12.4)$$

The contribution $Z_{2b}(E)$ to $Z_2(E)$ represents the absence from the Lorentzian-shaped quasiparticle peak of the excited states of the $(A - 1)$ system with excitation energy $|\omega - \epsilon_F| \gg |E(k) - W_{2a}(k) - \epsilon_F|$.

The familiar claim that the quasiparticle approximation is very good near the Fermi momentum thus refers to the fact that for fixed $k \approx k_F$ the spectral function presents a very narrow and pronounced peak when plotted versus ω . However, fig. 3.36 indicates that the area under this quasiparticle peak only represents a fraction (about seventy per cent) of the sum rule (2.19).

The case $k \ll k_F$ is schematically represented in fig. 3.38. The quasiparticle peak in the spectral function is quite broad. The area under a Lorentzian fit may sometimes be larger than unity.

Physical examples of the cases sketched in figs. 3.37 and 3.38 will be shown in section 4.7.

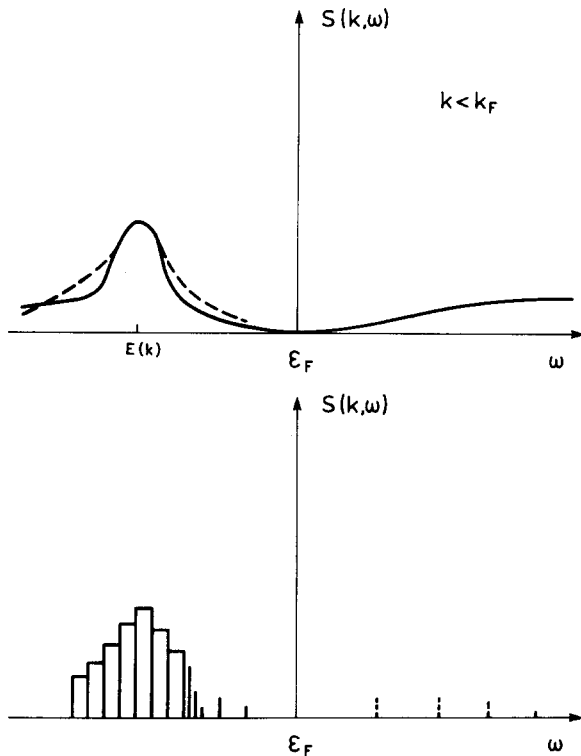


Fig. 3.38. The top part schematically represents the spectral function when k is significantly smaller than k_F . The dashed curve shows the quasiparticle Lorentzian. The bottom part corresponds to the case of a deeply bound orbit in a finite nucleus. The histogram recalls that the levels in the quasi-hole peak can no longer be resolved experimentally in pick-up or knock-out reactions; the spectrum of outgoing particles is in practice divided into energy bits. A physical example will be shown in fig. 4.41.

3.13. Screening corrections

3.13.1. Introduction

Until now, the discussion has been restricted to the first- and second-order contributions to the perturbation expansion of the mass operator. We have argued that the main conclusions should remain valid when higher-order terms are included. It is nevertheless necessary to investigate to what extent some of these higher-order terms may modify the quantities computed in second order.

One of the advantages of the diagrammatic representation is that it helps identifying subseries of the perturbation expansion which can be summed in closed form. This leads to various possibilities of rearranging the perturbation series via partial resummations.

The nature of the subseries which play an important quantitative role depends upon the physical system under consideration, in particular upon its density and the properties of the particle-particle interaction. In the following, we briefly survey three types of resummation. They correspond to the summation of ring diagrams (section 3.13.2), to the dilute hard sphere Fermi gas (section 3.14) and to Brueckner's particle-particle ladder summation (section 3.15).

3.13.2. Ring diagrams

Graph M_{2a} of fig. 3.8 is the generator of a series of diagrams of which one fifth-order term is denoted

by \mathcal{M}_{5a} in fig. 3.39. Similarly, graph \mathcal{M}_{2b} is the generator of a series of diagrams of which the graph \mathcal{M}_{5b} in fig. 3.39 is one example. These are called ring diagrams. Summing them up essentially amounts to replacing the one particle (*d*)–one hole (*j*) excitations of the core which appear in \mathcal{M}_{2a} and \mathcal{M}_{2b} by excitations computed from the random phase approximation. The inclusion of the ring diagrams yields the “screening corrections”. We shall see that these play an important role in dense systems, especially in the electron gas (section 3.20) and in liquid ^3He (section 3.19).

The ring diagrams can be summed in closed form if the particle–hole interaction $v_{SMT}(q)$ only depends upon the momentum transfer q , and upon the spin S , its projection M and the isospin T of the particle–hole excitation. Their sum reads [83]

$$\mathcal{M}^s(k; \omega) = -i \sum_{SMT} (2T+1) \sum_q \int \frac{d\gamma}{2\pi} \mathcal{G}_0(k-q; \omega-\gamma) v_{SMT}^2(q) \chi_{SMT}(q; \gamma) \quad (3.13.1)$$

where \mathcal{G}_0 is the Green function of the free Fermi gas (eq. (3.5)) and $\chi_{SMT}(q; \gamma)$ is the response function in the *SMT* channel: one has

$$\chi_{SMT}(q; \gamma) = \frac{\mathcal{L}(q; \gamma)}{1 + v_{SMT}(q) \mathcal{L}(q; \gamma)} \quad (3.13.2)$$

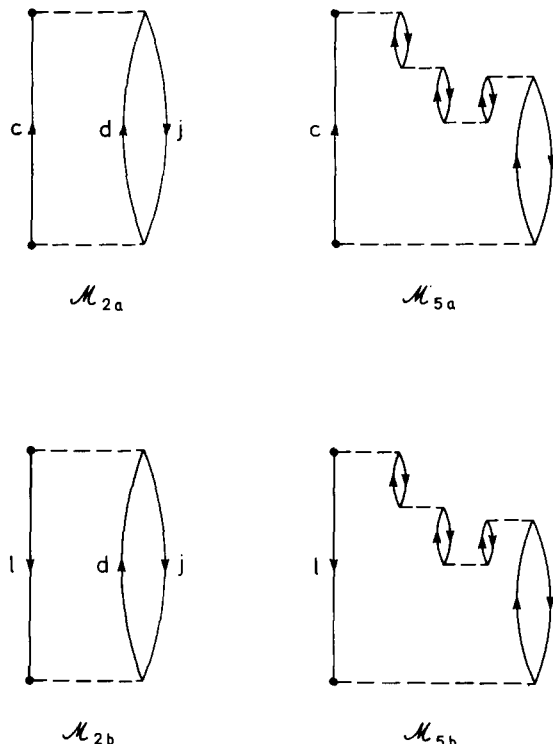


Fig. 3.39. The graphs \mathcal{M}_{5a} and \mathcal{M}_{5b} are examples of ring diagrams which yield the screening corrections to the second-order contributions \mathcal{M}_{2a} and \mathcal{M}_{2b} .

where $\mathcal{L}(q; \gamma)$ is the Lindhard function:

$$\mathcal{L}(q; \gamma) = 2 \sum_p \left\{ -\frac{n_<(p) n_>(p+q)}{\gamma - e(p+q) + e(p) + i\eta} + \frac{n_>(p) n_<(p+q)}{\gamma - e(p+q) + e(p) - i\eta} \right\}. \quad (3.13.3)$$

The second-order contribution M_2 is retrieved if one makes the approximation $\chi = \mathcal{L}$ in eq. (13.1).

3.13.3. Numerical results

Blaizot and Friman [83] have calculated the screening corrections in the case of the model defined by eqs. (10.13a,b). This modifies the second-order results which had been shown in figs. 3.21, 3.25 and 3.29 into those contained in figs. 3.40, 3.41 and 3.42, respectively. The slope of $V_S(E)$ at $E = \varepsilon_F$ is smaller than that of $V_2(E)$. As a consequence, the maximum value of $m_\omega^{(S)}(E)$ at $E \approx \varepsilon_F$ is smaller than that of $m_\omega^{(2)}(E)$. The enhancement peak of $m_\omega^{(S)}(E)$ is somewhat broader than that of $m_\omega^{(2)}(E)$. The dependence upon momentum of the k -mass $m_k^{(S)}$ is weaker than that of $m_k^{(2)}$. The enhancement of $m_S^*(E)$ is less marked than that of $m_2^*(E)$. Here the index S refers to ‘‘screened’’.

Blaizot and Friman [83] conclude that screening corrections have a significant influence on the enhancement of $m^*(E)$ in nuclear matter. We note, however, that caution must be exercised. Indeed, the calculations of the effective mass are based on the use of the relation (10.32). They are somewhat inaccurate because the derivatives contained in m_k and m_ω do not appear to have been calculated at the self-consistent energy (10.33). In any case, the calculations show that the screening corrections somewhat broaden the enhancement peak of the ω -mass in nuclear matter.

Screening corrections have also been considered in a model developed by Oset and Palanques-Mestre [120]. These authors compute the mass operator starting from a boson-exchange picture for the nucleon-nucleon interaction. They include explicitly the effect of π - and ρ -exchange. They compute the residue $Z(k) = m/m_\omega(k)$ at the quasiparticle pole and find results in semi-quantitative agreement with those shown in figs. 3.36 and 3.41.

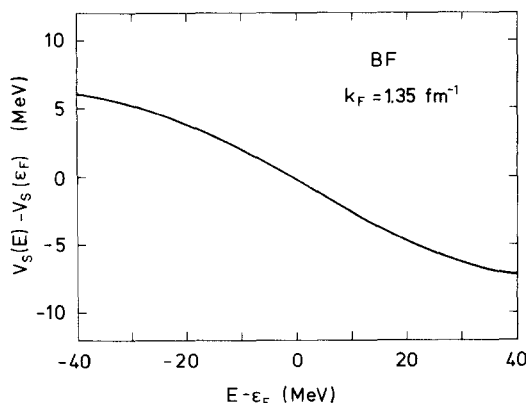


Fig. 3.40. Derived from ref. [83]. Dependence upon $E - \varepsilon_F$ of the difference $V_S(E) - V_S(\varepsilon_F)$, where $V_S(E)$ is the contribution of the ring diagrams to the self-energy, in the case of the interaction (10.13a, b) and of the Fermi momentum 1.35 fm^{-1} . This figure should be compared with fig. 3.21.

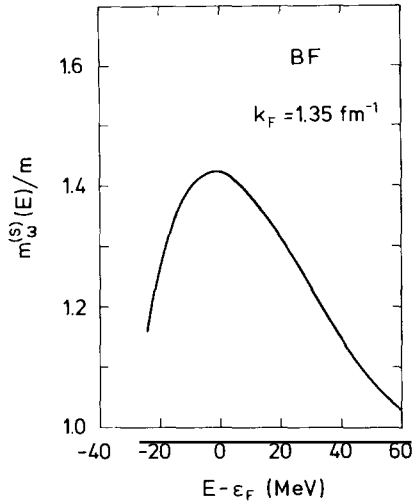


Fig. 3.41. Adapted from ref. [83]. Dependence upon $E - \epsilon_F$ of the ω -mass as calculated from the sum of the ring diagrams, in the case of the interaction (10.13a, b). This figure should be compared to fig. 3.25.

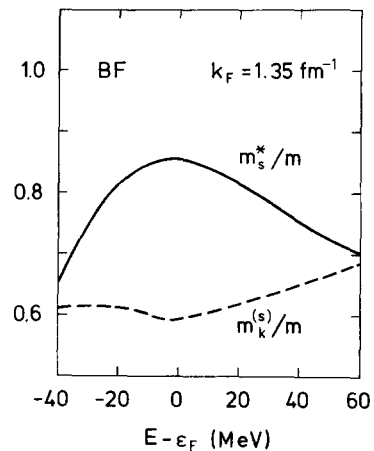


Fig. 3.42. Adapted from ref. [83]. Dependence upon $E - \epsilon_F$ of the k -mass (dashes) and of the effective mass (full curve) as calculated by adding the screening corrections to the quantities which had been plotted in fig. 3.29.

3.14. Hard-sphere dilute Fermi gas

3.14.1. Introduction

We have considered systems in which the interaction is sufficiently weak to enable one to calculate the quantities of interest from an expansion in powers of the strength of the interaction. This is not the case for most physical systems. Then it is necessary to rearrange the perturbation series by grouping and summing subseries, or to use different theoretical approaches (section 3.18).

One of the simplest uniform systems with singular interactions is the hard-sphere Fermi gas, in which the particles interact via a repulsive hard core of radius c . When the density of the system is small, so that

$$k_{FC} \ll 1, \quad (3.14.1)$$

all the quantities of interest can be expanded in powers of (k_{FC}) . Many of the results obtained in this model are valid for any normal dilute Fermi gas in the long wave length limit; in that case, c should be identified with the scattering length in free space [34].

The average energy per particle has been calculated up to order $(k_{FC})^4 \ln(k_{FC})$ [121]. Here, we shall discuss the properties of the mass operator; it has been computed up to order $(k_{FC})^2$ in ref. [88].

3.14.2. Second-order approximation

The first-order approximation to the mass operator $\mathcal{M}(k; \omega)$ of the dilute hard-sphere Fermi gas is independent of k and ω . Its expression reads

$$\mathcal{M}_1 = V_1 = \frac{2}{\pi m} k_{FC}^3. \quad (3.14.2)$$

The second-order contribution is the sum of three terms, which are represented in fig. 3.43. Their algebraic expressions are the following for particles with four degrees of freedom (2 for spin and 2 for isospin):

$$\mathcal{M}_{2a}(k; \omega) = \frac{96\pi^2 c^2}{m} \sum_{j, c, d} n_<(j) n_>(c) n_>(d) \frac{1}{\omega + e(c) - [e(d) - e(j)] + i\eta}, \quad (3.14.3)$$

$$\mathcal{M}_{2b}(k; \omega) = \frac{96\pi^2 c^2}{m} \sum_{j, l, d} n_<(l) n_<(j) n_>(d) \frac{1}{\omega - e(l) + [e(d) - e(j)] - i\eta}, \quad (3.14.4)$$

$$\mathcal{M}_{2c}(k) = -\frac{96\pi^2 c^2}{m} \mathcal{P} \sum_{j, a, b} n_<(j) \frac{1}{e(k) + e(j) - [e(a) + e(b)]}. \quad (3.14.5a)$$

On the right-hand side of eq. (14.5a), one must have

$$\mathbf{k} + \mathbf{j} = \mathbf{a} + \mathbf{b}, \quad (3.14.5b)$$

but \mathbf{a} and \mathbf{b} can be particle as well as hole momenta. We note that \mathcal{M}_{2c} is real and independent of the frequency variable ω . We shall write accordingly

$$\mathcal{M}_{2c}(k) = V_{2c}(k). \quad (3.14.6)$$

The order of each contribution (14.2)–(14.5a) is given by the power of c on the right-hand side. In keeping with the fact that one limits oneself to second order in the perturbation expansion, one can use in eqs. (14.3)–(14.5a) the zeroth-order approximation for the energy $e(q)$ which appears in the propagator, i.e.

$$e(q) = q^2/2m. \quad (3.14.7)$$

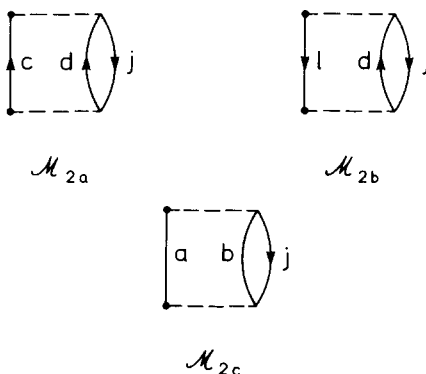


Fig. 3.43. Graphical representation of the three contributions to the mass operator $\mathcal{M}(k; \omega)$ which are of order $(k_F c)^2$ in the expansion of $\mathcal{M}(k; \omega)$ in powers of $(k_F c)$, for the hard-sphere dilute Fermi gas. Their algebraic expressions are given by eqs. (14.3)–(14.15b).

The comparison between the right-hand sides of eqs. (14.3) and (14.4) on the one hand and those of eqs. (8.2) and (9.1) on the other hand shows that in second order the dilute hard-sphere Fermi gas model essentially amounts to replacing all the matrix elements of the residual interaction by a constant.

In the present case, the rearrangement of the perturbation series has consisted in grouping the graphs whose sum can be expressed in terms of the reactance matrix K associated with the scattering of two free particles by the potential v . One has

$$\langle \mathbf{p}|K|\mathbf{p}'\rangle = \langle \mathbf{p}|v|\mathbf{p}'\rangle + \mathcal{P} \sum_{\mathbf{p}''} \langle \mathbf{p}|v|\mathbf{p}''\rangle \frac{m}{p^2 - p''^2} \langle \mathbf{p}''|K|\mathbf{p}'\rangle, \quad (3.14.8)$$

where \mathbf{p} , \mathbf{p}' and \mathbf{p}'' denote relative momenta. In the long wave length limit, i.e. for small values of p and p' one gets

$$\langle \mathbf{p}|K|\mathbf{p}'\rangle \approx 4\pi c/m, \quad (3.14.9)$$

where c is the scattering length. One is thus effectively using an interaction which is independent of the momentum transfer and which essentially amounts to a zero range interaction.

We shall use a notation similar to the one adopted in sections 3.8–3.12. We write for instance

$$\mathcal{M}_{2a}(k; \omega) = \mathcal{V}_{2a}(k; \omega) - i \mathcal{W}_{2a}(k; \omega), \quad (3.14.10)$$

$$V_{2a}(k) = \mathcal{V}_{2a}(k; k^2/2m), \quad (3.14.11)$$

$$V_2(k) = V_1 + V_{2a}(k) + V_{2b}(k) + V_{2c}(k), \quad (3.14.12)$$

$$W_2(k) = W_{2a}(k; k^2/2m). \quad (3.14.13)$$

3.14.3. Numerical results

The expansion parameter (k_{FC}) is only a scale parameter for all the quantities shown below. It can therefore be chosen arbitrarily in the numerical illustrations, and in that context need not be much smaller than unity. In ref. [88] the value $k_{FC} = 0.7$ was chosen because it yields approximately the numerical value of the depletion of the Fermi sea in nuclear matter as evaluated from a realistic interaction (compare fig. 3.35 with fig. 3.46 below).

The on-shell value $V_2(k)$ has been calculated algebraically by Galitskii [122]. From this quantity, one can calculate the second-order approximation to the effective mass; in ref. [88] it was defined by the following relation

$$m_2^*(k)/m = 1 - 2m \frac{dV_2(k)}{dk^2}. \quad (3.14.14)$$

This quantity is plotted in fig. 3.44. It displays a broad peak centred on the Fermi momentum. From the discussion in sections 3.8–3.10, one expects that this peak reflects the existence of an enhancement of the ω -mass

$$m_\omega^{(2)}(k) = m_\omega^{(2a)}(k) + m_\omega^{(2b)}(k) - m, \quad (3.14.15)$$

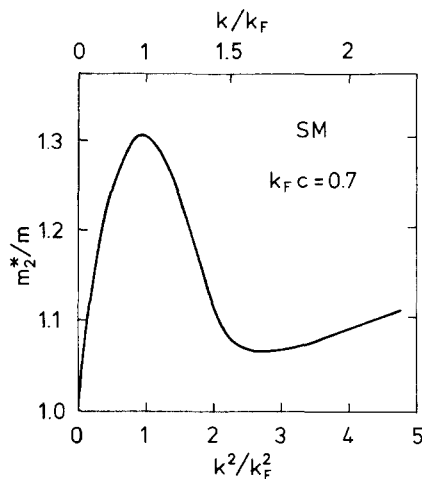


Fig. 3.44. Taken from ref. [88]. Momentum dependence of the effective mass m_2^*/m (eq. (14.4)) in the hard-sphere dilute Fermi gas for $k_{Fc}c = 0.7$.

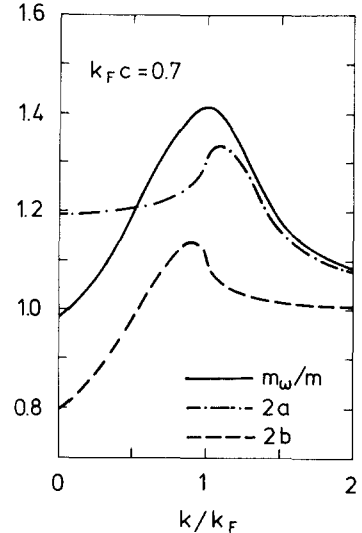


Fig. 3.45. Adapted from ref. [88]. Momentum dependence of the ω -mass $m_\omega^{(2)}/m$ (full curve), of $m_\omega^{(2a)}/m$ (dash-and-dot, eq. (14.16)) and of $m_\omega^{(2b)}/m$ (dashes, eq. (14.17)) in the case of a hard-sphere dilute Fermi gas for $k_{Fc} = 0.7$.

where

$$m_\omega^{(2a)}(k)/m = [1 - \partial \mathcal{V}_{2a}(k; \omega)/\partial \omega]_{\omega=k^2/2m}, \quad (3.14.16)$$

$$m_\omega^{(2b)}(k)/m = [1 - \partial \mathcal{V}_{2b}(k; \omega)/\partial \omega]_{\omega=k^2/2m}. \quad (3.14.17)$$

These quantities have been calculated in ref. [88]. They are plotted in fig. 3.45. The similarity between these results and those shown in figs. 3.22 and 3.24 is quite striking. This confirms that the main features of the enhancement of the ω -mass are largely independent of the interaction, unless screening corrections are sizeable.

The algebraic expression for the average momentum distribution of the dilute hard-sphere Fermi gas can be found in refs. [88, 123]; it is plotted in fig. 3.46. The ratio of the number of particles with momentum larger than k_F to the total number of particles has a very simple expression, namely $24(k_{Fc})^2/(5\pi^2)$ [123].

The quantities $n(k)$ and $k^2 n(k)$ decrease monotonically for $k > k_F$. This questions the validity of the assumption made in many calculations of higher-order corrections to the Brueckner–Hartree–Fock approximation for the binding energy of nuclear matter [92]. This assumption rests on the belief that a hard-core interaction preferentially gives rise to virtual excitations in which the two particles acquire momenta close to $\pi/2c \approx 3-4 \text{ fm}^{-1}$ [124]. This assumption may, however, have some validity for the partial waves for which tensor interactions play an important role [125].

The value of the k -mass in the hard-sphere dilute Fermi gas has been computed in ref. [88] from the approximation

$$\frac{m_2^*(k)}{2} = \frac{m_k^{(2)}(k)}{m} \cdot \frac{m_\omega^{(2)}(k)}{m} \quad (3.14.18)$$

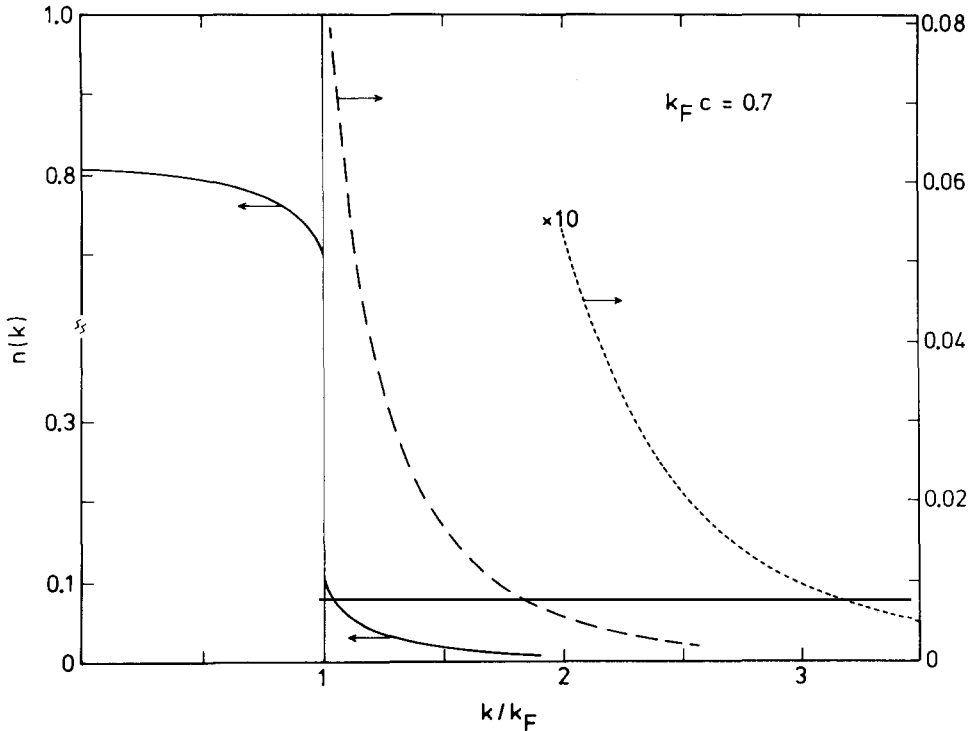


Fig. 3.46. Taken from ref. [88]. Momentum distribution in the correlated ground state of the dilute hard-sphere Fermi gas as calculated in second order in the expansion parameter ($k_F c$) for $k_F c = 0.7$.

which is valid in second order in $(k_F c)$. The results are represented by the short dashes in fig. 3.47. We note that $m_k^{(2)}$ has a shallow minimum for k close to k_F ; this is similar to the result found by Blaizot and Friman [83] in the case of second-order perturbation theory (fig. 3.29, see also figs. 3.27 and 3.42).

3.14.4. Subtracted dispersion relation

The procedure used in ref. [88] to calculate the quantities $m_\omega^{(2)}$, $m_\omega^{(2a)}$ and $m_\omega^{(2b)}$ was the following: Algebraic expressions valid for all values of k and ω have been obtained for the imaginary parts $\mathcal{W}_{2a}(k; \omega)$ and $\mathcal{W}_{2b}(k; \omega)$ of the quantities $\mathcal{M}_{2a}(k; \omega)$ and $\mathcal{M}_{2b}(k; \omega)$. Their real parts have been computed numerically, via dispersion relations. In the present case, however, the dispersion relation (8.26) is not applicable. Indeed, $\mathcal{W}_{2a}(k; \omega)$ increases like $\omega^{1/2}$ for large ω

$$\mathcal{W}_{2a}(k; \omega) \sim \frac{2}{\pi} k_F \left(\frac{\omega}{m}\right)^{1/2} (k_F c)^2. \quad (3.14.19)$$

The integral on the right-hand side of eq. (8.26) thus diverges. This problem can be circumvented by using the once subtracted dispersion relation ($\omega \neq \omega_0$)

$$\mathcal{V}_{2a}(k; \omega) = \mathcal{V}_{2a}(k; \omega_0) + (\omega - \omega_0) \frac{\mathcal{P}}{\pi} \int_{k^2/2m}^{\infty} \frac{\mathcal{W}_{2a}(k; \omega')}{(\omega' - \omega_0)(\omega - \omega')} d\omega', \quad (3.14.20)$$

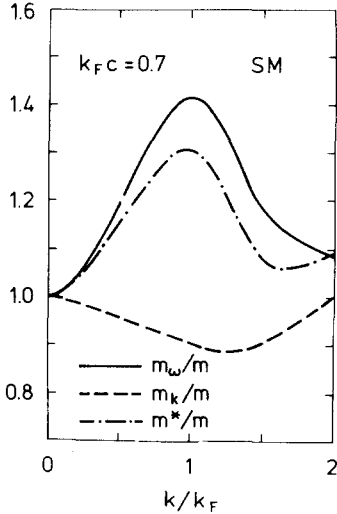


Fig. 3.47. Adapted from ref. [88]. Dependence upon k/k_F of the quantities m_2^*/m (full curve, eq. (14.14)), $m_\omega^{(2)}/m$ (long dashes, eq. (14.15)) and $m_k^{(2)}/m$ (short dashes, eq. (14.18)), in the case of the hard-sphere dilute Fermi gas for $k_{Fc} = 0.7$.

where ω_0 is arbitrary. Equation (14.20) determines $V_{2a}(k; \omega)$ only up to the constant $V_{2a}(k; \omega_0)$ but enables one to calculate the quantity $m_\omega^{(2a)}$ defined in eq. (14.16).

3.14.5. Summary

In the hard-sphere dilute Fermi gas, the ω -mass m_ω presents an enhancement centred near the Fermi energy. The effective mass m^* also has a broad enhancement, although the k -mass has a shallow minimum centred near the Fermi energy. The average momentum distribution is typical of a normal Fermi system. It is a monotonically decreasing function of the momentum. The imaginary part $\mathcal{W}_{2a}(k; \omega)$ increases like $\omega^{1/2}$ for large ω ; it can be related to $\mathcal{V}_{2a}(k; \omega)$ via a subtracted dispersion relation.

3.15. Hole line expansion

3.15.1. Introduction

We mentioned in section 3.14.1 that when the particle-particle interaction is strong the perturbation series must be rearranged by summing subseries. In the case of the dilute hard-sphere Fermi gas, the rearrangement is performed in such a way as to express the observables in terms of diagrams which involve the transition matrix for the scattering between two free particles rather than the particle-particle potential v . Brueckner [126, 127] realized that when the density of the system is not extremely small, it is more advantageous to express the observables in terms of a transition matrix which is modified in order to take into account the Pauli principle. This modified transition matrix is called the reaction matrix.

Many authors, in particular Bethe and collaborators, have improved and applied Brueckner's approach. The application of the resulting "hole line expansion" of Bethe and Brueckner for the binding energy of nuclear matter is reviewed in refs. [92, 124, 128, 129]; the most recent results are presented in ref. [130]. The extension of the Bethe-Brueckner hole line expansion to the study of the mass operator has been performed in ref. [42] and is briefly described in section 3.15.2. Numerical

results have been published in ref. [36]; those which are relevant in the present context are recalled in section 3.15.3.

3.15.2. Expansion of the mass operator

3.15.2.1. Brueckner–Hartree–Fock approximation

The algebraic expression of the contribution to the mass operator of the third-order term represented by the diagram \mathcal{M}_{3a} in fig. 3.48 is the following

$$\mathcal{M}_{3a}(k; \omega) = \sum_j n_<(j) \langle k, j | v_3[\omega] | k, j \rangle_t, \quad (3.15.1)$$

where

$$\begin{aligned} v_3[\omega] &= v \sum_{c, d} n_>(c) n_>(d) \frac{|c, d\rangle \langle c, d|}{\omega + e(j) - e(c) - e(d) + i\eta} v \\ &\times \sum_{c', d'} n_>(c') n_>(d') \frac{|c', d'\rangle \langle c', d'|}{\omega + e(j) - e(c') - e(d') + i\eta} v. \end{aligned} \quad (3.15.2)$$

By comparing these expressions with those of \mathcal{M}_1 (eq. (7.1)) and of \mathcal{M}_{2a} (eq. (8.2)), one realizes that the sum of \mathcal{M}_1 , \mathcal{M}_{2a} and of all the contributions which are obtained from \mathcal{M}_{2a} by adding an arbitrary number of interactions between the upward pointing particle lines c and d is given by

$$\mathcal{M}_{\text{BHF}}(k; \omega) = \sum_j n_<(j) \langle k, j | g[\omega + e(j)] | k, j \rangle_t, \quad (3.15.3)$$

where $g[\omega]$ is the solution of the integral equation

$$g[\omega] = v + v \sum_{c, d} n_>(c) n_>(d) \frac{|c, d\rangle \langle c, d|}{\omega - e(c) - e(d) + i\eta} g[\omega]. \quad (3.15.4)$$

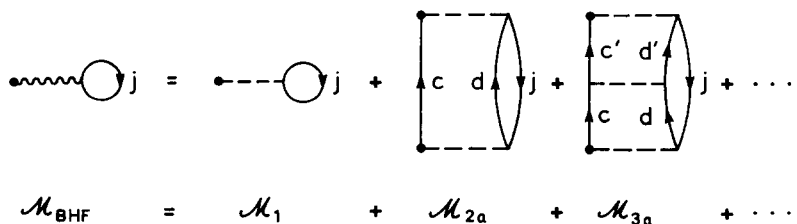


Fig. 3.48. The diagram on the left-hand side represents the Brueckner–Hartree–Fock approximation. It is the sum of the Hartree–Fock contribution \mathcal{M}_1 , of the contribution \mathcal{M}_{2a} (section 3.8) and of all the diagrams obtained from \mathcal{M}_{2a} by adding an arbitrary number of interactions between the particle lines c and d . The reaction matrix g is represented by a wiggly line and is said to be the sum of the particle–particle ladder. Only the direct terms are shown.

The operator $g[\omega]$ is called the *reaction matrix*. It depends upon the parameter ω , often called the “starting energy”. If one relaxes the condition that in eq. (15.4) the momenta c and d of the intermediate states must be larger than k_F and if one sets $e(c) = c^2/2m$, $e(d) = d^2/2m$, the reaction matrix g reduces to the transition matrix for the scattering of two free particles.

The quantity $\mathcal{M}_{\text{BHF}}(k; \omega)$ is the *Brueckner–Hartree–Fock approximation* to the mass operator. It is associated with the diagram at the left-hand side of fig. 3.48, where the wiggly line represents the reaction matrix. This diagram underlines the formal similarity between the Brueckner–Hartree–Fock and the Hartree–Fock approximation. Note, however, that $\mathcal{M}_{\text{BHF}}(k; \omega)$ is complex and depends upon ω . Since it is the sum of an infinite number of contributions belonging to the class (a) of the perturbation expansion (see fig. 3.48 and section 3.8.2.4), we write

$$\mathcal{M}_{\text{BHF}}(k; \omega) = \mathcal{V}_{\text{BHF}}(k; \omega) - i \mathcal{W}_{\text{BHF}}(k; \omega), \quad (3.15.5)$$

where

$$\mathcal{W}_{\text{BHF}}(k; \omega) \begin{cases} = 0 & \text{for } \omega < \varepsilon_F, \\ > 0 & \text{for } \omega > \varepsilon_F, \end{cases} \quad (3.15.6a)$$

$$(3.15.6b)$$

$$\mathcal{V}_{\text{BHF}}(k; \omega) = \frac{\mathcal{P}}{\pi} \int_{\varepsilon_F}^{\infty} \frac{\mathcal{W}_{\text{BHF}}(k; \omega')}{\omega - \omega'} d\omega'. \quad (3.15.7)$$

The latter dispersion relation may have to be replaced by a subtracted dispersion relation if v contains a hard core repulsion.

3.15.2.2. Hole line ordering

Bethe has argued that it is appropriate to group together all the graphs of the perturbation series which contain the same number of hole lines. This yields the hole line expansion.

The Brueckner–Hartree–Fock approximation is the sum of all the terms which contain only one hole line. The right-hand side of fig. 3.49 sketches a series of two-hole line diagrams of class (b) (section 3.8.2.4) which can be summed up in closed form. Their sum is represented on the left-hand side of fig.

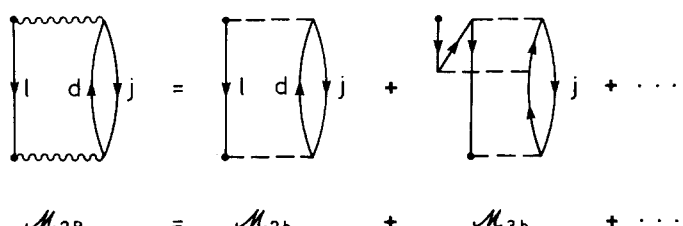


Fig. 3.49. The left-hand side represents one two-hole graph of the hole line expansion. It is obtained by summing an infinite series of diagrams of the perturbation expansion, of which \mathcal{M}_{2b} and \mathcal{M}_{3b} are typical examples.

3.49 and reads

$$\mathcal{M}_{2B}(k; \omega) = \frac{1}{2} \sum_{j, l, d} n_<(l) n_<(j) n_>(d) \frac{|(l, j | g[e(j) + e(l)] | k, d)|^2}{\omega + e(d) - e(j) - e(l) - i\eta}. \quad (3.15.8)$$

Note the formal analogy between \mathcal{M}_{2B} and \mathcal{M}_{2b} (eq. (9.11)).

3.15.2.3. Auxiliary potential

The energies $e(q)$ which appear in the equations above can be written in the form

$$e(q) = q^2/2m + U(q). \quad (3.15.9)$$

As in section 3.8.2.2, $U(q)$ is an auxiliary potential which should be chosen in such a way as to optimize the rate of convergence of the hole line expansion while still remaining manageable from a computational point of view. In the case of the mass operator, a convenient choice appears to be provided by the Brueckner–Hartree–Fock self-consistent condition

$$U(q) = \mathcal{V}_{BHF}(q; e(q)) \quad (3.15.10)$$

for all values of q [42]. The right-hand side of eq. (15.10) is a continuous function of q and the choice (15.10) is therefore referred to as the “continuous choice”.

The most appropriate choice of $U(q)$ for the calculation of the average binding energy per nucleon is a more debated problem [92]. All authors agree to adopt the self-consistent choice (15.10) for $q < k_F$: most take $U(q) = 0$ for $q > k_F$ [130], others adopt (15.10) either for $k_F < q < 2k_F$ [131] or for all q [75, 132, 133].

3.15.2.4. Effective mass

In the Brueckner–Hartree–Fock approximation, the ω -mass, the k -mass and the effective mass are given by (see eqs. (6.8)–(6.10))

$$\frac{m_\omega^{BHF}(k)}{m} = \left\{ 1 - \frac{\partial \mathcal{V}_{BHF}(k; \omega)}{\partial \omega} \right\}_{\omega=e(k)}. \quad (3.15.11)$$

$$\frac{m_k^{BHF}(k)}{m} = \left\{ 1 + \frac{m}{k} \frac{\partial \mathcal{V}_{BHF}(k; \omega)}{\partial \omega} \right\}_{\omega=e(k)}^{-1}, \quad (3.15.12)$$

$$\frac{m_{BHF}^*(k)}{m} = \left\{ 1 + \frac{m}{k} \frac{d}{dk} \mathcal{V}_{BHF}(k; e(k)) \right\}^{-1}. \quad (3.15.13)$$

One has

$$\frac{m_{BHF}^*(k)}{m} = \frac{m_\omega^{BHF}(k)}{m} \cdot \frac{m_k^{BHF}(k)}{m}, \quad (3.15.14)$$

provided that eqs. (15.9) and (15.10) are satisfied.

3.15.2.5. Average momentum distribution

The leading terms of the average momentum distribution are given by (see eqs. (11.6) and (11.7))

$$n_2^{\text{BB}}(k) = \begin{cases} \left[2 - \frac{m_{\omega}^{\text{BHF}}(k)}{m} \right] & \text{for } k < k_F, \\ \left[\frac{m_{\omega}^{(2\text{B})}(k)}{m} - 1 \right] & \text{for } k > k_F, \end{cases} \quad (3.15.15a)$$

$$(3.15.15b)$$

where

$$\frac{m_{\omega}^{(2\text{B})}(k)}{m} = \left\{ 1 - \frac{\partial}{\partial \omega} \mathcal{V}_{2\text{B}}(k; \omega) \right\}_{\omega=\epsilon(k)}. \quad (3.15.16)$$

3.15.2.6. Renormalized Brueckner–Hartree–Fock approximation

Figure 3.50 shows other two-hole line diagrams than $\mathcal{M}_{2\text{B}}$. The algebraic expression of graph \mathcal{M}_R is particularly simple:

$$\mathcal{M}_R(k; \omega) = \sum_j [1 - m_{\omega}^{\text{BHF}}(j)/m] \langle \mathbf{k}, j | g[\omega + e(j)] | \mathbf{k}, j \rangle_t. \quad (3.15.17)$$

From eqs. (15.3), (15.15a) and (15.17), one obtains the following expression for the sum of \mathcal{M}_R and \mathcal{M}_{BHF}

$$\mathcal{M}_{\text{RBHF}}(k; \omega) = \sum_{j(j < k_F)} n_2^{\text{BB}}(j) \langle \mathbf{k}, j | g[\omega + e(j)] | \mathbf{k}, j \rangle_t. \quad (3.15.18)$$

This is the renormalized Brueckner–Hartree–Fock approximation. Equations (15.3) and (15.18) show that the renormalized Brueckner–Hartree–Fock approximation takes some account of the depletion of the Fermi sea.

3.15.3. Numerical results

We now give a few numerical results taken from ref. [36]. They all have been obtained from Reid's hard-core nucleon–nucleon interaction [134] and from the continuous choice (15.10) for $U(q)$.

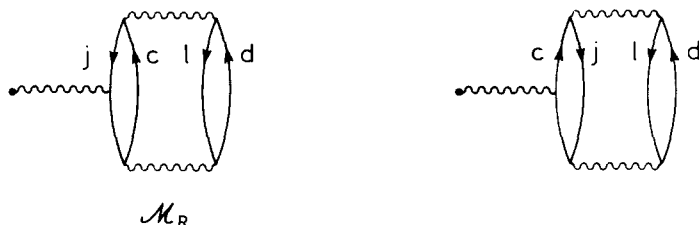


Fig. 3.50. Two diagrams which contain two hole lines. The sum $\mathcal{M}_{\text{RBHF}} = \mathcal{M}_{\text{BHF}} + \mathcal{M}_R$ yields the renormalized Brueckner–Hartree–Fock approximation.

3.15.3.1. Quasiparticle energy

In the Brueckner–Hartree–Fock approximation, the potential energy of a quasiparticle with energy e is given by

$$V_{\text{BHF}}(e) = \mathcal{V}_{\text{BHF}}(k(e); e), \quad (3.15.19)$$

where $k(e)$ is defined by the energy-momentum relation

$$e = k^2/2m + \mathcal{V}_{\text{BHF}}(k; e), \quad (3.15.20)$$

see eqs. (15.9) and (15.10). The value of $V_{\text{BHF}}(e)$ has been computed in ref. [135]; in the domain $10 \text{ MeV} < e < 100 \text{ MeV}$, the result can be represented (in MeV) by

$$V(e) \approx -56 + 0.3e. \quad (3.15.21)$$

This is in excellent agreement with the full line drawn in fig. 2.11. This gives confidence in the rate of convergence of the hole line expansion of the mass operator. The calculated imaginary part is also in good agreement with the empirical values for $200 \text{ MeV} > e > 50 \text{ MeV}$ [57, 58].

3.15.3.2. The ω -mass

The full curve in fig. 3.51 gives the dependence upon k/k_F of the ω -mass as calculated from eq. (15.11). These results are quite similar to those shown for $m_\omega^{(2a)}$ in figs. 3.10 and 3.24, see also fig. 3.45. The basic reason for this similarity is that the Brueckner–Hartree–Fock approximation sums up diagrams of type (a), as illustrated in fig. 3.48.

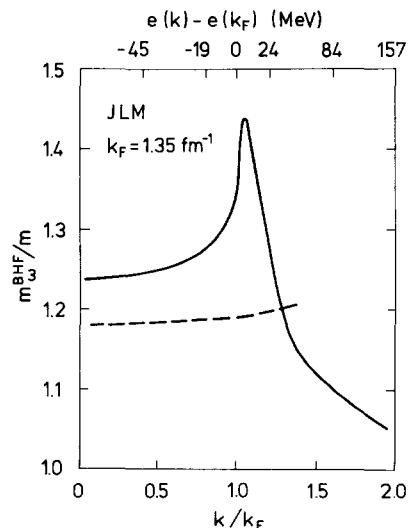


Fig. 3.51. Adapted from ref. [36]. The full curve represents the dependence upon k/k_F (lower scale) and upon $e(k) - e(k_F)$ (upper scale) of the ω -mass as evaluated in the Brueckner–Hartree–Fock approximation, see eqs. (15.3), (15.9), (15.10), in the case of Reid's hard-core interaction. The long dashes show the dependence upon k/k_F of the ω -mass which results if one sets $U(c) = U(d) = 0$ in eq. (15.4) ($c, d > k_F$) while keeping the self-consistent choice (15.10) for $U(j)$ ($j < k_F$). The Fermi momentum is equal to 1.35 fm^{-1} .

From our discussion in section 3.9, we expect that the inclusion of the contribution $m_\omega^{(2B)}$ (see eq. (15.16)) would make the enhancement peak of the ω -mass approximately two times broader than that of m_ω^{BHF} and raise the value of its maximum.

The average depletion of the Fermi sea is given by

$$1 - n_2^{\text{BB}}(\langle k \rangle) = m_\omega^{\text{BHF}}(\langle k \rangle)/m - 1 = \kappa, \quad (3.15.22)$$

where

$$\langle k \rangle = 0.75k_F \quad (3.15.23)$$

is the average value of k inside the Fermi sea. In the present case one has $\kappa \approx 0.25$. The quantity κ is called the smallness parameter and is believed to characterize the rate of convergence of the hole line expansion [42, 128, 136]. It has already been encountered in eqs. (8.61)–(8.65).

Equations (15.8) and (15.22) show that the value of the ω -mass in the renormalized Brueckner–Hartree–Fock approximation is approximately given by

$$m_\omega^{\text{RBHF}}(k) \approx 1 - (1 - \kappa) [1 - m_\omega^{\text{BHF}}(k)/m]. \quad (3.15.24)$$

This quantity has the same shape as $m_\omega^{\text{BHF}}(k)$, but the enhancement peak is somewhat broader and its maximum somewhat smaller [36].

3.15.3.3. The k -mass

The k -mass in the Brueckner–Fock approximation is defined by eq. (15.12). Its value is represented by the long dashes in fig. 3.52a. The property that it is a monotonically increasing function of k can be qualitatively understood from the fact that the Brueckner–Hartree–Fock approximation includes the Hartree–Fock term, for which a typical k -mass is shown in fig. 3.7. In addition, m_k^{BHF} contains the contribution of graphs of type (a); fig. 3.14 suggests that these yield a fairly constant contribution in the vicinity of the Fermi momentum.

The momentum dependence of the k -mass as calculated from the renormalized Brueckner–Hartree–Fock approximation is approximately the same as that of m_k^{BHF} [36]. We note, however, that the inclusion of the contribution of graphs like M_{2B} (fig. 3.49) could give rise to the appearance of a shallow minimum in the momentum dependence of the k -mass. This is suggested by the results shown in figs. 3.14, 3.27 and 3.29.

3.15.3.4. The effective mass

In the Brueckner–Hartree–Fock approximation, the effective mass can be obtained from the ω -mass and from the k -mass by using the relation (15.14). Its value is represented by the full curve in fig. 3.52.

Our discussion in the two preceding sections indicates that the inclusion of M_{2B} (fig. 3.49) would most probably render the enhancement of the effective mass broader and less pronounced. Furthermore, one should realize that the enhancement is less spectacular when the effective mass is plotted versus the quasiparticle energy, see fig. 3.52b.

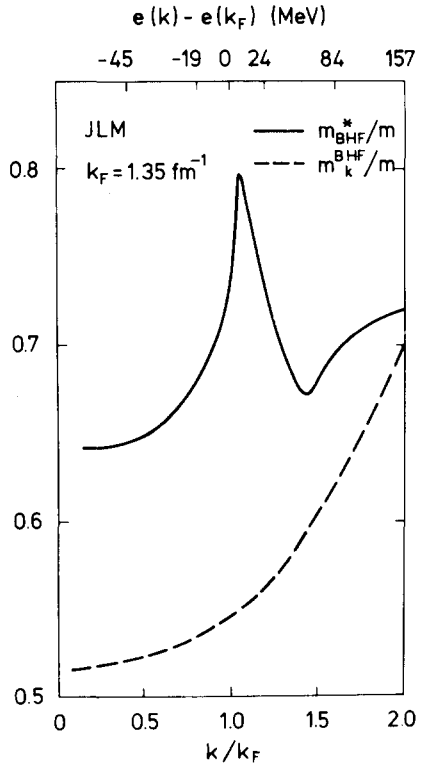


Fig. 3.52a. Adapted from ref. [36]. Dependence upon k/k_F (lower scale) and upon $e(k) - e(k_F)$ (upper scale) of the k -mass (dashes) and of the effective mass (full curve) as calculated from the Brueckner-Hartree-Fock approximation, see eqs. (15.3), (15.9), (15.10), (15.12) and (15.13), in the case of Reid's hard-core interaction. The Fermi momentum is equal to 1.35 fm^{-1} .

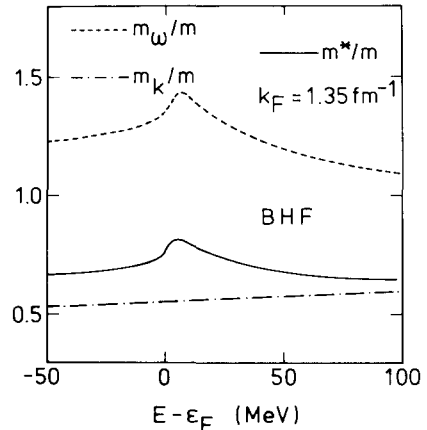


Fig. 3.52b. Dependence upon $E - \epsilon_F = e(k) - e(k_F)$ of the k -mass (dash-and-dot), of the ω -mass (dashes) and of the effective mass (full curve) as calculated in the Brueckner-Hartree-Fock approximation for the Fermi momentum $k_F = 1.35 \text{ fm}^{-1}$.

3.15.4. Summary

The Brueckner-Hartree-Fock approximation has the merit of enabling one to use as input realistic nucleon-nucleon interactions. It has led to the finding that the ω -mass is enhanced in the vicinity of the Fermi momentum. It suffers from the drawback that it does not include any diagram of class (b) (section 3.8.2.4), of which the contribution \mathcal{M}_{2B} shown in fig. 3.49 is an example. The inclusion of these contributions would broaden the enhancement peak of the ω -mass, and probably render less pronounced that of the effective mass in nuclear matter.

Finally, we mention the existence of another approach for evaluating the mass operator in nuclear matter, using realistic nucleon-nucleon interactions. Its starting point lies in the integro-differential set of equations which couple the one-, two-, three-, ... body Green functions [137]. This infinite set is truncated by assuming that the three-body Green function can be written as a linear combination of products of the one- and of the two-body Green functions. There exist several variants of this approximation; they rest on the assumption that the main correlations are those which take place between pairs of nucleons. It has been shown that each truncation amounts to summing a class of Feynman diagrams [138], but that the reverse is not true. The mass operator in nuclear matter has been

calculated along these lines in [139–144], see also references contained therein. This type of approach has been extended to finite nuclei by N. Vinh Mau et al. [103, 104, 145] and will be encountered in section 4.2.

3.16. Role of high-energy virtual excitations

3.16.1. Introduction

In sections 3.14 and 3.15 we outlined two methods for dealing with singular interactions. These interactions present the characteristic of being able to excite the core into virtual states with high excitation energy. The same holds true for forces which include tensor terms.

Highly excited virtual states cannot be included explicitly in calculation for finite nuclei since one must use a truncated configuration space. It is therefore of interest to investigate to what extent these highly excited states contribute to the dynamics of the mass operator, i.e. to the dependence of $\mathcal{M}(k; \omega)$ upon ω . This dependence is measured by the ω -mass. Below, we describe two arguments which indicate that the core states with high excitation energy yield a sizeable but energy-independent contribution to the ω -mass. This result is obtained in the case of nuclear matter but is expected to remain valid for nuclei, where high momentum states can also be described by plane waves.

3.16.2. Highly excited states in the Brueckner–Hartree–Fock approximation

We mentioned that in most calculations of the binding energy of nuclear matter one sets $U(q) = 0$ for $q > k_F$ in eq. (15.9). The reaction matrix which appears in the Brueckner–Hartree–Fock approximation (15.3) is then a solution of the integral equation

$$g[\omega + e(j)] = v + v \sum_{c, d} n_>(c) n_>(d) \frac{|c, d\rangle \langle c, d|}{\omega + e(j) - [(c^2 + d^2)/2m] + i\eta} g[\omega + e(j)]. \quad (3.16.1)$$

The on-shell value corresponds to $\omega = e(k)$; for $k < k_F$, the denominator D on the right-hand side of eq. (16.1) then fulfills the inequality

$$|D| > [(c^2 + d^2 - 2k_F^2)/2m] - 2U(k_F) \quad (3.16.2a)$$

$$> -2U(k_F). \quad (3.16.2b)$$

Since $U(k_F) \approx -70$ MeV, one has

$$|D| > 140 \text{ MeV}. \quad (3.16.2c)$$

Hence, the standard choice $U(q) = 0$ for $q > k_F$ corresponds to including virtual excited two particle–one hole states whose energy exceeds that of the polarizing nucleon by more than 140 MeV. This effectively suppresses any low-lying core excitations.

The corresponding Brueckner–Hartree–Fock approximation to the ω -mass which is obtained when one sets $U(c) = U(d) = 0$ on the right-hand side of eq. (15.4) is represented by the long dashes in fig. 3.51. This result indicates that the contribution of the high-lying core excitations essentially amounts to a background (of size ≈ 0.18) to the enhancement of the ω -mass near the Fermi energy.

3.16.3. Highly excited states and dispersion relation

We return to the model defined by eqs. (7.23), (7.25). The subtracted dispersion relation (14.20) yields

$$V_{2a}(\omega) - V_{2a}(\omega_F) = (\omega - \omega_F) \int_{\omega_F}^{\infty} \frac{W_{2a}(\omega')}{(\omega' - \omega_F)(\omega - \omega')} d\omega', \quad (3.16.3)$$

where ω_F is given by eq. (8.41). This quantity is represented by the full curve on the bottom of fig. 3.53 (compare with fig. 3.9).

From the asymptotic behaviour (14.19), it appears plausible to assume that the addition of a hard-core interaction would essentially amount to modifying the dependence of $W_{2a}(\omega)$ upon ω for large ω in the way represented by the dashed line in the upper part of fig. 3.53. The value of $V_{2a}(\omega) - V_{2a}(\omega_F)$ which would be obtained from this modified W_{2a} via the use of the subtracted dispersion relation (16.3) is represented by the dashed curve in the lower part of fig. 3.53. This dashed curve can approximately be obtained from the full curve by a rotation about the origin. This reflects the fact that the corresponding ω -masses essentially differ by a constant. This is confirmed in fig. 3.54.

Instead of adding a simulation of the excitations due to the hard core, one can investigate the role of highly excited core states by suppressing their contribution, i.e. by introducing a cut-off on the

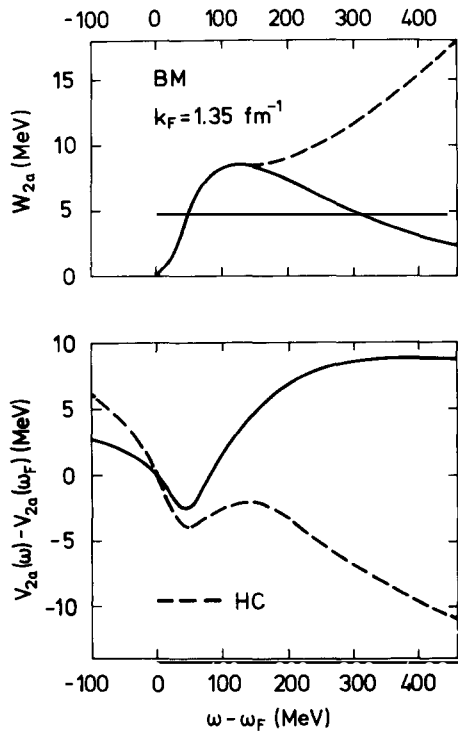


Fig. 3.53. Adapted from ref. [86]. The lower part shows the values of the difference $[V_{2a}(\omega) - V_{2a}(\omega_F)]$ which are obtained via the subtracted dispersion relation (16.3) when using as input the corresponding values of W_{2a} shown in the upper part.

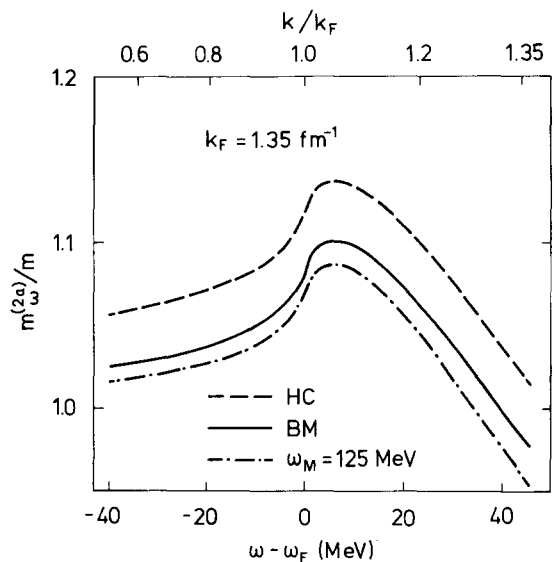


Fig. 3.54. Adapted from ref. [86]. The full curve and the short dashes represent the dependence upon ω of the quantity $m_\omega^{(2a)}/m = 1 - dV_{2a}/d\omega$, where V_{2a} is shown in fig. 3.53. The dash-and-dot curve shows the corresponding quantity as calculated from the truncated dispersion integral (16.4), for $\omega_M = 125$ MeV.

right-hand side of eq. (16.3). Let us accordingly introduce the quantity

$$[V_{2a}(\omega) - V_{2a}(\omega_F)]_M = (\omega - \omega_F) \int_{\omega_F}^{\omega_M + \omega_F} \frac{W_{2a}(\omega')}{(\omega' - \omega_F)(\omega - \omega')} d\omega'. \quad (3.16.4)$$

The corresponding ω -mass is represented by the dash-and-dot curve in fig. 3.54 for $\omega_M = 125$ MeV. It only differs from the full curve by a constant. An analytical discussion of this result has been given in ref. [113] in the framework of the model (10.27).

3.16.4. Conclusions

The main contribution of highly excited core polarized states to the ω -mass can be considered as a constant in the vicinity of the Fermi energy. This is natural from a physical point of view. Indeed, virtual states with excitation energy larger than $\omega_M - \omega_F$ cannot induce any rapid dependence upon ω in the domain $|\omega - \omega_F| \ll \omega_M - \omega_F$.

3.17. Statistical and dynamical quasiparticle energies

3.17.1. Introduction

Recent calculations of the temperature dependence of the specific heat of liquid ${}^3\text{He}$ will be surveyed in section 3.19. Some of these calculations involve “statistical quasiparticle energies”. The main purpose of the present section is to indicate *the origin* of the difference between the “statistical quasiparticle energy” and the “dynamical quasiparticle energy”. The latter is the one which has been introduced in section 3.4.

In eq. (4.11), the complex energy

$$\omega(k) = \varepsilon^{(D)}(k) \mp i \gamma^{(D)}(k) \quad (3.17.1)$$

of a quasiparticle has been defined as the pole of the one-body Green function. The upper index (D) refers to dynamical. These quasiparticle energies are associated with the elementary excitations of the system. The real part $\varepsilon^{(D)}(k)$ gives the excitation energy and the imaginary part $\gamma(k)$ yields the lifetime $\tau = (1/\gamma^{(D)})$ of the excitation. These dynamical quasiparticle energies appear in the microscopic derivations [146–149] of Landau’s theory of Fermi liquids, which had been introduced on intuitive grounds [150].

In a Landau description, the energy is written as a functional of the quasiparticle occupation number; the entropy and particle number are the same as for a system of noninteracting quasiparticles. The original microscopic justifications of Landau’s description rest on the assumption that the lifetime of the elementary excitations is large, i.e. that $\gamma^{(D)}(k)$ is small. These derivations were accordingly restricted to Fermi liquids at very low temperature.

It has been shown in refs. [151–153] that a Landau description can be used at any temperature if one adopts a proper definition for the quasiparticle energy. Balian and De Dominicis [152] thus distinguished between the *statistical quasiparticle energy* $\varepsilon^{(S)}(k)$ which should be used in a Landau description of equilibrium quantities at finite temperature and the *dynamical quasiparticle energy* $\varepsilon^{(D)}(k)$ which is associated with an elementary excitation of the system. This distinction appears to have been overlooked in several recent works on the thermodynamical properties of liquid ${}^3\text{He}$.

3.17.2. Landau's definition

Landau defined the energy of a quasiparticle with momentum k as the functional derivative of the energy B with respect to the momentum distribution of the noninteracting system. At zero temperature, this momentum distribution is given by $n_0(k) = n_<(k)$, see eqs. (3.3) and (3.6). Landau's definition then reads

$$\mathcal{E}^{(L)}(k) = \delta B / \delta n_<(k). \quad (3.17.2)$$

3.17.3. Second-order perturbation theory

In the standard perturbation expansion of B in powers of the strength of an effective interaction (sections 3.7–3.10) the second-order approximation reads

$$B = B_1 + B_2, \quad (3.17.3)$$

where

$$B_1 = \frac{1}{2} \sum_{\mathbf{k}} n_<(k) \left[\frac{k^2}{2m} + e_1(k) \right], \quad (3.17.4)$$

$$e_1(k) = k^2/2m + U_{HF}(k), \quad (3.17.5a)$$

$$U_{HF}(k) = \sum_j n_<(j) \langle \mathbf{k}, j | \hat{v} | \mathbf{k}, j \rangle_t, \quad (3.17.5b)$$

$$B_2 = -\frac{1}{4} \sum_{\substack{j, l \\ \mathbf{c}, \mathbf{d}}} n_<(j) n_<(l) n_>(d) n_>(c) \frac{|\langle \mathbf{j}, \mathbf{l} | \hat{v} | \mathbf{c}, \mathbf{d} \rangle_t|^2}{e_1(c) + e_1(d) - e_1(j) - e_1(l)}. \quad (3.17.6)$$

The contribution to $\mathcal{E}^{(L)}(k)$ of the first-order term B_1 yields the Hartree–Fock approximation to the quasiparticle energy, namely

$$\mathcal{E}_1^{(L)}(k) = k^2/2m + U_{HF}(k). \quad (3.17.7)$$

The second-order term (17.6) yields two contributions. The first one is obtained from the functional differentiation of the factors $n_<(j)$ and $n_<(l)$ on the right-hand side of eq. (17.6). It reads

$$\mathcal{E}_{2a}^{(L)}(k) = \frac{1}{2} \sum_{j, c, d} n_<(j) n_>(c) n_>(d) \frac{|\langle \mathbf{k}, j | \hat{v} | \mathbf{c}, \mathbf{d} \rangle_t|^2}{e_1(k) + e_1(l) - e_1(c) - e_1(d)}. \quad (3.17.8)$$

The second one arises from the factors $n_>(c)$ and $n_>(d)$ in eq. (17.6). Remembering that $n_>(c) = 1 - n_<(c)$, one obtains

$$\mathcal{E}_{2b}^{(L)}(k) = \frac{1}{2} \sum_{j, l, d} n_<(l) n_<(j) n_>(d) \frac{|\langle \mathbf{l}, \mathbf{j} | \hat{v} | \mathbf{k}, \mathbf{d} \rangle_t|^2}{e_1(k) + e_1(d) - e_1(l) - e_1(j)}. \quad (3.17.9)$$

The indices (2a) and (2b) are meant to emphasize the similarity between the right-hand sides of eqs. (17.8) and (17.9) on the one hand and those of eqs. (8.8) and (9.1) on the other hand.

3.17.4. Vanishing energy denominators

The energy denominators which appear on the right-hand side of eqs. (17.8) and (17.9) may vanish, in contrast to the denominator in the expression (17.6) for B_2 . Hence, the integrals in eqs. (17.8) and (17.9) must be specified by regularization procedures. Let us consider two examples.

(i) If one for instance takes principal value integrals and the choice (8.9) (i.e. $e(q) = e_1(q)$ in the expression of $\mathcal{M}_{2a}(k; \omega)$) one gets (see eqs. (8.14) and (9.4))

$$\mathcal{E}_{2a}^{(L)}(k) = \mathcal{V}_{2a}(k; e(k)), \quad (3.17.10)$$

$$\mathcal{E}_{2b}^{(L)}(k) = \mathcal{V}_{2b}(k; e(k)). \quad (3.17.11)$$

(ii) If one rather chooses to add $(+i\eta)$ to the denominator of expression (17.8) and $(-i\eta)$ to the denominator of eq. (17.9), one gets complex contributions to the quasiparticle energies; they read (see eqs. (8.8) and (9.1))

$$\mathcal{E}_{2a}^{(L)}(k) = \mathcal{M}_{2a}(k; e(k)), \quad (3.17.12)$$

$$\mathcal{E}_{2b}^{(L)}(k) = \mathcal{M}_{2b}(k; e(k)). \quad (3.17.13)$$

The choices (i) and (ii) for the regularization procedure yield in second order the same value for the real part of the Landau quasiparticle energy, which is the quantity of interest for the Landau description of the Fermi liquid. However, the choice of the regularization procedure becomes crucial if one considers terms of higher order than second in the perturbation expansion of $\mathcal{E}^{(L)}(k)$, because these contain products of denominators which can vanish [152, 154–156].

3.17.5. One third-order contribution

Some third-order contributions would be generated by the functional differentiation of B_2 if one would take into account the fact that the energies $e_1(q)$ in the denominator of eq. (17.6) depend upon $n_{<}(q)$ via eqs. (17.5a, b). In the present context, it is more convenient to consider that the energies $e_1(q)$ in the denominator of eq. (17.6) are fixed ($e_1(q) = q^2/m + U(q)$, see eq. (8.4)). This is a perfectly legitimate approach; it corresponds to the introduction of an external field in the zero-order Hamiltonian. The third-order contributions to $\mathcal{E}^{(L)}(k)$ then arise from the functional differentiation of the third-order contributions to the energy B .

Let us consider one example. The Brueckner–Hartree–Fock approximation to the energy reads (see eq. (15.3))

$$B_{\text{BHF}} = T_0 + \frac{1}{2} \sum_{\mathbf{k}, j} n_{<}(k) n_{<}(j) \langle \mathbf{k}, j | g[e(k) + e(j)] | \mathbf{k}, j \rangle_t, \quad (3.17.14)$$

where

$$T_0 = \sum_{\mathbf{k}} n_{<}(k) \frac{k^2}{2m} \quad (3.17.15)$$

is the kinetic energy of the free Fermi gas.

Let us expand the g -matrix in powers of v . Its third-order term is given by $v_3[e(k) + e(j)]$, see eq. (15.2). One particular third-order contribution to B is thus

$$B_{3a} = \frac{1}{2} \sum_{\mathbf{k}, \mathbf{j}} n_<(k) n_<(j) \langle \mathbf{k}, \mathbf{j} | v_3[e(k) + e(j)] | \mathbf{k}, \mathbf{j} \rangle_t. \quad (3.17.16a)$$

This contribution is represented by the diagram at the left-hand side of fig. 3.55. Its algebraic expression is

$$\begin{aligned} B_{3a} &= \frac{1}{2} \sum_{\mathbf{k}, \mathbf{j}} \sum_{\mathbf{c}, \mathbf{d}} \sum_{\mathbf{c}', \mathbf{d}'} n_<(k) n_<(j) n_>(c) n_>(d) n_>(c') n_>(d') \\ &\times \frac{\langle \mathbf{k}, \mathbf{j} | v | \mathbf{c}, \mathbf{d} \rangle \langle \mathbf{c}, \mathbf{d} | v | \mathbf{c}', \mathbf{d}' \rangle \langle \mathbf{c}', \mathbf{d}' | v | \mathbf{k}, \mathbf{j} \rangle_t}{[e(k) + e(j) - e(c) - e(d)][e(k) + e(j) - e(c') - e(d')]} . \end{aligned} \quad (3.17.16b)$$

Note that the denominator on the right-hand side never vanishes.

The functional differentiation of B_{3a} yields many contributions to $\mathcal{E}_{3a}^{(L)}(k)$. The most obvious one arises from the factor $n_<(k)$ on the right-hand side of eq. (17.16b); it reads

$$\mathcal{E}_{3a}^{(L)}(k) = \sum_j n_<(j) \langle \mathbf{k}, \mathbf{j} | \hat{v}_3[e(k) + e(j)] | \mathbf{k}, \mathbf{j} \rangle_t , \quad (3.17.17)$$

where

$$\begin{aligned} \hat{v}_3[e(k) + e(j)] &= v \sum_{\mathbf{c}, \mathbf{d}} n_>(c) n_>(d) \frac{|\mathbf{c}, \mathbf{d}\rangle \langle \mathbf{c}', \mathbf{d}'|}{e(k) + e(j) - e(c) - e(d)} v \\ &\times \sum_{\mathbf{c}', \mathbf{d}'} n_>(c') n_>(d') \frac{|\mathbf{c}', \mathbf{d}'\rangle \langle \mathbf{c}', \mathbf{d}'|}{e(k) + e(j) - e(c') - e(d')} . \end{aligned} \quad (3.17.18)$$

The right-hand side of this expression is ill-defined since the denominators can vanish.

The problem is more serious than in the second-order case because the real part of $\mathcal{E}_{3a}^{(L)}$ depends upon the regularization procedure. Let us give one example. If one regularizes the integrals by inserting

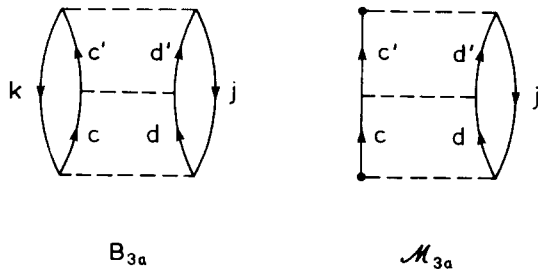


Fig. 3.55. Diagrams which represent the contribution B_{3a} (eq. (17.16a)) to the energy, and M_{3a} (eq. (15.1) and fig. 3.48) to the mass operator.

($+i\eta$) in both energy denominators of (17.18), one gets

$$\text{Re } \mathcal{E}_{3a}^{(L)}(k) = \mathcal{V}_{3a}(k; e(k)), \quad (3.17.19a)$$

see eqs. (8.13) and (15.1). Here Re stands for “the real part of”. One can as well choose principal value integrals on the right-hand side of eq. (17.18). One then obtains

$$\text{Re } \mathcal{E}_{3a}^{(L)}(k) = \mathcal{V}_{3a}(k; e(k)) - \pi^2 \sum_{\substack{j, c, d \\ c', d'}} n_<(j) n_>(c) n_>(d) n_>(c') n_>(d') \langle k, j | v | c, d \rangle \langle c, d | v | c', d' \rangle$$

$$\times \langle c', d' | v | k, j \rangle \delta[e(k) + e(j) - e(c) - e(d)] \delta[e(k) + e(j) - e(c') - e(d')]. \quad (3.17.19b)$$

This example illustrates that in third- (and of course also in higher-) order the choice of the regularization procedure is crucial.

3.17.6. Comments

We conclude from this example that Landau’s intuitive definition (17.2) for the quasiparticle energy must be supplemented by the specification of a regularization procedure. Pethick and Carneiro have in this context emphasized that “it is the necessity for a regularization procedure which makes most calculations of thermodynamic properties at finite temperature so complicated” [156].

The on-the-energy-shell value of the real part of the mass operator, $\varepsilon^{(D)} = \text{Re } \mathcal{M}(k; \omega(k))$, corresponds to the particular regularization prescription which is appropriate for the description of the elementary excitations of the system. It is not the one which should be used for the description of the thermodynamic properties of a normal Fermi liquid. The convention of using principal value integrals as in eq. (17.19b) is also not appropriate for a Landau description; the regularization procedure which should be used in that case has been derived by Balian and De Dominicis [152], see also refs. [151, 153]. It is quite involved and its description lies far outside the scope of the present review.

A physical explanation for the prescription of Balian and De Dominicis [152] has been given by Pethick and Carneiro [155]. This is quite useful because it also suggests a procedure for calculating the interaction between a quasiparticle and a quasi-hole [155–157].

3.17.7. Transition matrix, reactance matrix and phase shifts

3.17.7.1. Transition, reactance and reaction matrices

The importance of specifying the regularization procedure is familiar from scattering theory. Let us consider two-body scattering by a finite range potential v . The Hamiltonian reads

$$H = t + v, \quad (3.17.20)$$

where t is the kinetic energy operator. The transition matrix T is the solution of the Lippmann–Schwinger equation

$$T[E] = v + v(E - t + i\eta)^{-1} T[E]. \quad (3.17.21)$$

Note that the regularization procedure is the same as in the definition (15.4) of the reaction matrix

$g[E]$. The main difference between T and g is that in the latter those intermediate states $|c, d\rangle$ in which c and/or d are smaller than the Fermi momentum are excluded.

The reaction matrix should be distinguished from the reactance matrix K . The latter fulfills the integral equation

$$K[E] = v + v \mathcal{P}(E - t)^{-1} K[E], \quad (3.17.22)$$

where \mathcal{P} represents the prescription that principal value integrals should be used. The difference between $K[E]$ and $T[E]$ arises from energy-conserving collisions (as distinguished from virtual excitations). One has

$$T[E] = K[E] - i\pi K[E] \delta(E - t) T[E]. \quad (3.17.23)$$

Iterating the right-hand side, the real part of $T[E]$ reads

$$\text{Re } T[E] = K[E] - \pi^2 K[E] \delta(E - t) K[E] \delta(E - t) K[E] + \dots \quad (3.17.24)$$

Note the similarity of this expression with eq. (17.19b).

The operator whose expectation value gives the energy shift of the system when it is enclosed in a box is neither $\text{Re } T[E]$ nor $K[E]$ but [158, 159]

$$\Delta[E] = K[E] - \frac{1}{3}\pi^2 K[E] \delta(E - t) K[E] \delta(E - t) K[E]. \quad (3.17.25)$$

This gives a hint that the regularization procedure which is appropriate for a Landau description would lead to the replacement of the factor $(-\pi^2)$ by a factor $(-\frac{1}{3}\pi^2)$ in the second term on the right-hand side of eq. (17.19b).

3.17.7.2. Phase shift

The forward scattering amplitude is defined by

$$T(q) = \langle \mathbf{k}, \mathbf{j} | T[(k^2 + j^2)/2m] | \mathbf{k}, \mathbf{j} \rangle, \quad (3.17.26a)$$

where $\mathbf{q} = \mathbf{k} - \mathbf{j}$ is the momentum transfer. For s-wave scattering, $T(q)$ is related to the phase shift δ by

$$T(q) = -\frac{2\pi}{mq} e^{i\delta} \sin \delta. \quad (3.17.26b)$$

Note that $\delta = -kc$ for hard-sphere scattering (section 3.14). The diagonal matrix element of the reactance matrix yields

$$K(q) = -\frac{2\pi}{mq} \tan \delta, \quad (3.17.27)$$

while the matrix element of ΔE reads

$$\Delta E = -\frac{2\pi}{mq} \delta. \quad (3.17.28)$$

The energy shift is determined by δ rather than by $\tan \delta$ or $\cos \delta \sin \delta$ [160]. For small δ , one has

$$\delta = \tan \delta - \frac{1}{3} \tan^3 \delta + \dots; \quad (3.17.29)$$

the factor $(-\frac{1}{3})$ in the second term corresponds to the factor $-\frac{1}{3}$ in the second term of the right-hand side of eq. (17.25).

3.17.7.3. Discussion

The reminder above serves not only as an illustration of the difference between the results obtained from various regularization procedures. Indeed, we noted the close correspondence between the transition and the reaction matrix. It is thus not surprising that the relations recalled above have proved very useful in the evaluation of the interaction energy between a quasiparticle and a quasi-hole [155, 157].

3.17.8. Statements

In a Landau description of the thermodynamical properties of a Fermi liquid at equilibrium, the entropy has the same form as for a Fermi gas of free quasiparticles with energy $\varepsilon^{(S)}(k)$. These “statistical” quasiparticle energies are real quantities. They can be obtained from Landau’s functional derivative provided that appropriate regularization procedures are used to compute the integrals whose integrands involve products of denominators that can vanish.

The statistical quasiparticle energies are solutions of an equation formally similar to eq. (4.11), namely [152]

$$\varepsilon^{(S)}(k) = k^2/2m + M^{(S)}(k; \varepsilon^{(S)}(k)). \quad (3.17.30)$$

However, there exists no simple relationship between the “effective” mass operator $M^{(S)}(k; \omega)$ and the true mass operator. These two quantities have very different properties [152]. For instance, the quantity $\Sigma(k; \omega)$ (eq. (2.28)) has a cut along the real axis and is holomorphic in the whole cut complex ω -plane. In contrast, $M^{(S)}(k; \omega)$ has been defined on the real ω -axis; it can be continued analytically in the immediate vicinity of the real ω -axis along which it has no cut. This effective mass operator $M^{(S)}(k; \omega)$ is real for ω real.

For a dilute uniform system with density ρ , the dynamical quasiparticle energy (eq. (17.1)) is given by [152]

$$\mathcal{E}^{(D)}(k) \mp i \Gamma^{(D)}(k) \approx k^2/2m + \rho T_{kk} \quad (3.17.31)$$

where

$$T_{kk} = -\frac{2\pi}{mk} \sum_l (2l+1) \exp(i\delta_l) \sin \delta_l \quad (3.17.32)$$

is the forward scattering amplitude (17.26b). The statistical quasiparticle energy is then given by

$$\epsilon^{(S)}(k) = \frac{k^2}{2m} - \rho \frac{2\pi}{mk} \sum_l (2l+1) \delta_l. \quad (3.17.33)$$

Note the analogy with eqs. (17.28) and (17.33)

3.17.9. Conclusions

The statistical quasiparticle energies are useful when one wants to use a Landau description of equilibrium thermodynamics; they occur as a tool for performing summations needed in the evaluation of equilibrium properties. They need not be introduced for other descriptions [156, 161]. They do not describe the elementary excitations of the system: these are given by the dynamical quasiparticle energies.

3.18. The method of correlated basis functions

3.18.1. Introduction

The method of correlated basis functions presents over the hole line expansion the advantage of being applicable to dense systems such as ${}^3\text{He}$ and the electron gas. It is competitive with the hole line expansion in the case of nuclear matter.

The method has been initiated mainly by Feenberg, Clark and collaborators [162, 163]. It has made spectacular progress in recent years [111, 165] owing to the techniques developed in particular by Fantoni and Rosati [164], by Krotscheck and Ristig [166] and by Pandharipande and collaborators [167] for calculating expectation values of various operators with respect to trial wave functions. These techniques were first applied to the evaluation of upper bounds for the ground state energy. They have been extended to the ground state energy, to the mass operator and to related quantities.

3.18.2. Upper bound for the ground state energy

Let φ_0 denote some trial wave function and H the Hamiltonian. The quantity

$$\mathcal{U} = \langle \varphi_0 | H | \varphi_0 \rangle / \langle \varphi_0 | \varphi_0 \rangle \quad (3.18.1)$$

is an upper bound for the ground state energy

$$B = \langle \psi | H | \psi \rangle / \langle \psi | \psi \rangle ; \quad (3.18.2)$$

here ψ is the exact ground state wave function.

A trial wave function is called “of the Jastrow type” [168] if it has the form

$$\varphi_0 = \prod_{i < j} f_{ij}(x_i, x_j) |\psi_0\rangle = F_J |\psi_0\rangle , \quad (3.18.3)$$

where ψ_0 is the wave function of the free Fermi gas while $f(x_i, x_j)$ is a function of the coordinates x_i and x_j ($x = r, \sigma, \tau$). Fermi hypernetted chain summation procedures for approximating \mathcal{U} in that case are described in refs. [44, 166, 169]. Their accuracy is excellent as can be checked by comparing the results

with exact values of \mathcal{U} computed by Monte-Carlo techniques [170]. A formal comparison between the hypernetted chain approximation for \mathcal{U} and the Brueckner–Hartree–Fock approximation for B can be found in ref. [171].

If the Jastrow correlation factor F_J is sufficiently close to the exact two-particle correlation function, the upper bound \mathcal{U} is close to the energy B . This is not the case in nuclear matter where exchange forces are very large. One must therefore also consider trial functions of the form

$$\varphi_0 = \mathcal{S} \prod_{i < j} F(i, j) |\psi_0\rangle \quad (3.18.4)$$

where \mathcal{S} is a symmetrization operator and F is a sum of operators

$$F(i, j) = \sum_q f_q(r_{ij}) O_q(i, j), \quad (3.18.5)$$

where $O_q(i, j) = 1, \sigma_i \cdot \sigma_j, \tau_i \cdot \tau_j, (\sigma_i \cdot \sigma_j)(\tau_i \cdot \tau_j), \dots$. Up to eight different operators O_q have been included in the numerical calculations of \mathcal{U} in the case of nuclear matter [172]. The functions $f_q(r_{ij})$ usually contain parameters which are chosen by requiring that the corresponding value of \mathcal{U} be minimum; \mathcal{U} is calculated by performing Fermi hypernetted chain summations. This yields “optimized” correlation operators F_J or F .

In the case of nuclear matter, the recent estimates of the upper bound \mathcal{U} associated with trial functions of the form (18.4) are in fair agreement with the approximate value of B obtained from the hole line expansion [130].

Most calculations of liquid ^3He are based on the Lennard–Jones potential or on an improvement thereof [173, 174]. Radial correlation factors of the Jastrow type yield upper bounds for the average binding energy per particle which lie approximately 1.5 K above the experimental value which is -2.56 K at the experimental equilibrium density $\rho = 0.0166 \text{ \AA}^{-3}$ [175, 176]. Moreover, the calculated upper bound for the unpolarized ground state lies approximately 0.4 K above that for the ground state of the polarized system ^3He . This instability is cured if one introduces a spin dependence in the Jastrow correlation function [177].

Two main methods exist for bringing the calculated energy closer to the experimental result. (i) The first procedure consists in improving the choice of the trial wave function. One can for instance introduce three-body correlation factors and a momentum dependence in the two-body correlation factors; this lowers the upper bound to approximately -2 K [178]. (ii) The second procedure consists in evaluating the difference between the upper bound \mathcal{U} and the binding energy B via the method of correlated basis functions. In liquid ^3He , the calculated value of the difference ranges from 0.6 to 1.1 K, depending upon the choice of the Jastrow correlation factor f [112]. The difference $\mathcal{U} - B$ also removes the instability of the unpolarized system [179].

A cluster expansion has been constructed for the upper bound \mathcal{U} . The lowest-order term is given by a Hartree–Fock-type expression, namely [180, 181]

$$\mathcal{U}_1 = \frac{1}{2} \sum_k n_<(k) \left[\frac{k^2}{2m} + \varepsilon_1(k) \right], \quad (3.18.6)$$

where

$$\varepsilon_1(k) = k^2/2m + u(k), \quad (3.18.7a)$$

$$u(k) = \sum_j n_{<}(j) \langle \mathbf{k}, j | w | \mathbf{k}, j \rangle_t, \quad (3.18.7b)$$

$$w(1, 2) = \frac{1}{2} [f(1, 2), [\nabla_1^2 + \nabla_2^2, f(1, 2)]] + f(1, 2) v(1, 2) f(1, 2). \quad (3.18.8)$$

We recall that v is the bare particle-particle interaction.

3.18.3. Second-order approximation for the ground state energy

The wave functions of the excited states φ_m of the free Fermi gas form a complete set of Slater determinants. Here, the index m refers to the hole and particle momenta; for instance $\varphi_{ph} = a_p^+ a_h |\psi_0\rangle$. The correlated basis functions

$$\Phi_m = F |\varphi_m\rangle, \quad (3.18.9)$$

where F is a correlation operator, form a nonorthogonal set in which one can expand the true ground state wave function $|\psi\rangle$ and evaluate the quantities of interest.

In the resulting correlated basis functions method, the second-order approximation to the difference $\delta B = B - \mathcal{U}_1$ reads [182]

$$\begin{aligned} (\delta B)_2 &= -\frac{1}{4} \sum_{\substack{j, l \\ c, d}} n_{<}(j) n_{<}(l) n_{>}(c) n_{>}(d) \\ &\times \frac{\{|j, l| w |c, d\rangle_t + \frac{1}{2} [\varepsilon_1(c) + \varepsilon_1(d) - \varepsilon_1(j) - \varepsilon_1(l)] \langle j, l | f^2 - 1 | c, d \rangle_t|^2}{\varepsilon_1(c) + \varepsilon_1(d) - \varepsilon_1(j) - \varepsilon_1(l)}. \end{aligned} \quad (3.18.10)$$

The second term in the numerator on the right-hand side of eq. (18.10) arises from the property that the basis states $\{\varphi_m\}$ are not orthogonal.

The effective interaction of the correlated basis function method can be identified with the operator \hat{w} whose matrix elements are defined by

$$\begin{aligned} \langle j, l | \hat{w}(1, 2) | a, b \rangle &= \langle j, l | w(1, 2) | a, b \rangle \\ &+ \frac{1}{2} \{ \pm \varepsilon_1(a) \pm \varepsilon_1(b) \pm \varepsilon_1(j) \pm \varepsilon_1(l) \} \langle j, l | \mathcal{N}(1, 2) | a, b \rangle. \end{aligned} \quad (3.18.11)$$

Here, the (+) sign in front of $\varepsilon_1(q)$ is associated with a particle state ($q > k_F$) and the (-) sign with a hole state ($q < k_F$). The quantity $\mathcal{N}(1, 2)$ is defined by

$$\langle \psi_{p_1 p_2 h_1 h_2} | \psi_0 \rangle = \langle p_1 p_2 | \mathcal{N}(1, 2) | h_1, h_2 \rangle, \quad (3.18.12)$$

where \mathbf{p}_1 and \mathbf{p}_2 are particle momenta while \mathbf{h}_1 and \mathbf{h}_2 are hole momenta. These characterize φ_m in eq. (18.9). In lowest order, $\mathcal{N}(1, 2) = f^2(1, 2) - 1$.

3.18.4. Second-order approximation to the mass operator

The correlated basis functions method provides an expansion for the energy B . In refs. [5, 89, 95, 117, 183] the self-energy Σ has been defined by Landau's prescription

$$k^2/2m + \Sigma(k; \varepsilon_1(k)) = \delta B/\delta n_<(k). \quad (3.18.13)$$

In first order, this yields

$$\Sigma_1(k; \varepsilon_1(k)) = u(k), \quad (3.18.14)$$

where $u(k)$ is the Hartree–Fock-type potential given by eq. (18.7b).

In second order, one obtains two contributions similar to those of eqs. (17.8) and (17.9), namely

$$\Sigma_{2a}(k; \varepsilon_1(k)) = \frac{1}{2} \sum_{j, c, d} n_<(j) n_>(c) n_>(d) \frac{\langle \mathbf{k}, \mathbf{j} | \hat{w}(1, 2) | \mathbf{c}, \mathbf{d} \rangle_i|^2}{\varepsilon_1(k) + \varepsilon_1(j) - \varepsilon_1(c) - \varepsilon_1(d)}, \quad (3.18.15)$$

$$\Sigma_{2b}(k; \varepsilon_1(k)) = \frac{1}{2} \sum_{j, l, d} n_<(l) n_<(j) n_>(d) \frac{|\langle \mathbf{l}, \mathbf{j} | \hat{w}(1, 2) | \mathbf{k}, \mathbf{d} \rangle_i|^2}{\varepsilon_1(k) + \varepsilon_1(d) - \varepsilon_1(l) - \varepsilon_1(j)}. \quad (3.18.16)$$

3.18.5. Discussion

3.18.5.1. Problems

The definition of Σ via the right-hand side of eq. (18.13) encounters several problems.

(i) The discussion in section 3.17.4 shows that the right-hand sides of eqs. (18.15) and (18.16) are ill-defined quantities since one must specify a regularization procedure when the denominators vanish. The regularization prescription adopted in refs. [5, 89, 95, 117, 183] appears to have been patterned after the one which appears in the expressions (8.8) and (9.1) of \mathcal{M}_{2a} and \mathcal{M}_{2b} , respectively. This does not seem to have been justified. A proper derivation should probably start from the original definition of the time-ordered Green function [42, 149] and use Feynman diagrams [184].

(ii) A Landau-type definition (eq. (18.13)) can define a function of only one variable (k). In refs. [5, 89, 95, 117, 183] the off-the-energy-shell quantities $\Sigma_{2a}(k; \omega)$ and $\Sigma_{2b}(k; \omega)$ were constructed “by inspection, i.e. by considering higher-order diagrams (for B) which have the second-order self-energy insertions as subdiagrams” [5]. It is not clear to what extent this is a legitimate procedure. For instance, the diagrams for B never have vanishing energy denominators at zero temperature while these are encountered in the self-energy.

(iii) In refs. [5, 89, 95, 185] the following prescription was adopted to go off-the-energy shell and to regularize integrals which involve denominators that can vanish:

$$\Sigma_{2a}(k; \omega) = \frac{1}{2} \sum_{j, c, d} n_<(j) n_>(c) n_>(d) \frac{|\langle \mathbf{k}, \mathbf{j} | \tilde{w}[1, 2; \omega] | \mathbf{c}, \mathbf{d} \rangle_i|^2}{\omega + \varepsilon_1(l) - \varepsilon_1(c) - \varepsilon_1(d) + i\eta}, \quad (3.18.17)$$

$$\Sigma_{2b}(k; \omega) = \frac{1}{2} \sum_{j, l, d} n_<(l) n_<(j) n_>(d) \frac{|\langle \mathbf{l}, \mathbf{j} | \tilde{w}(1, 2; \omega) | \mathbf{k}, \mathbf{d} \rangle_i|^2}{\omega + \varepsilon_1(d) - \varepsilon_1(l) - \varepsilon_1(j) - i\eta}, \quad (3.18.18)$$

where (compare with eq. (18.11))

$$\langle \mathbf{k}, \mathbf{j} | \tilde{w}[1, 2; \omega] | \mathbf{c}, \mathbf{d} \rangle = \langle \mathbf{k}, \mathbf{j} | w(1, 2) | \mathbf{c}, \mathbf{d} \rangle + \frac{1}{2} \{ \varepsilon_1(c) + \varepsilon_1(b) + \varepsilon_1(k) - \varepsilon_1(j) - 2\omega \} \langle \mathbf{k}, \mathbf{j} | \mathcal{N}(1, 2) | \mathbf{c}, \mathbf{d} \rangle, \quad (3.18.19a)$$

$$\langle \mathbf{l}, \mathbf{j} | \tilde{\tilde{w}}[1, 2; \omega] | \mathbf{k}, \mathbf{d} \rangle = \langle \mathbf{l}, \mathbf{j} | w(1, 2) | \mathbf{k}, \mathbf{d} \rangle + \frac{1}{2} \{ \varepsilon_1(d) - \varepsilon_1(k) - \varepsilon_1(l) - \varepsilon_1(j) + 2\omega \} \langle \mathbf{l}, \mathbf{j} | \mathcal{N}(1, 2) | \mathbf{k}, \mathbf{d} \rangle. \quad (3.18.19b)$$

The dependence upon ω of \tilde{w} and $\tilde{\tilde{w}}$ hinders the use of the quantities $\Sigma_{2a}(k; \omega)$ and $\Sigma_{2b}(k; \omega)$ as approximations to the mass operator in equations in which related quantities (e.g. the spectral function) are integrated over ω , see e.g. eq. (2.20). It appears plausible that the ω -dependence of $\tilde{w}[\omega]$ and of $\tilde{\tilde{w}}[\omega]$ could be compensated by higher-order contributions of the correlated basis functions expansion [179]. It has been demonstrated by Krotscheck [185] that this holds in the case of the ring diagrams summation.

3.18.5.2. Advantages

(i) In the construction of the correlated basis $\{\Phi_m\}$, see eq. (18.9), one can use an optimized correlation function F which results from a Fermi hypernetted chain summation for the ground state energy (section 3.18.2). Then, the Hartree–Fock-type potential $u(k)$, eqs. (18.8b) and (18.14), already contains a summation over ring- and ladder diagrams [182]. Therefore it already includes some screening effects [89].

(ii) The correlated basis functions approach allows one to treat simultaneously and without double counting the main effect of the short-range correlations (via correlation operators) and of long-range correlations (via chain summations for the ground state wave function, summation of classes of diagrams in the correlated basis functions method and the self-consistent construction of the effective interaction), see [112] and references contained therein. It is also a promising approach to the microscopic investigation of nuclei with realistic nucleon–nucleon interactions.

(iii) In the present context, one advantage of the correlated basis functions approach is that it is applicable to dense systems, such as liquid ^3He and the electron gas for which the hole line expansion fails.

3.18.6. Numerical results

Numerical results obtained from the correlated basis functions approach in the case of liquid ^3He and of the electron gas will be described in sections 3.19 and 3.20, respectively.

Numerical results obtained in the case of nuclear matter have already been shown previously. Figures 3.26, 3.27, 3.30 and 3.32 showed values of the k -mass, of the ω -mass and of the effective mass as calculated from eqs. (18.14), (18.17) and (18.18); in the latter two equations, the dependence upon ω of \tilde{w} and $\tilde{\tilde{w}}$ has been dropped. The input is a semi-realistic nucleon–nucleon interaction.

Figure 3.31 shows the energy dependence of the effective mass as obtained from a more realistic nucleon–nucleon interaction. The full line is associated with the Hartree–Fock-type potential (18.14), see also ref. [186]. The dashed curves included the effect of the second-order corrections (18.17) and (18.18). It is not clear whether the ω -dependence of \tilde{w} and $\tilde{\tilde{w}}$ was included in the calculation.

The correlated ground state wave function obtained from the variational calculation alone can be used to calculate the average momentum distribution. The corresponding depletion of the Fermi sea is underestimated ($n(k_F - 0) - n(k_F + 0) \approx 0.85$). The inclusion of second-order corrections leads to the results shown in fig. 3.35.

3.19. Normal liquid ^3He

3.19.1. Introduction

In the present section we survey some recent theoretical progress in the investigation of the mass operator of normal liquid ^3He at zero temperature, of its effective mass and of the temperature dependence of its specific heat at low temperature. Emphasis is put on the relationship between these investigations and topics reviewed in the preceding sections.

The effective mass is proportional to the density of single-particle energies, see section 2.7.1 and eq. (6.1). This density appears as a coefficient in the expression of many observables. In particular, the specific heat per unit volume of a system of free particles with mass m_3^* is given by the following expression at low temperature ($k_B T \ll k_F^2/m_3^*$)

$$c_v^{(0)}(m_3^*) = \frac{1}{3} m_3^* k_F k_B^2 T, \quad (3.19.1)$$

where k_B is the Boltzmann constant. The Fermi momentum k_F is related to the density n by

$$n = (3\pi^2)^{-1} k_F^3. \quad (3.19.2)$$

At zero pressure and at saturation one has $n = 0.0166 \text{ \AA}^{-3}$ ($k_F = 0.79 \text{ \AA}^{-1}$).

Early [187, 188] as well as recent [189–192] measurements show that in normal liquid ^3He the effective mass m_3^* is significantly larger than the bare mass m_3 . Recent experimental values are shown in fig. 3.56. They yield $m_3^*/m_3 \approx 2.7$ at zero pressure.

Another striking feature of the recent experimental data [192] will be exhibited in section 3.19.3 below. It consists in the rapid dependence upon T of the temperature-dependent effective mass $M_S^*(T)$ defined by the following relation [193]

$$M_S^*(T)/m_3 = c_v(T)/c_v^{(f)}(T). \quad (3.19.3)$$

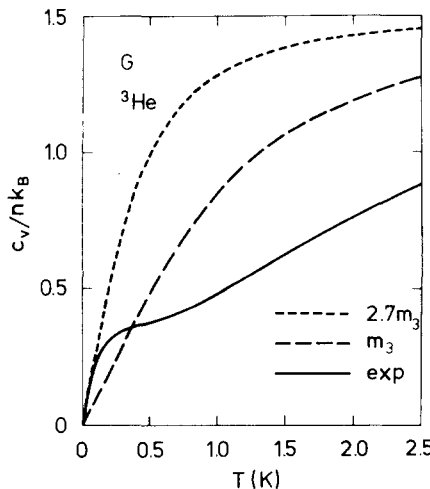


Fig. 3.56. Adapted from ref. [192]. Dependence upon the temperature ε of the specific heat per unit volume c_v in normal liquid ^3He . The full curve shows the experimental value, the long dashes correspond to a free Fermi gas of particles with mass m_3 and the short dashes to a free gas of particles with effective mass $m_3^* = 2.7m_3$. The number of atoms per unit volume is denoted by n ($n = 0.0166 \text{ \AA}^{-3}$).

Here $c_v(T)$ is the experimental value of the specific heat while $c_v^{(0)}(T)$ is the low-temperature limit of the specific heat of a free Fermi gas of atoms with bare mass m_3

$$\lim_{T \rightarrow 0} c_v^{(0)}(T) = \frac{1}{3} m_3 k_B k_F^2 T. \quad (3.19.4)$$

From eqs. (19.1)–(19.4) one obtains

$$\lim_{T \rightarrow 0} \frac{c_v(T)}{n k_B T} = \frac{\pi^2 k_B}{3 t_F^{(0)}} \frac{M_S^*(T=0)}{m_3}, \quad (3.19.5)$$

where $t_F^{(0)} = k_F^2/2m$ is the kinetic energy of a free ${}^3\text{He}$ atom with momentum k_F . We shall use the notation

$$m_3^*(0) = M_S^*(T=0). \quad (3.19.6)$$

The experimental data show that $M_S^*(T)$ has decreased from $2.7m_3$ at $T=0$ to the bare mass M_3 when T reaches 400 mK. This holds for a range of pressures which vary from 0 to 30 bar. It has recently been pointed out that this temperature dependence of $M_S^*(T)$ mainly reflects a rapid energy dependence of the statistical effective mass at zero temperature [3, 193]; the resulting model appears to account semi-quantitatively for the main features of the experimental value of $c_v(T)$ up to about 2 K [4].

The difficulties which must be overcome in a theoretical investigation are manifold. They primarily concern the construction of reliable approximation schemes for dense systems, the difference between statistical and dynamical quasiparticle energies and the fact that the quasiparticle energies depend upon the temperature besides their dependence upon the quasiparticle momentum.

In sections 3.19.2–3.19.5.4 we shall deal with an effective mass or an ω -mass which depends upon energy as in all the preceding sections. Finite temperature corrections will be mentioned in section 3.19.5.5. Equation (19.3) defines an effective mass $M_S^*(T)$ which depends upon the temperature. This can be considered mainly as a way of characterizing the energy dependence of the specific heat. We shall return to the temperature-dependent effective mass $M_S^*(T)$ of eq. (19.3) only in section 3.19.5.6 where we show experimental data.

3.19.2. Phenomenological fits

3.19.2.1. Theoretical formulae at low temperature

Let $f_k(T)$ denote the Fermi–Dirac distribution

$$f_k(T) = \{1 + e^x\}^{-1}, \quad (3.19.7)$$

where

$$x = [E(k) - E(k_F)]/k_B T. \quad (3.19.8)$$

The entropy per particle $S(T)$ and the specific heat per unit volume are given by

$$S(T) = -k_B \sum_k [f_k \ln f_k + (1-f_k) \ln(1-f_k)] \quad (3.19.9)$$

$$c_v(T) = nT \partial \mathcal{S}(T)/\partial T, \quad (3.19.10)$$

where n is the number of atoms per unit volume. In the case of a free Fermi gas at low temperature, these relations yield eq. (19.4).

For $k_B T \ll k_F^2/2m_3^*$, eqs. (19.7)–(19.10) give

$$c_v^{(E)}(T) = \frac{3nk_B}{k_F^3} \int_0^\infty k^2 \frac{x^2 e^x}{(1+e^x)^2} dk \quad (3.19.11)$$

where the upper index (E) refers to the fact that one uses the zero temperature quasiparticle spectrum. By converting the integration over k into an integration over x with the help of eq. (2.7.3), one obtains

$$c_v^{(E)}(T) = \frac{2k_F k_B^2 T}{\pi^2} \int_0^\infty m_S^*(xk_B T) x^2 \frac{e^x}{(1+e^x)^2} dx \quad (3.19.12)$$

where the index S on m_S^* refers to the use of “statistical” quasiparticle energies (section 3.17), and where one has allowed for the possibility that the effective mass depends upon the quasiparticle energy.

3.19.2.2. Empirical statistical quasiparticle energies

Equation (19.11) is an implicit equation for determining the statistical quasiparticle energy $E(k)$ from the experimental value of $c_v(T)$. Its resolution faces two main difficulties. Firstly, eq. (19.11) only holds in the limit of very low temperature; a correction $\Delta c_v^{(T)}(T)$ should be introduced in order to take into account the temperature dependence of the statistical quasiparticle spectrum [3, 193]. Secondly, eq. (19.11) is highly nonlinear.

The first difficulty has been disregarded by Fantoni, Pandharipande and Schmidt [4] who resorted to an analytical model to circumvent the second one. These authors wrote $E(k)$ in the following form

$$E(k) = \varepsilon_1(k) + V_2(E(k)), \quad (3.19.13)$$

with

$$\varepsilon_1(k) = k^2/(2m_3) + u(k). \quad (3.19.14)$$

Here, $u(k)$ is essentially the Hartree–Fock-type potential (18.7b), derived in the present case from a variational calculation performed at finite temperature [178]; its temperature dependence appears to be very small [4]. The value of $\varepsilon_1(k) - \varepsilon_1(k_F)$ is represented by the full curve in fig. 3.57. The input of the calculation is the ${}^3\text{He}$ – ${}^3\text{He}$ interaction of ref. [174].

The energy dependence of the correction term $V_2(E)$ has been evaluated in ref. [4] from the schematic model (10.27) of Brown and Rho [113], whose usefulness for the study of normal liquid ${}^3\text{He}$ had previously been demonstrated by Brown, Pethick and Zaringhalam [3]:

$$V_2(E) = \frac{\mathcal{P}}{\pi} \int_{-\infty}^{\infty} \frac{W(E')}{E - E'} dE' \quad (3.19.15)$$

with

$$W(E) = d \xi^2 / (\xi^2 + \xi_0^2) \quad (3.19.16a)$$

$$\xi = E - \varepsilon_1(k_F), \quad \xi_0 = E_0 - \varepsilon_1(k_F). \quad (3.19.16b)$$

Here, E_0 represents the average energy of the collective excitations (spin fluctuations) of normal liquid ${}^3\text{He}$ and d characterizes the strength of the coupling between a single-particle state near the Fermi surface and these collective excitations. One has [113]

$$V_2(E) = -d \xi \xi_0 / (\xi^2 + \xi_0^2). \quad (3.19.17)$$

Fantoni et al. [4] adopted the following parameter values

$$k_B^{-1}d = 3.08 \text{ K}, \quad k_B^{-1}\xi_0 = 1.1 \text{ K}. \quad (3.19.18)$$

These lead to the dashed curve in fig. 3.57. The corresponding specific heat per unit volume is represented by the long dashes in fig. 3.58. The semi-quantitative agreement between the dashed curve

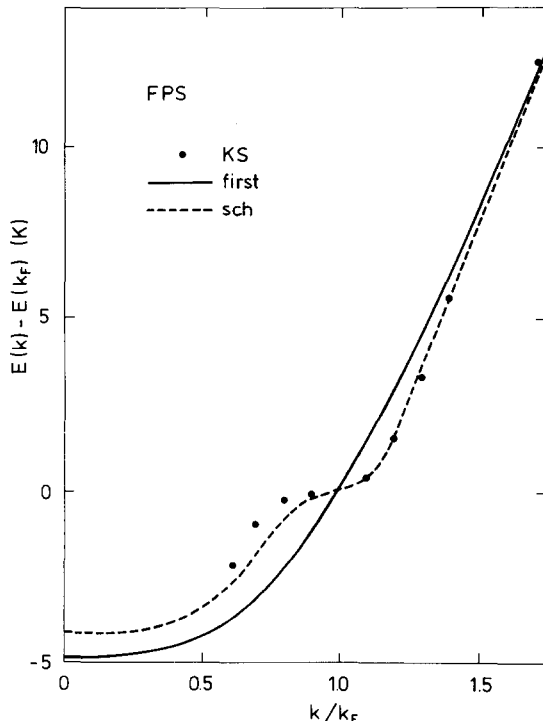


Fig. 3.57. Adapted from ref. [4]. Dependence of the difference $E(k) - E(k_F)$ upon the quasiparticle momentum in normal liquid ${}^3\text{He}$ ($n = 0.0166 \text{ \AA}^{-3}$). The full line corresponds to the variational approximation $E(k) \approx \varepsilon_1(k)$, see eq. (19.14). The dashed curve is obtained from the schematic model, eqs. (19.9)–(19.13). The full dots show the results obtained from a microscopic calculation performed in the framework of the correlated basis functions approach [5].

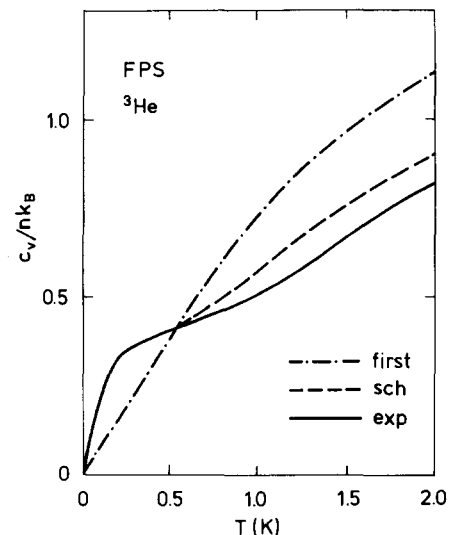


Fig. 3.58. Adapted from ref. [4]. Dependence upon the temperature of the specific heat per unit volume in normal liquid ${}^3\text{He}$ ($n = 0.0166 \text{ \AA}^{-3}$). The full curve shows the experimental result (see fig. 3.56). The other lines are obtained from eqs. (19.9)–(19.11). In the dash-and-dot curve, $E(k)$ has been approximated by $\varepsilon_1(k)$ (eq. (19.10)). The long dashes are obtained when $E(k)$ is calculated from the schematic model, eqs. (19.9)–(19.18).

and the experimental values (full curve) establishes that the schematic model (19.13)–(19.18) yields an approximate solution of eq. (19.11).

The momentum dependence of $E(k)$ can be characterized by the effective mass m_3^* , see eq. (6.1). In the schematic model (19.13), one has

$$\frac{m_3^*}{m_3} = \frac{m_k(k) m_\omega(k)}{m_3}, \quad (3.19.19)$$

where

$$d\epsilon_1(k)/dk = k/m_k(k). \quad (3.19.20)$$

$$m_\omega(k)/m_3 = [1 - dV_2(E)/dE]_{E=E(k)}. \quad (3.19.21)$$

The value of $m_k(k)/m$ is close to 0.8; it is fairly independent of k and of the temperature [4]. Equation (19.17) yields

$$m_\omega(k)/m_3 = 1 + d\xi_0[\xi_0^2 - \xi^2]/\{\xi^2 + \xi_0^2\}^2. \quad (3.19.22)$$

The ω -mass $m_\omega(k)$ thus reaches at $k = k_F$ a maximum equal to

$$m_\omega(k_F)/m_3 = 1 + d/\xi_0 \quad (3.19.23)$$

which is equal to 3.8 for the parameters (19.18). The ω -mass drops to the bare mass m_3 when k is such that $E(k) = E_0$, i.e. for $k_B^{-1}[E(k) - \epsilon_1(k_F)] = 1.1$ K in the case (19.18). Note that this temperature is significantly larger than the one (0.38 K, see fig. 3.56) for which the specific heat is equal to that of a free Fermi gas of particles with mass m_3 . This indicates that one must exert some caution when associating a temperature with an energy by means of the thermal averaging, see eq. (19.64) below.

The following physical interpretation of the enhancement of $m_\omega(k)$ is described in ref. [3] in terms of the response of the system to oscillations impressed by a time-dependent external potential. As long as the frequency ξ of the impressed oscillation is much smaller than the average energy ξ_0 of the spin fluctuations, the external potential can drive the collective excitations. When $\xi \approx \xi_0$, these collective excitations are “shaken off” i.e. become decoupled from the external oscillations and the ω -mass becomes equal to the bare mass.

3.19.3. Correlated basis function approach

The failure of the Hartree–Fock-type approximation (19.14) and the semi-quantitative agreement between the experimental value of the specific heat and the schematic model (19.13) both exhibit the importance of including dynamical effects in the calculation of the quasiparticle energies. These dynamical effects are contained in the polarization and correlation contributions to the mass operator.

A microscopic calculation of the mass operator of normal liquid ${}^3\text{He}$ requires an approximation scheme valid for dense Fermi systems. Although some early calculations [194, 195] have been performed in the framework of Brueckner’s theory, it is now generally believed that the rate of convergence of the hole line expansion (section 3.15) is too slow in the case of liquid ${}^3\text{He}$ [196]. Although a modified Brueckner–Hartree–Fock approximation has recently been proposed [197], the method of correlated basis functions appears better suited to this case of liquid ${}^3\text{He}$ [198].

Some variational calculations of an upper bound to the ground state energy and also of the ground state energy have already been mentioned in section 3.18.2. The first- and the second-order approximations to the mass operator are given by eqs. (18.14), (18.17) and (18.18). These expressions have been used in ref. [5]. The effective mass as calculated in the first-order approximation (18.14) is fairly independent of k and close to the one found in ref. [4], see eq. (19.14).

The second-order terms (18.17) and (18.18) yield a striking enhancement peak of $m_3^*(k)/m_3$; this is shown by the dashed curve in fig. 3.59. It is found in ref. [5] that the dependence upon k of $\Sigma_{2a}(k; \omega)$ and of $\Sigma_{2b}(k; \omega)$ is almost as strong as their dependence upon ω . Third-order corrections have also been evaluated in ref. [5], where it is not specified how the integrals containing vanishing energy denominators were regularized; the momentum dependence of the corresponding effective mass is represented by the full curve in fig. 3.59.

These results are in semi-quantitative agreement with the experimental temperature dependence of the specific heat [5]. This is also implied by the good agreement between the calculated quasiparticle energies (full dots in fig. 3.57) and those derived from the schematic model (19.13)–(19.18).

The difference between the second- and the third-order results shown in fig. 3.59 raises questions about the rate of convergence of the expansion. It therefore appears appropriate to perform the

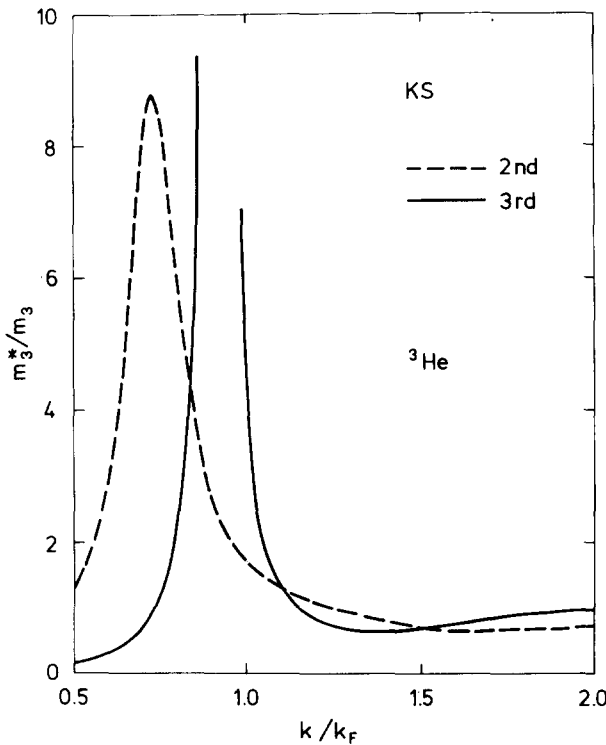


Fig. 3.59. Adapted from ref. [5]. Momentum dependence of the effective mass of normal liquid ${}^3\text{He}$ at density $n = 0.0166 \text{ \AA}^{-3}$, as calculated by the method of correlated basis functions. The dashed curve corresponds to the first- plus second-order contributions. The full line includes third-order contributions. The input is the ${}^3\text{He}-{}^3\text{He}$ potential of ref. [174].

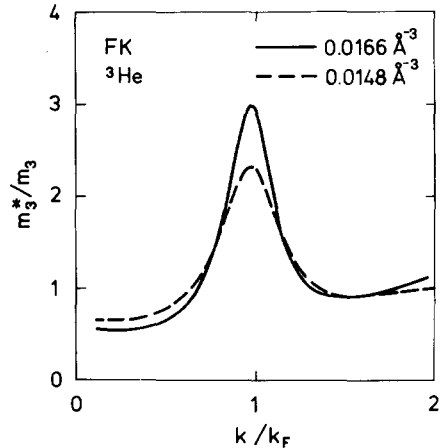


Fig. 3.60. Adapted from ref. [201]. Dependence upon k/k_F of the effective mass of normal liquid ${}^3\text{He}$ for $n = 0.0166 \text{ \AA}^{-3}$ (full curve) and $n = 0.0148 \text{ \AA}^{-3}$ (dashes). The calculation is based on the random phase approximation in the framework of the correlated basis functions approach [200].

summation of an infinite series of higher-order diagrams. A generalization of the random phase approximation to the correlated basis function approach has been developed in [112, 179, 199], see also references contained therein. This generalized random phase approximation has been applied to normal liquid ${}^3\text{He}$ in ref. [200]. The corresponding effective mass is represented in fig. 3.60. The input of the calculation is the particle-hole interaction and the particle-hole propagator of the polarization potential model [202]. The origin of the strong enhancement peak of $m_3^*(k)/m_3$ at $k \approx k_F$ lies in the attractive nature of the particle-hole interaction in the spin channel. The width of the calculated peak is fairly independent of the density and of the strength of the interaction. In contrast, the height of the peak very much depends upon the strength of the interaction and increases with the density [201].

Figure 3.61 shows that in the generalized random phase approximation of ref. [200] the effective mass presents a second enhancement peak for $k \approx 2.0\text{--}2.5k_F$. This second peak arises from the coupling of the single-particle states to the zero sound mode. It is very sensitive to the energy-momentum relation and the damping of this mode. The existence of this second peak appears to provide a qualitative explanation for the following problem. On the one hand, the temperature dependence of the specific heat at low temperature indicates that the effective mass $m_3^*(k)$ drops rapidly to m_3 when k becomes slightly different from the Fermi momentum. On the other hand, neutron scattering studies indicate that the effective mass $m_3^*(k)$ is on the average significantly larger than m_3 in the momentum range $k < 3k_F$ [203].

3.19.4. Spin-polarized liquid ${}^3\text{He}$

Spin-polarized liquid ${}^3\text{He}$ should soon become available in the laboratory [204]. The theoretical investigation of this system in the correlated basis function approach has been hindered by the fact that

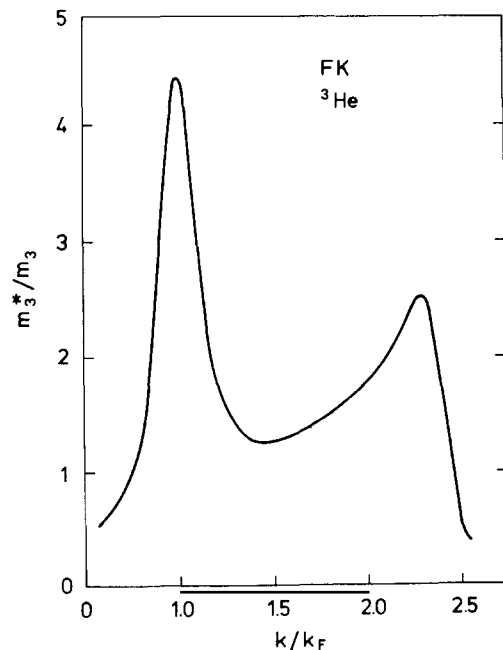


Fig. 3.61. Adapted from ref. [200]. Dependence upon k/k_F of the effective mass of normal liquid ${}^3\text{He}$ for $n = 0.0166 \text{ \AA}^{-3}$. The approximation scheme is the same as the one used in fig. 3.60, but the input parameters are slightly different.

the optimized trial wave function for the polarized system is unstable with respect to abnormal occupation [205, 206]. It has now been demonstrated that this instability is cured if one introduces an infinite subset of perturbative contributions computed in the framework of the correlated basis function approach [179]. This renders applicable the generalized random phase approximation of the correlated basis function approach [199]. The corresponding effective mass has been computed in ref. [179]. It is represented by the full line in fig. 3.62. The enhancement of the effective mass which exists for k close to k_F in the unpolarized system has practically disappeared in the polarized case.

A somewhat different result has been obtained by Glyde and Hernadi [207]. These authors used an improved version of the Brueckner–Hartree–Fock approximation. This version essentially amounts to choosing the auxiliary potential according to eq. (15.10). In addition, $U(q)$ includes the on-the-energy-shell value of the graph \mathcal{M}_{2B} of fig. 3.49, whose contribution is also taken into account when calculating the quantities of interest. This modified Brueckner–Hartree–Fock approximation appears successful in the case of unpolarized liquid ^3He [197]; the corresponding k -mass (including the contribution of \mathcal{M}_{2B}) is a smooth function of k , and the ω -mass $m_\omega(k)$ has an enhancement peak which reaches its maximum for k somewhat larger than k_F . In the case of spin-polarized liquid ^3He , Glyde and Hernadi [207] find that the effective mass still has an enhancement peak for k close to k_F ; this enhancement is approximately fifty per cent smaller than in the unpolarized case. The enhancement is due to the ω -mass in the polarized as well as in the unpolarized systems.

Figure 3.62 shows that the results obtained by Krotscheck, Clark and Jackson [179] are quite different. Indeed, their calculated ω -mass $m_\omega(k)$ is a smooth function of k . It would be of interest to decompose m_ω into contributions $m_\omega^{(a)}$ and $m_\omega^{(b)}$ (see eq. (10.17)) or, equivalently, to study the average momentum distribution in the ground state, see section 3.11.3. This would be helpful for understanding the puzzling difference between the results obtained in refs. [179] on the one hand and [207] on the other hand. The explanation probably lies in the fact that the generalized random phase approximation used in ref. [179] includes screening corrections (section 3.13). These may be quite large in the case of repulsive particle–hole interaction [83].

The results shown in fig. 3.62 are in semi-quantitative agreement with the value $m_{3\uparrow}^*(k_F)/m_3 \approx 0.8$ derived by Bedell and Quader [208] from a Landau description in which the adjustable parameter is the compression modulus. The latter is taken from Monte-Carlo calculations by Lhuillier and Levesque [209]. It is somewhat troublesome, however, that these Monte-Carlo calculations do not yield good agreement with the empirical energy in the case of unpolarized liquid ^3He . Note also that the model of ref. [208] does not involve the effective mass for $k \neq k_F$.

3.19.5. Dynamical effects and the Landau description

3.19.5.1. Introduction

A Landau description has the merit of enabling one to express many observables in terms of a few parameters [157, 210]. One can attempt to evaluate these parameters in terms of microscopic models [157, 210–212]. Brown, Pethick, Mishra and Zaringhalam [3, 193] have undertaken the task of blending the Landau description of liquid ^3He (which only involves quantities evaluated at the Fermi energy) with the dynamical effects reflected in the energy dependence of the effective mass.

3.19.5.2. Empirical fits to the specific heat at low temperature

Figure 3.63 represents the temperature dependence of the specific heat as measured at low pressure and at low temperature by Mota et al. [188]. These data are now somewhat superseded by those of Greywall and Busch [191, 192] but retain semi-quantitative validity. They can be fitted accurately with

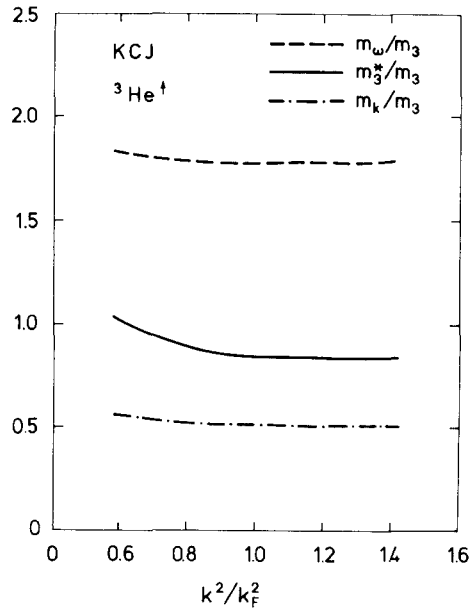


Fig. 3.62. Adapted from ref. [179]. Dependence upon k^2/k_F^2 of the effective mass m_3^*/m_3 (full curve), of the ω -mass m_ω/m_3 (long dashes) and of the k -mass m_k/m_3 (dash-and-dot) in the case of spin-polarized liquid ${}^3\text{He}$ at $n = 0.0166 \text{ \AA}^{-3}$. The calculation is based on the generalized random phase approximation of the correlated basis functions approach.

the expression

$$c_v/nk_B T = (4.63 - 22.5T/K) \text{ K}^{-1} \quad (3.19.24)$$

which only involves two parameters. The curve shown in fig. 3.63 represents another fit, namely

$$c_v/nk_B T = [2.93 + 57.4(T/K)^2 \ln(T/0.293K)] \text{ K}^{-1}, \quad (3.19.25)$$

which involves three adjustable parameters. In both cases the fits are quite good. Note that they lead to very different values of the effective mass $m_3^*(0)$ at zero temperature, see eqs. (19.5), (19.6).

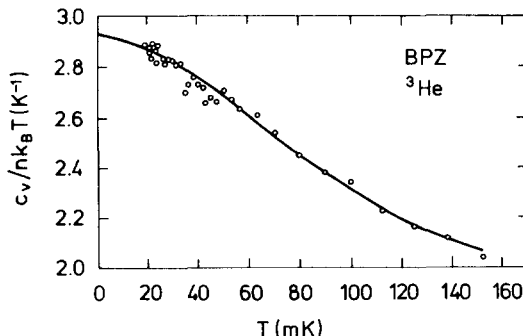


Fig. 3.63. Taken from ref. [157]. Temperature dependence of the specific heat per unit volume of normal liquid ${}^3\text{He}$. The dots are experimental values [188]; the full curve represents the algebraic fit (19.25).

There exists one apparent theoretical reason for attaching more meaning to the fit (19.25) than to the linear law (19.24). Indeed, we have seen in eq. (10.24) that a contribution proportional to $|\omega - \varepsilon_F|^3$ to the imaginary part of $\mathcal{M}(k; \omega)$ yields a contribution to the effective mass which is proportional to $(E - \varepsilon_F)^2 \ln|E - \varepsilon_F|$. The thermal averaging introduces a correspondence between $E - \varepsilon_F$ and temperature, see eq. (19.12). This leads to a contribution proportional to $T^2 \ln T$ to the ratio c_v/T , see eq. (19.5).

The argument that we just described contains two possible flaws:

(i) It refers to the dynamical single-particle energies, while the energies of interest for determining the thermodynamic properties are the statistical quasiparticle energies. This difficulty marred the early calculations of the coefficient of the $T^3 \ln T$ contribution to c_v [213–215]. This does not, however, imply that correct results cannot be obtained from a consistent evaluation of c_v in the framework of a model for the mass operator [155, 156, 161, 216].

(ii) The $T^3 \ln T$ contribution in the low-temperature expansion of $c_v(T)$ probably becomes important only for temperatures smaller than about 30 mK [3, 193, 217], i.e. for T smaller than the range of temperature used to derive the fit (19.25) to the experimental data.

The early theoretical attempts to calculate the temperature dependence of the specific heat of normal liquid ${}^3\text{He}$ are described in refs. [3, 157]. In the next section, we limit ourselves to the work described in refs. [3, 193] which satisfactorily encounters the problems (i) and (ii).

3.19.5.3. Energy dependence of the ω -mass at zero temperature

In refs. [3, 193], a model has been constructed for calculating the temperature dependence of the specific heat. In the present section, we focus on one ingredient of the model, namely the energy dependence of the ω -mass associated with the dynamical single-particle energies. The work of refs. [3, 193] is based on the dispersion relation (19.15) and involves the evaluation of the imaginary part $W(E')$ of the mass operator (assumed to be independent of k) in terms of the Landau parameters.

The central quantity of the Landau description is the scattering amplitude $T(\mathbf{p}, \mathbf{p}'; \mathbf{q}; t)$ where \mathbf{q} denotes the momentum transfer and t the energy transfer

$$T(\mathbf{p}, \mathbf{p}'; \mathbf{q}; t) = \langle \mathbf{p} - \mathbf{q}, \mathbf{p}' + \mathbf{q} | T(t) | \mathbf{p}, \mathbf{p}' \rangle, \quad (3.19.26)$$

$$t = [\varepsilon(\mathbf{p}) - \varepsilon(\mathbf{p} - \mathbf{q})] m_3^*/(q k_F). \quad (3.19.27)$$

Here, $\varepsilon(\mathbf{p})$ is the quasiparticle energy and m_3^* denotes the corresponding effective mass. One introduces the expansion

$$(m_3/m_\omega)^2 N(0) T(\mathbf{p}, \mathbf{p}'; \mathbf{q}; t) = \sum_L A_L^s(t) P_L(\hat{\mathbf{p}} \cdot \hat{\mathbf{p}}') + \boldsymbol{\sigma} \cdot \boldsymbol{\sigma}' \sum_L A_L^a(t) P_L(\hat{\mathbf{p}} \cdot \hat{\mathbf{p}}'), \quad (3.19.28)$$

where

$$N(0) = m_3^* k_F / \pi^2 \quad (3.19.29)$$

is the density of quasiparticle states at the Fermi surface, i.e. the number of quasiparticles (of both spins) per unit energy and per unit volume.

The coefficients A_L^s are related to the familiar parameters of Landau's theory. For instance,

$$A_0^a(t) = \frac{F_0^a}{1 + F_0^a L(t)}, \quad (3.19.30)$$

where $L(t) = \pi^2 \mathcal{L}(t)/mk_F$ is the Lindhard function (see eq. (13.3)) for $q/k_F \ll 1$, namely

$$L(t) = 1 + \frac{t}{2} \ln \left| \frac{1+t}{1-t} \right| + i \frac{\pi}{2} |t| \theta(1-|t|). \quad (3.19.31)$$

For $t \ll 1$, one has

$$L(t) \sim (1-t)^2 + i \frac{\pi}{2} |t| \theta(1-|t|). \quad (3.19.32)$$

Let $A_L^{s,a}$ denote the value of $A_L^{s,a}(t)$ for $t = 0$; for instance,

$$A_0^a = A_0^a(t=0). \quad (3.19.33)$$

It can be considered that the quantity F_0^s gives the s-wave part of the interaction between bare quasiparticles, while A_0^a yields the interaction between screened quasiparticles.

The parameter F_0^a plays an important role in liquid ${}^3\text{He}$. The relative magnetic susceptibility at low temperature, i.e. the susceptibility measured in units of the Pauli susceptibility reads

$$\chi_R = \frac{m_3^*/m_3}{1 + F_0^a}. \quad (3.19.34)$$

The fact that $F_0^a \approx -\frac{2}{3}$ is close to unity and that $m_3^*/m_3 \approx 3$ shows that χ_R is of order 10. Normal liquid ${}^3\text{He}$ is thus an incipient ferromagnet [35], i.e. a paramagnetic system which is close to being a ferromagnet. This leads to a strong coupling of the single-particle states to the low-lying “spin fluctuation modes”, sometimes called “paramagnons”. This expression refers to a model based on a zero range interaction [218] which is an adaptation of a model proposed by Berk and Schrieffer [219] for transition metals; the latter are also paramagnetic and nearly ferromagnetic, i.e. have a large spin susceptibility.

In view of the importance of the spin fluctuations in the present context, only the coefficient A_0^a on the right-hand side of eq. (19.28) has been retained in ref. [3]. This leads to the following expression for the imaginary part of the mass operator, if one uses the low t limit (19.32) for the Lindhard function:

$$W_\epsilon(\xi) \approx Df(y) \quad (3.19.35)$$

where

$$\xi = E - \epsilon_F, \quad y = \xi/\xi_0, \quad (3.19.36)$$

$$D = \frac{3}{4\pi} \frac{q_c^3}{m_3 k_F} \left[1 - \frac{8}{\pi^2 A_0^a} \right]^{-1}, \quad (3.19.37)$$

$$f(y) = \frac{2}{3}y^2 - \frac{1}{3}\pi|y|^3 + \frac{2}{3}y^3 \tan y + \frac{1}{3}\ln(1+y^2). \quad (3.19.38)$$

Here, ξ_0 is an energy which characterizes the spin fluctuations

$$\xi_0 = 2q_c k_F / (\pi m_3^* C), \quad (3.19.39)$$

$$C^2 = (A_0^a)^2 (1 - 8/\pi^2 A_a); \quad (3.19.40)$$

$q_c \ll k_F$ is a cut-off momentum introduced in integrals which involve the momentum transfer q . One can interpret ξ_0 as the average excitation energy of a paramagnon, i.e. of a quasiparticle-quasi-hole pair which has total spin 1 and a total momentum less than the cut-off value q_c .

For small values of y , one gets

$$W_\epsilon(\xi) \approx D \left(y^2 - \frac{\pi}{3}|y|^3 \right). \quad (3.19.41)$$

Note that in the present model the coefficients C and α on the right-hand side of eq. (10.21) are related. In the approximation (10.25), the inflection points of $m_\omega(E)$ occur at

$$E_i = \epsilon_F \pm \xi_0, \quad (3.19.42)$$

i.e. at the same energy as in the schematic model (19.16a) of Brown and Rho [113] (see eq. (19.22)) although this schematic model does not contain any contribution to $W(\xi)$ proportional to $|\xi|^3$. The coincidence between the values of E_i derived from (19.22) and (19.42) demonstrates that this absence of $|\xi|^3$ terms is irrelevant as far as the physical consequences are concerned. The main physical origin of the narrow enhancement peak of $m_\omega(E)$ lies in the fact that $W(E)$ increases faster for $|E| \approx |\xi_0|$ than for $|E| \ll |\xi_0|$, with $\xi_0 - \epsilon_F$ smaller than or comparable to ϵ_F .

In the approximations (19.35)–(19.38), the imaginary part $W(E')$ increases for large $|y|$. Then, however, the approximation (19.32) becomes unreliable. It turns out, that for $|y| \leq 1$, using the full expression (19.31) of the Lindhard function essentially amounts to multiplying the small y approximation (19.38) by a cut-off function $f_c(y)$, with [193]

$$f_c(y) = [1 - (y/7.5)^2] \theta(7.5 - |y|). \quad (3.19.43)$$

The final approximation for the imaginary part of the mass operator thus reads

$$W(\xi) = D f(y) f_c(y). \quad (3.19.44)$$

The corresponding value of the quasiparticle potential $V_2(y)$ can be computed from the dispersion relation (19.15). One finds that the schematic model (19.17) gives a good approximation to the results, provided that one takes [3]

$$d = \frac{2}{3}D; \quad (3.19.45)$$

the appearance of the factor 2/3 can be understood from the first term on the right-hand side of eq. (19.38). Figure 3.64 shows the functions

$$\frac{m_\omega(y)}{m_3} = 1 + \frac{2}{3} \frac{D}{E_0} \frac{[1 - y^2]}{[1 + y^{2/2}]}, \quad (3.19.46)$$

$$-\frac{3}{2} V_2(y)/D = y/(1 + y^2), \quad (3.19.47)$$

associated with the schematic model, see eqs. (19.17), (19.22) and (19.46); the quantity D has been taken equal to $3\xi_0$ in order to have $m_\omega(y=0) \approx 3m_3$ which is approximately the experimental value at low pressure provided that one omits the k -mass, see eq. (19.19). The value of ξ_0 is typically 1.14 K [3].

Figure 3.64 exhibits the rapid energy dependence of the ω -mass in normal liquid ${}^3\text{He}$. This property should be taken into account when computing the temperature dependence of the specific heat. This calculation involves the following two additional difficulties. (i) One must distinguish between the statistical and the dynamical quasiparticle energies. (ii) One must take into account the temperature dependence of the quasiparticle energy. These two effects have been evaluated for $T < 100$ mK [3, 193].

3.19.5.4. Statistical quasiparticle energies

The previous section dealt with the ω -mass associated with the mass operator, i.e. with the dynamical quasiparticle energy at zero temperature. The relation between statistical and dynamical quasiparticle energies has been worked out by Pethick and Carneiro [155]. As in section 3.17, we attach an index (D) or (S) to the quantities which refer to dynamical or to statistical quasiparticle energy, respectively. Let us write

$$m_\omega^{(S)}(\xi) = m_\omega(0) + \delta m_\omega^{(S)}(\xi) - \delta m_\omega(0), \quad (3.19.48)$$

$$m_\omega^{(D)}(\xi) = m_\omega(0) + \delta m_\omega^{(D)}(\xi) - \delta m_\omega(0), \quad (3.19.49)$$

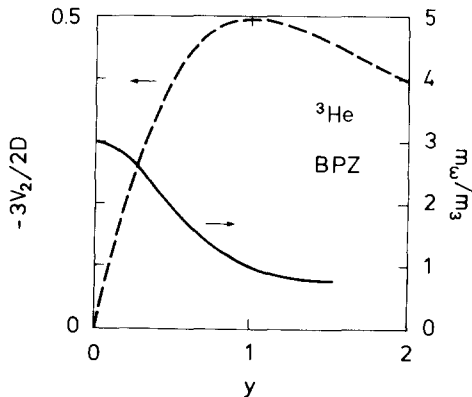


Fig. 3.64. Adapted from ref. [3]. Dependence upon y (eq. (19.36)) of the ω -mass $m_\omega(y)/m_3$ (right-hand scale) and of the quantity $-3 V_2(y)/2D$, see eqs. (19.48) and (19.49). The parameter D in eq. (19.48) has been taken equal to $3\xi_0$, in such a way that $m_\omega(0) \approx 3m_3$.

where one has taken into account the fact that the dynamical and the statistical ω -masses are equal at $\xi = 0$, see eq. (19.58) below. For $|\xi/\varepsilon_F| \ll 1$, one has [155]

$$\delta m^{(S)}(\xi) - \delta m_\omega(0) = \frac{B^{(S)}}{B^{(D)}} [\delta m_\omega^{(D)}(\xi) - \delta m_\omega(0)], \quad (3.19.50)$$

where the quantities $B^{(S)}$ and $B^{(D)}$ can be expressed in terms of the Landau parameters. If one only retains A_0^a , one finds

$$B^{(S)} = \frac{1}{8} \pi^2 (A_0^a)^3 - \frac{3}{2} (A_0^a)^2, \quad (3.19.51)$$

$$B^{(D)} = \frac{3}{8} \pi^2 (A_0^a)^3 - \frac{3}{2} (A_0^a)^2. \quad (3.19.52)$$

The difference of a factor 3 in the coefficients of $(A_0^a)^3$ in these two relations reflects the factor 1/3 in front of the second term on the right-hand side of eq. (17.25). In the limit of a ferromagnetic liquid, $F_0^a \rightarrow -1$, $A_0^a \rightarrow \infty$ (see eqs. (19.30), (19.34)) and $B^{(D)}/B^{(S)} \rightarrow 3$.

The expression of $B^{(D)}/B^{(S)}$ when A_1^a is taken into account is given in ref. [193]. It is found that [193]

$$2.30 \leq B^{(D)}/B^{(S)} \leq 2.42 \quad (3.19.53)$$

yields a good fit to the data in the whole range of pressures: $B^{(D)}/B^{(S)}$ increases from 2.31 at $P = 0$ to 2.42 at $P = 30$ bar.

Equation (19.50) gives the procedure for transforming the ξ -dependence of the dynamical ω -mass shown in fig. 3.64 into the ξ -dependence of the statistical ω -mass which should be used in the expression (19.12) of the specific heat. Let us denote by $c_v^{(0)}$ the specific heat of a Fermi gas of free quasiparticles with effective mass $m_3^*(0)$, see eq. (19.1). The energy dependence of the effective mass $m_3^*(\xi)$ introduces a correction $\Delta c_v^{(E)}$ to the specific heat

$$c_v^{(E)}(T) = c_v^{(0)} - \Delta c_v^{(E)}(T), \quad (3.19.54)$$

where (see eqs. (19.12) and (19.19))

$$\Delta c_v^{(E)}(T) = - \frac{2k_F k_B^2}{\pi^2} \frac{B^{(S)}}{B^{(D)}} \frac{m_k}{m} \int_0^\infty [\delta m_\omega^{(D)}(xk_B T) - \delta m_\omega^{(D)}(0)] \frac{x^2 e^x}{(1 + e^x)^2} dx; \quad (3.19.55)$$

the factor

$$m_k/m \approx 0.8 \quad (3.19.56)$$

has been assumed to be independent of x . This factor has been set equal to unity in ref. [193]. This is consistent with the fact that there it had also been omitted in the factor m_3^* which appears in the definition (19.39) of ξ_0 . Here, we shall also omit it for the sake of the consistency between our notation and that adopted in ref. [193]. We therefore write

$$m_S^*(\xi) = m_\omega^{(S)}(\xi). \quad (3.19.57)$$

3.19.5.5. Temperature dependence of the quasiparticle energy

In the preceding sections, we always dealt with quasiparticle energies at zero temperature. Actually, both the statistical and the dynamical quasiparticle energies depend upon T . For small values of $|\xi|/|\epsilon_F|$ and for low T , one has [155]

$$\xi^{(S,D)} = \xi + \frac{B^{(S,D)}}{24} \xi \frac{\xi^2 + \pi^2 k_B^2 T^2}{k_B^2 T_F^2} n \frac{\max[|\xi|, k_B T]}{k_B T_c^{(S,D)}}, \quad (3.19.58)$$

where

$$k_B T_F = k_F^2 / (2m_3^*(0)); \quad (3.19.59)$$

one has $T_F \approx 1.7$ K at low pressure. In eq. (19.58), $T_c^{(S)}$ and $T_c^{(D)}$ are cut-off temperatures. Note that eq. (19.58) yields eq. (19.50).

If one sets $T = 0$ in eq. (19.58), one gets

$$\xi^{(S)} = \xi + \frac{B^{(S)}}{24} \frac{\xi^3}{k_B^2 T_F^2} \ln \frac{|\xi|}{k_B T_c^{(S)}}. \quad (3.19.60)$$

The contribution to the specific heat which is proportional to $T^2 \ln T$ reads [3]

$$c_v(T) = c_v^{(0)} \left[1 - \frac{3}{10} B^{(S)} \frac{T^2}{T_F^2} \ln \frac{T}{T_c^{(c)}} \right], \quad (3.19.61)$$

where $T_c^{(c)}$ is a cut-off temperature and $c_v^{(0)}$ is defined in eq. (19.1). By comparing eqs. (19.60) and (19.61), one sees that the correction to $c_v(T)$ which is due to the $T^3 \ln T$ term is equal to the correction to the ω -mass $\delta m_\omega^{(S)}(\xi) - \delta m_\omega(0)$ at the energy

$$\xi_S = (12/5)^{1/2} \pi k_B T = 4.9 k_B T. \quad (3.19.62)$$

This result is useful for a rough estimate of the temperature T at which a correction $[\delta m_\omega^{(S)}(\xi_S) - \delta m_\omega(0)]$ to the ω -mass is likely to be felt by the specific heat.

The correction $\Delta c_v^{(T)}(T)$ to the specific heat which arises from the temperature dependence of the quasiparticle energy can be worked out explicitly for $T \leq 100$ mK. One finds [193]

$$\Delta c_v^{(T)}(T) = \frac{5}{7} \Delta c_v^{(E)}(T), \quad (3.19.63)$$

where $\Delta c_v^{(E)}(T)$ is given by eq. (19.55).

3.19.5.6. Fits to the experimental data

We recall that the k -mass m_k has been set equal to m_3 in refs. [3, 193]. It could be taken into account provided that it is assumed to be independent of ξ in the relevant domain. This would modify some of the constants listed in table IV of ref. [193].

Equations (19.1), (19.54), (19.55) and (19.63) enable one to calculate the specific heat in the domain

$T < 100$ mK for $0 < P < 30$ bar in the framework of this dynamical Landau model [193]. The value of $c_v(T = 20$ mK) has been fitted to the experimental value; this essentially fixes $m_3^*(0)$. The pressure determines the density n , and thereby k_F . The value of F_0^a is determined independently from the experimental value of the magnetic susceptibility, see eq. (19.34). The ratio $B^{(S)}/B^{(D)}$ is determined by F_0^a and by F_1^a . Two values of F_1^a have been considered in ref. [193], namely $F_1^a = 0$ and $F_1^a = -0.8$ [220]. The value of $m_3^*(0)$ determines that of $\delta m_\omega^{(D)}(0)$, which yields q_c , see eqs. (19.37)–(19.40). This in turn determines ξ_0 . In conclusion, the analysis involves only one adjustable parameter, namely $m_3^*(0)$.

Figures 3.65 and 3.66 show examples of fits obtained from this model. The notation is that of eq. (19.3), namely

$$M_S^*(T)/m_3 = c_v(T)/c_v^{(0)}(T). \quad (3.19.64)$$

The index S recalls that this quantity should be identified with the effective mass associated with the statistical quasiparticle energy. At zero pressure, one has [193] $m_3^*(0)/m_3 = 2.78$, $k_F = 8.28$ g cm sec $^{-1}$, $F_0^a = -0.7$, $q_c/k_F = 1.09$, $k_B^{-1}E_0 = 0.92$ K, $B^{(D)}/B^{(S)} = 2.31$. At $P = 30$ bar, these quantities become $m_3^*(0)/m_3 = 5.55$, $k_F = 9.28$ g cm sec $^{-1}$, $F_0^a = -0.75$, $q_c/k_F = 1.06$, $k_B^{-1}\xi_0 = 0.45$ K, $B^{(D)}/B^{(S)} = 2.43$. The value of the ratios ξ_0/T_F and q_c/k_F are practically independent of the pressure.

3.19.5.7. Discussion

The agreement between the model of refs. [3, 193] and the data is quite remarkable in view of the fact that only one parameter has been adjusted, namely the value of c_v at $T = 20$ mK. The enhancement of $m_\omega(\xi)$ for ξ close to 0 (i.e. for E close to ε_F) is an essential ingredient of the model. Except for a factor $m_k/m \approx 0.8$, the quantity $m_\omega(\xi)$ is equal to the effective mass m_S^* associated with the statistical quasiparticle energy.

The effective mass is related to the Landau parameters F_1^s by the usual equation

$$m_3^*/m_3 = 1 + \frac{1}{3}F_1^s. \quad (3.19.65)$$

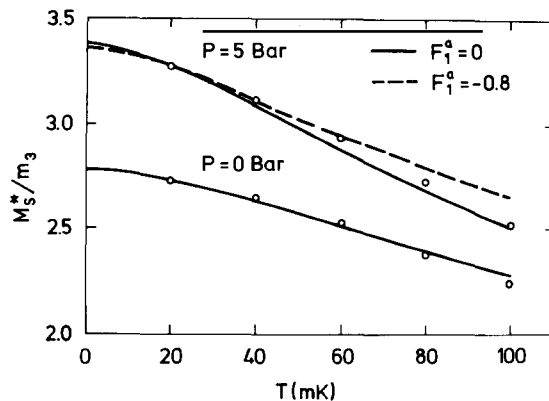


Fig. 3.65. Adapted from ref. [193]. Comparison between the experimental (dots, ref. [192]) and the calculated values of the quantity M_S^*/m_3 , see eq. (19.64), for pressures equal to 0 and to 5 bar, and for $F_1^a = 0$ (full curve) and $F_1^a = -0.8$ (dashes). The calculated result at $P = 0$ is insensitive to F_1^a .

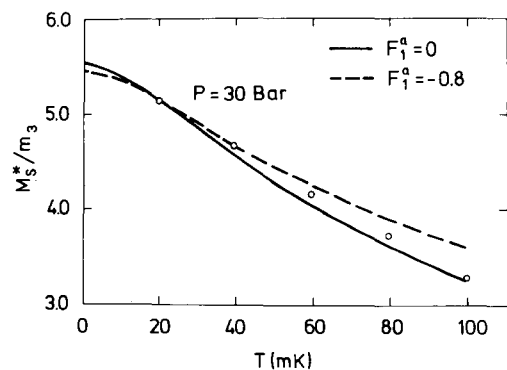


Fig. 3.66. Adapted from ref. [193]. Same as fig. 3.65, for $P = 30$ bar.

The energy dependence of m_3^* implies that F_1^* depends upon the quasiparticle energy in normal liquid ${}^3\text{He}$. Similarly, the fact that the magnetic susceptibility (19.34) is not affected by the $T^2 \ln T$ dependence of $m_8^*(T)$ [221] implies that F_0^a depends upon the quasiparticle energy. These dynamical effects call for a reexamination of the Landau description of normal liquid ${}^3\text{He}$. In particular, the analysis of inelastic neutron scattering [203, 222, 223] may have to be interpreted somewhat differently [3].

3.19.6. Summary

Various calculations of the effective mass in normal liquid ${}^3\text{He}$ at low temperature indicate that it has a narrow enhancement in the vicinity of the Fermi energy. This feature is found in microscopic calculations as well as in a Landau description. It should be taken into account in more phenomenological theories [220]. The enhancement of the effective mass is due to the coupling of single-particle states to spin fluctuations. It is strongly damped in the case of spin-polarized liquid ${}^3\text{He}$.

The energy dependence of the effective mass accounts quantitatively for the observed temperature dependence of the specific heat of normal liquid ${}^3\text{He}$ in the domain $T < 100 \text{ mK}$ and semi-quantitatively for its temperature dependence for $T < 1.5 \text{ K}$. The theoretical analysis in this wider range of temperature raises some problems. In particular, one should take into account the difference between statistical and dynamical quasiparticle energies and the possible role of the coupling of the single-particle excitations to the zero sound mode.

3.20. The electron gas

3.20.1. Definition

The “electron gas” is a homogeneous system in which electrons interact via the Coulomb potential and are immersed in a positively charged uniform background with the same absolute charge density as the electrons. It is also called the “one-component plasma” or the “jellium model”; the “jelly” is the continuous positive background.

The electron gas is characterized by a dimensionless parameter r_s which is related to the density n by

$$\frac{4\pi}{3} (r_s a_0)^3 = n^{-1}, \quad (3.20.1)$$

where $a_0 = \hbar^2/(m_e e^2) = 0.55 \text{ \AA}$ is the Bohr radius. Since $n = (3\pi^2)^{-1} k_F^3$ one has

$$r_s = 1.92/(k_F a_0); \quad k_F = 3.63/r_s (\text{\AA})^{-1}. \quad (3.20.2)$$

The kinetic energy of an electron with momentum k_F is equal to

$$t_F = k_F^2/(2m_e) = 50.1 r_s^{-2} (\text{eV}) = 3.68/r_s^2 \text{ Ry}. \quad (3.20.3)$$

The Hamiltonian of the electron gas reads

$$H = \sum_{\mathbf{k}} \frac{k^2}{2m} a_{\mathbf{k}}^\dagger a_{\mathbf{k}} + \frac{1}{2} \sum_{\mathbf{k}, \mathbf{k}', \mathbf{q}} v(\mathbf{q}) a_{\mathbf{k}+\mathbf{q}}^\dagger a_{\mathbf{k}'-\mathbf{q}}^\dagger a_{\mathbf{k}'} a_{\mathbf{k}}, \quad (3.20.4)$$

where

$$v(q) = 4\pi e^2/q^2 \quad (3.20.5)$$

is the Fourier transform of the Coulomb potential. The restriction $q \neq 0$ in the summation on the right-hand side of eq. (20.4) arises from the requirement that the direct Coulomb interaction energy between the electrons be cancelled by their interaction with the positively charged uniform background.

The electron gas is probably the model which has been most thoroughly investigated in many-body physics, see e.g. refs. [34, 35, 224–227]. Here, we discuss only a few topics chosen because of their relationship with dynamical features discussed in the preceding sections, namely the mass operator, the effective mass, the ω -mass and the momentum distribution. Already in 1958, Quinn and Ferrell [228] emphasized that the mass operator in the electron gas can be viewed as an “optical potential” for the electron.

3.20.2. The Hartree–Fock approximation

In the electron gas, the direct (Hartree) potential (7.3) vanishes because the direct Coulomb interaction between the electrons is cancelled by the direct interaction with the positively charged uniform background.

The Fock (exchange) contribution (7.4) is equal to [227]

$$V_F(k) = -\frac{e^2 k_F}{\pi} \left\{ 1 + \frac{1-y^2}{2y} \ln \left| \frac{1+y}{1-y} \right| \right\} \quad (3.20.6)$$

where

$$y = k/k_F. \quad (3.20.7)$$

As expected from section 3.7, the Fock mean field is nonlocal and static. The effective mass reduces to the k -mass which reads (see eqs. (6.9), (7.8) and (20.6))

$$m_{HF}^*(k)/m_e = \frac{2\pi k^2}{e^2 m_e k_F} \left[\frac{1+y^2}{y} \ln \left| \frac{1+y}{1-y} \right| - 2 \right]^{-1}. \quad (3.20.8)$$

In the Hartree–Fock approximation, the effective mass thus vanishes at $k = k_F$. This is in strong disagreement with the experimental value of the specific heat at low energy (see eq. (19.1)), which indicates that the effective mass m_e^* at the Fermi surface has the same magnitude as the bare electron mass m_e . This discrepancy exhibits the necessity of taking into account higher-order terms.

3.20.3. The random phase approximation

The second-order contribution to the mass operator involves singular integrals of the type

$$\int \frac{d^3 q}{q^4} (\dots).$$

This can be seen from eq. (8.2) in which one sets $\mathbf{c} = \mathbf{j} + \mathbf{q}$, $\mathbf{d} = \mathbf{j} - \mathbf{q}$ in order to take momentum conservation explicitly into account.

The divergence originates from the singularity of (20.5) at $q = 0$. This reminds of the case of hard-core interactions. It was discussed in sections 3.14 and 3.15 how one can handle singular interactions in the limit of a dilute system, i.e. of a system in which the average interparticle distance is larger than the range of the interaction. In that case, it was appropriate to perform partial summations by regrouping all the terms which have the same number of independent hole lines. The result is essentially an expansion in powers of $k_F c$, where c is the range of the strong component of the interaction.

This approach cannot be used in the electron gas since the interaction range is infinite. Then, the simplest limit to consider is that of a very dense system, i.e. of small r_s , see eq. (20.2). This suggests to rearrange the perturbation series for the mass operator by summing the dominant infinite terms which are of lowest order in r_s . These are the Feynman ring diagrams. This rearrangement yields a series expansion in powers of r_s . It can be summed in closed form. The result is given in eqs. (13.1)–(13.3). By adding expression (13.1) to the Fock contribution (20.6) one obtains the following “random phase approximation” to the mass operator:

$$\mathcal{M}_{\text{RPA}}(\mathbf{k}; \omega) = i \sum_{\mathbf{q}} \int \frac{d\gamma}{2\pi} v_{\text{RPA}}(\mathbf{q}; \gamma) \mathcal{G}_0(\mathbf{k} - \mathbf{q}; \omega - \gamma), \quad (3.20.9)$$

where

$$v_{\text{RPA}}(\mathbf{q}; \gamma) = v(\mathbf{q})/\varepsilon_{\text{RPA}}(\mathbf{q}; \gamma), \quad (3.20.10)$$

$$\varepsilon_{\text{RPA}}(\mathbf{q}; \gamma) = 1 + v(\mathbf{q}) \mathcal{L}(\mathbf{q}; \gamma). \quad (3.20.11)$$

The quantity ε_{RPA} is the random phase approximation to the dielectric constant; $v_{\text{RPA}}(\mathbf{q}; \gamma)$ plays the role of an effective (screened) Coulomb interaction. This effective interaction depends upon γ . In the static limit ($\gamma \rightarrow 0$) and for $q \ll k_F$, the Lindhard function becomes (see eq. (19.31))

$$\mathcal{L}(\mathbf{q}; 0) = \mu^2/4\pi e^2, \quad \mu^2 = (32/9\pi^4)^{1/3} r_s k_F^2. \quad (3.20.12)$$

One has then

$$v_{\text{RPA}}(\mathbf{q}) \approx 4\pi e^2/(q^2 + \mu^2). \quad (3.20.13)$$

Expression (20.13) is the Fourier transform of a Yukawa-type interaction; μ^{-1} can thus be interpreted as a screening distance.

One can also express in close form the static Lindhard function $\mathcal{L}(\mathbf{q}; 0)$ for arbitrary \mathbf{q} . Its real part reads

$$\text{Re } \mathcal{L}(\mathbf{q}; 0) = \frac{m_e k_F}{2\pi^2} \left\{ 1 - q^{-1} \left(1 - \frac{1}{4} q^2 \right) \ln \left| \frac{1 - \frac{1}{2}q}{1 + \frac{1}{2}q} \right| \right\}. \quad (3.20.14)$$

If one replaces in eq. (20.10) $\mathcal{L}(\mathbf{q}; \gamma)$ by $\text{Re } \mathcal{L}(\mathbf{q}; 0)$, one finds an effective interaction whose Fourier

transform is proportional to $v_{\text{eff}}(r) \sim \cos(2k_F r)/r^3$ for large r ; this effective interaction presents oscillations of wave number $(2k_F)$ which are called the “Friedel oscillations”.

The random phase approximation is derived from the high-density limit, i.e. for $r_s < 1$. In free-electron type metals, r_s varies between 1.8 and 5.6. The random phase approximation is not reliable for these realistic densities. It has nevertheless been quite often used for r_s larger than unity, with the belief that it yields the main features of the dynamical corrections to the Hartree–Fock approximation. Moreover, it has been argued that in some formulations the expansion parameter is $r_s/(1+r_s)$ rather than r_s [229].

The random phase approximation (20.9) also encounters problems with the value (20.11) of $\varepsilon_{\text{RPA}}(q; \gamma)$ at large q , for the main reason that it fails to take into account the fact that short-range correlations are smaller between electrons of parallel spins; these electrons are indeed kept apart by the Pauli principle [225]. One way of accounting for this effect has been suggested by Hubbard (quoted in [230]). It essentially amounts to replacing in eq. (20.10) ε_{RPA} by

$$\varepsilon_{\text{RPA}}^H(q; \gamma) = 1 + f(q) v(q) \mathcal{L}(q; \omega) \quad (3.20.15a)$$

where

$$f(q) \approx \frac{q^2}{2(q^2 + k_F^2 + q_{\text{TF}}^2)}, \quad (3.20.15b)$$

$$q_{\text{TF}}^2 = 4k_F/\pi a_0. \quad (3.20.15c)$$

3.20.4. Off-the-energy-shell values of the imaginary part of the mass operator

The imaginary part $\mathcal{W}(k; \omega)$ of the mass operator is usually easier to calculate than its real part. It has been computed as a function of ω (for fixed k) by Bose et al. [231]. Some of their results are shown in fig. 3.67. One can distinguish two main contributions to the imaginary part \mathcal{W} :

(i) The first one arises from the q -domain in (20.9) in which the imaginary part $\varepsilon_{\text{RPA}}(q; \gamma)$ differs from zero. This yields the “quasiparticle contribution” represented by the full curve in fig. 3.67.

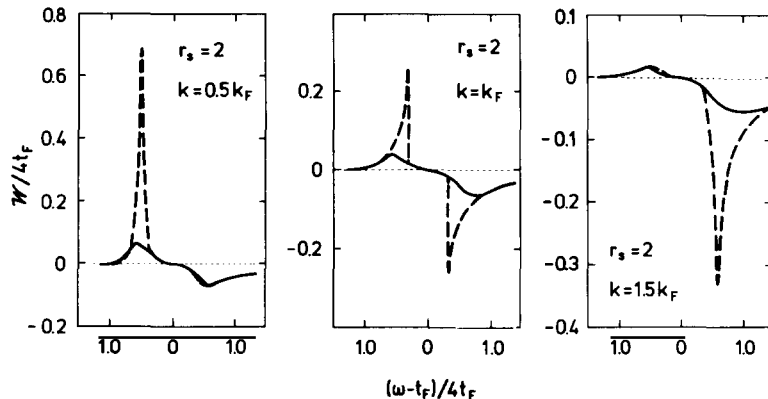


Fig. 3.67. Adapted from ref. [231]. Dependence upon $(\omega - t_F)/4t_F$, where $t_F = k_F^2/2m_e$, of the imaginary $\mathcal{W}(k; \omega)/4t_F$ of the mass operator of the electron gas for $r_s = 2$ and (from left to right) for $k/k_F = 0.5, 1$ and 1.5 . The full curves give the quasiparticle contribution and the dashes the plasmon contribution.

(ii) The second one arises from the q -domain in which $\text{Im } \varepsilon_{\text{RPA}}(q; \gamma) = 0$. It corresponds to the excitation of plasmons, i.e. of long-range high-frequency oscillations. This plasmon contribution only exists if [232]

$$k < k_c \approx 4k_F \left\{ (1 + 2m_e \omega_p / k_F^2)^{1/2} - 1 \right\}, \quad (3.20.16a)$$

where

$$\omega_p = (12/r_s^3) \text{ Ry} \quad (3.20.16b)$$

is the plasmon frequency. The energy-momentum relation for the plasmon frequency is

$$\text{Re } \varepsilon(q; \omega(q)) = 0. \quad (3.20.17)$$

3.20.5. Off-the-energy-shell values of the real part of the mass operator

Once $\mathcal{W}(k; \omega)$ is known, the real part $\mathcal{V}(k; \omega)$ can be found from the dispersion relation (2.35) which reduces to

$$\mathcal{V}(k; \omega) = V_F(k) + \frac{\mathcal{P}}{\pi} \int \frac{\mathcal{W}(k; \omega')}{\omega - \omega'} d\omega', \quad (3.20.18)$$

where $V_F(k)$ is the Fock contribution (20.6).

The values of $\mathcal{W}(k; \omega')$ shown in fig. 3.67 indicate that $\mathcal{V}(k; \omega)$ has a rather complicated dependence upon ω . Figure 3.68 gives a typical example for $k < k_F$; only the plasmon contribution has been retained. In that example, the energy-momentum relation (4.12), namely

$$E = k^2/2m_e + \mathcal{V}(k; E) \quad (3.20.19)$$

has three roots, labelled by ω_1 , ω_2 and ω_3 in fig. 3.68.

The root ω_1 corresponds to the familiar quasiparticle energy. The spectral function as calculated from eq. (2.32) has a δ -function peak of strength $Z_1 = 0.56$, see fig. 3.69. If the quasiparticle contribution to $\mathcal{W}(k; \omega')$ would be included, see fig. 3.67, this delta function would become a narrow quasiparticle peak.

At the frequency $\omega_2 \approx \omega_p$, the value of $\mathcal{W}(k; \omega_2)$ is quite large. This quasiparticle state thus has a very short lifetime and the spectral function only displays a broad bump in the vicinity of ω_2 .

The value of $\mathcal{W}(k; \omega_3)$ is very small in the case of fig. 3.68. In this example, the spectral function therefore has a second narrow peak at ω_3 , with strength $Z_3 = 0.35$ (see fig. 3.69). This excitation is called a “plasmaron” [234–236]. It has been interpreted as a hole coupled to a cloud of plasmons, i.e. to real plasmons with various wave lengths.

Figures 3.70 and 3.71 show results for three values of k . For $k \approx k_F$, only one strong peak exists in the calculated spectral function; this is the standard quasiparticle peak. For $k = 0.6k_F$ and for $k = 1.4k_F$, there exist three roots of the energy-momentum relation (20.18). For $k = 0.6k_F$ two of these roots lead to a narrow peak of the spectral function, as in fig. 3.69. The peak which is closest to $k^2/2m_e$ is the standard quasiparticle peak; the other one is associated with the plasmaron.

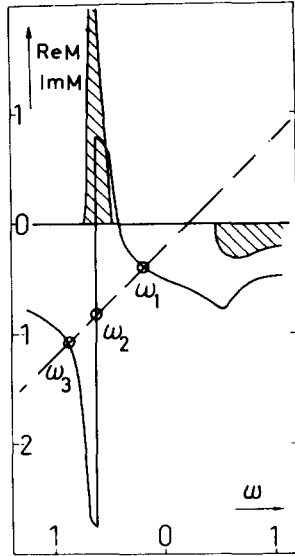


Fig. 3.68. Taken from ref. [233]. Dependence upon ω of $W(k; \omega)$ (in Ry, shaded domain) and of $V(k; \omega)$ (in Ry, full curve) for the electron gas in the case $r_s = 4$ and $k = 0.4k_F$; one has $\epsilon_F = -0.17$ Ry. The plasmon frequency is $\omega_p = 0.43$ Ry. One has $\omega_1 - \omega_2 = 1.02\omega_p$, $\omega_1 - \omega_3 = 1.59\omega_p$. The dashed straight line shows the function $\omega + \epsilon_F - k^2/2m_e$. The zero of ω has been set equal to $k_F^2/2m_e = 0.23$ Ry.

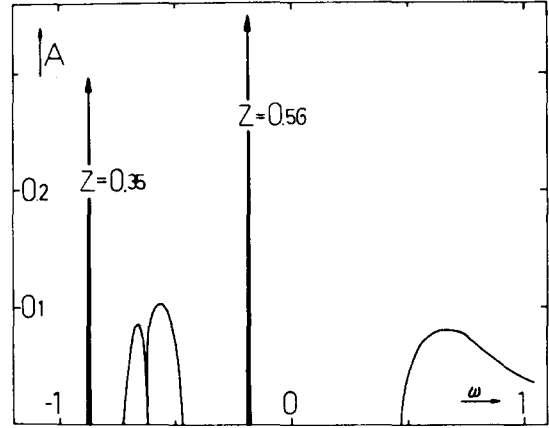


Fig. 3.69. Taken from ref. [233]. Spectral function $A(k; \omega) = S(k; \omega)$ (in Ry⁻¹) as calculated from eq. (2.32), for the mass operator shown in fig. 3.68. The zero of ω has been set equal to $k_F^2/2m_e = 0.23$ Ry.

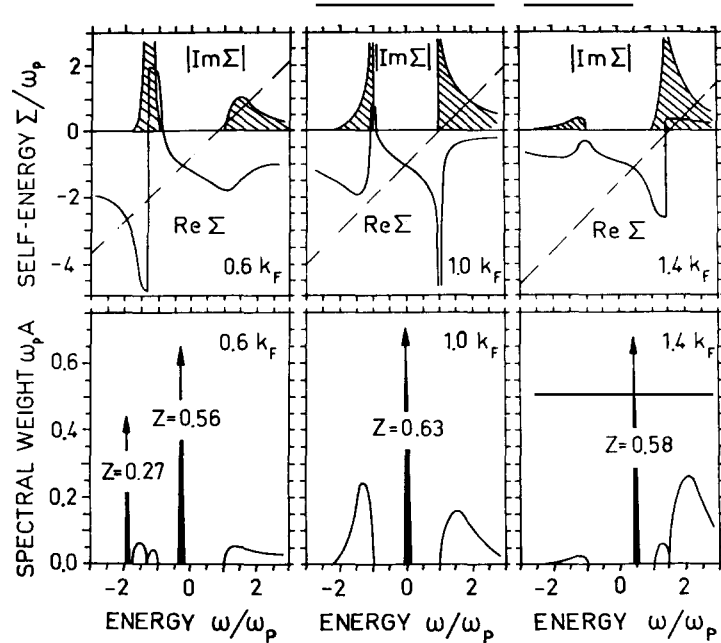


Fig. 3.70. Taken from ref. [229]. Dependence upon ω/ω_p of the real part $V(k; \omega)/\omega_p$ and of the imaginary part $W(k; \omega)/\omega_p$ of the mass operator (upper part) and of the spectral function $\omega_p A(k; \omega)$ (lower part), for the electron gas with $r_s = 5$ and for the momenta $k = 0.6 k_F$, $k = k_F$ and $k = 1.4 k_F$ [234]. The quantity ω_p is the plasmon frequency, see eq. (20.16b). Only the plasmon contribution to the mass operator has been retained [234] [see fig. 3.67]. The straight dashed lines show the function $(\omega - k^2/2m_e)/\omega_p$. The zero of ω has been set at the energy $k_F^2/2m_e$.

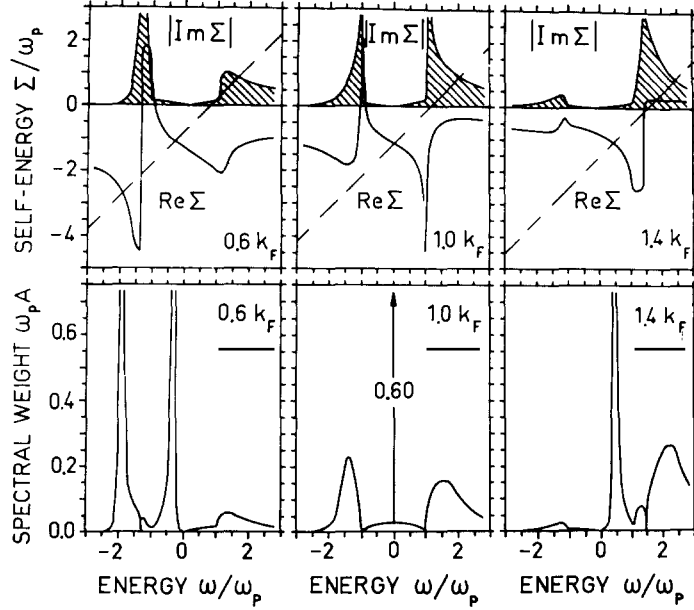


Fig. 3.71. Taken from ref. [229]. Same as fig. 3.70, except that the quasiparticle contribution is now included in the mass operator (see fig. 3.67) [236].

The simplified plasmon model associated with fig. 3.70 is analogous to the polaron model [237]. The imaginary part of the corresponding mass operator has a logarithmic singularity at the frequency [234]

$$\omega + t_F = k^2/2m_e \mp \omega_p, \quad (3.20.20a)$$

since

$$\mathcal{W}_p(k; \omega + t_F) \approx -\frac{\omega_p}{2ka_0} \ln |k^2/2m_e \mp \omega_p - \omega - t_F|. \quad (3.20.20b)$$

The upper sign is associated with $k < k_F$, and the lower sign with $k > k_F$. The dispersion relation (20.18) then implies that in this model the real part $\mathcal{V}(k; \omega)$ of the mass operator has a finite discontinuity at the frequency (20.20a); the size of the step is small and equal to $\pi\omega_p/(2ka_0)$. For $k = k_F$, the discontinuity becomes a logarithmic singularity at $\omega \approx k_F/2m_e + \omega_p - t_F$.

Figure 3.71 indicates that these features retain a semi-quantitative validity when the full Lindhard function is used, i.e. when the quasiparticle contribution is included, see fig. 3.67. It has, however, been suggested that the plasmaron pole disappears if vertex corrections are taken into account [238]. Hence, we consider here figs. 3.68–3.71 as semi-realistic illustrations of the possible existence of several roots of the energy-momentum relation (20.19) in the case of the electron gas.

3.20.6. Momentum distribution

The average momentum distribution $n(k)$ in the electron gas can be calculated from eq. (2.13). The values shown in fig. 3.72 have been obtained from the random phase approximation (10.9) for the mass

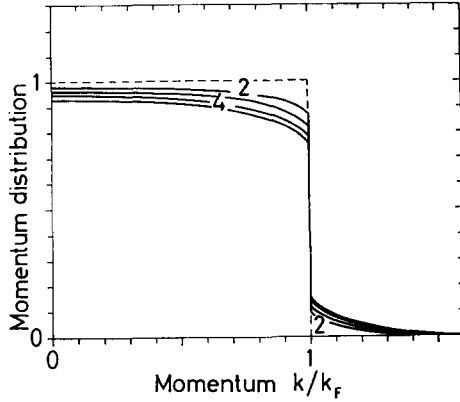


Fig. 3.72. Taken from ref. [236]. Average momentum distribution in the electron gas as calculated from the random phase approximation, for $r_s = 2, 3, 4$ and 5 .

operator. The momentum distribution determines the X-ray Compton scattering double differential cross section [239, 240]. This process is analogous to the $(e, e'p)$ knock-out reaction used in nuclear physics to measure the momentum distribution of the nucleons.

In the Born approximation, the inelastic X-ray scattering cross section from electrons in the conduction band is proportional to $J(Q)$, with [241]

$$\frac{d^2\sigma}{d\omega d\Omega} \propto J(Q) = \int_{|Q|}^{\infty} k n(k) dk, \quad (3.20.21a)$$

where

$$Q = k/2 - \omega m_e/k \quad (3.20.21b)$$

and ω denotes the energy transfer.

In the noninteracting gas, the momentum distribution is the step function (2.2) and the corresponding $J_0(Q)$ is the inverted parabola:

$$J_0(Q) = \frac{1}{2}(k_F^2 - Q^2) \theta(k_F - Q) \quad (3.20.22)$$

represented by the dashes on the left-hand side of fig. 3.73. The presence of momenta $k > k_F$ in the interacting electron gas gives rise to a high- Q tail in $J(Q)$. This is sketched by the full line on the left-hand side of fig. 3.73.

Metallic Na is close to a homogeneous electron gas (with $r_s = 3.97$) in the sense that the interaction between the conduction electrons and the ion core electrons is small and that its Fermi surface is nearly spherical. The right-hand side of fig. 3.73 shows a comparison between the experimental data [241] and the theory [242, 243] in the case of Na. The agreement is only qualitative: the calculated depletion of the Fermi sea is too small.

The discontinuity of the slope of $J(Q)$ at $Q = k_F$ is determined by the difference (see eq. (2.5))

$$Z(k_F) = n(k_F - 0) - n(k_F + 0). \quad (3.20.23)$$

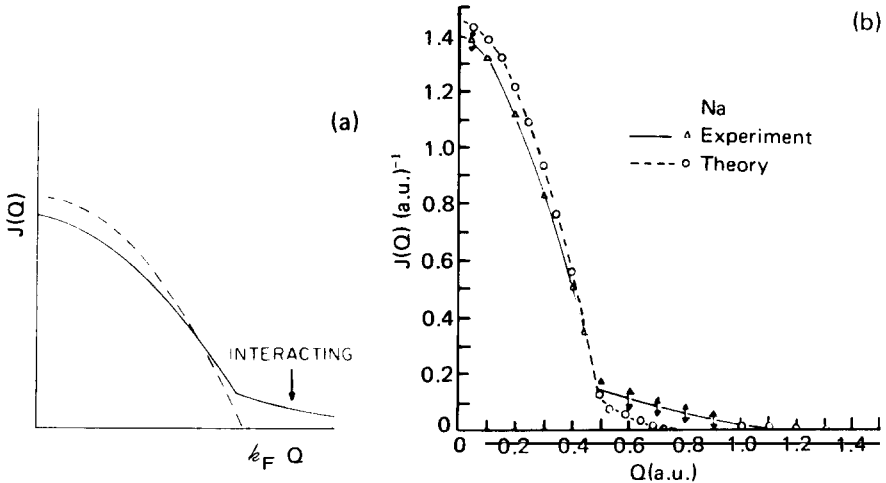


Fig. 3.73. Taken from ref. [227]. The left-hand side sketches the values of $J(Q)$ (eq. (20.21a)) in the case of the noninteracting (dashes) or of an interacting (full line) electron gas. The right-hand side compares the experimental results in Na ([241], triangles joined by a full line) with the values derived from the momentum distribution calculated by Daniel and Vosko [242] and Lam [243] in the case of an electron gas with $r_s = 4$ (open circles, joined by a dashed line).

The experimental data shown in fig. 3.73 yield $Z(k_F) \approx 0.55 \pm 0.15$ for $r_s = 3.97$. This is compared in fig. 3.74 with values calculated from various versions and improvements of the random phase approximation.

Lantto [245] has calculated the momentum distribution associated with a Jastrow trial wave function optimized by using the Fermi hypernetted chain approximation, see section 3.18.2. In fig. 3.75, his results are compared with the random phase approximation.

With the availability of the Green function Monte-Carlo method [246], one may consider that the ground state wave function of the electron gas is known with an accuracy which is limited only by the computing time devoted to the calculation. This ground state wave function enables one to obtain the average momentum distribution. The results are compared in fig. 3.76 with the variational calculation of Lantto [245].

The gap $Z(k_F)$ is the inverse of the ω -mass $m_\omega(k_F)/m_e$, see eq. (5.18). It can be computed from the correlated basis function approach. This leads to values [248] which are in close agreement with those obtained by Lantto in the whole range $1 \leq r_s \leq 5$.

3.20.7. Energy distribution

The energy spectrum of the electrons with momentum k is given by

$$g(\omega) = \int S(k; \omega) d^3k. \quad (3.20.24)$$

A typical frequency dependence of this quantity is shown in fig. 3.77. The approximately parabolic contribution in the domain $\varepsilon_F < \omega < 0$ (i.e. $\omega > -0.17$ Ry in fig. 3.77) arises from the standard quasiparticle peak associated with the root labelled ω_1 in fig. 3.68. The full curve at the left extends approximately from ω_2 to ω_3 . The plasmaron root ω_3 leads to the small peak at the extreme left in fig.

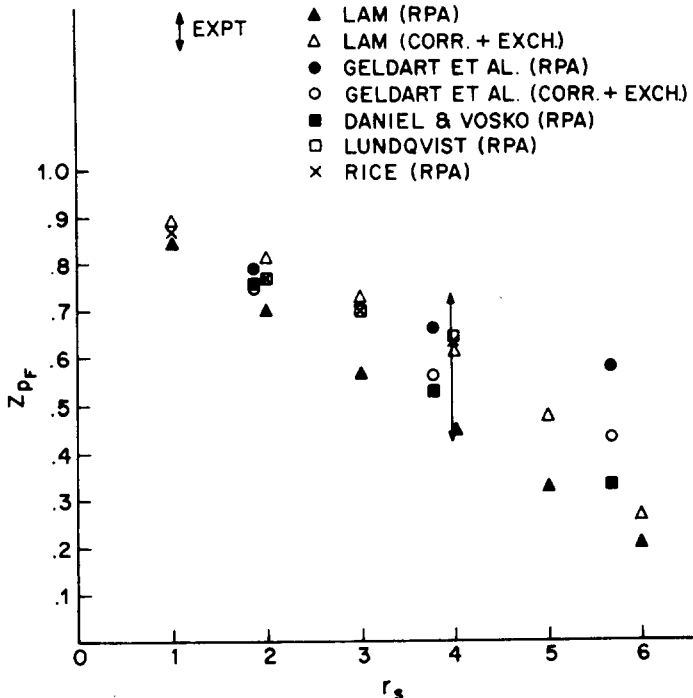


Fig. 3.74. Taken from ref. [241]. Dependence upon r_s of the quantity $Z_{p_F} = Z(k_F)$ (see eq. (20.23)). The calculated values are from refs. [243] (open and full triangles), [244] (full and open dots), [242] (full squares), [236] (open squares) and [230] (crosses). The vertical bar shows the value deduced from the analysis of the X-ray Compton profile of Na [241].

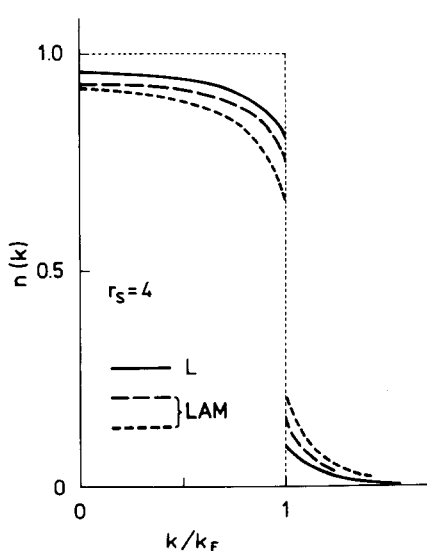


Fig. 3.75. Adapted from ref. [245]. Momentum distribution in the electron gas for $r_s = 4$. The two dashed curves correspond to the random phase approximation and to an improvement thereof [243]. The full curve is derived from an optimized Jastrow trial wave function [245].

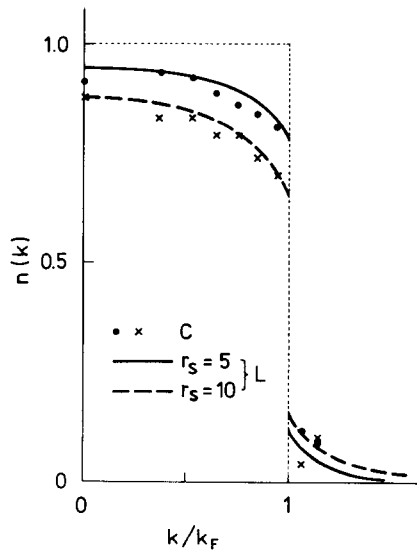


Fig. 3.76. Adapted from ref. [245]. Momentum distribution in an electron gas with $r_s = 5$ (full curve, full dots) and $r_s = 10$ (dashed curve, crosses). The curves are derived from an optimized Jastrow trial wave function [245]. The dots and the crosses are obtained from a Monte-Carlo calculation of the electron gas [247].

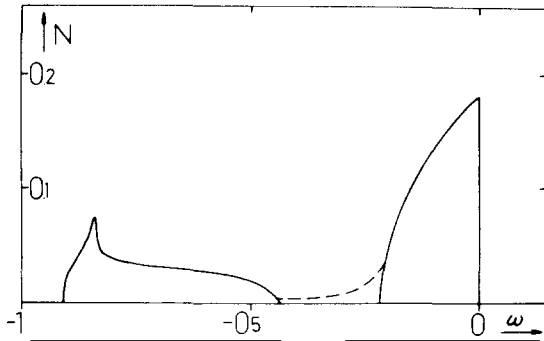


Fig. 3.77. Taken from ref. [233]. Dependence upon ω of the quantity $N(\omega) = (32\pi k_F^3)^{-1}g(\omega)$ (see eq. (20.24), in Ry^{-1}) for the electron gas with $r_s = 4$ and for $\omega < \omega_F$. The zero of ω has been set equal to $\omega_F = 0.17 \text{ Ry}$. The full curve is computed from the spectral function of the plasmon model of fig. 3.69. The dashed curve indicates the modification brought by the quasiparticle contribution (see fig. 3.67).

3.77. The values of $g(\omega)$ for ω contained between ω_2 and ω_3 may give rise to observable effects in soft X-ray emission and absorption [249]. Their detection [250, 251] is rendered difficult by the existence of other effects [252].

3.20.8. On-the-energy-shell value of the mass operator

The on-the-energy-shell value of the mass operator is given by $\mathcal{M}(k; E(k))$ where $E(k)$ is the quasiparticle root of the energy-momentum relation (20.19). We drop the upper (NL) index in eqs. (4.14) and (4.17) and write

$$\mathcal{M}(k; E(k)) = V(k) \mp i W(k). \quad (3.20.25)$$

As discussed in section 3.4, the quantities $V(k)$ and $[2 W(k)]^{-1}$ yield the potential energy and the mean lifetime of a quasiparticle.

The quasiparticle approximation is meaningful only if the spectral function $S(k; \omega) \equiv A(k; \omega)$ has a well-defined peak when plotted versus ω . Figure 3.78 shows that this is the case in a wide range of values for k .

The Fock contribution $V_F(k)$ is represented by the dashed line at the bottom of fig. 3.79. It has a vertical slope at $k = k_F$, in keeping with eq. (20.8). This feature is eliminated by the random phase approximation to $V(k)$, which is shown by the full line at the bottom of fig. 3.79. The potential energy is quite flat for k close to k_F . Figures 3.70, 3.71 and eq. (20.20b) make one expect that this is no longer the case when k is so large that $E(k) - \epsilon_F$ becomes comparable to the plasmon energy, at which the channel for decay of an electron into one electron and a plasmon becomes open. Figures 3.80 and 3.81 confirm this expectation. For $k/k_F = 2$ one has $E(k) \approx 12 \text{ eV}$ in the case $r_s = 4$ [253]. In practice one can use $E(k) \approx k^2/2m_e$ for $k/k_F > 2$, as suggested by fig. 3.79.

The on-the-energy-shell value $W(k)$ of the imaginary part of the mass operator is shown in figs. 3.82 and 3.83. For $k/k_F < 1.5$ the imaginary part mainly originates from the quasiparticle contribution, see fig. 3.67. It suddenly increases when k reaches the threshold for creation of a plasmon; there, the imaginary part $W(k)$ has a logarithmic singularity in a simplified plasmon model, see eq. (20.20b). The mean free path of an electron is related to $W(k)$ by eq. (5.14). Figure 3.84 shows that the mean free

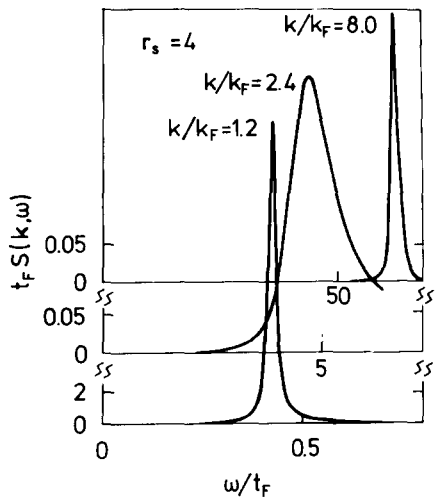


Fig. 3.78. Adapted from ref. [253]. Dependence upon ω of the spectral function $S(k, \omega)$ for an electron gas with $r_s = 4$ for $k/k_F = 1.2$, 2.4 and 8.0. Here, $t_F = k_F^2/2m_e = 0.23$ Ry is the unperturbed Fermi energy. The zero of ω has been set equal to the unperturbed Fermi energy $t_F = k_F^2/2m_e = 0.23$ Ry. The calculation has been performed in the framework of the random phase approximation.

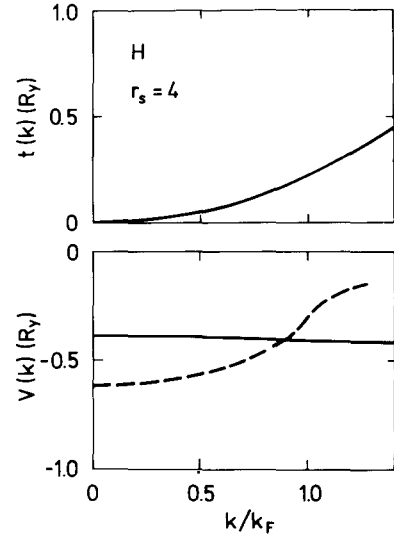


Fig. 3.79. Adapted from ref. [254]. Dependence upon k/k_F of the kinetic energy $t_k = k^2/2m_e$ (upper part) and of the real part $V(k)$ of the on-the-energy-shell mass operator (lower part) for an electron gas with $r_s = 4$. The dashed curve represents the Fock contribution (20.6). The full curve gives $V(k)$ in the random phase approximation (20.9).

path calculated from the random phase approximation [253] is in fair agreement with the experimental value. It is not clear which one of equations (5.14) or (5.20) has been used in fig. 3.84; figure 3.86 below shows that the difference between these two expressions should not exceed 20 per cent.

3.20.9. Effective mass

The effective mass $m_e^*(k)$ is defined by eq. (6.6). In the random phase approximation, the value of

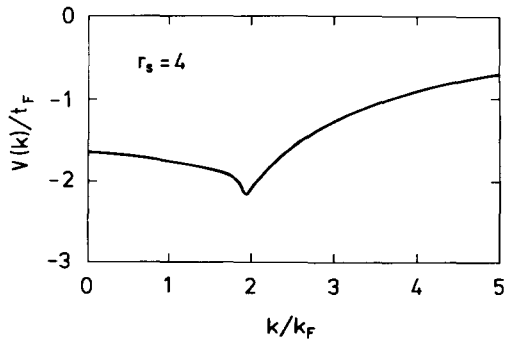


Fig. 3.80. Adapted from ref. [253]. Dependence upon k/k_F of the potential energy $V(k)/t_F$ of a quasiparticle, as calculated in an electron gas with $r_s = 4$ from the random phase approximation ($t_F = k_F^2/2m_e = 0.23$ Ry).

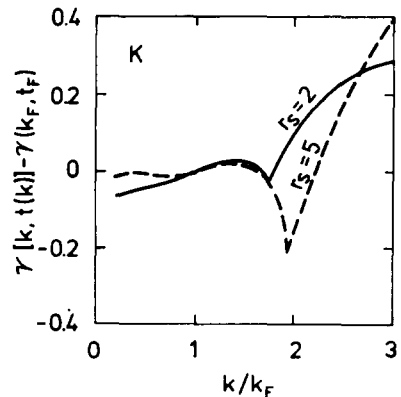


Fig. 3.81. Adapted from ref. [248]. Dependence upon k/k_F of the difference $Y(k, t(k)) = k^2/2m_e - Y(k_F, t_F) \approx V(k) - V(k_F)$ (in units of $t_F = k_F^2/2m_e$) in the case of an electron gas with $r_s = 2$ (full curve) and $r_s = 5$ (dashes), as calculated from the random phase approximation in the framework of the correlated basis functions approach.

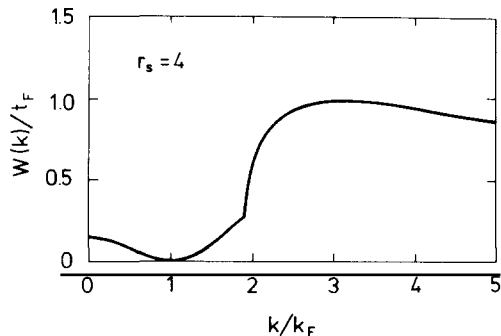


Fig. 3.82. Adapted from ref. [253]. Dependence upon k/k_F of the imaginary part $W(k)/t_F$ of the on-the-energy-shell mass operator for an electron gas with $r_s = 4$ ($\epsilon_F = 0.23$ Ry), as calculated from the random phase approximation.

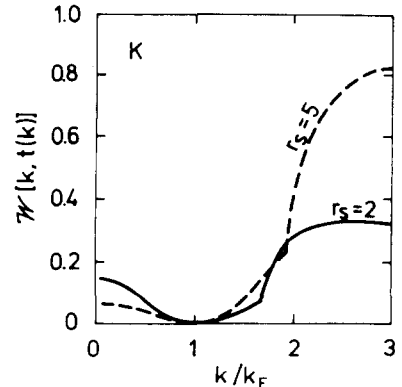


Fig. 3.83. Adapted from ref. [248]. Dependence upon k/k_F of the quantity $W(k, k^2/2m_e) \approx W(k)$ (in units $k^2/2m_e$) in the case of an electron gas with $r_s = 2$ (full curve) and $r_s = 5$ (dashes), as calculated from the random phase approximation in the framework of the correlated basis functions approach.

$m_e^*(k_F)$ of the effective mass at the Fermi surface of the electron gas differs from the bare electron mass m_e by less than six per cent in the whole range $1 \leq r_s \leq 4$, see e.g. ref. [230].

Figure 3.85 shows the momentum dependence of the effective mass $m_e^*(k)$ recently calculated in the framework of the random phase approximation of the correlated basis functions approach [248]. The structure near $k/k_F = 2$ reflects the opening of the plasmon channel, see fig. 3.83.

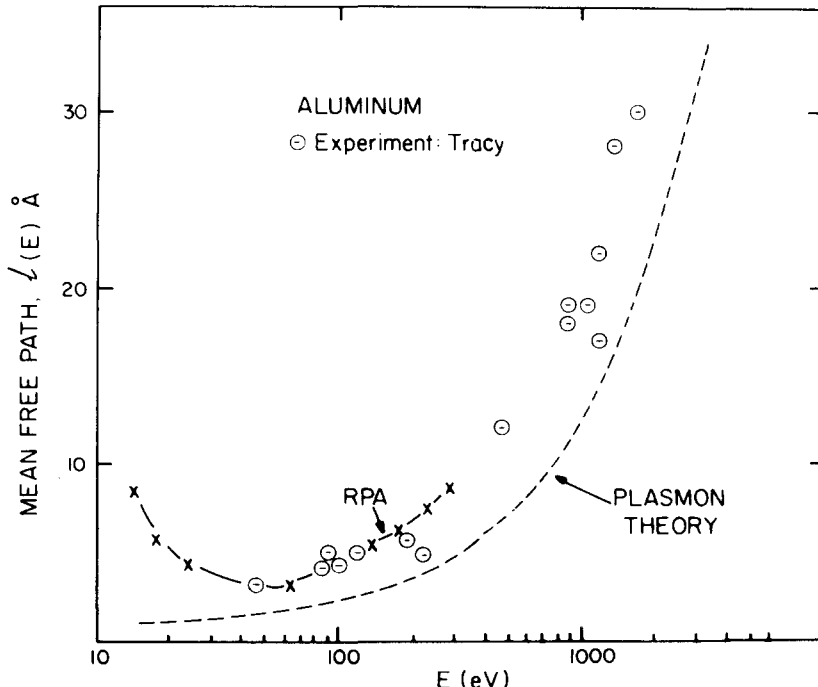


Fig. 3.84. Taken from ref. [227]. Dependence upon energy of the mean free path of electrons in aluminium ($r_s = 2.05$). The experimental values (circles) are from Tracy [255]. The crosses have been calculated from eq. (5.20) with $W(k_0(E); E)$ computed in the random phase approximation [253]. The short dashes are derived from a pure plasmon model.

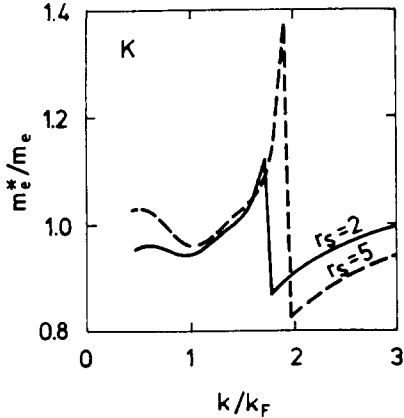


Fig. 3.85. Adapted from ref. [248]. Dependence upon k/k_F of the effective mass m_e^*/m_e as calculated from the random phase approximation of the correlated basis function approach, for an electron gas with $r_s = 2$ (full line) and $r_s = 5$ (dashes).

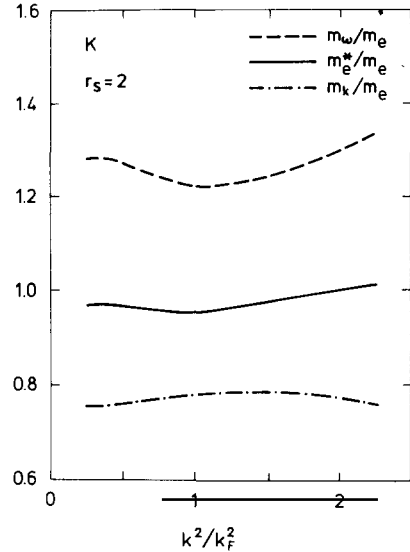


Fig. 3.86. Adapted from ref. [248]. Dependence upon k^2/k_F^2 of the effective mass m_e^*/m_e (full line), of the ω -mass m_ω/m_e (long dashes) and of the k -mass m_k/m_e (dash-and-dot), as calculated from the random phase approximation of the correlated basis function approach, for an electron gas with $r_s = 2$.

We recall that the effective mass can be written as the product of the ω -mass by the k -mass:

$$\frac{m_e^*(k)}{m_e} = \frac{m_\omega(k)}{m_e} \frac{m_k(k)}{m_e}, \quad (3.20.26a)$$

$$Z(k) = m_e/m_\omega(k), \quad (3.20.26b)$$

see eqs. (6.11), (5.19). Values of $Z(k_F)$ have been shown in fig. 3.74. The dependence upon k^2/k_F^2 of the quantities $m_e^*(k)$, $m_\omega(k)$ and $m_k(k)$ is represented in fig. 3.86.

In the case of the electron gas, the screening correction is so important that there exists no enhancement of $m_e^*(k)$ near the Fermi momentum. The interesting structure in that case occurs near the plasmon energy. As expected from our earlier discussion of nuclear matter and of liquid ${}^3\text{He}$, this structure of $m_e^*(k)$ is mainly due to the ω -mass, or equivalently to the quasiparticle strength, see eq. (20.26b). The latter quantity is plotted in fig. 3.87 together with the imaginary part $Y(k)$ of the residue of the one-body Green function at the quasiparticle pole:

$$Z(k) + i Y(k) = \left\{ 1 - \frac{\partial}{\partial \omega} \mathcal{M}(k; \omega) \right\}_{\omega=E(k)}^{-1}, \quad (3.20.27)$$

see eq. (4.16). The fact that $Y(k)$ is comparable to $Z(k)$ for $k/k_F \approx 2$ implies that the quasiparticle peak of the spectral function is asymmetric, see e.g. eq. (2.95) of ref. [36]. The detailed behaviour of $Z(k)$ and of $Y(k)$ for k close to $2k_F$ is expected to be modified by corrections to the random phase approximation [253].

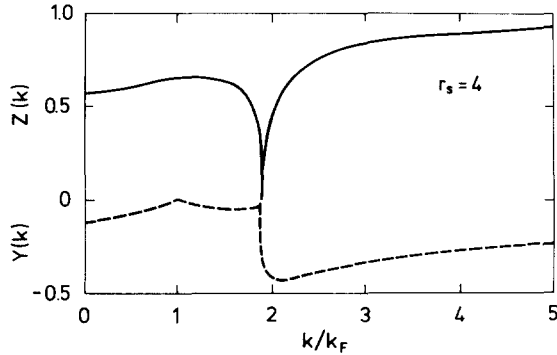


Fig. 3.87. Adapted from ref. [253]. Dependence upon k/k_F of the quasiparticle strength (upper part) and of the imaginary part $Y(k)$ of the residue of the Green function at the quasiparticle pole, see eq. (20.27), in the case of the electron gas ($r_s = 4$) and as calculated from the random phase approximation.

3.20.10. Effect of the electron–phonon interaction

3.20.10.1. Phonons

In the electron gas, the ions are assumed to be frozen and their charge is smeared out to form the positively charged background. In real solids, the background is neither uniform nor frozen. The band structure renders the Fermi surface nonspherical; it also introduces a contribution to the effective mass which reflects the curvature of the energy band near its minimum. Since we only consider uniform systems, we do not discuss this effect; it is quite small in Na [256].

The ions are not frozen. They can vibrate; their quantized modes are the phonons. The typical magnitude of the phonon energies is given by the Debye frequency ω_D

$$\omega_D = 18\pi^2 n c_s, \quad (3.20.28)$$

where c_s is the average velocity of the sound waves. Phonon energies are typically contained in the range 10–30 meV in most metals. In Na, $\omega_D \approx 13$ meV. This implies that the effect of the electron–phonon coupling on the self-energy of an electron becomes negligible when $\omega - \varepsilon_F$ is larger than 100 meV. This domain is quite small compared to the Fermi energy ε_F which is of the order of 10 eV. This is sketched in fig. 3.88.

3.20.10.2. Effective mass

Although the electron–phonon interaction yields a small contribution to the quasiparticle energy, it considerably influences the value of the effective mass in the energy domain

$$|\omega - \varepsilon_F| < \omega_D. \quad (3.20.29)$$

The k -mass $m_k(E)$ is a smooth function of E . One may assume that it is a constant in the domain (20.29) in which its value can be approximated by the k -mass of the electron gas model [258]. In the domain (20.29) and in a free-electron type metal [224, 256] one writes accordingly

$$\frac{m^*}{m_e} \approx \frac{m_{bs}^*}{m_e} \left\{ 1 + \frac{m_e^*}{m_e} + \frac{m_\omega^{ep}}{m_e} \right\}, \quad (3.20.30)$$

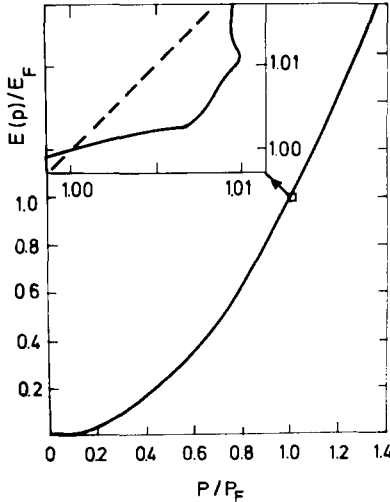


Fig. 3.88. Taken from ref. [257]. The inset shows the modification of the quasiparticle spectrum $E(k)/\epsilon_F$ of the electron gas (dashed line) introduced in the immediate vicinity of the Fermi surface by the electron–phonon coupling.

where m_{bs}^* is the band structure mass ($\approx m_e$ in Na), m_e^* is the effective mass of the electron gas model and m_ω^{ep} is the ω -mass which arises from the electron–phonon coupling.

3.20.10.3. One-phonon exchange

Migdal [258] has shown that the contribution of the electron–phonon coupling to the electron self-energy can be accurately evaluated from the one-phonon contribution, which reads [224]

$$\mathcal{M}_{ep}(k; \omega) = i \sum_q \int \frac{d\gamma}{2\pi} \mathcal{G}_0(k - q; \omega - \gamma) |g_{RPA}(q)|^2 D(q; \gamma), \quad (3.20.31a)$$

where $D(q; \gamma)$ is the phonon Green function

$$D(q; \gamma) = \frac{2\omega_q \sqrt{\epsilon_{RPA}(q; 0)}}{\gamma^2 - \omega_q^2 + i\eta}, \quad (3.20.31b)$$

$$\omega_q = \left\{ \frac{4\pi}{M(1 + \mu^2/q^2)} \right\}^{1/2} Z \epsilon_n, \quad (3.20.31c)$$

$$g_{RPA}(q) = \frac{2\pi e^2}{q^2} \left[\frac{Z^2 n}{\pi e^2 M} \right]^{1/4} / \epsilon_{RPA}(q; 0). \quad (3.20.31d)$$

Here, Z is the ion charge, M its mass and μ is given by eq. (20.12). The quantity $g_{RPA}(q)$ can be interpreted as the dressed electron–phonon interaction. Equations (20.9) and (20.31a) lead to eq. (20.30) for the effective mass.

An equivalent form for \mathcal{M}_{ep} is the following [227]

$$\mathcal{V}_{\text{ep}}(k; \omega) = \text{Re } \mathcal{M}_{\text{ep}}(k; \omega) = - \int_0^\infty du F^2(u) \ln \frac{|u + \omega - \varepsilon_F|}{|u - \omega - \varepsilon_F|}, \quad (3.20.32a)$$

$$\mathcal{W}_{\text{ep}}(k; \omega) = \text{Im } \mathcal{M}_{\text{ep}}(k; \omega) = \pi \int_0^\infty du F^2(u) [n_0(u + \omega - \varepsilon_F) + n_0(\omega - \varepsilon_F - u)], \quad (3.20.32b)$$

where $n_0(k)$ is the momentum distribution of the free Fermi gas, see eq. (2.1). The quantity $F^2(u)$ is an average phonon frequency spectrum. It can be measured in electron tunneling experiments [259, 260]. Since the momentum dependence of \mathcal{M}_{ep} can be neglected [258], we write

$$V_{\text{ep}}(\omega) = \mathcal{V}_{\text{ep}}(k; \omega), \quad (3.20.32c)$$

$$W_{\text{ep}}(\omega) = \mathcal{W}_{\text{ep}}(k; \omega). \quad (3.20.32d)$$

3.20.10.4. Einstein model

In the rest of this section, we set the zero of the frequency variable ω at the Fermi energy ε_F . In an Einstein model all the phonons have the same energy ω_E :

$$F^2(u) = F_0^2 \delta(u - \omega_E). \quad (3.20.33a)$$

In that simple model, one has [261]

$$V_{\text{ep}}(\omega) = \text{Re } \mathcal{M}_{\text{ep}}(\omega) = -F_0^2 \ln \left| \frac{\omega + \omega_E}{\omega - \omega_E} \right| \quad (3.20.33b)$$

$$W_{\text{ep}}(\omega) = \text{Im } \mathcal{M}_{\text{ep}}(\omega) \begin{cases} = -\pi F_0^2 \text{sgn}(\omega) & \text{if } |\omega| > \omega_E \\ = 0 & \text{if } |\omega| < \omega_E \end{cases}. \quad (3.20.33c)$$

The contribution of the electron–phonon coupling to the ω -mass is given by

$$\frac{m_\omega^{\text{ep}}(\omega)}{m_e} = 1 - \frac{d}{d\omega} V_{\text{ep}}(\omega). \quad (3.20.34)$$

In this Einstein model, the ω -mass at the Fermi surface is equal to

$$m_\omega^{\text{ep}}(0)/m = 2\pi F_0/\omega_E = 1 + \lambda. \quad (3.20.35)$$

The quantities $V_{\text{ep}}(\omega)$ and $W_{\text{ep}}(\omega)$ are shown in fig. 3.89 in the case $\lambda = 0.5$. The ω -mass $m^{\text{ep}}(E)/m$ is equal to 1.5 at $E = 0$: it increases to $+\infty$ at the degenerate phonon energy $\omega_E = 0$, and then increases from $-\infty$ at $\omega_E + 0$ to unity as $E \rightarrow \infty$.

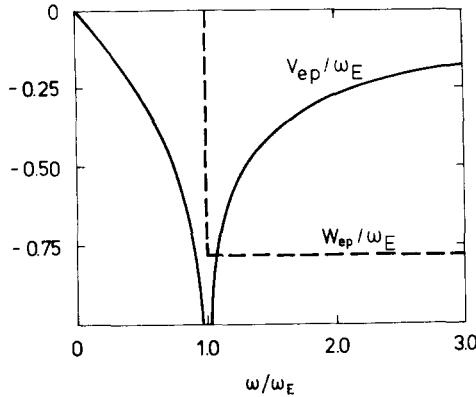


Fig. 3.89. Taken from ref. [262]. Dependence upon ω/ω_E of the real part (full line) and of the imaginary part (dashes) of the contribution M_{ep} of the electron-phonon coupling to the mass operator in an Einstein model. The parameter λ in eq. (20.35) has been taken equal to 0.5. The zero of frequency is taken equal to the Fermi energy.

3.20.10.5. Sodium

The quantity $M_{ep}(\omega)$ of eq. (20.31a) has been calculated in many works, especially for $\omega = \varepsilon_F$. For the purpose of illustration, we choose the example of metallic Na and the calculation reported in ref. [263].

The calculated dependence upon ω of the imaginary part $W_{ep}(\omega)$ is shown in fig. 3.90. The imaginary part first increases like $(\omega - \varepsilon_F)^2$. It then rapidly increases for $\omega \approx \omega_D$ and seems to saturate at $\omega \approx 1.2\omega_D$. The corresponding real part is plotted in fig. 3.91. For $\omega < 0.5\omega_D$, it is in semi-quantitative agreement with the Einstein model with $\lambda = 0.19$, $\omega_E = \omega_D$. It shows a minimum at $\omega \approx 1.2\omega_D$ where the ω -mass (20.34) becomes equal to the bare electron mass, see fig. 3.92. Results similar to those given in figs. 3.88 and 3.92 had been shown by Buckingham [265] as early as 1951.

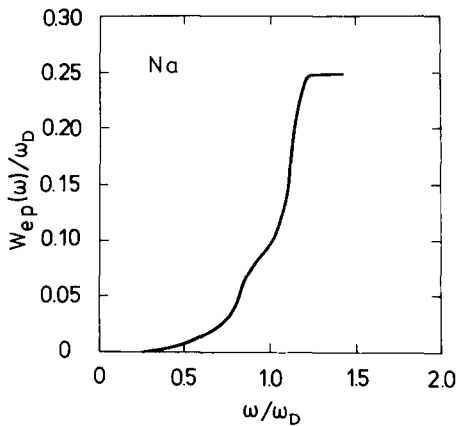


Fig. 3.90. Adapted from ref. [263]. Dependence upon ω of the imaginary part $W_{ep}(\omega)$ of the contribution of the electron-phonon coupling to the mass operator of electrons in Na. The unit $\omega_D = 13$ meV is the Debye energy and the zero of ω has been set equal to the Fermi energy.

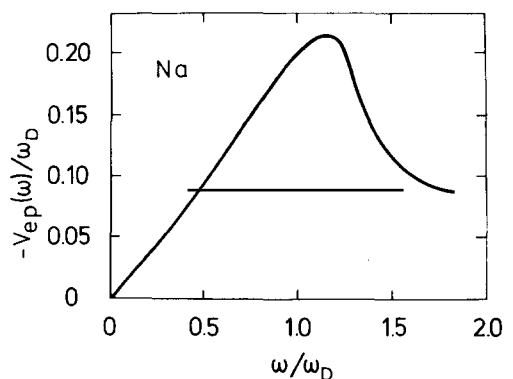


Fig. 3.91. Adapted from ref. [263]. Dependence upon ω of the real part $V_{ep}(\omega)$ of the contribution of the electron-phonon coupling to the mass operator of electrons in Na. The unit is the Debye energy ω_D .

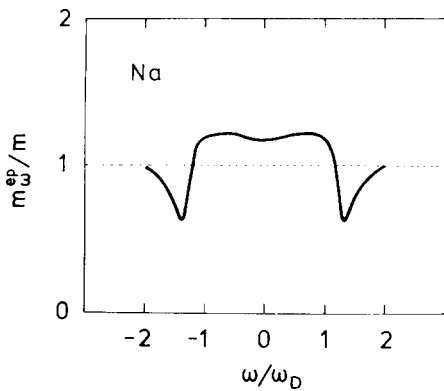


Fig. 3.92. Adapted from ref. [264]. Dependence upon ω/ω_D of the ω -mass (eq. (20.34)) associated with the electron-phonon coupling in Na. The zero of ω has been set at the Fermi energy.

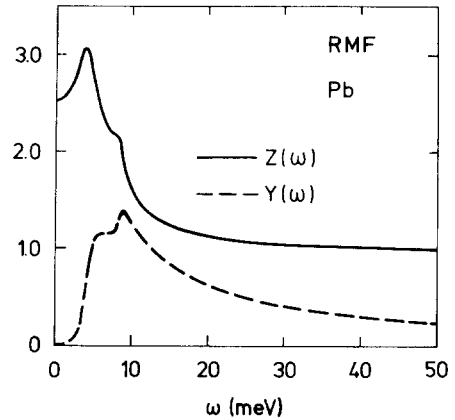


Fig. 3.93. Adapted from ref. [260]. Dependence upon energy of the quantities (see eq. (20.36)) $Z(\omega)$ (full curve) and $Y(\omega)$ (dashes) in Pb, as obtained from a superconducting tunneling experiment. The zero of E has been set at the Fermi energy ϵ_F .

3.20.10.6. Lead

The quantity $F^2(u)$ which appears in eqs. (20.32a) and (20.32b) can be measured by electron tunneling in superconductors [259, 260]. This enables one to calculate $V_{ep}(\omega)$ and $W_{ep}(\omega)$. We show results obtained in the case of Pb. They imply some averaging over the Fermi surface which is not spherical in that case; the band structure moreover yields a contribution $m_{bs}^*/m \approx 1.1$ to the effective mass [256].

Figure 3.93 shows the values of $Z(\omega)$ and of $Y(\omega)$, with

$$Z(\omega) + i Y(\omega) = \left\{ 1 - \frac{d}{d\omega} \mathcal{M}_{ep}(\omega) \right\}^{-1}, \quad (3.20.36)$$

see eq. (20.27). We recall that $m_\omega(E)/m_e = [Z(E)]^{-1}$. The self-energy can be computed from

$$\mathcal{M}_{ep}(u) = \int_0^u \{1 - [Z(E) + i Y(E)]^{-1}\} dE. \quad (3.20.37)$$

The real and the imaginary parts of $\mathcal{M}_{ep}(u)$ are shown in fig. 3.94. They are qualitatively similar to the results computed in the case of Na, see figs. 3.90 and 3.91. In the case of Pb, the value of the ω -mass at the Fermi surface is quite large: $m_\omega(0)/m_e \approx 3.5$. Since the Fermi surface is not spherical in Pb, this should be considered as an average value. The value of $Z(\omega)$ in Pb has been calculated in ref. [266].

Figure 3.94 shows that the imaginary part of $\mathcal{M}_{ep}(u)$ has the same size as its real part for $u < 10$ meV. Hence, only a limited meaning can be attached to the energy momentum relation represented by the inset in fig. 3.88. This is exhibited in fig. 3.95. There, the vertical bar has a length equal to $|2 W_{ep}(k)|$ and is a rough measure of the width of the quasiparticle peak associated with the momentum k . The quasiparticle energy $E(k)$ is defined by

$$E(k) = k^2/2m_e + \operatorname{Re} \mathcal{M}_{ep}(E(k)). \quad (3.20.38)$$

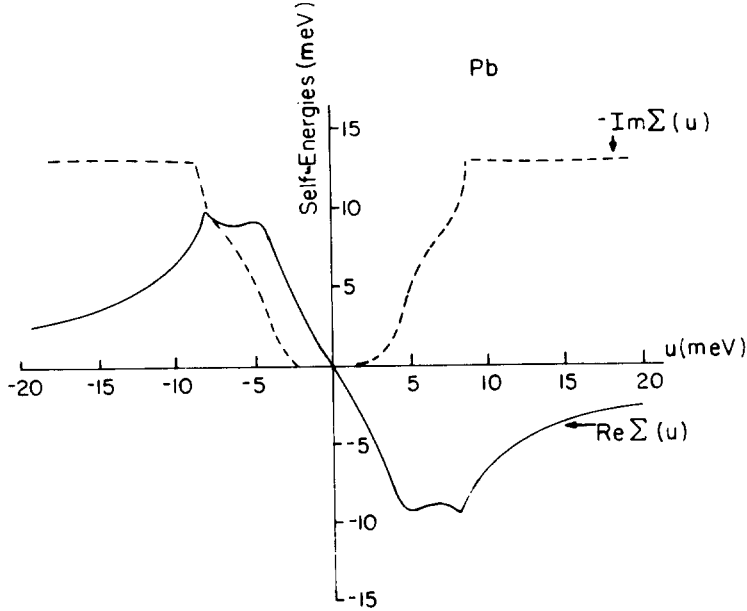


Fig. 3.94. Taken from ref. [227]. Dependence upon energy of the real (full curve) and of the imaginary (dashes) parts of $\Sigma(u) = M_{ep}(u)$ as calculated from fig. 3.93 [257]. Here, $u = \omega - \varepsilon_F$.

3.20.10.7. Influence on observables

The effective mass m^* of electrons in metals is given by eq. (20.30). It has a narrow enhancement in the energy domain $|E - \varepsilon_F| < \omega_D$, where ω_D is the Debye energy.

Some observables are affected by this renormalization of the effective mass, most are not [267, 268]. This is summarized in a survey by Grimwall [257]. The enhancement influences the value of the electronic specific heat at low temperature, see eq. (19.1). In contrast, the spin susceptibility is not affected by the contribution of the electron-phonon coupling to the ω -mass.

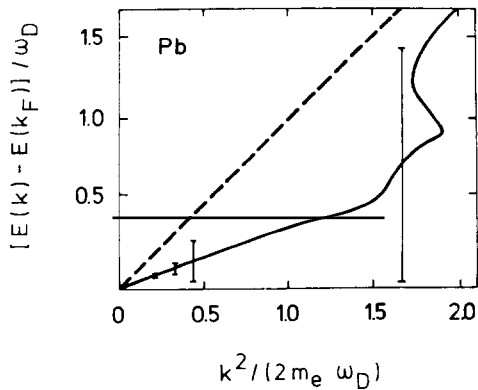


Fig. 3.95. Adapted from ref. [262]. The dashes show the energy-momentum relation in the electron gas. The full line takes into account the electron-phonon coupling in ^{208}Pb , see fig. 3.94 and eq. (20.38). The vertical bars indicate the size of the width of the quasiparticle peak. The Debye frequency is denoted by ω_D .

3.20.11. Conclusions

There exist numerous reliable investigations of the mass operator in the case of the electron gas at high density. The calculated effective mass is close to the bare electron mass near the Fermi surface because the difference $1 - (m_k/m_e)$ happens to be approximately equal to the difference $(m_\omega/m_e) - 1$. Strong dynamical effects exist when the quasiparticle energy is close to the plasmon energy.

In metals, the electron–phonon interaction leads to a narrow enhancement of the ω -mass $m_\omega(E)$ in the domain $|E - \varepsilon_F| < \omega_D$ where ω_D ($\approx 10\text{--}30$ meV) is a typical phonon energy. This can be calculated accurately at high density because the random phase approximation is then reliable and the electron–phonon vertex is known [258]. Since we limit our discussion to uniform systems, we did not discuss complications related to the fact that in most metals the Fermi surface is not spherical.

3.21. Hindsight

In sections 3.2–3.6 we have defined the one-body Green function, the mass operator, their quasiparticle approximation and related quantities. This discussion applies to any normal uniform system. The dynamical effects are contained in the ω -mass m_ω/m , whose inverse is the strength of the quasiparticle.

Sections 3.7–3.10 have mainly been devoted to the investigation of the first- and of the second-order approximations to the mass operator, to the momentum distribution and to the quasiparticle strength. Numerical examples have been given which are simplified models of nuclear matter. In that case, the ω -mass has an enhancement centred on the Fermi energy ε_F ; its width is comparable to ε_F . Screening corrections tend to broaden the enhancement peak of the ω -mass in nuclear matter. It is difficult, however, to make a quantitative statement because the screened particle–hole interaction is not known in that case.

Nuclear interactions are strong for small internuclear distances. Hence, one cannot apply a straightforward perturbation expansion in powers of the strength of the interaction. The perturbation series must be rearranged by performing partial summation as in the dilute Fermi gas model (section 3.14) or in the hole line expansion (section 3.15). The short-range part of the interaction leads to the virtual excitation of high-lying core states. This only introduces a smooth background under the enhancement peak of the ω -mass near the Fermi surface (section 3.16).

The method of correlated basis functions has been outlined in section 3.17. It provides a powerful method for the calculation of the properties of dense as well as of dilute systems. Normal liquid ^3He and the electron gas provide typical examples of dense systems.

Significant progress has recently been accomplished in the description of the temperature dependence of the specific heat of normal liquid ^3He at low temperature (section 3.19). This progress has been stimulated by works on the energy dependence of the effective mass in the case of nuclear matter and of nuclei. In a detailed calculation based on a Landau-type description, a distinction must be made between dynamical and statistical quasiparticle energies (section 3.17).

The theory of the dense electron gas (section 3.20) is quite satisfactory because the Coulomb interaction is known and the random phase approximation is reliable. Dynamical effects occur when the quasiparticle energy is close to the plasmon energy. In metals, the electron–phonon interaction leads to a strong and narrow enhancement of the ω -mass near the Fermi energy. This is due to the smallness of the phonon excitation energies. A similar situation is encountered in the case of nuclei.

4. Single-particle motion in nuclei

4.1. Introduction

In chapter 2, we recalled some of the empirical properties which point to the approximate validity of the concept of single-particle motion in nuclei. Equation (2.0.3) gives the general form of a single-particle wave equation ($\hbar = 1$)

$$-\frac{1}{2m} \nabla^2 \varphi_E(\mathbf{r}) + \int d^3 r' \mathcal{M}(\mathbf{r}, \mathbf{r}'; E) \varphi_E(\mathbf{r}') = E \varphi_E(\mathbf{r}). \quad (4.1.1)$$

Positive values of the single-particle energy E correspond to scattering states; negative values of E are associated with bound single-particle states, see fig. 2.2.

We shall see that if one identifies \mathcal{M} with the mass operator of the (A)-nucleon system, the discrete eigenvalues of eq. (1.1) in the domain $E < 0$ yield the bound state energies of the nuclei with ($A - 1$) and with ($A + 1$) nucleons, respectively. For $E > 0$ the asymptotic behaviour of $\varphi_E(\mathbf{r})$ yields the elastic scattering phase shift of a nucleon by the target nucleus (A). Hence, the mass operator appears to be a good candidate for the single-particle potential.

This is in keeping with our discussion of uniform systems in chapter 3. In the present case, however, this identification faces the main problem that both the energy dependence and the nonlocality of $\mathcal{M}(\mathbf{r}, \mathbf{r}'; E)$ are very complicated in finite systems. For instance, $\mathcal{M}(\mathbf{r}, \mathbf{r}'; E)$ has many poles on the real E -axis. It has been hinted at the end of section 2.11.4 that the latter difficulty can be circumvented by considering the operator

$$\mathcal{M}(\mathbf{r}, \mathbf{r}'; E + \frac{1}{2}i\Delta) = V_{HF}(\mathbf{r}, \mathbf{r}') + \mathcal{N}(\mathbf{r}, \mathbf{r}'; E + \frac{1}{2}i\Delta), \quad (4.1.2)$$

where $V_{HF}(\mathbf{r}, \mathbf{r}')$ is the Hartree–Fock field while Δ is an averaging energy interval. This operator is a more plausible candidate for the empirical single-particle potential. Its overall energy dependence is rather smooth. For $|E - \varepsilon_F| > 10\text{--}20 \text{ MeV}$, its nonlocality appears to be fairly simple and similar to the nonlocality of the mass operator in the case of uniform systems. Little is known on the nonlocality of \mathcal{N} for $|E - \varepsilon_F| < 10 \text{ MeV}$. We shall call \mathcal{N} the “dispersion correction” to the Hartree–Fock approximation. It is the sum of the polarization and correlation corrections discussed in chapter 3.

Two main procedures have been applied to handle the nonlocality of \mathcal{N} . The first one consists in considering the quantity

$$\mathcal{Q}(\mathbf{r}; E) = \int d^3 r' \mathcal{N}(\mathbf{r}, \mathbf{r}'; E + \frac{1}{2}\Delta). \quad (4.1.3)$$

The second method is based on the Hartree–Fock representation of the operator \mathcal{N}

$$\mathcal{N} = \sum_{\alpha, \alpha'} |\varphi_\alpha^{(0)}\rangle \mathcal{N}_{\alpha\alpha'} \left(E + \frac{i}{2}\Delta\right) \langle \varphi_{\alpha'}^{(0)}|, \quad (4.1.4a)$$

and assumes that the matrix $\mathcal{N}_{\alpha\alpha'}(E)$ is diagonal

$$\mathcal{N}_{\alpha\alpha'}\left(E + \frac{i}{2}\Delta\right) \approx \mathcal{N}_\alpha\left(E + \frac{i}{2}\Delta\right) \delta_{\alpha\alpha'}. \quad (4.1.4b)$$

For a bound single-particle state $\varphi_\alpha^{(0)}$, $\alpha = \{n, l, j, m\}$; for a scattering state, $\alpha = \{E, l, j, m\}$.

This brief discussion suggests that the case of nuclei is considerably more complicated than that of uniform systems, from a conceptual as well as from a practical point of view. Let us for instance consider the ω -mass which constitutes the cornerstone of our survey. At least four possible definitions have been used in the literature, namely

$$\frac{m_\omega(\mathbf{r}; E)}{m} = 1 - \frac{d}{dE} \operatorname{Re} \mathcal{Q}(\mathbf{r}; E), \quad (4.1.5)$$

$$\frac{m_\omega^{(\alpha)}(E)}{m} = 1 - \frac{d}{dE} \operatorname{Re} \mathcal{N}_\alpha\left(E + \frac{i}{2}\Delta\right), \quad (4.1.6)$$

$$\frac{\bar{m}_\omega(E)}{m} = 1 - \frac{d}{dE} \operatorname{Re} \langle \mathcal{N}_\alpha\left(E + \frac{i}{2}\Delta\right) \rangle_\alpha, \quad (4.1.7)$$

$$\frac{m_\omega(\varepsilon_\alpha^{(0)})}{m} = 1 - \left[\frac{d}{dE} \operatorname{Re} \mathcal{N}_\alpha\left(E + \frac{i}{2}\Delta\right) \right]_{E=\varepsilon_\alpha^{(0)}}. \quad (4.1.8)$$

Here, Re stands for “the real part of”. In eq. (1.7), $\langle \rangle_\alpha$ denotes an average over some levels α . In eq. (1.8) $\varepsilon_\alpha^{(0)}$ is the single-particle energy associated with $\varphi_\alpha^{(0)}$.

4.2. The mass operator in finite systems

4.2.1. Definitions

The n -body Green function is defined as follows

$$G_n(x_1, \dots, x_n; x'_1, \dots, x'_n) = (-i)^n \langle \Psi_0^{(A)} | T[a(x_1) \dots a(x_n) a^+(x'_n) \dots a^+(x'_1)] | \Psi_0^{(A)} \rangle, \quad (4.2.1)$$

where $\Psi_0^{(A)}$ is the normalized exact ground state wave function of the (A)-particle system, while T denotes the time-ordering operator and x represents the space and time variables $x = (\mathbf{r}, t)$. We omit any explicit reference to the spin degree of freedom.

In the case $n = 1$ one recovers the one-body Green function of eq. (3.2.24b). Its Fourier transform $G(\mathbf{r}, \mathbf{r}'; \omega)$ has the Lehmann representation

$$G(\mathbf{r}, \mathbf{r}'; \omega) = \sum_h \frac{\varphi_h(\mathbf{r}) \varphi_h^*(\mathbf{r}')}{\omega - \omega_h - i\eta} + \sum_p \frac{\varphi_p(\mathbf{r}) \varphi_p^*(\mathbf{r}')}{\omega - \omega_p + i\eta}, \quad (4.2.2)$$

where

$$\varphi_h(\mathbf{r}) = \langle \psi_h^{(A-1)} | a(\mathbf{r}) | \psi_0^{(A)} \rangle, \quad (4.2.3a)$$

$$\varphi_p(\mathbf{r}) = \langle \psi_0^{(A)} | a(\mathbf{r}) | \psi_p^{(A+1)} \rangle. \quad (4.2.3b)$$

Here $\psi_h^{(A-1)}$ is a suitably normalized eigenstate of the Hamiltonian of the $(A-1)$ -particle system with energy $E_h^{(A-1)}$, $\psi_p^{(A+1)}$ is an eigenstate of the $(A+1)$ -particle system with energy $E_p^{(A+1)}$, and

$$\omega_p = E_p^{(A+1)} - E_0^{(A)}, \quad \omega_h = E_0^{(A)} - E_h^{(A-1)}, \quad (4.2.4)$$

where $E_0^{(A)}$ is the energy of $\Psi_0^{(A)}$. The closure relation yields

$$\sum_p \varphi_p(\mathbf{r}) \varphi_p^*(\mathbf{r}') + \sum_h \varphi_h(\mathbf{r}) \varphi_h^*(\mathbf{r}') = \delta(\mathbf{r} - \mathbf{r}'). \quad (4.2.5)$$

The analog of the defining equation (3.2.25) for the mass operator \mathcal{M} reads

$$[\omega + (2m)^{-1} \nabla_{\mathbf{r}}^2] G(\mathbf{r}, \mathbf{r}'; \omega) = \delta(\mathbf{r} - \mathbf{r}') + \int d^3 r' \mathcal{M}(\mathbf{r}, \mathbf{r}'; \omega) G(\mathbf{r}, \mathbf{r}'; \omega). \quad (4.2.6)$$

4.2.2. Single-particle wave function

Equations (2.2) and (2.6) yield

$$[\omega_p + (2m)^{-1} \nabla^2] \varphi_p(\mathbf{r}) - \int d^3 r' \mathcal{M}(\mathbf{r}, \mathbf{r}'; \omega_p) \varphi_p(\mathbf{r}') = 0. \quad (4.2.7)$$

This single-particle wave equation has two remarkable properties.

(i) It has discrete eigenvalues which correspond to the excitation energies of the bound states of the $(A+1)$ -particle system; it can also be checked that it has discrete eigenvalues which correspond to the energies of the bound states of the $(A-1)$ -particle system, see eqs. (2.4).

(ii) In the continuum ($\omega_p > 0$), the asymptotic form of the radial part $r^{-1} u_p(r)$ of $\varphi_p(\mathbf{r})$ yields for large r

$$u_p(r) \sim \exp(-ik_p r) + S_{pp}(\omega_p) \exp(ik_p r), \quad (4.2.8a)$$

where

$$(2m)^{-1} k_p^2 = \omega_p. \quad (4.2.8b)$$

The quantity $S_{pp}(\omega_p)$ is the exact diagonal (elastic scattering) element of the scattering matrix; this has first been demonstrated by Bell and Squires [48], see also refs. [269–272]. Our presentation follows that of refs. [273] and [50]. It can only be considered as a heuristic proof since we did not sufficiently specify the boundary conditions satisfied by $\Psi_p^{(A+1)}$ and $\Psi_h^{(A-1)}$.

It seems that there does not yet exist a derivation of (2.8a) which treats correctly the centre-of-mass motion. This is a rather academic problem in the case of atomic physics [50] since there it is logical to start from an unperturbed one-body Green function associated with a static one-body (Hartree–Fock) potential centred on the nucleus. In the nuclear case there is no obvious origin around which to centre this one-body potential [269].

4.2.3. Analytical properties of the one-body Green function

The analytical properties of $G(\mathbf{r}, \mathbf{r}'; \omega)$ in the complex ω -plane are schematically represented in fig. 4.1 [274]. The one-body Green function has a right-hand cut which runs below the real ω -axis between $\omega = \varepsilon_t^+$ and $\omega = +\infty$. Here, ε_t^+ is the threshold energy of the first inelastic channel. The one-body Green function has a left-hand cut which runs above the real ω -axis and extends from $-\infty$ to ε_t^- with

$$\varepsilon_t^- = E_0^{(A)} - E_0^{(A-2)}. \quad (4.2.9)$$

The left-hand cut corresponds to the possibility of the decay of the $(A-1)$ into the $(A-2)$ nucleus.

The one-body Green function has discrete poles ω_h between ε_t^- and ε_F^- with

$$\varepsilon_F^- = E_0^{(A)} - E_0^{(A-1)}; \quad (4.2.10a)$$

these poles correspond to bound states of the $(A-1)$ nucleus with excitation energy (see eqs. (2.4))

$$E_X^{(A-1)} = \varepsilon_F^- - \omega_h. \quad (4.2.11a)$$

The Green function also has poles ω_p on the real axis between $\omega = \varepsilon_F^+$ and $\omega = 0$, where

$$\varepsilon_F^+ = E_0^{(A+1)} - E_0^{(A)}. \quad (4.2.10b)$$

These correspond to bound states of the $(A+1)$ nucleus with excitation energy

$$E_X^{(A+1)} = \omega_p - \varepsilon_F^+, \quad (4.2.11b)$$

see eqs. (2.4).

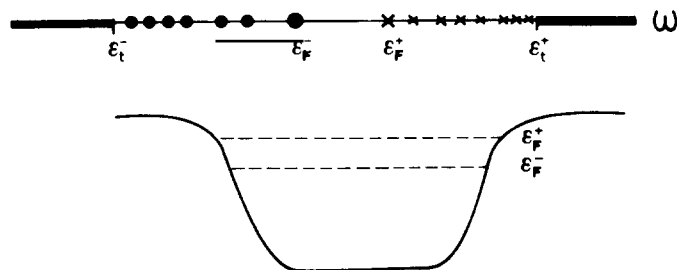


Fig. 4.1. Schematic representation of the singularities of the one-body Green function $G(\mathbf{r}, \mathbf{r}'; \omega)$ in the complex ω -plane. The left-hand cut runs above the real axis between $-\infty$ and ε_t^- . The right-hand cut runs below the real axis between ε_t^+ and $+\infty$. The discrete poles (full dots) between ε_t^- and ε_F^- correspond to bound states of the $(A-1)$ nucleus with excitation energies given by eq. (2.11a). The discrete poles (crosses) between ε_F^+ and 0 correspond to bound states of the $(A+1)$ nucleus with excitation energies given by eq. (2.11b). In an independent-particle model of the (A) nucleus, ε_F^- is the energy of the last occupied orbit and ε_F^+ that of the first unoccupied orbit.

Let us illustrate this description with two examples. In the case of neutrons in ^{208}Pb one has (see figs. 2.4 and 2.6)

$$\begin{aligned} \varepsilon_t^+ &= 2.6 \text{ MeV}, & \varepsilon_t^- &= -14.08 \text{ MeV}, \\ \varepsilon_F^+ &= -3.93 \text{ MeV}, & \varepsilon_F^- &= -7.34 \text{ MeV}. \end{aligned} \quad (4.2.12)$$

In the case of neutrons in ^{40}Ca , one has (see figs. 2.7 and 2.8)

$$\begin{aligned} \varepsilon_t^+ &= 3.4 \text{ MeV}, & \varepsilon_t^- &\approx -29 \text{ MeV}, \\ \varepsilon_F^+ &= -8.36 \text{ MeV}, & \varepsilon_F^- &= -15.73 \text{ MeV}. \end{aligned} \quad (4.2.13)$$

4.2.4. Hartree–Fock approximation

The Hartree–Fock approximation is the first-order term of the expansion of the mass operator in powers of the strength of the nucleon–nucleon interaction. It is given by eq. (3.7.6) in the case of a uniform medium. In the present case it reads

$$V_{\text{HF}}\varphi_k^{(0)} = V_{\text{H}}(\mathbf{r})\varphi_k^{(0)}(\mathbf{r}) - \int V_{\text{F}}(\mathbf{r}, \mathbf{r}')\varphi_k^{(0)}(\mathbf{r}') d\mathbf{r}', \quad (4.2.14a)$$

where the expressions of the Hartree and of the Fock contributions are

$$V_{\text{H}}(\mathbf{r}) = \sum_j n_<(j) \langle \varphi_j^{(0)}(\mathbf{r}') | v(\mathbf{r}, \mathbf{r}') | \varphi_j^{(0)}(\mathbf{r}') \rangle, \quad (4.2.14b)$$

$$V_{\text{F}}(\mathbf{r}, \mathbf{r}') = \sum_j n_<(j) \varphi_j^{(0)}(\mathbf{r}')^* v(\mathbf{r}, \mathbf{r}') \varphi_j^{(0)}(\mathbf{r}), \quad (4.2.14c)$$

where $n_<(j) = 1$ for the A deepest bound single-particle orbits and $=0$ for other values of j .

In the case of a finite system, the orthonormal single-particle wave functions must be determined self-consistently according to the equation

$$-(2m)^{-1} \nabla^2 \varphi_k^{(0)} + V_{\text{HF}}\varphi_k^{(0)} = \varepsilon_k^{(0)}\varphi_k^{(0)}. \quad (4.2.14d)$$

The Hartree–Fock potential is nonlocal, static (i.e. independent of ω) and Hermitian. The single-particle energies $\varepsilon_k^{(0)}$ are real. They take discrete values ($\varepsilon_k^{(0)} < 0$, bound single-particle states) and continuous values ($\varepsilon_k^{(0)} > 0$, scattering single-particle states), see fig. 2.2.

The Hartree–Fock basis has the property of minimizing the following ground state expectation value of the Hamiltonian H

$$E^{(0)} = \langle \phi_0 | H | \phi_0 \rangle, \quad (4.2.15a)$$

where ϕ_0 is a Slater determinant built from the A deepest bound orbitals $\varphi_j^{(0)}$. The Hartree–Fock approximation cannot be used in conjunction with realistic nucleon–nucleon interactions. Practical

calculations involve effective interactions v whose parameters are adjusted in such a way that the Hartree–Fock energy $E^{(0)}$, the density $\rho^{(0)}(\mathbf{r})$

$$\rho^{(0)}(\mathbf{r}) = \sum_j n_{<}(j) |\varphi_j^{(0)}(\mathbf{r})|^2, \quad (4.2.16)$$

and the Fermi energy are in good agreement with the empirical values. Here, we only consider doubly closed shell nuclei. We also omit the Coulomb interaction and write the equations in the case $N = Z$ only.

Skyrme-type interactions (see section 3.7.7) have been widely used [19, 275] because they are successful and simple to handle in computations. The latter property is a consequence of the fact that they enable one to write $E^{(0)}$ as an integral of an energy density which only depends upon $\rho^{(0)}(\mathbf{r})$ and upon the kinetic energy density $\tau^{(0)}(\mathbf{r})$:

$$E^{(0)} = \int d^3r \mathcal{H}(\rho^{(0)}, \tau^{(0)}), \quad (4.2.15b)$$

$$\tau^{(0)}(\mathbf{r}) = (2m)^{-1} \sum_j n_{<}(j) |\nabla \varphi_j^{(0)}|^2.$$

The Hartree–Fock equation (2.14) reads in this case

$$\{-\nabla \cdot [2m_{Sk}^*(\mathbf{r})]^{-1} \nabla + \mathcal{V}_{HF}(\mathbf{r})\} \varphi_k^{(0)}(\mathbf{r}) = \varepsilon_k^{(0)} \varphi_k^{(0)}(\mathbf{r}). \quad (4.2.17)$$

In the case of the simple Skyrme interaction (3.7.27) one has

$$\frac{m_{Sk}^*(\mathbf{r})}{m} = \frac{8}{8 + m \rho^{(0)}(\mathbf{r}) (3t_1 + 5t_2)}, \quad (4.2.18)$$

$$\mathcal{V}_{HF}(\mathbf{r}) = \frac{3}{4} t_0 \rho^{(0)}(\mathbf{r}) + \frac{1}{16} (3t_1 + 5t_2) \tau^{(0)}(\mathbf{r}) + \frac{1}{32} (5t_2 - 9t_1) \nabla^2 \rho^{(0)} + \frac{3}{16} t_3 [\rho^{(0)}]^2. \quad (4.2.19)$$

Let $r^{-1} u_k^{(0)}(\mathbf{r})$ denote the radial part of $\varphi_k^{(0)}(\mathbf{r})$. The function

$$u_k^{(L)}(\mathbf{r}) = [m_{Sk}^*(\mathbf{r})/m]^{1/2} u_k^{(0)}(\mathbf{r}) \quad (4.2.20a)$$

fulfills the equation [276]

$$\frac{1}{2m} \left\{ -\frac{d^2 u_k^{(L)}(\mathbf{r})}{dr^2} + \frac{l(l+1)}{r^2} u_k^{(L)}(\mathbf{r}) \right\} + \mathcal{V}_{HF}^{(L)}(\mathbf{r}; \varepsilon_k^{(0)}) u_k^{(L)}(\mathbf{r}) = \varepsilon_k^{(0)} u_k^{(L)}(\mathbf{r}), \quad (4.2.20b)$$

where $\mathcal{V}_{HF}^{(L)}$ is a local potential which depends linearly upon energy:

$$\mathcal{V}_{HF}^{(L)}(\mathbf{r}; E) = \mathcal{V}_{HF}^{(L)}(\mathbf{r}) + [1 - m_{Sk}^*(\mathbf{r})/m] E; \quad (4.2.21a)$$

the potential

$$\mathcal{V}_{\text{HF}}^{(L)}(r) = \frac{m_{\text{Sk}}^*(r)}{m} \left[\mathcal{V}_{\text{HF}}(r) - \frac{1}{8} m_{\text{Sk}}^*(r) \left\{ \frac{d}{dr} [m^*(r)]^{-1} \right\}^2 + \frac{1}{4} \frac{d^2}{dr^2} \{m_{\text{Sk}}^*(r)\}^{-1} \right] \quad (4.2.21b)$$

has a Woods-Saxon type shape.

Equations (2.20b)–(2.21a) show that the Skyrme–Hartree–Fock eigenvalues and potential scattering phase shifts can be computed from a local potential well whose depth is a linear function of energy. The “Skyrme effective mass” quoted in the literature refers to the nuclear matter value (3.7.28) of m_{Sk}^* at the saturation density $\rho^{(0)} = 0.17 \text{ fm}^{-3}$. Figure 4.2 shows the neutron single-particle energies in the valence shells of ^{208}Pb , in the case of the Skyrme III interaction ($m_{\text{Sk}}^*/m = 0.76$) and of the Skyrme V interaction ($m_{\text{Sk}}^*/m = 0.38$). As expected from our discussion in section 2.7, the calculated density of single-particle energies decreases with decreasing m_{Sk}^* and is smaller than the experimental one in both cases. We note that the Skyrme III interaction is rather successful in reproducing the ground states global properties ($E^{(0)}$ and $\rho^{(0)}(r)$) of ^{208}Pb and that it moreover approximately yields the empirical energy dependence of the mean field at positive energy, see eqs. (2.4.1) and (2.21a). Therefore, it appears logical to interpret the difference between the experimental and the Hartree–Fock single-particle energies as a signal that large dispersion corrections exist in the two valence shells of ^{208}Pb , i.e. in the domain

$$|E - \varepsilon_F| < 10 \text{ MeV} \quad (4.2.22)$$

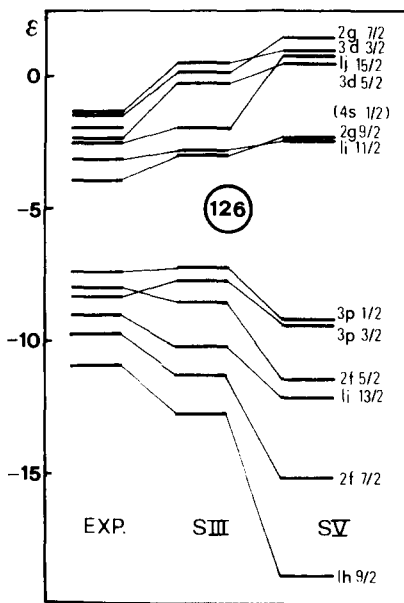


Fig. 4.2. Taken from ref. [19]. Comparison between the experimental single-neutron energies in the valence shells of ^{208}Pb (left, see fig. 2.6) and the values calculated in the Hartree–Fock approximation with a Skyrme III (SIII, middle) and a Skyrme V (SV, right) interaction.

where

$$\varepsilon_F = \frac{1}{2}(\varepsilon_F^+ + \varepsilon_F^-) \approx -5.6 \text{ MeV}. \quad (4.2.23)$$

One consequence of these dispersion corrections should be that the effective mass of the full single-particle field is enhanced in the vicinity of the Fermi energy.

4.2.5. Approximation for the dispersion corrections

4.2.5.1. Introduction

We have learned from the discussion of normal liquid ${}^3\text{He}$ and of the electron gas that the dispersion corrections can lead to a narrow enhancement of the effective mass near the Fermi energy provided that there exist low-lying core excited states which are strongly coupled to the single-particle motion. This is the case in medium-weight and heavy nuclei since they have strongly collective surface vibrations at low energy. In the present context, it is thus essential that the approximation scheme chosen for describing the dispersion corrections be such that the low-lying collective modes of the core are correctly described. This is usually done in the framework of the random phase approximation.

One approach of this type has been developed by N. Vinh Mau [145]. She starts from the infinite set of equations which couples the one-, two-, three-, ... body Green functions. This set is truncated by writing the three-body Green function G_3 as a sum of products $G_1 G_2$ [137]. This essentially amounts to assuming that it is sufficient to include the interaction between a pair of nucleons and that the correlation between this pair and a third particle can be neglected. We alluded to this type of approach at the end of section 3.15.4. It has been used in practically all the microscopic calculations of the dispersion corrections in medium-weight nuclei at low energy.

4.2.5.2. Random phase approximation

The full expression for the mass operator in the random phase approximation can be found in ref. [145]. Here, we only give this expression in the simple case of a Skyrme-type interaction (3.7.27a, b) when one omits the particle-particle and hole-hole ladders which lead to pairing vibrations. Furthermore, we set t_1 and t_2 equal to zero.

Let us call $\Psi_\lambda^{(A)}$ the eigenstates of H for the (A)-nucleon system as calculated in the random phase approximation, E_λ the corresponding excitation energy and $\rho_\lambda(r)$ the transition density defined by

$$\rho_\lambda(r) Y_{\lambda\mu}(\hat{r}) = \langle \Psi_0^{(A)} | a^+(r) a(r) | \Psi_\lambda^{(A)} \rangle. \quad (4.2.24)$$

The particle-hole interaction is obtained by taking the second functional derivative of $E^{(0)}$ with respect to the occupation number. It reads [277]

$$v(\mathbf{r}_1, \mathbf{r}_2) = v_T(r_{12}) \delta(\mathbf{r}_1 - \mathbf{r}_2), \quad (4.2.25a)$$

where the index T refers to the isospin of the particle-hole mode; one has

$$v_0(r) = \frac{3}{4}t_0 + \frac{3}{8}t_3 \rho^{(0)}(r), \quad (4.2.25b)$$

$$v_1(r) = -\frac{1}{4}t_0(1 + 2x_0) - \frac{1}{8}t_3 \rho^{(0)}(r), \quad (4.2.25c)$$

where we used the notation introduced in eqs. (3.7.27a, b) and (2.16).

The various terms which appear in the random phase approximation for the mass operator are represented in fig. 4.3. The corresponding algebraic expression is the following [96]

$$\mathcal{M}^{\text{RPA}}(\mathbf{r}, \mathbf{r}'; \omega) = V_{\text{HF}}(\mathbf{r}, \mathbf{r}') + \mathcal{N}^{\text{RPA}}(\mathbf{r}, \mathbf{r}'; \omega) - \mathcal{N}^{(2)}(\mathbf{r}, \mathbf{r}'; \omega), \quad (4.2.26)$$

where $\mathcal{N}^{(2)}$ is the second-order contribution, while

$$\mathcal{N}^{\text{RPA}}(\mathbf{r}, \mathbf{r}'; \omega) = \sum_{ljm} \mathcal{N}_{lj}^{\text{RPA}}(\mathbf{r}, \mathbf{r}'; \omega) \mathcal{Y}_{lj}^m(\hat{\mathbf{r}}) \mathcal{Y}_{lj}^{m*}(\hat{\mathbf{r}}'), \quad (4.2.27a)$$

$$\mathcal{N}_{lj}^{\text{RPA}}(\mathbf{r}, \mathbf{r}'; \omega) = \mathcal{N}_{lj}^{(a)}(\mathbf{r}, \mathbf{r}'; \omega) + \mathcal{N}_{lj}^{(b)}(\mathbf{r}, \mathbf{r}'; \omega), \quad (4.2.27b)$$

$$\begin{aligned} \mathcal{N}_{lj}^{(a)}(\mathbf{r}, \mathbf{r}'; \omega) &= \sum_c \sum_{\lambda \neq 0} n_>(c) \frac{u_c^{(0)}(\mathbf{r}) u_c^{(0)*}(\mathbf{r}')}{\omega - \varepsilon_c^{(0)} - E_\lambda + i\eta} v_0(\mathbf{r}) v_0(\mathbf{r}') \\ &\times |\langle l j \| Y_\lambda \| l_c j_c \rangle|^2 \rho_\lambda(\mathbf{r}) \rho_\lambda(\mathbf{r}'), \end{aligned} \quad (4.2.28a)$$

$$\begin{aligned} \mathcal{N}_{lj}^{(b)}(\mathbf{r}, \mathbf{r}'; \omega) &= \sum_h \sum_{\lambda \neq 0} n_<(h) \frac{u_h^{(0)}(\mathbf{r}) u_h^{(0)*}(\mathbf{r}')}{\omega - \varepsilon_h^{(0)} + E_\lambda - i\eta} v_0(\mathbf{r}) v_0(\mathbf{r}') \\ &\times |\langle l j \| Y_\lambda \| l_h j_h \rangle|^2 \rho_\lambda(\mathbf{r}) \rho_\lambda(\mathbf{r}'). \end{aligned} \quad (4.2.28b)$$

Here, $r^{-1} u_d^{(0)}(\mathbf{r})$ ($d = c$ or h) is the radial part of the Hartree–Fock single-particle wave function and we only included isoscalar core excitations.

4.2.5.3. Discussion

The upper indices (a) and (b) in eqs. (2.28a, b) have been used to emphasize the formal analogy with

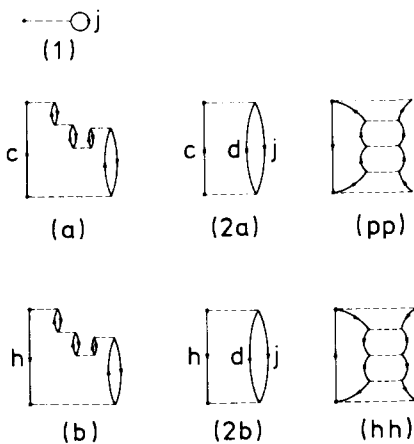


Fig. 4.3. Diagrammatic representation of the terms which are included in the random phase approximation for the mass operator. Graph (1) is the Hartree–Fock approximation. Graphs (a) and (b) are associated to expressions (2.28a) and (2.28b). The sum of the graphs (2a) and (2b) yields the second-order double-counting correction $\mathcal{N}^{(2)}$. The contribution of the particle–particle and hole–hole ladder graphs (pp) and (hh) have been omitted in the expressions given in section 4.2.5.2.

the case of uniform systems, see expressions (3.8.8) and (3.9.1). The core excited states are evaluated in the random phase approximation, which involves terms of arbitrary order in the strength of the effective interaction. In contrast, the interaction between the additional particle (or hole) and the core excited states is evaluated only up to second-order.

The approximation (2.28a, b) illustrates the analytic structure expected from our discussion in section 4.2.3. The (a)-component of the mass operator has poles at the energies $[E_\lambda + \epsilon_c^{(0)}]$ of the core excited states plus one additional nucleon. The imaginary part of $\mathcal{N}^{(a)}(r, r'; \omega)$ becomes different from zero when ω is larger than the minimum value of E_λ ($\lambda \neq 0$). The corresponding branch cut runs below the real axis.

The second-order contribution $\mathcal{N}^{(2)}$ on the right-hand side of eq. (2.26) has been introduced to avoid a double counting [96, 103, 145] of the second-order term. It has been interpreted as a nonorthogonality correction in ref. [105]. This term has many poles, located at the unperturbed two-particle one-hole and two-hole one-particle energies. The physical meaning of these poles is not obvious. They may introduce in the one-body Green function poles which have a residue larger than unity. This might be an indication that the approximation (2.26) is inappropriate if $\mathcal{N}^{(2)}$ is not negligible. It is usually found that $\mathcal{N}^{(2)}$ has only a small influence on all the calculated quantities, see e.g. [278]. In refs. [103, 145] the approximation (2.26) has been derived by starting from an exact expression for \mathcal{M} which involves G_1 , G_2 and G_3 ; G_3 was then approximated by a sum of products $G_1 G_2$. It is not obvious that the corresponding value \mathcal{M}^{RPA} of \mathcal{M} is related to the approximation of G_1 by the Dyson equation (2.6), see ref. [138].

4.2.5.4. Nuclear field theory

The collective excitations of the core can in many ways be considered as phonons. Hence, it is appealing to develop a theoretical framework in which the basic ingredients would be boson (vibration) and fermion (single-particle) degrees of freedom. This faces the following problem. Since the vibrations themselves are built from the single-particle degrees of freedom which already exhaust all nuclear degrees of freedom, the joint boson–fermion basis is overcomplete. Care must therefore be exercised to avoid double counting. This problem is handled by the “nuclear field theory”, see [279] and references contained therein. This theory is perturbative in nature. The expansion parameter is Ω^{-1} , where Ω is the effective degeneracy of the subspace allowed for the fermions.

In the nuclear field theory, a large fraction of the correlations is contained in the basis states. Each diagram of the perturbation expansion is a sum of many Feynman diagrams. For instance, graphs (c) and (d) of fig. 4.4 are sums of Feynman diagrams similar to those involved in the random phase approximation.

The nuclear field theory can include the coupling of single-particle states to pairing phonons; this coupling is represented by graphs (e) and (f) in fig. 4.4. The theory can cope with isovector as well as with isoscalar core excitations. The double counting correction $\mathcal{N}^{(2)}$ on the right-hand side of eq. (2.26) also appears in this approach [281].

4.2.5.5. Coupling to isoscalar vibrations

The low-lying collective core excitations are isoscalar. For these, the transition density (2.24) has the shape [61, 277]

$$\rho_\lambda(r) = \frac{\beta_\lambda R_0}{(2\lambda + 1)^{1/2}} \frac{dp^{(0)}(r)}{dr}. \quad (4.2.29a)$$

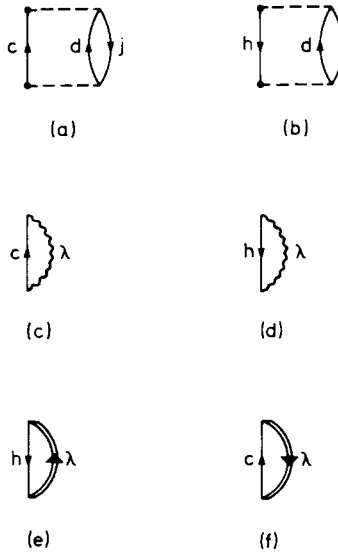


Fig. 4.4. Graphs which represent various contributions to the mass operator in the nuclear field theory. The sum of the graphs (a) and (b) yields the second-order contribution $\mathcal{N}^{(2)}$. Graphs (c) and (d) give the lowest-order dynamical correction in the particle-vibration model. Graphs (e) and (f) represent the coupling of a single-particle state to a pairing phonon [73, 280].

For these collective states, the particle-vibration coupling can be described by means of the zero-range transition potential

$$\delta U = \frac{\beta_\lambda R_0}{(2\lambda + 1)^{1/2}} \frac{dU_0(r_1)}{dr_1} Y_{\lambda\mu}(\hat{r}_1) \delta(r_1 - r_2) \quad (4.2.29b)$$

where $U_0(r)$ is a Woods-Saxon potential of depth ≈ 50 MeV and of radius R_0 , while β_λ characterizes the strength of the coupling.

The expression of the corresponding random phase approximation is summarized in refs. [282] and [283]. The calculations determine the excitation energies E_λ and the zero-point amplitudes $\beta_\lambda/(2\lambda + 1)^{1/2}$ associated with the vibration. The only free parameter is the ratio κ between the actual strength of the residual interaction and its self-consistent value (see eq. (6.74) of ref. [284]). This ratio can be adjusted in such a way that the isoscalar dipole mode, which corresponds to the motion of the centre of mass of the nucleus and thus to a spurious state, falls at zero excitation energy. In a self-consistent calculation κ would be equal to one. As shown in ref. [277] the transition potential (2.29b) provides with an accurate approximation to the function $v_0(r) \rho_\lambda(r) Y_{\lambda\mu}(\hat{r})$ appearing in eqs. (2.28a, b). The terms which are included in this approach are labelled (c) and (d) in fig. 4.4, where λ should then be an isoscalar collective mode.

4.3. The average nucleon-nucleus potential

4.3.1. Generalized optical-model potential

Our discussion of eq. (2.7) indicates that the mass operator $\mathcal{M}(\mathbf{r}, \mathbf{r}'; \omega)$ can be considered as a nucleon-nucleus potential for a nucleon with energy ω . However, it cannot be identified with the

empirical nucleon–nucleus potential. Indeed, the latter is rather simple while $\mathcal{M}(\mathbf{r}, \mathbf{r}'; \omega)$ is very complicated if dispersion corrections to the Hartree–Fock approximation are taken into account. In particular, it has many poles for real values of ω . For $\omega < 0$, these poles are related to bound state energies. In the domain $0 < \omega < \varepsilon_i^+$ they lead to narrow resonances in the elastic scattering cross section. For ω larger than ε_i^+ , $\mathcal{M}(\mathbf{r}, \mathbf{r}'; \omega)$ still has a wild ω -dependence since it has poles close to the branch cut on the unphysical sheet; these poles correspond to resonances in the elastic and inelastic cross sections.

Hence, the mass operator $\mathcal{M}(\mathbf{r}, \mathbf{r}'; \omega)$ cannot be identified with the shell-model or the optical-model potential. It should be identified with the quantity called the “generalized” optical-model potential in nuclear reaction theory [100, 106, 107, 285–287].

4.3.2. Optical-model potential

By definition, the optical-model potential is required to yield the energy average $\langle S_{pp}(E) \rangle$ of $S_{pp}(E)$ in the interval $E - \frac{1}{2}\Delta \leq E \leq E + \frac{1}{2}\Delta$. If one defines $\langle S_{pp}(E) \rangle$ by

$$\langle S_{pp}(E) \rangle = \frac{\Delta}{2\pi} \int_{-\infty}^{\infty} \frac{S_{pp}(E')}{(E - E')^2 + \frac{1}{4}\Delta^2} dE', \quad (4.3.1)$$

one has [78]

$$\langle S_{pp}(E) \rangle = S_{pp}(E + \frac{1}{2}i\Delta). \quad (4.3.2)$$

Equations (2.7), (2.8a) and (3.2) suggest that the optical-model potential at the energy E can be identified with the quantity

$$V_{HF}(\mathbf{r}, \mathbf{r}') + \mathcal{N}(\mathbf{r}, \mathbf{r}'; E + \frac{1}{2}i\Delta) = \mathcal{M}(\mathbf{r}, \mathbf{r}'; E + \frac{1}{2}i\Delta), \quad (4.3.3)$$

see eq. (1.2). This was foreseen by Bell and Squires [48] and is indeed a good approximation [107, 288, 289]. This is indicated by the model which has been discussed in section 2.11 in the case of bound states, and that we now extend to elastic scattering.

4.3.3. Doorway state model

Let us consider the following model. We call

$$H_0 = t + V_{HF} \quad (4.3.4)$$

the model Hamiltonian, v the residual interaction, H the full Hamiltonian, see eq. (2.11.2). We denote by $|\phi_0\rangle$ and $|\phi_\alpha\rangle$ ($\alpha = 1, \dots, M$) bound normalized eigenstates of H_0 and by $|\chi_E\rangle$ scattering eigenstates of H_0

$$H_0 |\phi_0\rangle = E_0 |\phi_0\rangle, \quad (4.3.4a)$$

$$H_0 |\phi_\alpha\rangle = E_\alpha |\phi_\alpha\rangle, \quad (4.3.4b)$$

$$H_0 |\chi_E\rangle = E |\chi_E\rangle, \quad \langle \chi_E | \chi_{E'} \rangle = \delta(E - E'). \quad (4.3.4c)$$

We assume that

$$\langle \phi_\alpha | v | \chi_E \rangle = 0 \quad (\alpha = 1, \dots, M), \quad (4.3.4d)$$

$$\langle \phi_\alpha | H | \phi_{\alpha'} \rangle = \varepsilon_\alpha \delta_{\alpha\alpha'} \quad (\alpha, \alpha' = 1, \dots, M), \quad (4.3.4e)$$

$$\langle \phi_0 | v | \phi_0 \rangle = \varepsilon_0, \quad (4.3.4f)$$

and use the notation

$$\langle \phi_0 | v | \phi_\alpha \rangle = v_{\alpha 0}, \quad (4.3.4g)$$

$$\langle \phi_0 | v | \chi_E \rangle = v_0(E). \quad (4.3.4h)$$

Equations (3.4d) and (3.4h) imply that the complicated states $|\phi_\alpha\rangle$ ($\alpha = 1, \dots, M$) are coupled to the continuum $|\chi_E\rangle$ only via the “doorway” configuration $|\phi_0\rangle$. We assume that the target is a pure shell-model configuration. In the standard theoretical example of a doorway state, $|\phi_0\rangle$ is a two particle–one hole state. With minor redefinitions, the formulae below are also valid in the case when $|\phi_0\rangle$ is a single-particle configuration [290]. This is the case that we now consider.

The scattering matrix of this model is given by [29, 107, 289]

$$S_{pp}(E) = \exp(2i\delta) G_p(E)/[G_p(E)]^*, \quad (4.3.5)$$

where δ is the potential scattering phase shift due to the Hartree–Fock field, while

$$G_p(E) = \left[E - \varepsilon_0 - F_0(E) - \sum_{\alpha=1}^M \frac{v_{\alpha 0}^2}{E - \varepsilon_\alpha} \right]^{-1}, \quad (4.3.6)$$

where

$$F_0(E) = \int_0^\infty \frac{v_0^2(E')}{E - E' + i\eta} dE' \quad (4.3.7a)$$

$$= f_0 - \frac{1}{2}i\Gamma_0^\uparrow, \quad (4.3.7b)$$

with

$$\Gamma_0^\uparrow = 2\pi v_0^2(E), \quad f_0 = \mathcal{P} \int_0^\infty \frac{v_0^2(E')}{E - E'} dE'. \quad (4.3.8)$$

It can be checked that $G_p(E)$ is the particle part of the one-body Green function of the model, see eq. (3.2.16) [32].

The quantity F_0 arises from the coupling of $|\phi_0\rangle$ to the continuum; Γ_0^\uparrow is called the escape width. If F_0 is set to zero, one recovers the model of section 2.11, see eq. (2.11.34). The dispersion contribution to the self-energy is given by

$$M_p(E) = F_0(E) + \sum_{\alpha=1}^M \frac{v_{\alpha 0}^2}{E - \varepsilon_\alpha}; \quad (4.3.9)$$

if one makes the plausible assumptions that δ , f_0 and Γ_0^\uparrow are independent of energy in the domain of interest, the poles of $G_p(E)$ are identical to those of $S_{pp}(E)$. They correspond to the $(M+1)$ compound nuclear resonances of the model.

4.3.4. Quasiparticle energies in nuclei

Equations (3.2) and (3.5) show that the poles of the energy average $\langle S_{pp}(E) \rangle$ are the same as the poles of $G_p(E + \frac{1}{2}i\Delta)$. If the approximations used in connection with eqs. (2.11.11), (2.11.12), (2.11.22) and (2.11.23) are valid, one has

$$G_p(E + \frac{1}{2}i\Delta) = \{E - \varepsilon_0 - f_0 - \delta_0 E + \frac{1}{2}i[\alpha + \Gamma_0^\uparrow + \Gamma_0^\downarrow]\}^{-1}. \quad (4.3.10)$$

This quantity has a pole located at the energy $\tilde{E}_0 - \frac{1}{2}i(\Delta + \Gamma_0)$, with

$$\tilde{E}_0 = \varepsilon_0 + f_0 + \delta_0 E \quad (4.3.11a)$$

$$\Gamma_0 = \Gamma_0^\uparrow + \Gamma_0^\downarrow. \quad (4.3.11b)$$

In a finite system, it is convenient to introduce a shell-model representation, cf. eq. (1.4a):

$$G_{\alpha\alpha'}(\omega) = G_{ij}^{nn'}(\omega) \delta_{ii'} \delta_{jj'}. \quad (4.3.12)$$

Engelbrecht and Weidenmüller [32] define the energy \mathcal{E}_{Nlj} of a quasiparticle with quantum numbers l, j as a pole of $g_{ij}^{nn'}(\omega \pm \frac{1}{2}i\Delta)$, where the plus sign corresponds to $\omega > \varepsilon_F$ and the minus sign to $\omega < \varepsilon_F$. For E close to $\text{Re } \mathcal{E}_{Nlj}$, one can write (if $\text{Im } \mathcal{E}_{Nlj}$ is sufficiently small) [32]

$$G_{ij}^{nn'}\left(\omega + \frac{i}{2}\Delta\right) \approx \frac{\langle n|N\rangle \langle N|n'\rangle}{E - \mathcal{E}_{Nlj}} [Z_{Nnn'}^{ij} + iY_{Nnn'}^{ij}]^{-1} + G_{Nnn'}^{B,ij}(\omega) \quad (4.3.13)$$

where

$$Z_{Nlj}^{nn'} + iY_{Nlj}^{nn'} = \left[1 - \frac{d}{d\omega} \mathcal{N}_{nn'}^{ij}(\omega) \right]_{\omega=\mathcal{E}_{Nlj}}^{-1}, \quad (4.3.14)$$

compare with eqs. (3.4.15) and (3.20.36).

4.3.5. Quasiparticle wave functions

The quantities $\langle n|N\rangle$ give the coefficients of the shell-model representation of the quasiparticle wave

function $\varphi_{Nlj}(r)$:

$$\varphi_{Nlj}(r) = \sum_n \langle n | N \rangle \varphi_{nlj}^{(0)}(r). \quad (4.3.15)$$

These wave functions are complex; they become real and normalizable in the limit $\text{Im } \mathcal{E}_{Nlj} \rightarrow 0$. Even in that limit, however, they are not orthogonal because $\mathcal{M}_{nn}^{lj}(\omega + \frac{1}{2}i\Delta)$ depends upon ω . A very rough estimate yields [32]

$$\langle \varphi_{nlj} | \varphi_{(n+1)lj} \rangle \approx |Z_{lj}^{nn} - 1|. \quad (4.3.16)$$

In the following, we assume for simplicity that $\mathcal{M}_{lj}^{nn'}(\omega + \frac{1}{2}i\Delta)$ is diagonal in the principal quantum numbers n, n' and usually drop any explicit reference to n .

4.3.6. Discussion

The model discussed above and the one described in section 2.11 show that in the case of bound as well as of scattering states the quasiparticle energies should be defined as the poles of $G_{lj}(\omega \pm \frac{1}{2}i\Delta)$ which lie close to the real axis. One can then closely follow the discussion carried out in section 3.4 in the case of uniform systems. In keeping with eqs. (1.2) and (1.4a, b) let us call $\mathcal{N}_{lj}(\omega)$ the shell-model representation of the dispersion corrections to the Hartree–Fock field. The one-body Green function reads

$$G_{lj}(\omega) = \{\omega - \varepsilon_{lj}^{(0)} - \mathcal{N}_{lj}(\omega)\}^{-1}. \quad (4.3.17)$$

We introduce the notation

$$\Delta V_{lj}(\omega) \equiv \Delta V(\omega, lj) = \text{Re } \mathcal{N}_{lj}(\omega + \frac{1}{2}i\Delta), \quad (4.3.18a)$$

$$W_{lj}(\omega) \equiv |\text{Im } \mathcal{N}_{lj}(\omega + \frac{1}{2}i\Delta)|. \quad (4.3.18b)$$

The quasiparticle approximation to $G_{lj}(\omega)$ is given by

$$G_{lj}^{\text{QP}}(\omega) = \frac{Z_{lj}}{\omega - \varepsilon_{lj} + \frac{1}{2}i[2Z_{lj}W_{lj}(\varepsilon_{lj}) + \Delta]}, \quad (4.3.19)$$

where

$$\varepsilon_{lj} = \varepsilon_{lj}^{(0)} + \Delta V_{lj}(\varepsilon_{lj}), \quad (4.3.20)$$

$$Z_{lj} = \left\{ 1 - \frac{d}{d\omega} \Delta V_{lj}(\omega) \right\}_{\omega=\varepsilon_{lj}}^{-1}. \quad (4.3.21)$$

The corresponding approximation to the spectral function is

$$S_{ij}^{\text{OP}}(\omega) = (2\pi)^{-1} \frac{Z_{ij}^2(2W_{ij}(\varepsilon_{ij}) + \Delta)}{(\omega - \varepsilon_{ij})^2 + \frac{1}{4}[2Z_{ij}W_{ij}(\varepsilon_{ij}) + \Delta]^2}. \quad (4.3.22)$$

As in section 3.8.2.4, we shall occasionally distinguish between two main types of contributions to $\mathcal{N}_{ij}(\omega)$:

$$\mathcal{N}_{ij}(\omega) = \mathcal{N}_{ij}^{(a)}(\omega) + \mathcal{N}_{ij}^{(b)}(\omega). \quad (4.3.23)$$

They have the main property that

$$W_{ij}^{(a)}(\omega) = 0 \quad \text{for } \omega < \varepsilon_F, \quad (4.3.24a)$$

$$W_{ij}^{(b)}(\omega) = 0 \quad \text{for } \omega > \varepsilon_F. \quad (4.3.24b)$$

4.3.7. Dispersion relation

Let us for definiteness consider the random phase approximation (2.26) and omit the second-order correction $\mathcal{N}^{(2)}$. One has

$$\Delta V_{ij}^{(a)}(\omega) = \text{Re} \sum_{c_+} \frac{|\langle 0_+ | v | c_+ \rangle|^2}{\omega - E_{c_+} + \frac{1}{2}i\Delta} + \frac{\mathcal{P}}{\pi} \int_{\varepsilon_F^-}^{\infty} \frac{W_{ij}^{(a)}(\omega')}{\omega - \omega'} d\omega' \quad (4.3.25a)$$

$$\Delta V_{ij}^{(b)} = \text{Re} \sum_{c_-} \frac{|\langle 0_- | v | c_- \rangle|^2}{\omega - E_{c_-} - \frac{1}{2}i\Delta} + \frac{\mathcal{P}}{\pi} \int_{-\infty}^{\varepsilon_F^-} \frac{W_{ij}^{(b)}(\omega')}{\omega - \omega'} d\omega'. \quad (4.3.25b)$$

Here, we use a schematic notation [91] where $|c_+\rangle$ denotes a bound state of the $(A+1)$ nucleus (in the random phase approximation, see the crosses in fig. 4.1), while $|0_+\rangle$ represents the ground state of nucleus (A) coupled to a Hartree–Fock single-particle state with quantum numbers (l, j) . Similarly, $|c_-\rangle$ is a bound state of the $(A-1)$ nucleus (in the random phase approximation, see full dots in fig. 4.1), while $|0_-\rangle$ represents the ground state of (A) coupled to a Hartree–Fock single-hole state with quantum numbers (l, j) . One has

$$W_{ij}^{(a)}(\omega) = \pi \sum_{c_+} \langle 0_+ | v | c_+ \rangle^2 \delta(\omega - E_{c_+}), \quad (4.3.26a)$$

$$W_{ij}^{(b)}(\omega) = \pi \sum_{c_-} \langle 0_- | v | c_- \rangle^2 \delta(\omega - E_{c_-}). \quad (4.3.26b)$$

Equation (3.25a) was first derived by Feshbach [106] in the case of the generalized optical-model potential, i.e. in the limit $\Delta \rightarrow 0$.

On the basis of the model developed in section 2.11, it has been proposed in ref. [91] to replace the first term on the right-hand sides of eqs. (3.25a) by

$$\frac{\mathcal{P}}{2\pi} \int_{\varepsilon_F^+}^{\varepsilon_i^+} \frac{\Gamma_{ij}^\downarrow(\omega')}{\omega - \omega'} d\omega', \quad (4.3.27a)$$

where

$$\Gamma_{ij}^\downarrow(\omega') = 2W_{ij}(\omega') \quad (4.3.27b)$$

is the spreading width of the quasibound single-particle state with quantum numbers (l, j) , see eqs. (2.11.17) and (2.11.21). This assumption enables one to write

$$\Delta V_{ij}^{(a)}(\omega) \approx \frac{\mathcal{P}}{\pi} \int_{\varepsilon_F^+}^{\infty} \frac{W_{ij}^{(a)}(\omega')}{\omega - \omega'} d\omega'. \quad (4.3.28a)$$

Similarly, one obtains

$$\Delta V_{ij}^{(b)} \approx \frac{\mathcal{P}}{\pi} \int_{-\infty}^{\varepsilon_F^-} \frac{W_{ij}^{(b)}(\omega')}{\omega - \omega'} d\omega'. \quad (4.3.28b)$$

In view of eqs. (3.24a, b), there is no need to attach an index (a) or (b) to $W_{ij}(\omega)$, although we shall occasionally do so. These dispersion relation type equations are formally identical to the relations (3.8.27), (3.9.9) which were encountered in the case of a uniform medium.

In practice the parameters of the effective interaction which enters in the Hartree–Fock field V_{HF} are chosen in such a way that the Hartree–Fock approximation to the Fermi energy ε_F is approximately equal to the empirical value. Hence, it is useful to define the dispersion corrections via the following subtracted dispersion relations (see eq. (3.8.27))

$$\Delta V_{ij}^{(a)}(\omega) = (\varepsilon_F^+ - \omega) \frac{\mathcal{P}}{\pi} \int_{\varepsilon_F^+}^{\infty} \frac{W_{ij}(\omega')}{(\omega' - \varepsilon_F^+) (\omega' - \omega)} d\omega', \quad (4.3.29a)$$

$$\Delta V_{ij}^{(b)}(\omega) = (\varepsilon_F^- - \omega) \frac{\mathcal{P}}{\pi} \int_{-\infty}^{\varepsilon_F^-} \frac{W_{ij}(\omega')}{(\omega' - \varepsilon_F^-) (\omega' - \omega)} d\omega'. \quad (4.3.29b)$$

The full dispersion correction is given by

$$\Delta V_{lj}(\omega) = \Delta V_{lj}^{(a)}(\omega) + \Delta V_{lj}^{(b)}(\omega); \quad (4.3.30)$$

it is very small for $\omega = \varepsilon_F$.

4.4. Dispersion relation approach

4.4.1. Introduction

The real part of the dispersion correction can be evaluated from eqs. (3.29a, b) if the quantities $W_{lj}(\omega)$ are known. In the “dispersion relation approach” of refs. [64, 90, 91, 291] it is assumed that $W_{lj}(\omega)$ is independent of the quantum numbers l and j . This has the following two consequences.

(i) $\mathcal{N}(\mathbf{r}, \mathbf{r}'; \omega + \frac{1}{2}i\Delta)$ is local:

$$\mathcal{N}(\mathbf{r}, \mathbf{r}'; \omega \pm \frac{1}{2}i\Delta) \approx [\Delta V(\mathbf{r}; \omega) \mp i W(\mathbf{r}; \omega)] \delta(\mathbf{r} - \mathbf{r}'). \quad (4.4.1)$$

(ii) For $\omega > 0$, the quantity $W(\mathbf{r}; \omega)$ can be identified with the modulus of the empirical value of the imaginary part of the optical-model potential. For $\omega < 0$, one can estimate $W(\omega)$ from the spreading widths of the quasibound single-particle states, or extract it from theoretical models. Here, we ignore the fact that there exists a difference of a factor m/m_{HF}^* between the value of $W(\mathbf{r}; \omega)$ and the empirical value (see (3.5.14)); this is indeed compensated by a factor m_{HF}^*/m by which one should multiply $\Delta V(\mathbf{r}; \omega)$ before adding it to the local equivalent of the Hartree–Fock potential, see eqs. (3.5.14) and (3.5.23) [91].

4.4.2. Validity of the basic assumption

The basic assumption of the dispersion relation approach is that $\text{Im } \mathcal{N}(\mathbf{r}, \mathbf{r}'; \omega + \frac{1}{2}i\Delta) = W(\mathbf{r}, \mathbf{r}'; \omega + \frac{1}{2}i\Delta)$ is local. The accuracy of this approximation must be evaluated by referring to microscopic calculations or by comparing the results of the approach with empirical data.

One can construct local potentials which yield the same eigenvalues and elastic scattering phase shift as nonlocal ones provided that their nonlocality is sufficiently simple, see ref. [7] and section 3.5.2. Hence, the fact that experimental elastic scattering and total cross sections can be fitted with the help of local optical-model potentials only implies that the nonlocality of $\mathcal{N}(\mathbf{r}, \mathbf{r}'; \omega + \frac{1}{2}i\Delta)$ is rather simple for $\omega > 0$. It could for instance be similar to that encountered in the case of nuclear matter, i.e. have approximately a Gaussian dependence upon $|\mathbf{r} - \mathbf{r}'|$ [102]. This is confirmed by recent microscopic calculations [103–105]. The dispersion relation approach could be extended to include this type of nonlocality.

In the domain $\varepsilon_{\text{t}}^- < \omega < \varepsilon_{\text{t}}^+$ which includes the two valence shells, the number of core states which can effectively be excited is not large. Angular momentum and parity conservation can then play a significant role. Therefore, the possibility cannot be excluded that the dependence of $\Delta V_{lj}(\omega)$ (and correspondingly of $W_{lj}(\omega)$) upon l and j could be large and unpredictable. However, figs. 2.6 and 4.2 suggest that this is not the case. Indeed, they show that even in the valence shells the dependence of the single-particle energies upon l and j is not very strong in the case of ^{208}Pb , in the sense that the energy shift between the Hartree–Fock single-particle energies $\varepsilon_{nlj}^{(0)}$ and the experimental single-particle energies ε_{nlj} appear to depend mainly upon the difference $\varepsilon_{nlj} - \varepsilon_F$ rather than upon the quantum numbers l and j . This is exhibited in figs. 4.5a and 4.5b. There, the full dots show the dependence upon

$\varepsilon_{nlj} - \varepsilon_F$ of the difference

$$\Delta\varepsilon_{nlj} = (\varepsilon_{nlj} - \varepsilon_F) - (\varepsilon_{nlj}^{(0)} - \varepsilon_F^{(0)}) \quad (4.4.2)$$

in the case of neutrons and of protons in ^{208}Pb . The energies $\varepsilon_{nlj}^{(0)}$ have been computed from a Woods-Saxon potential whose depth depends linearly upon energy:

$$V^{(0)}(r; E) = \frac{V^0 + \beta(E - \varepsilon_F)}{1 + \exp[(r - R)/a]} \quad (4.4.3)$$

We argued in section 4.2 that the potential (4.3) yields eigenvalues $\varepsilon_{nlj}^{(0)}$ which are quite close to those which result from a Skyrme-Hartree-Fock potential with effective mass

$$m_{\text{Sk}}^*/m = 1 - \beta. \quad (4.4.4)$$

The full dots in figs. 4.5a, b define an average trend exhibited by the dashed curve. The calculation of this average is the aim of the dispersion relation approach. If the fluctuations of $\Delta\varepsilon_{nlj}$ about the average were as large as the average itself, it would be meaningless to try to approximately account for the polarization and correlation effects by introducing a simple correction to the Hartree-Fock potential well.

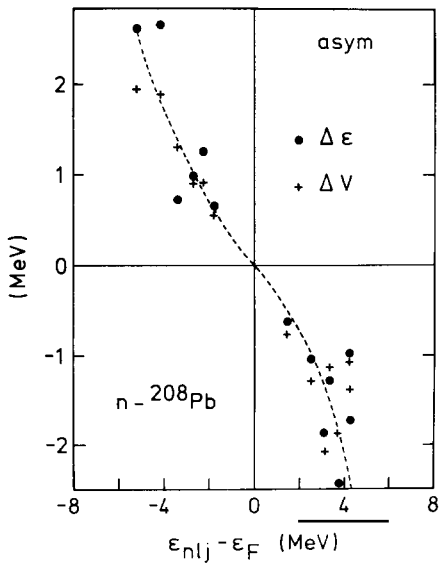


Fig. 4.5a. Adapted from ref. [291]. The full dots represent the dependence upon $\varepsilon_{nlj} - \varepsilon_F$ of the quantity $\Delta\varepsilon_{nlj}$ defined by eq. (4.2), in the case of neutrons in ^{208}Pb . The first-order energies $\varepsilon_{nlj}^{(0)}$ have been computed from the Woods-Saxon potential (4.3), with $\beta = 0.37$. The dashes sketch the average behaviour of $\Delta\varepsilon_{nlj}$. The crosses have been computed from the dispersion relation approach, see eq. (4.15).

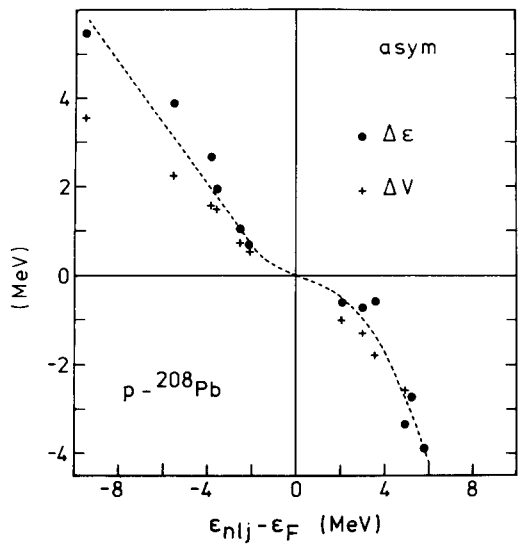


Fig. 4.5b. Adapted from ref. [291]. Same as fig. 4.5a, for protons in ^{208}Pb . In this case $\beta = 0.43$.

4.4.3. Imaginary part of the potential at negative energy

In light- and medium-weight nuclei one can measure experimentally the spreading width Γ_{ij}^j of bound quasiparticle states. Equation (3.27b) then yields empirical values for $W_{ij}(\varepsilon_{ij})$ for $\varepsilon_{ij} < 0$. The full dots in fig. 4.6 show a compilation of these values for nuclei with mass number $12 \leq A \leq 60$; the open dots correspond to the imaginary part of empirical optical-model potentials. The lines are simply drawn through the empirical values. It is remarkable that they are symmetric with respect to $E = \varepsilon_F$. This feature also holds if one considers ^{40}Ca alone rather than a compilation which involves many nuclei [91].

This symmetry had already been encountered in the case of a uniform medium, see fig. 3.19. It reflects the property that the phase space for nucleon decay of e.g. $^{207}\text{Pb}^*$ and $^{209}\text{Pb}^*$ is approximately the same at the same excitation energy. In the case of nuclear matter, the symmetry is restricted to $\omega - \omega_F < 80$ MeV because momentum conservation makes $W^{(b)}(E)$ vanish for large $|E - \varepsilon_F|$. This restriction may also exist in nuclei. Microscopic calculations of $W^{(a)}(\omega)$ and of $W^{(b)}(\omega)$ in ^{208}Pb also lead to values which are approximately symmetric with respect to ε_F in the case of protons in ^{208}Pb for $|E - \varepsilon_F| < 20$ MeV, see fig. 4.54 below. This justifies the approximation made in the dispersion relation approach that the imaginary part of the optical-model potential is symmetric about the Fermi energy ε_F in the energy range $|E - \varepsilon_F| \leq 30$ MeV [64, 90, 91, 291].

4.4.4. Volume integrals

4.4.4.1. Imaginary part

The elastic scattering cross sections are not very sensitive to the detailed geometrical shape of the optical-model potential well [295]. They mainly depend upon the volume integral per nucleon of the real and of the imaginary parts:

$$J_V(E) = 4\pi A^{-1} \int V(r; E) r^2 dr, \quad (4.4.5a)$$

$$J_W(E) = 4\pi A^{-1} \int W(r; E) r^2 dr. \quad (4.4.5b)$$

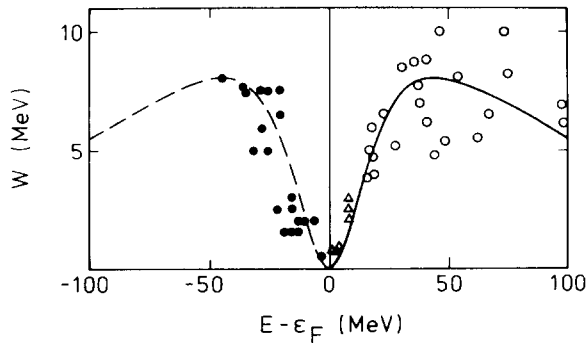


Fig. 4.6. Taken from ref. [90]. Dependence upon $E - \varepsilon_F$ of the strength of the imaginary part of the optical-model potential for nuclei with mass number $12 \leq A \leq 60$. The full dots are obtained from the spreading widths compiled in ref. [25]. The triangles are derived from neutron strength functions [292, 293]. The open dots are deduced from the analysis of elastic scattering cross sections [294].

Figure 4.7 shows the dependence upon $(E - \varepsilon_F^+)$ of J_W in the case of protons in ^{208}Pb . In the domain $E - \varepsilon_F^+ < 30$ MeV, the empirical values have been fitted with polynomials of the form

$$J_W = \sum_{n=N}^{N+4} a_n (E - \varepsilon_F^+)^n. \quad (4.4.6a)$$

The upper part of fig. 4.7 corresponds to $N = 4$, the lower part to $N = 2$.

In the domain $E - \varepsilon_F^+ > 30$ MeV, two extrapolations have been considered. The dashed curve in fig. 4.7 decreases like

$$J_W(E) \sim (E - \varepsilon_F^+) \exp(E - \varepsilon_F^+) \quad (4.4.6b)$$

for large E . The full curve in fig. 4.7 has the following asymptotic behaviour for large $|E|$

$$J_W(E) \sim (E - \varepsilon_F^+)^{1/2}; \quad (4.4.6c)$$

this mocks up the effect of a hard core in the nucleon-nucleon interaction, see eq. (3.4.19) and fig. 3.53. The difference between the results obtained from the two extrapolations will give an indication of the importance played by the highly excited core states, see sections 3.16 and 4.5.4.

In all cases, it is assumed that for $E < \varepsilon_F^-$ the value of J_W is the symmetric with respect to ε_F of the

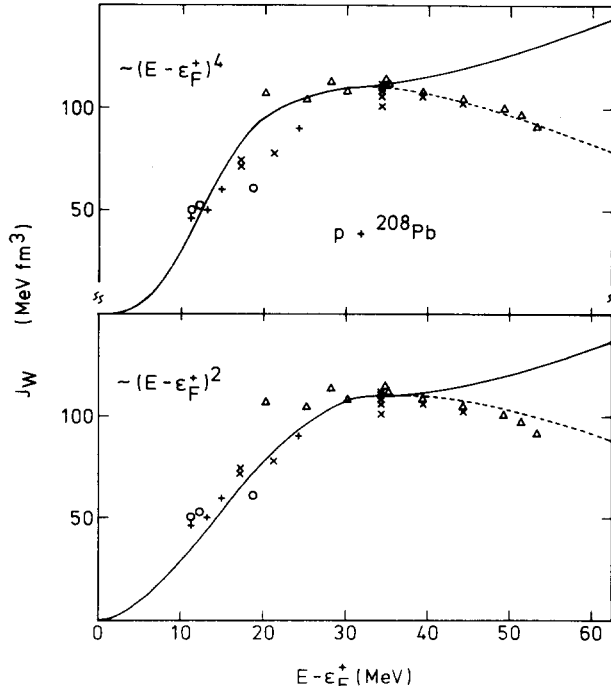


Fig. 4.7. Taken from ref. [291]. Dependence upon $E - \varepsilon_F^+$ of the quantity J_W in the case of protons in ^{208}Pb . The dots, triangles and crosses are empirical values and the curves are different fits, as explained in the text (see eqs. (4.6a, b, c)).

parametrization which corresponds to eqs. (4.6a, b). The results shown below correspond to the “asymmetric” case in which the parametrization corresponding to (4.6b) is adopted for $E < \varepsilon_F^- - 30$ MeV while the parametrization associated with (4.6c) is adopted for $E > \varepsilon_F^+ + 30$ MeV.

4.4.4.2. Real part

The volume integral per nucleon of the real part of the sum of the dispersion corrections can be computed from the volume integral of eqs. (3.29a, b). The result is shown in fig. 4.8 for the two parametrizations of J_w shown in fig. 4.7.

This dispersion correction must be added to the volume integral per nucleon of the local equivalent of the Hartree–Fock field. The latter is approximately a linear function of energy:

$$J_{HF}(E) = J_{HF}^{(0)} + \alpha(E - \varepsilon_F). \quad (4.4.7a)$$

The parameter $J_{HF}^{(0)}$ is fitted to the empirical value of the Fermi energy. The parameter α is determined by the energy dependence of the empirical optical-model potential for $E - \varepsilon_F \approx 40$ MeV. This yields the curves shown in fig. 4.9a. The corresponding values of α are 3.9 fm^3 (full curve) and 4.4 fm^3 (dash-and-dot curve).

The binding energy of a single-particle state mainly depends upon the volume integral of the shell-model potential well. It is, however, slightly influenced by the geometrical shape of the potential. In fig. 4.9a the volume integral per nucleon has been taken from ref. [296]. In fig. 4.9b, the dots for $E - \varepsilon_F > 10$ MeV are taken from the real part of an empirical optical-model potential determined from proton elastic scattering experiments [66]. The dots for $E - \varepsilon_F < 10$ MeV are obtained by fitting the observed energies of the bound proton single-particle states with a potential well which has the same geometrical shape as the one used for scattering states [64]. The curve is drawn by eye through these empirical points. The energy dependence of the average effective mass derived from this curve is in good agreement [64] with the one calculated from the dispersion relation approach and shown in fig. 4.10 below.

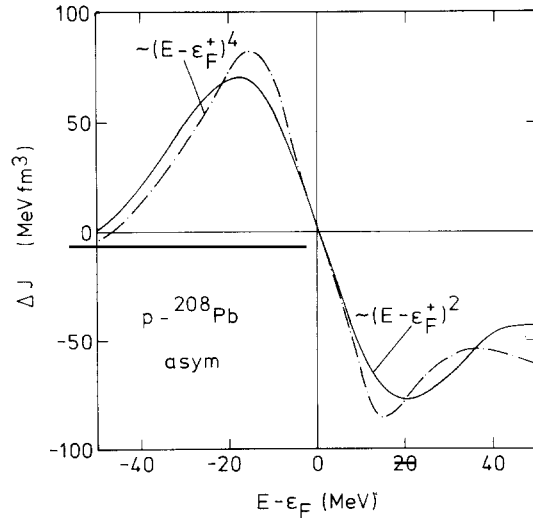


Fig. 4.8. Taken from ref. [291]. Dependence upon $E - \varepsilon_F^\pm$ of the volume integral per nucleon of the sum of the dispersion corrections (a) and (b) in the case of protons in ^{208}Pb , as evaluated from eqs. (3.29a, b) with the inputs shown in fig. 4.7.

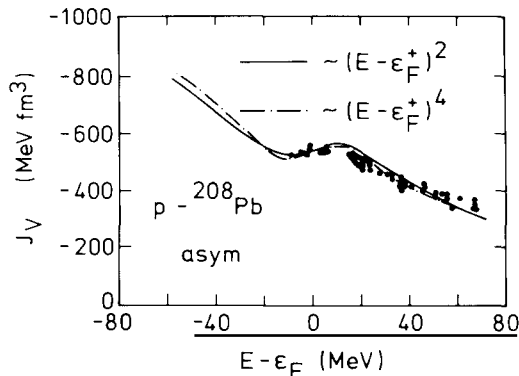


Fig. 4.9a. Taken from ref. [291]. Energy dependence of the volume integral per nucleon of the real part of the optical-model potential, in the case of protons in ^{208}Pb . The dots are empirical values [296]. The curves are obtained from the dispersion relation approach. The full line uses as input the bottom of fig. 4.7, while the dashed curve is derived from the top of fig. 4.7.

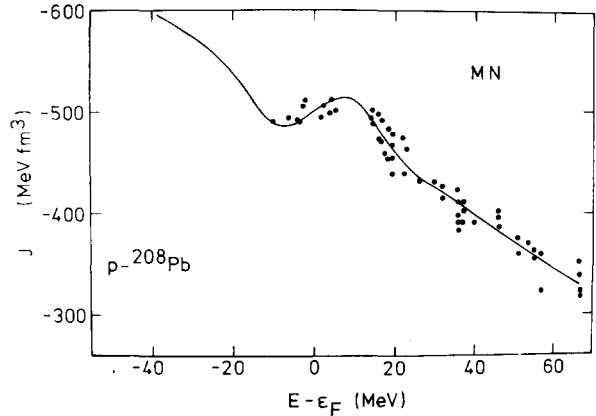


Fig. 4.9b. Adapted from ref. [64]. Dependence upon $E - \epsilon_F$ of empirical values of the volume integral per nucleon of the real part of an optical-model potential whose depth is determined by $p - ^{208}\text{Pb}$ scattering experiments ($E - \epsilon_F > 10$ MeV) [66] and by the observed single-particle energies for protons in ^{208}Pb , see fig. 2.6. The shape of the potential well is the same for all the dots, in contrast to the case of fig. 4.9a. The curve is drawn by eye through the empirical points.

4.4.4.3. The average ω -mass

The volume integral per nucleon J_V is related to the depth V_0 of the Woods-Saxon potential by

$$V_0 = G J_V \quad (4.4.7b)$$

where G is a purely geometrical coefficient. In the case of the parametrization (2.7.11) one has

$$G = (9.25)^{-1} \text{ fm}^{-3}. \quad (4.4.7c)$$

The coefficients α of eq. (4.7a) and β of eq. (4.3) are related by

$$\beta = G\alpha \approx 1 - m_{Sk}^*/m \quad (4.4.7d)$$

where m_{Sk}^* is the Skyrme-Hartree-Fock effective mass, see eq. (4.4). The full curve in fig. 4.9 corresponds to $m_{Sk}^*/m = 0.57$ and the dash-and-dot line to $m_{Sk}^*/m = 0.52$. The difference between these values and the effective mass for neutrons ($m_{Sk}^*/m \approx 0.7$, see ref. [291]) can be ascribed to the energy dependence of the symmetry potential.

One can associate an average ω -mass to the value of ΔJ plotted in fig. 4.8 via the definition

$$\langle m_\omega(E)/m \rangle = 1 - G_\Delta \frac{d}{dE} [\Delta J(E)]. \quad (4.4.8)$$

The geometric factor G_Δ is different from G since in general $\Delta V(r; E)$ does not have a Woods-Saxon shape; we shall see that the radial shape of $\Delta V(r; E)$ is energy-dependent. The authors of ref. [291]

took

$$G_\Delta = (9.5)^{-1} \text{ fm}^{-3} \quad (4.4.7e)$$

which is intermediate between the value (4.7c) and that associated with the derivative of a Woods-Saxon potential well. This yields the values of $\langle m_\omega(E)/m \rangle$ shown in fig. 4.10. Since the value (4.7e) of G_Δ is somewhat arbitrary, the ordinate scale of fig. 4.10 only has a semi-quantitative meaning. Figure 4.10 exhibits the property that the average ω -mass for protons in ^{208}Pb has a narrow enhancement in the vicinity of the Fermi energy. A similar result holds for neutrons in ^{208}Pb [91]. Figure 4.9a (see also fig. 4.9b and fig. 1 of ref. [64]) shows that the calculated enhancement is in semi-quantitative agreement with the empirical data.

It is of interest to plot separately the contributions of the corrections (a) and (b) to the average ω -mass, see eqs. (3.29a, b). These contributions are shown in fig. 4.11 in the case of neutrons in ^{208}Pb . The curves are in keeping with the discussion carried out in sections 3.8 and 3.9, compare with figs. 3.22 and 3.24.

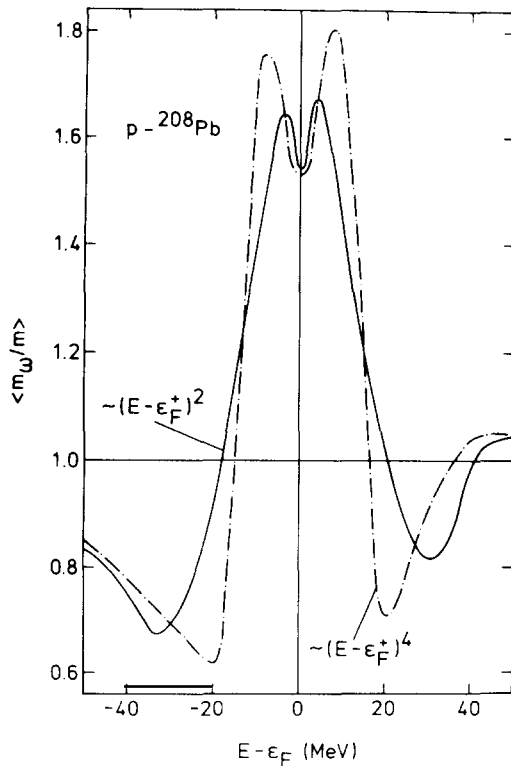


Fig. 4.10. Taken from ref. [291]. Energy dependence of the average ω -mass defined by eq. (4.8), in the case of protons in ^{208}Pb and as derived from the curves shown in fig. 4.8.

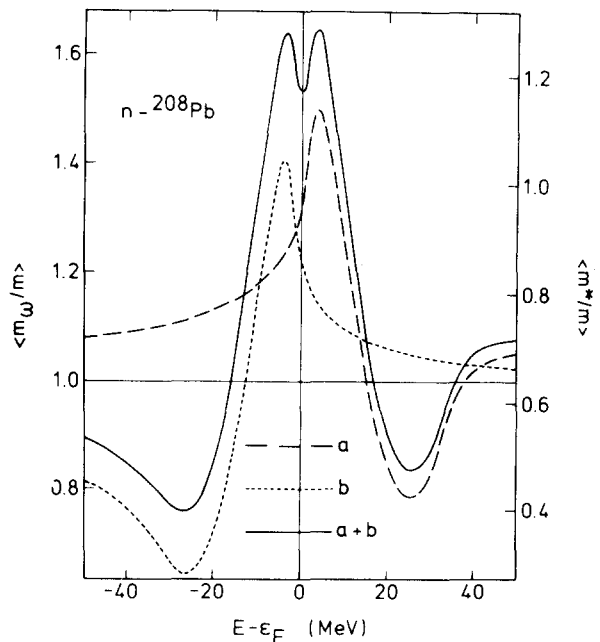


Fig. 4.11. Taken from ref. [91]. The full curve represents the energy dependence of the average ω -mass (left-hand scale) of neutrons in ^{208}Pb , using as input values of $J_W(E)$ which vanish as $(E - \epsilon_F^+)^2$ at low energy. The other curves show the contributions (a) (long dashes) and (b) (short dashes) of eqs. (3.29a) and (3.29b). The right-hand scale gives the average effective mass as estimated from $\langle m^*/m \rangle = \langle m_\omega/m \rangle - \beta$, with $\beta = 0.37$ (see fig. 4.5a).

4.4.5. Radial dependence

Within the basic approximation (4.1) of the dispersion relation approach, the radial dependence of $\Delta V(r; E)$ can be obtained from eqs. (3.29a, b):

$$\Delta V^{(a)}(r; E) = (\varepsilon_F^+ - E) \frac{\mathcal{P}}{\pi} \int_{\varepsilon_F^+}^{\infty} \frac{W^{(a)}(r; E')}{(E' - \varepsilon_F^+)(E' - E)} dE', \quad (4.4.9a)$$

$$\Delta V^{(b)}(r; E) = (\varepsilon_F^- - E) \frac{\mathcal{P}}{\pi} \int_{-\infty}^{\varepsilon_F^-} \frac{W^{(b)}(r; E')}{(E' - \varepsilon_F^-)(E' - E)} dE', \quad (4.4.9b)$$

$$\Delta V(r; E) = \Delta V^{(a)}(r; E) + \Delta V^{(b)}(r; E). \quad (4.4.10)$$

On the right-hand side of eq. (4.9a), $W^{(a)}(r; E')$ is the imaginary part of the empirical optical-model potential. It is assumed in refs. [91, 291] that $W^{(b)}(r; \varepsilon_F^- - E') = W^{(a)}(r; E' - \varepsilon_F^+)$ in the domain $|E' - \varepsilon_F| < 30$ MeV. For large $|E'|$, we shall consider the case in which it is assumed that $W^{(b)}(E')$ decreases (see eq. (4.6b)) and that $W^{(a)}$ increases (see eq. (4.6c)). This “asymmetric” assumption is not crucial; approximately the same results are obtained in the “symmetric” case when $W^{(a)}(E')$ is assumed to decrease for large E' [90, 91, 291]. This is in keeping with the discussion carried out in section 3.16.

The values of $\Delta V(r; E)$ obtained from eqs. (4.9a, b) and (4.10) are shown in fig. 4.12 for several values of $E - \varepsilon_F$, in the case of neutrons in ^{208}Pb . While the value of ΔV at the nuclear centre is a monotonically decreasing function of energy, its energy dependence at the nuclear surface is quite complicated. It is therefore useful to introduce the r -dependent ω -mass $m_\omega(r; E)$ defined by the

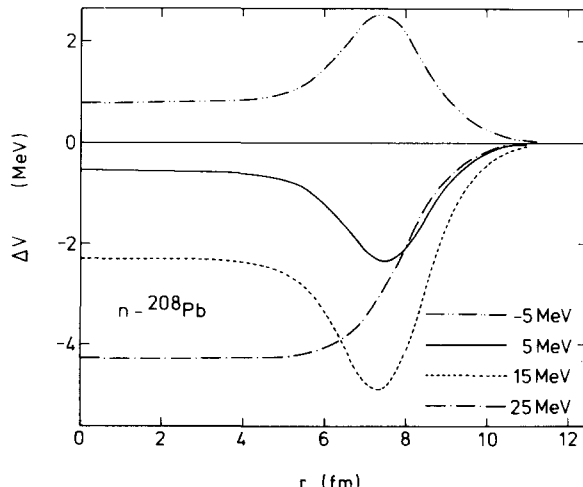


Fig. 4.12. Taken from ref. [91]. Radial dependence of the dispersion correction to the Hartree–Fock potential in the case of neutrons in ^{208}Pb , for $E - \varepsilon_F = -5, +5, +15$ and $+25$ MeV.

following relation

$$\frac{m_\omega(r; E)}{m} = 1 - \frac{d}{dE} [\Delta V(r; E)], \quad (4.4.11)$$

see eq. (1.5). The energy dependence of $m_\omega(r; E)$ in the case of neutrons in ^{208}Pb is plotted in figs. 4.13 and 4.14 for $r = 0$ and for $r = 7.54$ fm, respectively. At the nuclear centre, the ω -mass $m_\omega(0; E)$ has a very broad enhancement, comparable to the one found in the case of nuclear matter (see e.g. figs. 3.22, 3.24). The value of $m_\omega(0; E)$ is almost independent of E in the domain $-20 \text{ MeV} < E - \epsilon_F < 20 \text{ MeV}$. At the nuclear surface, $m_\omega(R_W; E)$ has a narrow enhancement peak. This indicates that near the Fermi energy the dispersion correction mainly arises from the coupling of the single-particle to low-lying surface vibrations of the core.

We now turn to the real part of the full quasiparticle potential. It is given by

$$V(r; E) = V_{\text{HF}}^{(0)}(r; E) + \Delta V(r; E). \quad (4.4.12)$$

Here, $V_{\text{HF}}^{(0)}(r; E)$ is the local equivalent of the Hartree–Fock potential, see eq. (2.21a). It can be approximated by the Woods–Saxon potential $V^{(0)}(r; E)$ given by eq. (4.3). The difference between the energy dependence of $m_\omega(0; E)$ and of $m_\omega(R_W; E)$ implies that the radial shape of $\Delta V(r; E)$ is a sensitive function of E in the vicinity of the Fermi energy. This is confirmed in fig. 4.15, which shows that $\Delta V(r; E)$ has the shape of a Woods–Saxon potential to which a surface term is added. This implies

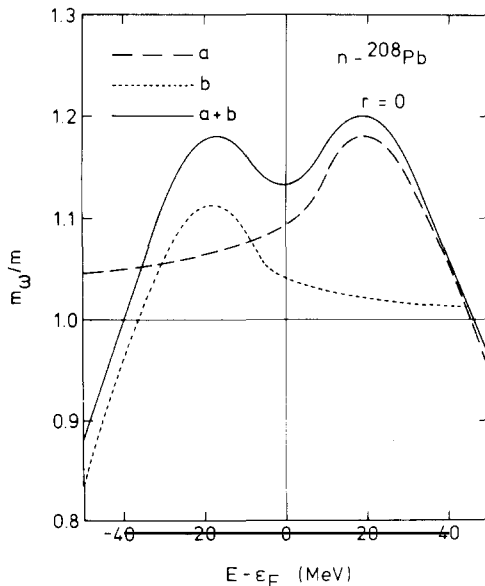


Fig. 4.13. Taken from ref. [91]. The full curve shows the energy dependence of the value $m_\omega(r = 0; E)$ of the ω -mass at the nuclear centre in the case of neutrons in ^{208}Pb . The other curves give the contributions $m_\omega^{(a)}(E)/m$ of $\Delta V^{(a)}$ (eq. (4.9a), long dashes) and of $m_\omega^{(b)}(E)/m$ of $\Delta V^{(b)}$ (eq. (4.9b), short dashes).

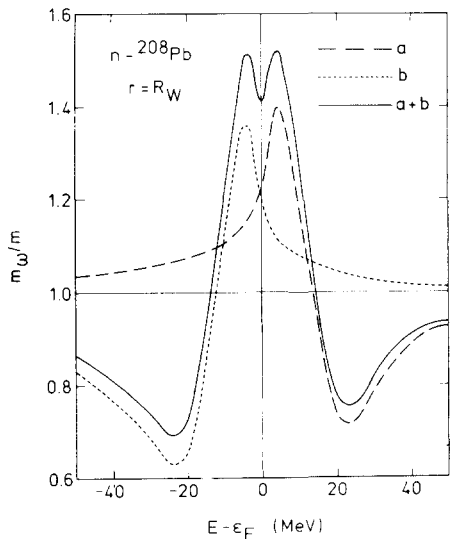


Fig. 4.14. Taken from ref. [91]. The full curve shows the energy dependence of the value $m_\omega(r = R_W; E)$ of the ω -mass at the nuclear surface ($R_W = 7.54$ fm), in the case of neutrons in ^{208}Pb . The other curves give the contributions of $\Delta V^{(a)}$ (eq. (4.9a), long dashes) and of $\Delta V^{(b)}$ (eq. (4.9b), short dashes).

that the full potential (4.12) has a Woods-Saxon shape; the effect of $\Delta V(r; E)$ is to modify the surface geometry of $V(r; E)$ (as compared to $V^0(r; E)$) for E close to the Fermi energy [298]. This is exhibited in fig. 4.16.

4.4.6. Shell occupation probability

Recent electron scattering experiments yield information on the probability n_{lj} that a given proton subshell is occupied [299]. The discussion contained in section 3.11 can be extended to finite systems. The occupation probability of the subshell $\{l, j\}$ is given by

$$n_{lj}^{(a)} \approx \left\{ 1 + \frac{d}{d\omega} \Delta V_{lj}^{(a)}(\omega) \right\}_{\omega=\epsilon_{lj}} \quad (4.4.13a)$$

for $\omega < \epsilon_F^-$, i.e. for shells which are fully occupied in the independent particle approximation, see eq. (3.11.4). It is given by

$$n_{lj}^{(b)} \approx \left\{ - \frac{d}{d\omega} \Delta V_{lj}^{(b)}(\omega) \right\}_{\omega=\epsilon_{lj}} \quad (4.4.13b)$$

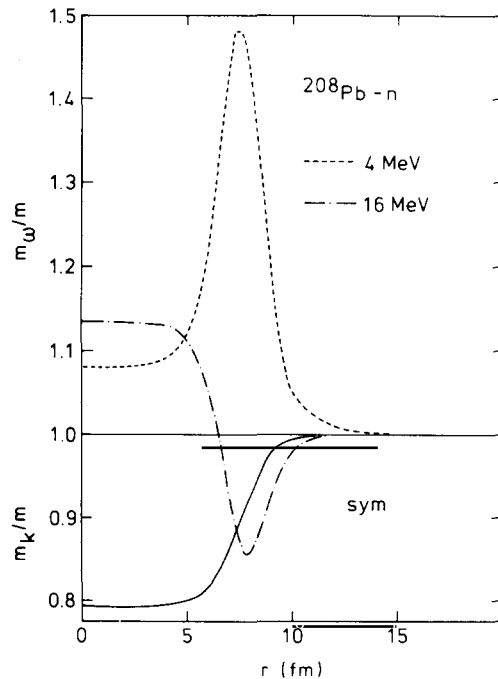


Fig. 4.15. Taken from ref. [297]. Radial dependence of the ω -mass in the case of neutrons in ^{208}Pb for $E - \epsilon_F = 4$ MeV (short dashes) and $E - \epsilon_F = 16$ MeV (dash-and-dot). The full curve represents a typical radial dependence of the Skyrme-Hartree-Fock effective mass, see eq. (2.18).

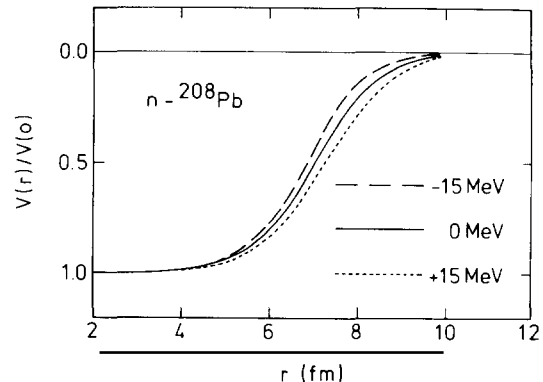


Fig. 4.16. Taken from ref. [91]. Radial dependence of the full quasiparticle potential $V(r; E)/V(0; E)$ in the case of neutrons in ^{208}Pb . In eq. (4.12), $V_F^{(1)}$ has been identified with $V^0(r; E)$ (see eq. (4.3) where $V^0 = -51$ MeV, $\beta = 0.37$) and is represented by the full curve. The long dashes correspond to $E - \epsilon_F = -15$ MeV and the short dashes to $E - \epsilon_F = +15$ MeV.

for $\omega > \epsilon_F^+$, i.e. for subshells which are unoccupied in the independent particle approximation, see eq. (3.11.8).

In the dispersion relation approach these expressions are approximated by

$$n_{lj} \approx n(\epsilon_{lj}) = 2 - \langle m_\omega^{(a)}(\epsilon_{lj})/m \rangle \quad (4.4.14a)$$

for $\epsilon_{lj} < \epsilon_F$, and by

$$n_{lj} \approx n(\epsilon_{lj}) = \langle m_\omega^{(b)}(\epsilon_{lj})/m \rangle - 1 \quad (4.4.14b)$$

for $\epsilon_{lj} > \epsilon_F$, see eqs. (3.11.6) and (3.11.7). Figure 4.17 shows the function $n(E)$ as calculated from the values $\langle m_\omega^{(a)}(E)/m \rangle$ and of $\langle m_\omega^{(b)}(E)/m \rangle$ which had been plotted in fig. 4.11. We note the similarity with the case of nuclear matter (see figs. 3.33–3.35) and of the electron gas (see figs. 3.75 and 3.76).

4.4.7. Single-particle energies

If one assumes that the dispersion correction $\Delta V(r; E)$ is sufficiently small to be treated in first-order perturbation theory, the associated energy shift can be approximated by the expression

$$\Delta V_{nlj} = \langle \varphi_{nlj}^{(0)} | \Delta V(r; \epsilon_{nlj}^{(0)}) | \varphi_{nlj}^{(0)} \rangle, \quad (4.4.15)$$

where $\varphi_{nlj}^{(0)}$ is the normalized eigenstate associated with the Woods–Saxon potential (4.3). The values of ΔV_{nlj} are represented by the crosses in figs. 4.5a and 4.5b; they fall rather close to the average behaviour of $\Delta \epsilon_{nlj}$ (eq. (4.2)) represented by the dashed line. This confirms the semi-quantitative success of the dispersion relation approach.

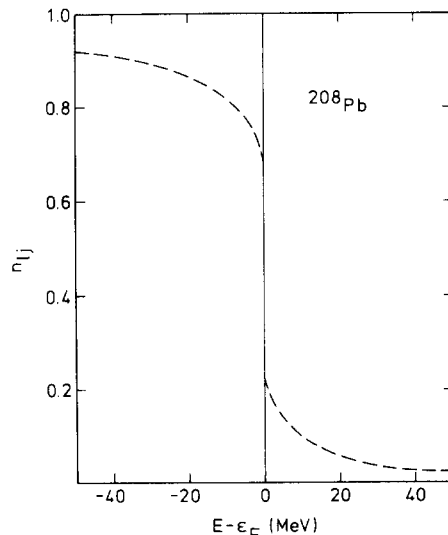


Fig. 4.17. Taken from ref. [300]. Dependence upon $E - \epsilon_F$ of the orbit occupation probability $n(E)$ as defined by eqs. (4.14a, b), in the case of neutrons in ^{208}Pb . Here, E is the binding energy of the single-particle orbit.

For the sake of comparison with other calculations, we show in fig. 4.18a the observed neutron single-particle energies in ^{208}Pb (see fig. 2.6), the Hartree–Fock single-particle energies $\varepsilon_{nlj}^{(0)}$ as calculated from the Woods–Saxon potential well (4.3) (with $\beta = 0.37$, $V^0 = -44$ MeV and the geometry (3.3.1)) and the quasiparticle energies

$$\varepsilon_{nlj} = \varepsilon_{nlj}^{(0)} + \Delta V_{nlj}. \quad (4.4.16)$$

An average particle–hole energy gap can be defined by the difference

$$\Delta\omega = \langle \varepsilon_p \rangle - \langle \varepsilon_h \rangle, \quad (4.4.17)$$

with

$$\langle \varepsilon_p \rangle = \sum_{\text{uno}} (2j+1) \varepsilon_{nlj} / \sum_{\text{uno}} (2j+1), \quad (4.4.18a)$$

$$\langle \varepsilon_h \rangle = \sum_{\text{occ}} (2j+1) \varepsilon_{nlj} / \sum_{\text{occ}} (2j+1), \quad (4.4.18b)$$

where “uno” and “occ” refer to the subshells of the normally “unoccupied” and “occupied” valence shells, respectively. One has with obvious notations

$$\Delta\omega_{\text{obs}} = 6.50 \text{ MeV}, \quad (4.4.19a)$$

$$\Delta\omega^{(0)} = 9.64 \text{ MeV}, \quad (4.4.19b)$$

$$\Delta\omega = 6.65 \text{ MeV}; \quad (4.4.20a)$$

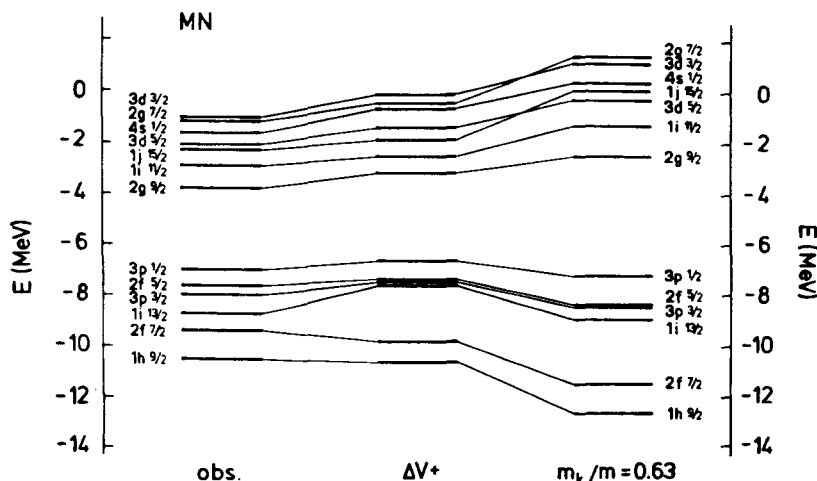


Fig. 4.18a. Adapted from ref. [291]. Neutron quasiparticle energies in ^{208}Pb . The observed values (see fig. 2.6) are shown at the left-hand side, and the Hartree–Fock values $\varepsilon_{nlj}^{(0)}$ of the right-hand side ($m_k/m = 1 - \beta = 0.63$, see eq. (4.3)). The middle column gives the quasiparticle energies as calculated from the dispersion relation approach, see eq. (4.16).

the latter value is the one derived from eqs. (4.16), (4.18b). The dispersion correction therefore brings the average particle hole gap in close agreement with the observed value. This also holds for protons in ^{208}Pb [291].

We note that the ratio

$$\Delta\omega^{(0)}/\Delta\omega = 1.45 \quad (4.4.20b)$$

is in fair agreement with the average value $\langle m_\omega(E)/m \rangle$ of the ω -mass near the Fermi energy, see fig. 4.11. We recall that the value of $\langle m_\omega(E)/m \rangle$ (not its E -dependence) depends upon the choice of the geometrical parameter G_Δ in eq. (4.7e). In the vicinity of the Fermi energy, $\Delta V(r; E)$ is surface-peaked. Therefore, the value $G_\Delta = (9.5)^{-1} \text{ fm}^{-3}$ is an overestimate, whence also the value of $\langle m_\omega(E)/m \rangle$ shown in fig. 4.11.

The centroid energies (4.18a) and (4.18b) are essentially the first moments of the distribution of the energies ε_{nlj} of the orbits of each valence shell. The variance of this distribution is defined by

$$\sigma_p^2 = \sum_{\text{uno}} (2j+1) [\varepsilon_{nlj} - \langle \varepsilon_p \rangle]^2, \quad (4.4.21a)$$

$$\sigma_h^2 = \sum_{\text{occ}} (2j+1) [\varepsilon_{nlj} - \langle \varepsilon_h \rangle]^2. \quad (4.4.21b)$$

The variance measures the bunching of the single-particle energies within the shell [301]. The gross features of each valence shell can then be represented by assuming that the single-particle energies ε_{nlj} of the shell have a Gaussian distribution with centroid $\langle \varepsilon_p \rangle$ (or $\langle \varepsilon_h \rangle$) and variance σ_p (or σ_h). Figure 4.18b shows the Gaussians which are obtained from, respectively, the Hartree–Fock approximation, the

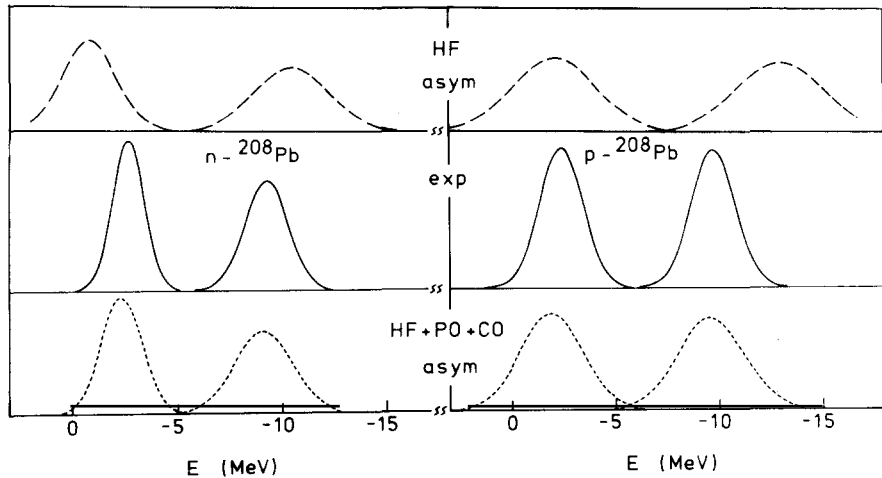


Fig. 4.18b. Adapted from ref. [291]. Gross structure of the valence shells for neutrons (left) and protons (right) in ^{208}Pb , as obtained by assuming a Gaussian distribution of the single-particle energies in each shell, with centroid $\langle \varepsilon_p \rangle$ (or $\langle \varepsilon_h \rangle$) and with variance σ_p (or σ_h), see eqs. (4.18a, b) and (4.21a, b). The observed single-particle energies yield the full curves in the middle part of the figure. The Hartree–Fock approximation is shown at the top, while the curves at the bottom include the dispersion corrections.

observed energies and the dispersion relation approach. The dispersion corrections yield a good agreement between the calculated and the observed centroids. They also reduce, but not sufficiently, the variance as compared to its Hartree-Fock value. It should be kept in mind that the variance depends sensitively upon the geometry assumed for $V_{\text{HF}}^{(L)}(r; E)$ and upon the spin-orbit coupling.

4.4.8. Schematic models

The results presented in section 4.4.4 are analogous to those obtained in the case of nuclear matter. Hence, the schematic models which have been discussed in section 3.10.5 are also useful in the case of nuclei.

This was first used by Brown and Rho [113] who pointed out that the algebraic formula (3.10.27), namely

$$W^{\text{BR}} = \frac{d(E - \varepsilon_F)^2}{(E - \varepsilon_F)^2 + E_0^2}, \quad (4.4.22a)$$

with

$$d = 12 \text{ MeV}, \quad E_0 = 22.4 \text{ MeV}, \quad (4.4.22b)$$

yields a good fit to the empirical points shown in fig. 4.6. The dispersion integral

$$\Delta V(E) = (E - \varepsilon_F) \frac{\mathcal{P}}{\pi} \int_{-\infty}^{\infty} \frac{W^{\text{BR}}(E')}{(E' - \varepsilon_F)(E - E')} dE' \quad (4.4.23)$$

can be calculated analytically and yields

$$\Delta V^{\text{BR}}(E) = -d \frac{E_0(E - \varepsilon_F)}{(E - \varepsilon_F)^2 + E_0^2}. \quad (4.4.24)$$

The corresponding ω -mass

$$m_{\omega}^{\text{BR}}(E)/m = 1 - \frac{d}{dE} \Delta V^{\text{BR}}(E) \quad (4.4.25)$$

is plotted in fig. 4.19 for the parameter values (4.22). This result is quite close to the one which had been computed in ref. [90] from the curves shown in fig. 4.6.

This schematic model omits the particle-hole gap associated in a given nucleus to the difference between the energy ε_F^- of the last occupied orbit and the energy ε_F^+ of the first unoccupied orbit. One can take approximately that difference into account by writing

$$\Delta V(E) = \Delta V^{(\text{a})}(E) + \Delta V^{(\text{b})}(E), \quad (4.4.26a)$$

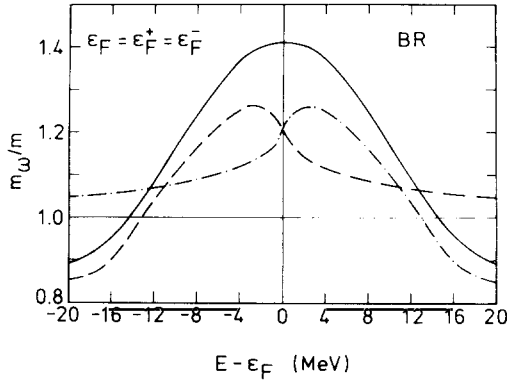


Fig. 4.19. Taken from ref. [115]. The full curve shows the energy dependence of the ω -mass as calculated from the schematic model of Brown and Rho, see eqs. (3.10.27), (4.22a) and (4.23). The parameter values (4.22b) are adapted to a range of nuclei with mass numbers $12 \leq A \leq 60$, see fig. 4.6. The dash-and-dot and the dashed curves give the contributions of $\Delta V^{(a)}$ and of $\Delta V^{(b)}$ obtained by setting $\epsilon_F^+ = \epsilon_F^- = \epsilon_F$ in eqs. (4.26b) and (4.26c), respectively.

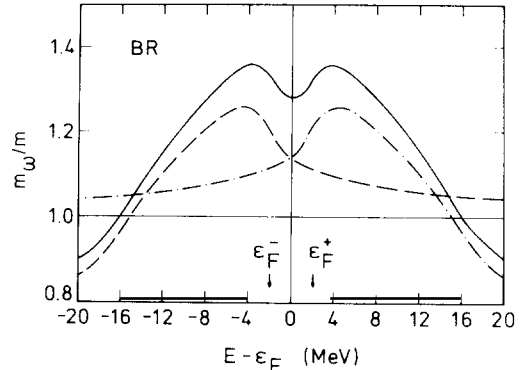


Fig. 4.20. Taken from ref. [115]. Energy dependence of the ω -mass in the schematic model defined by eqs. (4.26a)–(4.27c). The arrows point to the values adopted for ϵ_F^+ and ϵ_F^- .

with

$$\Delta V^{(a)}(E) = (E - \epsilon_F) \int_{\epsilon_F^+}^{\infty} \frac{W^{(a)}(E')}{(E' - \epsilon_F)(E - E')} dE', \quad (4.4.26b)$$

$$\Delta V^{(b)}(E) = (E - \epsilon_F) \int_{-\infty}^{\epsilon_F^-} \frac{W^{(b)}(E')}{(E' - \epsilon_F)(E - E')} dE'. \quad (4.4.26c)$$

The ω -mass associated with expression (3.26a) is plotted in fig. 4.20 for the same functional form (4.22a) of $W(E')$, more precisely for

$$W^{(a)}(E') = d \frac{(E' - \epsilon_F^+)^2}{(E' - \epsilon_F^+)^2 + E_0^2} \theta(E' - \epsilon_F^+), \quad (4.4.27a)$$

$$W^{(b)}(-E') = W^{(a)}(E'), \quad (4.4.27b)$$

and for the differences

$$\epsilon_F^+ - \epsilon_F = \epsilon_F - \epsilon_F^- = 2 \text{ MeV}, \quad (4.4.27c)$$

adapted to the case of neutrons in ^{208}Pb . The enhancement of the ω -mass now presents one bump on each side of ϵ_F , in qualitative agreement with the results shown in fig. 4.11.

The parameter values (4.22b) have been fitted to the empirical data contained in fig. 4.6. These correspond to a set of light nuclei. Figure 4.21 shows that the value (22.4 MeV) of the parameter E_0 given in eq. (4.22b) is too large for the case of ^{208}Pb , for which $E_0 \approx 12$ MeV would be more appropriate. The lowering of the value of E_0 with increasing A mainly reflects the decreasing value of the average excitation energy of the most collective core excitations.

Figure 4.21 also shows two other fits. The long dashes correspond to the following schematic model [115]

$$W^{\text{JM}}(E) = 9 \frac{(E - \epsilon_F)^4}{(\epsilon - \epsilon_F)^4 + 13.27^4} \text{ MeV}. \quad (4.4.28)$$

The full curve in fig. 4.21 corresponds to the schematic model (3.10.28a, b) which had been fitted in ref. [114] to values of $W(E)$ calculated in a microscopic model in the energy domain $0 < E - \epsilon_F < 10$ MeV. The ω -masses associated with the three schematic models of fig. 4.21 are shown in fig. 4.22. The origin of the difference between the dashed curve and the dash-and-dot line is the same as that of the difference between figs. 4.20 and 4.21, namely the fact that expression (4.28) rises much more slowly than expression (4.22a) for E close to ϵ_F . The narrow dip presented by the full curve in fig. 4.22 for $E \approx 9$ MeV reflects the existence of a peak in the corresponding $W(E)$, see figs. 4.21 and 3.28. The fact that the value of $m_\omega(E)$ at $E = \epsilon_F$ is smaller for the full curve than for the two other cases is due to the smaller values taken by the corresponding $W(E)$ for $E > 10$ MeV [115].

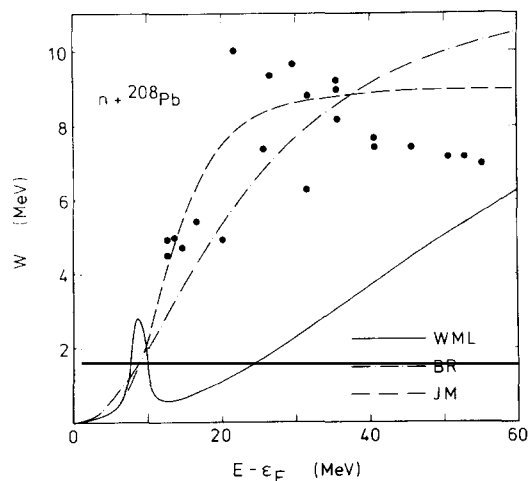


Fig. 4.21. Taken from ref. [115]. The dots show the strength of the imaginary part of the empirical optical-model potential as obtained by multiplying by the geometrical factor $G_\Delta = (9.5)^{-1} \text{ fm}^{-3}$ the volume integrals plotted in fig. 4.7. The dash-and-dot curve represents the schematic model defined by eqs. (4.22a, b). The long dashes correspond to the schematic model (4.28). The full curve shows the schematic model defined by eqs. (3.10.28a, b) which has been illustrated in fig. 3.28.

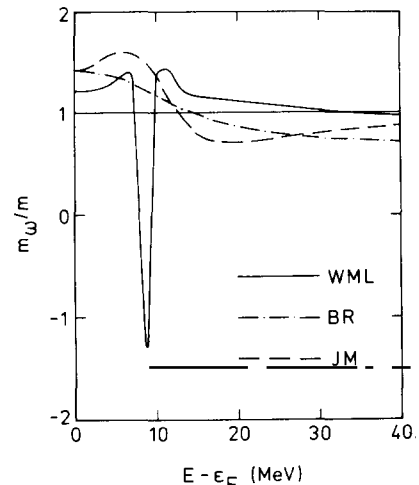


Fig. 4.22. Taken from ref. [115]. The three curves represent the dependence of the ω -mass in the case of the three schematic models for W shown in fig. 4.21.

4.4.9. Discussion

The dispersion relation approach can only deal with average properties of quasiparticle levels. In its present form, it neglects the nonlocality of the dispersion corrections and, by the same token, any dependence upon the orbital angular momentum and the parity of the subshells. It could be improved by including simple forms of nonlocality.

Even in its present simplified form, the dispersion relation approach turns out to be quite successful as far as the average of the empirical properties of quasiparticles in ^{208}Pb are concerned. It predicts that the ω -mass at the nuclear surface presents a narrow enhancement which is centred near the Fermi energy and has a width equal to about 10 MeV. In view of the similarity between the dispersion relation approach and the case of uniform systems, we expect from sections 3.19 and 3.20 that this width is closely related to the average excitation energy of collective core excitations. Since these are surface vibrations, it is natural that the narrow enhancement of the ω -mass takes place at the nuclear surface.

4.5. Core excitations in ^{208}Pb

4.5.1. Introduction

Figure 4.2 shows that the dispersion corrections increase the density of quasiparticle energies as compared to the Hartree–Fock approximation. This is reflected in an increase of the effective mass near the Fermi energy. The discussion of normal liquid ^3He and of electrons in metals (sections 3.19 and 3.20) makes one expect that low-lying collective core excitations play a dominant role in determining the height and the width of the enhancement of the effective mass. In the present section, we briefly survey the results of some microscopic calculations of the low-lying collective excitations of ^{208}Pb . These calculations have all been carried out in the framework of the random phase approximation. They differ mainly by the choice of the unperturbed single-particle energies, of the particle–hole coupling and of the size of the configuration space.

4.5.2. Experimental information

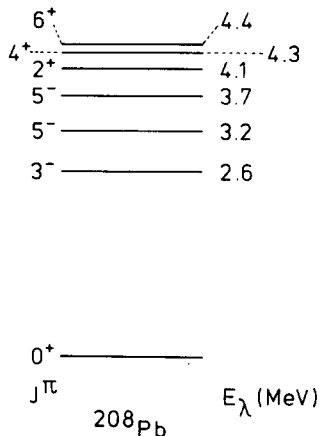
The low-lying collective states of ^{208}Pb are strongly excited in inelastic hadron and electron scattering. The experimental values of the excitation energy, angular momentum and parity of these states are shown in fig. 4.23 and in table 4.1, and their $B(E\lambda)$ values are gathered in the second column of table 4.2. All these states have isoscalar character.

4.5.3. Theoretical calculations

The one particle–one hole excitation spectrum of ^{208}Pb gives little isoscalar strength at low energy. The random phase approximation brings the strength down in energy and thereby accounts for the observed low-lying collective excitations. Figure 4.24 shows the example of the strength distribution for isoscalar 2^+ states in ^{208}Pb . Realistic theoretical calculations of the low-lying core excited states should therefore be based on the random phase approximation. Some results are gathered in tables 4.1 and 4.2.

Column (a) refers to the calculation of Ring and Speth [305]. These authors adopt the observed single-particle energies as input (see fig. 2.6). The particle–hole potential is a Landau–Migdal type density-dependent contact interaction whose parameters are fitted to the experimental values of the electric and magnetic moments of ^{207}Pb , ^{209}Pb , ^{207}Tl and ^{209}Tl , and of the energy and $B(E\lambda)$ values of the lowest 3^- and 2^+ collective excitations of ^{208}Pb . The configuration space includes two main shells above and two main shells below the Fermi energy, and a Woods–Saxon single-particle field.

Column (b) refers to the results of Bernard and Nguyen Van Giai [61, 96]. The single-particle basis is

Fig. 4.23. Low-lying collective excitations of ^{208}Pb , from the data reported in refs. [302–304].

derived from the Skyrme III–Hartree–Fock approximation, and the corresponding particle–hole interaction is given by eqs. (2.25a, b, c). The equations of the random phase approximation are solved in coordinate space [277]. The configuration space includes all the hole states, and all the particle states with energy smaller than 50 MeV. The calculation covers the 0^+ , 2^+ , 3^- and 4^+ core excited states.

Column (c) contains the results of ref. [306]. The authors adopt the observed single-particle energies in the valence shells and use oscillator wave functions. The interaction is a Landau–Migdal-type contact force to which finite range one-pion and one-rho meson exchange potentials are added. The configuration space includes two main shells on each side of the Fermi energy.

Table 4.1

Excitation energies of the collective low-lying states of ^{208}Pb . The observed (obs) values are taken from refs. [302–304]. The calculated energies have been obtained from refs. [305] (column (a)), [96] (b), [306] (c), [307] (d), [308] (e) and [278] (f)

J^π	$E_\lambda \text{ (MeV)}$						
	obs	(a)	(b)	(c)	(d)	(e)	(f)
3^-	2.6	2.6	2.8	2.6	2.6	2.6	2.9
5^-	3.2	3.4		3.4	3.3	3.3 3.8	3.4
5^-	3.7	3.8		4.3		4.3	3.9
2^+	4.1	4.5	6.1	4.6	5.0 5.3	4.4	4.6 5.7
4^+	4.3	4.7	4.4	4.7	5.0 5.6	4.7	4.9 5.7
6^+	4.4	4.8		4.8	4.9 5.6	4.8	5.0 5.4

Table 4.2
 $B(E\lambda)$ values of the collective low-lying excitations of ^{208}Pb . The notation is the same as in table 4.1

J^π	$B(E\lambda) \quad (\text{fm}^2\lambda)$					
	obs	(a)	(c)	(d)	(e)	(f)
3^-	7.7×10^5	5.5×10^5	5.1×10^5	8.7×10^5	4.3×10^5	3.1×10^5
5^-	4.5×10^8	2.9×10^8	3.2×10^5	9.0×10^8	2.2×10^8	4.5×10^7
			8.6×10^5			
5^-	3.2×10^8	3.0×10^8	1.5×10^7		2.7×10^8	1.6×10^8
2^+	3.0×10^3	3.1×10^3	3.0×10^3	2.5×10^3	2.3×10^3	1.3×10^3
				1.2×10^3		4.5×10^3
4^+	1.3×10^7	7.6×10^6	1.1×10^7		6.0×10^6	1.1×10^6
6^+	2.3×10^{10}	2.1×10^{10}	3.8×10^{10}	2.8×10^{10}	1.8×10^{10}	1.9×10^9
				1.6×10^{10}		6.6×10^9

Column (d) is derived from the work of Bortignon et al. [283, 307]. The single-particle states are obtained from the Skyrme III–Hartree–Fock approximation; all the hole states are included, and all particle states up to 40 MeV. The random phase approximation is treated as outlined in section 4.2.5.4.

Column (e) gives the results of Fiebig and Wambach [308]. The single-particle wave functions are obtained from a Woods–Saxon potential and the associated energies are close to those of the Skyrme III–Hartree–Fock approximation [114]. The configuration space consists of the two main shells on each side of the Fermi energy. The effective interaction is a Landau–Migdal contact force to which finite range one-pion and one-rho exchange potentials are added.

Column (f) refers to [278]. The single-particle energies and wave functions and the configuration space are approximately the same as in column (e). The effective interaction is the “M3Y potential” [310], renormalized by a factor $Z_{ij}^{1/2} = (m/m_\omega^h)^{1/2}$ (as calculated in ref. [306]) for each particle and hole which belongs to the valence shells and by a factor $Z_{ij}^{1/2} = \sqrt{0.9}$ for a particle (or a hole) which belongs to another shell.

4.5.4. High-lying core excitations

The theoretical description of core excitations with high multipolarity (and/or with large energy) requires the use of a large configuration space. Then, the momentum dependence of the residual interaction may be significant. The contribution of these core excitations to the dispersion corrections is not negligible [313] and deserves further investigations, see section 4.6.4.

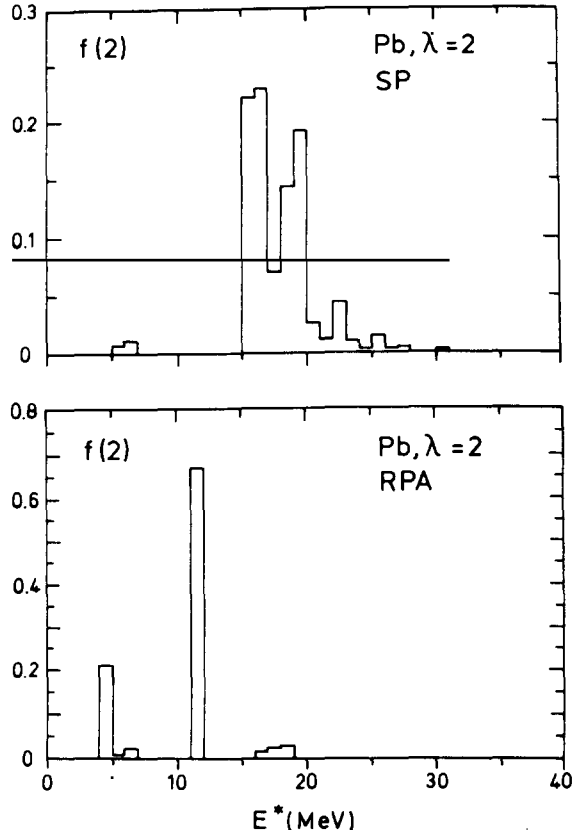


Fig. 4.24. Adapted from ref. [309]. Fraction of the energy-weighted sum rule for the 2^+ isoscalar excitations in ^{208}Pb (oscillator strength), grouped in energy bins of 1 MeV. The upper part corresponds to the one particle-one hole states as computed from the Skyrme III-Hartree-Fock basis, the lower part to the random phase approximation based on the schematic interaction of ref. [283], see section 4.2.5.5.

4.6. Microscopic calculations of the quasiparticle energies of the valence shells in ^{208}Pb

4.6.1. Introduction

There exist many calculations of the dispersion corrections to the single-particle energies in the valence shells of ^{208}Pb , especially in the case of neutrons. The main purpose of the present section is to survey their main features, similarities and differences. We follow the historical order and label the calculations by the names of their authors. We unfortunately overlooked the interesting work of Platonov [314].

4.6.2. Bertsch and Kuo

Stimulated by the case of normal liquid ^3He , Bertsch and Kuo [2] calculated the dispersion corrections in ^{40}Ca and in ^{208}Pb . They used second-order perturbation theory, see graphs (a) and (b) of fig. 4.4. In the case of ^{208}Pb , the uncorrelated core states up to 25 MeV excitation energy were considered; this includes the $0 \hbar\omega$, $2 \hbar\omega$ and part of the $4 \hbar\omega$ excitations. Experimental single-particle energies were used as input. The interaction was of the Kuo-Brown type [316].

The authors give numerical results for the proton subshells which belong to the valence main shell located above the Fermi energy. The calculated dispersion corrections increase their binding energy by

Table 4.3a

Synthetic overview of theoretical calculations of quasiparticle properties in ^{208}Pb . The columns are associated with refs. [2] (1), [311] (2), [312] (3) and [313] (4). Neutron particle and hole states are denoted by ν and ν^{-1} , respectively, and protons by π and π^{-1} . The first four lines give the value of $\langle m_\omega/m \rangle$ as defined by eq. (7.29). The fifth row outlines the nature of the graphs which are calculated. The sixth line gives the configuration space, and the seventh row the particle-hole interaction. The eighth row indicates whether the double counting correction $\mathcal{N}^{(2)}$ in eq. (2.26) has been included. The ninth line specifies whether the self-consistent one pole approximation (3.20) has been solved

	<u>BK 68</u>	<u>RW 73</u>	<u>HS 76</u>	<u>PRS 80</u>
ν	1.15	1.25	1.28	1.20
ν^{-1}		1.19	1.16	1.25
π	1.32	1.34	1.47	1.16
π^{-1}		1.31	1.24	1.19
int.	$0\hbar\omega, 2\hbar\omega, \text{part } 4\hbar\omega$ $(\text{HO}; \tau=0+1, \sigma=0+1)$ obs	$0\hbar\omega, 1\hbar\omega, 2\hbar\omega$ $\lambda^\pi = 2^+, 3^-, 6^+, 4^-$ (WS, HO basis) $\sigma = 0+1$ obs	$0\hbar\omega$ $\lambda^\pi = 2^+, 3^-, \dots, 10^+$ $(\tau = 0+1)$ obs	$0\hbar\omega, 9\hbar\omega$ $\lambda^\pi = 2^+, 3^-, \dots, 9^-$ $(\tau = 0+1, p-h)$ $\lambda^\pi = 0^+, 2^+, \dots, 8^+$ $(\pi, \nu, \text{pair add+subs})$
j		Hamada-Johnston (G-matrix)	Landau-Migdal	mult. - mult. ($r\lambda$) self. cons. k_λ
correct doub. count				
pert.	x		x	
one-pole approx.		x		x
	1	2	3	4
				BE 84019

about 2 MeV. Only the $g_{9/2}$ and the $i_{11/2}$ neutron subshells were considered. Their energy remains approximately unaffected by the dispersion corrections.

The authors gave a rough evaluation of the ω -mass associated with the valence shells, see eq. (1.8). They obtained $m_\omega/m \approx 1.32$ in the case of protons and $m_\omega/m \approx 1.15$ in the case of neutrons. According to this estimate, the dispersion corrections would thus reduce the average particle-hole gap $\Delta\omega$ (see eq. (4.17)) by about 30 per cent in the case of protons and by about 15 per cent in the case of neutrons. These results are summarized in column (1) of table 4.3a.

Table 4.3b

Same as table 4.3a, for the calculations reported in refs. [96] (5), [306] (6), [315] (7), [114] (8) and [278] (9)

	BG 80	LK 81	BBDM83	WML 81	SRK 83
ν	1.29	1.37	1.33	1.27	1.30
ν^{-1}	1.62	1.68	1.41		
π		1.71	1.29	1.37	1.43
π^{-1}		1.43	1.61		1.49
int.	50 MeV (HF box) $\lambda^\pi = 0^+, 1^-, \dots, 4^+$ ($\tau=0+1$)	$0\hbar\omega, 1\hbar\omega, 2\hbar\omega$ $\lambda^\pi = 0^+, 2^+, \dots, 8^+$ (HO) $1^+, 2^-, \dots, 4^-$ ($\tau=0+1; \sigma=0+1$) obs	ϵ_h unrestr. $\epsilon_p \leq 40$ MeV $\lambda^\pi \leq 2^+, 3^-, \dots, 10^+$ ($\tau=0$) HF Skyrme III (box)	2 shells above ϵ_F below ϵ_F $\lambda^\pi = 0^+, 2^+, \dots, 13^+$ $1^+, 2^-, \dots, 14^-$ ($\tau=0+1; \sigma=0+1$) scaled WS ($m^*/m=.7$)	$0\hbar\omega-3\hbar\omega$ WS ($\tau=0+1; \sigma=0+1$) scaled WS ($m^*/m=.7$)
j	HF r-space	Landau-Migdal	mult - mult. (du/dr) self cons λ	Landau - Migdal plus $\pi\pi$ and ρ exch. potns	M3Y, renormalized particle hole int.
	Skyrme III				
correct doub. count	x	x	x		x
pert.		x			
one - pole approx.	x		x	x	x
Ref	5	6	7	8	9

BE 8402C

4.6.3. Hamamoto and Siemens

Inelastic nucleon scattering exhibits the existence in the nuclei with mass number 209 and 207 of multiplets of states which can be described as a particle or a hole coupled to a low-lying vibration of the ^{208}Pb core, see e.g. [317]. The work of ref. [2] should thus be improved by taking the collectivity of the core excited states into account. This was undertaken by Ring and Werner [311]; we defer a discussion of their work until section 4.7 since these authors focused upon the distribution of single-particle strength and did not compute the dispersion corrections to the single-particle energies.

Collectivity effects in the calculation of the dispersion corrections to the quasiparticle energies have been evaluated by Hamamoto and Siemens [312]. These authors used a degenerate harmonic oscillator basis (no spin-orbit coupling) and a self-consistent multipole-multipole interaction [284]. This model does not yield the empirical properties of the low-lying collective core excitations. These were thus added a posteriori in an ad hoc manner.

The dispersion corrections have been evaluated from graphs (c) and (d) of fig. 4.4 with the following two drastic simplifications.

(i) The included virtual excitations are only those in which the particle or the hole single-particle state belongs to the valence main shells, see column 3 of table 4.3a.

(ii) Only graph (c) of fig. 4.4 is included for evaluating the energy shift of a quasiparticle state which lies above the Fermi energy, while only graph (d) is included for a quasiparticle state which lies below the Fermi energy.

One striking feature of the results of ref. [312] is that the high-lying core excitations yield the major contribution to the dispersion correction to the average particle-hole gap $\Delta\omega$ defined by eq. (4.17). This is probably an artifact due to the simplifications (i) and (ii) above.

Hamamoto and Siemens started from the observed single-particle energies. In order to facilitate the comparison with other calculations, we have added in fig. 4.25 the energy shifts ΔV_{nlj} calculated in ref. [312] to an “unperturbed” spectrum obtained by multiplying by $m/m^* = 1/0.7$ the difference $\varepsilon_{nlj} - \varepsilon_F$ between the observed single-particle energies (see fig. 2.6) and the observed Fermi energy:

$$\varepsilon_{nlj}^{(0)} - \varepsilon_F = \frac{m}{m^*} (\varepsilon_{nlj} - \varepsilon_F). \quad (4.6.1)$$

We moreover left the Fermi energy unchanged. The calculated values shown in the middle column in fig. 4.25 are thus defined by

$$(\varepsilon_{nlj})_{\text{calc}} = \varepsilon_{nlj}^{(0)} + \Delta V_{nlj} - \Delta V_F, \quad (4.6.2a)$$

where

$$\Delta V_F = \sum_{\substack{\text{occ} \\ \text{uno}}} (2j+1) \Delta V_{nlj}. \quad (4.6.2b)$$

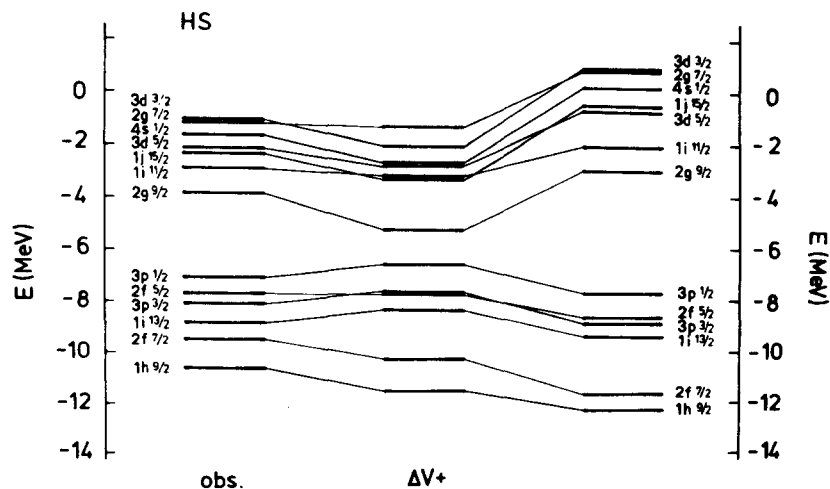


Fig. 4.25. Representation of the results of Hamamoto and Siemens [312] for the neutron quasiparticle energies in valence shells of ^{208}Pb . The column at the left gives the observed values, see fig. 2.6. The column at the right is obtained by dilating this observed spectrum by a factor $m/m^* = 1/0.7 = 1.43$, see eq. (6.1). The energies shown in the middle column are derived by adding the energy shifts calculated in ref. [312] to the levels at the right, while leaving the Fermi energy unchanged (see eqs. (6.2a, b)).

The convention (6.2a, b) facilitates the comparison between the results obtained by various authors. It does not affect the value of the calculated correction to the average particle-hole gap $\Delta\omega$ defined by eq. (4.17). In ref. [312] the calculated dispersion correction to $\Delta\omega$ is equal to

$$\delta\omega \approx -3.2 \text{ MeV} \quad (4.6.3)$$

in the case of neutrons in ^{208}Pb and to -4.2 MeV for protons in ^{208}Pb . In this calculation, the low-lying collective core excitations would only yield a contribution equal to -0.7 MeV in both cases. If one defines an average ω -mass by the ratio

$$m_\omega/m = 1 - \delta\omega/\Delta\omega^{(0)}, \quad (4.6.4)$$

one obtains in the present case

$$m_\omega/m \approx 1.34 \quad \text{for neutrons}, \quad (4.6.5a)$$

$$m_\omega/m \approx 1.40 \quad \text{for protons}. \quad (4.6.5b)$$

Here, we took $\Delta\omega^{(0)} = 9.3$ for neutrons and $\Delta\omega^{(0)} = 10.4 \text{ MeV}$ for protons, in keeping with eq. (6.1).

4.6.4. Perazzo, Reich and Sofia

The model used by Perazzo, Reich and Sofia [313] for the core excited states is essentially the same as the one which had been adopted by Hamamoto and Siemens [312] (see also ref. [280]) with the main improvement that these authors do not introduce the drastic simplifications labelled (i) and (ii) in section 4.6.3. The contribution of graphs (c) and (d) of fig. 4.4 are included, with $\lambda \leq 9$ ($E_\lambda < 70 \text{ MeV}$); the single-particle states (c or h) in the intermediate state cover 9 shells of the degenerate harmonic oscillator. Observed single-particle energies were used for the valence shells; the eigenvalues of the degenerate harmonic oscillator were taken for the other shells. In addition, Perazzo et al. include pairing phonons, see column (4) of table 4.3a and graphs (e) and (f) of fig. 4.4 ($\lambda \leq 8$).

Perazzo et al. calculate proton as well as neutron quasiparticle energies in the valence shells of ^{208}Pb by solving eq. (3.20). Figure 4.26 summarizes their results in the case of neutrons. The calculated dispersion correction to the average particle-hole gap is

$$\delta\omega = -1.25 \text{ MeV}, \quad (4.6.6)$$

when the pairing modes are omitted; the contribution of the isoscalar bosons to this value of $\delta\omega$ is equal to -0.59 MeV . If the second term on the right-hand side of eq. (3.20) is replaced by $\Delta V_{ij}(\varepsilon_{ij}^{(0)})$, the calculated value of $\delta\omega$ becomes -1.72 MeV .

These calculated values of $\delta\omega$ are considerably smaller in absolute magnitude than those which had been obtained by Hamamoto and Siemens [312]. The analysis carried out by Perazzo et al. [313] shows that this reflects the inaccuracy of the assumptions labelled (i) and (ii) in section 4.6.3. This is illustrated in fig. 4.27.

Perazzo, Reich and Sofia [313] also evaluated the contributions to $\delta\omega$ of all the phonons with given multipolarity λ as a function of λ . Figure 4.28 shows that the contributions of the even and odd multipolarities are out of phase. This is mainly due to parity conservation. Let us for simplicity

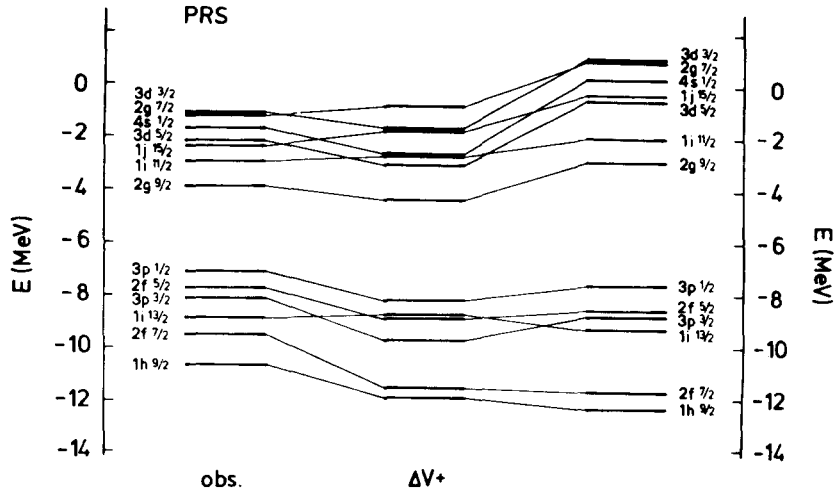


Fig. 4.26. Representation of the results of Perazzo, Reich and Sofia [313] for the neutron quasiparticle energies in the valence shells of ^{208}Pb . The notation is the same as in fig. 4.25.

disregard the intruder $j_{15/2}$ and $i_{13/2}$ subshells of the two valence main shells, whose parity differs from that of the other subshells of the same shell. Let us furthermore focus on the case of the 3^- core excitation and on the graph (c) of fig. 4.4. In this graph we only consider intermediate single-particle states which belong to the valence shell. The graph (c) then differs from zero (and is attractive) for all the hole states, i.e. for all the orbits of the main shell below the Fermi energy. Because of parity conservation, graph (c) vanishes for all the particle states, i.e. for all the orbits of the main shell above the Fermi energy. In this simplified model, the coupling via graph (c) of fig. 4.4 of the 3^- phonon to the

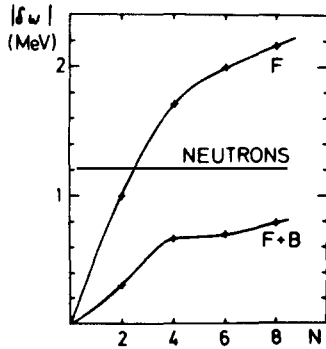


Fig. 4.27. Adapted from ref. [313]. Dependence upon the number N of major shells (allowed for the intermediate single-particle states) of the absolute value of the dispersion correction to the average particle-hole gap for neutrons in ^{208}Pb . Only 2^+ and 3^- bosons are taken into account. The curve labelled F (forward) shows the result obtained when only graph (c) of fig. 4.4 is included for particle states and only graph (d) for hole states. The curve $F + B$ (forward + backward) takes the sum of graphs (c) and (d) into account for particles as well as for hole states.

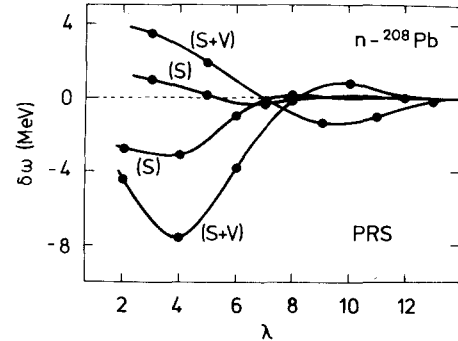


Fig. 4.28. Adapted from ref. [313]. Contribution of the core excited states with multipolarity λ to the dispersion correction $\delta\omega$ to the average particle-hole gap as calculated by Perazzo, Reich and Sofia [313] in the case of neutrons in ^{208}Pb . The labels S and V refer to isoscalar and isovector modes, respectively.

single-particle states therefore does not affect the energy of the particle valence states and increases the binding of the hole valence states. In the same way, one finds that the coupling via graph (d) of fig. 4.4 of the 3^- phonon to the single-particle states increases the energy of the particle valence states and does not affect the binding energy of the quasi-hole valence states. This explains why the contribution to $\delta\omega$ of the multipolarity $\lambda = 3$ is positive: the average particle-hole gap is increased by the coupling to the 3^- collective state. This was not the case in ref. [312] because of the simplifying assumptions (i) and (ii) in section 4.6.3.

Another striking feature of fig. 4.28 is that the contribution to $\delta\omega$ of the high-lying isovector core excitations is as large as that of isoscalar states for small λ and is larger than the isoscalar contribution for large λ . It should be kept in mind, however, that the decrease of $\delta\omega$ due to the high-lying core states is ambiguous in the sense that these can be included in the Hartree-Fock contribution via a suitable redefinition of the effective interaction.

When pairing phonons are included (graphs (c) and (f) of fig. 4.4), the dispersion correction to the average particle-hole gap changes from -1.25 MeV (see eq. (6.5)) to -1.10 MeV. Their effect therefore seems to be small. This is in keeping with the results of ref. [318] in which it was found that the pairing modes only yield a small contribution to the imaginary part W_{ij} of the average nuclear field.

From eq. (6.6), one finds that the average effective mass as defined by eq. (6.4) is equal to

$$m_\omega/m \approx 1.15 \text{ for neutrons .} \quad (4.6.7a)$$

Similarly, one obtains

$$m_\omega/m \approx 1.1 \text{ for protons .} \quad (4.6.7b)$$

4.6.5. Bernard and Nguyen Van Giai

V. Bernard and Nguyen Van Giai [96] use the Skyrme III-Hartree-Fock single-particle basis and the corresponding particle-hole interaction given by eqs. (2.25a, b, c). Because of the zero-range nature of the Skyrme interaction, expression (2.28a, b) diverge if the sums over c and λ (or over h and λ) are unrestricted. In the calculation reported in ref. [96] the sum over h extends over all hole states. The sum over λ is restricted to the $\lambda = 0^+, 2^+, 3^-$ and 4^+ isoscalar modes with $E_\lambda < 30$ MeV, see column (b) of table 4.1 and column (5) of table 4.3b. The core excited states with unnatural parity are omitted.

In eq. (2.26), the second-order contribution $\mathcal{N}^{(2)}$ is computed by using only the single-particle states with energies $\epsilon_c^{(0)} < 50$ MeV, by discretizing this single-particle energy spectrum by enclosing the system in a spherical box of radius 15 fm and by assuming that all the uncorrelated core excited states lie at 21 MeV excitation energy.

In ref. [96], the quasiparticle energies are calculated by solving eqs. (2.26)–(2.28b) and (3.18a), (3.20). The averaging interval Δ which appears in eq. (3.18a) is set equal to zero. We show below that the value of Δ is largely irrelevant as far as the quasiparticle energies in the valence shells are concerned. The main results of ref. [96] are summarized in fig. 4.29.

The calculated dispersion correction to the average particle-hole gap is equal to

$$\delta\omega = -1.9 \text{ MeV .} \quad (4.6.8)$$

The corresponding value of the average effective mass as defined by eq. (6.4) is equal to

$$m_\omega/m \approx 1.2 , \quad (4.6.9)$$

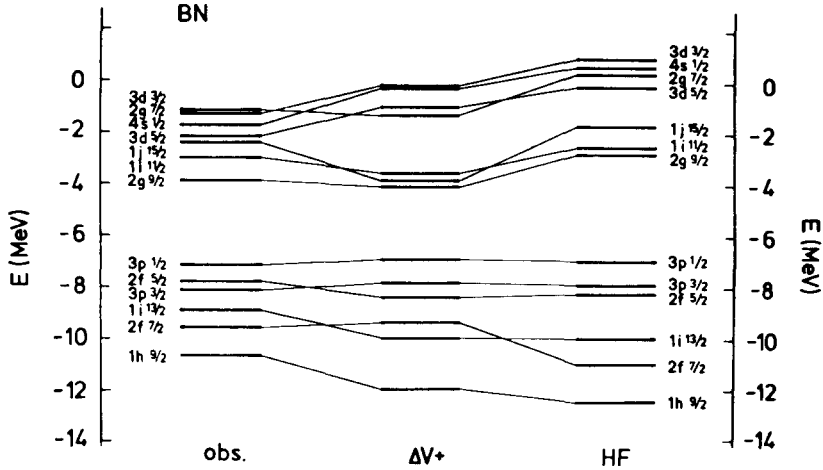


Fig. 4.29. Representation of the results of Bernard and Nguyen Van Giai [96] for the neutron quasiparticle energies in the valence shells of ^{208}Pb . The observed values are plotted on the left-hand side and the results of the Skyrme III–Hartree–Fock approximation on the right-hand side. The middle column gives the quasiparticle energies, see section 4.6.5.

if one takes in eq. (6.4) the unperturbed average particle–hole gap $\Delta\omega^{(0)} = 8.8$ MeV which corresponds to the Skyrme III–Hartree–Fock approximation.

4.6.6. Bortignon, Broglia, Dasso and Mahaux

Bortignon et al. [315] start from single-particle energies calculated from the Skyrme III–Hartree–Fock approximation and shown in the right-hand column of fig. 4.30. The difference between these energies and those plotted on the right-hand side of fig. 4.29 is mainly due to a difference in the numerical treatment of the spin–orbit coupling. All the hole states are included as well as all (discretized) single-particle energies with $\varepsilon_c^{(0)} < 50$ MeV.

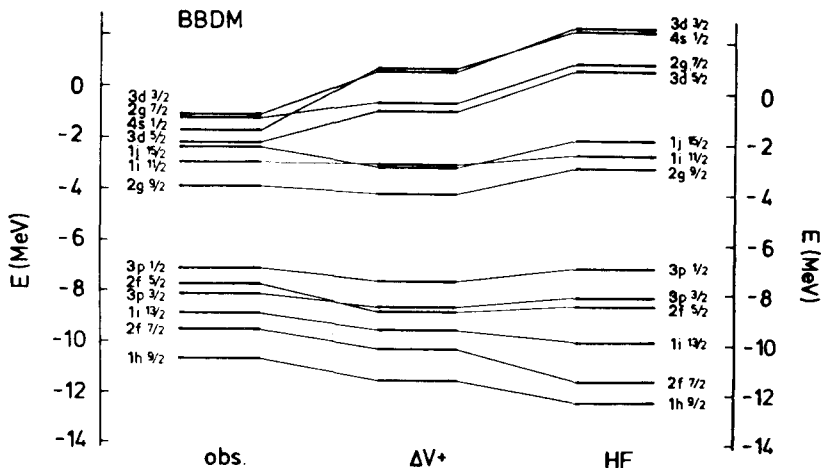


Fig. 4.30. Representation of the results of Bortignon et al. [315] for the neutron quasiparticle energies in the valence shells of ^{208}Pb . The notation is the same as in fig. 4.29.

The core excited states are computed from the random phase approximation outlined in section 4.2.5.4, see columns (d) of tables 4.1 and 4.2. All isoscalar modes with $\lambda \leq 10^+$ and $E_\lambda < 30$ MeV were included. The second-order term $\mathcal{N}^{(2)}$ in eq. (2.26) is evaluated by using the unperturbed response function, see the upper part of fig. 4.24. The core excited states with unnatural parity are omitted.

The quasiparticle energies are obtained by solving eqs. (2.26)–(2.28b) and (3.18a), (3.20) where the averaging interval Δ is set equal to zero. The results are summarized in fig. 4.30. The calculated dispersion correction to the average particle–hole gap is equal to

$$\delta\omega \approx -1.8 \text{ MeV}. \quad (4.6.10)$$

The corresponding effective mass (eq. (6.4)) is approximately the same as in eq. (6.9):

$$m_\omega/m \approx 1.2. \quad (4.6.11)$$

4.6.7. Wambach, Mishra and Li Chu-hsia

The single-particle basis adopted by Wambach, Mishra and Li Chu-hsia [114] is restricted to two main shells on each side of the Fermi energy. The single-particle energies are the same as those shown in the right-hand columns of figs. 4.25 and 4.26. The core excited states are calculated from a Landau–Migdal type interaction, see ref. [308] and columns (e) of tables 4.1 and 4.2. The isoscalar and isovector core excited modes with $\lambda < 14$ are included, as well as unnatural parity states.

The quasiparticle energies of the main neutron shell above the Fermi energy are computed from eq. (3.20) with $\Delta = 1$ MeV. The results are summarized in fig. 4.31. The calculated dispersion corrections produce a bunching of the quasiparticle energies as compared to the unperturbed ones which are close to those obtained from the Skyrme III–Hartree–Fock approximation. Since the authors did not perform calculations for the valence shell below the Fermi energy, one cannot derive from their work the dispersion correction to the average particle–hole gap. If one makes the crude assumption that $\delta\omega = 2(\langle \epsilon_p \rangle - \langle \epsilon_p^{(0)} \rangle)$, one finds

$$\delta\omega \approx -1.6 \text{ MeV} \quad (4.6.12)$$

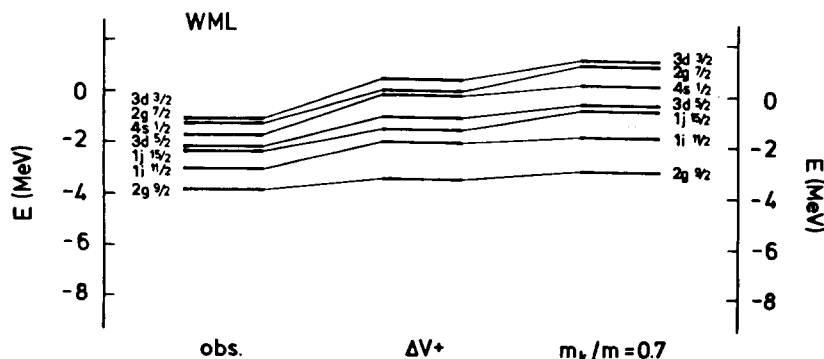


Fig. 4.31. Adapted from ref. [114]. Representation of the results obtained by Wambach et al. [114] for the neutron quasiparticle energies of the valence shell which is located above the Fermi energy in ^{208}Pb . The notation is the same as in fig. 4.25.

for neutrons and $\delta\omega \approx -2.7$ MeV for protons. The corresponding ω -mass as defined by eq. (6.4) is equal to

$$m_\omega/m \approx 1.2 \quad (4.6.13)$$

in the case of neutrons and to 1.3 in the case of protons.

4.6.8. Sommermann, Ratcliff and Kuo

The single-particle wavefunctions and energies used by Sommermann et al. [278] are approximately the same as those adopted by Wambach et al. [114]. The core excited states are computed as outlined in section 4.5.3 in connection with columns (f) of tables 4.1 and 4.2. The core excitation energies are smaller than approximately 40 MeV. Excitations with unnatural parity are taken into account.

The quasiparticle energies of the protons in the two valence shells of ^{208}Pb and of the neutrons in the valence shell above the Fermi energy are obtained from eq. (3.20), with $\Delta = 1$ MeV. The results obtained in the case of neutrons are summarized in fig. 4.32. If one assumes that the dispersion correction to the average particle-hole gap is equal to $2(\langle\epsilon_p\rangle - \langle\epsilon_p^{(0)}\rangle)$, one finds

$$\delta\omega \approx -1.1 \text{ MeV} \quad (4.6.14)$$

for neutrons and $\delta\omega \approx -3$ MeV for protons in ^{208}Pb . The corresponding ω -mass as defined by eqs. (6.4) and (6.1) is then equal to

$$m_\omega/m \approx 1.1 \quad (4.6.15)$$

in the case of neutrons and 1.3 in the case of protons.

4.6.9. Role of the energy averaging

The quasiparticle energies are calculated from eq. (3.20). This is referred to as the one-pole approximation in tables 4.3a, b. Equation (3.18a) shows that the energy shift $\Delta V_b(E)$ which appears in this equation depends upon the energy averaging interval Δ . This averaging was introduced because the correction $N_b(E)$ to the Hartree-Fock has many poles on the real E -axis or close to the real E -axis. We note, however, that $N_b(E)$ has no pole in an energy interval which contains the Fermi energy.

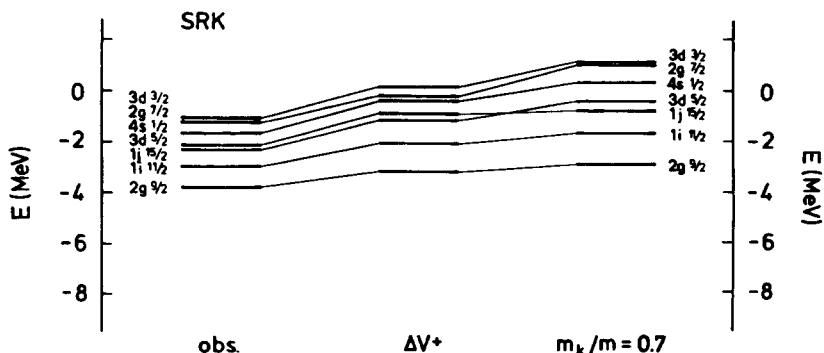


Fig. 4.32. Derived from ref. [278]. Representation of the results obtained by Sommermann et al. [278] for the neutron quasiparticle energies of the valence shell which is located above the Fermi energy in ^{208}Pb . The notation is the same as in fig. 4.25.

Let us consider the example of the valence neutron shell which lies above the Fermi energy in ^{208}Pb . The quantity $\mathcal{N}_{ij}(E)$ has no pole in the energy domain D_{ij} where

$$D_{ij} = (\varepsilon_h^{(0)} - E_\lambda)_{\max}^{ij}, \quad (\varepsilon_c^{(0)} + E_\lambda)_{\min}^{ij}. \quad (4.6.16)$$

Here, $(\varepsilon_c^{(0)} + E_\lambda)_{\min}^{ij}$ is the minimum value of the energy of the intermediate state in graph (c) of fig. 4.4 which has angular momentum j and parity $(-1)^j$. Correspondingly, $(\varepsilon_h^{(0)} - E_\lambda)_{\max}^{ij}$ is the maximum value of the energy of the intermediate state in graph (d) of fig. 4.4 which has angular momentum j and parity $(-1)^j$. The quantity $\mathcal{N}_{ij}(E)$ has a pole at each end point of the domain D_{ij} .

Let us for instance consider results of ref. [315] for the neutron $1i_{11/2}$ orbit, for which $\varepsilon_{i11/2}^{(0)} \approx -2.8$ MeV in the case of the Skyrme III–Hartree–Fock approximation. The value of $(\varepsilon_c^{(0)} + E_\lambda)_{\min}^{i,11/2}$ is equal to (see fig. 4.30 and column (d) of table 4.1)

$$\varepsilon_{j15/2}^{(0)} + E_{3-} \approx (-2.0 + 2.6) \text{ MeV} = 0.6 \text{ MeV}; \quad (4.6.17a)$$

the coupling to this intermediate state is moreover very weak because it requires a spin flip transition. The value of $(\varepsilon_h^{(0)} - E_\lambda)_{\max}^{i,11/2}$ is equal to

$$\varepsilon_{p11/2}^{(0)} - E_{5-} \approx (-7.2 - 3.5) \text{ MeV} = -10.7 \text{ MeV}. \quad (4.6.17b)$$

Hence, the function $\mathcal{N}_{i11/2}(E)$ is a real, smooth and decreasing function of E in the domain

$$D_{i11/2} = (-10.7 \text{ MeV}, +0.6 \text{ MeV}). \quad (4.6.17c)$$

Inside the energy domain (6.17c), there exists no physical reason for introducing an average of $\mathcal{N}_{ij}(E)$ over energy. This is exhibited in figs. 4.33 and 4.34 which show that in the domain the function

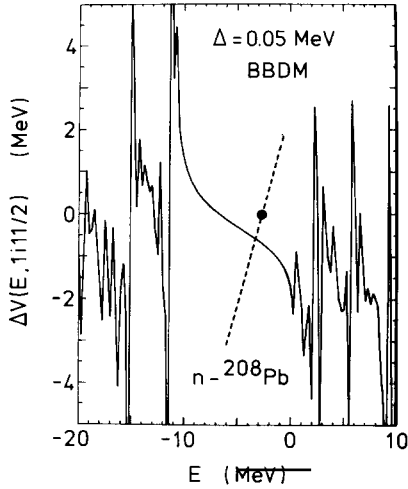


Fig. 4.33. Dependence upon the energy E of the quantity $\Delta V_{i11/2}(E)$ for the $1i_{11/2}$ neutron orbit in ^{208}Pb (see eq. (3.18a)) for the value $\Delta = 0.05$ MeV of the energy-averaging interval. The theoretical model is the one described in section 4.6.6 [315]. The dashed straight line represents the function $E - \varepsilon_{i11/2}^{(0)}$ and the location of $\varepsilon_{i11/2}^{(0)} = -2.8$ MeV is indicated by a full dot.

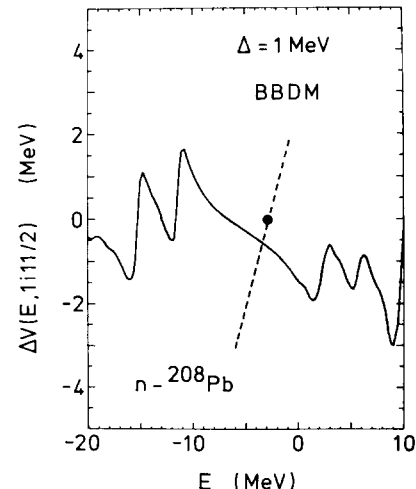


Fig. 4.34. Same as fig. 4.33, for the value $\Delta = 1$ MeV of the energy-averaging interval.

$\Delta V_{i11/2}(E)$ defined by eq. (3.18a) is independent of the energy-averaging interval Δ , except near the end points of the domain $D_{i11/2}$.

This property holds for the subshells which lie in the vicinity of the Fermi energy. It need not be valid for orbits which lie farther away from ε_F . Let us consider the example of the $(1h_{9/2})$ neutron orbit for which $\varepsilon_{h9/2}^{(0)} \approx -12.7$ MeV in the Skyrme III–Hartree–Fock approximation [96]. The lower limit of the domain $D_{h9/2}$ in which $\mathcal{N}_{h9/2}(E)$ has no singularity is given by

$$\varepsilon_{i13/2}^{(0)} - E_{3^-} = (-10.2 - 2.6) \text{ MeV} = -12.8 \text{ MeV} \quad (4.6.17d)$$

which lies very close to $\varepsilon_{h9/2}^{(0)}$. The quantity $\text{Re } \mathcal{N}_{h9/2}(E)$ has a pole on the real axis at the energy -12.8 MeV. In that example, eq. (3.20) has two roots which lie close to one another. They essentially correspond to the eigenvalues of the Hamiltonian matrix in the subspace defined by the two configurations $(h_{9/2})^{-1}$ and $3^-_*(1i_{13/2})^{-1}$.

Another well-known example is the $j_{15/2}$ neutron single-particle configuration, whose Skyrme III–Hartree–Fock energy lies close to the energy of the intermediate state $3^-_* 2g_{9/2}$, see e.g. ref. [317]. In this case, one usually calls “quasiparticle energy” the root of eq. (3.20) which is associated with the largest spectroscopic factor, see section 4.7.4.

Let us return to the simpler case where $\mathcal{N}_{ij}(E)$ is a smooth function of E in the vicinity of $\varepsilon_{ij}^{(0)}$, even for $\Delta = 0$. Then, the quasiparticle energy ε_{ij} defined by eq. (3.20) is very approximately independent of the size of the energy averaging Δ . In the example of the $1i_{11/2}$ neutron orbit, this quasiparticle energy is given by the abscissa of the intersection point between the full curve and the straight dashed line in figs. 4.33 and 4.34. In that case, one can furthermore expand the right-hand side of eq. (3.20) and write

$$\varepsilon_{ij} \approx \varepsilon_{ij}^{(0)} + \Delta V_{ij}(\varepsilon_{ij}^{(0)}) + (\varepsilon - \varepsilon_{ij}^{(0)}) \left[\frac{d}{dE} (\Delta V_{ij}(E)) \right]_{E=\varepsilon_{ij}^{(0)}}. \quad (4.6.18)$$

This yields

$$\varepsilon_{ij} \approx \varepsilon_{ij}^{(0)} + Z_{ij}^{(0)} \Delta V_{ij}(\varepsilon_{ij}^{(0)}) \quad (4.6.19)$$

where

$$Z_{ij}^{(0)} = \left\{ 1 - \frac{d}{dE} \Delta V_{ij}(E) \right\}_{E=\varepsilon_{ij}^{(0)}}^{-1}. \quad (4.6.20)$$

A comparison with eq. (1.8) shows that

$$[Z_{ij}^{(0)}]^{-1} = m_{\omega}^{(ij)}(\varepsilon_{ij}^{(0)})/m. \quad (4.6.21)$$

If the approximation (6.18) is accurate, Z_{ij} is the residue of the one-body Green function $G_{ij}(E)$ at the quasiparticle pole. Equations (3.13)–(3.15) show that Z_{ij} measures the probability of finding the quasiparticle in the form of a particle. Equations (2.2)–(2.3b) show why the quantity Z_{ij} is often called the “spectroscopic factor” of the quasiparticle state with quantum numbers $\{n, l, j\}$. We return to this point in section 4.7.4.

4.6.10. Polarization and correlation corrections

In eq. (2.27b) we distinguished the contributions (a) and (b) to the dispersion correction \mathcal{N}_{ij} to the mass operator. In the particle-vibration coupling model, the contribution (a) is represented by the graph labelled (c) in fig. 4.4 and the contribution (b) by the graph labelled (d).

The interest of handling separately these two contributions has been exhibited in chapter 3 and in section 4.4. We mentioned in connection with fig. 3.18 that the contribution $\mathcal{N}_{ij}^{(a)}$ is often called the polarization correction and the contribution $\mathcal{N}_{ij}^{(b)}$ the correlation contribution, but that this terminology is appropriate to particle states proper, i.e. to a quasiparticle state whose energy ε_{ij} lies above the Fermi energy.

By introducing eq. (2.27b) into the definition (3.18a, b) of $\Delta V_{ij}(E)$ and $W_{ij}(E)$, we obtain with obvious notations

$$\Delta V_{ij}(E) = \Delta V_{ij}^{(a)}(E) + \Delta V_{ij}^{(b)}(E), \quad (4.6.22)$$

$$W_{ij}(E) = W_{ij}^{(a)}(E) + W_{ij}^{(b)}(E). \quad (4.6.23)$$

The main properties of $\mathcal{N}_{ij}^{(a)}(E)$ and of $\mathcal{N}_{ij}^{(b)}(E)$ are that

$$\text{Im } \mathcal{N}_{ij}^{(a)}(E) = 0 \quad \text{for } E < \varepsilon_F^+, \quad (4.6.24a)$$

$$\text{Im } \mathcal{N}_{ij}^{(b)}(E) = 0 \quad \text{for } E > \varepsilon_F^- . \quad (4.6.24b)$$

Because of the appearance of the energy-averaging interval Δ in the definition (3.18b) of $W_{ij}(E)$, the properties (6.24a, b) are not exactly fulfilled by $W_{ij}^{(a)}(E)$ and $W_{ij}^{(b)}(E)$. Since $\Delta < \varepsilon_F^+ - \varepsilon_F^-$, one can nevertheless write for all practical purposes

$$W_{ij}^{(a)}(E) \approx 0 \quad \text{for } E < \varepsilon_F, \quad (4.6.25a)$$

$$W_{ij}^{(b)}(E) \approx 0 \quad \text{for } E > \varepsilon_F. \quad (4.6.25b)$$

This has been widely used in section 4.4, see e.g. eqs. (4.9a, b), where we saw that

$$\Delta V_{ij}^{(a)}(E) < 0, \quad \frac{d}{dE} \Delta V_{ij}^{(a)}(E) < 0 \quad \text{for } E < \varepsilon_F, \quad (4.6.26a)$$

$$\Delta V_{ij}^{(b)}(E) > 0, \quad \frac{d}{dE} \Delta V_{ij}^{(b)}(E) < 0 \quad \text{for } E > \varepsilon_F. \quad (4.6.26b)$$

Let us illustrate these properties by considering the example of the $1i_{11/2}$ neutron orbit in ^{208}Pb . The corresponding quantities $W_{1i_{11/2}}^{(a)}(E)$ and $W_{1i_{11/2}}^{(b)}(E)$ are given in fig. 4.35, while $\Delta V_{1i_{11/2}}^{(a)}(E)$ and $\Delta V_{1i_{11/2}}^{(b)}(E)$ are plotted in fig. 4.36, in the case $\Delta = 1$ MeV. The full $\Delta V_{1i_{11/2}}(E)$ has been shown in fig. 4.34.

4.6.11. Discussion

The calculated quasiparticle energies in the valence shells of ^{208}Pb as calculated from eq. (3.20) are

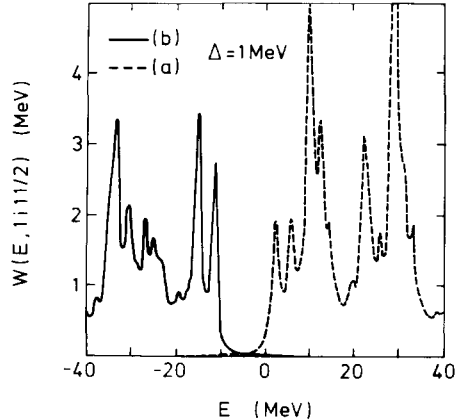


Fig. 4.35. Dependence upon the energy E of the quantities $W_{1i1/2}^{(a)}(E)$ (dashes) and $W_{1i1/2}^{(b)}(E)$ (full curve) in the case of the $1i_{11/2}$ neutron orbit in ^{208}Pb , and for the energy-averaging interval $\Delta = 1 \text{ MeV}$. The theoretical model is the one described in section 4.6.6 [315].

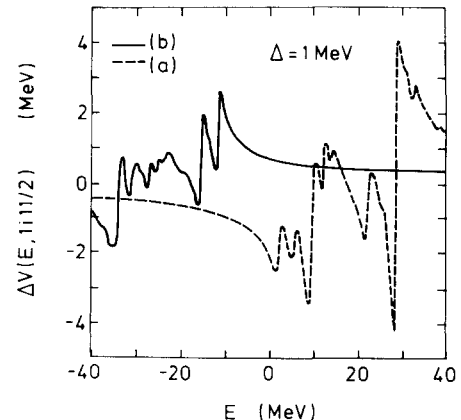


Fig. 4.36. Dependence upon the energy E of the quantities $\Delta V_{1i1/2}^{(a)}(E)$ (dashes) and $\Delta V_{1i1/2}^{(b)}(E)$ (full curve) in the case of the $1i_{11/2}$ neutron orbit in ^{208}Pb . The energy averaging interval Δ is equal to 1 MeV . The sum of $\Delta V_{1i1/2}^{(a)}(E)$ and $\Delta V_{1i1/2}^{(b)}(E)$ yields the value of $\Delta V_{1i1/2}(E)$ shown in fig. 4.34. The theoretical model is the one described in section 4.6.6 [315].

largely independent of the value chosen for the energy-averaging interval Δ . All calculations show that the average particle-hole energy gap is reduced by the dispersion correction to the Hartree-Fock approximation. This reflects the features that $\Delta V_i(E)$ is a decreasing function of E in the vicinity of the Fermi energy and that

$$\Delta V_i(\varepsilon_F) \approx 0 \quad (4.6.27)$$

in most calculations. The decreasing nature of $\Delta V_i(E)$ in the energy interval $(\varepsilon_F^-, \varepsilon_F^+)$ is a general property, independent of the approximation scheme. The smallness of $\Delta V_i(\varepsilon_F)$ derives from the approximate cancellation of the attractive correction $\Delta V_i^{(a)}(\varepsilon_F)$ by the repulsive correction $\Delta V_i^{(b)}(\varepsilon_F)$. In turn, this reflects the approximate symmetry of $W_i(E)$ with respect to $E = \varepsilon_F$.

While all calculations share these common features, the numerical results obtained by various authors can be widely different. This is illustrated by the calculated values of the dispersion correction to the average particle-hole energy gap for neutrons in ^{208}Pb , namely $\delta\omega = -3.2 \text{ MeV}$ [312], -1.25 MeV [313], -1.9 MeV [96], -1.8 MeV [307, 315], $\approx -1.6 \text{ MeV}$ [114] and $\approx -1.1 \text{ MeV}$ [278].

In some microscopic calculations [312, 313] $\varepsilon_{ni}^{(0)}$ has been identified with the observed single-particle energies rather than with values associated with the Hartree-Fock approximation. Equations (2.28a, b) hint that this yields smaller values for $|\delta\omega|$. This is in keeping with the comparison between the results of ref. [313] on the one hand, and those of refs. [96, 307] on the other hand. The large value of $|\delta\omega|$ obtained in ref. [312] is probably due to the inaccuracy of the approximations labelled (i) and (ii) in section 4.6.3.

Since $\delta\omega$ is a correction to the average particle-hole gap $\Delta\omega^{(0)}$, it is gratifying that $|\delta\omega|$ is smaller if $\Delta\omega^{(0)}$ is smaller. Indeed this stabilizes the calculated value of the corrected particle-hole gap $\Delta\omega = \Delta\omega^{(0)} + \delta\omega$ with respect to the choice of the single-particle energies. In this respect, the fact that we added in figs. 4.25 and 4.26 the value of $\Delta V_i(\varepsilon_F)$ to a Skyrme III-Hartree-Fock-type energy spectrum can be criticized; this was performed for the sole purpose of illustration.

Other sources of difference between the various calculations of ΔV_{ij} are the number of shells allowed for the intermediate single-particle states (in the graphs (c) and (d) of fig. 4.4), the number of core excited states and the nature of the particle-hole interaction. All these features can lead to large differences between the values calculated by various authors for the functions $\Delta V_{ij}(E)$ and $W_{ij}(E)$. This is illustrated by the comparison between fig. 4.37a on the one hand and fig. 4.37b on the other hand. This shows that the calculated individual values of the individual functions $\Delta V_{ij}(E)$ and of $W_{ij}(E)$ are questionable. The possibility exists that the calculations are more reliable as far as average properties are concerned. We describe below that there exist several ways of performing averages. The prescription which should be adopted depends upon the physical observable that one wants to describe.

4.7. Distribution of the single-particle strength and subshell occupation probabilities

4.7.1. Spectroscopic factors

Above, we used the basic assumption that the one-body Green function is diagonal in the $\{\varphi_\alpha^{(0)}\}$ representation. Within that assumption, eq. (2.2) yields

$$G_{\alpha\alpha}(\omega) = \sum_h \frac{S_{h\alpha}}{\omega - \omega_h - i\eta} + \sum_p \frac{S_{p\alpha}}{\omega - \omega_p + i\eta}. \quad (4.7.1)$$

The quantities

$$S_{h\alpha} = |\langle \psi_h^{(A-1)} | a_\alpha | \psi_0^{(A)} \rangle|^2 \quad (4.7.2a)$$

$$S_{p\alpha} = |\langle \psi_0^{(A)} | a_\alpha | \psi_p^{(A+1)} \rangle|^2 \quad (4.7.2b)$$

are, respectively, the spectroscopic factors of the level h of the $(A-1)$ nucleus and of the level p of the $(A+1)$ nucleus for the Hartree-Fock single-particle state with quantum numbers $\alpha = \{n, l, j, m_j\}$.

Equation (7.1) shows that the spectroscopic factors are the residues of the one-body Green function $G_{\alpha\alpha}$ at the poles which lie on the real axis. Here, we neglect the complication that highly excited states

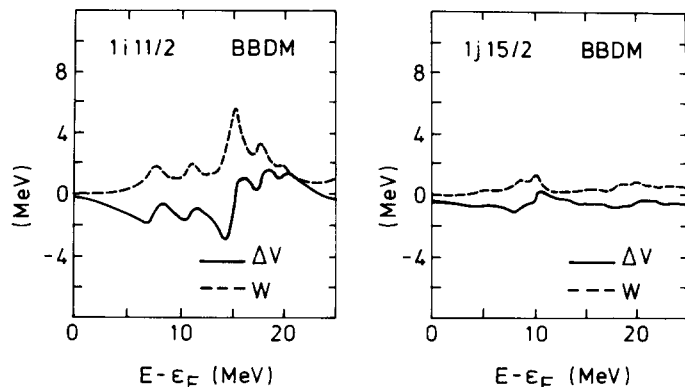


Fig. 4.37a. Dependence upon $E - \epsilon_F$ of the quantities $\Delta V_{ij}(E)$ (full curves) and $W_{ij}(E)$ (dashes) as calculated by Bortignon et al. [315] for the $1i_{11/2}$ and the $1j_{15/2}$ neutron orbits in ^{208}Pb , from the model outlined in section 4.6.6.

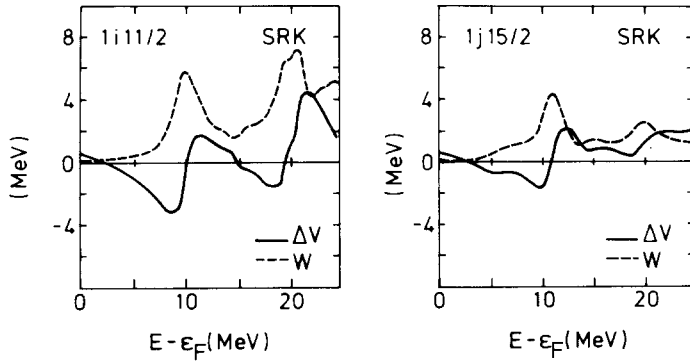


Fig. 4.37b. Adapted from ref. [278]. Same quantities as in fig. 4.37a, as calculated by Sommermann et al. from the model outlined in section 4.6.8.

of ^{207}Pb and of ^{209}Pb may lie above the threshold for particle emission, i.e. the existence of the branch cuts shown in fig. 4.1. One has then

$$S_{h\alpha} = \left\{ 1 - \frac{d}{dE} \mathcal{N}_{\alpha\alpha}(E) \right\}_{E=\omega_h}^{-1}, \quad (4.7.3a)$$

$$S_{p\alpha} = \left\{ 1 - \frac{d}{dE} \mathcal{N}_{\alpha\alpha}(E) \right\}_{E=\omega_p}^{-1}. \quad (4.7.3b)$$

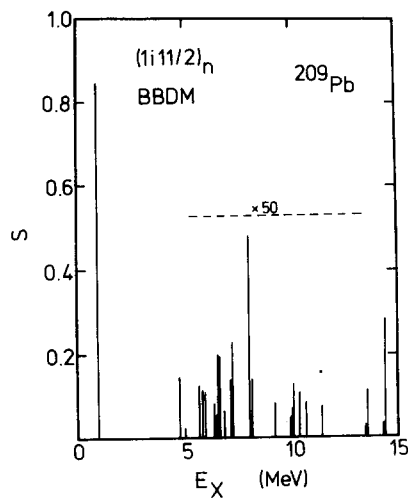


Fig. 4.37c. Dependence of the spectroscopic factors of the $(1i_{11/2})_n$ neutron orbit upon the excitation energy E_x in ^{209}Pb . The spectroscopic factor (0.85) of the lowest state is equal to the quasiparticle strength. The spectroscopic factors of the higher lying $(11/2)^+$ excitations have been multiplied by 50. The sum of the spectroscopic factors shown in this figure is equal to $1 - n_{1i_{11/2}}$, where $n_{1i_{11/2}} \approx 0.06$ is the occupation probability of the $1i_{11/2}$ neutron orbit in the correlated ^{208}Pb core, see eqs. (7.6b) and (7.12b) [315].

4.7.2. Sum rule

The closure relation (2.5) yields the sum rule

$$\sum_h S_{h\alpha} + \sum_p S_{p\alpha} = 1, \quad (4.7.4)$$

which is equivalent to (2.9.11). It states that the full strength of the single-particle state α must be found in the nuclei $(A+1)$ and $(A-1)$. The strength is distributed over many levels of these two nuclei, with excitation energies $E_h^{(A-1)}$ and $E_p^{(A+1)}$, see eq. (2.4).

4.7.3. Occupation probability of subshells in the core

Let us for instance consider the $1i_{13/2}$ neutron single-particle state. Its strength is contained in many $13/2^+$ excited states of the nuclei ^{207}Pb and ^{209}Pb . These levels can be excited with pick-up and stripping reactions, e.g. the $^{208}\text{Pb}(^3\text{He}, \alpha)$ and $^{208}\text{Pb}(\alpha, ^3\text{He})$ reactions. In the limit of the independent particle model, the full strength of the $1i_{13/2}$ single-particle state would be contained in the lowest $13/2^+$ excited state of ^{207}Pb with excitation energy $\varepsilon_{13/2}^{(0)} - \varepsilon_{p1/2}^{(0)}$. Because of the existence of dynamical interactions, this strength is distributed over many levels of ^{207}Pb , and also over many levels of ^{209}Pb . The latter feature arises from the core correlations. These are responsible for the fact that the $1i_{13/2}$ orbit, which would be fully occupied in the independent particle model, is partly empty. Its occupation probability in ^{208}Pb is given by $(\varepsilon_{ij}^{(0)} < \varepsilon_F)$

$$n_{ij} \approx \left\{ 1 + \frac{d}{dE} \mathcal{N}_{ij}^{(a)}(E) \right\}_{E=\varepsilon_{ij}^{(0)}}. \quad (4.7.5a)$$

We note that $\mathcal{N}_{ij}^{(a)}(E)$ is real and is a smooth function of E in the domain $E < \varepsilon_F$, as illustrated by fig. 4.36. Therefore one has

$$\Delta V_{ij}^{(a)}(E) = \text{Re } \mathcal{N}_{ij}^{(a)}(E + \frac{1}{2}i\Delta) \approx \mathcal{N}_{ij}^{(a)}(E) \quad (4.7.6a)$$

for $E < \varepsilon_F$. One can thus write the occupation probability of a normally fully occupied subshell in the form

$$n_{ij} \approx \left\{ 1 + \frac{d}{dE} \Delta V_{ij}^{(a)}(E) \right\}_{E=\varepsilon_{ij}^{(0)}}. \quad (4.7.7a)$$

In the case of a normally unoccupied (l', j') subshell of ^{208}Pb , e.g. the $1i_{11/2}$ orbit, the existence of core correlations renders it partly occupied. Its occupation probability in the core is given by

$$n_{l'j'} \approx - \left\{ \frac{d}{dE} \mathcal{N}_{l'j'}^{(b)}(E) \right\}_{E=\varepsilon_{l'j'}^{(0)}}. \quad (4.7.5b)$$

We note that $\mathcal{N}_{l'j'}^{(b)}(E)$ is a smooth real function of E for $E > \varepsilon_F$, as illustrated by fig. 4.36. One has therefore

$$\Delta V_{l'j'}^{(b)}(E) = \text{Re } \mathcal{N}_{l'j'}^{(b)}(E + \frac{1}{2}i\Delta) \approx \mathcal{N}_{l'j'}^{(b)}(E) \quad (4.7.6b)$$

for $E > \varepsilon_F$. Equation (7.5b) can therefore be written in the form

$$n_{l'j'} \approx - \left\{ \frac{d}{dE} \Delta V_{l'j'}^{(b)}(E) \right\}_{E=\varepsilon_{lj}^{(0)}} . \quad (4.7.7b)$$

We have calculated from eqs. (7.7a, b) the occupation probabilities in the case of ^{208}Pb and in the framework of the particle-vibration coupling model outlined in section 4.6.6, see column (7) of table 4.3b. The results are represented by the full dots in fig. 4.38a. A dashed curve has been drawn through the calculated dots in order to exhibit the similarity between their trend and the results which had been shown in fig. 4.17. There, the depletion of the normally fully occupied subshells is much larger than the one found in the present microscopic calculation. This can be understood by the fact that microscopic calculations cannot take into account the part of the depletion which is due to the coupling to highly excited core configurations; the dashes in fig. 3.51 indicate that the corresponding depletion may be as large as 0.2.

Figures 4.38b, c show the occupation probabilities calculated by Dechargé and Gogny [344, 345] in the case of Gogny's D1 effective nucleon-nucleon interaction; the corresponding Hartree-Fock single-particle energies in the valence shells are plotted in fig. 4.38d.

4.7.4. Quasiparticle strengths in the valence shells

Let us consider the example of the lowest-lying level of the $(A-1)$ nucleus with angular momentum j and parity $(-1)^j$. Its spectroscopic factor is equal to the residue of the one-body Green function at the

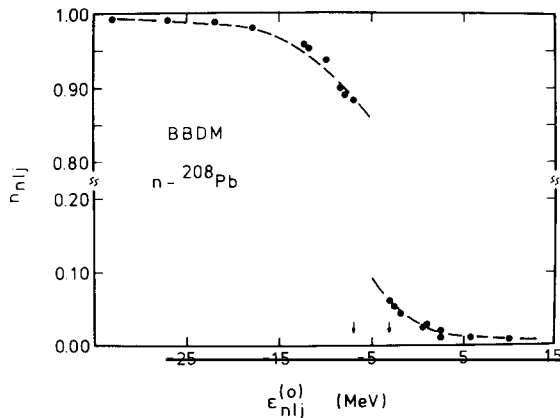


Fig. 4.38a. Occupation probability of neutron orbits in the correlated ^{208}Pb nucleus plotted versus the single-particle energy $\varepsilon_{nlj}^{(0)}$ computed in the Skyrme III-Hartree-Fock approximation. The calculation is based on eqs. (7.7a, b). It is performed in the framework of the particle-vibration coupling model of ref. [283], see column (7) of table 4.3b. In order of increasing energy, the dots correspond to the $1f_{7/2}$, $2p_{1/2}$, $1g_{7/2}$, $1h_{11/2}$, $1h_{9/2}$, $2f_{5/2}$, $2f_{7/2}$, $1i_{13/2}$, $3p_{3/2}$ and $3p_{1/2}$ hole states, and to the $2g_{9/2}$, $1i_{11/2}$, $1j_{15/2}$, $3d_{5/2}$, $2g_{7/2}$, $4s_{1/2}$, $3d_{3/2}$, $2h_{11/2}$ and $2h_{9/2}$ particle states. The dashed curve has been drawn by eye through the calculated dots in order to exhibit their trend. The arrows show the location of $\varepsilon_F^- = \varepsilon_{3p_{1/2}}^{(0)}$ and of $\varepsilon_F^+ = \varepsilon_{2g_{9/2}}^{(0)}$.

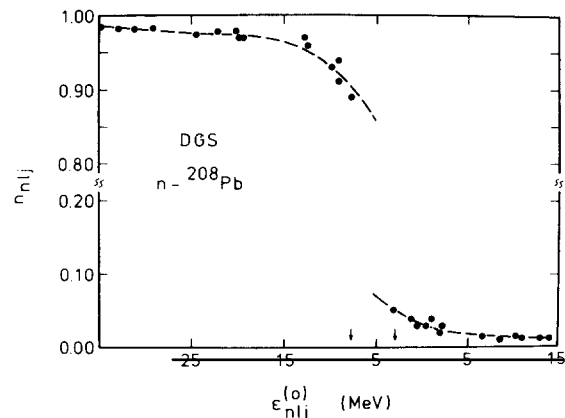


Fig. 4.38b. Derived from ref. [345]. Occupation probability of neutron orbits in the correlated ^{208}Pb nucleus plotted versus the single-particle energy $\varepsilon_{nlj}^{(0)}$ computed in the Hartree-Fock approximation with the D1 effective interaction of Gogny; the energies $\varepsilon_{nlj}^{(0)}$ are shown in fig. 4.38d. The calculation is based on eqs. (7.7a, b). In order of increasing energy, the dots correspond to the $1f_{5/2}$, $2p_{3/2}$, $2p_{1/2}$, $1g_{9/2}$, $1g_{7/2}$, $2d_{5/2}$, $2d_{3/2}$, $3s_{1/2}$, $1h_{11/2}$, $1h_{9/2}$, $2f_{7/2}$, $1i_{13/2}$, $3p_{3/2}$, $2f_{5/2}$ and $3p_{1/2}$ hole states, and to the $2g_{9/2}$, $1i_{11/2}$, $1j_{15/2}$, $3d_{5/2}$, $2g_{7/2}$, $4s_{1/2}$, $3d_{3/2}$, $2h_{11/2}$, $1k_{17/2}$, $1j_{13/2}$, $3f_{7/2}$, $3f_{5/2}$ and $4p_{3/2}$ particle states. The dashed curve has been drawn by eye through the calculated dots. The arrows show the location of $\varepsilon_F^- = \varepsilon_{3p_{1/2}}^{(0)}$ and of $\varepsilon_F^+ = \varepsilon_{2g_{9/2}}^{(0)}$.

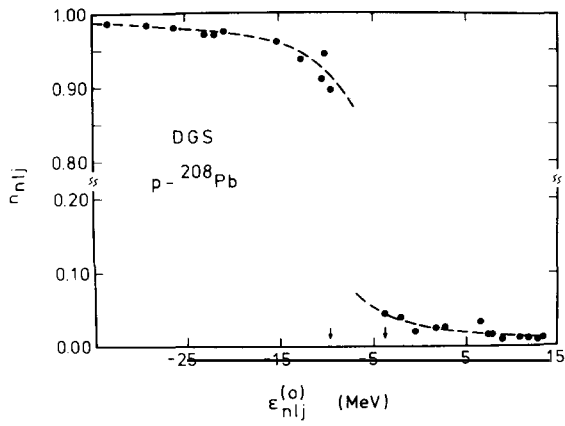
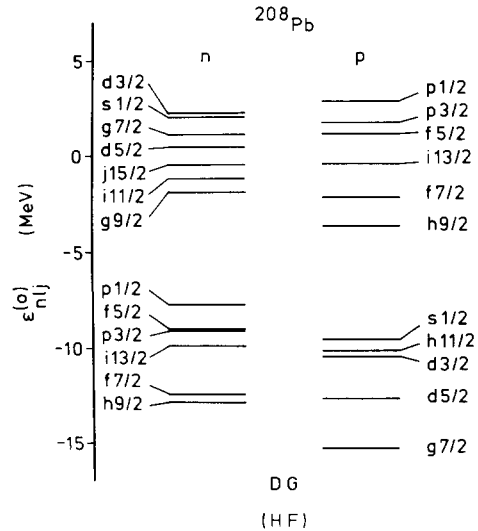


Fig. 4.38c. Derived from ref. [345]. Occupation probability of proton orbits in the correlated ^{208}Pb nucleus plotted versus the single-particle energy $\epsilon_{nlj}^{(0)}$ computed in the Hartree-Fock approximation with the D1 effective interaction of Gogny. The energies $\epsilon_{nlj}^{(0)}$ are shown in fig. 4.38d. The calculation is based on eqs. (7.7a, b). In order of increasing energy, the dots correspond to the $1f_{7/2}$, $1f_{5/2}$, $2p_{3/2}$, $2p_{1/2}$, $1g_{9/2}$, $1g_{7/2}$, $2d_{5/2}$, $2d_{3/2}$, $1h_{11/2}$ and $3s_{1/2}$ hole states, and to the $1h_{9/2}$, $2f_{7/2}$, $1i_{13/2}$, $2f_{5/2}$, $3p_{3/2}$, $3p_{1/2}$, $1i_{11/2}$, $2g_{9/2}$, $1j_{15/2}$, $2g_{7/2}$, $3d_{5/2}$, $3d_{3/2}$ and $4s_{1/2}$ particle states. The dashed curve has been drawn by eye through the calculated dots in order to exhibit their trend. The arrows show the location of $\epsilon_F^- = \epsilon_{3s_{1/2}}^{(0)}$ and of $\epsilon_F^+ = \epsilon_{1h_{9/2}}^{(0)}$.



independent particle model of the ^{208}Pb core. The corresponding quantity $\Delta V_{i11/2}(E)$ has been plotted in figs. 4.33 and 4.34 for the values $\Delta = 0.05$ MeV and $\Delta = 1$ MeV of the averaging interval, respectively. In the limit $\Delta = 0$, one has $\Delta V_{i11/2}(E) = \mathcal{N}_{i11/2}(E)$. This quantity has many poles on the real axis. They are located near the energies where $\Delta V_{i11/2}(E)$ presents sharp wiggles in fig. 4.33. Near each of these poles, there exist one root of the equation

$$\omega_{ij} = \varepsilon_{ij}^{(0)} + \mathcal{N}_{ij}(\omega_{ij}), \quad (4.7.9)$$

i.e. one pole of the one-body Green function. In addition, eq. (7.9) has one root located at the intersection between the full curve and the straight dashed line in figs. 4.33 and 4.34; this is the quasiparticle pole. The residue at this pole is called the quasiparticle strength or the spectroscopic factor of the quasi-pure $11/2^+$ excited state located at 0.77 MeV excitation energy in ^{209}Pb . The binding energy of the corresponding quasiparticle orbit is equal to $\varepsilon_F^+ + 0.77$ MeV = -3.16 MeV. This observed value should be compared with the result of the calculation shown in fig. 4.33 which yields $\varepsilon_{i11/2} = -3.37$ MeV.

The value of the corresponding spectroscopic factor as obtained from fig. 4.33 and eq. (7.8a) is equal to

$$Z_{i11/2} = 0.85. \quad (4.7.10)$$

Since $\Delta V_{ij}(E) = \Delta V_{ij}^{(a)}(E) + \Delta V_{ij}^{(b)}(E)$, one can write (see eq. (3.12.2))

$$Z_{ij} \approx Z_{ij}^{(a)} \cdot Z_{ij}^{(b)} \quad (4.7.11)$$

with

$$Z_{ij}^{(a)} \approx \left\{ 1 - \frac{d}{dE} \Delta V_{ij}^{(a)}(E) \right\}_{E=\varepsilon_{ij}}^{-1}, \quad (4.7.12a)$$

$$Z_{ij}^{(b)} \approx \left\{ 1 - \frac{d}{dE} \Delta V_{ij}^{(b)}(E) \right\}_{E=\varepsilon_{ij}}^{-1}. \quad (4.7.12b)$$

The relation (7.11) has the interest of exhibiting the existence of two physical reasons why the spectroscopic factor is smaller than unity. The first reason is that the single-particle strength is partly contained in higher-lying $11/2^+$ excited states of ^{209}Pb ; this effect is represented by the factor $Z_{i11/2}^{(a)}$ which is found equal to

$$Z_{i11/2}^{(a)} \approx 0.89, \quad (4.7.13a)$$

see fig. 4.36. The second reason is that the $i_{11/2}$ orbit is partly occupied in the correlated ^{208}Pb core and can therefore not be fully excited in a stripping reaction. This effect is represented by the factor

$$Z_{i11/2}^{(b)} \approx 0.94, \quad (4.7.13b)$$

see fig. 4.36. This physical interpretation of $Z_{i11/2}^{(b)}$ is in keeping with the relation

$$Z_{i11/2}^{(b)} \approx 1 - n_{i11/2}, \quad (4.7.14a)$$

where $n_{i11/2}$ is the probability that the $1i_{11/2}$ orbit is occupied in the correlated ^{208}Pb core, see eqs. (7.6b) and (7.12b).

A fraction $(1 - Z_{i11/2}) \approx 0.15$ of the $(1i_{11/2})$ single-particle strength is not contained in the lowest $(11/2)^+$ excited state of ^{209}Pb . Part (≈ 0.06) of this missing strength is contained in other $(11/2)^+$ excited states of ^{209}Pb and is displayed in fig. 4.37c. The rest of the missing strength is located in excited states of ^{207}Pb , see fig. 4.40b below.

One can investigate the contribution of individual core excited states λ to the value of

$$-\frac{d\mathcal{N}_i(E)}{dE}, \quad (4.7.15)$$

see eqs. (2.28a, b). Detailed results have been published by Li and Klemt [306]. These authors use a theoretical approach very similar to the one described in section 7.6.7, see column (6) of table 4.3b. In the example of the $1i_{11/2}$ orbit, they find

$$Z_{i11/2} = 0.67. \quad (4.7.14b)$$

We note that this result is much smaller than the one computed by Bortignon et al. and reported in eq. (7.10). It is also much smaller than the value $Z_{i11/2} = 0.86$ calculated by Bernard and Nguyen Van Giai [96]. In ref. [306] it is found that the contributions of the core excited states to the derivative (7.15) are the following: 0.004 ($\lambda = 0^+$), 0.032 ($\lambda = 1^-$), 0.070 ($\lambda = 1^+$), 0.043 ($\lambda = 2^-$), 0.044 ($\lambda = 2^+$), 0.071 ($\lambda = 3^-$), 0.020 ($\lambda = 4^-$), 0.055 ($\lambda = 4^+$), 0.033 ($\lambda = 5^-$), 0.058 ($\lambda = 6^+$), 0.019 ($\lambda = 7^+$), 0.036 ($\lambda = 8^+$). The largest contribution arises from the 3^- vibration. It is remarkable, however, that the contribution of the unnatural parity states is comparable to that of the natural parity vibrations. This explains why the spectroscopic factor $Z_{i11/2}$ computed in ref. [306] is much smaller than the value computed in refs. [96, 315] in which the unnatural parity states are omitted. This is also true for the spectroscopic factors of the other subshells of the valence shells.

4.7.5.2. The $1i_{13/2}$ orbit

The $1i_{13/2}$ neutron orbit is fully occupied in the independent particle model of the ^{208}Pb core. The corresponding one-body Green function has poles at the roots of the equation

$$\omega = \varepsilon_{i13/2}^{(0)} + \mathcal{N}_{i13/2}(\omega), \quad (4.7.16)$$

where $\varepsilon_{i13/2}^{(0)} \approx -10.2$ MeV in the case of the Skyrme III–Hartree–Fock approximation. Each root $\omega_h < \varepsilon_F^-$ corresponds to a level of ^{207}Pb with excitation energy

$$E_h = \varepsilon_F^- - \omega_h = -7.34 - \omega_h \text{ MeV}. \quad (4.7.17)$$

The root $\varepsilon_{i13/2}$ which lies closest to $\varepsilon_{i13/2}^{(0)}$ is the quasiparticle pole. In the model of Bernard and Nguyen Van Giai [96] one has (see fig. 4.29)

$$\varepsilon_{i13/2} \approx -10.1 \text{ MeV}, \quad (4.7.18a)$$

while in that of Bortignon et al. [315], one has (see fig. 4.30)

$$\varepsilon_{i13/2} \approx -9.8 \text{ MeV}. \quad (4.7.18b)$$

These results should be compared with the observed value

$$\varepsilon_{i13/2} \approx -8.9 \text{ MeV}, \quad (4.7.18c)$$

see fig. 2.6. The calculated excitation energy of the lowest $13/2^+$ level of ^{207}Pb is given by the difference $|\varepsilon_{i13/2} - \varepsilon_{p1/2}|$. Its experimental value is 1.63 MeV. The calculation gives

$$|-10.1 + 7.1| \text{ MeV} = 3.2 \text{ MeV} \quad (4.7.19a)$$

in the case of ref. [96] (see fig. 4.39) and

$$|-9.8 + 7.8| \text{ MeV} = 2 \text{ MeV} \quad (4.7.19b)$$

in the case of ref. [283] (see fig. 4.40a).

The roots $\omega_h < \varepsilon_{i13/2}$ correspond to $13/2^+$ excited states of ^{207}Pb with higher energy. The first few ones are shown in figs. 4.39 and 4.40a; the length of the vertical segment attached to each excitation energy represents the value of the corresponding spectroscopic factor as calculated from eq. (7.3a). We recall that part of the $i_{13/2}$ single-particle strength is located in $13/2^+$ excited states of ^{209}Pb , see eqs. (7.3b) and (7.4).

In sections 4.3.4–4.3.7 it was argued that the quasiparticle properties can be described by the one-body Green function $G_y(\omega \pm \frac{1}{2}i\Delta)$ taken at the complex energy $\omega \pm \frac{1}{2}i\Delta$, where Δ is an energy-averaging interval. The corresponding expression for the spectral function reads (see eqs. (2.11.19) and

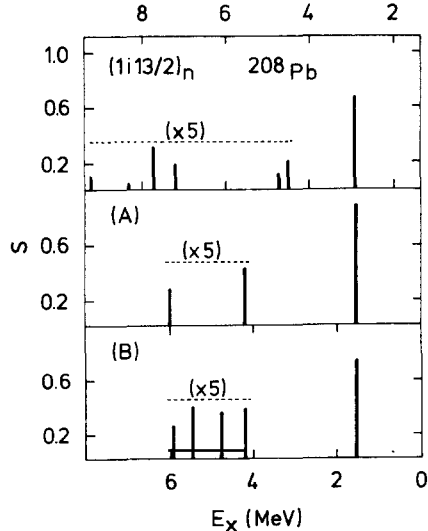


Fig. 4.39. Taken from ref. [319]. The upper part shows the calculated spectroscopic factors of $13/2^+$ low excited states in ^{207}Pb ; the upper horizontal scale gives the calculated excitation energies; the theoretical model is the one outlined in eqs. (2.28a, b). The middle and the lower parts give the spectroscopic factors derived from $^{208}\text{Pb}(^3\text{He}, \alpha)$ pick-up reactions, as reported in refs. [320] (middle part, (A)) and [321] (lower part, (B)); the corresponding excitation energy should be read on the lower abscissa.

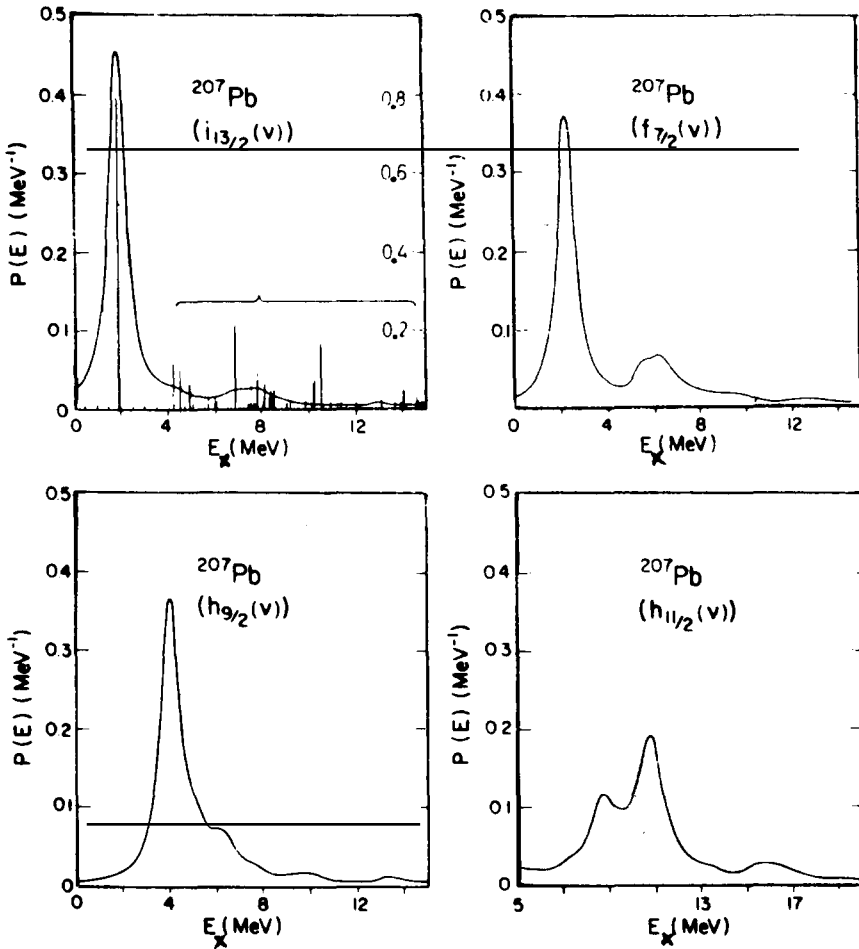


Fig. 4.40a. Taken from ref. [283]. The full curves give dependence upon excitation energy of calculated spectral functions (see eq. (7.20)), for $\Delta = 1$ MeV, for several neutron orbits. The spectroscopic factor of each calculated $13/2^+$ level of ^{207}Pb is represented by a vertical straight line (right-hand scale); except for that of the lowest excited state, all the spectroscopic factors have been multiplied by ten.

(2.11.20))

$$S_{ij}(\omega) = P_{ij}(\omega) = \frac{1}{2\pi} \frac{2W_{ij}(\omega) + \Delta}{[\varepsilon_{\alpha}^{(0)} + \Delta V_{ij}(\omega) - \omega]^2 + \frac{1}{4}[2W_{ij}(\omega) + \Delta]^2}. \quad (4.7.20)$$

In figs. 4.40a and 4.40b, the functions $P_{ij}(\omega)$ are plotted for $\Delta = 1$ MeV in five cases, namely for the neutron orbits $1i_{13/2}$, $2f_{7/2}$, $1h_{9/2}$, $1h_{11/2}$ and $1i_{11/2}$. The first three orbits belong to the valence shell located below the Fermi energy in ^{208}Pb . In these cases, the spectral function exhibits a narrow peak at the calculated energy of the lowest excited state of ^{207}Pb with angular momentum and parity $(13/2)^+$, $(7/2)^-$ and $(9/2)^-$, respectively. We emphasize that the full width at half-maximum of this narrow peak is equal to the averaging interval Δ and has no physical meaning.

The $1h_{11/2}$ orbit belongs to the second shell below the Fermi energy in ^{208}Pb . The corresponding spectral function $P_{h_{11/2}}(\omega)$ has a broad peak whose width is equal to $\Delta + 2W_{h_{11/2}}(\varepsilon_{h_{11/2}}) \approx 4$ MeV,

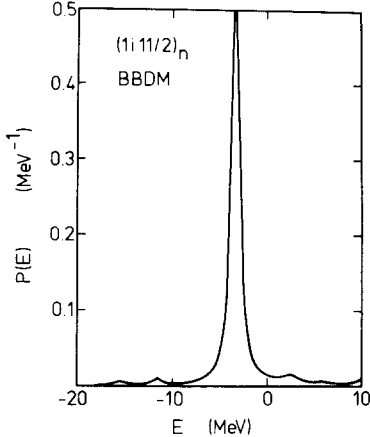


Fig. 4.40b. Energy dependence of the spectral function $P(E)$ for the $1i_{11/2}$ neutron orbit as calculated from eq. (7.20) [315]. The part of the curve located at $E > \varepsilon_F \approx -6$ MeV corresponds to strength contained in the ^{208}Pb nucleus. The part located at $E < \varepsilon_F$ corresponds to the ^{207}Pb nucleus. The width of the quasiparticle peak at $\varepsilon_{1i_{11/2}} = -3.37$ MeV is entirely due to the energy-averaging interval ($\Delta = 1$ MeV).

where $\varepsilon_{h11/2}$ is the quasiparticle energy of the $1h_{11/2}$ orbit. This case is semi-quantitatively similar to the one described by eq. (2.11.22), see also fig. 3.38. Figure 4.41 shows the distribution of spectroscopic factors in this case, as calculated by Nguyen Van Giai. The spectral function (7.20) is essentially obtained by folding the distribution of the spectroscopic factors with a Lorentzian of width Δ , see also figs. 2.16 and 2.17.

In the cases shown in figs. 4.40a, 4.40b and 4.41, the quasiparticle approximation (3.22) for the spectral function is rather accurate in the vicinity of the quasiparticle energy ε_i . We note, however, a

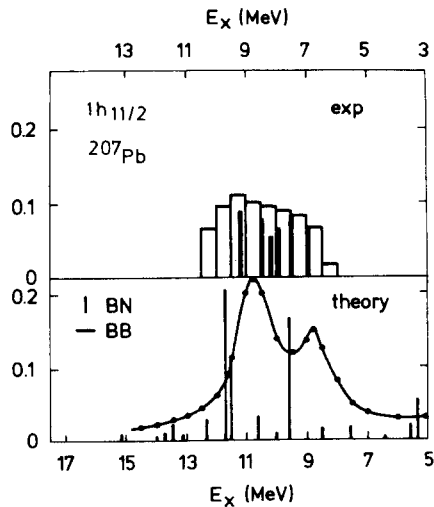


Fig. 4.41. Taken from ref. [322]. The upper part represents the distribution of the $1h_{11/2}$ single-particle strength as measured between 6.7 and 10.5 MeV excitation energy in ^{207}Pb by the $^{208}\text{Pb}({^3\text{He}}, \alpha)$ pick-up experiments reported in refs. [320, 323]; the measured excitation energy is shown on the upper horizontal scale. The lower part gives the spectroscopic factors (vertical segments) as calculated in ref. [319] and the spectral functions $P_{h11/2}$ (full curve with dots) as calculated in ref. [283], versus the calculated excitation energy given by the lower horizontal scale.

significant difference between valence subshells and a deeply bound orbit. In the case of a valence subshell which does not lie too far away from the Fermi energy, the spectroscopic factor of the first excited state is much larger than that of the other excited states with the same angular momentum and parity. In the case of a more deeply bound state, the spectroscopic factors of the levels whose excitation energy is contained in the domain

$$(\varepsilon_{lj} - \varepsilon_F^- - 2W_{lj}(\varepsilon_{lj}), \quad \varepsilon_{nlj} - \varepsilon_F^- + 2W_{lj}(\varepsilon_{lj})) \quad (4.7.21)$$

have comparable magnitude.

4.7.5.3. The $1h_{9/2}$ orbit

We noted in connection with eq. (6.17d) that the Skyrme III-Hartree-Fock energy $\varepsilon_{h9/2}^{(0)} = -12.7$ MeV of the $(1h_{9/2})$ neutron orbit is close to the energy (≈ -12.8 MeV) of the $\{(1i_{13/2})^{-1}*3^-\}$ configuration. A diagonalization of the Hamiltonian performed in the subspace spanned by these two configurations will therefore yield two excited states of ^{207}Pb . This is illustrated in the upper part of fig. 4.42. The spectroscopic factors derived from the full calculation are represented in the lower part. One of the spectroscopic factors is equal to 0.44 [96]. It is quite smaller than unity but is nevertheless much larger than the other spectroscopic factors and can be associated with the residue of the quasiparticle pole. This case represents a transition situation between a quasi-hole state which is primarily contained in a single excited state of ^{207}Pb and a quasi-hole state which corresponds to a bunch of excited states of

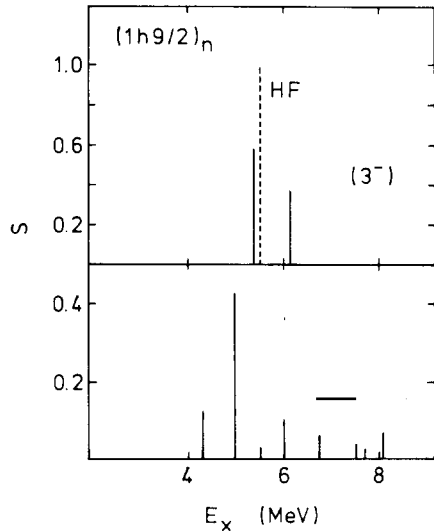


Fig. 4.42. Taken from ref. [319]. Dependence upon the calculated excitation energy E_x of the calculated spectroscopic factor of the $9/2^-$ excited states of ^{207}Pb . The dashed line corresponds to the Hartree-Fock approximation. The full segments in the upper part correspond to the case where only the lowest 3^- excited core state is taken into account, see eqs. (2.28a, b). The lower part represents the results of a full calculation performed in the framework of the model outlined in section 4.6.5 and in column (5) of table 4.3b.

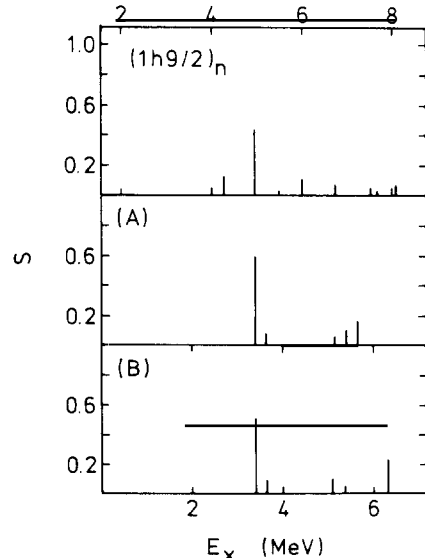


Fig. 4.43. Taken from ref. [319]. The top part shows the calculated spectroscopic factors of the $9/2^-$ excited states of ^{207}Pb , see bottom of fig. 4.42. The middle and lower parts give the spectroscopic factors as measured in refs. [323] (A) and [320] (B) by means of the $^{208}\text{Pb}({}^3\text{He}, \alpha)$ pick-up reaction. The horizontal scales correspond to the calculated (top) and experimental (bottom) excitation energies.

^{207}Pb (microgiant quasiparticle resonance, see e.g. figs. 3.38 and 4.41). Figure 4.43 presents a comparison between the calculated and the measured spectroscopic factors.

4.7.5.4. The $1j_{15/2}$ orbit

Ring and Werner [311] calculated the distribution of single-particle strengths in ^{207}Tl , ^{207}Pb , ^{209}Bi and ^{209}Pb . Only nine core excited states, with energies smaller than 4.7 MeV, were included. They were obtained as outlined in section 4.5.3 in connection with columns (a) of tables 4.1 and 4.2. Unnatural as well as natural parity states are taken into account.

The authors adjusted the value of $\varepsilon_y^{(0)}$ in such a way that the quasiparticle pole ε_y falls at the observed energy. Therefore, the calculation only yields information on the distribution of the single-particle strength. It does not take the Pauli principle into account. Because of the smallness of the excitation energies allowed for the core excitations, the results of ref. [311] cannot be considered as quantitatively realistic.

Figure 4.44 shows the results obtained in ref. [311] in the case of the $1j_{15/2}$ neutron orbit. Since the negative parity of the orbit is opposite to the positive parity of the other subshells of the same main shell, the core excited states with negative parity are expected to have a large influence on the calculated distribution of the single-particle strength. This is confirmed by the work of Li and Klemt

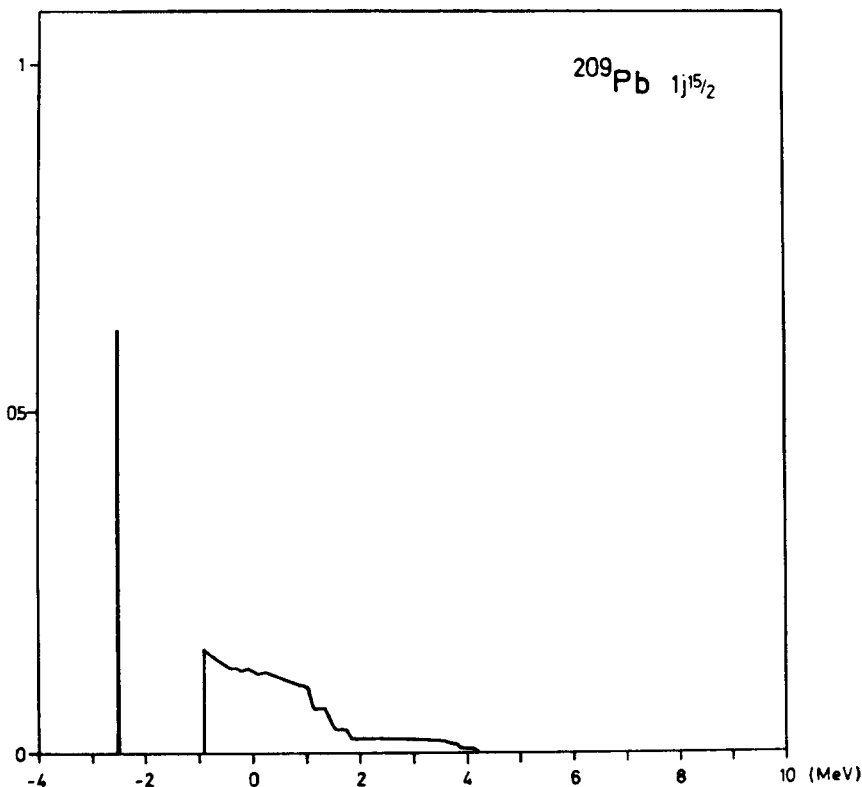


Fig. 4.44. Taken from ref. [311]. Calculated distribution of the $(1j_{15/2})$ single-particle strength in ^{209}Pb . The histogram above -0.9 MeV (which corresponds to $3.9 - 0.9 = 3\text{ MeV}$ excitation energy in ^{209}Pb) is obtained by averaging the calculated strength over an energy interval of 1 MeV.

[306] who find that the contribution of the 3^- vibrations to the derivative (7.15) is equal to 0.52; that of the 5^- vibrations is equal to 0.08; all the other contributions are smaller than 0.04. In ref. [311] the quasiparticle strength $Z_{j15/2}$ is equal to 0.62, while in ref. [306] it is found equal to 0.55.

4.7.5.5. The $2g_{9/2}$ and the $1g_{9/2}$ orbits

The observed $2g_{9/2}$ quasiparticle energy lies at $\varepsilon_F^+ = -3.93$ MeV, right above the Fermi energy. It belongs to the valence shell $N = 6$. The $1g_{9/2}$ quasiparticle belongs to the main shell $N = 4$, with a quasiparticle energy located between -20 MeV and -30 MeV; it appears that part of the $1g_{9/2}$ single-particle strength has been detected in $^{208}\text{Pb}({}^3\text{He}, \alpha)$ pick-up reactions [320–323]. Here, we are not concerned with the comparison between theoretical calculations and empirical information. Rather, we use results calculated in the case of the $2g_{9/2}$ and of the $1g_{9/2}$ neutron orbits as an illustration of the main differences between a valence subshell and a deeply bound subshell. The approximation scheme is the same as in ref. [283]; the averaging interval Δ is taken equal to 1 MeV.

The quantity $\Delta V_{2g_{9/2}}$ defined by eq. (3.18a) is plotted in fig. 4.45a. This case is similar to that of the $1i_{11/2}$ orbit illustrated in fig. 4.34. The Hartree–Fock single-particle energy $\varepsilon_{2g_{9/2}}^{(0)}$ is equal to -3.3 MeV. The quasiparticle energy is given by the intersection between the full curve and the dashed line; this yields

$$\varepsilon_{2g_{9/2}} = -4.1 \text{ MeV}, \quad (4.7.22a)$$

which should be compared with the empirical value $\varepsilon_F^+ = -3.93$ MeV. The corresponding spectroscopic factor is equal to

$$Z_{2g_{9/2}} = 0.77; \quad (4.7.22b)$$

the values calculated by other authors are 0.86 (ref. [311]), 0.79 (ref. [313]), 0.75 (ref. [96]), 0.73 (ref. [306]) and 0.82 (ref. [278]).

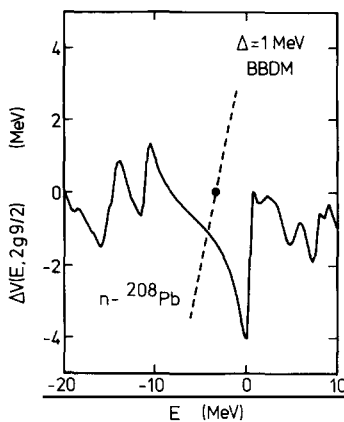


Fig. 4.45a. Energy dependence of the quantity $\Delta V_{2g_{9/2}}(E)$ defined by eq. (3.18a), for the energy-averaging interval $\Delta = 1$ MeV. The straight dashed line represents $E - \varepsilon_{2g_{9/2}}^{(0)}$, where $\varepsilon_{2g_{9/2}}^{(0)} = -3.3$ MeV is derived from the Skyrme III-Hartree-Fock approximation. The approximation scheme is that of ref. [283].

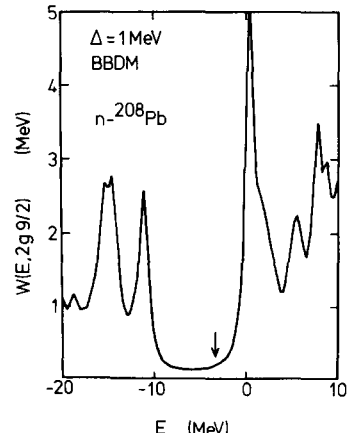


Fig. 4.45b. Energy dependence of the quantity $W_{2g_{9/2}}(E)$ defined by eq. (3.18b), for $\Delta = 1$ MeV. The location of the Skyrme III-Hartree-Fock approximation to the single-particle energy is indicated by an arrow. The large peak of $W_{2g_{9/2}}(E)$ at $E \approx 0.5$ MeV is due to the coupling to the $\{1j_{15/2}\}_* 3^-$ configuration.

The imaginary part $W_{2g9/2}(E)$ of $\mathcal{N}_{2g9/2}(E + \frac{1}{2}i\Delta)$ is plotted in fig. 4.45b. The smallness of $W_{2g9/2}(E)$ for $-10 \text{ MeV} < E < 0 \text{ MeV}$ reflects the fact that the ground state of ^{209}Pb is a quasi-pure single-particle state. The fraction of the $2g_{9/2}$ single-particle strength which is not contained in the ground state of ^{209}Pb is located in excited $9/2^+$ states of ^{209}Pb and in $9/2^+$ excited states of ^{207}Pb . This is exhibited by the strength function contained in fig. 4.45c (see eq. (7.20)).

The situation is quite different in the case of the deeply bound $1g_{9/2}$ neutron orbit, which is illustrated in figs. 4.46a-c. The quantity $\Delta V_{1g9/2}(E)$ is shown in fig. 4.46a. The Skyrme III–Hartree–Fock single-particle energy is equal to -25.6 MeV . The quasiparticle energy as defined by eq. (3.20) is equal to

$$\varepsilon_{1g9/2} = -27 \text{ MeV}. \quad (4.7.23)$$

However, fig. 4.46b shows that

$$W_{1g9/2} = W_{1g9/2}(\varepsilon_{g9/2}) \quad (4.7.24a)$$

is larger in absolute magnitude than

$$\Delta V_{1g9/2} = \Delta V_{1g9/2}(\varepsilon_{1g9/2}). \quad (4.7.24b)$$

Furthermore, the energy dependence of $W_{1g9/2}(E)$ is as strong as that of $\Delta V_{1g9/2}(E)$ for values of E contained in the energy interval

$$D_{1g9/2} = (\varepsilon_{1g9/2} - W_{1g9/2}, \varepsilon_{1g9/2} + W_{1g9/2}). \quad (4.7.25a)$$

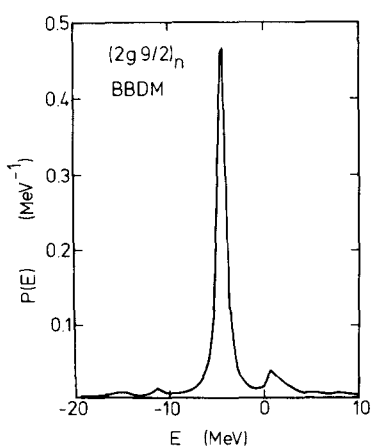


Fig. 4.45c. Energy dependence of the spectral function $P(E)$ for the $2g_{9/2}$ neutron orbit, as calculated from eq. (7.20) [315]. The energy-averaging interval Δ is equal to 1 MeV.

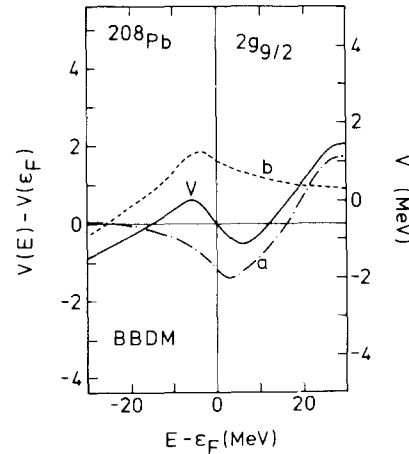


Fig. 4.45d. The full curve represents the gross structure of $\Delta V_{2g9/2}(E) = (V_{2g9/2}(E) - V_{2g9/2}(\varepsilon_F))$, in the domain $-30 \text{ MeV} < E - \varepsilon_F < 30 \text{ MeV}$. The dash-and-dot give the contribution $\Delta V_{2g9/2}^{(a)}(E)$ for $\Delta \approx \text{several MeV}$ (see eq. (7.6a)). The short dashes represent $\Delta V_{2g9/2}^{(b)}(E)$. The approximation scheme is the one outlined in section 4.6 and in the column (7) of table 4.3b.

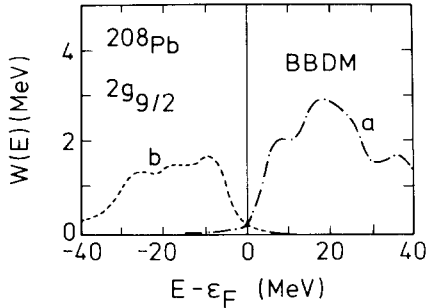


Fig. 4.45e. Gross structure of $W_{2g9/2}^{(a)}(E)$ and of $W_{2g9/2}^{(b)}(E)$ (see eq. (6.23)), with the same notation as in fig. 4.45d.

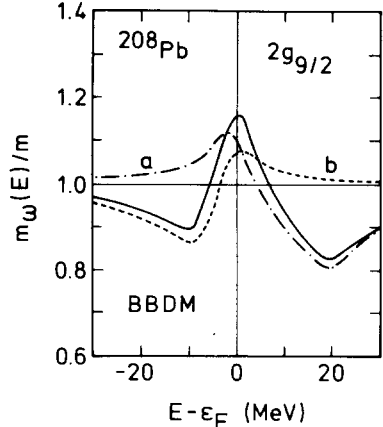


Fig. 4.45f. Gross structure of the ω -mass $m_ω^{(2g9/2)}(E)/m = 1 - d[\Delta V_{2g9/2}(E)]/dE$, see eq. (1.6). The dash-and-dot line and the short dashes represent the contributions of $\Delta V_{2g9/2}^{(a)}(E)$ and of $\Delta V_{2g9/2}^{(b)}(E)$, respectively.

This indicates that the real part of the pole of the one-body Green function $G_{1g9/2}(\omega + \frac{1}{2}i\Delta)$ cannot be accurately calculated from the relation (3.20). Relatedly, the quasiparticle approximations (3.19) and (3.22) only have a limited significance.

Figure 4.46c shows that the spectral function $P_{1g9/2}(E)$ has a broad bump in the vicinity of $\epsilon_{1g9/2}$, with a width about equal to $2W_{g9/2}$. However, the shape of this bump can only be qualitatively reproduced by a Lorentzian. The quasiparticle strength $Z_{1g9/2}$ which appears in eq. (3.22) should be replaced by the energy average value $\langle Z_{1g9/2} \rangle$ of the quantity (see eq. (1.6))

$$Z_{1g9/2}(E) = m/[m_\omega^{(1g9/2)}(E)] = \left\{ 1 - \frac{d}{dE} \Delta V_{1g9/2}(E) \right\}^{-1} \quad (4.7.26)$$

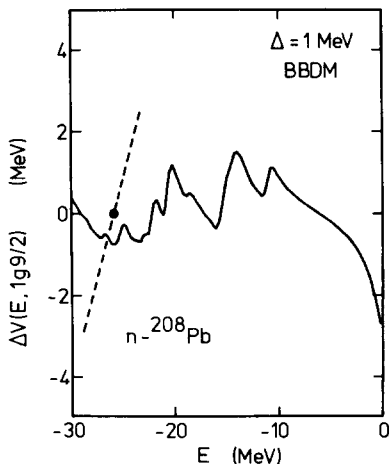


Fig. 4.46a. Same as fig. 4.45a, in the case of the $1g_{9/2}$ neutron orbit [315]. The value of $\epsilon_{1g9/2}^{(0)}$ is equal to -25.6 MeV.

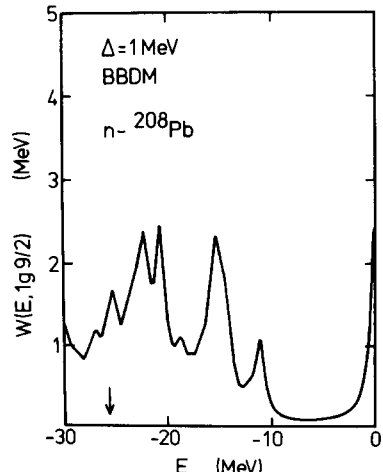


Fig. 4.46b. Same as fig. 4.45b, in the case of the $1g_{9/2}$ neutron orbit [315]. The location of $\epsilon_{1g9/2}^{(0)}$ is indicated by an arrow.

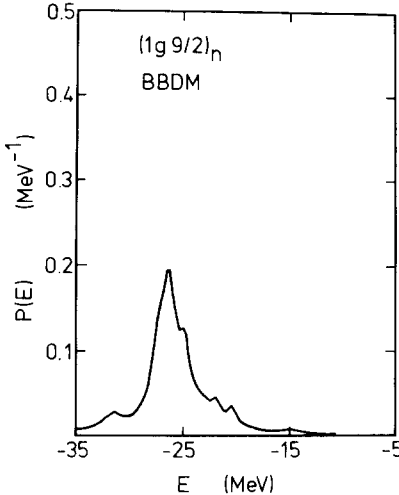


Fig. 4.46c. Same as fig. 4.45c, in the case of the $1g_{9/2}$ neutron orbit [315].

over values of E contained in the energy domain $D_{1g9/2}$ defined by eq. (7.25a). In the present case this average value is close to unity. We note that it could be larger than unity. This does not violate the sum rule (7.4) since $\langle Z_{1g9/2} \rangle$ is not directly related to a spectroscopic factor or to a sum of spectroscopic factors.

If $\langle Z_{1g9/2} \rangle$ is larger than unity, this implies that the Lorentzian fit to the quasiparticle bump of the spectral function contains more single-particle strength than the sum of the actual spectroscopic factors of all the levels, and a fortiori than the sum of the spectroscopic factors of the levels contained in the energy domain $D_{1g9/2}$ defined by eq. (7.25). In the present case,

$$\langle Z_{1g9/2} \rangle \approx 1. \quad (4.7.27)$$

It is rather natural to find that $\langle Z_{nlj} \rangle$ is larger than the calculated value of the spectroscopic factor of a valence shell. Indeed, the energy $\varepsilon_{nlj}^{(0)}$ of a deeply bound orbit is close to many energies $\varepsilon_h^{(0)} - E_\lambda$ (see eq. (2.28b)). Hence, the $\{n, l, j\}$ configuration finds many nearby configurations $\{h^{-1} * \lambda\}$ with which it can mix via the effective interaction. A large fraction of the calculated single-particle strength can therefore remain contained within the broad quasi-hole peak (see fig. 3.38). The situation is different in the case of a valence subshell. Indeed, most $\{h^{-1} * \lambda\}$ configurations then lie several MeV away from $\varepsilon_{nlj}^{(0)}$. These configurations suck part of the single-particle strength away from the quasiparticle peak (which in that case reduces to a single state). This necessarily renders Z_{nlj} smaller than unity in the case of a valence subshell.

Let us now return to the $(2g_{9/2})$ single-particle orbit. Figures 4.45a, b show that the corresponding values of $\Delta V_{2g9/2}(E)$ and of $W_{2g9/2}(E)$ are strong functions of energy for $|E - \varepsilon_F| > 4$ MeV, even though an energy-averaging interval $\Delta = 1$ MeV has been introduced. In some applications, a larger value of Δ may be of interest. This would smoothen the narrow wiggles in $\Delta V_{2g9/2}(E)$ and in $W_{2g9/2}(E)$ and may mock up the role played by more complicated core excitations. Furthermore, the narrow structures of $\Delta V_{2g9/2}(E)$ and of $W_{2g9/2}(E)$ are model-dependent (see e.g. figs. 4.37a and 4.37b). It is therefore instructive to consider the gross behaviour of $\Delta V_{2g9/2}(E)$ and of $W_{2g9/2}(E)$ over a wide energy interval. This is performed in figs. 4.45d–4.45f.

We note that although the $(2g_{9/2})$ neutron orbit is unoccupied in the uncorrelated ^{208}Pb core, the quantity $W_{2g9/2}(E)$ is different from zero for $E < \varepsilon_F$. It is moreover approximately symmetric about $E = \varepsilon_F$. The quantity $\Delta V_{2g9/2}(E)$ is approximately skew-symmetric about $E = \varepsilon_F$. The ω -mass $m_\omega^{(2g9/2)}(E)$ has a peak centred on $E = \varepsilon_F$, with a full width at half-maximum approximately equal to 10 MeV.

4.7.6. Comparison between calculations of the quasiparticle strengths in the valence shells

Table 4.4 summarizes the results obtained by several groups for the quasiparticle strength Z_{lj} of the valence subshells for neutrons in ^{208}Pb . We recall that for these subshells Z_{lj} can be identified with the spectroscopic factor, and that it is related to the on-the-energy-shell value of the ω -mass (1.6) by eq. (7.8b), namely

$$Z_{lj} = \{m^{(lj)}(\varepsilon_{lj})/m\}^{-1}. \quad (4.7.28)$$

As expected, the calculated values of Z_{lj} sensitively depend upon the theoretical approximations. Figure 4.47a shows the level-average

$$\langle m_\omega/m \rangle = \sum_j [(2j+1)m_\omega^{(lj)}(\varepsilon_{lj})] / \sum_j [(2j+1)m], \quad (4.7.29)$$

where the sum runs over all the subshells of a given main valence shell of ^{208}Pb . Typically, the level-average

Table 4.4

Compilation of the spectroscopy factors Z_{nj} (see eq. (7.8a)) of the subshells which belong to the valence neutron shells of ^{208}Pb . The numbering of the columns is the same as in tables 4.3a and 4.3b: column (2) corresponds to ref. [311], (3) to [312], (4) to [313], (5) to [96], (6) to [306], (7) to [315], (8) to [114], and (9) to [278]

$n \ell j$	Z_{nj}							
3d 3/2	0.88	0.72	0.79	0.80	0.72	0.65	0.86	0.84
4s 1/2	0.92	0.76	0.79	0.82	0.80	0.68	0.93	0.86
2g 7/2	0.83	0.80	0.81	0.86	0.61	0.74	0.79	0.72
3d 5/2	0.90	0.78	0.78	0.83	0.77	0.75	0.93	0.85
1j 15/2	0.62	0.66	0.79	0.71	0.55	0.70	0.66	0.73
2g 9/2	0.89	0.86	0.79	0.75	0.73	0.77	0.87	0.82
1i 11/2	0.97	0.94	0.88	0.86	0.67	0.85	0.83	0.75
<hr/>								
3p 1/2	0.95	0.94	0.78	0.73	0.79	0.84		
3p 3/2	0.92	0.91	0.74	0.82	0.73	0.81		
2f 5/2	0.94	0.94	0.82	0.76	0.71	0.82		
1i 13/2	0.87	0.92	0.83	0.72	0.62	0.78		
2f 7/2	0.70	0.75	0.70	0.59	0.53	0.58		
1h 9/2	0.84	0.82	0.81	0.44	0.51	0.60		
	2	3	4	5	6	7	8	9

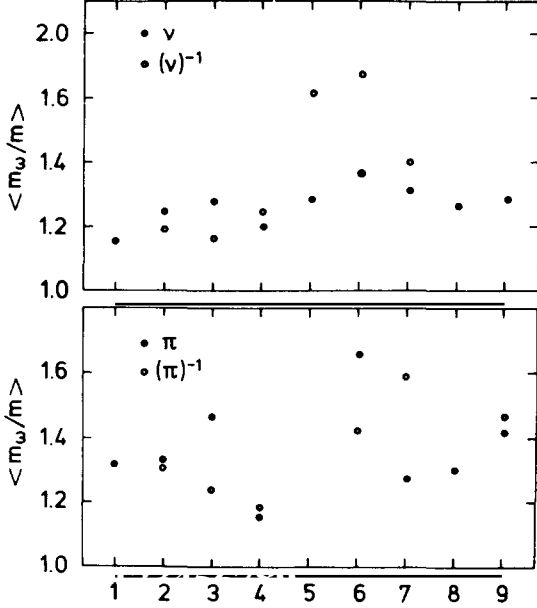


Fig. 4.47a. Compilation of the values of the level average $\langle m_\omega/m \rangle$ (see eq. (7.29)) calculated by various authors for the proton and neutron valence shells in ^{208}Pb . The numbering in the abscissa is the same as in tables 4.3a and 4.3b: (1) corresponds to ref. [2], (2) to [311], (3) to [312], (4) to [313], (5) to [96], (6) to [306], (7) to [315], (8) to [114] and (9) to [278].

$\langle m_\omega/m \rangle$ is contained in the range

$$1.2 < \langle m_\omega/m \rangle < 1.4 \quad (4.7.30a)$$

in the case of the neutron valence shells, and in the range

$$1.3 < \langle m_\omega/m \rangle < 1.6 \quad (4.7.30b)$$

in the case of the proton valence shells.

The average $\langle m_\omega/m \rangle$ appears to be somewhat larger in the case of protons than in the case of neutrons. The authors of ref. [278] suggest that this may be due to the role of the attractive part of the tensor component of the interaction, and to the fact that the protons are more likely than valence neutrons to form $T = 0$ states with the core nucleons, because of the existence of a neutron excess.

The value of $\langle m_\omega/m \rangle$ is particularly large in the case of neutron holes in the calculations of refs. [96] and [306], see columns (5) and (6) of fig. 4.47a. This is related to the very small value of the calculated spectroscopic factors of the $2f_{7/2}$ and $1h_{9/2}$ quasiparticle states, see table 4.4. In turn, this is due to the near-degeneracy of these single-particle states with a $\{(h)^{-1}*\lambda\}$ configuration. This has been illustrated at the top of fig. 4.42 in the case of the $(1h_{9/2})$ orbit.

The value of $\langle m_\omega/m \rangle$ shown in fig. 4.47a has a tendency to increase with the number of core excited states included in the calculation. For instance, the calculated spectroscopic factors are normally smaller in ref. [306] (column (6)) than in ref. [311] (column (2)). We also saw in section 4.7.5.1 that unnatural parity states play a significant role in reducing the spectroscopic factors.

The spectroscopic factor of the intruder ($1j_{15/2}$) quasiparticle state is smaller than that of the other subshells of the same $N = 6$ shell. This is due to the fact that the ($1j_{15/2}$) configuration can be coupled to $\{c*3^-\}$ configurations where c also belongs to the $N = 6$ shell.

The dependence of $\langle m_\omega/m \rangle$ upon the size of the configuration space has been discussed in refs. [313] and [324] in the case of the values shown in the column (4) of table 4.3a and of fig. 4.47a. Figure 4.47b represents the dependence of the level-average of the spectroscopic factor upon the number N of shells allowed for the single-particle in the intermediate state. It shows that the average spectroscopic factor is not very sensitive to the value of N provided that $N > 4$. Figure 4.47c gives the contribution to the difference $1 - \langle m_\omega/m \rangle$ of the core excitations with multipolarity λ . It exhibits the importance of the 3^- excitations.

4.7.7. Conclusions

We have shown that in the case of a valence subshell the quasiparticle strength is identical to the spectroscopic factor. It is necessarily smaller than unity. The spectral function (7.20) then has a narrow peak (whose width has no physical meaning) and a small background located on each side of this narrow peak, and usually disconnected from it.

For a deeply bound subshell, the spectral function has a broad bump whose area is measured by the energy average $\langle Z_{ij} \rangle$ of the quantity defined by eq. (7.26). This average can be larger or smaller than unity. It approximately gives the area of a Lorentzian fit to the distribution of the spectroscopic factors of the levels contained in the energy interval

$$D_{nlj} = (\varepsilon_{nlj} - \langle W_{nlj} \rangle, \quad \varepsilon_{nlj} + \langle W_{nlj} \rangle). \quad (4.7.25b)$$

The full width at half-maximum of this Lorentzian is approximately given by twice the energy average $\langle W_{nlj} \rangle$ of $W_{nlj}(E)$ in the domain (7.25b).

These conclusions have been illustrated by the results of several calculations. The borderline between the case of a deeply bound subshell and that of a valence subshell is not always as sharply defined as we just outlined. For instance, fig. 4.48 shows that in the calculation reported in ref. [311] the distribution of the strength of the deeply bound $3s_{1/2}$ subshell behaves almost as that of a valence subshell. This may, however, be due to the simplifying assumptions made and to the very restricted subspace used in ref. [311].

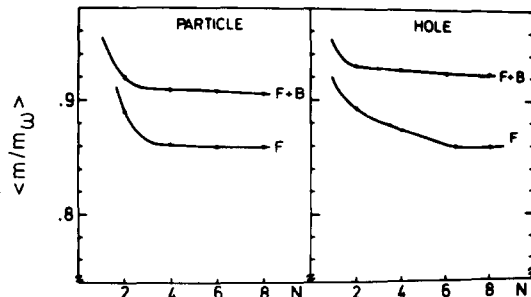


Fig. 4.47b. Adapted from ref. [313]. Dependence upon the number N of major shells (allowed for the intermediate single-particle states) of the value of $\langle m/m_\omega \rangle$ in the case of the neutron valence shell located above the Fermi energy (left) and for the valence shell which lies below the Fermi energy (right). The notation is the same as in fig. 4.27.

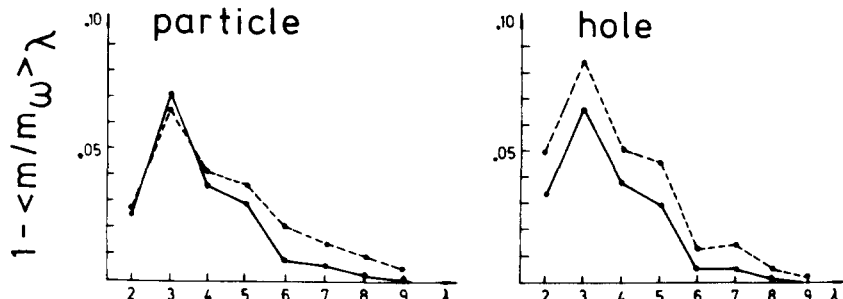


Fig. 4.47c. Adapted from ref. [324]. Dependence upon λ of the contribution of the core excited states with multipolarity λ to the value of $1 - \langle m/m_w \rangle$ in the case of the particle (left) and of the hole (right) valence shells. The full curves are derived from isoscalar core excitations while the dashed lines also include isovector excitations.

It should also be kept in mind that microscopic calculations are based on an effective particle–hole (or particle–vibration) interaction. By their very nature, these calculations cannot describe the phenomena associated with the existence of strong short-range forces in nuclei. These short-range forces lead to the virtual excitation of high-lying configurations of the ($A - 1$) and ($A + 1$) nuclei. Hence, the sum of the actual spectroscopic factors of the levels with excitation energy less than about 30 MeV is likely to be closer to 0.8 than to unity [325]. The same feature is responsible for the fact that the

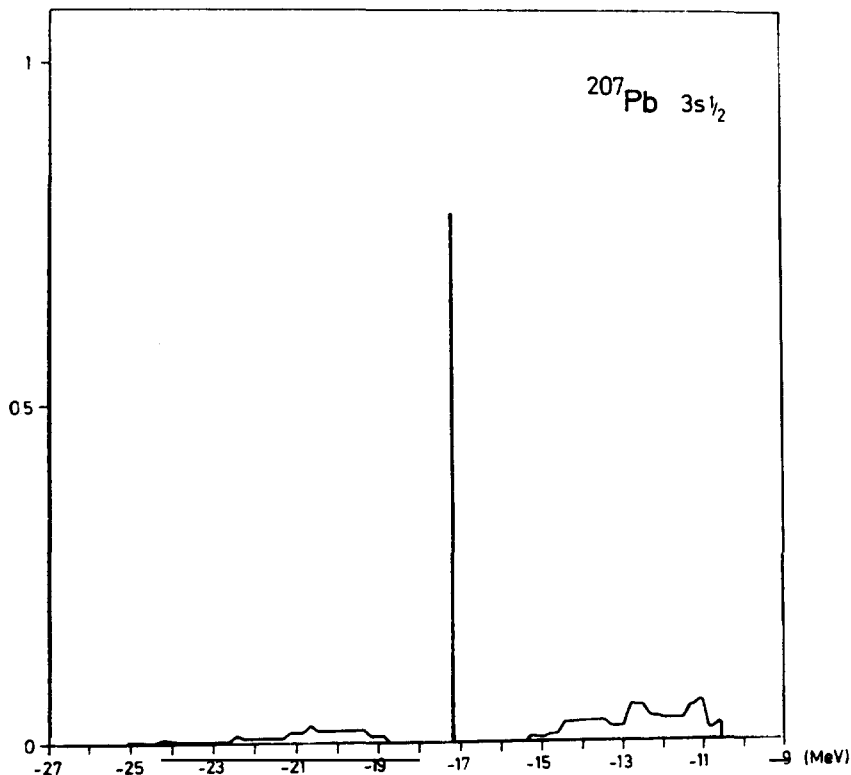


Fig. 4.48. Taken from ref. [311]. Calculated distribution of the $(3s_{1/2})$ single-particle strength in ^{207}Pb . The notation is the same as in fig. 4.44.

microscopic calculations lead to a smaller depletion of the Fermi sea of the correlated core than the dispersion relation approach, compare figs. 4.17 and 4.38a–c.

4.8. Level dependence of the dispersion corrections

4.8.1. Energy shift

Equation (3.20) shows that the dispersion correction to the Hartree–Fock single-particle energy $\varepsilon_{ij}^{(0)}$ is given by the value of $\Delta V_{ij}(E)$ at $E = \varepsilon_{ij}$, where ε_{ij} is the quasiparticle energy. The difference $|\varepsilon_{ij}^{(0)} - \varepsilon_{ij}|$ is smaller than 2 MeV. Hence, the only portion of the curve $\Delta V_{ij}(E)$ which is of interest inasmuch as the quasiparticle energy is concerned is the segment contained in the energy interval $(\varepsilon_{ij}^{(0)} - 2 \text{ MeV}, \varepsilon_{ij}^{(0)} + 2 \text{ MeV})$. This segment is denoted by the shaded area in fig. 4.49, which corresponds to the example of the $1i_{11/2}$ neutron orbit shown in fig. 4.34.

We had concluded from figs. 4.5a, b that the plot versus ε_{ij} of the semi-empirical values of the quantities

$$\Delta V_{ij} = \Delta V_{ij}(\varepsilon_{ij}) \approx \Delta V_{ij}(\varepsilon_{ij}^{(0)}) = \Delta V_{ij}^{(0)} \quad (4.8.1)$$

delineate a fairly well-defined average dependence upon ε_{ij} for the subshells which belong to the valence shells. Let us investigate whether such a well-defined trend also emerges from the microscopic calculations and whether this property can be extrapolated to values of ε_{ij} which lie in shells located far away from the Fermi energy.

In the upper part of fig. 4.50, we have gathered the segments analogous to the one shown in fig. 4.48

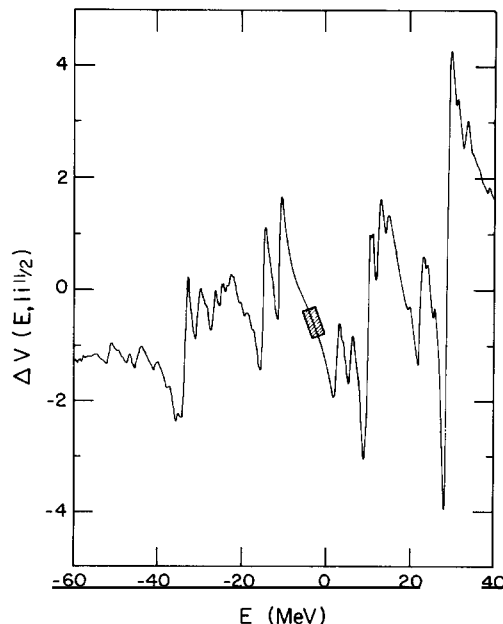


Fig. 4.49. Taken from ref. [326]. The curve shows the dependence upon energy of the quantity $\Delta V_{111/2}(E)$, see fig. 4.34; the averaging interval is $\Delta = 1 \text{ MeV}$. The shaded segment is centred on the Skyrme III–Hartree–Fock single-particle energy $\varepsilon_{111/2}^{(0)} = -2.8 \text{ MeV}$.

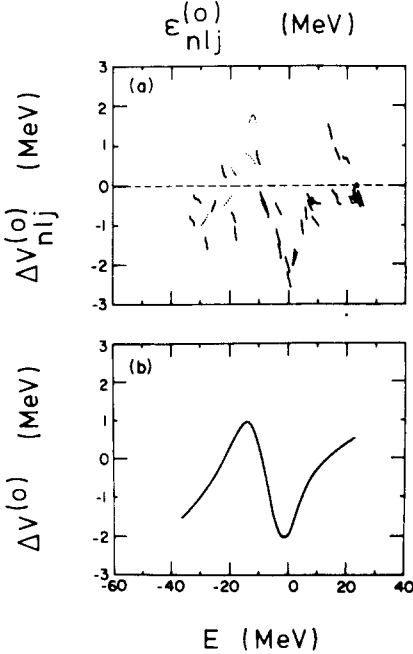


Fig. 4.50. Taken from ref. [326]. Dependence upon the Skyrme III-Hartree-Fock single-particle energy $\varepsilon_{nlj}^{(0)}$ of the values of $\Delta V_{nlj}(\varepsilon_{nlj}^{(0)})$ for forty neutron orbits in ^{208}Pb . A dotted segment indicates that $\varepsilon_{nlj}^{(0)}$ falls in a wiggly part of $\Delta V_{nlj}(E)$; the corresponding segment is then associated with the gross structure of $\Delta V_{nlj}(E)$ which is the one which would emerge if one increased the value of the averaging interval Δ or included a larger density of states in the configuration space.

for the 40 single-particle states whose energy extends from that of $1f_{7/2}$ subshell to that of the $4d_{3/2}$ orbit, i.e. for the energy range $-35 \text{ MeV} < \varepsilon_{nlj}^{(0)} < +25 \text{ MeV}$. The distribution of these segments follows a fairly well-defined pattern which is represented in the curve $\Delta V^{(0)}(E)$ shown in the lower part of fig. 4.50. This curve has been drawn by eye through the calculated segments.

The property that on the average $\Delta V_{nlj}^{(0)}$ depends smoothly upon $\varepsilon_{nlj}^{(0)}$ shows that one can approximately reduce the empirical values of the quasiparticle energies by introducing a continuous energy dependence in the parameters of the shell-model potential. This is in keeping with the results derived from the dispersion relation approach in section 4.4.

The results shown in fig. 4.50 have been calculated in the framework of the particle-vibration coupling model outlined in section 4.6.6. In the case of the valence subshells, the value of ΔV_{nlj} defined by eq. (8.1) can be obtained from the various calculations described in section 4.6. For instance, the open dots in fig. 4.51 show the dependence upon $\varepsilon_{nlj} - \varepsilon_F$ ($\varepsilon_F \approx -6 \text{ MeV}$) of the quantities ΔV_{nlj} derived from fig. 4.31 and from a similar calculation performed in the case of protons. This calculation is restricted to the main valence shell which lies above the Fermi energy. The results are nevertheless sufficient to confirm that the calculated values follow a fairly well-defined pattern in this energy domain.

4.8.2. The on-shell ω -mass

When a small perturbation $\Delta V_{nlj}^{(0)}$ which depends smoothly upon $\varepsilon_{nlj}^{(0)}$ is added to $\varepsilon_{nlj}^{(0)}$, it introduces a relative change

$$\frac{d(\Delta V_{nlj}^{(0)})}{d(\varepsilon_{nlj}^{(0)})} = 1 - m_\omega(\varepsilon_{nlj}^{(0)})/m, \quad (4.8.2)$$

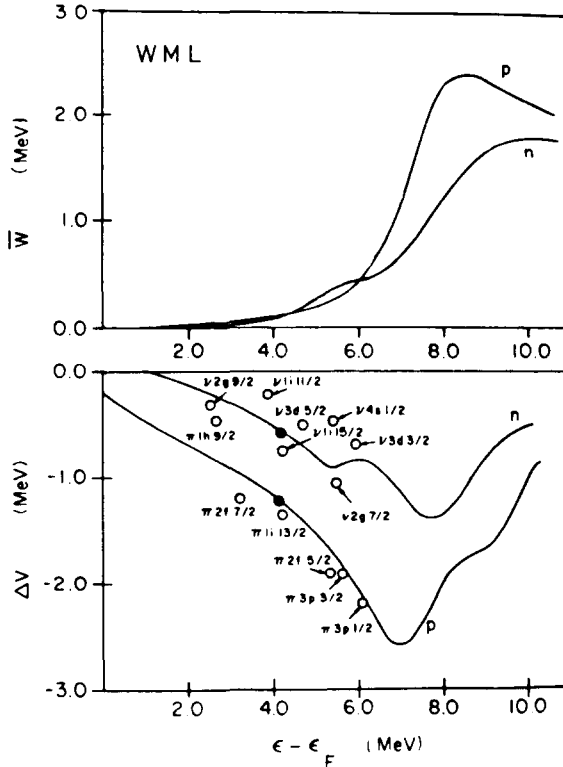


Fig. 4.51. Adapted from ref. [114]. The dots in the lower part show the dependence upon $\epsilon_{nlj} - \epsilon_F$ ($\epsilon_F \approx -6$ MeV) of the quantities ΔV_{nlj} defined by eq. (8.1), as derived from the calculation of Wambach et al. [114] for the proton and neutron orbits which belong to the main valence shell which lies above the Fermi energy in ^{208}Pb . The curves shown in the upper part show the dependence upon $E - \epsilon_F$ of the level-average $\bar{W}(E)$ defined by eq. (9.1a), where the sum over α runs over the subshells of the valence shell. The curves in the lower part are obtained from $\bar{W}(E)$ via the dispersion relation (9.5) with the assumption $\bar{W}(E - \epsilon_F) = \bar{W}(\epsilon_F - E)$. The full dots are located at the abscissae $\langle \epsilon_p \rangle - \epsilon_F$ and give the value of $\bar{\Delta V}(\langle \epsilon_p \rangle)$; here $\langle \epsilon_p \rangle$ is the centroid energy defined by eq. (4.18a) (for neutrons and protons, respectively).

to the single-particle energies. Equation (8.2) defines the on-the-energy-shell ω -mass:

$$m_\omega^{(0)}(E)/m = 1 - d(\Delta V^{(0)}(E))/dE. \quad (4.8.3)$$

The density of the quasiparticle energies in the vicinity of E is inversely proportional to $m_\omega^{(0)}(E)/m$. Our notation is in keeping with eq. (1.8). The quantity $m_\omega^{(0)}(E)/m$ is represented by the full curve in fig. 4.52.

We argued in connection with eq. (6.19) that the quasiparticle energies are approximately given by

$$\epsilon_{lj} \approx \epsilon_{lj}^{(0)} + Z_{lj}^{(0)} \Delta V_{lj}^{(0)}, \quad (4.8.4a)$$

where $Z_{lj}^{(0)}$ is defined by eq. (6.20). If we make the crude assumption that the slope of the functions $\Delta V_{nlj}(E)$ of E follow the pattern $\Delta V^{(0)}(E)$ for E close to $\epsilon_{nlj}^{(0)}$, one has

$$Z_{lj}^{(0)} \approx m/[m_\omega^{(0)}(\epsilon_{lj}^{(0)})]. \quad (4.8.4b)$$

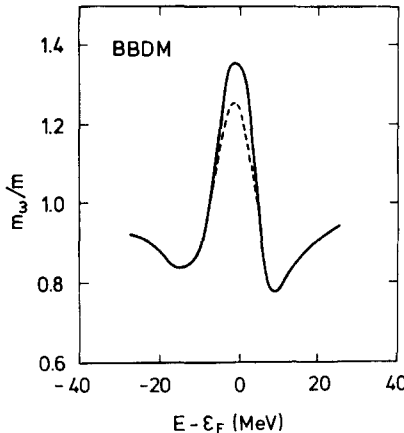


Fig. 4.52. The full curve represents the dependence upon $E - \epsilon_F$ of the ω -mass $m_\omega^{(0)}(E)/m$ defined by eq. (8.3), where $\Delta V^{(0)}(E)$ is the function shown at the bottom of fig. 4.49. The dashed curve gives the value of the ω -mass $m_\omega(E)/m$ defined by eq. (8.4c).

This suggests the introduction of a modified on-shell ω -mass via the relation

$$m_\omega(E)/m = 1 - [m/m_\omega^{(0)}(E)][d(\Delta V^{(0)}(E))/dE]. \quad (4.8.4c)$$

This quantity is represented by the dashed curve in fig. 4.52.

The density of the Skyrme–Hartree–Fock single-particle energies $\epsilon_{nlj}^{(0)}$ is approximately inversely proportional to the Skyrme–Hartree–Fock effective mass $m_{Sk}^* = m_{Sk}^*(0)$ defined by eq. (2.18). The density of the quasiparticle energies in the vicinity of E is proportional to the density of these Hartree–Fock single-particle energies and, in addition, is inversely proportional to the ω -mass $m_\omega(E)$. Hence, the density of the quasiparticle energies in the vicinity of E is approximately inversely proportional to the effective mass $m^*(E)$ defined by the following relation

$$\frac{m^*(E)}{m} = \frac{m_{Sk}^*}{m} \cdot \frac{m_\omega(E)}{m}, \quad (4.8.5a)$$

which can be compared with eq. (3.6.11). If the effective interaction is not of the Skyrme type, the quantity m_{Sk}^* should be replaced by the Hartree–Fock approximation m_{HF}^* to the effective mass, which can have a smooth monotonic dependence upon E :

$$\frac{m^*(E)}{m} = \frac{m_{HF}^*(E)}{m} \cdot \frac{m_\omega(E)}{m}. \quad (4.8.5b)$$

4.9. Level-averages of the dispersion corrections

4.9.1. Introduction

In the dispersion relation approach described in section 4.4, the corrections to the mass operator are evaluated in the space representation, and it has been assumed that these corrections are local. The corresponding dispersion corrections to the single-particle energies $\epsilon_{nlj}^{(0)}$ depend upon the whole set of

quantum numbers $\{n, l, j\}$. However, they mainly depend upon the difference $\varepsilon_{nlj}^{(0)} - \varepsilon_F$; this is illustrated in figs. 4.5a and 4.5b. In the microscopic calculations described in sections 4.6–4.8 the dispersion corrections to the mass operator are evaluated in the (Hartree–Fock) shell-model representation. Here too, it turns out that the corresponding dispersion corrections to the single-particle energies $\varepsilon_{nlj}^{(0)}$ mainly depend upon the difference $\varepsilon_{nlj}^{(0)} - \varepsilon_F$; this is illustrated in figs. 4.50 and 4.51.

Inasmuch as one is primarily interested in the trend of the dispersion corrections, it therefore appears meaningful to perform level averages. We thus introduce the quantities ($\alpha = \{n, l, j\}$)

$$\bar{W}(E) = \left\{ \sum_{\alpha} (2j_{\alpha} + 1) \right\}^{-1} \sum_{\alpha} (2j_{\alpha} + 1) W_{\alpha}(E), \quad (4.9.1a)$$

$$\bar{\Delta V}(E) = \left\{ \sum_{\alpha} (2j_{\alpha} + 1) \right\}^{-1} \sum_{\alpha} (2j_{\alpha} + 1) \Delta V_{\alpha}(E), \quad (4.9.1b)$$

$$\frac{\bar{m}_{\omega}(E)}{m} = 1 - \frac{d}{dE} \bar{\Delta V}(E). \quad (4.9.2)$$

This notation is in keeping with eq. (1.7). The meaningfulness of performing these level-averages will partly be evaluated by comparing the outcome of this approach to the results described in the previous sections. We note that the quantities $\bar{W}(E)$ and $\bar{\Delta V}(E)$ depend upon the nature and the number of the subshells introduced in the sum over α on the right-hand side of eqs. (9.1a, b).

4.9.2. Average over the levels of a valence shell

Figure 4.53 shows the calculated energy dependence of $W_{nlj}(E)$ for $E > \varepsilon_F$ for the proton and neutron valence subshells located above the Fermi energy in ^{208}Pb [114]. There exist noticeable differences between the energy dependence of the various $W_{nlj}(E)$. We note, however, that the corresponding contribution to the dispersion correction to the single-particle energies is given by

$$\Delta V_{lj}^{(a)} \approx \frac{\mathcal{P}}{\pi} \int_{\varepsilon_F^+}^{\infty} \frac{W_{lj}^{(0)}(E')}{\varepsilon_{nlj}^{(0)} - E'} dE', \quad (4.9.3)$$

see eqs. (3.28a) and (8.1). Figure 4.53 shows that $W_{lj}^{(a)}(E') = 0$ for $E' - \varepsilon_F < 5 \text{ MeV}$. Hence, the use of the principal value prescription in eq. (9.3) is not required in practice. Moreover, $\Delta V_{lj}^{(a)}$ is not very much influenced by the wiggles in $W_{lj}^{(a)}(E')$ which are located at $E' - \varepsilon_F > 10 \text{ MeV}$. It thus appears meaningful to perform the level-averages (9.1a, b), where the sum over α now runs over the subshells of the valence shell located above the Fermi energy.

The resulting values of $\bar{W}(E)$ are shown in the upper part of fig. 4.51. By assuming that $\bar{W}(E)$ is symmetric about the Fermi energy

$$\bar{W}(E - \varepsilon_F) = \bar{W}(\varepsilon_F - E), \quad (4.9.4)$$

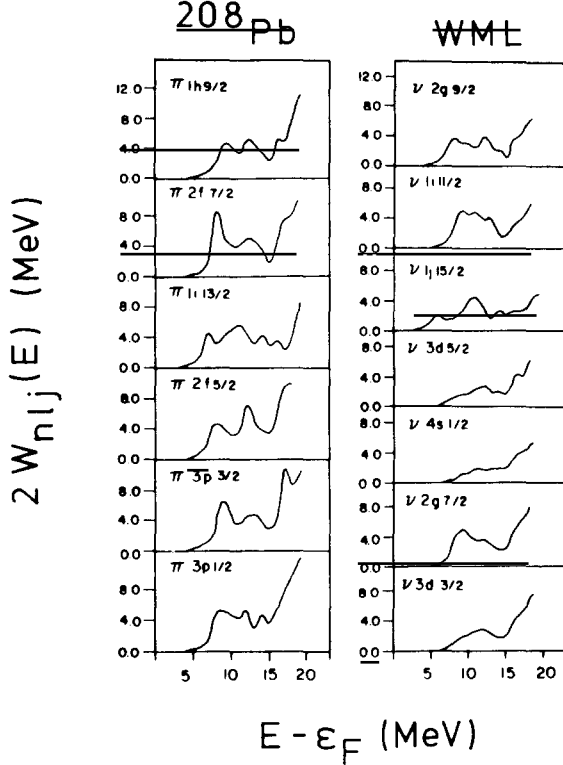


Fig. 4.53. Adapted from ref. [114]. Dependence upon $E - \varepsilon_F$ of $2W_{nlj}(E)$ (see eq. (3.18b)) for $E > \varepsilon_F$ and for the proton (left) and neutron (right) valence subshells located above the Fermi energy. The theoretical framework is outlined in section 4.6.7 and in column (8) of table 4.3b. The averaging interval Δ is equal to 2 MeV.

the following dispersion relation (see eqs. (4.26a–c))

$$\overline{\Delta V}(E) \approx \frac{\mathcal{P}}{\pi} \int \frac{\bar{W}(E')}{E - E'} dE' \quad (4.9.5)$$

yields the values of $\overline{\Delta V}(E)$ represented by the curves in the lower part of fig. 4.51. The fair agreement between these curves and the calculated open dots illustrates the meaningfulness of performing level-averages over the subshells of one valence shell.

This calculation involves the assumption that $\bar{W}(E)$ is symmetric about ε_F . A similar assumption had been made in the dispersion relation approach described in section 4.4. Figure 4.54 shows that it is fairly accurate in the case of the two proton valence shells in ^{208}Pb .

It is only for values of E contained within the energy range spanned by the energies of the valence shell, typically for the average value $E = \langle \varepsilon_p \rangle$, that the quantities $\overline{\Delta V}(E)$ and $\bar{W}(E)$ have a straightforward physical meaning in terms of quasiparticle properties. There, these quantities coincide with the on-shell values discussed in section 4.8. In particular, the fact that for $E - \varepsilon_F > 10$ MeV the calculated $\bar{W}(E)$ is much smaller than the strength of the imaginary part of the empirical optical-model potential (see fig. 4.21) is not necessarily worrisome.

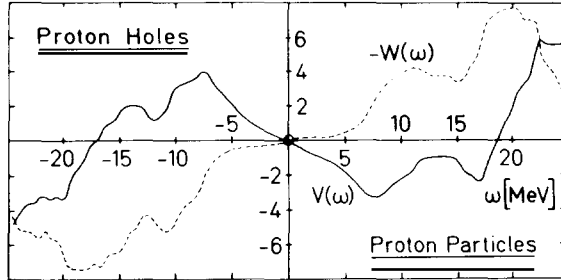


Fig. 4.54. Taken from ref. [278]. Dependence upon $\omega = E - \epsilon_F$ of the quantities $-W(\omega) = -\bar{W}(\omega)$ and $V(\omega) = \bar{V}(\omega)$ defined by eqs. (9.1a, b) in which the sum over α runs over the subshells of the proton valence shells in ^{208}Pb . The theoretical framework is outlined in section 4.6.8 and in column (9) of table 4.3b. The averaging interval Δ is equal to 1.5 MeV.

The value of $\bar{V}(E)$ for $E \neq \langle \epsilon_p \rangle$ gives the average potential energy of a quasiparticle which is carried out of the energy shell. This is of interest in cases where the quasiparticles of the valence shell enter in the microscopic description of a very collective core excitation [327].

Figures 4.37a and 4.37b illustrate the fact that the calculated quantities $\Delta V_{nj}(E)$ and $W_{nj}(E)$ are quite sensitive to the theoretical approximation scheme. One may wonder whether the level-averaging does not diminish this dependence. Figures 4.55a and 4.55b show that this is to some extent true. The quantities $\bar{V}(E)$ calculated in refs. [278, 315] only differ by a constant for $E - \epsilon_F < 5$ MeV. In this energy domain, $\bar{W}(E)$ also takes approximately the same values in the two cases, but it has essentially no physical meaning. Indeed, $\bar{W}(E)$ at low energy differs from zero only because one has introduced a large energy-averaging interval Δ .

In the domain $E - \epsilon_F > 7$ MeV, the full and dashed curves shown in, respectively, figs. 4.55a and 4.55b are quite different. In particular, $\bar{W}(E)$ shows a peak at $E - \epsilon_F \approx 10$ MeV in the calculations reports in ref. [278] (see also figs. 4.21 and 4.51, ref. [114]), while this peak is absent in the dashed curve of fig. 4.55b. This difference is not yet understood. We note that $E \approx \epsilon_F + 10$ MeV corresponds to

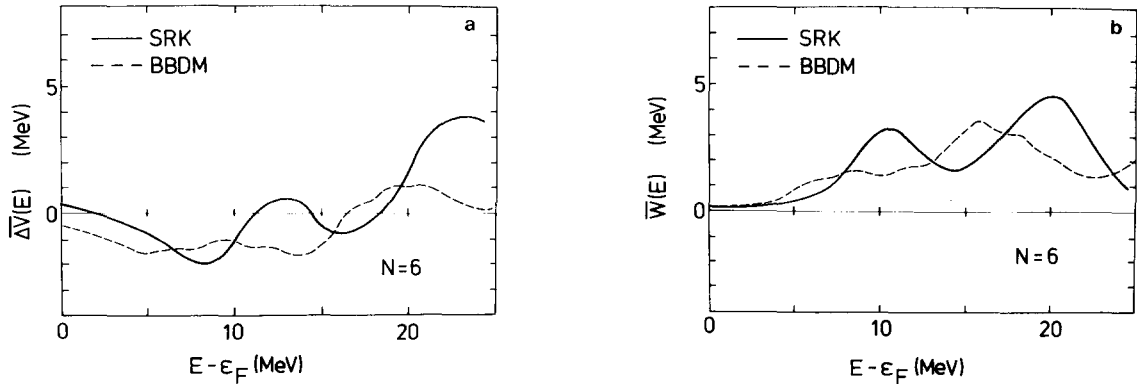


Fig. 4.55. (a) Dependence upon $E - \epsilon_F$ ($\epsilon_F = -6$ MeV) of the quantity $\bar{V}(E)$ defined by eq. (9.1b), where the sum over α runs over the levels of the $N = 6$ neutron shell, i.e. the neutron valence shell located just above the Fermi energy in ^{208}Pb . The full curve is taken from ref. [278] (see column (9) of table 4.3b); it is associated with the averaging interval $\Delta = 1.5$ MeV. The dashes correspond to $\Delta = 1$ MeV and to the approximation scheme outlined in column (7) of table 4.3b [315]. (b) Same as (a) in the case of $\bar{W}(E)$ (see eq. (9.1a)).

$E \approx \langle \epsilon_p \rangle + 6$ MeV. Hence, this peak should be due to core states located at approximately 6 MeV excitation energy. The physical origin of this calculated peak is thus difficult to understand. Indeed, it can also not be accounted for by the existence of a group of $\{c_*\lambda\}$ excitations (see graph (c) of fig. 4.4) at the energy $\langle \epsilon_p \rangle_{N=7} + E_3^- \approx 14$ MeV, where $\langle \epsilon_p \rangle_{N=7}$ is the average energy of the $N = 7$ neutron shell. These excitations probably correspond to the appearance of a maximum of $\bar{W}(E)$ at $E - \epsilon_F \approx 20$ MeV in the full curve of fig. 4.55b. We conclude that the differences between various microscopic calculations are significant and require further investigations.

Figures 4.56a and 4.56b show the results obtained in refs. [114] and [278] for the level-average ω -mass $\bar{m}_\omega(E)$ defined by eq. (9.2). This quantity has a straightforward interpretation for E equal to the on-shell value $\langle \epsilon_p \rangle \approx \epsilon_F + 4$ MeV (see fig. 4.51). Indeed, one has

$$\langle Z_{ij} \rangle \approx m / \bar{m}_\omega(\langle \epsilon_p \rangle) \quad (4.9.6)$$

where $\langle Z_{ij} \rangle$ is the average spectroscopic factor of the valence shell, see eq. (7.28). Figures 4.56a and 4.56b yield $\bar{m}_\omega(\langle \epsilon_p \rangle)/m \approx 1.27$ and 1.30, respectively. These results are in good agreement with the values quoted in the first line of the columns (8) and (9) of table 4.3b. They imply that (see eqs. (7.29) and (9.6))

$$\langle m_\omega / m \rangle \approx \bar{m}_\omega(\langle \epsilon_p \rangle) / m. \quad (4.9.7)$$

The assumption (9.4) entails that $\overline{\Delta V}(\epsilon_F) = 0$. In the domain $0 < |E| < 9$ MeV the functions $\Delta V_{nij}(E)$ are moreover approximately linear functions of energy, see e.g. figs. 4.34 and 4.45a. Then, one can check that

$$\bar{m}_\omega(\langle \epsilon_p \rangle) \approx m_\omega(\langle \epsilon_p \rangle) \quad (4.9.8)$$

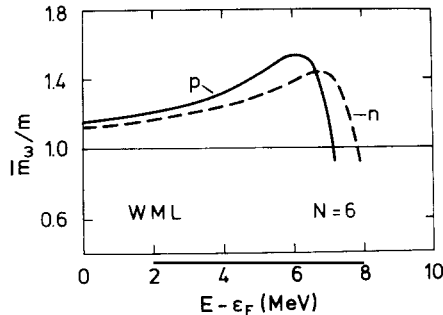


Fig. 4.56a. Adapted from ref. [114]. Dependence upon $E - \epsilon_F$ of the quantity $\bar{m}_\omega(E)/m = 1 - d[\Delta \bar{V}(E)]/dE$, where $\overline{\Delta V}(E)$ is represented by the full curves in the lower part of fig. 4.51. The latter figure shows that $\bar{m}_\omega(E)$ should present a narrow wiggle at $E = \epsilon_F \approx 6$ MeV in the case of neutrons; this wiggle has apparently been omitted in the present drawing.

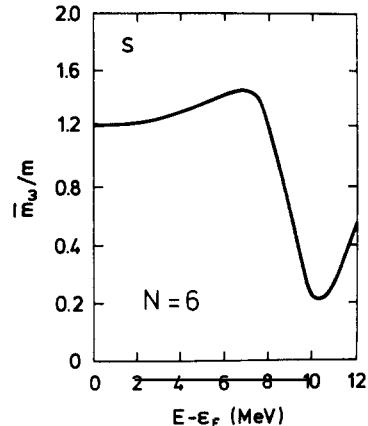


Fig. 4.56b. Adapted from ref. [278]. Dependence upon $E - \epsilon_F$ of the quantity $\bar{m}_\omega(E)/m$ defined by eq. (9.2), where the sum over α runs over the orbits of the $N = 6$ neutron shell, i.e. the neutron valence shell which lies above the Fermi energy in ^{208}Pb . One has $\bar{m}_\omega(\omega) = 1 - dV(\omega)/d\omega$, where $\omega = E - \epsilon_F$ and $V(\omega)$ is represented by the full curve in fig. 4.54.

where $m_\omega(E)$ is the on-shell value defined by eq. (8.4c). The comparison between fig. 4.52 and figs. 4.56a, b shows that the approximation (9.8) is fairly well fulfilled.

The physical significance of $\bar{m}_\omega(E)$ for off-shell values of E (i.e. for $E \neq \langle \varepsilon_p \rangle$) is not straightforward in terms of quasiparticle energies. This quantity determines the variation of the average potential energy of a quasiparticle when it is carried off its energy shell. For large values of the difference $E - \langle \varepsilon_F \rangle$, the quantity $\bar{m}_\omega(E)$ is furthermore expected to depend sensitively upon the size of the energy averaging interval Δ . This is implied by the comparison between figs. 4.33 and 4.34.

The dispersion relation (9.5) shows that the sudden drop of $\bar{m}_\omega(E)/m$ for $E - \varepsilon_F \approx 7$ or 8 MeV in figs. 4.56a and 4.56b reflects the existence of a maximum of the calculated $\bar{W}(E)$ at $E - \varepsilon_F \approx 10$ MeV in the full curves of figs. 4.51 and 4.55b. We mentioned that the origin of this maximum is not clear, and that it is not present in the calculation represented by the dashed curve in fig. 4.55b. The latter leads to an ω -mass $\bar{m}_\omega(E)/m$ which remains close to unity in the domain $5 \text{ MeV} < E - \varepsilon_F < 15 \text{ MeV}$. This can be seen from eq. (9.2) and from the dashed curve in fig. 4.55a.

4.9.3. Average over the levels of the next-to-the-valence shell

For $14 \text{ MeV} > E - \varepsilon_F > 9 \text{ MeV}$, the on-the-energy-shell average quantities are defined by the right-hand side of eqs. (9.1a, b) and (9.2) in which the sum over α runs over the subshells of the $N = 7$ main neutron shell, i.e. the shell which lies right above the $N = 6$ valence neutron shell. The corresponding values of $\Delta V(E)$ and of $\bar{W}(E)$ are plotted in figs. 4.57a and 4.57b. As in figs. 4.55a and 4.55b, we note differences between the results obtained from two approximation schemes. In both cases, however, the on-shell value $\Delta \bar{V}(\langle \varepsilon_p \rangle_{N=7})$ is quite small, which is in keeping with the results shown in fig. 4.50. The on-shell value $\bar{W}(\langle \varepsilon_p \rangle_{N=7})$ is approximately equal to 2 MeV in both cases; this is in fair agreement with the empirical trend shown in fig. 4.21.

4.9.4. Average over the levels of two shells

We note a rather striking similarity between figs. 4.55a and 4.57a, and between figs. 4.55b and 4.57b. This suggests that the gross structure of $\bar{W}(E)$ probably mainly reflects the energy and the degree of

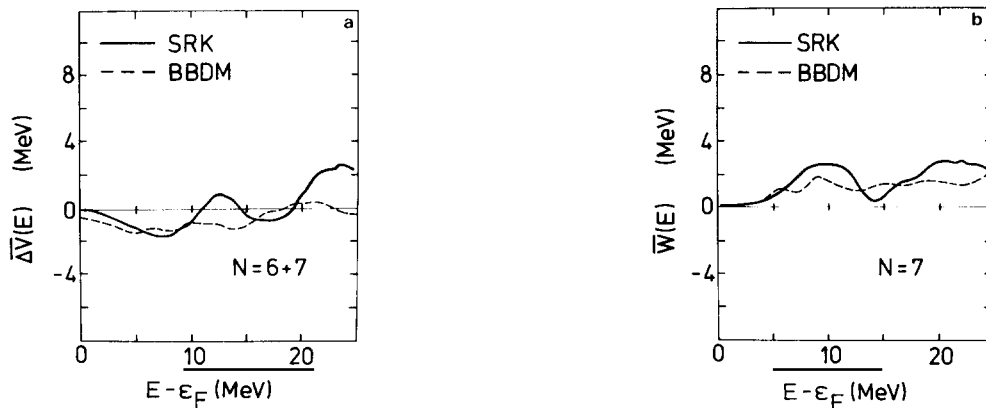


Fig. 4.57. (a) Dependence upon $E - \varepsilon_F$ ($\varepsilon_F = -6$ MeV) of the quantity $\Delta \bar{V}(E)$ defined by eq. (9.1b), in which the sum over α runs over the levels of the $N = 7$ main neutron shell. The full curve is taken from ref. [278] (see column (9) of table 4.3b); it is associated with the averaging interval $\Delta = 1.5$ MeV. The dashes are obtained from the model outlined in column (7) of table 4.3b; they are associated with $\Delta = 1$ MeV. (b) Same as (a) in the case of $\bar{W}(E)$ (see eq. (9.1a)).

collectivity of the core excitations, and that it is meaningful to include the levels of both the $N = 6$ and $N = 7$ shells in the sum over α which appears in the definitions (9.1a) and (9.1b) of $\bar{W}(E)$ and $\bar{\Delta}V(E)$. The results are shown in figs. 4.58a and 4.58b.

4.9.5. Average over the levels of many shells

One problem with the quantities shown in figs. 4.54–4.58b is that they are associated with rather specific level-averages. The similarity between average quantities derived from the $N = 6$ shell, from the $N = 7$ shell, and from the combination of these two shells suggests that a meaningful average can be introduced in which the sum over α in eqs. (9.1a,b) runs over *all* the subshells included in the calculation.

This has first been performed in ref. [328]. Figure 4.59 shows the value of $\bar{W}(E)$ obtained from eq. (9.1a) by letting the sum over α run over the 39 orbits contained in the $N = 2$ to the $N = 8$ neutron shells, i.e. whose energies range from that of the $1d_{5/2}$ orbit up to that of the $4d_{3/2}$ subshell. The quantity $\bar{\Delta}V(E)$ shown in fig. 4.59 has been obtained from $\bar{W}(E)$ by making use of the dispersion relation (9.5).

The dashed curve in fig. 4.60 has been computed from the definition (9.2) of $\bar{m}_\omega(E)$, with $\bar{\Delta}V(E)$ given by the dashed curve in fig. 4.59. The histogram has been calculated from the formula

$$\bar{m}_\omega(E)/m = 1 - \left\{ \sum_\alpha (2j_\alpha + 1) \right\}^{-1} \frac{d}{dE} \left[\sum_\alpha \Delta V_\alpha(E)/dE \right]. \quad (4.9.9)$$

The good agreement between the histogram and the dashed curve in fig. 4.60 confirms the accuracy of the dispersion relation (9.5).

Actually, each of the two curves contained in fig. 4.59 is a smoothed average of a curve which presents narrow fluctuations. This is exhibited in fig. 4.61. There, the trend of the wiggly line $\bar{\Delta}V(E)$ is represented by the dashed curve, which has been drawn by eye. The quantity $\bar{m}_\omega(E)$ plotted in fig. 4.62 has been computed from eq. (9.2) where $\bar{\Delta}V(E)$ has been identified with the dashed curve contained in fig. 4.61.

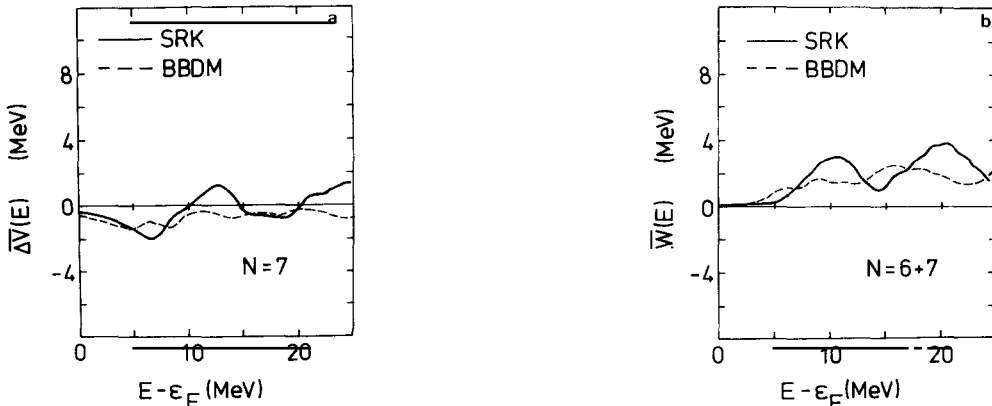


Fig. 4.58. (a) Dependence upon $E - \epsilon_F$ of the quantity $\bar{\Delta}V(E)$ defined by eq. (9.1b) in which the sum over α runs over the levels of the $N = 6$ and $N = 7$ main neutron shells. The notation is the same as in 4.57a. (b) Same as (a) in the case of $\bar{W}(E)$ (see eq. (9.1a)).

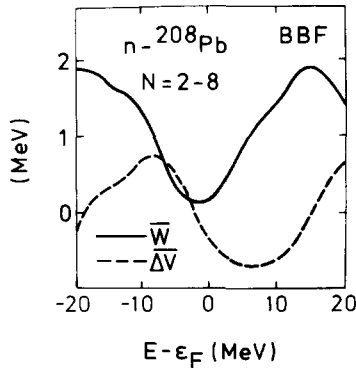


Fig. 4.59. Adapted from ref. [328]. Dependence upon $E - \varepsilon_F$ of the quantities $\bar{W}(E)$ and $\bar{\Delta}V(E)$ defined by eqs. (9.1a) and (9.5). In eq. (9.1a), the sum over α runs over the 39 neutron orbits contained in the $N = 2$ to the $N = 8$ main neutron shells. The approximation scheme is the one outlined in section 4.6.6 and in column (7) of table 4.3b. The averaging interval Δ is equal to 1 MeV.

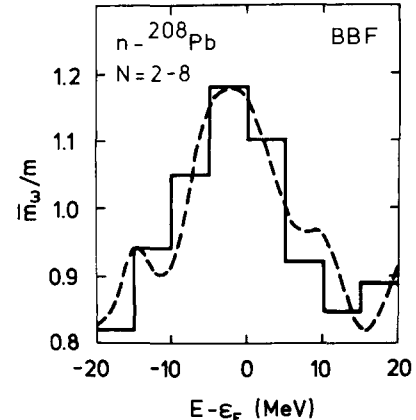


Fig. 4.60. Adapted from ref. [328]. Dependence upon $E - \varepsilon_F$ of the ω -mass $\bar{m}_\omega(E)$ defined by eq. (9.2), in which $\bar{\Delta}V(E)$ is taken from fig. 4.59 (dashed curve) or from eq. (9.1b) (histogram).

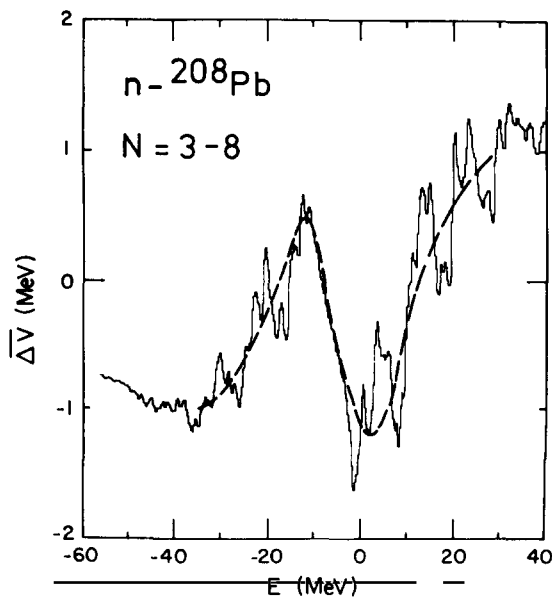


Fig. 4.61. The full line gives the dependence upon E of the quantity $\bar{\Delta}V(E)$ defined by eq. (9.1b), in which the sum over α runs over all the levels of the $N = 3$ to the $N = 8$ main neutron shells. The averaging interval Δ is equal to 1 MeV. The theoretical approach is the one outlined in section 4.6.6 and in column (7) of table 4.3b. The dashed curve has been drawn by eye.

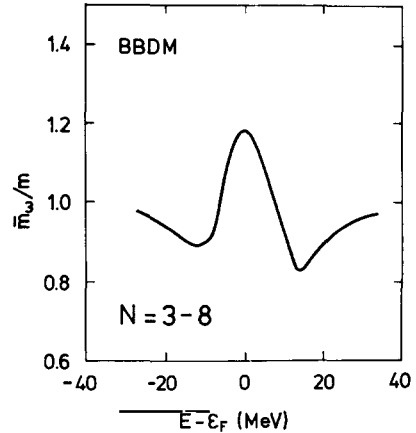


Fig. 4.62. Dependence upon $E - \varepsilon_F$ ($\varepsilon_F = -6$ MeV) of the ω -mass defined by eq. (9.2), where $\bar{\Delta}V(E)$ is identified with the dashed curve shown in fig. 4.61.

4.9.6. Discussion

The results shown in figs. 4.59–4.62 have been obtained by performing an average over many shells. Hence, they do not refer to any particular set of orbits. This is also the property which was sought by performing in fig. 4.50 the compilation of the on-shell values $\Delta V_{nlj}(\varepsilon_{nlj})$ and by associating to this compilation an average pattern $\Delta V^{(0)}(E)$, and the ω -mass shown in fig. 4.52.

The quantities plotted in fig. 4.52 on the one hand and in fig. 4.62 on the other hand are quite close to one another. There also exists a great similarity between these results and those which would be obtained in the dispersion relation approach if one would replace the curve in fig. 4.7 by another fit which would rapidly decrease for $E > 40$ MeV, in order to mock up effects associated with the use of a truncated configuration space in microscopic calculations [115].

It is not clear whether the striking similarity between the results obtained in sections 4.4, 4.8 and 4.9 has a deep-lying origin. In particular, it would be of interest to investigate the implication on the dependence of $\Delta V_{nlj}(E)$ upon E , of $\Delta V_{nlj}(\varepsilon_{nlj})$ upon ε_{nlj} and of $\Delta V(E)$ upon E of the basic assumption made in the dispersion relation approach, namely that the spatial nonlocality of the dispersion correction has a simple character.

The interest of the results obtained in sections 4.8 and 4.9 is that the calculated averages no longer carry any orbit quantum numbers. This suggests that one can include the average effect of the dispersion corrections by introducing an appropriate smooth energy dependence in the parameters of the shell-model potential, see also fig. 4.16.

One must, however, remain aware of the fact that the calculated level-averages may hide effects associated with angular momentum or with parity conservation. This is hinted by figs. 4.63a and 4.63b, in which we performed separately the average over the subshells with positive and with negative parity.

4.10. Dispersion corrections in spatial coordinate representation

The microscopic calculations described in sections 4.6–4.9 deal with the (Hartree–Fock) shell-model representation of the dispersion corrections to the mass operator, see eq. (1.4a). These calculations can, however, also be used to evaluate the dispersion correction in the space representation. This applies in particular to the work of Bernard and Van Giai outlined in section 4.6.5. These authors evaluated the

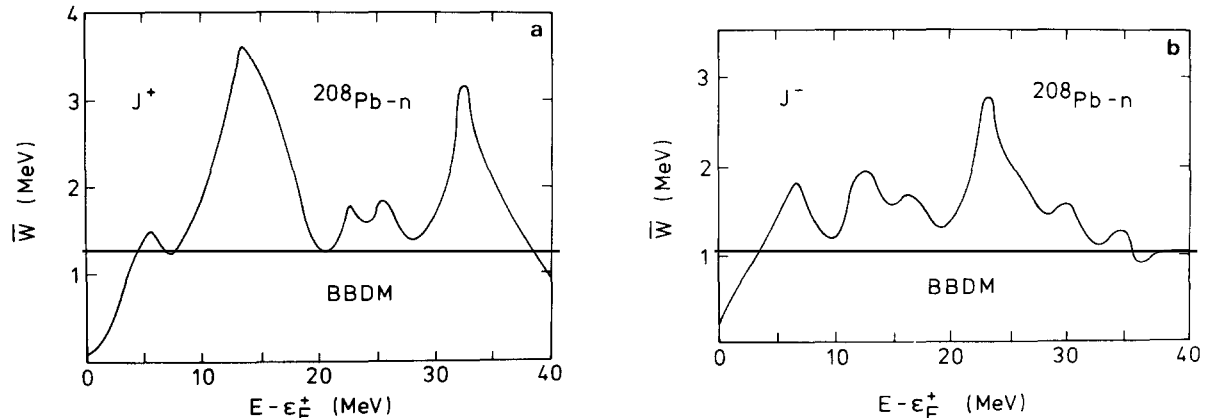


Fig. 4.63. (a) Dependence upon $E - \varepsilon_F^+$ ($\varepsilon_F^+ = -3.9$ MeV) of the quantity $\bar{W}(E)$ defined in eq. (9.1a), where the sum over α runs over all the positive parity levels which are contained in the $N = 5$ main neutron shell. (b) Same as (a) in the case of the negative parity levels contained in the $N = 6$ main neutron shell.

quantities $\mathcal{N}_{ij}^{(a)}(\mathbf{r}, \mathbf{r}'; \omega)$ and $\mathcal{N}_{ij}^{(b)}(\mathbf{r}, \mathbf{r}'; \omega)$ defined by eqs. (2.28a, b). They first considered positive energies, typically $5 \text{ MeV} < \omega < 30 \text{ MeV}$. In this energy range, the nonlocality of

$$\mathcal{W}^{\text{RPA}}(\mathbf{r}, \mathbf{r}'; \omega) = \text{Im } \mathcal{N}^{\text{RPA}}(\mathbf{r}, \mathbf{r}'; \omega) \quad (4.10.1)$$

is rather simple. Indeed, it turns out that \mathcal{W}^{RPA} mainly depends upon the combinations

$$\mathbf{R} = \frac{1}{2}(\mathbf{r} + \mathbf{r}'), \quad \mathbf{s} = \mathbf{r} - \mathbf{r}' \quad (4.10.2)$$

and is fairly independent of the angle between \mathbf{R} and \mathbf{s} [103]. One can then write

$$\mathcal{W}^{\text{RPA}}(\mathbf{R}, \mathbf{s}; \omega) = \sum_{ij} \frac{2j+1}{4\pi} \mathcal{W}_{ij}(\mathbf{r}, \mathbf{r}'; \omega) \quad (4.10.3a)$$

where $\mathbf{r} = \mathbf{R} + \frac{1}{2}\mathbf{s}$, $\mathbf{r}' = \mathbf{R} - \frac{1}{2}\mathbf{s}$ and

$$\mathcal{W}_{ij}(\mathbf{r}, \mathbf{r}'; \omega) = \text{Im } \mathcal{N}_{ij}(\mathbf{r}, \mathbf{r}'; \omega), \quad (4.10.3b)$$

see eq. (2.27a). The dependence of $\mathcal{W}(\mathbf{R}, \mathbf{s}; \omega)$ upon \mathbf{R} gives the radial dependence of the imaginary part of the optical-model potential. Its dependence upon \mathbf{s} corresponds to its spatial nonlocality. It turns out that $\mathcal{W}(\mathbf{R}, \mathbf{s} = 0; \omega)$ is strongly peaked at the nuclear surface, i.e. at $\mathbf{R} \approx 7.2 \text{ fm}$. The dependence of $\mathcal{W}(\mathbf{R}, \mathbf{s}; \omega)$ upon \mathbf{s} for $\mathbf{R} \approx 7.2 \text{ fm}$ has a Gaussian shape with a nonlocality range $\beta \approx 1 \text{ fm}$ [61]. The real part of $\mathcal{N}(\mathbf{r}, \mathbf{r}'; \omega)$ has similar properties. This type of nonlocality resembles the one encountered in the case of nuclear matter, see eq. (3.7.17) [102].

In a recent work, Nguyen Van Giai and Pham Van Thieu [329] assumed that these properties are also valid in the energy range $|\omega - \varepsilon_F| < 10 \text{ MeV}$. They write accordingly

$$\text{Re } \mathcal{N}^{\text{RPA}}(\mathbf{r}, \mathbf{r}'; \omega + \frac{1}{2}i\Delta) \approx \Delta \mathcal{V}(\mathbf{R}, \mathbf{R}; \omega) \exp(-s^2/\beta^2) \quad (4.10.4a)$$

$$|\text{Im } \mathcal{N}^{\text{RPA}}(\mathbf{r}, \mathbf{r}'; \omega + \frac{1}{2}i\Delta)| = \Delta \mathcal{W}(\mathbf{R}, \mathbf{R}; \omega) \exp(-s^2/\beta^2) \quad (4.10.4b)$$

with $\beta \approx 1 \text{ fm}$. They introduce the quantities

$$\Delta V(\mathbf{R}; \omega) = \int \text{Re } \mathcal{N}(\mathbf{r}, \mathbf{r}'; \omega) d^3s \quad (4.10.5a)$$

$$= (\beta \sqrt{\pi})^3 \sum_{ij} \frac{2j+1}{4\pi} \Delta \mathcal{V}_{ij}(\mathbf{R}, \mathbf{R}; \omega), \quad (4.10.5b)$$

$$W(\mathbf{R}; \omega) = (\beta \sqrt{\pi})^3 \sum_{ij} \frac{2j+1}{4\pi} \mathcal{W}_{ij}(\mathbf{R}, \mathbf{R}; \omega). \quad (4.10.6)$$

These quantities turn out to be strongly surface-peaked [329]. Figure 4.64 shows their dependence upon $E - \varepsilon_F$ for $\mathbf{R} = 7.35 \text{ fm}$. The energy dependence of $\Delta V(\mathbf{R}; E)$ can be characterized by the

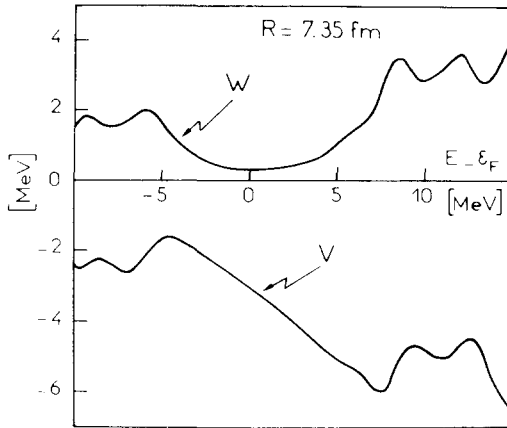


Fig. 4.64. Taken from ref. [329]. Dependence upon $E - \epsilon_F$ ($\epsilon_F \approx -6$ MeV) of the quantities $W(R; E)$ and $\Delta V(R; E)$ defined by eqs. (10.5b) and (10.6), in the case of protons in ^{208}Pb and for $R = 7.35$ fm. The energy averaging interval Δ is equal to 2 MeV. The approximation scheme is outlined in section 4.6.5 and in column (5) of table 4.3b.

derivative

$$\bar{m}(R; E)/m = 1 - d[\Delta V(r; E)]/dE. \quad (4.10.7a)$$

The comparison between this relation and eq. (4.11) shows that

$$\bar{m}(R; E)/m \approx m_\omega(R; E)/m. \quad (4.10.7b)$$

The quantity $\bar{m}(R; E)/m$ is represented in fig. 4.65 in the case of protons in ^{208}Pb . Note the similarity with the results obtained from the dispersion relation approach shown in fig. 4.15.

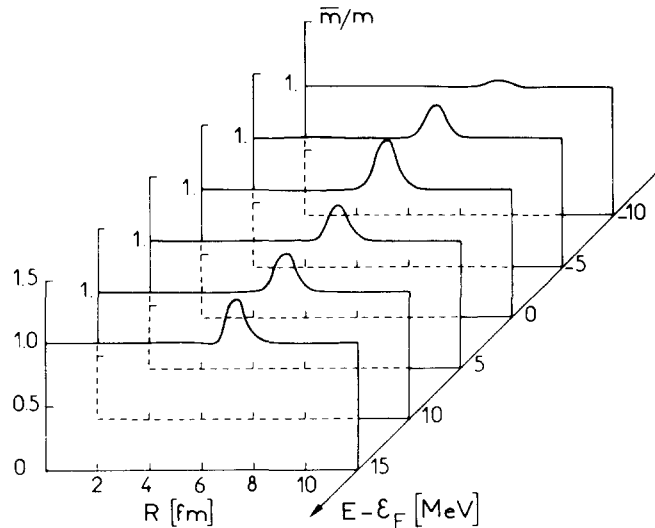


Fig. 4.65. Taken from ref. [329]. Dependence upon R and $E - \epsilon_F$ of the ω -mass $\bar{m}(R; E)$ defined by eq. (10.7a), in the case of protons in ^{208}Pb .

A radial-dependent effective mass $m^*(R; E)$ can be defined by the relation

$$\frac{m^*(R; E)}{m} = \frac{\bar{m}(R; E)}{m} \frac{m_{\text{Sk}}^*(R)}{m}, \quad (4.10.8)$$

where $m_{\text{Sk}}^*(R)$ is the Skyrme III–Hartree–Fock approximation to the effective mass, see eqs. (2.18), (4.12) and (8.5a). The quantity $m^*(R; E)$ is represented in fig. 4.66.

It has recently been proposed that for small values of $|E - \varepsilon_F|$ the simple form of nonlocality assumed in eq. (10.4a) may become inaccurate [324]; in this work, however, the nonlocality of the Hartree–Fock potential was omitted. It would be of interest to examine to what extent the approximation (10.4a) is accurate for $E \approx \varepsilon_F$ and at the nuclear surface, i.e. in the domain where $\Delta V(R; E)$ is appreciably different from zero.

4.11. Implications, applications and questions

4.11.1. Introduction

Much progress has recently been accomplished in calculating the dispersion corrections to the mass operator in nuclei. Some implications of these recent works have already been described, in particular concerning the density of quasiparticle energies, the energy dependence of the volume integral of the mean field, the lifetime of the quasiparticle states, the spectroscopic factor of quasi-pure single-particle excitations and the distribution of the single-particle strengths.

Last but not least, we discussed the possibility of taking the average effect of the dispersion corrections into account by introducing simple modifications to the shell-model potential. At positive energies, it is for instance well-known that the dispersion corrections transform the shell model into the optical model. To what extent this is also possible at negative energy is an interesting problem which amounts to probing the limitations of the concept of quasiparticles.

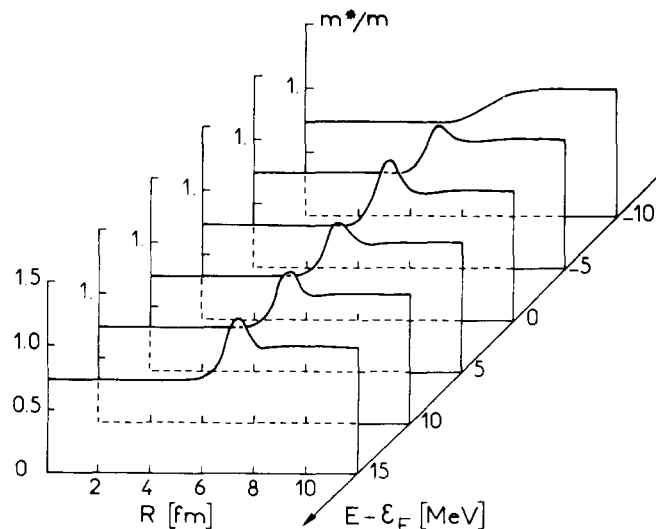


Fig. 4.66. Taken from ref. [329]. Dependence upon R and $E - \varepsilon_F$ of the effective mass $m^*(R; E)$ defined by eq. (10.8), in the case of protons in ^{208}Pb .

Other consequences of the dynamical content of the shell-model potential have recently been conjectured. Below, we outline some of these contributions.

4.11.2. Correction to giant resonance energies

Brown, Dehesa and Speth [330] pointed out that the collective energy shift associated with a giant resonance brings its particle and hole single-particle constituents out of their energy shell, and that this may lead to large dynamical corrections to the collective energy shift.

This idea has been pursued in refs. [113, 114, 308, 331–334]. These various approaches have been compared in ref. [327]; it was concluded that the effective particle–hole gap appropriate to a giant resonance is approximately given by

$$\varepsilon_{ph}^{\text{eff}} = \langle \varepsilon_p^{(0)} \rangle - \langle \varepsilon_h^{(0)} \rangle + 2\overline{\Delta V}(\langle \varepsilon_p^0 \rangle - \varepsilon_F + C), \quad (4.11.1)$$

where C is the collective energy shift. Here, $\overline{\Delta V}(E)$ is the quantity plotted in figs. 4.54 and 4.55a in the case of $(1\hbar\omega)$ excitations; it is the quantity plotted in fig. 4.57a in the case of $(2\hbar\omega)$ excitations.

In ref. [327], a schematic model was used for the purpose of illustration. It is oversimplified and unreliable for quantitative estimates. If one considers for instance the giant dipole resonance in ^{208}Pb , it is safer to rely on fig. 4.55a. In that case, $C \approx 5 \text{ MeV}$ and $\langle \varepsilon_p^{(0)} \rangle - \varepsilon_F + C \approx 9 \text{ MeV}$. According to the dashed line in fig. 4.55a, the effective particle–hole gap is then close to the observed particle–hole gap ε_{ph} ; it is somewhat smaller than ε_{ph} in the case of the calculation of ref. [278].

The prescription (11.1) is quite crude. In a proper dynamical theory the dispersion correction to the particle and the hole interfere with the vertex corrections. These corrections in which a phonon is exchanged between the particle and the hole are of the same order of magnitude as the dispersion corrections and of opposite sign for density vibrations. The interference between the vertex corrections and the dispersion corrections is important to obtain a quantitative description of both damping widths and centroids of giant resonances [282, 283].

4.11.3. Correction to the level density parameter

The level density ρ at the nuclear excitation energy E is usually written in the form

$$\ln \rho = 2\sqrt{QE} \quad (4.11.2)$$

where Q is called the level density parameter. Barranco and Treiner [335] have shown that

$$Q \approx \frac{\pi^2}{2} \sum_{q=p,n} \int \frac{\rho_q(r) m_q^*(r)}{k_{Fq}^2(r)} d^3r \quad (4.11.3)$$

where $k_{Fq}(r) = [3\pi^2\rho_q(r)]^{1/3}$ is the local Fermi momentum. When the effective mass $m_q^*(r)$ is identified with its Skyrme III–Hartree–Fock approximation, eq. (11.3) yields a too small value for the level density parameter. It is shown in ref. [336] that this discrepancy disappears if one takes into account the surface peaking of $m_q^*(r)$ which is produced by the dispersion corrections, see fig. 4.66.

4.11.4. Energy dependence of the Coulomb correction

Equations (3.5.25) and (3.5.26) show that the effective Coulomb energy felt by a proton is given by

$V_C + \Delta_C$, where V_C is the standard value of the Coulomb energy while

$$\Delta_C \approx [(m^*/m) - 1] V_C \quad (4.11.4)$$

is the Coulomb correction due to the spatial nonlocality of the nuclear mean field. Figure 4.11 shows that $\langle m^*/m \rangle$ is a function of energy. Hence, Δ_C is expected to be a function of the proton energy, and to vary from $\approx -0.4ZA^{-1/3}$ MeV at $E \approx 30$ MeV to ≈ 0 at $E = \varepsilon_F$ [64].

4.11.5. Energy dependence of the symmetry potential

In ^{208}Pb , the empirical value of $\langle m^*/m \rangle_p$ for 30 MeV protons is smaller than the value of $\langle m^*/m \rangle_n$ for 30 MeV neutrons:

$$\langle m^*/m \rangle_{E_p \approx 30 \text{ MeV}} \approx \langle m^*/m \rangle_{E_n \approx 30 \text{ MeV}} - 0.16. \quad (4.11.5)$$

This reflects the fact that the absolute value of the depth of the empirical symmetry potential decreases with increasing energy. Since $\langle m^*/m \rangle_{E \approx \varepsilon_F} \approx 1$ for protons as well as for neutrons, this implies that $\langle m_\omega(E)/m \rangle_{E \approx \varepsilon_F}$ is larger for protons than for neutrons and, correspondingly, that the depth of the symmetry potential is significantly larger for weakly bound single-particle states than at positive energy. This is confirmed by recent empirical analyses [64, 67, 337].

4.11.6. Temperature dependence of surface properties

The free energy per nucleon is given by an expression which involves the integral [338]

$$\int m^*(r) \rho^{1/3}(r) d^3r, \quad (4.11.6)$$

where $m^*(r)$ is the value of the radial-dependent effective mass for energies close to the Fermi energy. Figures 4.15 and 4.66 show that $m^*(r)$ is peaked at the nuclear surface. This peaking affects the temperature dependence of the surface properties, in particular the temperature dependence of the fission barrier height [339].

4.11.7. Temperature dependence of the parameters of the Migdal interaction

It was pointed out in section 3.19 that some parameters of the Landau–Migdal interactions in liquid ^3He depend upon temperature. Similar effects are expected in nuclei [340].

4.11.8. Gravitational collapse of stars

The equation of state which describes the gravitational collapse of stars involves the level density parameter Q which appears in eq. (11.2). It is therefore affected by the radial and by the energy dependence of the effective mass [341].

4.11.9. Density distribution in nuclei

The charge density distributions $\rho_p(r)$ in heavy nuclei as calculated in the Hartree–Fock approximation displays marked oscillations in the nuclear interior [275], while the experimental data show that $\rho_p(r)$ is a very flat function of r [342]. The oscillations of the theoretical density distributions are somewhat damped if one includes the depletion of the normally occupied states in the framework of the

random phase approximation [343], but this is not sufficient to account for the experimental data. Ma and Wambach [344] reach a similar result by including phenomenologically a surface peaking in the effective mass, see fig. 4.66.

The short-range part of the nucleon–nucleon force introduces a coupling to highly excited core states. This very much increases the depletion of the Fermi sea (compare figs. 4.17 and 4.38) and is expected to produce a strong damping of the oscillations of the calculated density distribution. The proper theoretical method for evaluating this effect has not yet been constructed.

4.11.10. Occupation probability of the $3s_{1/2}$ proton orbit in ^{206}Pb

The comparison between the experimental charge density distributions of ^{206}Pb and ^{205}Tl strongly suggests that the normally occupied $3s_{1/2}$ proton orbit in ^{206}Pb is depleted by as much as thirty per cent [299, 343]. This is in keeping with the results shown in fig. 4.17, but not with those contained in fig. 4.38c or evaluated in refs. [344, 345]. This again points to the importance of short-range correlations and raises the challenge of finding a proper way of including them.

4.11.11. Radial dependence of valence orbits

In favourable cases, the magnetic form factor of individual valence orbits can be accurately measured [343], although meson exchange corrections introduce some uncertainty in the analysis of the data. Ma and Wambach [346] have proposed that this form factor is significantly influenced by the radial dependence of the ω -mass $\bar{m}(R; E)$, see fig. 4.65.

4.11.12. Dispersion corrections in other nuclei

All the theoretical results shown in the previous sections have been obtained in the particular case of the ^{208}Pb nucleus. It would be of much interest to perform similar investigations in the case of other nuclei, in particular of other closed shell nuclei [348, 349]. Fragmentary results have been published in the case of ^{40}Ca [91], on which work is in progress [307, 350]. The importance of charge-exchange excitations should be studied.

5. Postface

In the simplest version of the nuclear shell model, it is assumed that the nucleons move independently of one another in a static mean field. This is necessarily an oversimplification of the physical reality, but many experiments indicate that it has some degree of validity.

In a somewhat more realistic description, it is taken into account that the nucleons interact with the rest of the nucleus and drag core excitations. One then speaks of the motion of quasiparticles. Since quasiparticles include effects of collisions, their group velocity is smaller than that of particles with the same wavelength. This effect is measured by a quantity called here the ω -mass; it has been introduced in section 3.6 in the case of nuclear matter. The ω -mass $m_\omega(E)$ is a function of the energy E of the quasiparticle. It characterizes the dynamical content of the shell model and forms the cornerstone of the present report.

In chapter 2, we reviewed some empirical data which point to the necessity of using quasiparticles rather than particles for describing many properties of nuclei.

In chapter 3, we discussed theoretical procedures for introducing the concept of a quasiparticle and for evaluating its main properties in the case of a uniform Fermi liquid. It turns out that the

independent particle model corresponds to the Hartree–Fock approximation to the mean field, while collisions introduce dispersion corrections often called polarization and correlation contributions. These dispersion corrections also modify the momentum distribution of the ground state of a Fermi gas. They have been evaluated by means of various theoretical techniques, surveyed in sections 3.13–3.18.

These techniques enable one to investigate the properties of the quasiparticles in nuclear matter, in normal liquid ^3He and in the electron gas. In these three cases it is found that the ω -mass $m_\omega(E)$ presents a maximum centred on the Fermi energy ε_F . In nuclear matter, the width of this enhancement peak is comparable to the kinetic energy of a particle at the Fermi surface. It is much smaller than this kinetic energy in normal liquid ^3He (section 3.19), and also in the electron gas if one takes the electron–phonon coupling into account (section 3.20). In the latter two cases, the width of the enhancement of the ω -mass is comparable to the energy E_λ of the low-lying collective excitations of the medium, i.e. the spin fluctuations ($E_\lambda \approx 10^{-5}$ eV) in normal liquid ^3He and the phonons ($E_\lambda \approx 10^{-2}$ eV) in the electron gas. The physical interpretation of this narrow peak of $m_\omega(E)$ is that once the difference $E - \varepsilon_F$ is larger than E_λ , the collective excitations are decoupled from the quasiparticle, whose group velocity therefore increases.

Since nuclei also have low-lying collective excitations ($E_\lambda \approx$ several MeV), one expects that the corresponding ω -mass also presents a narrow enhancement. Empirical properties and theoretical calculations in the case of ^{208}Pb confirm this expectation (chapter 4). In this case, however, parity and angular momentum conservation considerably complicates the conceptual picture as well as the theoretical calculations. Furthermore, the nuclear surface plays a predominant role in the enhancement of the ω -mass since the most collective low-lying core excitations are surface vibrations.

The title of the present survey is patterned after that of a paper [325] by G.E. Brown, who has made decisive contributions to the understanding of the dynamical content of the shell model. We owe much to his stimulation. We also benefited from discussions with J.-P. Blaizot, J. Dechargé, D. Gogny, E. Krotscheck, V.L. Mishra, H. Ngô and c. Pethick. We are grateful to the many secretaries who typed portions of various versions of the present work. Special thanks are due to Ms. M.-Cl. Pontus, who diligently typed the entire final version, carefully took care of the numbering of the references and realized many of the original and adapted figures.

References

- [1] G.E. Brown, J.H. Gunn and P. Gould, Nucl. Phys. 46 (1963) 598.
- [2] G.F. Bertsch and T.T.S. Kuo, Nucl. Phys. A112 (1968) 204.
- [3] G.E. Brown, C.J. Pethick and A. Zaringhalam, J. Low Temp. Phys. 48 (1982) 349.
- [4] S. Fantoni, V.R. Pandharipande and K.E. Schmidt, Phys. Rev. Lett. 48 (1982) 878.
- [5] E. Krotscheck and R.A. Smith, Phys. Rev. B27 (1983) 4222.
- [6] H. Feshbach, C.E. Porter and V.F. Weisskopf, Phys. Rev. 96 (1954) 448.
- [7] F.G. Perey and B. Buck, Nucl. Phys. 32 (1962) 353.
- [8] J. Blomqvist and S. Wahlborn, Arkiv Fysik 16 (1960) 545.
- [9] J.M. Blatt and V.F. Weisskopf, *Theoretical Nuclear Physics* (Wiley, New York, 1952) ch. VIII.
- [10] A.E. Taylor and E. Wood, Phil. Mag. 44 (1953) 95.
- [11] P.H. Bowen, J.P. Scanlon, G.H. Stafford, J.J. Thresher and P.E. Hodgson, Nucl. Phys. 22 (1961) 640.
- [12] J.D. Lawson, Phil. Mag. 44 (1953) 102.
- [13] M.G. Mayer and J.H.D. Jensen, *Elementary Theory of Nuclear Shell Structure* (Wiley, New York, 1955).
- [14] C. Ellegaard, J. Kantele and P. Vedelsby, Nucl. Phys. A129 (1969) 113.
- [15] A. Bohr and B.R. Mottelson, *Nuclear Structure*, vol. I (Benjamin, New York, 1969).

- [16] G. Muehllehner, A.S. Poltorak, W.C. Parkinson and R.H. Bassel, Phys. Rev. 159 (1967) 1039.
- [17] M. Bauer, E. Hernandez-Saldana, P.E. Hodgson and J. Quintanilla, J. Phys. G8 (1982) 525.
- [18] W.T.H. Van Oers, H. Haw, N.E. Davison, A. Ingemarsson, B. Fagerström and G. Tibell, Phys. Rev. C10 (1974) 307.
- [19] P. Quentin and H. Flocard, Ann. Rev. Nucl. Sci. 28 (1978) 523.
- [20] S. Galès, Nucl. Phys. A354 (1981) 193c.
- [21] J. Mougey, Nucl. Phys. A396 (1983) 39c.
- [22] J. Mougey, M. Bernheim, A. Bussière, A. Gillebert, Phan Xuan Hö, M. Priou, D. Royer, I. Sick and G.J. Wagner, Nucl. Phys. A262 (1976) 461.
- [23] G.J. Wagner, P. Doll, K.T. Knöpfle and G. Mairle, Phys. Lett. 57B (1975) 413.
- [24] P. Doll, G.J. Wagner, K.T. Knöpfle and G. Mairle, Nucl. Phys. A263 (1976) 210.
- [25] G. Jacob and T.A.J. Maris, Rev. Mod. Phys. 45 (1973) 6.
- [26] R. Sartor and C. Mahaux, Phys. Rev. 21C (1980) 2613.
- [27] A. Stuirbrink, G.J. Wagner, K.T. Knöpfle, L.K. Pao, G. Mairle, H. Riedesel, K. Schindler, V. Bechtold and L. Friedrich, Z. Phys. A297 (1980) 307.
- [28] J.P. Jeukenne and C. Mahaux, Nucl. Phys. A136 (1969) 49.
- [29] C. Mahaux, Ann. Rev. Nucl. Sci. 23 (1973) 193.
- [30] A.M. Lane, R.G. Thomas and E.P. Wigner, Phys. Rev. 98 (1955) 693.
- [31] A.E.L. Dieperink and P.J. Brussaard, Z. Phys. 261 (1973) 117.
- [32] C.A. Engelbrecht and H.A. Weidenmüller, Nucl. Phys. A184 (1972) 385.
- [33] R. Guardiola and J. Ros, eds., The Many-Body Problem. Jastrow versus Brueckner Theory (Springer Verlag, Berlin, 1981).
- [34] A.L. Fetter and J.D. Walecka, Quantum Theory of Many-Particle Systems (McGraw-Hill, 1971).
- [35] G.E. Brown, Many-Body Problems (North-Holland Publ. Comp., Amsterdam, 1972).
- [36] J.P. Jeukenne, A. Lejeune and C. Mahaux, Phys. Reports 25C (1976) 83.
- [37] A.B. Migdal, Sov. Phys. JETP 5 (1957) 333.
- [38] J.M. Luttinger, Phys. Rev. 119 (1960) 1153.
- [39] D.S. Koltun, Phys. Rev. Lett. 28 (1972) 182.
- [40] D.S. Koltun, Phys. Rev. C9 (1974) 484.
- [41] A.E.L. Dieperink and T. de Forest, Ann. Rev. Nucl. Sci. 25 (1975) 1.
- [42] J. Hüfner and C. Mahaux, Ann. Phys. (N.Y.) 73 (1972) 525.
- [43] M. Bernheim, A. Bussière, A. Gillebert, J. Mougey, Phan Xuan Hö, M. Priou, D. Royer, I. Sick and G.J. Wagner, Phys. Rev. Lett. 32 (1974) 898.
- [44] A. Faessler, S. Krewald and G.J. Wagner, Phys. Rev. C11 (1975) 2069.
- [45] G.M. Vagradov, F.A. Gareev and J. Bang, Nucl. Phys. A278 (1977) 319.
- [46] A.E.L. Dieperink, P.J. Brussaard and R.Y. Cusson, Nucl. Phys. A180 (1972) 110.
- [47] G.A. Baker Jr., M.F. Hind and J. Kahane, Phys. Rev. C2 (1970) 841.
- [48] J.S. Bell and E.J. Squires, Phys. Rev. Lett. 3 (1959) 96.
- [49] M. Namiki, Progr. Theor. Phys. (Kyoto) 23 (1960) 629.
- [50] P. Driessens, H.S. Taylor and T. Scott, Physica Scripta 21 (1980) 272.
- [51] J.M. Luttinger, Phys. Rev. 121 (1961) 942.
- [52] R. Sartor, Phys. Lett. 69B (1977) 6.
- [53] P. Nozières, Theory of Interacting Fermi Systems (W.A. Benjamin, Inc., 1964) p. 350.
- [54] M. Baranger, Nucl. Phys. A149 (1970) 225.
- [55] S.Y. Lee, F. Osterfeld, K. Tam and T.T.S. Kuo, Phys. Rev. C24 (1981) 329.
- [56] B. Buck and R. Lipperheide, Nucl. Phys. A368 (1981) 141.
- [57] J.W. Negele and K. Yazaki, Phys. Rev. Lett. 47 (1981) 71.
- [58] S. Fantoni, B.L. Friman and V.R. Pandharipande, Phys. Lett. 104B (1981) 89.
- [59] C. Mahaux, Phys. Rev. 28C (1983) 1848.
- [60] J.W. Negele, Comm. Nucl. Part. Phys. 12 (1983) 1.
- [61] V. Bernard and Nguyen Van Giai, Nucl. Phys. A327 (1979) 397.
- [62] J.P. Schiffer, Nucl. Phys. A335 (1980) 348.
- [63] J. Dabrowski, Phys. Lett. 8 (1964) 90.
- [64] C. Mahaux and H. Ngô, Phys. Lett. 126B (1983) 1.
- [65] J.P. Jeukenne, A. Lejeune and C. Mahaux, Phys. Rev. C15 (1977) 10.
- [66] J. Rapaport, Phys. Lett. 70B (1977) 141; Phys. Reports 87 (1982) 25.
- [67] F.S. Dietrich, R.W. Finlay, S. Mellem, G. Randers-Pehrson and F. Petrovich, Phys. Rev. Lett. 51 (1983) 1629.
- [68] J.P. Jeukenne, A. Lejeune and C. Mahaux, Phys. Rev. C16 (1977) 80.
- [69] F.A. Brieva and J.R. Rook, Nucl. Phys. A291 (1977) 299.
- [70] H.V. Von Geramb, in: The Interactions between Medium Energy Nucleons in Nuclei-1982, ed. H.O. Meyer (American Institute of Physics, 1983) p. 44.

- [71] C. Mahaux, in: The Interactions between Medium Energy Nucleons in Nuclei-1982, ed. H.O. Meyer (American Institute of Physics, 1983) p. 20.
- [72] F.G. Perey, in: Direct Interactions and Nuclear Reaction Mechanisms, eds. E. Clementel and C. Villi (Gordon and Breach, New York, 1963) p. 125.
- [73] R. Peierls and N. Vinh Mau, Nucl. Phys. A343 (1980) 1.
- [74] J.R. Rook, Nucl. Phys. A370 (1981) 125.
- [75] J.P. Jeukenne, A. Lejeune and C. Mahaux, Phys. Lett. 59B (1975) 208.
- [76] A.B. Migdal, Nucl. Phys. 30 (1962) 239.
- [77] V.F. Weisskopf, Nucl. Phys. 3 (1957) 423.
- [78] G.E. Brown, Rev. Mod. Phys. 31 (1959) 893.
- [79] K.A. Brueckner, Quantum Theory, vol. III, ed. D.R. Bates (Academic Press, New York, 1962) p. 286.
- [80] G.E. Brown, Unified Theory of Nuclear Models and Forces (North-Holland Publ. Comp., Amsterdam, 1971) p. 180.
- [81] K.M. Khanna and P.K. Barkhai, Nucl. Phys. A243 (1975) 298.
- [82] J.P. Jeukenne and C. Mahaux, Z. Phys. A302 (1981) 233.
- [83] J.P. Blaizot and B.L. Friman, Nucl. Phys. A372 (1981) 69.
- [84] H.A. Bethe, Phys. Rev. 103 (1956) 1353.
- [85] S.A. Moszkowski and B.L. Scott, Ann. Phys. (N.Y.) 11 (1960) 65.
- [86] V. Bernard and C. Mahaux, Phys. Rev. C23 (1981) 888.
- [87] D. Vautherin and D.M. Brink, Phys. Lett. 32B (1970) 149.
- [88] R. Sartor and C. Mahaux, Phys. Rev. 21C (1980) 1546.
- [89] E. Krotscheck, R.A. Smith and A.D. Jackson, Phys. Lett. 104B (1981) 421.
- [90] C. Mahaux and H. Ngô, Phys. Lett. 100B (1981) 285.
- [91] C. Mahaux and H. Ngô, Nucl. Phys. A378 (1982) 205.
- [92] C. Mahaux, in: The Many-Body Problem. Jastrow versus Brueckner Theory, eds. R. Guardiola and J. Ros (Springer Verlag, Berlin, 1981) p. 1.
- [93] H. Orland and R. Schaeffer, Nucl. Phys. A299 (1978) 442.
- [94] G.L. Shaw, Ann. Phys. (N.Y.) 3 (1959) 509.
- [95] A.D. Jackson, E. Krotscheck, D.E. Meltzer and R.A. Smith, Nucl. Phys. A386 (1982) 125.
- [96] V. Bernard and Nguyen Van Giai, Nucl. Phys. A348 (1980) 75.
- [97] B.H. Brandow, in: Lectures in Theoretical Physics, vol. 11, ed. K.T. Mahanthappa (Gordon and Breach, New York, 1969).
- [98] H.A. Bethe, B.H. Brandow and A.G. Petschek, Phys. Rev. 129 (1963) 225.
- [99] B. Gyarmati, R.G. Lovas, T. Vertse and P.E. Hodgson, J. Phys. G7 (1981) L209.
- [100] H. Feshbach, Ann. Rev. Nucl. Sci. 8 (1958) 49.
- [101] J.P. Blaizot and B.L. Friman, private communication to C. Mahaux (1981).
- [102] G. Ripka, Nucl. Phys. 42 (1963) 75.
- [103] N. Vinh Mau and A. Bouyssy, Nucl. Phys. A257 (1976) 189.
- [104] A. Bouyssy, H. Ngô and N. Vinh Mau, Nucl. Phys. A371 (1981) 173.
- [105] F. Osterfeld, J. Wambach and V.A. Madsen, Phys. Rev. C23 (1981) 179.
- [106] H. Feshbach, Ann. Phys. (N.Y.) 5 (1958) 357.
- [107] C. Mahaux and H.A. Weidenmüller, Shell-Model Approach to Nuclear Reactions (North-Holland Publ. Comp., Amsterdam, 1969).
- [108] S. Fantoni and V.R. Pandharipande, Nucl. Phys. A427 (1984) 473.
- [109] B.L. Friman and E.M. Nyman, Nucl. Phys. A302 (1978) 365.
- [110] T.F. Hammann and Q. Ho-Kim, Nuovo Cim. 64B (1969) 356; 14A (1973) 633(E).
- [111] J.W. Clark, in: The Many-Body Problem. Jastrow versus Brueckner Theory, eds. R. Guardiola and J. Ros (Springer Verlag, Berlin, 1981) p. 184 and references contained therein.
- [112] E. Krotscheck, R.A. Smith, J.W. Clark and R.M. Panoff, Phys. Rev. B24 (1981) 6383.
- [113] G.E. Brown and M. Rho, Nucl. Phys. A372 (1981) 397.
- [114] J. Wambach, V.K. Mishra and Li Chu-hsia, Nucl. Phys. A380 (1982) 285.
- [115] J.P. Jeukenne and C. Mahaux, Nucl. Phys. A394 (1983) 445.
- [116] J. Wambach, private communication.
- [117] S. Fantoni, B.L. Friman and V.R. Pandharipande, Nucl. Phys. A399 (1983) 51.
- [118] R. Sartor, Nucl. Phys. A289 (1977) 329.
- [119] R.S. Poggio and A.D. Jackson, Phys. Rev. Lett. 35 (1975) 1211.
- [120] E. Oset and A. Palanques-Mestre, Nucl. Phys. A359 (1981) 289.
- [121] R.F. Bishop, Ann. Phys. (N.Y.) 77 (1973) 106.
- [122] V.M. Galitskii, Sov. Phys. JETP 7 (1958) 104.
- [123] R. Sartor and C. Mahaux, Phys. Rev. C25 (1982) 677.
- [124] B.D. Day, Rev. Mod. Phys. 39 (1967) 719.
- [125] B.D. Day, private communication.

- [126] K.A. Brueckner, C.A. Levinson and H.M. Mahmoud, Phys. Rev. 95 (1954) 217;
K.A. Brueckner and C.A. Levinson, Phys. Rev. 97 (1955) 1344;
K.A. Brueckner, Phys. Rev. 97 (1955) 1353.
- [127] K.A. Brueckner, Phys. Rev. 103 (1956) 172.
- [128] H.A. Bethe, Ann. Rev. Nucl. Sci. 21 (1971) 93.
- [129] H.S. Köhler, Phys. Reports 18 (1975) 217.
- [130] B.D. Day, Phys. Rev. C24 (1983) 1203.
- [131] Z.Y. Ma and T.T.S. Kuo, Phys. Lett. 127B (1983) 137.
- [132] C. Mahaux, Nucl. Phys. A328 (1979) 24.
- [133] P. Grangé and A. Lejeune, Nucl. Phys. A327 (1979) 335.
- [134] R.V. Reid Jr., Ann. Phys. (N.Y.) 50 (1968) 411.
- [135] J.P. Jeukenne, A. Lejeune and C. Mahaux, Phys. Rev. C10 (1974) 1391.
- [136] C. Mahaux, in: Microscopic Optical Potentials, ed. H.V. Von Geramb (Springer Verlag, Berlin, 1979) p. 1.
- [137] P.C. Martin and J. Schwinger, Phys. Rev. 115 (1959) 1342.
- [138] R.D. Mattuck and A. Theumann, Adv. Phys. 20 (1971) 721.
- [139] A.S. Reiner (Rinat), Phys. Rev. 133 (1964) B1105.
- [140] M. Weigel and G. Wegmann, Fortschr. Phys. 19 (1971) 451.
- [141] H. Gall and M.R. Weigel, Z. Phys. A276 (1976) 45.
- [142] C. Marville, Z. Phys. A279 (1976) 175.
- [143] C. Marville and P. Haensel, Nucl. Phys. A295 (1978) 445.
- [144] C. Marville and P. Haensel, Z. Phys. A284 (1978) 83 and references contained therein.
- [145] N. Vinh Mau, in: Theory of Nuclear Structure: Trieste Lectures 1969 (International Atomic Energy Agency, 1970) p. 931.
- [146] L.D. Landau, Sov. Phys. JETP 8 (1959) 70.
- [147] A.A. Abrikosov and I.M. Khalatnikov, Rept. Progr. Phys. 22 (1959) 329.
- [148] P. Nozières, *Le Problème à N Corps* (Dunod, Paris, 1963).
- [149] A.A. Abrikosov, L.P. Gorkov and I.E. Dzyaloshinsky, *Methods of Quantum Field Theory in Statistical Physics* (Prentice Hall, Inc., 1963).
- [150] L.D. Landau, Sov. Phys. JETP 3 (1957) 920.
- [151] J.M. Luttinger, Phys. Rev. 174 (1968) 263.
- [152] R. Balian and C. De Dominicis, Ann. Phys. (N.Y.) 62 (1971) 229.
- [153] J.M. Luttinger and Y.T. Liu, Ann. Phys. (N.Y.) 80 (1973) 1.
- [154] C. Bloch, in: *Studies in Statistical Mechanics*, vol. III, eds. J. de Boer and G.E. Uhlenbeck (North-Holland Publ. Comp., Amsterdam, 1965) p. 1.
- [155] C.J. Pethick and G.M. Carneiro, Phys. Rev. A7 (1973) 304.
- [156] G.M. Carneiro and C.J. Pethick, Phys. Rev. B11 (1975) 1106.
- [157] G. Baym and C.J. Pethick, in: *The Physics of Liquid and Solid Helium*, part II, eds. K.H. Bennemann and J.B. Ketterson (J. Wiley & Sons, New York, 1978) p. 1.
- [158] N. Fukuda and R.G. Newton, Phys. Rev. 103 (1956) 1558.
- [159] B.S. DeWitt, Phys. Rev. 103 (1956) 1565.
- [160] K. Gottfried, *Quantum Mechanics* (Benjamin, New York, 1966).
- [161] E. Riedel, Z. Phys. 210 (1968) 403.
- [162] J.W. Clark and E. Feenberg, Phys. Rev. 113 (1959) 388.
- [163] E. Feenberg, *Theory of Quantum Fluids* (Academic Press, New York, 1969).
- [164] S. Fantoni and S. Rosati, Lett. Nuovo Cim. 16 (1976) 531.
- [165] E. Krotscheck and J.W. Clark, Nucl. Phys. A328 (1979) 73.
- [166] E. Krotscheck and M.L. Ristig, Nucl. Phys. A242 (1975) 389.
- [167] V.R. Pandharipande and R.B. Wiringa, Nucl. Phys. A266 (1976) 269.
- [168] R. Jastrow, Phys. Rev. 98 (1955) 1479.
- [169] G. Ripka, Phys. Reports 56 (1979) 1.
- [170] D. Ceperley, G.V. Chester and M.H. Kalos, Phys. Rev. B16 (1977) 3081.
- [171] G. Ripka, Nucl. Phys. A314 (1979) 115.
- [172] L.E. Lagaris and V.R. Pandharipande, Nucl. Phys. A359 (1981) 349.
- [173] J. de Boer and A. Michels, Physica 5 (1938) 945.
- [174] R.A. Azziz, V.P.S. Nain, J.S. Carley, W.L. Taylor and G.T. McConville, J. Chem. Phys. 70 (1979) 4330.
- [175] J.G. Zabolitzky, Phys. Rev. A16 (1977) 1258.
- [176] J.W. Clark, E. Krotscheck and R.M. Panoff, J. Phys. (Paris) 41 (1980) C7-197.
- [177] J.C. Owen and G. Ripka, Phys. Rev. B25 (1982) 4914.
- [178] K.E. Schmidt and V.R. Pandharipande, Phys. Rev. B19 (1979) 2504; Riv. Nuovo Cim. 6, ser. 3, no. 4 (1983).
- [179] E. Krotscheck, J.W. Clark and A.D. Jackson, Phys. Rev. B28 (1983) 5088.
- [180] M.L. Ristig, W.J. Ter Louw and J.W. Clark, Phys. Rev. C3 (1971) 1504.

- [181] M.L. Ristig, W.J. Ter Louw and J.W. Clark, Phys. Rev. C5 (1972) 695.
- [182] J.W. Clark, P.M. Lam and W.J. Ter Louw, Nucl. Phys. A255 (1975) 1.
- [183] G.E. Brown, Rev. Mod. Phys. 43 (1971) 1.
- [184] A.D. Jackson, A. Lande and R.A. Smith, Phys. Reports 86 (1982) 55.
- [185] E. Krotscheck, private communication.
- [186] B. Friedman and V.R. Pandharipande, Phys. Lett. 100B (1981) 205.
- [187] T.R. Roberto and S.G. Sydoriak, Phys. Rev. 98 (1955) 1672.
- [188] A.C. Mota, R.P. Platzeck, R. Rapp and J.C. Wheatley, Phys. Rev. 177 (1969) 266.
- [189] T.A. Alvesalo, T. Haavasoja, P.C. Main, M.T. Manninen, J. Ray and L.M.M. Rehn, Phys. Rev. Lett. 43 (1979) 1509.
- [190] T.A. Alvesalo, T. Haavasoja, M.T. Manninen and A.T. Soinne, Phys. Rev. Lett. 44 (1980) 1076.
- [191] D.S. Greywall and P.A. Busch, Phys. Rev. Lett. 49 (1982) 146.
- [192] D.S. Greywall, Phys. Rev. B27 (1983) 2747; B29 (1984) 4933.
- [193] V.K. Mishra, G.E. Brown and C.J. Pethick, J. Low Temp. Phys. 52 (1983) 379.
- [194] K.A. Brueckner and J.L. Gammel, Phys. Rev. 109 (1958) 1040.
- [195] E. Østgaard, Phys. Rev. 176 (1968) 351.
- [196] H.B. Ghassib, R.H. Ibarra and J.M. Irvine, Ann. Phys. (N.Y.) 85 (1974) 378.
- [197] H.R. Glyde and S.I. Hernadi, Phys. Rev. B28 (1983) 141.
- [198] H.T. Tan and E. Feenberg, Phys. Rev. 176 (1968) 370.
- [199] E. Krotscheck, Phys. Rev. A26 (1982) 3536.
- [200] B.L. Friman and E. Krotscheck, Phys. Lett. 49 (1982) 1705.
- [201] E. Krotscheck, in: Quantum fluids and Solids – 1983 (Sanibel), eds. E.D. Adams and G.G. Ihss (AIP, New York, 1983) p. 132.
- [202] C.H. Aldrich III and D. Pines, J. Low Temp. Phys. 25 (1976) 673.
- [203] K. Sköld, C.A. Pelizzari, R. Kleb and G.E. Ostrowski, Phys. Rev. Lett. 37 (1976) 842.
- [204] B. Castaing and P. Nozières, J. Phys. (Paris) 40 (1979) 257.
- [205] M. de Llano, A. Plastino and J.G. Zabolitzky, Phys. Rev. C20 (1979) 2418.
- [206] M. de Llano, A. Plastino and J.G. Zabolitzky, Phys. Rev. C22 (1980) 314.
- [207] H.R. Glyde and S.I. Hernadi, in: Quantum Fluids and Solids – 1983 (Sanibel), eds. E.D. Adams and G.G. Ihss (AIP, New York, 1983) p. 171; Phys. Rev. B29 (1984) 3873.
- [208] K.S. Bedell and K.F. Quader, Phys. Lett. 96A (1983) 91.
- [209] C. Lhuillier and D. Levesque, Phys. Rev. B23 (1981) 2203.
- [210] T.L. Ainsworth, K.S. Bedell, G.E. Brown and K.F. Quader, J. Low Temp. Phys. 50 (1983) 319.
- [211] S. Babu and G.E. Brown, Ann. Phys. (N.Y.) 78 (1973) 1.
- [212] O. Sjöberg, Ann. Phys. (N.Y.) 78 (1973) 39.
- [213] W. Brenig and H.J. Mikeska, Phys. Lett. 24A (1967) 322.
- [214] D.J. Amit, J.W. Kane and H. Wagner, Phys. Rev. Lett. 19 (1967) 425; Phys. Rev. 175 (1968) 313; 326.
- [215] V.J. Emery, Phys. Rev. 170 (1968) 205.
- [216] W. Brenig, H.J. Mikeska and E. Riedel, Z. Phys. 206 (1967) 439.
- [217] W.F. Brinkman and S. Engelsberg, Phys. Rev. 169 (1968) 417.
- [218] S. Doniach and S. Engelsberg, Phys. Rev. Lett. 17 (1966) 750.
- [219] N.F. Berk and J.R. Schrieffer, Phys. Rev. Lett. 17 (1966) 433.
- [220] K. Levin and O.T. Valls, Phys. Reports 98 (1983) 1.
- [221] G.M. Carneiro and C.J. Pethick, Phys. Rev. B16 (1977) 1933.
- [222] C.H. Aldrich III and D. Pines, J. Low Temp. Phys. 32 (1978) 689.
- [223] M.T. Béal-Monod, J. Low Temp. Phys. 37 (1979) 123.
- [224] J.R. Schrieffer, Theory of Superconductivity (Benjamin, New York, 1964).
- [225] D. Pines and P. Nozières, The Theory of Quantum Liquids, vol. I (W.A. Benjamin, New York, 1966).
- [226] R.D. Mattuck, A Guide to Feynman Diagrams in the Many-Body Problem, 2nd ed. (McGraw-Hill, 1976).
- [227] G.D. Mahan, Many-Particle Physics (Plenum Press, 1981).
- [228] J.J. Quinn and R.A. Ferrell, Phys. Rev. 112 (1958) 812.
- [229] L. Hedin and S. Lundqvist, in: Solid State Physics, vol. 23, eds. F. Seitz, D. Turnbull and H. Ehrenreich (Academic Press, New York, 1969) p. 1.
- [230] T.M. Rice, Ann. Phys. (N.Y.) 31 (1965) 100.
- [231] S.M. Bose, A. Bardasis, A.J. Glick, D. Hone and P. Longe, Phys. Rev. 155 (1967) 379.
- [232] J.J. Quinn, Phys. Rev. 126 (1962) 1453.
- [233] L. Hedin, B.I. Lundqvist and S. Lundqvist, Solid State Comm. 5 (1967) 237.
- [234] B.I. Lundqvist, Physik Kondensierte Materie 6 (1967) 193.
- [235] B.I. Lundqvist, Physik Kondensierte Materie 6 (1967) 206.
- [236] B.I. Lundqvist, Physik Kondensierte Materie 7 (1968) 117.
- [237] G.D. Mahan and C.B. Duke, Phys. Rev. 149 (1966) 705.

- [238] P. Minnhagen, *J. Phys.* C7 (1974) 3013.
- [239] J.W.M. Du Mond, *Phys. Rev.* 33 (1929) 643.
- [240] P.M. Platzman and N. Tzoar, *Phys. Rev.* A139 (1965) 410.
- [241] P. Eisenberger, J. Lam, P.M. Platzman and P. Schmidt, *Phys. Rev. B* 6 (1972) 3671.
- [242] E. Daniel and S.H. Vosko, *Phys. Rev.* 120 (1960) 2041.
- [243] J. Lam, *Phys. Rev.* B3 (1971) 3243.
- [244] D.J.W. Geldart, A. Houghton and S.H. Vosko, *Can. J. Phys.* 42 (1964) 1938.
- [245] L.J. Lantto, *Phys. Rev.* B22 (1980) 1380.
- [246] D.M. Ceperley and B.J. Alder, *Phys. Rev. Lett.* 45 (1980) 566.
- [247] D.M. Ceperley, quoted in ref. [245];
see also D.M. Ceperley, G.V. Chester and M.H. Kalos, *Phys. Rev.* B16 (1977) 3081.
- [248] E. Krotscheck, *Ann. Phys. (N.Y.)* 155 (1984) 1.
- [249] R.A. Ferrell, *Rev. Mod. Phys.* 28 (1956) 308.
- [250] G.A. Rooke, *Phys. Lett.* 3 (1963) 234.
- [251] W.J. Pardee, G.D. Mahan, D.E. Eastman, R.A. Pollak, L. Ley, F.R. McFeely, S.P. Kowalezyk and D.A. Shirley, *Phys. Rev.* B11 (1975) 3614.
- [252] P. Longe, in: *Advances in X-Ray Spectroscopy*, eds. C. Bennelle and C. Mandé (Pergamon Press, 1982) p. 254.
- [253] B.I. Lundqvist, *Phys. Stat. Sol.* 32 (1969) 273.
- [254] L. Hedin, *Phys. Rev.* 139 (1965) A796.
- [255] J. Tracy, *J. Vac. Sci. Technol.* 11 (1974) 280.
- [256] N.W. Ashcroft and J.W. Wilkins, *Phys. Lett.* 14 (1965) 285.
- [257] G. Grimvall, *Physica Scripta* 14 (1976) 63.
- [258] A.B. Migdal, *Sov. Phys. JETP* 34 (1958) 996.
- [259] H. Hermann and A. Schmid, *Z. Phys.* 211 (1968) 313.
- [260] J.M. Rowell, W.L. McMillan and W.L. Feldmann, *Phys. Rev.* 180 (1969) 658.
- [261] S. Engelsberg and J.R. Schrieffer, *Phys. Rev.* 131 (1963) 993.
- [262] G. Grimvall, *The Electron-Phonon Interaction in Metals* (North-Holland Publ. Comp., Amsterdam, 1981).
- [263] G. Grimvall, *Phys. Kondens. Materie* 6 (1967) 15.
- [264] G. Grimvall, *J. Phys. Chem. Solids* 29 (1968) 1221.
- [265] M.J. Buckingham, *Nature* 168 (1951) 281.
- [266] G. Grimvall, *Phys. Kondens. Materie* 9 (1969) 283.
- [267] R.E. Prange and A. Sachs, *Phys. Rev.* 158 (1967) 672.
- [268] A.J. Leggett, *Ann. Phys. (N.Y.)* 46 (1968) 76.
- [269] J.S. Bell, in: *Lectures on the Many-Body Problem*, ed. E.R. Caianiello (Academic Press, New York, 1962) p. 91.
- [270] A.L. Fetter and K.M. Watson, in: *Advances in Theoretical Physics*, ed. K.A. Brueckner (Academic Press, New York, 1965) p. 115.
- [271] W. Brenig, *Z. Phys.* 202 (1967) 340.
- [272] D.H.E. Gross, *Nucl. Phys.* A129 (1969) 45.
- [273] A.B. Migdal, *Theory of Finite Fermi Systems and Applications to Atomic Nuclei* (Interscience, New York, 1967).
- [274] D.H.E. Gross and R. Lipperheide, *Nucl. Phys.* A150 (1970) 449.
- [275] J.W. Negele, *Rev. Mod. Phys.* 54 (1982) 913.
- [276] C.B. Dover and Nguyen Van Giai, *Nucl. Phys.* A190 (1972) 373.
- [277] G.F. Bertsch and S.F. Tsai, *Phys. Reports* 18C (1975) 126.
- [278] H.M. Sommermann, K.F. Ratcliff and T.T.S. Kuo, *Nucl. Phys.* A406 (1983) 109.
- [279] P.F. Bortignon, R.A. Broglia, D.R. Bes and R. Liotta, *Phys. Reports* 30C (1977) 305.
- [280] S.L. Reich, H.M. Sofia and D.R. Bes, *Nucl. Phys.* A233 (1974) 105.
- [281] D.R. Bes, R.A. Broglia, G.G. Dussel, R.J. Liotta and R.P.J. Perazzo, *Nucl. Phys.* A260 (1976) 77.
- [282] G.F. Bertsch, P.F. Bortignon and R.A. Broglia, *Rev. Mod. Phys.* 55 (1983) 287.
- [283] P.F. Bortignon and R.A. Broglia, *Nucl. Phys.* A371 (1981) 405.
- [284] A. Bohr and B.R. Mottelson, *Nuclear Structure*, vol. II (W.A. Benjamin, Inc., 1975).
- [285] H. Feshbach, *Ann. Phys. (N.Y.)* 19 (1962) 287.
- [286] R. Lipperheide, *Nucl. Phys.* 89 (1966) 97.
- [287] F. Villars, in: *Fundamentals of Nuclear Theory*, eds. A. de Shalit and C. Villi (IAEA, Vienna, 1967).
- [288] R. Lipperheide, *Z. Phys.* 202 (1967) 58.
- [289] H. Feshbach, A.K. Kerman and R.H. Lemmer, *Ann. Phys. (N.Y.)* 41 (1967) 230.
- [290] W.L. Wang and C.M. Shakin, *Phys. Lett.* 32B (1970) 421.
- [291] C. Mahaux and H. Ngô, *Nucl. Phys.* A410 (1983) 271.
- [292] B.L. Cohen, *Amer. J. Phys.* 33 (1965) 1011.
- [293] B.L. Cohen, *Concepts in Nuclear Physics* (McGraw-Hill, 1973) p. 324.
- [294] M.M. Giannini, G. Ricco and A. Zucchiatti, *Ann. Phys. (N.Y.)* 124 (1980) 208.
- [295] F.G. Perey, in: *Nuclear Spectroscopy and Reactions*, ed. J. Cerny (Academic Press, New York, 1974) part B, p. 137.
- [296] M. Bauer, E. Hernandez-Saldana, P.E. Hodgson and J. Quintanilla, *J. Phys. G8* (1982) 525.

- [297] C. Mahaux and H. Ngô, *Physica Scripta* 27 (1983) 74.
- [298] G.R. Satchler, *Isospin in Nuclear Physics*, ed. D.H. Wilkinson (North-Holland Publ. Comp., Amsterdam, 1969) p. 389.
- [299] J.M. Cavedon, B. Frois, D. Goutte, M. Huet, Ph. Leconte, C.N. Papanicolas, H.H. Phan, S.K. Platchkov, S. Williamson, W. Boeglin and I. Sick, *Phys. Rev. Lett.* 49 (1982) 978.
- [300] C. Mahaux, in: Proc. 1983 Conf. on Coincidence Reactions with Electromagnetic Probes (NIKHEF, Amsterdam).
- [301] Y. Yariv, T. Ledergerber and H.C. Pauli, *Z. Phys.* A278 (1976) 225.
- [302] M. Nagao and Y. Torizuka, *Phys. Lett.* 37B (1971) 383.
- [303] M.B. Lewis, *Nuclear Data Sheets* 5 (1971) 243.
- [304] H.P. Morsch, C. Sükösd, M. Rogge, P. Turek, H. Machner and C. Mayer-Böricker, *Phys. Rev.* C22 (1980) 489.
- [305] P. Ring and J. Speth, *Phys. Lett.* 44B (1973) 477.
- [306] C.H. Li and V. Klemt, *Nucl. Phys.* A364 (1981) 93.
- [307] P.F. Bortignon, unpublished, see also ref. [283].
- [308] H.R. Fiebig and J. Wambach, *Nucl. Phys.* A386 (1982) 381.
- [309] R.A. Broglia, C.H. Dasso and A. Winther, in: Proc. LXXVII Enrico Fermi Schools of Physics, eds. R.A. Broglia, C.H. Dasso and R.A. Ricci (North-Holland Publ. Comp., Amsterdam, 1981) p. 327.
- [310] G.F. Bertsch, J. Borysowicz, H. McManus and W.G. Love, *Nucl. Phys.* A284 (1977) 399.
- [311] P. Ring and E. Werner, *Nucl. Phys.* A211 (1973) 198.
- [312] I. Hamamoto and P. Siemens, *Nucl. Phys.* A269 (1976) 199.
- [313] R.P.J. Perazzo, S.L. Reich and H.M. Sofia, *Nucl. Phys.* A339 (1980) 23.
- [314] A.P. Platonov, *Sov. J. Nucl. Phys.* 34 (1981) 342.
- [315] P.F. Bortignon, R.A. Broglia, C.H. Dasso and C. Mahaux, unpublished.
- [316] T.T.S. Kuo and G.E. Brown, *Nucl. Phys.* 85 (1966) 40.
- [317] I. Hamamoto, *Phys. Reports* 10C (1974) 63.
- [318] G.F. Bertsch, P.F. Bortignon, R.A. Broglia and C.H. Dasso, *Phys. Lett.* 80B (1979) 161.
- [319] Nguyen Van Giai, in: Proc. on Highly Excited States in Nuclear Reactions, eds. H. Ikegami and M. Muraoka (Osaka Univ., 1980) p. 682.
- [320] J. Guillot, J. Van de Wiele, H. Langevin-Joliot, E. Gerlic, J.P. Didelez, G. Duhamel, G. Perrin, M. Buenerd and J. Chauvin, *Phys. Rev.* C21 (1980) 879.
- [321] H. Langevin-Joliot, E. Gerlic, J. Guillot, M. Sakai, J. Van de Wiele, A. Devaux, P. Force and G. Landaud, *Phys. Lett.* 114B (1982) 103.
- [322] S. Galès, in: Proc. 1980 Masurian Summer School (Mikolajki, Poland).
- [323] S. Galès, G.M. Crawley, D. Weber and B. Zwieglinski, *Phys. Rev.* C18 (1978) 2475.
- [324] O. Civitarese, R.P.J. Perazzo, S.L. Reich and M. Saraceno, *Z. Phys.* A311 (1983) 135.
- [325] G.E. Brown, *Comments Nucl. Part. Phys.* 3 (1969) 136.
- [326] P.F. Bortignon, R.A. Broglia, C.H. Dasso and C. Mahaux, *Phys. Lett.* 140B (1984) 163.
- [327] H.M. Sommermann and C. Mahaux, *Nucl. Phys.* A411 (1983) 27.
- [328] P.F. Bortignon, R.A. Broglia, C.H. Dasso and Fu De-ji, *Phys. Lett.* 108B (1982) 247.
- [329] Nguyen Van Giai and Pham Van Thieu, *Phys. Lett.* 126B (1983) 421.
- [330] G.E. Brown, J.S. Dehesa and J. Speth, *Nucl. Phys.* A330 (1979) 290.
- [331] G.E. Brown and S. Raman, *Comments Nucl. Part. Phys.* 9 (1980) 79.
- [332] J. Wambach and J. Speth, *Phys. Lett.* 94B (1980) 458.
- [333] J. Wambach and R. Fiebig, in: Spin Excitations in Nuclei, Telluride, Colorado, March 25–27, 1982.
- [334] H.M. Sommermann, T.T.S. Kuo and K.F. Ratcliff, *Phys. Lett.* 112B (1982) 108.
- [335] M. Barranco and J. Treiner, *Nucl. Phys.* A351 (1981) 269.
- [336] M. Prakash, J. Wambach and Z.Y. Ma, *Phys. Lett.* 128B (1983) 141.
- [337] D.S. Flynn, *Phys. Rev.* C27 (1983) 2381.
- [338] X. Campi and S. Stringari, *Nucl. Phys.* A337 (1980) 313.
- [339] X. Campi and S. Stringari, *Z. Phys.* A309 (1983) 239.
- [340] S.O. Bäckman, G.E. Brown, V. Klemt and J. Speth, *Nucl. Phys.* A345 (1980) 202.
- [341] H.A. Bethe, G.E. Brown, J. Applegate and J.M. Lattimer, *Nucl. Phys.* A324 (1979) 487.
- [342] B. Frois, J.B. Bellicard, J.M. Cavedon, M. Huet, P. Leconte, P. Ludeau, A. Nakada, Phan Zuan Hö and I. Sick, *Phys. Lett.* 38 (1977) 152.
- [343] B. Frois, J.M. Cavedon, D. Goutte, M. Huet, Ph. Leconte, C.N. Papanicolas, X.H. Phan, S.K. Platchkov and S.E. Williamson, *Nucl. Phys.* A396 (1983) 409c.
- [344] D. Gogny, in: Nuclear Physics with Electromagnetic Interactions, eds. H. Arenhövel and D. Drechsel (Springer Verlag, 1979) p. 88; corrected in: Proc. Los Alamos Conf. on Nuclear Structure with Intermediate Energy Probes, Jan. 14–16, 1980.
- [345] J. Decharge and L. Sips, *Nucl. Phys.* A407 (1983) 1; J. Decharge and D. Gogny, private communication.
- [346] Z.Y. Ma and J. Wambach, *Nucl. Phys.* A402 (1983) 275.
- [347] S.K. Platchkov, J.B. Bellicard, J.M. Cavedon, B. Frois, D. Goutte, M. Huet, Ph. Leconte, X.H. Phan, P.K.A. de Witt Huberts, L. Lapikas and I. Sick, *Phys. Rev.* C25 (1982) 2318.
- [348] T. Björnstadt, J. Blomqvist, G.T. Ewan, B. Jonson, K. Kawade, A. Kerek, S. Mattsson and K. Sistermich, *Z. Phys.* A306 (1982) 95.
- [349] B. Fogelberg and J. Blomqvist, *Phys. Lett.* 137B (1984) 20.
- [350] C. Mahaux and H. Ngô, *Nucl. Phys.* A431 (1984) 486.

Note added in proof

The following recent works are directly related to the topics covered in our Report. The momentum distribution in nuclear matter has been evaluated [351]. Some properties of the mass operator in a semi-infinite medium have been derived [352]. The momentum and the frequency dependence of the imaginary part of the mass operator in nuclear matter are discussed in ref. [353], in which these results are extended to nuclei by means of a semi-classical approximation. Some effects of the depletion of the Fermi sea have been considered [354].

[351] M.R. Flynn, J.W. Clark, O. Bohigas and S. Stringari, Nucl. Phys. A427 (1984) 253.

[352] H. Esbensen and G.F. Bertsch, Phys. Rev. Lett. 52 (1984) 2257.

[353] R.W. Hasse and P. Schuck, Nucl. Phys. A438 (1985) 157.

[354] V.R. Pandharipande, C.N. Papanicolas and J. Wambach, Phys. Rev. Lett. 53 (1984) 1133.